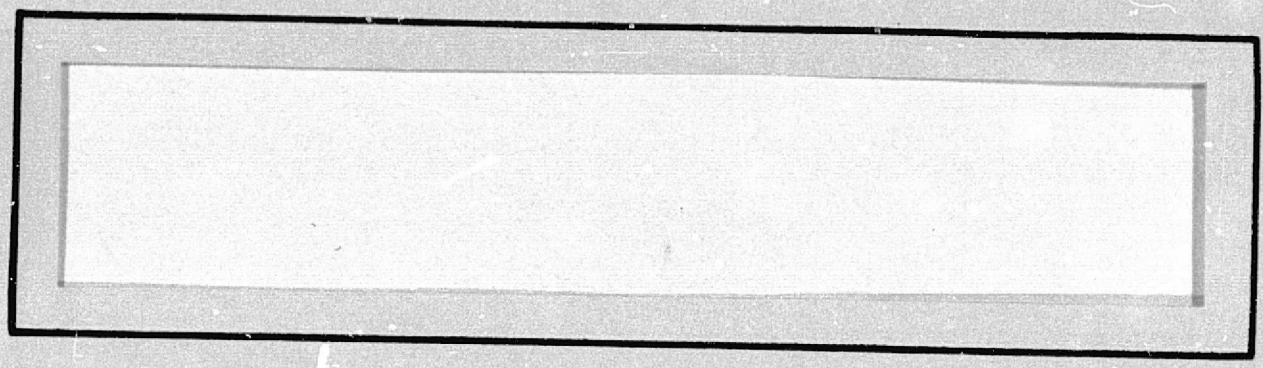

Axiomatix

(NASA-CR-160135) SHUTTLE ORBITER KU-BAND RADAR/COMMUNICATIONS SYSTEM DESIGN EVALUATION Final Report (Axiomatix, Los Angeles, Calif.) 410 p HC A18/MF A01 CSCL 17I G3/32

N79-19187

Unclas
16362

SHUTTLE ORBITER KU-BAND RADAR/COMMUNICATIONS SYSTEM DESIGN EVALUATION

FINAL REPORT

Contract No. NAS 9-15515A

Prepared for

NASA Lyndon B. Johnson Space Center
Houston, Texas 77058

Prepared by

Axiomatix
9841 Airport Boulevard, Suite 912
Los Angeles, California 90045

Axiomatix Report No. R7902-2
February 12, 1979

TABLE OF CONTENTS

Page

Appendix

LIST OF TABLES

LIST OF FIGURES

Page

1.0 EXECUTIVE SUMMARY

1.1 Purpose of Effort and Degree of Performance

The overall objective of the effort has been to critique the design and assess the performance of the Orbiter Ku-band radar/communication equipment. The work has three principal aspects:

(1) Review the architecture of the HAC Ku-band equipment and assess the design in regard to compatibility with NASA performance requirements over the specified environments.

(2) Review data from tests performed by HAC on the Ku-band breadboard hardware and the engineering model and identify any discrepancies between predicted (design analysis) performance and measured (test data analysis) performance and provide recommendations to NASA in those areas not providing satisfactory performance.

(3) Evalute the Ku-band hardware product design and identify any problem areas with recommendations for possible alternatives.

The degree of results produced with respect to objective (2) is directly proportional to design and test data available from the Ku-band radar/communication equipment contractor, HAC. Additional testing by HAC, Rockwell and NASA is needed before full evaluations are possible.

1.2 General Approach to the Activity

The general approach has been to work with cognizant NASA personnel and individuals at RI and HAC to ascertain directions taken. A vital part of this activity has involved Axiomatix attendance and participation in the regular monthly program reviews as well as all special meetings at HAC. These latter gatherings usually involved detailed discussions on design and specification issues that surfaced at the regular monthly reviews.

Each month, Axiomatix prepared a Monthly Technical Report which contained a brief summary of all relevant technical activity, including design reviews, technical conferences, design and analysis efforts and results, critical problem areas, and a forecast of effort for the next monthly reporting period. In addition, Axiomatix prepared a report for each of the tasks. This Final Report summarizes the results of these reports.

1.3 Contents of the Final Report

This report provides information on all activities with which Axiomatix was involved during CY78.

Section 2.0 is an expanded introduction which addresses the in-depth nature of the tasks and indicates continuity of the reported effort and results with previous work and related contracts.

Two major modes of operation exist in the Ku-band system, namely, the radar mode and the communication mode, as seen in Figure 1. The Ku-band radar system is designed to search for a target in a designated or undesignated mode, then track the detected target, which might be cooperative (active) or passive, providing accurate estimates of the target range, range rate, angle and angle rate to enable the Orbiter to rendezvous with this target. The radar mode is described along with a summary of its predicted performance in Section 3.0. The principal subunit that implements the radar function is the Electronics Assembly 2 (EA-2). The relationship of EA-2 to the remainder of the Ku-band system is shown in Figure 2. Section 4.0 presents a block diagram of EA-2 including the main command and status signals between EA-2 and the other Ku-band units.

The Ku-band communication mode is designed to enable the Orbiter to communicate with the Tracking and Data Relay Satellite (TDRS). This requires angle tracking of the TDRS as well as a forward link to receive from the TDRS and a return link to transmit to it. Various functions have to be performed in order to recover the data in the forward link. The main functions can be summarized in tracking the received carrier, despreading of any existing spread spectrum signal, then either passing the signal through an amplifier and line driving stage (buffering) or detecting the data by performing bit and frame synchronization before sending it to the Orbiter. Two modes can be selected in the return link whereby both channels are quadriphase modulated on a subcarrier, then either quadriphase modulated with a third channel on a carrier in one of the modes or added to the third channel to frequency modulate a carrier. Detailed descriptions of the forward and return links are discussed in Sections 5.0 and 6.0 respectively.

In order to operate the Ku-band system and select the required modes, various power supply voltages and command signals are generated.

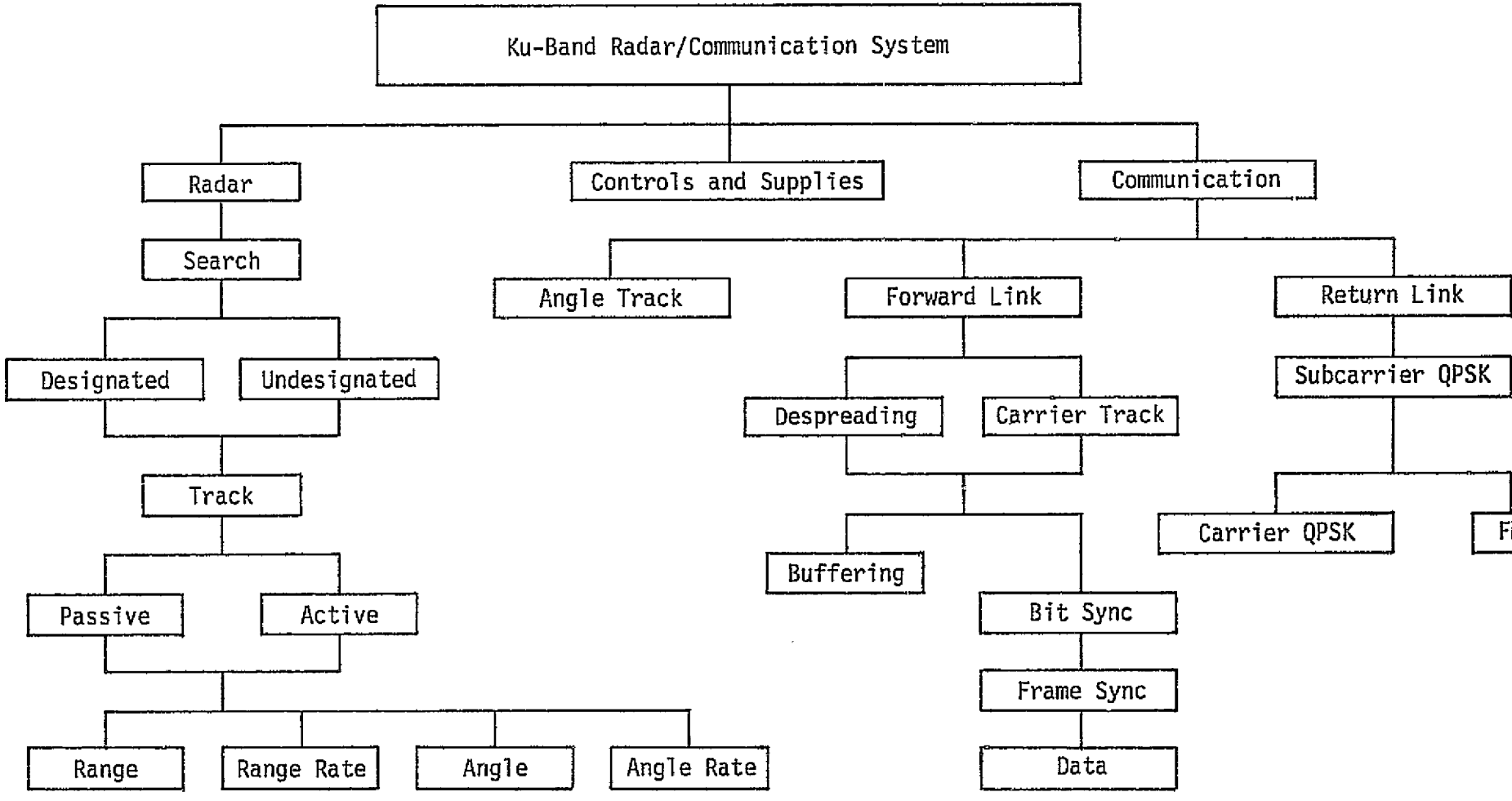

Figure 1. Ku-Band Radar/Communication System Modes Block Diagram

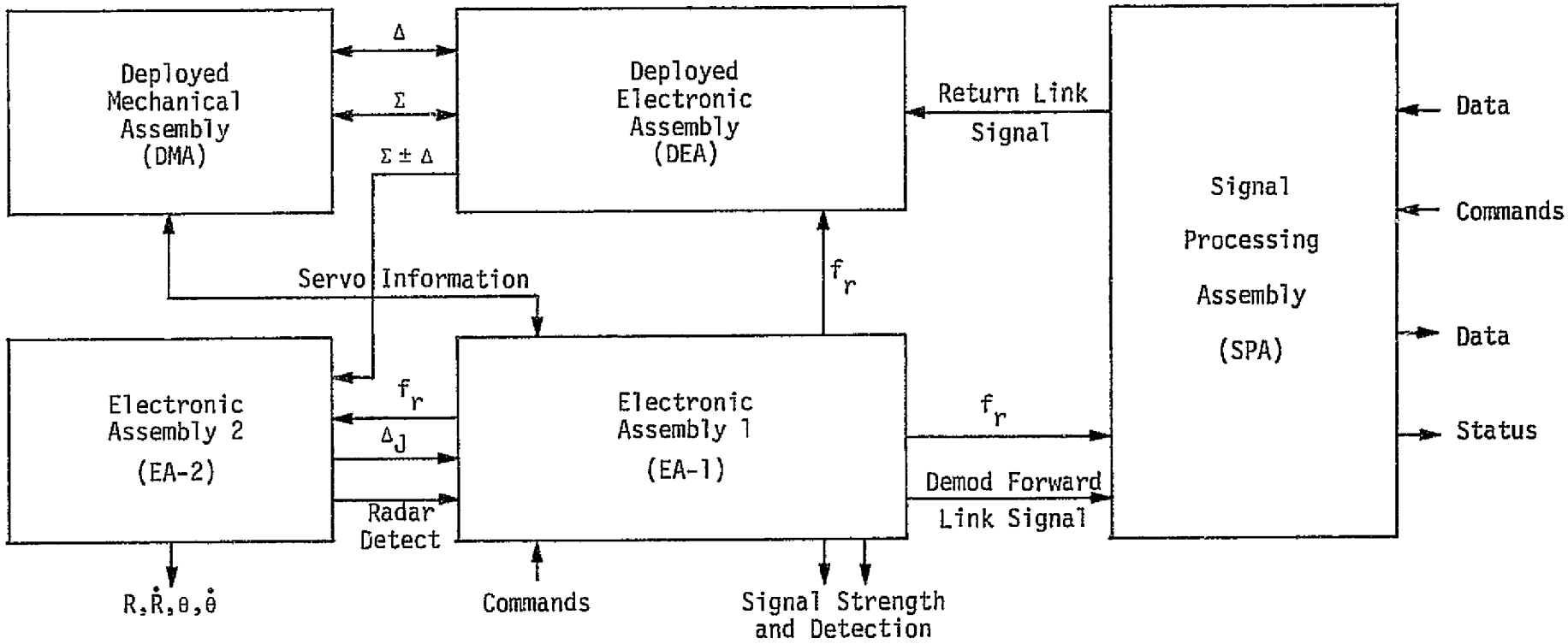

f_r = reference frequency

Figure 2. Ku-Band System Subunits

These are briefly discussed as part of Sections 7.0, 8.0 and 9.0, which are devoted to the description and discussion of the actual subunits being built by HAC and which are shown in Figure 2 with the major signals between the units as well as between the units and the Orbiter. As shown in this figure, these units are:

1. Deployed Mechanical Assembly (DMA)
2. Deployed Electronic Assembly (DEA)
3. Electronic Assembly 1 (EA-1)
4. Electronic Assembly 2 (EA-2) (presented in Section 4.0)
5. Signal Processing Assembly (SPA)

The product design considerations for the Ku-band integrated radar and communication equipment are presented in Section 10.0. The equipment, as designed by HAC, is comprised of four line replaceable units (LRU). One of these LRUs is a deployed assembly (DA) located within the payload bay. It is deployable upon opening the payload bay door. The other three LRUs are EA-1, EA-2, and SPA.

Finally, Section 11.0 presents a cumulative index of the major HAC documents describing the Ku-band radar/communication system. The intent of the index is to provide a cohesive reference to the various documents describing the system. Information relevant to any one of the subsystems may be contained in several documents; the index should help those who are familiar with the system to access needed information and those who are not to gain an understanding of the functions of the system.

1.4 Design Evaluation Summary

This section presents a summary of the major potential problems found in this study. The potential problems in each Ku-band system subunit are identified, and possible alternatives are suggested when this is applicable.

1.4.1 Deployed Mechanical Assembly

There are two major areas of concern pertaining to the Ku-band antenna system:

(1) Although the specifications require the antenna sidelobes to be at least 18 dB below the main lobe, the current test figures show

that the sidelobes can be as high as 14 dB below the main lobe. This might create a problem in sidelobe discrimination, especially in the radar mode.

(2) Since the primary TDRS search mode is now the GPC designate because of the inability of the TDRS angle tracking circuitry to withstand a large rate of signal power change, it was recommended that the wide beam horn polarization be changed to linear polarization. This would help the sidelobe rejection capabilities in the radar mode.

1.4.2 Deployed Electronic Assembly

The DEA test data show that the unit is meeting the specifications in all major tests performed. It should be noted, however, that the transmitter/receiver microwave subunit has not yet been adequately documented, which limits the ability of analyzing it in more detail for any potential problems.

1.4.3 Electronic Assembly 1

The receiver part of the EA-1 appears to be meeting the specifications. In particular, (1) with the loop SNR predicted for the Costas loop of the forward link, the data detection capability of the loop is degraded very little within the C/N_0 operational range; (2) the computations show that a maximum acquisition time of 70 msec is needed in no-noise for the Costas loop to pull-in; and (3) both analysis and experimental data show that the tau-dither loop is expected to meet the tracking specifications of 0.022 chips. A worst-case degradation is not expected to exceed 0.14 dB.

One aspect of the PSK data demodulator design which requires closer examination is that of using the 5.92 kHz "dither" signal in modes other than CW reception. For the CW mode, the dither signal is obviously required to provide the sideband which can be utilized by an AC coupled Costas loop for coherent carrier acquisition and tracking. However, for the case when biphase-L data is being received, the requirement for a dither waveform is questionable because the spectrum of the data does not contain DC, i.e., the carrier, anyway. Locking up to and tracking of such biphase-L data with an AC coupled loop should not present a problem.

Introduction of an asynchronous dither signal into the received IF signal biphase modulation and subsequent removal of this signal from the baseband data by a chopper may result in "glitches" which, in turn, may degrade the BER performance.

Consequently, it is recommended that the function of the dither signal during reception of the biphase-L data be reexamined and, if it is not found to be justifiable, use of dither in the data receive mode be discontinued.

As far as the scanning function of the EA-1, the data presented at the PDR points out that the 30% overlap specification is not met. The HAC digital simulation results show that the overlap is about 25% in the radar main scan and only 12% in the communication main scan. This problem deserves special attention due to its impact on the system performance in the search mode.

1.4.4 Electronic Assembly 2

The radar mode, which is the primary function of the EA-2, appears to be meeting specifications in most cases of interest. The major problems in the EA-2 can be summarized as:

(1) Detection margins are negative for the worst-case design and are marginal for the average-losses design at 10 nmi. An increase in the scanning time from 1 min to 2 min is recommended to assure adequate performance.

(2) Angle rate accuracies are marginal for some ranges and the angle rate transient response to accelerations normal to the line-of-sight does not settle fast enough within the specifications. Any attempt to widen the angle loop bandwidth to improve transient response will have an inverse effect on the steady-state tracking performance of the loop. It is believed that, unless major design changes are made, a compromise between steady-state performance and transient performance of the angle tracking loop has to be worked out.

(3) There is a discrepancy between the range rate logarithmic discriminant error calculated by Axiomatix and that calculated by Hughes. This might be due to the method that HAC is implementing to map between the doppler offset and the expected mean of the discriminant. Further HAC documentation is needed before this discrepancy can be resolved.

(4) It is believed that the angle and angle rate measurements for large targets will not be dependable at close ranges. These ranges are functions of the target size and shape. It is recommended that further analysis be performed before an optimum solution to this problem is reached.

It should be emphasized that a close agreement is found between analytical performance curves derived by Axiomatix and available data supplied by HAC.

1.4.5 Signal Processing Assembly

The detailed evaluation of the SPA data is discussed in Section 9.0. The two main functions of the SPA are the forward link bit synchronization and frame decommutation and the return link baseband three-channel signal modulation.

The first and main function of the SPA forward link signal processing is to establish bit synchronization before frame decommutation can take place. The bit synchronizer implemented by HAC includes an anbiguity resolver which distinguishes midbit transitions from between-bit transitions of the incoming 216 kbps biphase-L data. The detailed analysis of the bit synchronizer is presented in Appendix E.

A description of the ambiguity resolver and numerical results of the performance analysis are presented in Section 9.3, with the complete performance analysis presented in Appendices F and G. However, no test data is available yet for comparison.

Several observations can be made concerning the bit synchronizer:

(1) The calculations show that the degradation in signal-to-noise ratio due to imperfect bit timing does not exceed 0.75 dB for $R_d \geq 2$ dB ($R_d = E_b/N_0$), which is well below the specifications of 1.0 dB and in agreement with most of the available data. Some test data, however, show that, for high temperatures (85°C), the loss can be between 1-1.5 dB.

(2) For given values of in-phase decision threshold and transition density, tracking jitter decreases with an increase in signal-to-noise ratio, R_d. This is intuitively correct because better performance should be expected at higher signal-to-noise ratios. It is pointed out, however, that the test data supplied by HAC show a reverse trend at high R_d, where

the loss which is proportional to the tracking jitter is shown to increase with the increase of signal-to-noise ratio.

(3) The test data show that, in order for the bit synchronizer loop to acquire and maintain lock over the full temperature range of -20°C to 85°C, signal-to-noise ratios of 2 dB and 5.9 dB might be needed for random data and alternating data, respectively. At the same time, the available test data show that acquisition is taking place down to 0 dB with a wide frequency pull-in margin that exceeds by far the specifications of ±22 Hz. Though a possible small margin of signal-to-noise ratio above 0 dB might be warranted to allow for component aging, the value of 5.9 dB is believed to be high for such tolerances.

1.4.6 System Software

In order to assure proper functioning of the Ku-band system hardware, the system software has to be completed. The lack of documentation of the software design, the required memory size, and the cycle time make it impossible to evaluate this important part of the Ku-band system. This constitutes a major problem in the evaluation of the system and cannot be resolved before adequate documentation is made available.

1.5 Continuing Effort

Axiomatix will continue to support the overall Ku-band system developments and, in particular, all activities associated with development of the Ku-band avionic hardware. During CY79, this effort will include:

(1) Development test performance evaluation
(2) Qualification test performance evaluation
(3) Radar range test evaluation
(4) Ku-band high-gain antenna/widebeam horn design evaluation.

In addition, Axiomatix will be working with all concerned agencies (principally, NASA, RI and HAC) to solve design and operational problems in a timely, efficient, low-cost manner.

2.0 INTRODUCTION

This Final Report summarizes the design evaluation and performance assessment of the Orbiter Ku-band radar/communication equipment being developed by Hughes Aircraft Company (HAC) under subcontract from Rockwell International (RI).

2.1 Statement of Work

2.1.1 Objectives

The overall objective of the effort has been to critique the design and assess the performance of the Orbiter Ku-band radar/communication equipment. The work has three principal aspects:

(1) Review the architecture of the HAC Ku-band equipment and assess the design in regard to compatibility with NASA performance requirements over the specified environments.

(2) Review data from tests performed by HAC on the Ku-band breadboard hardware and the engineering model, identify any discrepancies between predicted (design analysis) performance and measured (test data analysis) performance, and provide recommendations to NASA in those areas not providing satisfactory performance.

(3) Evaluate the Ku-band hardware product design and identify any problem areas with recommendations for possible alternatives.

2.1.2 Stipulated Tasks

The contract statement of work calls out the following tasks:

"Task #1. Ku-Band Equipment Design Evaluation

> The contractor shall perform evaluation analysis of the Ku-band design as depicted in the Ku-band contractor schematic diagrams. The contractor shall assess the design in regard to compatibility with NASA performance requirements over the specified environments. In addition, the contractor shall identify areas of the design that may involve high technical risk or marginal performance and recommend alternate designs. The results of the Ku-band Equipment Design Evaluation shall be detailed in the Design Evaluation Report.

Task #2. Ku-Band Breadboard Test Analysis

The contractor shall provide analysis of Ku-band breadboard hardware test data as presented by the Ku-band contractor. The contractor shall verify that the test data supports the NASA requirements. The contractor shall identify any discrepancies between predicted (design analysis) performance and measured (test data analysis) performance of the breadboard hardware, and provide recommendations to the NASA in those areas not providing satisfactory performance. The results of the Ku-band Breadboard Test Analysis shall be reported in the Test Data Analysis Report.

Task #3. Ku-Band Product Design Analysis

The contractor shall provide evaluation of the Ku-band hardware product design. This shall include, but not be limited to, review of the box layouts, enclosure design, partitioning, board layouts, and test signals. The contractor shall identify any problem areas identified and recommend possible alternates. The results of the Ku-band Product Design Analysis shall be reported in the Product Design Evaluation Report.

Task #4. Ku-band Engineering Model Data Analysis

The contractor shall provide evaluation analysis of the Ku-band engineering model test data presented by the Ku-band contractor. The contractor shall verify that the test data supports the NASA requirements. The contractor shall identify discrepancies between the expected performance, based on design analysis and breadboard test data, and the performance measured during engineering model tests. The results of the Ku-band Engineering Model Data Analysis shall be reported in the Prototype Data Analysis Report."

2.1.3 General Approach

The general approach has been to work with cognizant NASA personnel and individuals at RI and HAC to ascertain directions taken. A vital part of this activity has involved Axiomatix attendance and participation in the regular monthly program reviews, as well as all special meetings, at HAC. These latter gatherings usually involved detailed discussions on design and specification issues that surfaced at the regular monthly reviews.

Each month, Axiomatix prepared a Monthly Technical Report which contained a brief summary of all relevant technical activity, including design reviews, technical conferences, design and analysis efforts and

results, critical problem areas, and a forecast of effort for the next monthly reporting period. In addition, Axiomatix prepared a report for each of the first three tasks. The report covering the fourth task is included in this Final Report along with summaries of the work performed under the first three tasks.

2.1.4 Continuity with Previous Work and Relationship to Parallel Work

The subject contract effort was new for CY78; however, previous activity was carried out under contract NAS 9-14614, "Study to Investigate and Evaluate Means of Optimizing the Radar/Communications Functions." The work performed under the subject contract was strongly interrelated to parallel efforts; contract NAS 9-15240C, "Shuttle Ku-Band and S-Band Communications Implementation Study," forms the system framework which ties the Ku-band communication equipment to the overall Tracking and Data Relay Satellite System (TDRSS) network and addresses the system interfaces.

2.2 Scope of the Final Report

The integrated Ku-band communication/radar system is described here from two separate points of view. The first is concerned with the signal flow during various operating functions of the system, while the second is devoted to describing the functions and operation of the various subunits currently being implemented by HAC.

Two major modes of operation exist in the Ku-band system, namely, the radar mode and the communication mode, as seen in Figure 3. The Ku-band radar system is designed to search for a target in a designated or undesignated mode, then track the detected target, which might be cooperative (active) or passive, providing accurate estimates of the target range, range rate, angle and angle rate to enable the Orbiter to rendezvous with this target. The radar mode is described along with a summary of its predicted performance in Section 3.0. The principal subunit that implements the radar function is the Electronics Assembly 2 (EA-2). The relationship of EA-2 to the remainder of the Ku-band system is shown in Figure 4.

Section 4.0 presents a block diagram of EA-2 including the main command and status signals between EA-2 and the other Ku-band units.

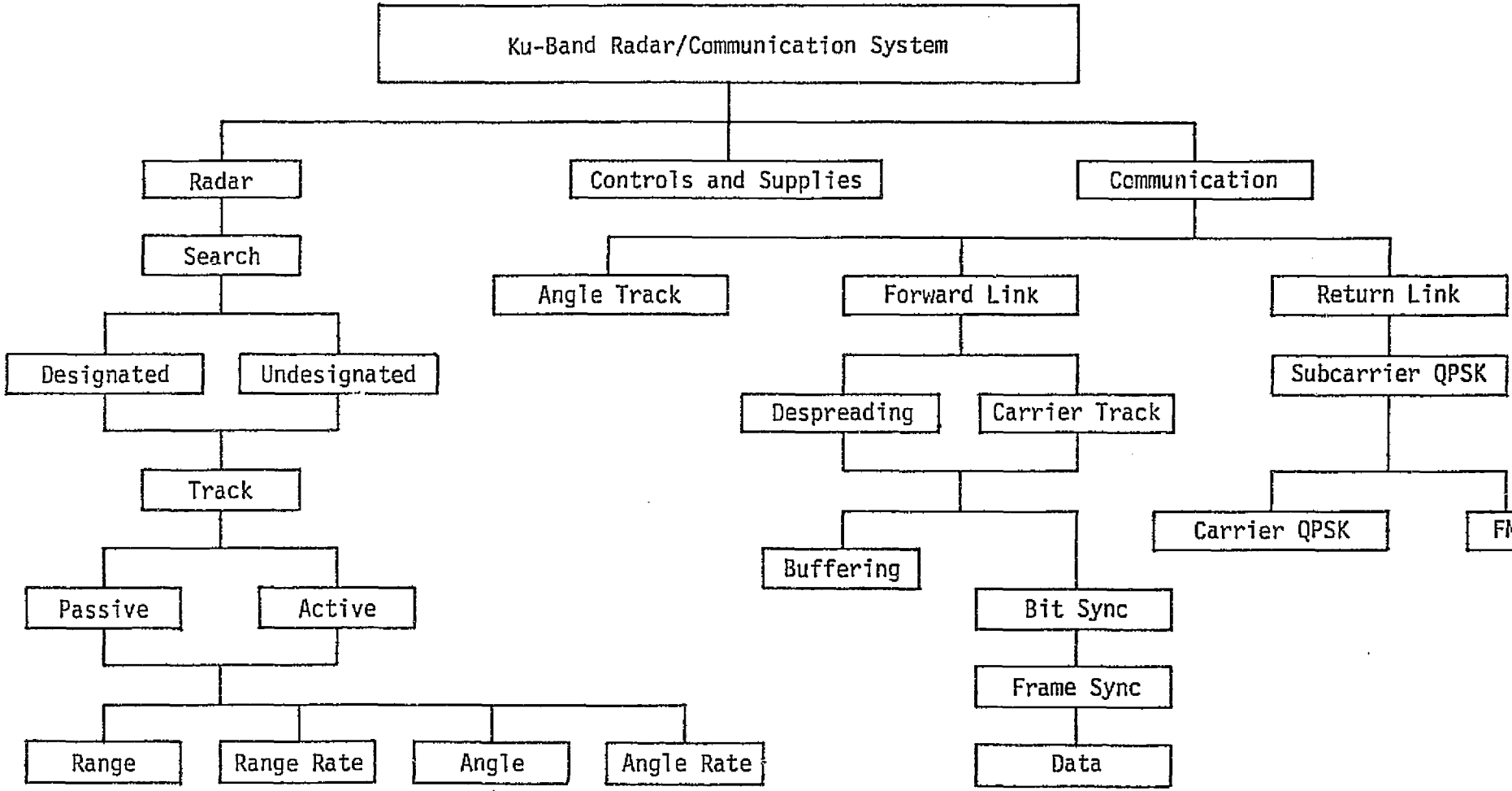

Figure 3. Ku-Band Radar/Communication System Modes Block Diagram

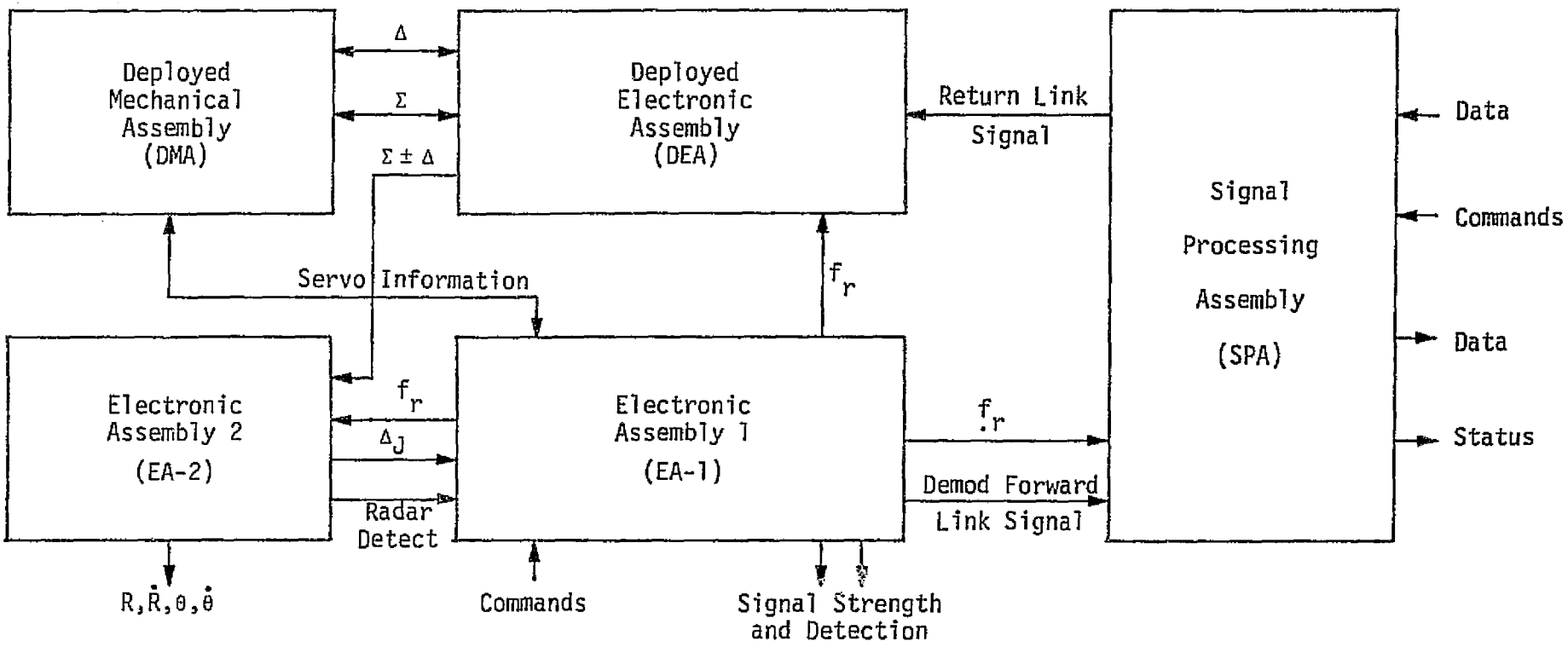

f_r = reference frequency

Figure 4. Ku-Band System Subunits

Section 4.0 also identifies the major existing problems in the radar mode of operation.

The Ku-band communication mode is designed to enable the Orbiter to communicate with the Tracking and Data Relay Satellite (TDRS). This requires angle tracking of the TDRS as well as a forward link to receive from the TDRS and a return link to transmit to it. Various functions have to be performed in order to recover the data in the forward link. The main functions can be summarized in tracking the received carrier, despreading of any existing spread spectrum signal, then either passing the signal through an amplifier and line driving stage (buffering) or detecting the data by performing bit and frame synchronization before sending it to the Orbiter. Two modes can be selected in the return link whereby both channels are quadriphase modulated on a subcarrier, then either quadriphase modulated with a third channel on a carrier in one of the modes or added to the third channel to frequency modulate a carrier. Detailed descriptions of the forward and return links are discussed in Sections 5.0 and 6.0, respectively.

In order to operate the Ku-band system and select the required modes, various power supply voltage and command signals are generated. These are briefly discussed as part of Sections 7.0, 8.0 and 9.0, which are devoted to the description and discussion of the actual subunits being built by HAC and which are shown in Figure 4 with the major signals between the units as well as between the units and the Orbiter. As shown in the figure, these units are:

1. Deployed Mechanical Assembly (DMA)
2. Deployed Electronic Assembly (DEA)
3. Electronic Assembly 1 (EA-1)
4. Electronic Assembly 2 (EA-2) (presented in Section 4.0)
5. Signal Processing Assembly (SPA)

Also in Sections 7.0, 8.0 and 9.0, the major existing problems in these subunits are identified as a result of evaluating the available test data and comparing it to the predicted performance.

The product design considerations for the Ku-band integrated radar and communication equipment are presented in Section 10.0. The equipment, as designed by HAC, is comprised of four line replaceable units (LRU).

One of these LRUs is a deployed assembly (DA) located within the payload bay. It is deployable upon opening the payload bay door. The other three three LRUs are EA-1, EA-2, and SPA.

These LRUs are located inside the Orbiter cabin in the avionics bay. The DA consists of the two major subassemblies, the DEA and the DMA. The detailed description of the product design of the Ku-band system is discussed in Appendix H. It should be pointed out that, since the only available literature concerning the product design is that from HAC, most of the material describing the product design has been extracted from the various contractor (HAC) reports.

Finally, Section 11.0 presents a cumulative index of the major HAC documents describing the Ku-band radar/communication system. The intent of the index is to provide a cohesive reference to the various documents describing the system. Information relevant to any one of the subsystems may be contained in several documents; the index should help those who are familiar with the system to access needed information and those who are not to gain an understanding of the functions of the system. It is recommended that the index be expanded and updated as additional documents become available from HAC, as well as from other sources.

2.3 Evaluation and Recommendation Summary

This section presents a summary of the major potential problems found in this study. The potential problems in each Ku-band system subunit are identified, and possible alternatives are suggested when this is applicable.

2.3.1 Deployed Mechanical Assembly

There are several problems pertaining to the Ku-band antenna system:

(1) Although the specifications require the antenna sidelobes to be at least 18 dB below the main lobe, the current test figures show that the sidelobes can be as high as 14 dB below the main lobe. This might create a problem in sidelobe discrimination, especially in the radar mode.

(2) Since the primary TDRS search mode is now the GPC designate because of the inability of the TDRS angle tracking circuitry to withstand

a large rate of signal power change, it was recommended that the widebeam horn polarization be changed to linear polarization. This would help the sidelobe rejection capabilities in the radar mode. A study should be performed to investigate the need for circular polarization of the widebeam horn in the communication mode.

(3) As discussed in Section 7.1.1, the monopulse feed presents a potential tracking problem in one plane. An explanation of the possible null degradation phenomenon is first outlined in Section 7.1.1, and a subsequent corrective measure employing curved dipoles is developed. Finally, some design considerations are included to minimize blockage effects.

2.3.2 Deployed Electronic Assembly

The DEA test data as summarized below show that the unit is meeting the specifications in all the major tests performed. It should be noted, however, that the transmitter/receiver microwave subunit has not yet been adequately documented, which limits the ability of analyzing it in more detail for any potential problems.

(1) The low noise RF amplifier (LNA), which is a three-stage gallium-arsenide (GaAs) field effect transistor (FET) unit, is meeting the gain specifications of 20 dB over a temperature range of -18°C to 60°C. Because the maximum input signal in the communications mode is -92.6 dBm, resulting in an output of about -70 dBm (input signal plus amplifier gain), it is evident that this amplifier does not present a dynamic range limitation to the communications signal. Furthermore, the 13,725 MHz spur (a sixth harmonic of the 2287.5 MHz S-band signal) is estimated at about -60 dBm at the input to this amplifier. This results in a -38 dBm output, which is still significantly below the 1 dB compression point. Thus, sufficient dynamic range is provided for handling the spur as well as the signal.

The bandpass filter which follows the LNA has a bandwidth which is sufficiently wide to accommodate the radar signal band, yet its roll-off is such as to provide more than the specified 20 dB of rejection of the image frequency band.

(2) The S-band spur problem has been resolved by implementing the Gunn-VCO circuitry at the exciter/receiver subunits.

(3) All the tested TWT amplifiers have provided 55W to 60W over the radar frequency band and 60W over the communication band. Several tests have also been conducted on various aspects of the TWT operation and they all seem to be meeting the specifications.

(4) The gain imbalance requirement of less than 3 dB between the sum channel and the difference channel has been tested. A maximum of less than 1 dB has been quoted.

(5) The input and output saturation tests show that the DEA is meeting the specifications in this respect. The ambient temperature for these tests has not been specified, however.

2.3.3 Electronic Assembly 1

The receiver part of the EA-1 appears to be meeting the specifications. In particular:

(1) With the loop SNR predicted for the Costas loop of the forward link, the data detection capability of the loop is degraded very little within the C/N_0 operational range.

(2) The computations show that a maximum acquisition time of 70 msec is needed in no-noise for the Costas loop to pull-in. The available data over the C/N_0 range of 60-80 dB and a temperature range of -20°C to 80°C also show that the acquisition time varies between 60-195 msec. All of the above indicate that the 200 msec requirement on acquisition time will present no problem with the present forward link power budget. In addition, the experimental data indicate that the acquisition probability of 0.99 can be achieved by the Costas loop at a C/N_0 of 61 dB-Hz over the temperature range of -20°C to 65°C and a frequency offset of ±150 kHz. Consequently, the possible widening of the Costas loop bandwidth during acquisition does not seem to present a potential problem.

(3) Both the analysis and the experimental data show that the tau-dither loop is expected to meet the tracking specifications of 0.022 chip. The tests were performed over the full expected temperature range. The degradation in this loop can also be considered negligible. A worst-case degradation is not expected to exceed 0.14 dB.

One aspect of the PSK data demodulator design which requires closer examination is that of using the 5.92 kHz "dither" signal in

modes other than CW reception. For the CW mode, the dither signal is obviously required to provide the sideband which can be utilized by an AC coupled Costas loop for coherent carrier acquisition and tracking. However, for the case when biphase-L data is being received, the requirement for a dither waveform is questionable because the spectrum of the data does not contain DC, i.e., the carrier, anyway. Locking up to and tracking of such biphase-L data with an AC coupled loop should not present a problem.

Introduction of an asynchronous dither signal into the received IF signal by biphase modulation and subsequent removal of this signal from the baseband data by a chopper may result in "glitches" which, in turn, may degrade the BER performance.

Consequently, it is recommended that the function of the dither signal during reception of the biphase-L data be reexamined and, if it is not found to be justifiable, use of dither in the data receive mode be discontinued.

As far as the scanning function of the EA-1, the data presented at the PDR points out that the 30% overlap specification is not met. The HAC digital simulation results show that the overlap is about 25% in the radar main scan and only 12% in the communication main scan. This problem deserves special attention due to its impact on system performance in the search mode.

2.3.4 Electronic Assembly 2

The radar mode, which is the primary function of the EA-2, appears to be meeting specifications in most cases of interest. The major problems in the EA-2 can be summarized as:

(1) Detection margins are negative for the worst-case design and are marginal for the average-losses design at 10 nmi. An increase in the scanning time from 1 min to 2 min is recommended to assure adequate performance.

(2) Angle rate accuracies are marginal for some ranges and the angle rate transient response to accelerations normal to the line-of-sight does not settle fast enough within the specifications. Any attempt to widen the angle loop bandwidth to improve the transient response will have an inverse effect on the steady-state tracking performance of the loop.

It is believed that, unless major design changes are made, a compromise between steady-state performance and transient performance of the angle tracking loop has to be worked out.

(3) There is a discrepancy between the range rate logarithmic discriminant error calculated by Axiomatix and that calculated by HAC. This might be due to the method that HAC is implementing to map between the doppler offset and the expected mean of the discriminant. Further HAC documentation is needed before this discrepancy can be resolved.

(4) It is believed that the angle and angle rate measurements for large targets will not be dependable at close ranges. These ranges are functions of the target size and shape. It is recommended that further analysis be performed before an optimum solution to this problem is reached.

It should be emphasized that a close agreement is found between the analytical performance curves derived by Axiomatix and the available data supplied by HAC.

2.3.5 Signal Processing Assembly

The detailed evaluation of the SPA data is discussed in Section 9.0. The two main functions of the SPA are the forward link bit synchronization and frame decommutation and the return link baseband three-channel signal modulation. A summary of the results is presented in this section.

2.3.5.1 Forward Signal Processing

The first and main function of SPA forward link signal processing is to establish bit synchronization before frame decommutation can take place. The bit synchronizer implemented by HAC includes an ambiguity resolver which distinguishes midbit transitions from between-bit transitions of the incoming 216 kbps biphase-L data. The detailed analysis of the bit synchronizer is presented in Appendix E.

A description of the ambiguity resolver and numerical results of the performance analysis are presented in Section 9.3, with the complete performance analysis presented in Appendices F and G. However, no test data is available yet for comparison.

Several observations can be made concerning the bit synchronizer.

1. For a given value of bit energy-to-noise spectral density ratio (R_d) and a given transition density (p_t), the in-phase decision threshold, which is used to decide the polarity of a given bit or the inability to decide that polarity, has an optimal value (η_{opt}). Since no threshold value has been quoted by HAC, a value of 0.3 was selected to obtain quantitative results. A typical value of bit time and loop bandwidth product ($B_L T$) was selected to be 10^{-2}. The calculations show that the degradation in signal-to-noise ratio due to imperfect bit timing does not exceed 0.75 dB for $R_d \geq 2$ dB, which is well below the specifications of 1.0 dB and in agreement with most of the available data. Some test data, however, show that, for high temperatures (85°C), the loss can be between 1.0 and 1.5 dB. Though such losses are not believed to present any problem to overall system performance, a closer look at the data and the breadboard setting is needed to verify the validity of the test data.

It is also worth noting that the selection of the value of $B_L T$ is a compromise between tracking accuracy and ability of the loop to track long streams of ones or zeros.

2. For given values of in-phase decision threshold and transition density, the tracking jitter decreases with an increase in signal-to-noise ratio, R_d. This is intuitively correct because better performance should be expected at higher signal-to-noise ratios. It is pointed out, however, that the test data supplied by HAC show a reverse trend at high R_d, where the loss which is proportional to the tracking jitter is shown to increase with an increase in signal-to-noise ratio. It is believed that the test setup is the cause of this problem and a closer look at the setup is believed essential to obtain better test data.

3. The mean-squared tracking jitter is considerably more sensitive to values of decision threshold greater than η_{opt} than it is to $\eta < \eta_{opt}$. This sensitivity itself diminishes with decreasing p_t and increasing R_d. At fixed R_d, one cloncludes that the mean-squared tracking jitter decreases with decreasing p_t. (NOTE: Decreasing NRZ transition density implies increasing between-bit transitions in the Manchester biphase-L coded waveform. In fact, $p_t = 0$ results in a square-wave data waveform at twice the bit rate.)

4. As discussed in detail in Appendix E, windowing the in-phase I&Ds to half a bit (as in the HAC design), results in a 3 dB SNR penalty

for making decisions on the midbit and between-bit transitions relative to performing full-bit in-phase I&Ds.

5. The test data show that, in order for the bit synchronizer loop to acquire and maintain lock over the full temperature range of -20°C to 85°C, signal-to-noise ratios ($R_d = E_b/N_0$) of 2 dB and 5.9 dB might be needed for random data and alternating data, respectively. The available test data at the same time show that acquisition is taking place down to 0 dB with a wide frequency pull-in margin that exceeds by far the specifications of ±22 Hz. Though a possible small margin of signal-to-noise ratio above 0 dB might be warranted to allow for component aging, the value of 5.9 dB is believed to be high for such tolerances.

2.3.5.2 Return Link Signal Processing

Two areas of concern were discussed in analyzing the test data:

1. Variations in power distribution between the three channels were analyzed using the latest link budgets. It was found that the expected variations in the power ratio distribution of the three channels in the return link do not create any problem in meeting the specified probabilities of error at the TDRSS because of the high return link signal-to-noise ratios.

2. The expected performance of the TDRS bit synchronizer for a given amount of asymmetry in the high data rate channel was presented. It is believed that the proposed asymmetry compensator should provide adequate means for reducing symmetry in the forward link to within the specified 10%. This will limit loss due to asymmetry to a maximum of a few tenths of a dB. Test results are not yet available. Such results are needed before passing a final judgment on the performance of the compensator and the resulting degradation due to asymmetry.

2.3.6 System Software

In order to assure the proper functioning of the Ku-band system hardware, the system software has to be completed. The lack of documentation of the software design, the required memory size, and the cycle time make it impossible to evaluate this important part of the Ku-band system. This constitutes a major problem in the evaluation of the system and cannot be resolved before adequate documentation is made available.

3.0 DESCRIPTION AND PERFORMANCE OF THE KU-BAND RADAR

The objective of the Ku-band radar system on the Shuttle Orbiter is to detect the presence of a target and then obtain continuous accurate estimates of the various target parameters, namely, its range, range rate (velocity), azimuth, elevation angle, and angle rates. The target is usually detected when the radar is in the search mode, while the accurate estimates are obtained in the track mode. It is the objective of this section to describe the overall radar block diagram, explain its operation in both the search and track modes, and summarize its expected performance.

The radar employs coherent processing over each RF frequency transmitted, and noncoherent postdetection integration (PDI). Following the intermediate amplifiers, in-phase and quadrature-phase baseband signals are sampled and digitized (A/D converted), providing target amplitude and phase information. For longer range search and acquisition ($R > 0.42$ nmi), 16 doppler filters are formed, covering the doppler interval defined by the repetition rate. This is an ambiguous doppler interval; this ambiguity is removed via differentiation of the range estimates.

The magnitudes of the doppler filters outputs are determined and summed over the number of RF frequencies (noncoherent postdetection integration). This result is then compared to a threshold. The threshold is set from noise measurements so as to maintain a constant false alarm probability (CFAP). This can be implemented by any of several methods.

In the search mode, only the sum channel is processed. When the threshold is exceeded and target detection is declared, the auxiliary antenna signal is processed, and its magnitude is compared to that of the main antenna to eliminate sidelobe detected targets. The auxiliary antenna has a peak gain which is approximately 20 dB less than that of the main antenna. Also, the sidelobes of the main antenna are approximately 20 dB down from the main lobe. This provides roughly a 20 dB main lobe/guard antenna ratio to detect and eliminate sidelobe targets. It should be emphasized that a lobe/guard of only 14 dB has been measured during preliminary tests.

In the modes for which angle tracking is required, namely, GPC acquisition and autotrack, the sum plus angle error channels are processed. The azimuth and elevation error signals are time-multiplexed, thereby eliminating the need for a second and third matched processing channel.

A general block diagram is now presented and explained in more detail; the functions of the individual blocks are then described.

3.1 Ku-Band Radar Block Diagram

The Shuttle Ku-band radar block diagram is shown in Figure 5. The antenna assembly consists of a main antenna and an auxiliary antenna, followed by the deployed mechanical assembly (DMA) and the deployed electronics assembly (DEA), where various switching and filtering operations take place, as explained in Section 3.2. The antenna assembly is followed by several IF mixing stages to bring the carrier frequency down to a stable IF of $f_0 = 78.143$ MHz. The output of the I-Q stage that follows is a pair of baseband signals which are in phase and in quadrature with the input signal. The operation of the previous two stages is discussed in Section 3.3. The available information is converted by an A/D converter to digital data which samples both channels at a rate of $f_s = 480$ ksps, which is slightly larger than the Nyquist rate of the baseband signals at the output of the I-Q stage. (The LPF bandwidth in both the I and Q channels is equal to 237 kHz.) The output of the A/D converter is a set of complex numbers which undergo various stages of digital processing before estimates of the target parameters (range, velocity, azimuth angle, elevation angle) are obtained. The first processing stage is a presumming stage, followed by a set of range gates and doppler filters consecutively. The arrangement of the gates is varied for the two modes of operation. Two cases are distinguished in the search mode. When a range designation is not available, four range gates per pulse are used, whereas two overlapping range gates are used when range designation is provided. The width of each of the two range gates is $3\tau/2$, where τ is the pulse width. In the track mode, there are only two nonoverlapping gates, an early gate and a late gate, each of width τ seconds.

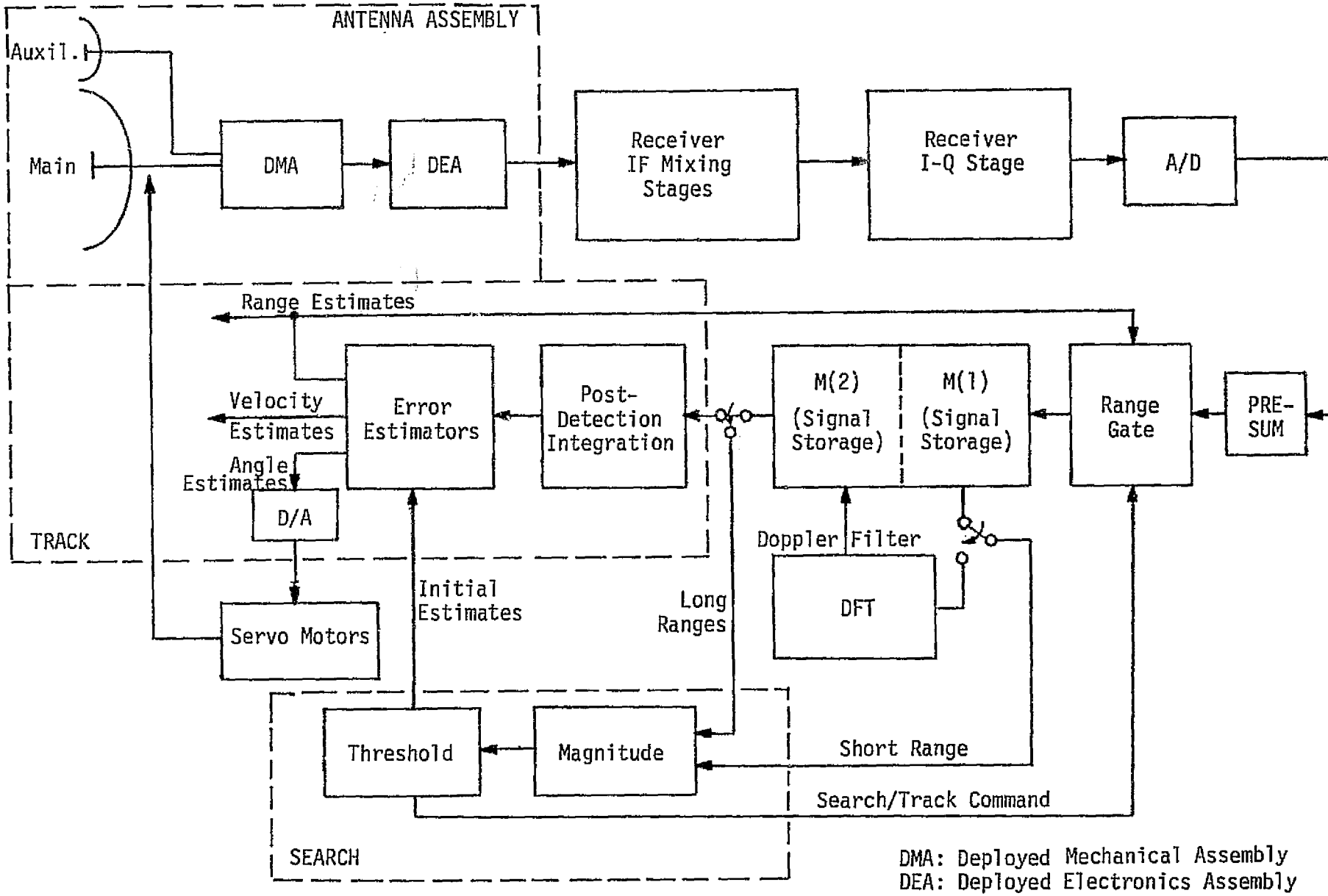

Figure 5. Radar Block Diagram

For long ranges, the magnitudes of the outputs of the doppler filters are summed over the RF frequencies and compared to a threshold to detect the existence of a target. For short ranges ($R < 0.42$ nmi), the detection takes place without using any doppler filtering.

Once a target is detected, the radar is switched to a track mode and the digital signals undergo post-detection integration, followed by an error estimation unit which is initiated by the crude estimate obtained by the search mode operation.

In the following sections, a detailed discussion of the various stages in the block diagram is presented, along with an analysis of the signal timing in both the search mode and the track mode.

3.2 Antenna Assembly

The antenna assembly is illustrated in Figure 6. (For a more detailed illustration, see [1].) The main antenna has a gain $G = 38.5$ dB. There is also an auxiliary antenna whose gain is $G = 20$ dB, which is used to guard against target effects on the sidelobes of the main antenna. Three signals emerge from the antenna, namely, the sum signal (Σ) which carries the received signal, and two angle signals (ΔAZ and ΔEL) which supply the azimuth and elevation angle information. The Σ signal is passed through a bandpass filter (BPF), whose center frequency can be adjusted by a centralized frequency synthesizer in the exciter to be one of the five frequencies (13.779 GHz, 13.831 GHz, 13.883 GHz, 13.935 GHz, 13.987 GHz). The angle signals ΔAZ and ΔEL are passed through a selecting switch which selects one of the signals at a time at a rate of 93 Hz. The output of the switch is then passed through a phase encoder whose rate is twice that of the selecting switch. A typical sequence of signals out of the encoder is shown in Figure 7. The encoded angle signal is then passed through a matching BPF to that of the Σ signal. The two signals are then passed through the T/R switch to the receiver IF mixing stage.

When angle track is operating, there are four antenna error dwell periods at each RF, during which the azimuth and elevation error signals are processed. During each error dwell period, 32 doppler filter outputs (via DFT) are computed.

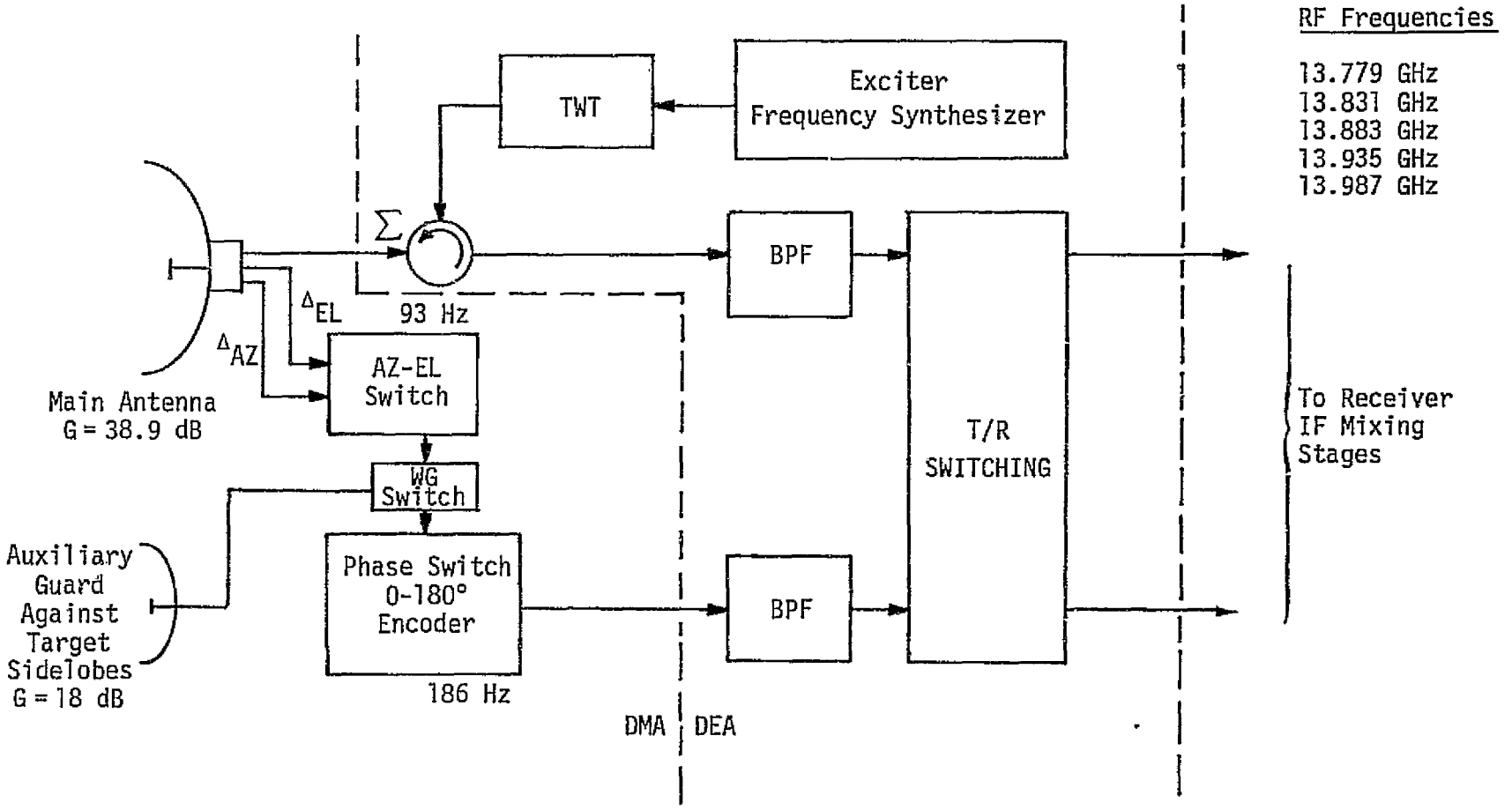

Figure 6. Antenna Assembly

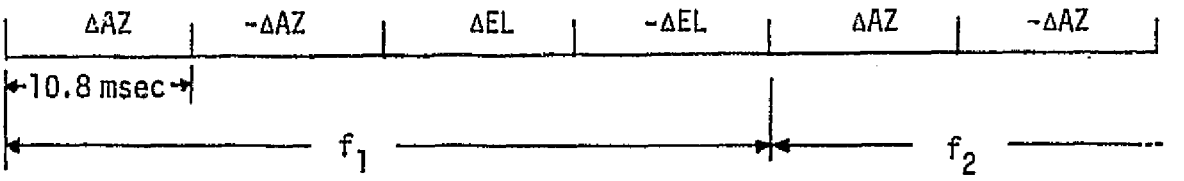

Figure 7. TDMA and Phase Encoder Output of Angle Error Information During Angle Track

3.3 IF Mixing and I-Q Stages

The antenna assembly is followed by two stages of IF amplifiers and filters, where the frequency of the signal is beaten down to a stable 78.143 MHz, as shown in Figure 8. In this stage, the power in the Σ-channel is divided in two equal parts to be used for communication and the radar. This results in a loss of 3 dB in signal-to-noise ratio due to this power split. Following the first down converter stage, a solid-state diode receiver blanking switch is included in each channel (DS1, DS2). These switches are controlled by a blanking logic to perform four functions: (1) preventing excessive leakage into the receiver during transmission; (2) switching the sum channel only during search; (3) switching the difference channel only during the main lobe/sidelobe discrimination test; and (4) switching both channels during track. The radar Σ-channel is then combined with the Δ-channel to form the multiplexed signal ($\Sigma \pm \Delta$). Only one-fourth of the power available in the Δ-channel is used when forming $\Sigma \pm \Delta$, as seen in Figure 8. The multiplexed signal is then passed through an in-phase and quadrature-phase detector (I-Q), where it is converted to two baseband signals. The two signals are converted to digital data using an A/D converter whose sampling frequency is slightly higher than twice the bandwidth of the signal to reduce the aliasing error to less than 0.5 dB. All computations after the A/D converter are carried out digitally. The sampling frequency is equal to 480 Hz. For long-range search, when the pulse width is 66.4 μsec, this corresponds to 32 samples/pulse from each channel of the I-Q detector for each range gate period. These samples are summed at the PRESUM stage to give a complex number that represents every received pulse.

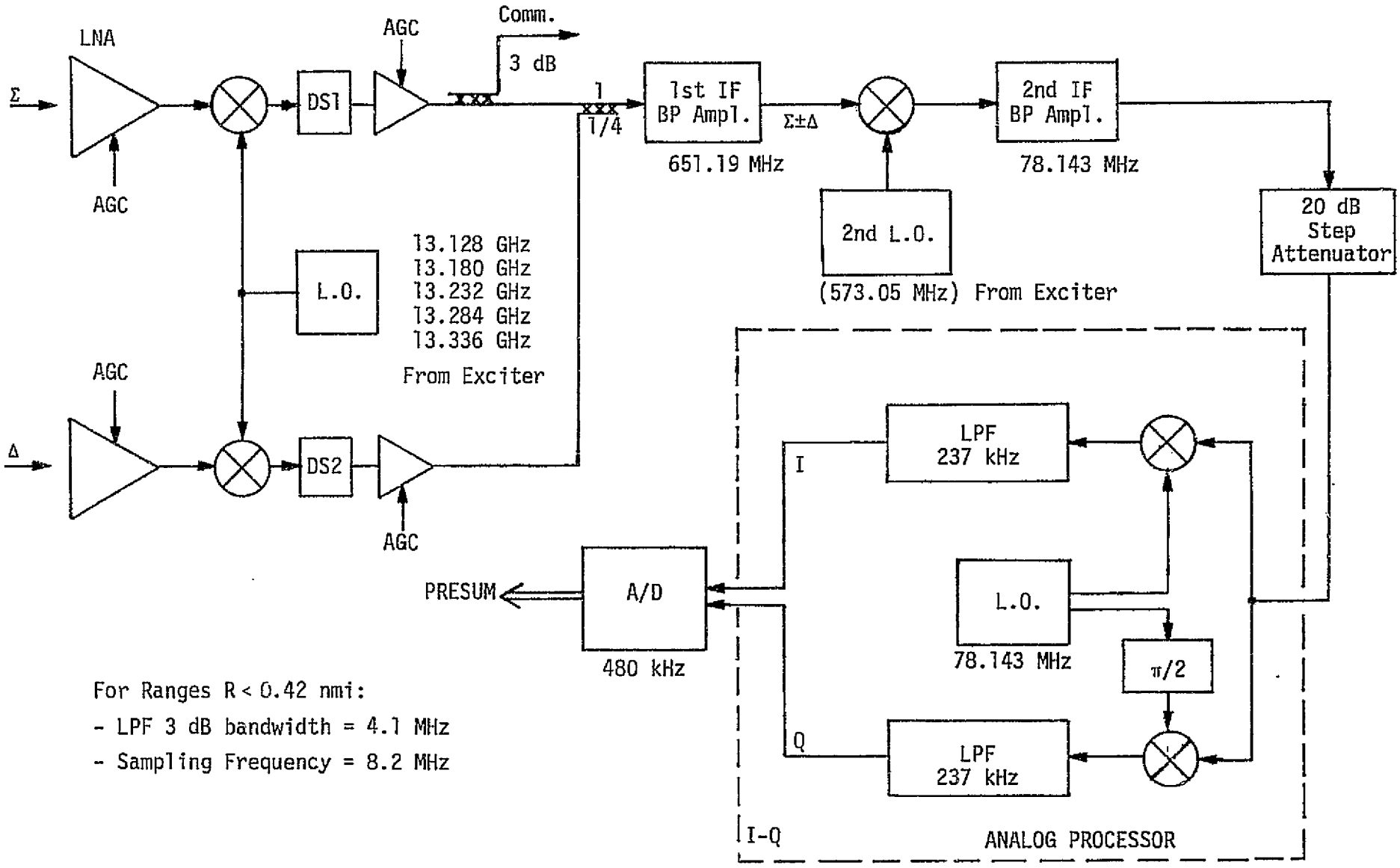

Figure 8. Simplified IF Mixing and I-Q Stages

3.4 Signal Parameters

Before explaining the different modes of operation, it is important to discuss the signals that are being used. The signals are RF pulses with a duration (τ) and a pulse repetition frequency (PRF) that are functions of the designated range. Frequency diversity, using five RF frequencies, is used in both the search and track modes. The five RF frequencies are generated in the DEA using a common swept Gunn oscillator with the communication mode. As explained in more detail in Section 6.5, the 83rd harmonic of a 156 MHz reference frequency from EA1 is mixed with the output of the Gunn VCO and fed into a loop filter and a comparator. A zero beat is detected as shown in Figure 9 whenever the resulting frequency is a multiple of 52 MHz. A bank of five BPFs is used to select the 52×i MHz signals ($i = 3,4,5,6,7$) which are fed back to the sweep control logic that locks the VCO at five discrete frequencies starting with 13.128 GHz and differing by multiples of 52 MHz. These frequencies are then mixed with 651 MHz (generated from the reference 156 MHz, as explained in Section 6.5) to yield the required five frequencies.

Switches SW1 and SW2 are used for selecting communication or radar signals, and switch SW1 is used to obtain the TWT bypass mode for the close range operation.

Table 1 lists the five frequencies [2] which are cycled in a given pattern which is convenient for the manual operation mode [3]. The table also shows the associated PRFs for different ranges [2]. The various signal timings are summarized in Table 2 for the search mode and in Table 3 for the track mode [2]. The PRF values used in the tables are those corresponding to the middle IF frequency. It is noted that the integration time corresponds to slightly more than five frequency dwell times in order to allow for computation time at the end of every spatial dwell in the search mode and every accuracy estimate calculation in the track mode.

The AGC operation in the Ku-band radar consists of a linear AGC and a set of five step attenuators. Their operation is summarized in Figure 10, where the hysteresis effect of the step attenuators can be observed. The linear AGC has a range of 25 to 30 dB. At the extremes

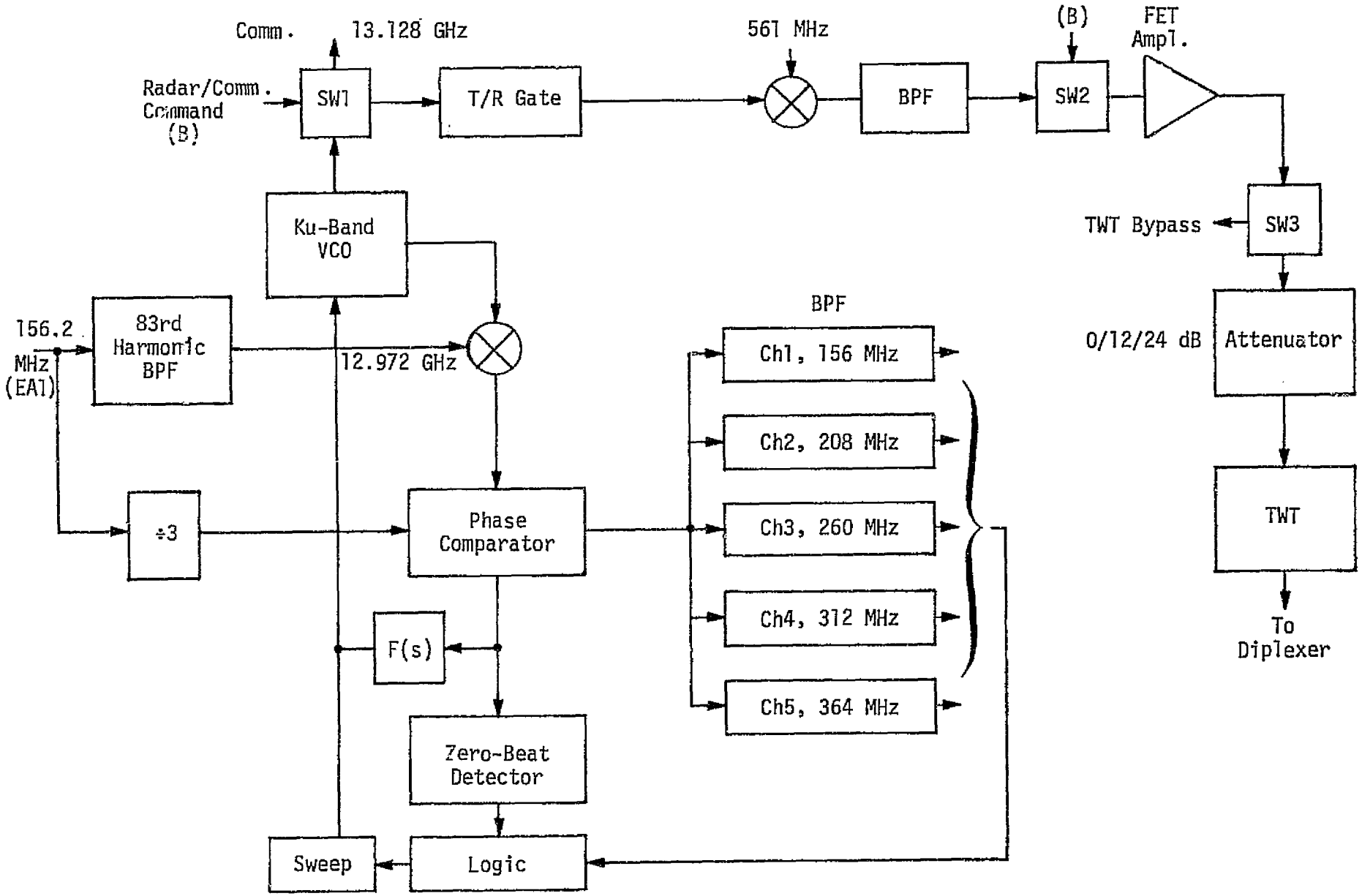

Figure 9. Radar RF Frequency Generation

Table 1. Frequency Synthesizer Frequencies for the First IF Mixing L.O. (in GHz)

		F_1	F_2	F_3	F_4	F_5
	Frequency	13.779	13.831	13.883	13.935	13.987
PRF (Hz)	Long Ranges R > 9.5 nmi	3009	2998	2987	2976	2965
	Short Ranges R < 9.5 nmi	7017	6994	6970	6946	6923

Table 2. Signal Parameters for Various Designated Ranges in Search Mode

Designated Range (nmi)	τ (μsec)	PRF (Hz)	Frequency Dwell Time (msec)	Integration Period (msec)
7.2 -	66.4	2987	5.36	28.6
3.8 - 7.2	33.2	6970	2.29	12.2
1.9 - 3.8	16.6	6970	2.29	12.2
0.95 - 1.9	8.3	6970	2.29	12.2
0.42 - 0.95	4.15	6970	2.29	12.2
- 0.42	0.122	6970	2.29	12.2

Table 3. Signal Parameters for Various Designated Ranges in Track Mode

Designated Range (nmi)	τ (μsec)	PRF (Hz)	Frequency Dwell Time (msec)	Integration Period (msec)
9.5 -	33.2	2987	21.44	116
3.8 - 9.5	16.6	6970	9.18	51.2
1.9 - 3.8	8.3	6970	9.18	51.2
0.95 - 1.9	4.15	6970	9.18	51.2
0.42 - 0.95	2.07	6970	9.18	51.2
- 0.42	0.122	6970	9.18	51.2

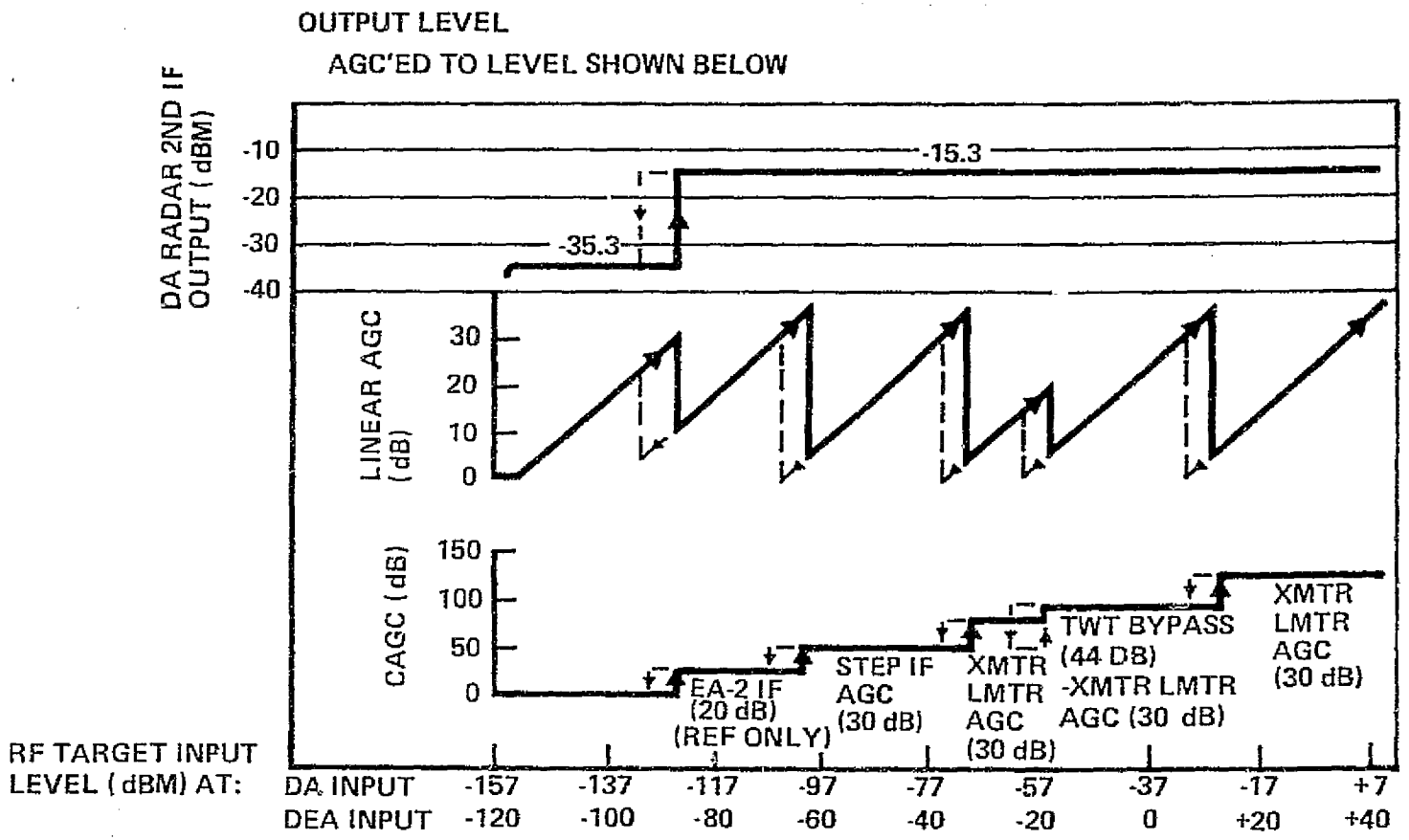

Figure 10. Description of AGC Operation for the Ku-Band Radar (Reprinted from [14])

of the linear range, a step attenuator is inserted which extends the limits of operation of the AGC. As can be seen from Figure 10, when all five step attenuators are taken into account, the dynamic range of the AGC is in excess of 125 dB.

The only region of possible concern is the transient response of the AGC after one of the step attenuators has been either inserted or deleted. The transient response does appear to be fast enough so that there is no problem in this area.

3.5 The Search Mode

In explaining the search mode operation, the long-range signal format is chosen for demonstration. All other ranges follow the identical processing except for the short range ($R < 0.42$ nmi), which does not utilize the doppler filters.

Sixteen pulses are transmitted at each RF frequency. The duration of each pulse is 66.4 μsec, while the time between consecutive pulses is 335 μsec. Four range gates (R_1, R_2, R_3, R_4) are used to cover the target range when no range designation is available. When range designation is available, two overlapping range gates are used around the designated range. The width of each gate in this case is three-halves the pulse width [2].

For each RF frequency, 64 complex numbers are stored in a memory designated as M(1), as shown in Figure 11. The output of each range gate at every RF frequency is passed through a bank of 16 doppler filters, uniformly spread over $[f_c, f_c + PRF]$, and implemented as discrete Fourier transforms (DFT). The magnitudes of the outputs of these filters are calculated and compared to precalculated thresholds. The target is detected when the magnitude of one or two outputs of adjacent doppler filters pertaining to one or two range gates is exceeded. Initial estimates of the range and the range rate of the target are calculated from the knowledge of the doppler filters and range gates whose outputs have exceeded the threshold. These initial estimates are fed into the error estimators as initial conditions to start the successive estimation process in the track mode. The thresholds are calculated to produce an error alarm rate of one false alarm per hour.

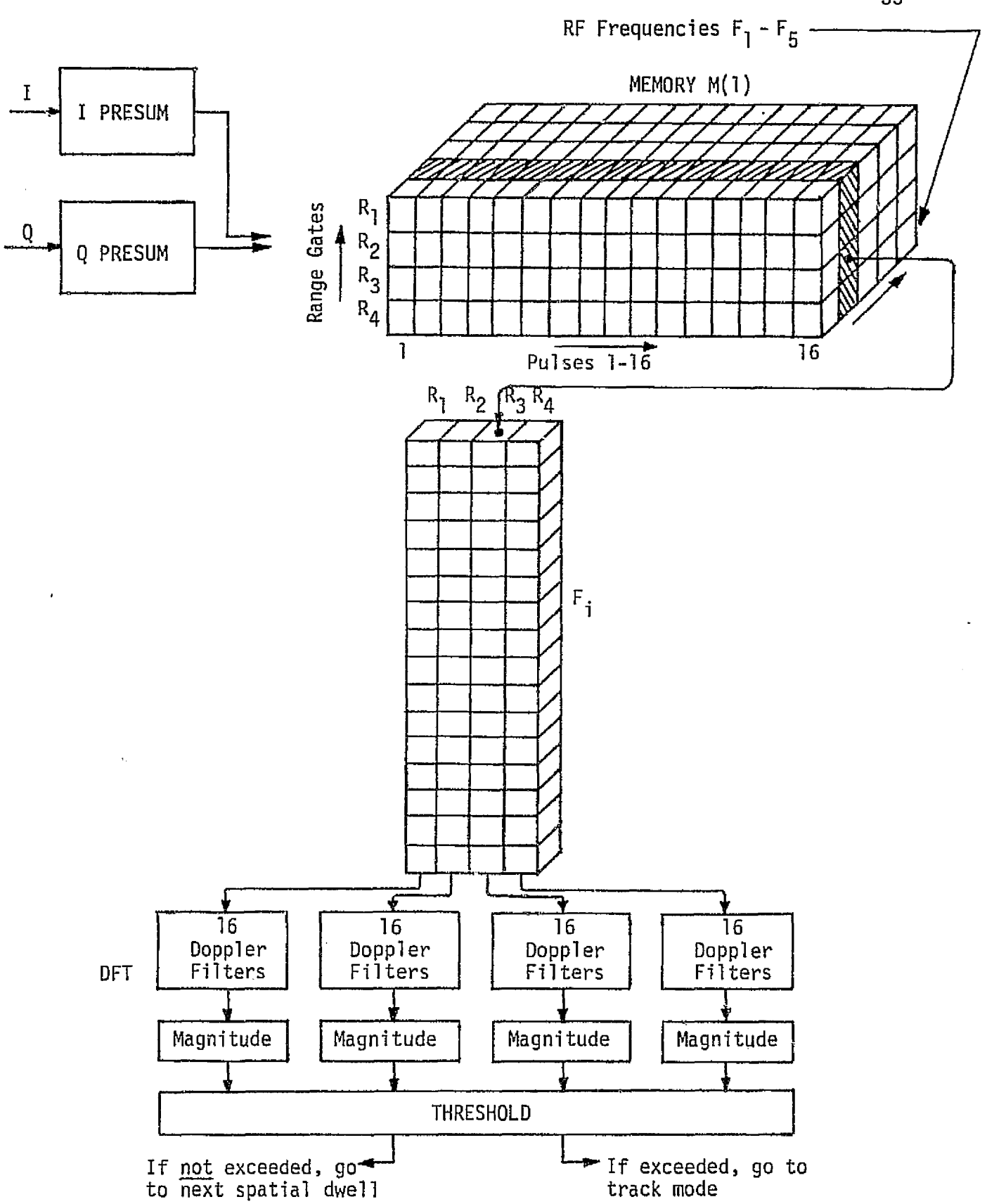

Figure 11. Search Mode Signal Processing

For short ranges ($R < 0.42$ nmi), a single short pulse is transmitted at a PRF of 6970 Hz [2]. The width of the pulse is equal to 0.122 μsec. The detection is carried out by finding the magnitude of the return signal over the time period corresponding to 0.42 nmi and comparing it continuously to a threshold. If the threshold is not exceeded, the receiver waits for the second transmitted pulse and the process is repeated. The number of pulses transmitted at every RF frequency is 16. The RF frequencies used in the short-range detection are the same as those used in long-range detection. For short ranges, once the threshold is exceeded, a hit is declared. Five hits are required before declaring detection. Tracking is started once the target is detected. The initial range estimate is obtained by finding the time that elapses between the transmission of the pulse and the exceeding of the threshold. This is done by implementing a range bin clock and a counter, as seen in Figure 12.

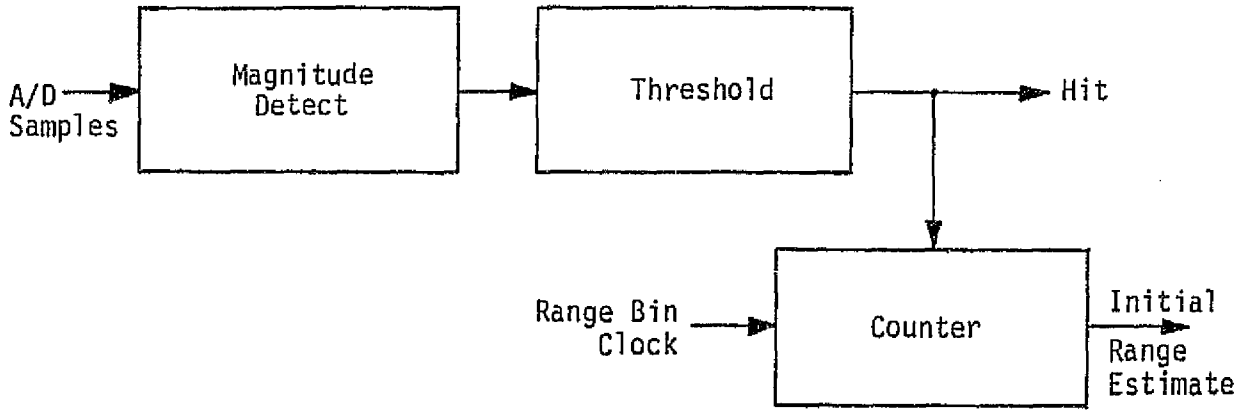

Figure 12. Short-Range Detection

3.6 The Track Mode

3.6.1 Signal Format and Block Diagram

The block diagram for track mode processing is shown in Figure 13. All the computations involved in obtaining the tracking accuracies are digital. The separate blocks in the figure are explained in detail in subsequent sections.

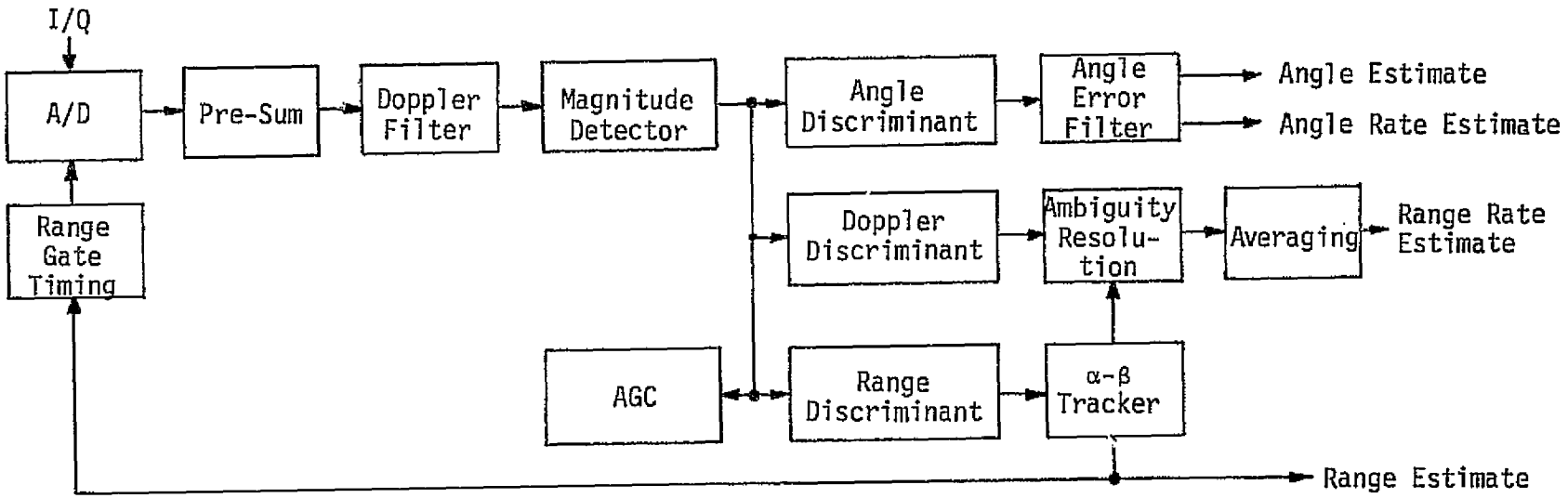

Figure 13. Track Processing Block Diagram

The signal in the track mode consists of 64 pulses for each RF frequency, instead of the 16 pulses in the search mode, as shown in Figure 14 [3]. For long-range tracking, the frequency dwell time is equal to 21.44 msec. Each frequency dwell time is divided into four time slots by the switching combination of SW1 and the phase encoder switch in the antenna assembly. The signals in the succeeding time slots are $\Sigma + \Delta AZ$, $\Sigma - \Delta AZ$, $\Sigma + \Delta EL$, and $\Sigma - \Delta EL$, respectively. The time slots are arranged so that the first two are used to measure the azimuth angle, while the last two are used for the elevation angle. Each one of the previous time slots consists of 16 pulses. The pulses are passed through two nonoverlapping gates, an early gate and a late gate, which are located around a predicted estimate of the range, $R_p(n)$, from the processor timing unit. The width of each gate is equal to the pulse width. The output of each range gate is a complex number $z(I,J,L,K)$, which is a function of four parameters (I,J,L,K):

I denotes the RF frequency being transmitted; $I = 1,2,\ldots,5$

J denotes the time slot in each frequency such that

- $J = 1$ corresponds to $\Sigma + \Delta AZ$
- $J = 2$ corresponds to $\Sigma - \Delta AZ$
- $J = 3$ corresponds to $\Sigma + \Delta EL$
- $J = 4$ corresponds to $\Sigma - \Delta EL$

K denotes a particular pulse in each time slot; $K = 1,2,\ldots,16$

L denotes the range gate under consideration,

- $L = -1$ corresponds to early gate
- $L = +1$ corresponds to late gate.

Figure 14 illustrates the signal format in the track mode. The computation time is not included in the figure.

3.6.2 Doppler Filtering

The outputs of the range gates are stored in a memory bank, designated for illustration as M(1). For all combinations of I, J, and L, the series of 16 pulses ($K = 1,2,\ldots 16$) are passed through a bank of 32 doppler filters, as shown in Figure 15 [2]. The doppler filters are uniformly spread over $[f_c, f_c + f_{PRF}]$. The overlapping of adjacent filters results in a doppler filter loss, which has to be taken into consideration. The outputs of the doppler filters are designated as

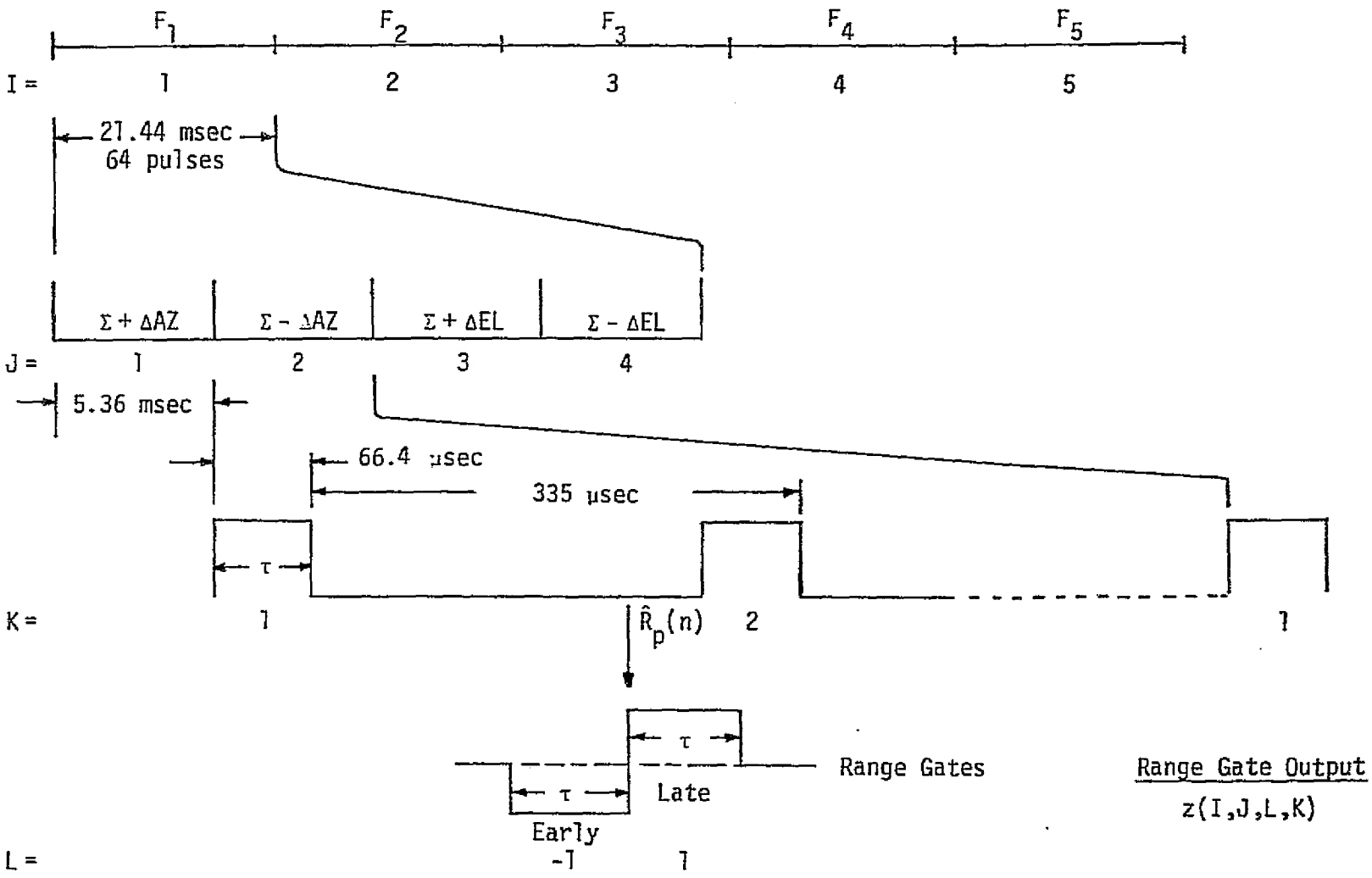

Figure 14. Track Mode Signal Format

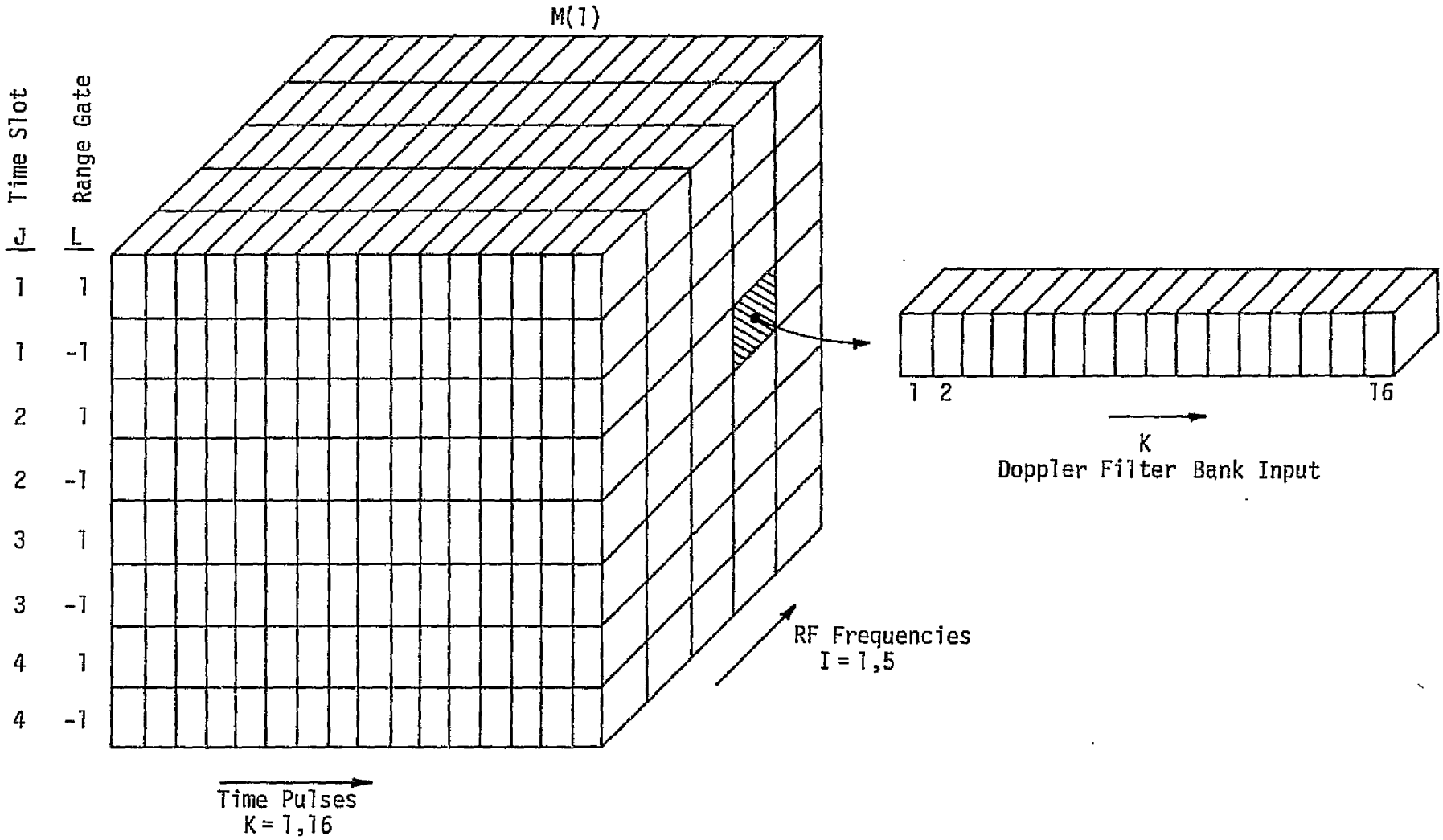

Figure 15. Pictorial Illustration of Memory Bank M(1)

$\omega(I,J,L,M)$, where M denotes a particular filter ($M = 0,1,\ldots,31$). Since doppler filtering is accomplished by digital Fourier transforms (DFT), $\omega(I,J,L,M)$ is given by

$$\omega(I,J,L,M) = \sum_{K=1}^{16} z(I,J,L,K)\, e^{-(j2\pi KM)/16}$$

$$= x(I,J,L,M) + j\,y(I,J,L,M)\,. \qquad (1)$$

Implementing doppler filters using a DFT (or an FFT) might result in losses due to the lack of proper match between the pulse bandwidths, the PRF, and the bandwidth of the DFT.

The outputs of the doppler filters are stored in a memory bank designated as M(2), as shown in Figure 16. Only the outputs of three adjacent filters are processed further, namely, the output of the filter whose center frequency is closest to the actual doppler and the outputs of the filters adjacent to it. If the middle filter is designated as M_1, then the outputs of filters $M_1 - 1$, M_1, and $M_1 + 1$ are processed further through the post-integration stage. The output of M_1 is used in computing the range, as well as the angle discriminants, while the outputs of $M_1 - 1$ and $M_1 + 1$ are used in computing the range rate (doppler) discriminant.

3.6.3 Post-Integration

The outputs of each of the doppler filters $M_1 - 1$, M_1, and $M_1 + 1$ consist of 40 memory cells from the memory M(2), as shown in Figure 16. The 40 cells correspond to five RF frequencies ($I = 1,2,\ldots,5$), two range gates ($L = \pm 1$), and four time slots ($J = 1,2,3,4$). Each one of these cells carries a complex number $\omega(I,J,L,M)$, whose magnitude is found by finding $\theta = \tan^{-1}\left(y(I,J,L,K)/x(I,J,L,K)\right)$ by table look-up and then rotating $\omega(I,J,L,K)$ by an angle θ to find the magnitude. This procedure uses Programmable Read Only memories (PROM) and is easier to implement than multiplying the number with its conjugate. These magnitudes are added in different manners to form the post-detection integration (PDI) outputs. To be able to demonstrate the logical procedure for adding these magnitudes, the memory cells under consideration are redrawn for a given RF frequency F_i, as shown in Figure 17.

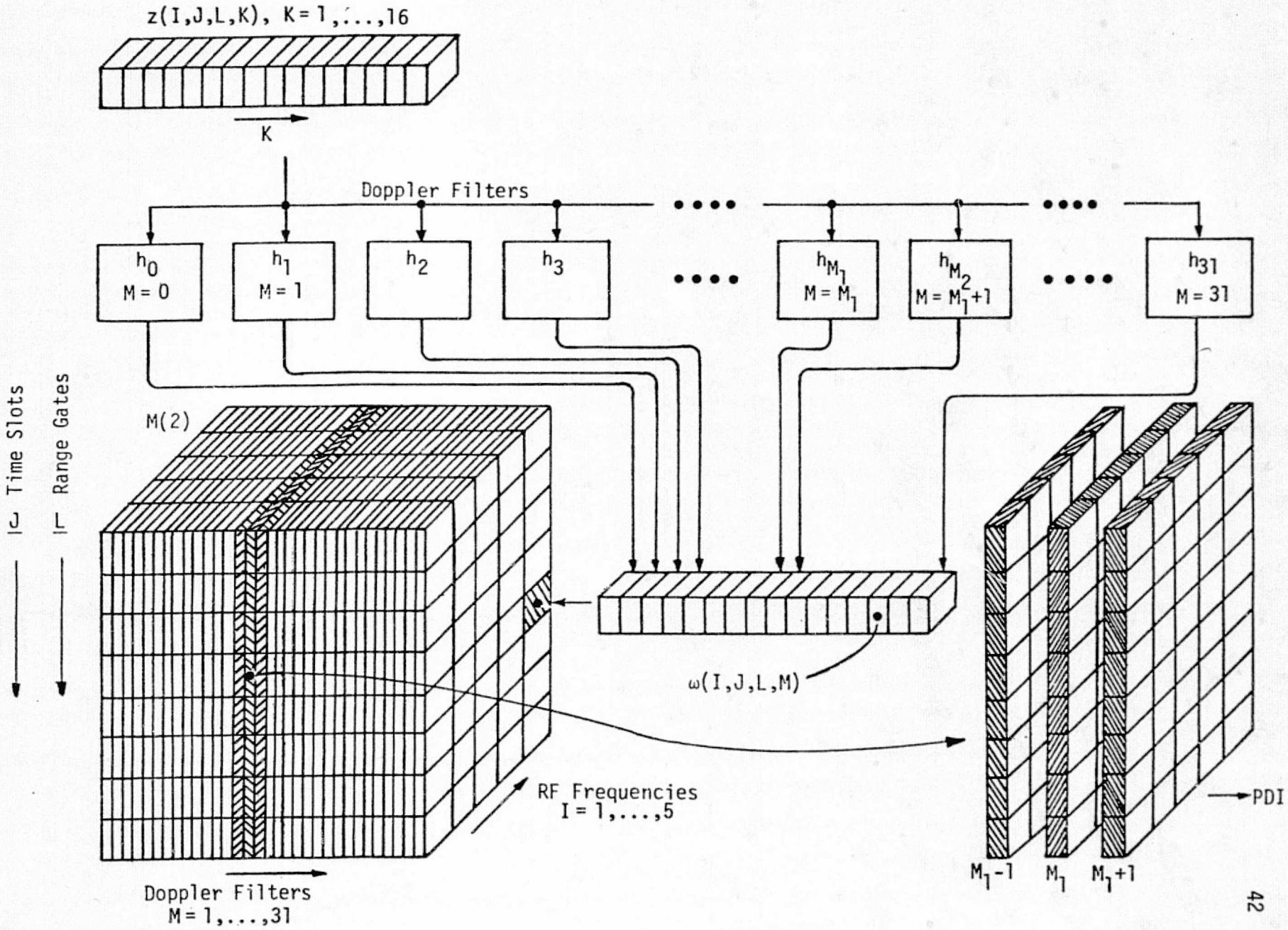

Figure 16. Pictorial Illustration of Memory Bank M(2)

Eight sums are formed at the output of the post-detection integrator—two corresponding to each of the four parameters of interest, namely, range, range rate, azimuth angle, and elevation angle. As mentioned previously, for range and angle accuracy computations, the output of the doppler filter M_1 is used, whereas the outputs of the two adjacent filters $M_1 - 1$ and $M_1 + 1$ are used for range rate computation.

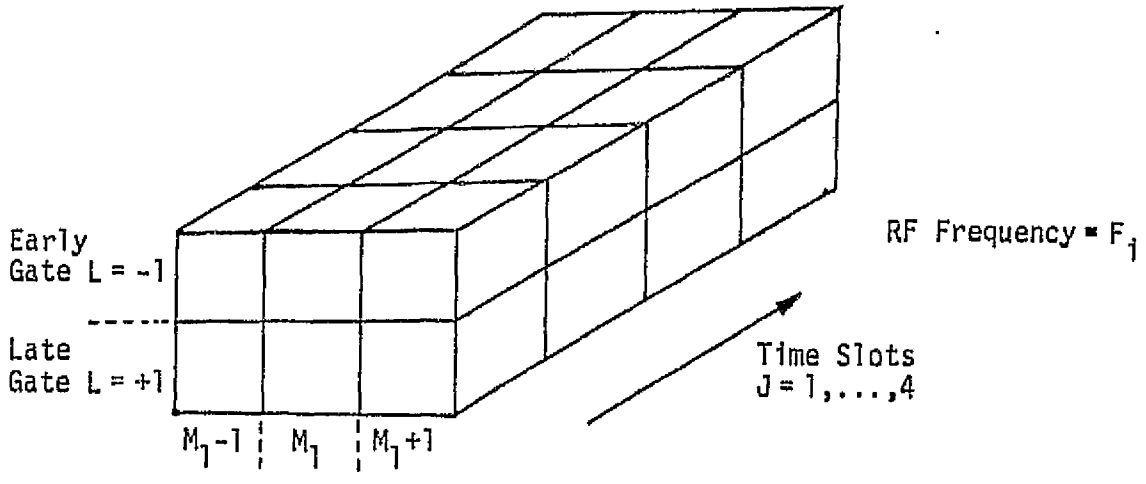

Figure 17. Memory Cells Storing $\omega(I,J,L,M)$ for a Given RF

3.6.4 Range PDI Outputs

The two range outputs are formed by the post-detection integration, one corresponding to the early gate and the other corresponding to the late gate. They are denoted $S_R(L=-1)$ and $S_R(L=+1)$. The R denotes the range and the L denotes the early or late gate. They are formed by using the output of the middle doppler filter (M_1). Thus, to obtain $S_R(L=-1)$, the magnitude of all the complex numbers pertaining to the early gate and the filter M_1 are added over all the RF frequencies. $S_R(L=+1)$ is obtained in a similar fashion using the late gate.

3.6.5 Range Rate (Doppler) PDI Outputs

The doppler PDI outputs are designated as $S_D(M=M_1-1)$ and $S_D(M=M_1+1)$ and are obtained by summing the magnitudes of the numbers out of the doppler filters $M_1 - 1$ and $M_1 + 1$, respectively (Figure 17).

Each sum is taken over the two gates, the four time slots, and all the RF frequencies.

3.6.6 Angle PDI Outputs

To obtain the two PDI outputs for the azimuth (elevation) angle information, the output of the doppler filter M_1 is used to obtain the magnitudes of the first (last) two time slots corresponding to $\Sigma + \Delta AZ$ and $\Sigma - \Delta AZ$ ($\Sigma + \Delta EL$ and $\Sigma - \Delta EL$) which are added over all RF frequencies to give $S_{AZ}(J=1)$ and $S_{AZ}(J=2)$ [$S_{EL}(J=3)$ and $S_{EL}(J=4)$], respectively. As in the range rate case, the outputs of both the early and late range gates are used and are summed.

3.6.7 Logarithm Discriminant Formation

The purpose of the logarithm discriminant is to obtain an estimate of the error (error signal), including sign, of the various parameters under consideration. Since the following approximation is valid for small x:

$$\ln \frac{1+x}{1-x} \simeq 2x ; \qquad x \ll 1 , \tag{2}$$

then, if x represents the errors in the parameters under consideration, this error can be computed by forming the logarithm of $(1+x)/(1-x)$. The mathematical derivation of the variance of the logarithmic estimator is formed in [4], where the maximum likelihood estimator of the form

$$\hat{x} = \log \frac{\sum_i |U_i|^2}{\sum_i |V_i|^2} \tag{3}$$

is analyzed. U_i and V_i represent a pair of voltages whose difference is proportional to the target parameter being measured. Since the target range, range rate, and orientation angles are mathematical duals of each other, it is the objective of the following discussion to relate $|U_i|^2$ and $|V_i|^2$ to the various outputs of the PDI, as illustrated in Figure 17.

3.6.8 Range Discriminant

In the formation of the range discriminant, a sum signal (S) and a difference signal (D) are formed such that

$$S = S_R(L=-1) + S_R(L=+1)$$

$$D = S_R(L=-1) - S_R(L=+1)\,, \tag{4}$$

where $S_R(\ )$ is defined in Section 3.6.4.

Since the output of the early gate is a measure of $R-\Delta R$, where ΔR is an absolute error in the range, and the output of the late gate is a measure of $R+\Delta R$, then S is a measure of the range R and D is a measure of the absolute range error. Then, replacing S by R and D by ΔR, it can be stated that

$$S_R(L=-1) \propto R-\Delta R$$

$$S_R(L=+1) \propto R+\Delta R\,. \tag{5}$$

(A proportionality constant might be added; however, this coefficient will drop when taking the logarithms.)

Let

$$S_R(L=-1) \equiv \sum_{i=1}^{20} |U_i|^2$$

and

$$S_R(L=+1) \equiv \sum_{i=1}^{20} |V_i|^2\,, \tag{6}$$

where N = 20 is the number of samples used in calculating a single range error estimate. It corresponds to four time slots over five RF frequencies. It is now easy to see that

$$\ln \frac{\sum_{i=1}^{20} |U_i|^2}{\sum_{i=1}^{20} |V_i|^2} = \frac{2\Delta R}{R} \triangleq 2R_\varepsilon\,, \tag{7}$$

where R_ε is the required range error signal. This procedure for obtaining a normalized estimate of range error estimate is illustrated in Figure 18.

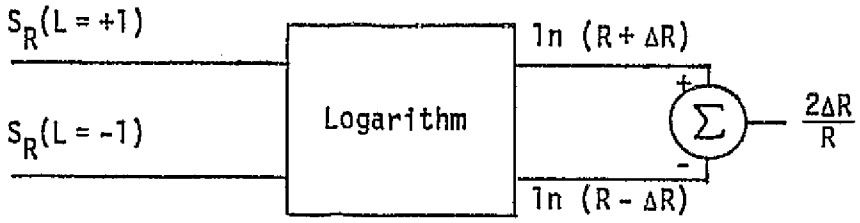

Figure 18. Range Discriminant

3.6.9 Doppler (Range Rate) Discriminant

A similar argument can be stated for the doppler discriminant. In this case, however, the number of samples used to calculate a doppler error estimate is equal to 40. This is because both the outputs of the early gate and late gate are used in the computation which is also carried over four time slots and five RF frequencies. Thus, from Section 3.6.5.

$$\ln \frac{\sum_{i=1}^{40} |U_i|^2}{\sum_{i=1}^{40} |V_i|^2} \simeq 2 \frac{S_D(M=M_1-1) + S_D(M=M_1+1)}{S_D(M=M_1-1) - S_D(M=M_1+1)} \simeq 2\dot{R}_\varepsilon . \qquad (8)$$

3.6.10 Angle Discriminants

As has already been noted, the magnitudes of the samples from the DFT corresponding to both the early and late range gates are summed to form an on-target gate and then integrated over the transmitter frequency cycle. This means that the number of samples used per calculation of an angle error estimate is equal to 10 for two range gates and five RF frequencies. The sum and difference samples of an angle error are then log-converted and subtracted to form the normalized angle errors for the elevation and azimuth channels. The error signals are then D/A converted and sent to the servo filters and finally to the servo motors.

The angle error signals are given by

$$2\Delta_\varepsilon AZ \triangleq \ln \frac{S_{AZ}(J=1)}{S_{AZ}(J=2)} = \frac{2\,\Delta AZ}{\Sigma}$$

$$2\Delta_\varepsilon EL \triangleq \ln \frac{S_{EL}(J=3)}{S_{EL}(J=4)} = \frac{2\,\Delta EL}{\Sigma} \quad . \tag{9}$$

These error signals are used to obtain the various required estimates pertaining to the parameters under consideration.

Since the error signals are obtained successively as new readings are processed, they will be denoted by $R_\varepsilon(n)$, $\dot{R}_\varepsilon(n)$, $\Delta_\varepsilon AZ(n)$, and $\Delta_\varepsilon EL(n)$, where (n) denotes the nth error signal being processed by the logarithm discriminant.

The angle error signals $\Delta_\varepsilon AZ$ and $\Delta_\varepsilon EL$ are fed into loop filters as shown in Figure 19 to obtain two sets of estimates:

(1) Angle estimates $\hat{\Delta}AZ$ and $\hat{\Delta}EL$, which are fed back to the servo motors.

(2) Angle rate estimates $\hat{\dot{\Delta}}AZ$ and $\hat{\dot{\Delta}}EL$, which are displayed for the astronauts for visual reading.

The range and range rate error signals, however, are fed into the processor timing unit to obtain various required estimates, as discussed in the following section.

3.6.11 Processor Timing, Range and Range Rate Prediction

The processor timing stage consists of two substages. The first is called the α-β tracker [5] and the second is designated as the ambiguous doppler resolver and corrector, as shown in Figure 20. The α-β tracker is employed to give a smoothed estimate of the current range $\hat{R}_s(n)$, a predicted estimate of the next range reading $\hat{R}_p(n+1)$, and a smoothed estimate of the range rate $\hat{\dot{R}}_s(n)$. This latter value is used along with the range rate error signal $\dot{R}_\varepsilon(n)$ as inputs to the ambiguous doppler resolver and corrector whose output is fed through a sliding window to produce a smoothed corrected doppler estimate $\hat{\dot{R}}_{sc}(n)$ and a predicted corrected doppler estimate $\hat{\dot{R}}_{pc}(n+1)$. The doppler estimates $\hat{\dot{R}}_{sc}(n)$ and $\hat{\dot{R}}_{pc}(n+1)$ are obtained by averaging (smoothing) m previous estimated values that are stored in a special memory (sliding

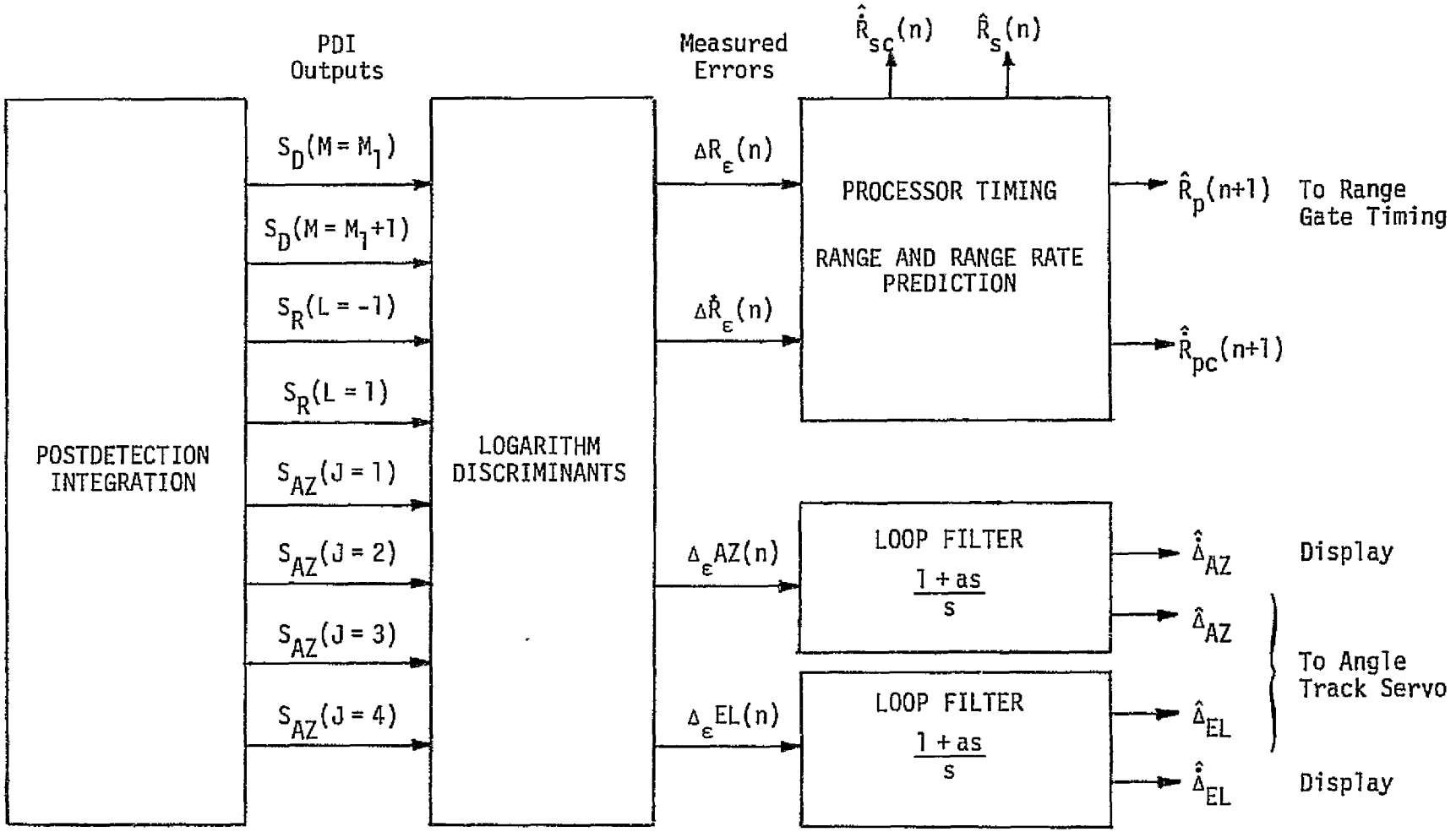

Figure 19. PDI and Parameter Estimators

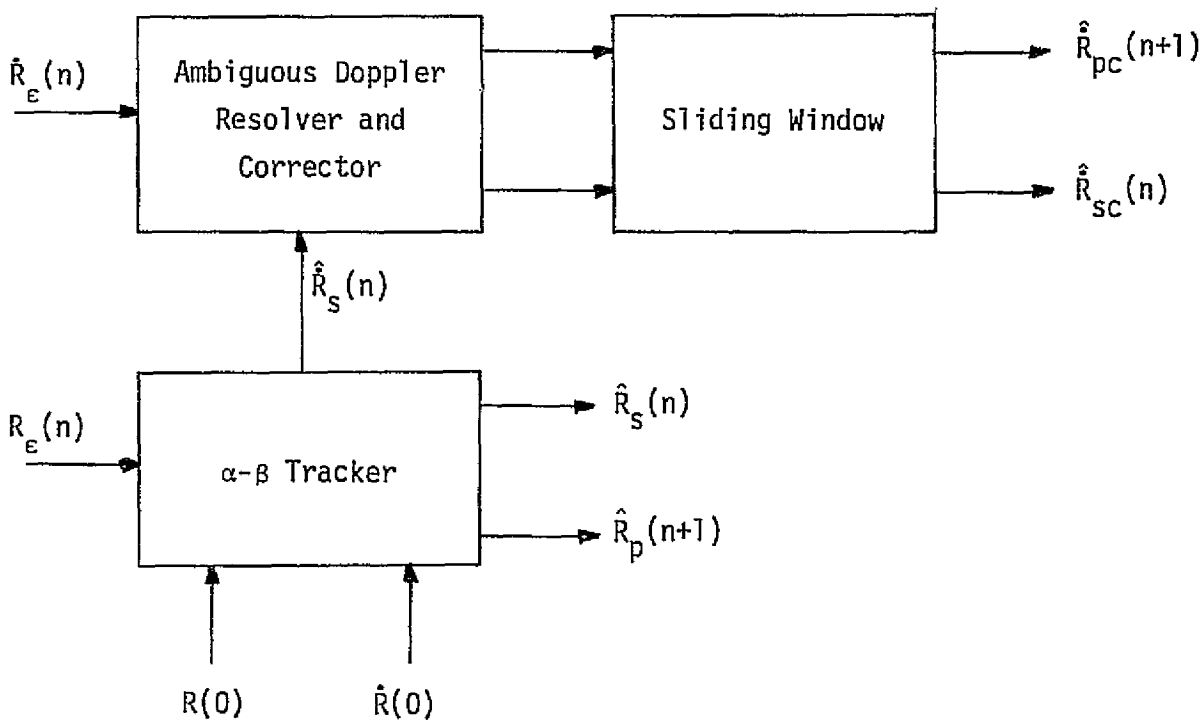

Figure 20. Processor Timing Stage

window averaging). The number of estimates (m) being used is dependent on the designated range [2]. For long ranges ($R > 9.5$ nmi), m is equal to 2 while, for shorter ranges, it is equal to 4.

These estimates are used for various purposes, which are summarized in Table 4.

Table 4. Processor Timing Stage Outputs

Estimate	$\hat{R}_p(n+1)$	$\hat{R}_s(n)$	$\hat{R}_{sc}(n)$	$\hat{R}_{pc}(n+1)$
Use	Adjust early and late gates location	Display	Display	Select doppler filters

Whereas the location of the range gates is adjusted as a result of every new range estimate, the location of the doppler filters remains unchanged. The range rate estimates are used to select the filter M_1 whose center frequency is closest to the estimated doppler. This filter remains unchanged until the doppler error changes appreciably to make the estimated doppler frequency closer to a different filter center frequency.

The operation of the ambiguous doppler resolver and corrector is explained in detail in [6].

This completes the description of the Ku-band radar system. Sufficient detail has been given so that accurate performance estimates can be made in both the search and track modes of operation. More detailed functional flow and block diagrams are given in [1]. In subsequent sections, a summary of anticipated performance is given for all aspects of the search and track modes of the Ku-band radar.

3.7 Ku-Band Radar Performance in Target Acquisition (Passive Target)

A fundamental part of the operation of the Ku-band radar is the capability to detect and reacquire the target at all ranges less than 10 nmi. The acquisition capability of the present configuration of the Ku-band radar is summarized in this section. The development in Appendix A of [6] is used extensively.

The primary emphasis in the evaluation of the Ku-band radar during acquisition is "how the radar performs." Comparison will be made to the specification values, but no heavy emphasis is placed on it. In those situations where the performance does not meet the specification requirements, reasonable alternatives are proposed which will provide satisfactory performance in all rendezvous profiles.

3.7.1 Target Detection Processing Losses

The target detection processing losses as they are presently estimated are summarized in Table 5. The losses anticipated by both Hughes and Axiomatix are shown. The reasons for the agreements and disagreements are detailed in [6,7].

The totals of the losses are used in evaluating radar detection performance. It is noted that the difference between the average losses and worst case losses is 4.0 dB. In the next section, the differences in these losses and their implications are discussed.

3.7.2 Radar Detection Performance Philosophy

The losses summarized in the last section demonstrate two approaches in establishing a radar detection performance philosophy. The differences center around what is to be taken into account when averages are performed. The "Hughes" approach is to average over all target positions and velocities when carrying out an average. The "Axiomatix" approach is somewhat more pessimistic in that the average is carried out over thermal noise, target scintillation effects, and other radar parameters. This is done, however, for a target located at the worst possible velocity and worst possible angular position.

There is merit to both approaches. Therefore, the detection results to be subsequently presented are carried out under both performance philosophies.

In the one case, the design philosophy is that

$$\text{Average } P_d = 0.99$$

for a 1 square meter target. In the latter case, the design philosophy is that

$$\text{Average } P_d \geq 0.99$$

for a 1 square meter target for all target velocities and spatial positions.

Table 5. Summary of Target Detection Processing Losses

		Hughes (average) (dB)	Axiomatix (worst case) (dB)
Transmit Loss		3.7	3.7
Beam Shape Loss		2 (avg)	3.2 (max)
Pre-Sum Mismatch		0.57	0.57
Constant FAP		1.7	1.7
Doppler Mismatch		1.1 (avg)	3.9 (max)
Range Gate Straddle			
	Designated Mode	1.76	1.76
	Undesignated Mode*	$L_{str} = f(R)$	$L_{str} = f(R)$
Processor Loss		1.25	1.25
Totals	Designated Mode	12.08	16.08
	Undesignated Mode	$10.32 + L_{str}$	$14.32 + L_{str}$

*The range gate straddle loss in the undesignated mode varies from 0 dB to 6 dB, depending on the range. For details, see [6,7].

3.7.3 Radar Detection Performance

Based on the losses summarized above, the Ku-band radar detection performance is summarized. In Figures 21 and 22, the target detection design margins are plotted versus range for both the designated range and undesignated range modes of operation. Except for the losses, all radar equation parameters are the same as used in Appendix A of [6]. In Figure 21, the worst case losses of Table 5 are used. Also, a transmitted power of 50 watts is used, although the present system configuration consists of a 60-watt TWT. This is approximately 0.8 dB improvement. For the range designation mode, a design margin of 0 dB is obtained at approximately 9.3 nmi. For the undesignated range mode, it is about 7.5 nmi. The design margin for the undesignated range mode deteriorates as the range is reduced in the interval of 8 nmi to 11 nmi because, in this interval, the range gate straddling loss is increasing faster than the factor R^{-4} gain in the radar equation. At 12 nmi, the design margin is -4.5 dB for the range designated mode and -5.1 dB for the undesignated range mode.

In Figure 22, the design margin is shown versus range for the average losses in Table 5. In this case, a 0 dB design margin is obtained at approximately 11.7 nmi; at 12 nmi, the design margin is greater than -1 dB. These results are close to those quoted in [8] by HAC. The HAC results are shown as two dots in Figure 22.

The cumulative detection probability is plotted versus range for the worst case in Figure 23; both $M = 1$ and $M = 2$ scans are shown. It is seen that the two-scan case uniformly outperforms the single-scan case for both the designated and undesignated range modes. In these computations, a transmitted power of 60 watts was used.

Inspection of Figure 23 reveals that, depending on the range, the cumulative detection probability for the designated range can be both smaller and larger than that for the undesignated case. This is also the case for the design margins in Figures 21 and 22. At 12 nmi, the cumulative detection probability is approximately 75% for two scans and approximately 50% for one scan. This is the case for both the designated and undesignated range modes.

The design margins can be significantly improved without altering the present design by allowing more time (greater than 1 min) to

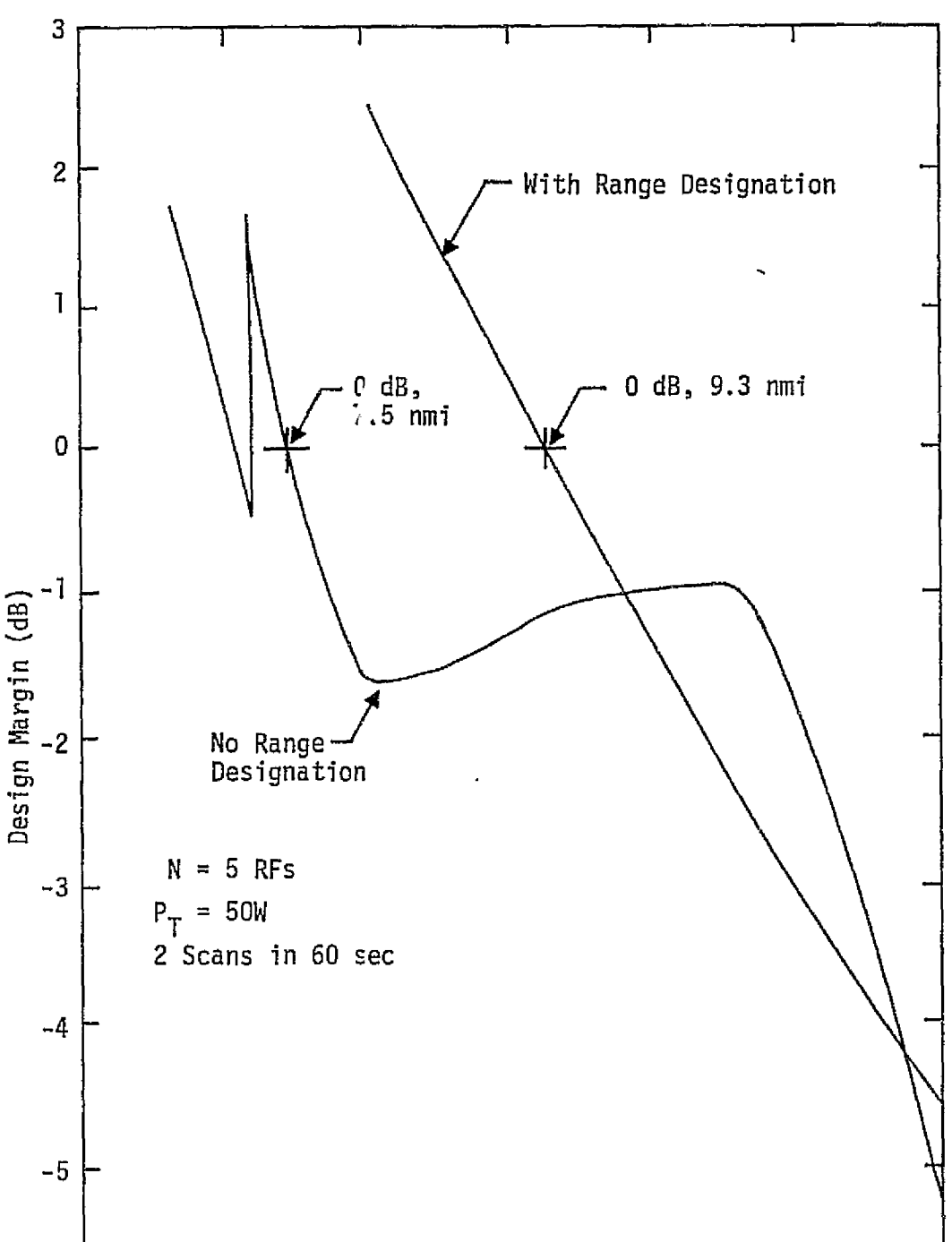

Figure 21. Target Detection Design Margin Versus Range for Worst Case Losses in Table 5

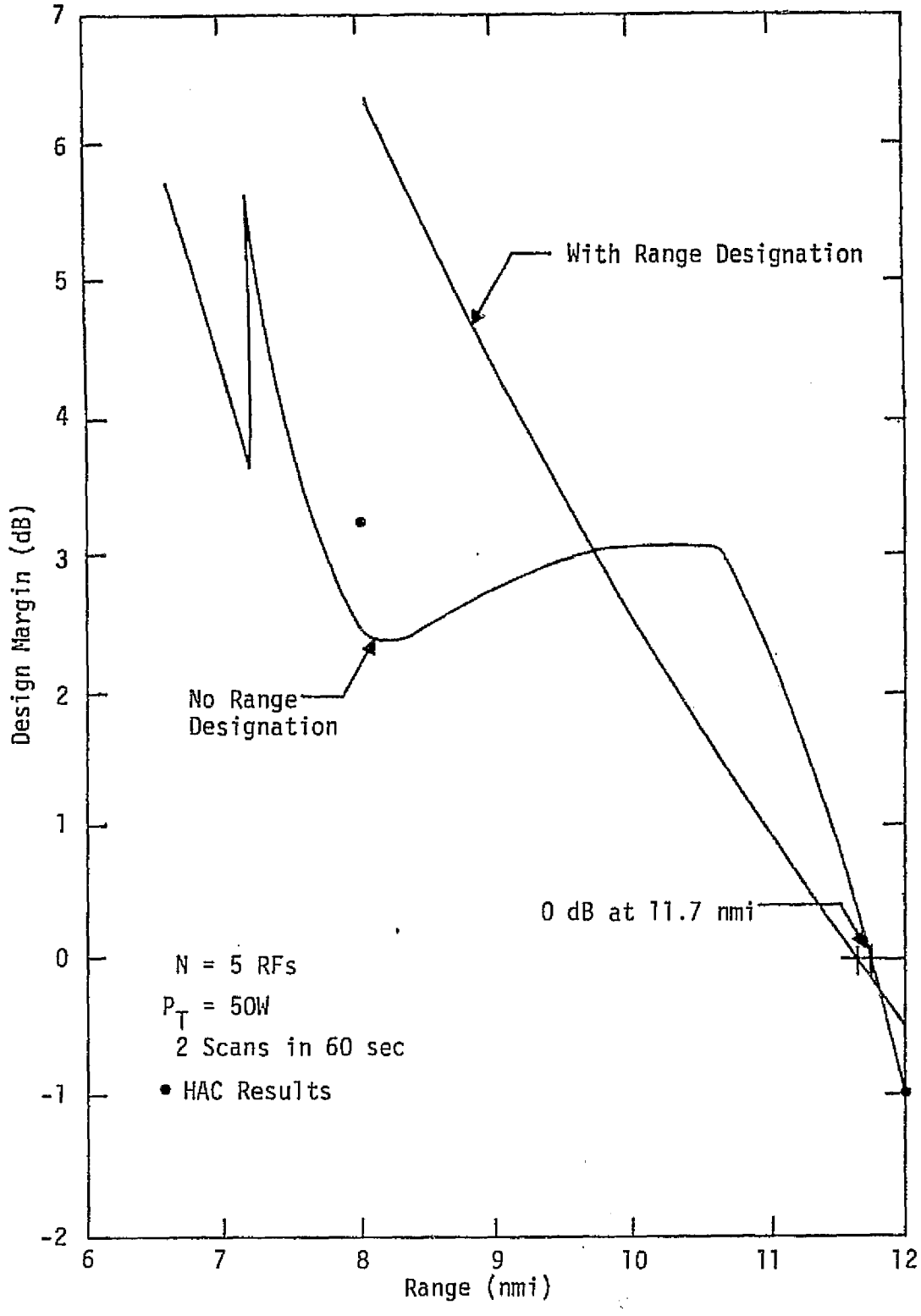

Figure 22. Target Detection Design Margins Versus Range for Average Losses in Table 5

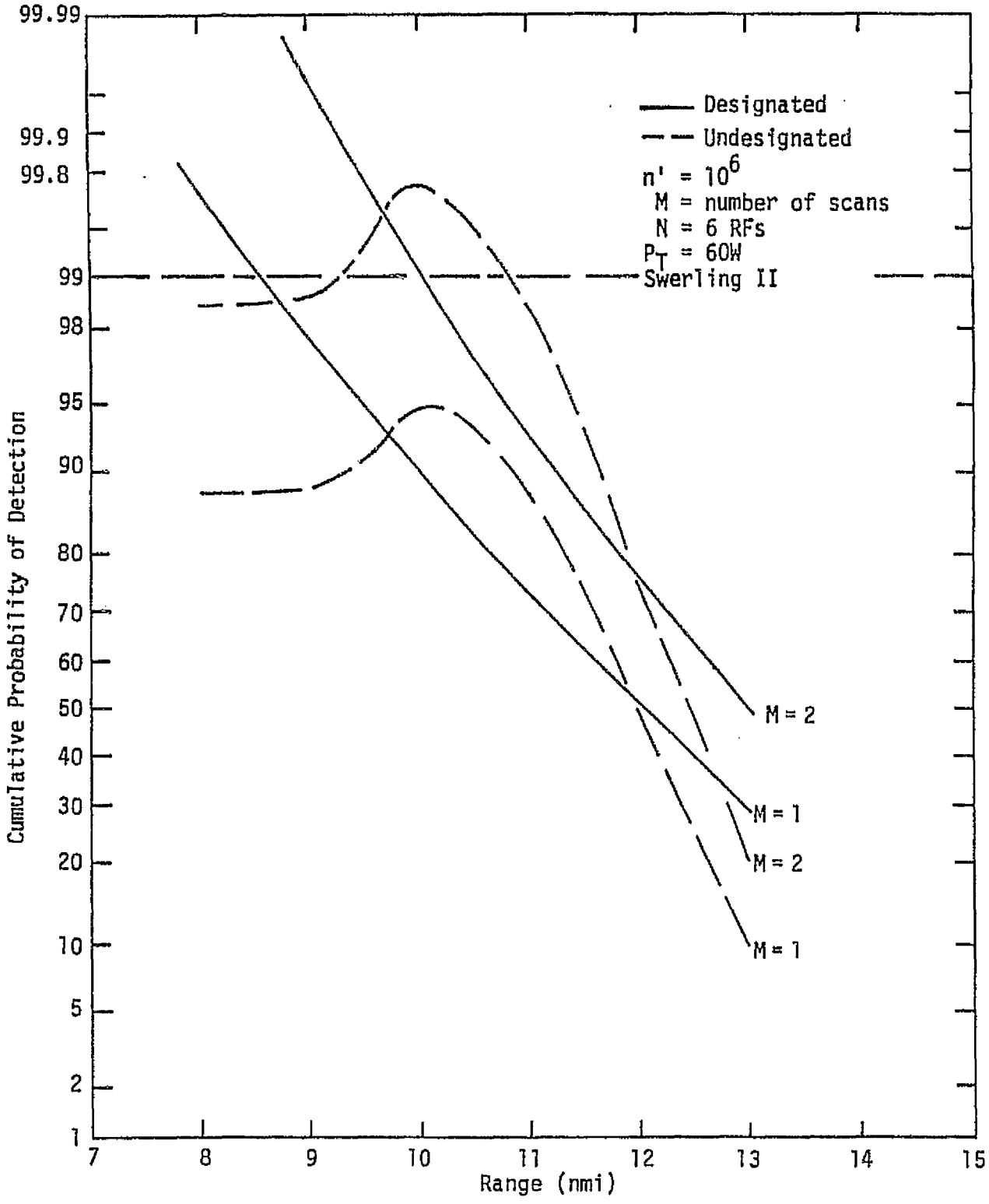

Figure 23. Cumulative Detection Probability Versus Range for Worst Case Losses in Table 5

illuminate the search volume. The scan rate is held fixed at two scans per minute in Figure 24, where the cumulative detection probability is plotted versus range. The gain in performance is significant. At 11.3 nmi, for example, by increasing the total scan time from 1 minute to 2 minutes, the cumulative detection probability increases from 90% to 99%.

3.7.4 Alternatives and Recommendations

If the design philosophy of average losses is acceptable, then the design margin at 12 nmi is within a few tenths of 0 dB with a 50-watt TWT and approximately 0 dB with a 60-watt TWT.

If the design philosophy of worst case losses is preferred, the design margin is between -4 dB and -5.2 dB. As shown above, however, there is significant improvement in performance by maintaining the same scan rate and allowing the total search time to increase from 1 minute to 2 minutes. This increases the total number of scans from 2 to 4, and keeps the present radar configuration entirely intact and thereby has virtually no hardware implications. For worst case losses, a 0 dB design margin is obtained at a range of 11.3 nmi. We recommend this alternative, and this recommended design point is shown in Figure 24.

Another alternative which applies to the range designate mode only is to narrow somewhat the two range gates during search. How much they can be narrowed is a function of the anticipated range designate accuracy. We do not have a recommendation for this alternative. It could be implemented in addition to the recommended alternative above. If one has any doubt about the range designate accuracy, however, this alternative does not appear satisfactory.

3.7.5 Detection of an Active Target

In the detection mode of an active target at 300 nmi, there is a positive design margin of greater than 2.5 dB. There does not appear to be any problem with the present radar configuration in regard to the detection of active targets at maximum range.

3.8 Point Target Tracking

The tracking performance of a point target of the Ku-band radar is described twofold. First, the effects of thermal noise and target

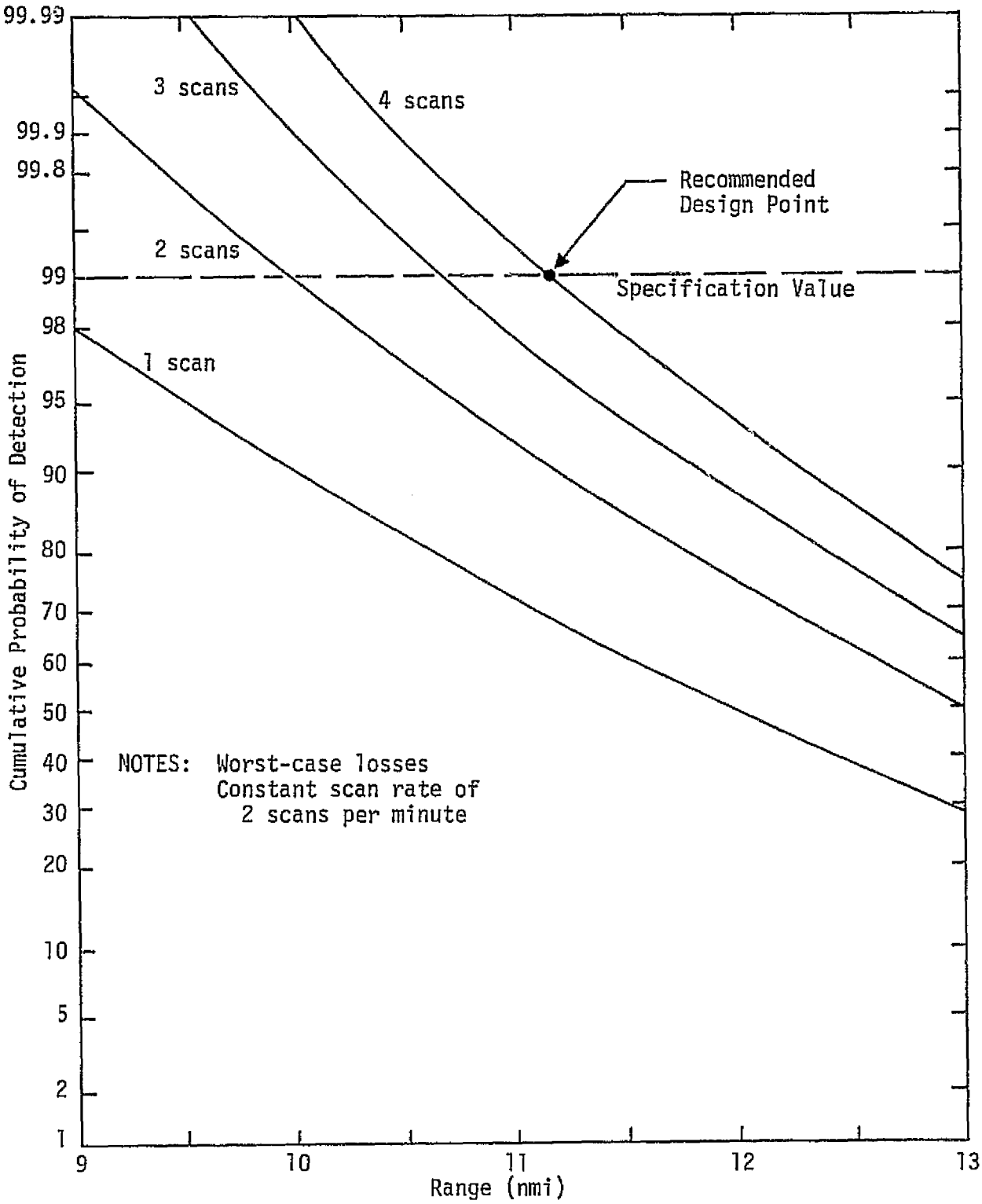

Figure 24. Cumulative Detection Probability Versus Range for Various Scans

amplitude scintillation are given. The tracking capability is then given in the presence of relative accelerations along and perpendicular to the LOS. Emphasis is placed on the recovery time after an acceleration.

3.8.1 Thermal Noise and Target Scintillation Effects on Tracking Accuracies for Passive Point Targets

The tracking accuracies of the four variables being tracked (range, range rate, angle, and angle rate) are presented as functions of range and compared to the existing specifications, as well as to the available HAC data. It is to be noted that there are two factors affecting the results:

(1) Thermal noise and target scintillation which become the dominating factors at long ranges.

(2) Quantization effects in the Ku-band radar [6] which uses 4 bits of quantization, resulting in a signal-to-noise ratio at the output of the A/D converter equal to

$$(SNR)_{out} = \left[\frac{1}{1 + \left[1 + (SNR)_{in}\right](0.0129)}\right](SNR)_{in}, \qquad (10)$$

where $(SNR)_{in}$ is SNR at the input of the A/D converter. Note that, for high $(SNR)_{in}$, the limit of $(SNR)_{out}$ is 18.9 dB. The signal at the output of the A/D converter is presumed with a resulting gain in $(SNR)_{out}$ equal to 16 (12.04 dB). It is easy to see from the above that, at high input SNR (close range), the resulting SNR saturates at

$$SNR = 18.9 + 12.04 = 30.94 \text{ dB}, \qquad (11)$$

which makes the quantization effect the major contributing factor to the tracking accuracies. The combined effect of both factors is taken into account in all subsequent calculations.

There are many parameters in the various tracking loops that are varied with the designated range. The parameters used in these calculations are the latest available from HAC and are summarized in Table 6.

3.8.2 Angle and Angle Rate Tracking Accuracies

The angle and angle rate tracking accuracies are presented together because the angle rate estimation is carried out in the angle tracking loop. Figures 25 and 26 illustrate the variations of $3\sigma_\theta$ and

Table 6. Summary of Tracking Loop Parameters (Passive Target)

Parameter	Range (nmi)						Remarks
	> 9.5	9.5-3.8	3.8-1.9	1.9-0.95	0.95-0.42	0.42	
d_t	0.099	0.116	0.058	0.029	0.0144	0.00085	Duty factor
τ_E (msec)	5.36	2.29	2.29	2.92	2.29	2.29	$1/B_F$
Δ (μsec)	33.2	16.6	8.3	4.15	2.07	0.122	Pulse width
α	0.0566	0.1132	0.2263	0.2263	0.4526	0.4803	
β	0.000884	0.00354	0.0283	0.0283	0.1132	0.1202	
B_F (Hz)	186	437	437	437	437	437	Doppler filter bandwidth
m	2	4	4	4	4	4	Number of averaged samples
T_s (msec)	107.2	45.9	45.9	45.9	45.9	45.9	
$L_{\theta,\dot{\theta}}$	16.90	16.83	16.83	16.83	16.83	16.83	Angle and angle rate losses
$L_{R,\dot{R}}$	9.49	9.42	9.42	9.42	9.42	9.42	Range and range rate losses
K	0.0288	0.0288	0.2221	0.5685	0.5685	0.5685	Angle loop gain
τ (sec)	12	12	4.25	2.7	2.7	2.7	Angle loop time constant
PRF (Hz)	2987	6970	6970	6970	6970	6970	

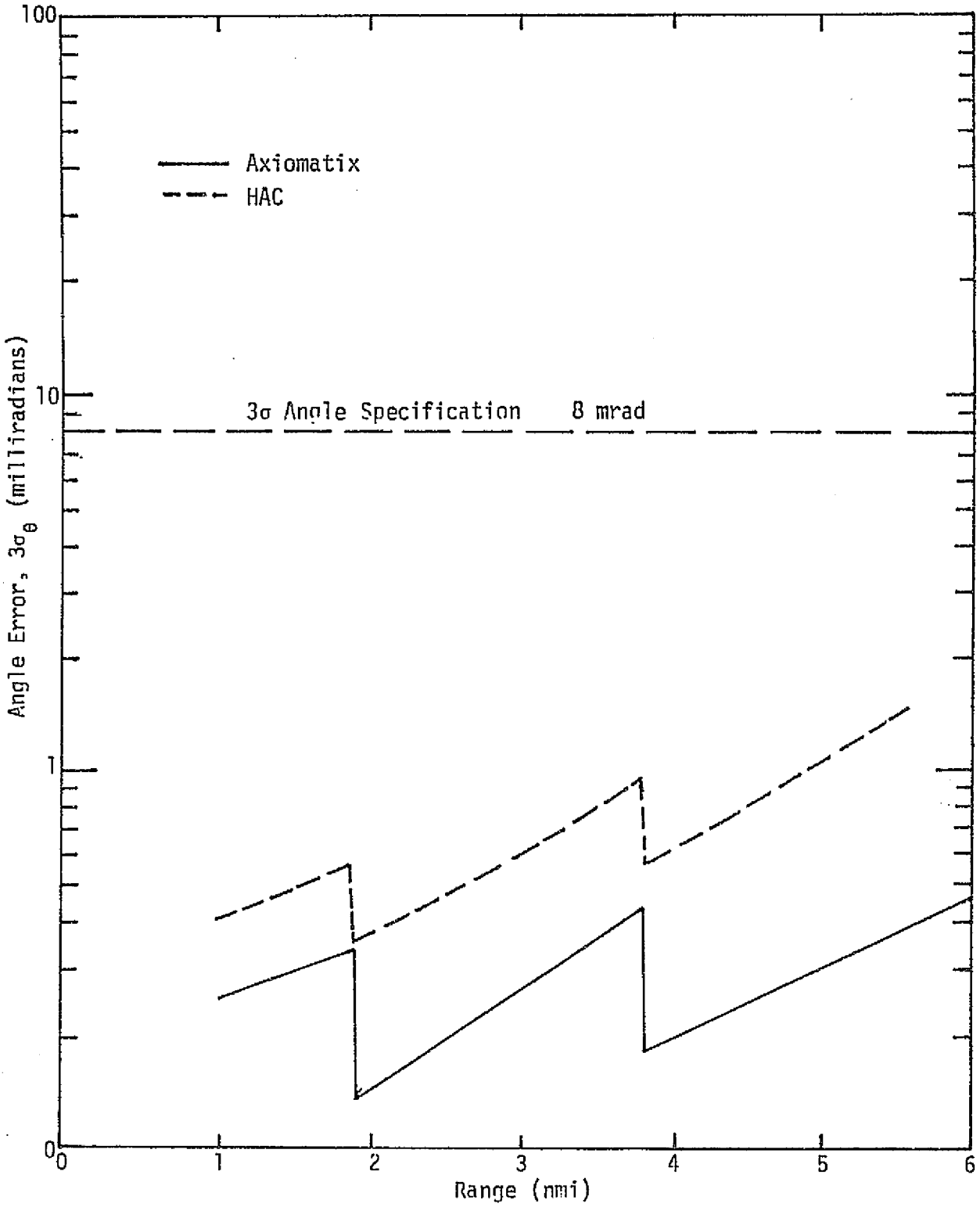

Figure 25. Angle Tracking Error of Passive Point Target Due to Thermal Noise and Target Scintillation Versus Range

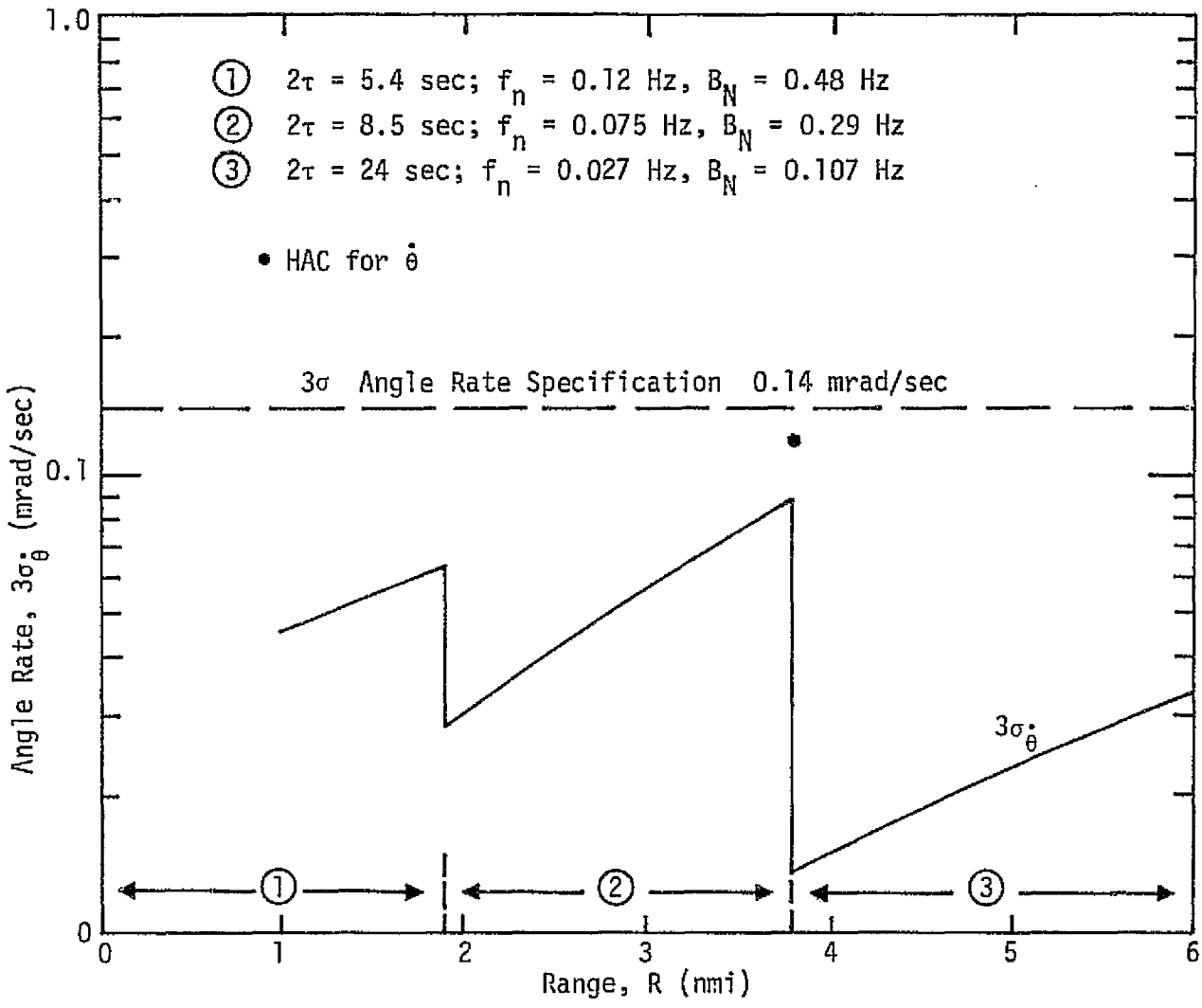

Figure 26. Angle Rate Estimation of a Passive Point Target Due to Thermal Noise and Target Scintillation Versus Range

$3\sigma_{\dot{\theta}}$ with range, along with the data obtained from HAC [9]. These performance predictions are developed in [6,7]. It is obvious that both the angle and angle rate accuracies meet the design specifications. The design margin in the angle rate tracking, however, is much less than that for the angle. This is due to the fact that the loop filter in the former has been widened to provide faster recovery from acceleration transients. It is believed that increasing the gain K slightly or effectively increasing the natural frequency f_n would improve the transient performance of the loop while maintaining the random error within or very close to specifications. It should be pointed out that, although some differences exist between the Axiomatix and HAC angle and angle rate performance curves, both results show the same trend and are well below specification limits. One area of concern is the angle rate accuracy at close range when the target accelerates in a direction orthogonal to the line of sight. Performance curves for angle rate tracking are presented in Section 3.8.2.1. In addition, since simulation efforts are underway to obtain additional data on the tracking capabilities of the Ku-band radar, normalized tracking errors are introduced in Section 3.8.2.2 which are independent of the Ku-band radar parameters that are range dependent.

3.8.2.1 Angle Rate Tracking Accuracy

This section is concerned with the angle rate tracking accuracy when the target accelerates in a direction perpendicular to the line of sight. This is of special importance in any rendezvous mission when retro rockets are fired to adjust the rendezvous trajectory. The analysis of the angle rate performance in an acceleration environment was presented in detail in [6]. No attempt will be made to repeat the analysis, and only new performance curves are presented.

The angle rate estimation takes place in the angle tracking loop whose gain K and time constant τ are given in Table 6, along with the other tracking loop parameters for a passive target. The noise-free assumption is warranted, especially at short ranges, because of the existing high SNR at these ranges. Figures 27, 28, and 29 illustrate the normalized angle rate error as a function of time for various parameters of interest. The actual angle rate error $\Delta\dot{\theta}(t)$ in mrad/sec is obtained by scaling the plots vertically in proportion to the actual acceleration (a) in ft/sec^2. This implies that the actual angle rate error at a given time

is equal to that obtained from the figures times the acceleration perpendicular to the line of sight in ft/sec^2.

Figure 27 illustrates the angle rate error due to acceleration at a range R = 0.5 nmi for burn times T = 1, 3 and 5 sec, which are typical expected burn times. It is easily observed that the recovery time, which is the time required for the error to settle within the specified 3σ accuracy of 0.14 mrad/sec, varies between 2 sec for T = 1 sec and 3.5 sec for T = 3 sec. These figures represent recovery times when the acceleration a = 1 ft/sec; they increase with the increase in acceleration. It should also be pointed out that, in order to obtain the cumulative angle rate error, the error due to acceleration should be added to the errors caused by thermal noise, bias, glint, etc.

Figures 28 and 29 illustrate the angle rate due to acceleration with range R as a parameter for burn times T of 1 and 3 sec, respectively. Similar observations can be made here. In addition, it can be seen that the error decreases with range and that the response at various ranges differs due to the variations in the angle tracking loop parameters as seen in Table 6.

It should be emphasized that all of these results assume a point target which is an ideal assumption suitable for analysis. Target effects are discussed in [7] and are believed to make major contributions to the error at short ranges.

3.8.2.2 Normalized Tracking Accuracies

Normalized tracking error expressions suitable for simulation purposes are derived in this section for the three parameters of interest, namely, range, range rate and angle. The angle rate rms error is shown in [7] to be proportional to the angle error and hence will not be discussed further. The rms tracking error due to thermal noise and target amplitude scintillation is developed in [6], where it is shown that

$$\sigma_R = \frac{\Delta c}{16}(B_{NR}T_s)^{1/2}\frac{\sigma_{XR}(SNR)}{\sqrt{\rho_R(SNR)}} \quad \text{for range,} \tag{12}$$

$$\sigma_{\dot{R}} = \frac{c\,B_F}{16\,f_c}\frac{1}{\sqrt{m}}\frac{\sigma_{\dot{X}R}(SNR)}{\sqrt{\rho_{\dot{R}}(SNR)}} \quad \text{for range rate,} \tag{13}$$

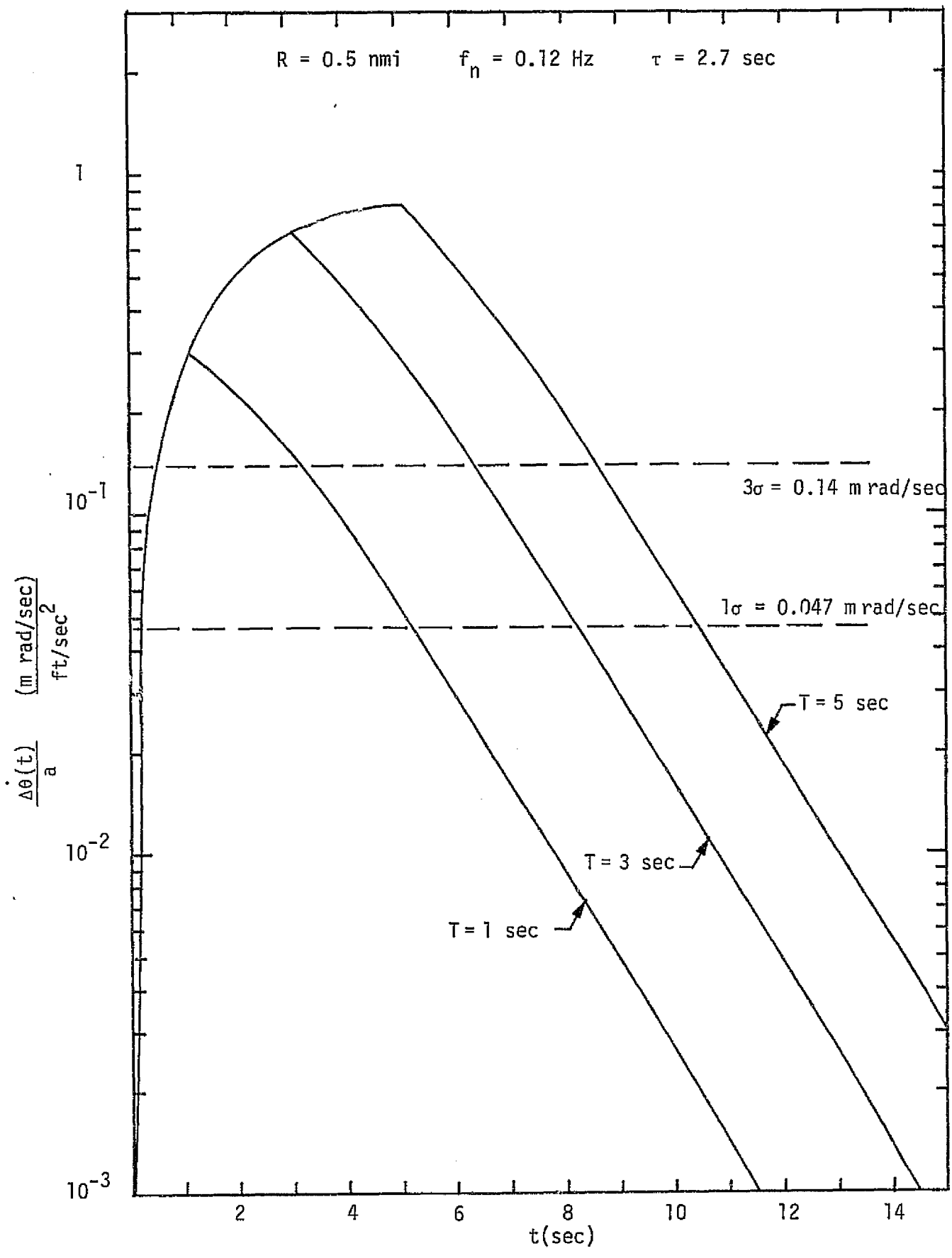

Figure 27. Angle Rate Accuracy with Acceleration Perpendicular to the Line of Sight with Burn Time as a Parameter; R = 0.5 nmi.

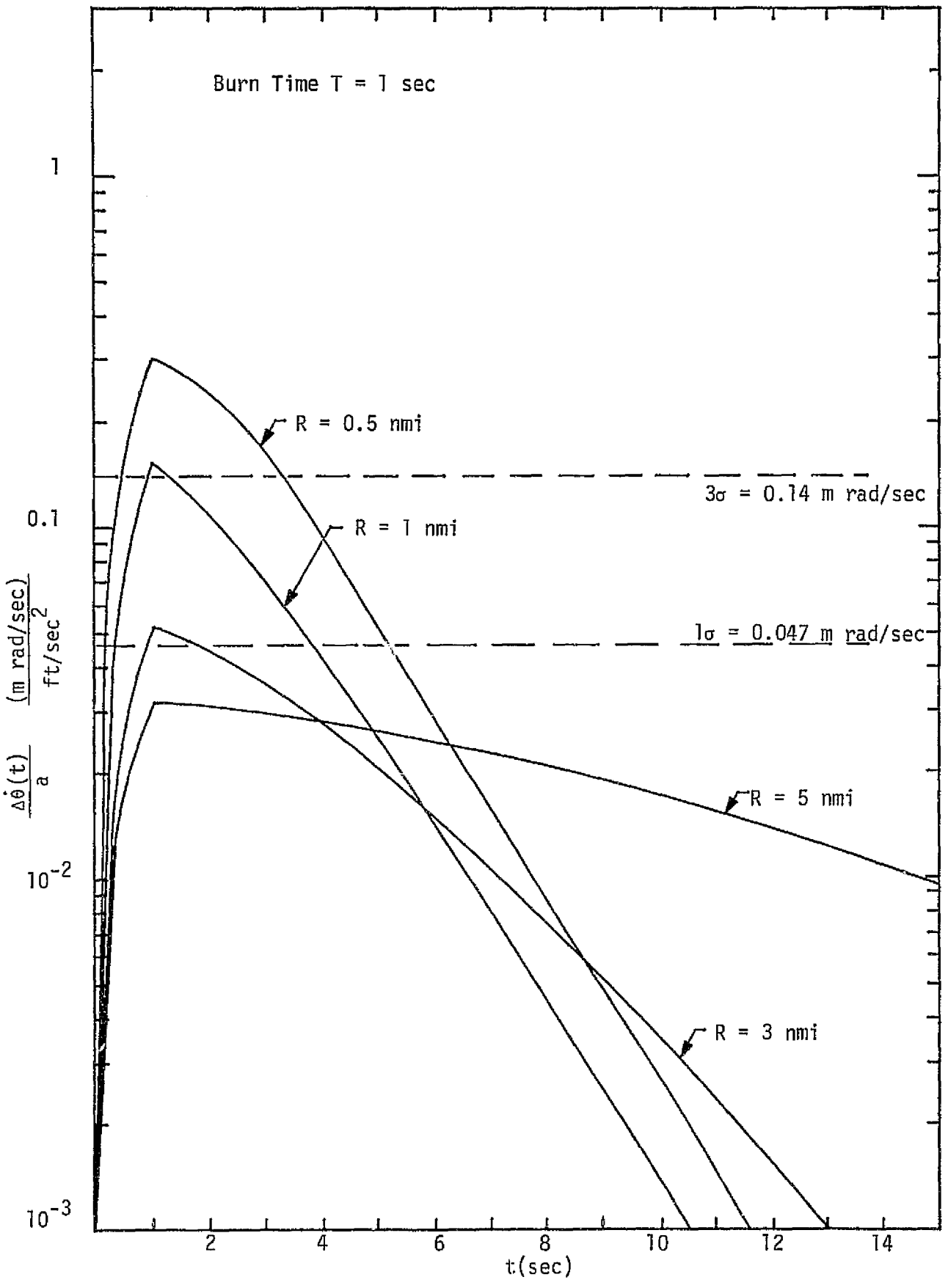

Figure 28. Angle Rate Accuracy with Acceleration Perpendicular to the Line of Sight with Range as a Parameter; Burn Time T = 1 sec.

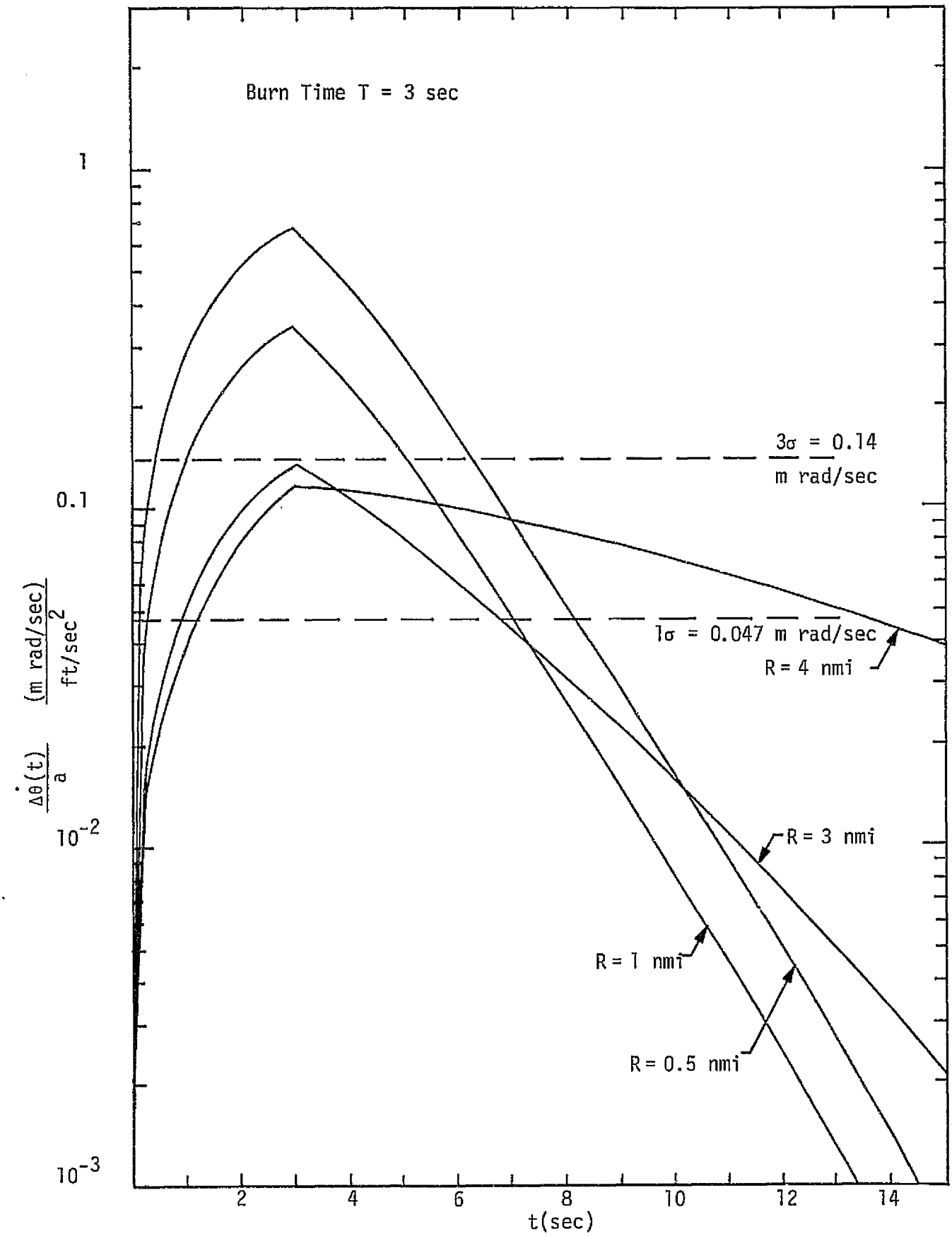

Figure 29. Angle Rate Accuracy with Acceleration Perpendicular to the Line of Sight with Range as a Parameter; Burn Time T = 3 sec.

and $$\sigma_\theta = \frac{\theta_B}{4}(B_{N\theta}\, T_s)^{1/2}\, \frac{\sigma_{X\theta}(SNR)}{\sqrt{\rho_\theta(SNR)}} \tag{14}$$

for angle, where c is the velocity of light in free space, f_c is the carrier frequency (13.85 GHz), and θ_B is the antenna beamwidth (1.6°). B_{NR} and $B_{N\theta}$ are the single-sided noise bandwidths of the range and angle tracking loops, respectively. They are given by

$$B_{NR} = \frac{8\rho_R \alpha^2 + \beta}{4\alpha T_s} \tag{15}$$

$$B_{N\theta} = \frac{K\tau^2 + 1}{4\tau}\,. \tag{16}$$

The parameters α, β, T_s, K, τ, Δ, B_F and m are system parameters that vary with range and are given along with their description in Table 1. Finally, $\sigma_{X\zeta}(SNR)$ is the normalized tracking standard deviation for the measured parameter ζ, and $\rho_\zeta(SNR)$ is the normalized correlation coefficient of ζ. The parentheses emphasize the dependence of $\sigma_{X\zeta}$ and ρ_ζ on the signal-to-noise ratio (SNR) [6].

In order to obtain normalized tracking accuracies, which are independent of the above system parameters, we define

$$\sigma_{\zeta N} \triangleq \frac{\sigma_\zeta}{C_\zeta} = \frac{\sigma_{X\zeta}}{\sqrt{\rho_\zeta}}\,, \tag{17}$$

where ζ denotes any one of the three parameters of interest and C_ζ are constants that depend on the above system parameters, namely,

$$C_R \triangleq \frac{\Delta c}{16}\sqrt{B_{NR}\, T_s} \tag{18a}$$

$$C_{\dot{R}} = \frac{c\, B_F}{16\, f_c}\,\frac{1}{\sqrt{m}} \tag{18b}$$

$$C_\theta \triangleq \frac{\theta_B}{4}\sqrt{B_{N\theta}\, T_s}\,. \tag{18c}$$

Figures 30 and 31 illustrate the normalized tracking accuracies σ_{RN}, $\sigma_{\dot{R}N}$, and $\sigma_{\theta N}$ as functions of the signal-to-noise ratio (SNR) at the

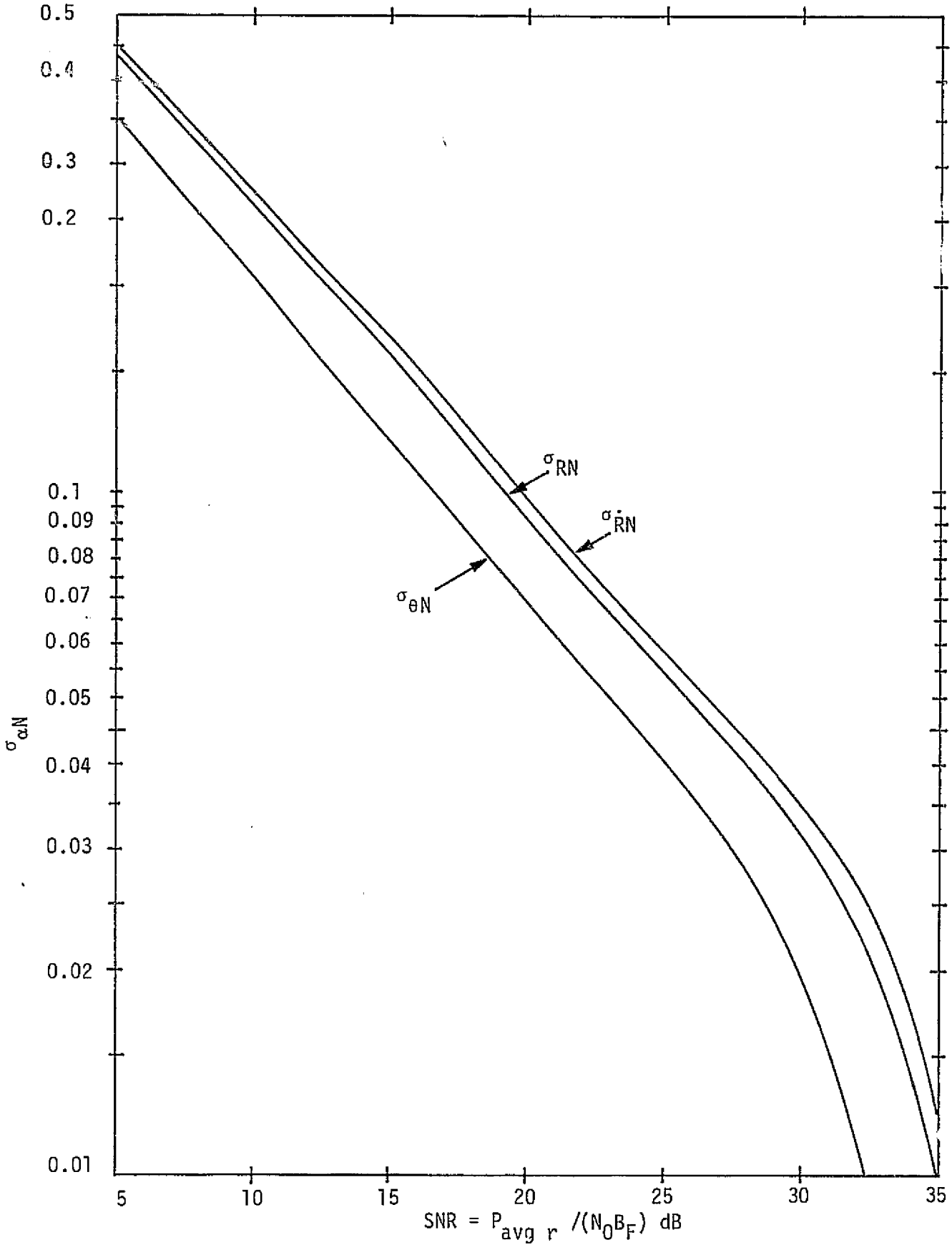

Figure 30. Normalized Tracking Accuracies versus SNR at High SNR

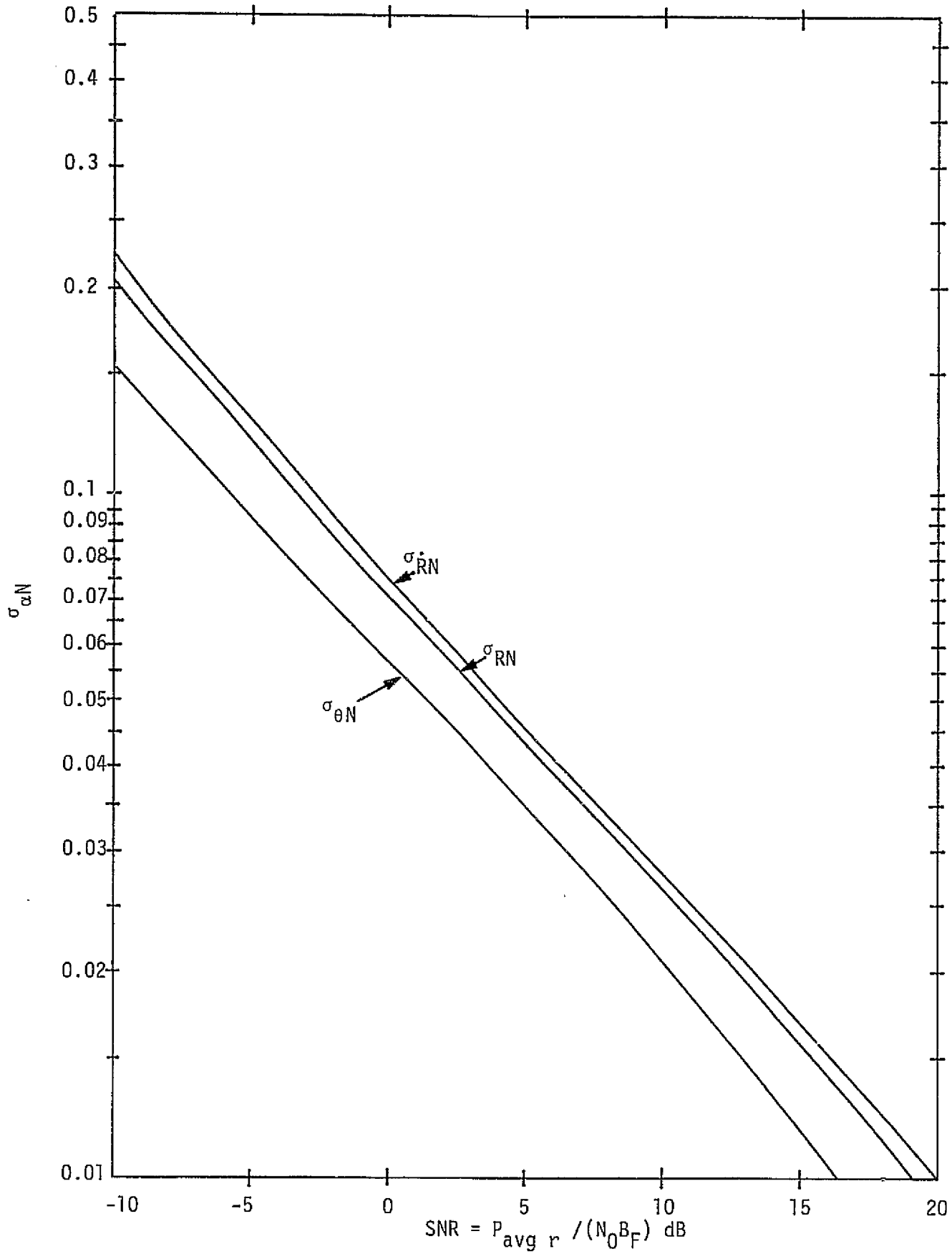

Figure 31. Normalized Tracking Accuracies versus SNR at Low SNR

output of the doppler filters for high and low SNRs, respectively. SNR is defined as

$$SNR \triangleq \frac{P_{avg\,r}}{N_0 B_F}, \tag{19}$$

where $P_{avg\,r}$ is the average received power, B_F is the one-sided doppler filter bandwidth, and N_0 is the single-sided noise spectral density in W/Hz.

These curves can be used to obtain the tracking accuracy of any of the three parameters at any range after multiplying the proper reading with the appropriate constant from (18a), (18b), or (18c).

3.8.3 Range Tracking Accuracies

Figure 32 illustrates the variations of the range error at ranges ($R < 6$ nmi) with the latest values of α and β as parameters. The figure also shows the latest performance curve presented by HAC [10] for comparison purposes. There are four points to observe:

(1) The range tracking performance of a passive point target due to thermal noise and target scintillation is well below the specifications, especially at close range.

(2) The flat portions of the curve at ranges $R < 1$ nmi are due to quantization limiting effects.

(3) The difference between the Axiomatix and HAC performance curves is believed to be due to the automatic gain control (AGC) which has not been taken into account in the analysis.

(4) Although the accuracies at close range drop below 10 feet, it is believed that 10 feet is the best achievable accuracy because of the sensitivity of the display meters. As shown in [6], the range accuracy meets the specifications up to 9.5 nmi.

3.8.4 Range Rate Tracking Accuracy

The evaluation of $\sigma_{\dot{R}}$ for various ranges ($2 \leq R \leq 12$ nmi) is shown in Figures 33 and 34. Figure 33 illustrates range rate errors at long ranges and shows the effect of varying the number of averaged samples (m) at 9.5 nmi. Figure 34 illustrates the calculated range rate errors at short ranges and compares them with those presented by HAC [10]. As is obvious

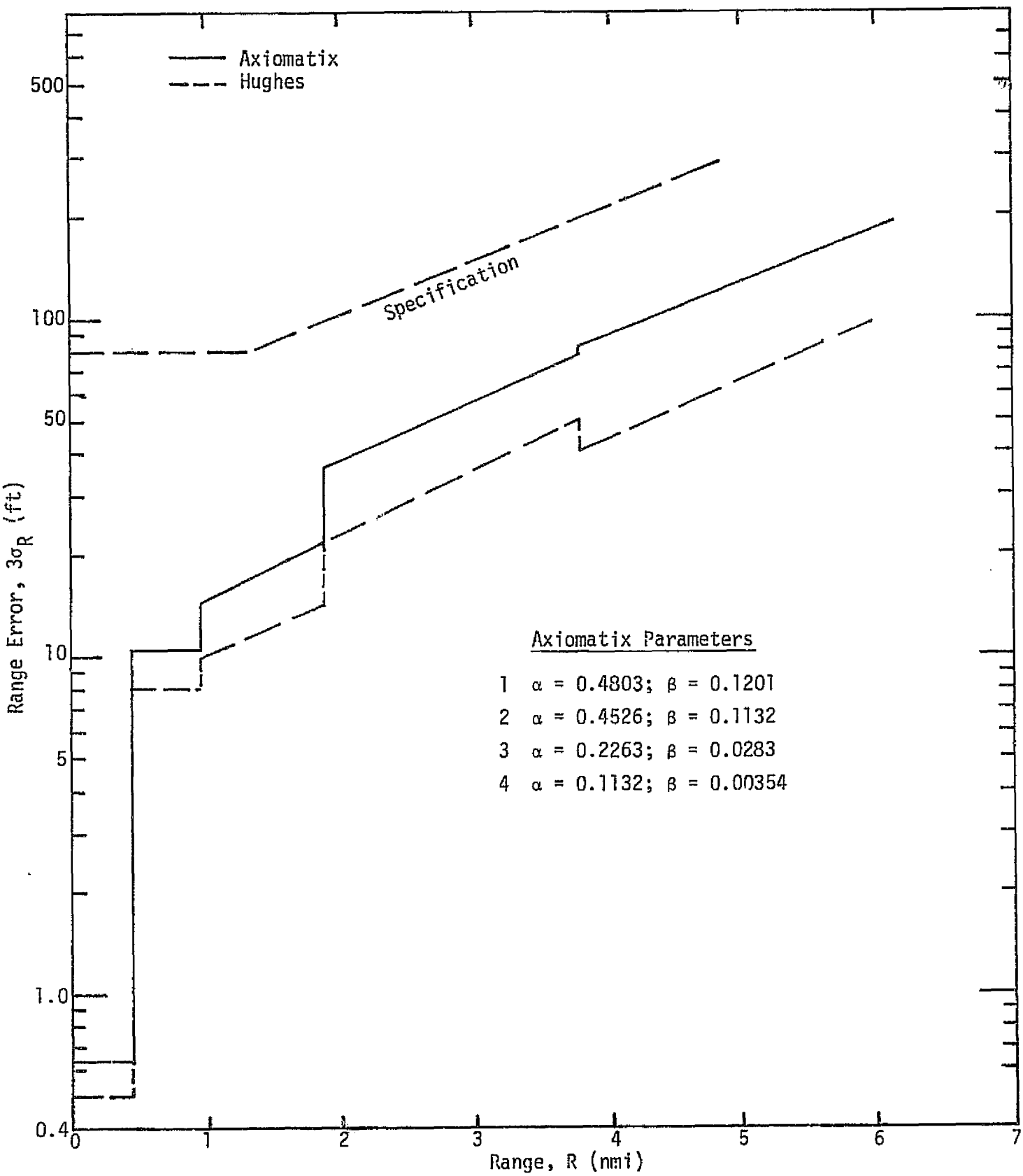

Figure 32. RMS Range Tracking Error of Passive Point Targets at Close Range Versus Range

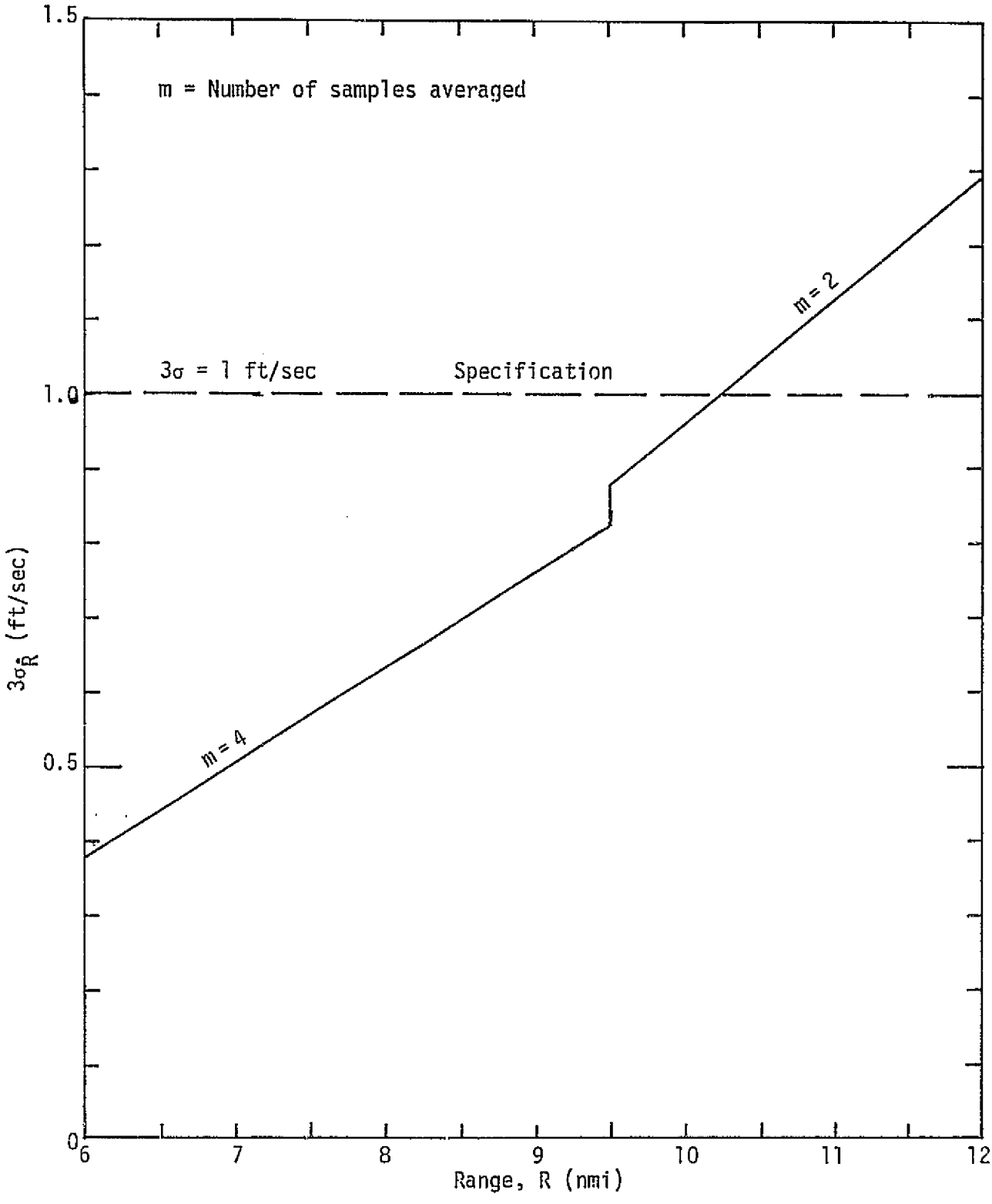

Figure 33. RMS Range Rate Tracking Error Due to Thermal Noise and Target Scintillation of Passive Point Targets Versus Range (Long Ranges)

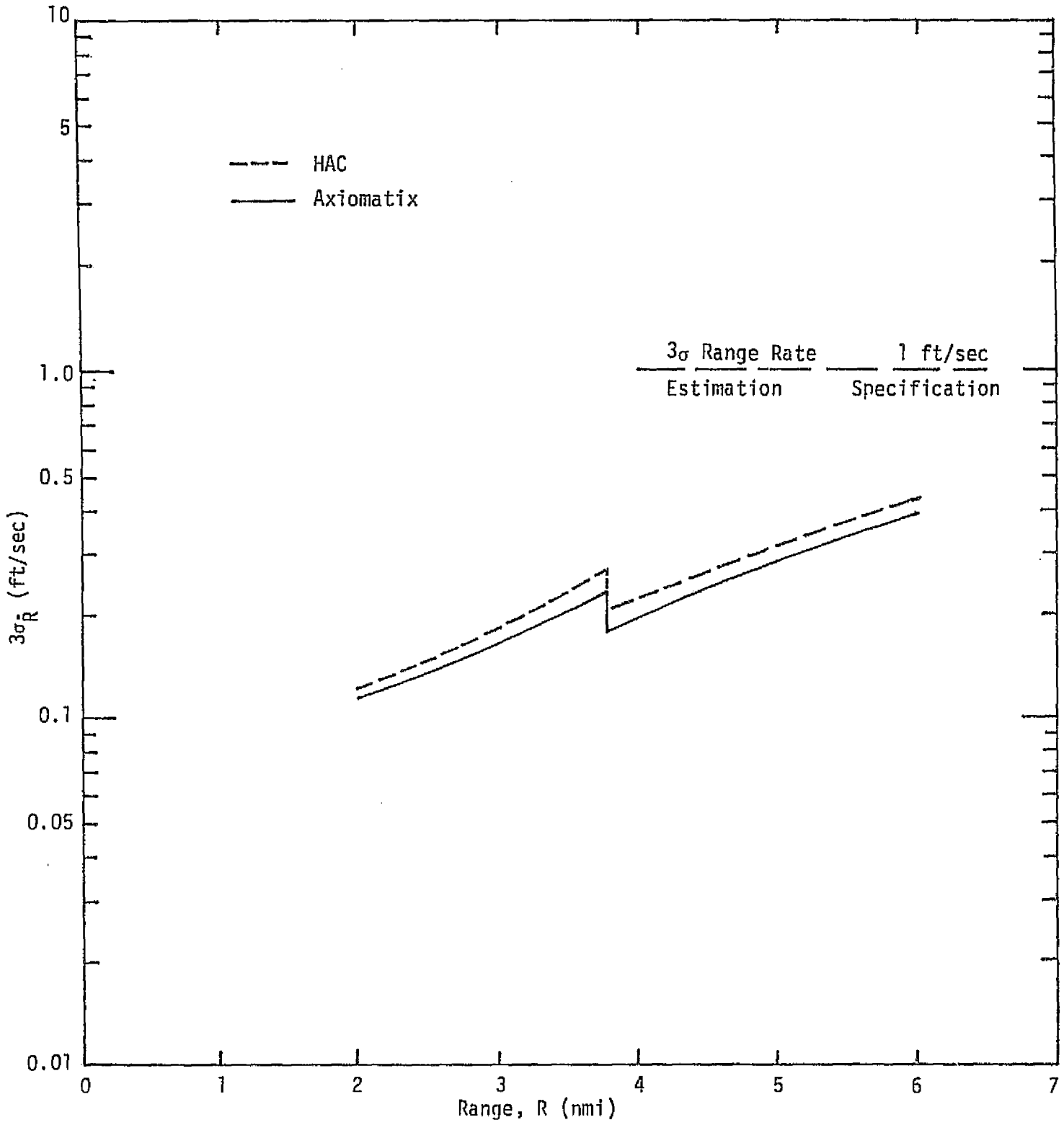

Figure 34. RMS Range Rate Tracking Error Due to Thermal Noise and Target Scintillation of Passive Point Targets Versus Range (Short Ranges)

from the figure, the range rate accuracies meet the specifications for all ranges below the specified 10 nmi. The same is true for short ranges [7].

3.8.5 Effects of Point Target Accelerations

This section investigates the performance of the Ku-band radar system in the tracking mode when constant acceleration takes place. Two extreme cases can be distinguished; the first will be referred to as radial acceleration which is achieved by firing retro rockets in the direction of the LOS. This causes the range to vary as a quadratic function of time rather than as a linear function of time, which occurs in the case of a constant approaching velocity (range rate). The second case will be referred to as tangential acceleration, which is an acceleration in a direction perpendicular to the LOS, causing a quadratic variation in the target angle being tracked. Since both the azimuth and elevation angles are tracked similarly [6], this section will not distinguish between the two angles.

The results of an analysis of the tracking loops in the presence of acceleration is presented in this section for a deterministic input. The deterministic input is a realistic assumption for the range of interest, namely, close range when the SNR is high.

3.8.6 Radial Acceleration

A constant radial acceleration causes the range to change as a quadratic function of time without affecting the angle measurements. A detailed analysis of the effect of radial acceleration is presented in [7]. A typical response of the loop to radial accelerations is shown in Figure 35, which shows the variations of error ΔR for a radial acceleration of $A = 0.1$ g and a burn time of $T = 10$ sec at a range of 2 nmi. It can be easily seen that the error due to 0.1 g acceleration is well below the 1σ specification for the range error ($1\sigma = 40$ ft at 2 nmi). Since it is believed that the value of the acceleration (A) will actually be of the same order of magnitude as 0.1 g or less, no problems are anticipated in tracking radial accelerations during target approach.

3.8.7 Tangential Acceleration

While it was shown that the radial acceleration affects the range measurements, the tangential acceleration has a direct effect on the angle and angle rate measurements [6,7].

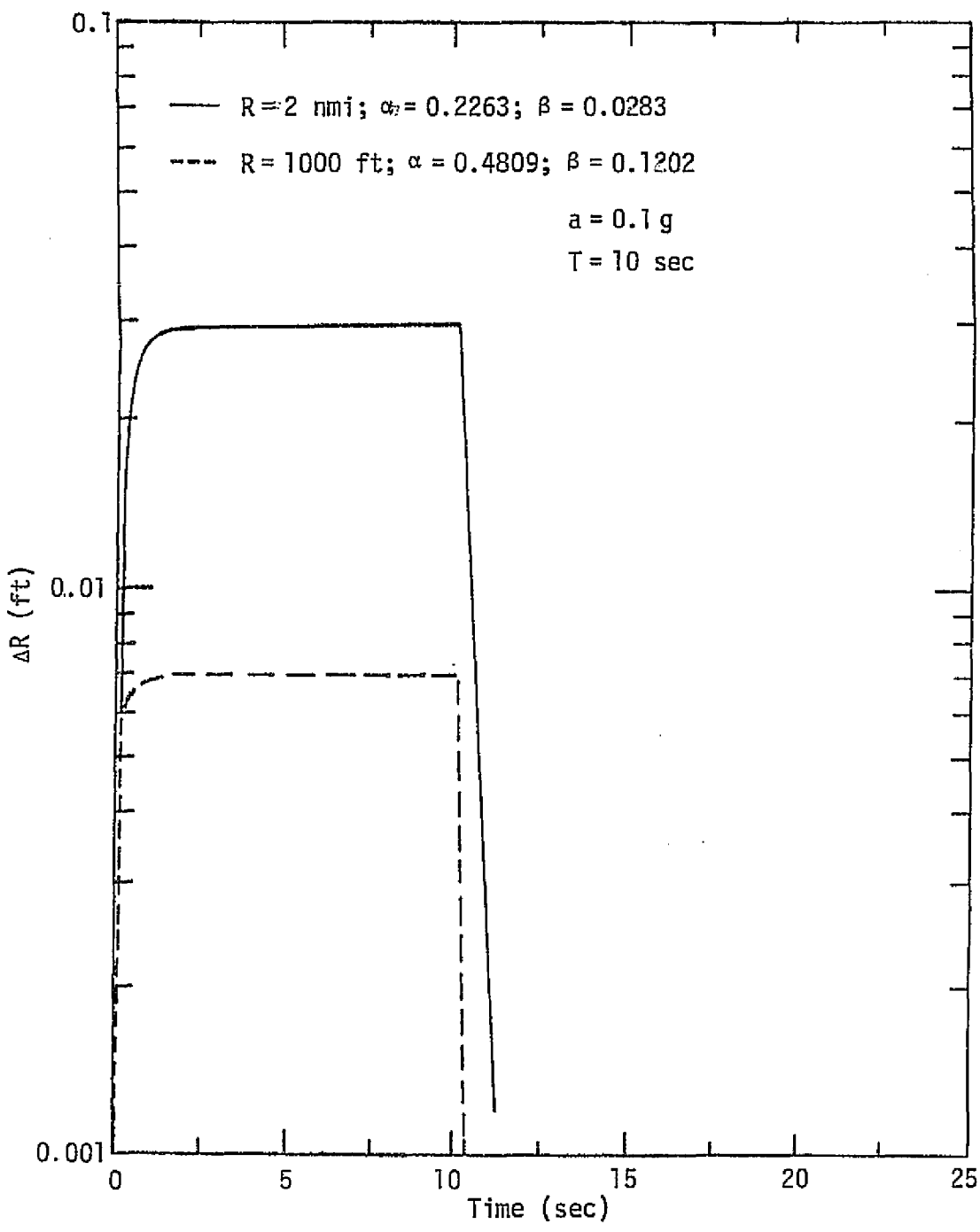

Figure 35. Range Error Due to Constant Acceleration Lasting T Seconds (R = 2 nmi)

The angle and angle rate transient accuracies are discussed in detail in [6,7]. Figures 36 and 37 illustrate these accuracies with range as a parameter with a burn time T = 10 sec and an acceleration A = 0.1 g. Using these figures and [5,6], it can be concluded that the angle error due to acceleration is always less than 3σ and is less than 1σ for all the cases considered except for ranges less than 1000 feet and burn times larger than 2 seconds. In the latter two cases, the recovery time, which can be defined as the time required after the burn to reside below the specifications (1σ), is equal to 4 seconds. Since the actual amplitudes of acceleration are believed to be in the range of 0.1 g or less, the angle errors due to tangential accelerations are not believed to constitute a major problem for angle tracking.

It is evident, however, that the angle rate errors due to acceleration exceed the 3σ angle rate specifications for all cases studied. For the close range of 1000 feet, the recovery times to reside within 1σ of the angle rate specifications are 8, 8.75, 9.25, and 9.30 sec for burn times of 1, 2, 5 and 10 sec, respectively. All of these recovery times exceed the desired 2-sec recovery time. In order to reduce the angle rate acceleration errors to the desired levels, the equivalent noise bandwidth of the angle tracking loop has to be widened considerably, which would result in an appreciable increase in the angle and angle rate errors due to thermal noise. It is believed that, short of major design changes, any attempt to reduce the angle rate recovery times to within the desired value of 2 sec is unrealistic.

A compromise can be worked out in such a way as to make the thermal noise tracking accuracy of the angle rate marginal and improve on the transient performance by widening the angle loop noise bandwidth. The extent of this compromise is dependent on the navigation needs of the astronauts.

Responses from other values of accelerations for any of the cases in this section can be obtained simply by scaling the desired value with respect to that shown on the appropriate figure. This is due to the fact that, at high values of SNR and the small accelerations considered, the systems are nearly linear. The same scaling cannot be carried out in the time dimension, however.

1 R = 10 nmi; f_n = 0.027 Hz; 2τ = 24 sec; B_N = 0.107 Hz
2 R = 2 nmi; f_n = 0.075 Hz; 2τ = 8.5 sec; B_N = 0.29 Hz
3 R = 1000 ft; f_n = 0.12 Hz; 2τ = 5.4 sec; B_N = 0.48 Hz

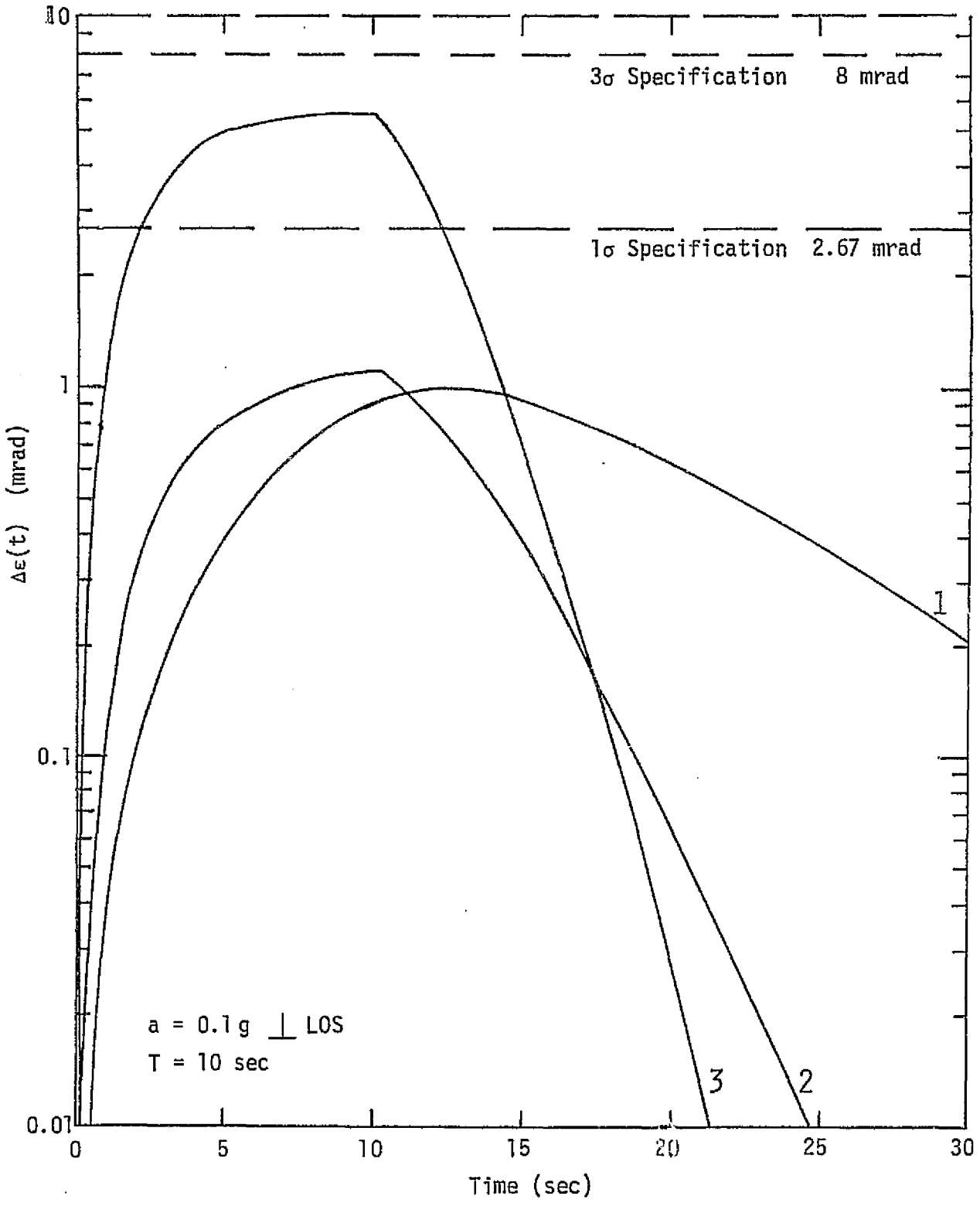

Figure 36. Angle Error Due to Tangential Acceleration With Range as a Parameter

1 R = 10 nmi; f_n = 0.027 Hz; 2τ = 24 sec; B_N = 0.107 Hz
2 R = 2 nmi; f_n = 0.075 Hz; 2τ = 8.5 sec; B_N = 0.29 Hz
3 R = 1000 ft; f_n = 0.12 Hz; 2τ = 5.4 sec; B_N = 0.48 Hz

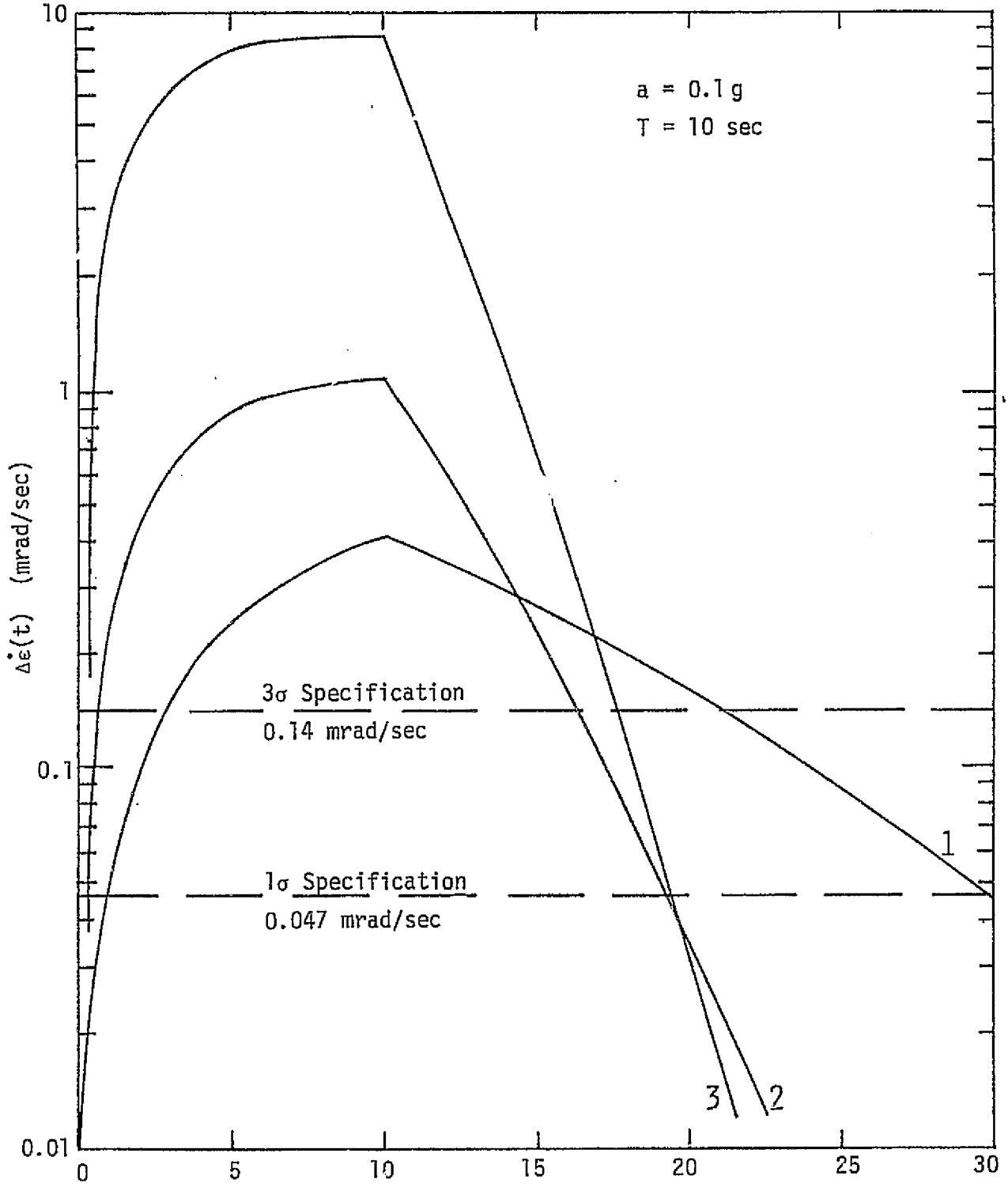

Figure 37. Angle Rate Error Due to Acceleration With Range as a Parameter

4.0 ELECTRONIC ASSEMBLY 2

The block diagram of the Electronic Assembly 2 (EA-2) is shown in Figure 38, with the main command and status signals indicated. Since the unit is implemented mainly for use in the radar mode and discussed in detail in Section 3.0, no detailed discussion of the radar signal flow is presented here. This section is devoted to explaining the main command signals between EA-2 and the other Ku-band units, as well as pointing out the major existing problems in the radar mode of operation.

The 78 MHz radar ($\Delta + \Sigma$) signal is received from the DEA receiver by the EA-2 analog processor, which applies 20 dB of automatic gain control before mixing it with two quadrature 78 MHz reference signals. The reference signals are generated from a 156 MHz signal from EA-1. The resulting orthogonal signals are filtered by a variable bandwidth video filter before being A/D converted by four bit encoders to digital signals.

As explained in Section 3.0, the resulting complex signal is pre-summed and the output of the pre-sum is filtered using discrete Fourier transforms (DFT) to approximately determine the doppler frequency. Sixteen filters are used in the search mode and 32 filters are used in the track mode.

Post-detection is used to detect the presence of targets and to send a signal to EA-1 declaring the detection of a target. In the track mode, the signal is sent to a logarithmic discriminator that forms the error signals for the range, range rate and angle tracking loops. It also puts out a signal to be used by the AGC block to generate the required AGC signal for use in the DEA and the analog processor.

The range tracking loop outputs three main signals. The first is used by the timing and mode control circuits to adjust the positions of the range gates. The second is used in the open range rate tracking loop to resolve range rate ambiguity, and the third is sent to the interface circuits before sending it to EA-1. The angle tracking loop is also used to generate angle rate estimates for both the azimuth and elevation angles. Its outputs are used in the EA-1 control electronics to adjust the antenna position and are sent to the Orbiter via the interface with EA-1.

One of the most critical aspects of EA-2 is the timing and mode control block which receives commands from the interface indicating the

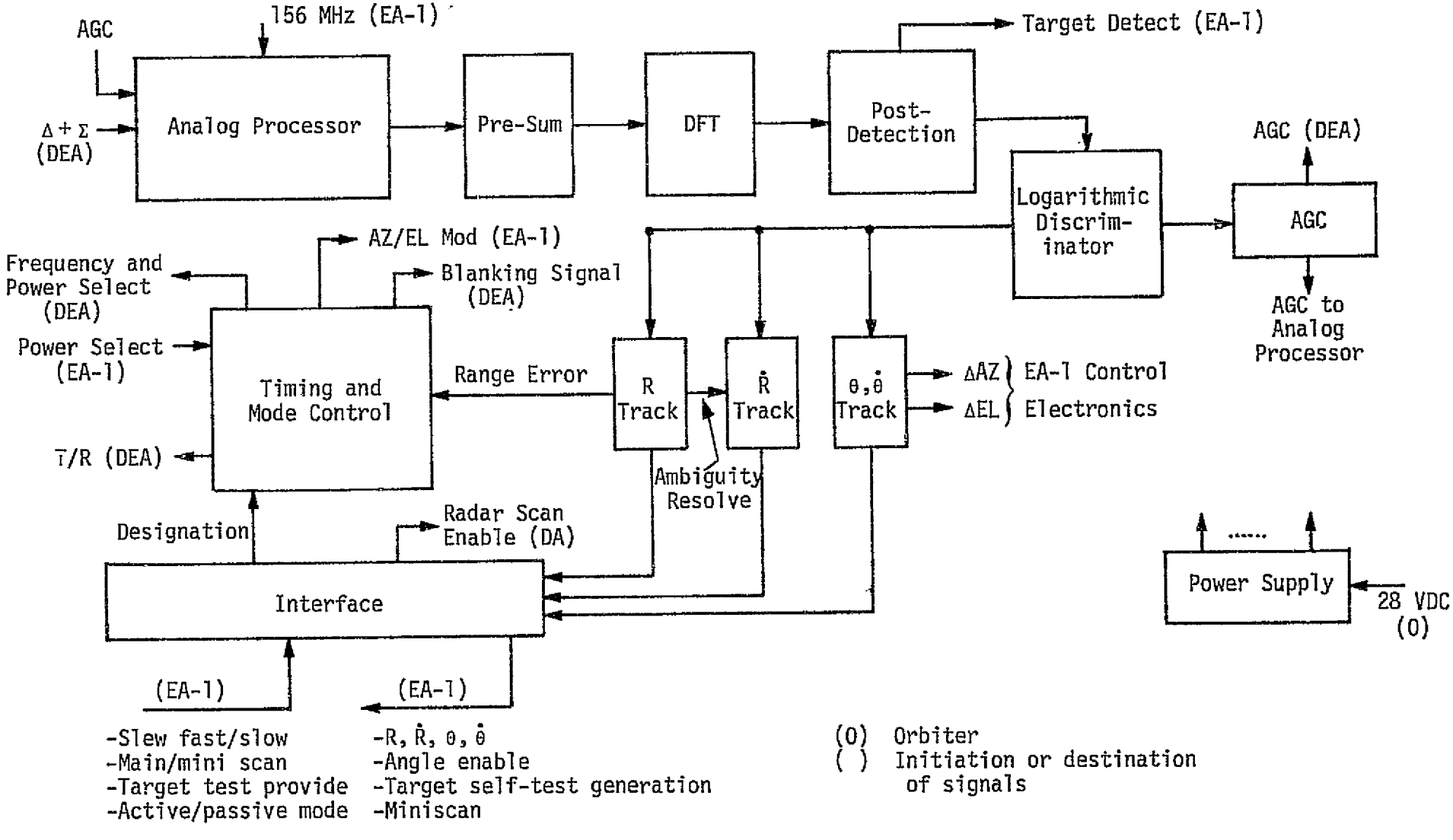

Figure 38. Electronic Assembly 2 Block Diagram

designations of targets in the designated mode or switching the system to the undesignated mode. It also receives information concerning whether the target is active or passive. All of these commands are sent from EA-1 to EA-2 via the interface circuity. The timing circuit also receives a command directly from EA-1 so as to direct an attenuator at the DEA to select the proper radar signal power to be transmitted. It also controls the timing and selection of the five radar frequencies generated at the DEA for frequency diversity purposes in the passive mode or chooses the middle frequency in the active mode. The transmit/receive (T/R) gates in the DMA and DEA are also controlled by signals from the timing and control circuitry which, in addition, control the operation of the blanking signal that is generated in the DEA (exciter) to appropriately switch the diode switches in the DEA (receiver) (see Section 3.3). Another important signal issued by this block is the Az/El modulated signal which is used by the EA-1 angle servo in the radar mode to control the torque on the antenna driving motors. The timing and controls also monitor the antenna steering mode and the range designation word during search.

The main signals received or sent by the EA-2 interface can be summarized as follows:

(1) Signals to EA-1

- Range, range rate, angle and angle rate measurements in the track mode
- Angle enable signal which implies that acquisition is completed
- Target self-test generation in the self-test mode
- Miniscan signal to be used after search is terminated and acquisition is to be initiated

(2) Signals from EA-1

- Slew rate of the antenna which is used in the search mode sequence
- A main or miniscan signal
- A signal that initiates target test
- Mode (active or passive)
- Various other signals, including designation, antenna steering, etc.

A more detailed and lengthy description of sequencing and other control signals can be found in [1] and [11].

The major problems in EA-2, as shown in Section 3.0, can be summarized as:

(1) The detection margins are negative for the worst-case design and are marginal for average losses design at 10 nmi. An increase in the scanning time is recommended to assure adequate performance with minimal hardware impact.

(2) The angle rate accuracies are marginal for some ranges, and the angle rate transient responses to acceleration normal to the line-of-sight do not settle fast enough to meet the specifications. Any attempt to widen the angle loop bandwidth to improve the transient response will have an adverse effect on the steady-state tracking performance of the loop. It is believed that, unless major design changes are made, a compromise between the steady-state performance and the transient performance of the angle tracking loop has to be worked out.

(3) There is a discrepancy between the range rate logarithmic discriminant error calculated by Axiomatix and that calculated by HAC. This might be due to the method HAC uses to implement the mapping between the doppler offset and the expected mean of the discriminant [7]. Further HAC documentation is needed before resolving this discrepancy.

(4) It is believed that the angle and angle rate measurements for large targets will not be dependable at close ranges. These ranges are functions of the target size and shape. It is believed that further analysis has to be performed before an optimum solution to the problem is reached.

5.0 FORWARD LINK

The function of the forward link is to receive the communication signal from the TDRS and process this signal before handing it over to the various Orbiter equipments. The processing starts at the DA by downconverting and power amplifying the signal. Recovery of the carrier and despreading of the signal whenever a spread spectrum signal exists are carried out in EA-1. Two modes exist in the SPA which result in either buffering the data before sending it to the Orbiter or demodulating the data and then sending it to the Orbiter. The demodulation of the data involves the ability to achieve bit synchronization and frame synchronization.

In order to adequately describe the forward link, the input signal and noise levels are traced to give the maximum and minimum expected signal-to-noise ratios at various parts of the system. A summary of these signal levels is given in Section 5.1, with the detailed analysis carried out in Appendix A, which also includes the tracking performance of the Costas loop (used in EA-1 to recover the carrier) and the tau-dither loop (used in EA-1 to track the PN code). Section 5.2 discusses the signal flow in the DA and EA-1, while Section 5.3 discusses the two modes that exist in the SPA and the signal processing involved in each mode.

5.1 Input Signal and Noise Levels

The received signal-to-noise ratio at the output of the Shuttle antenna depends on the effective isotropic radiated power (EIRP) delivered by the TDRS, the distance between the Shuttle and the TDRS (path loss), and the Ku-band antenna geometry.

To provide a satisfactory forward link performance, the Shuttle Ku-band communication receiver must accommodate a range of received power levels. Using the Ku-band antenna gain of 38.5 dB and the corresponding effective area A_e, Figure 39 illustrates the power densities at the Ku-band Orbiter antenna and the corresponding power levels versus TDRS EIRP and range. The range changes [12] result in the path loss variations shown in Table 7.

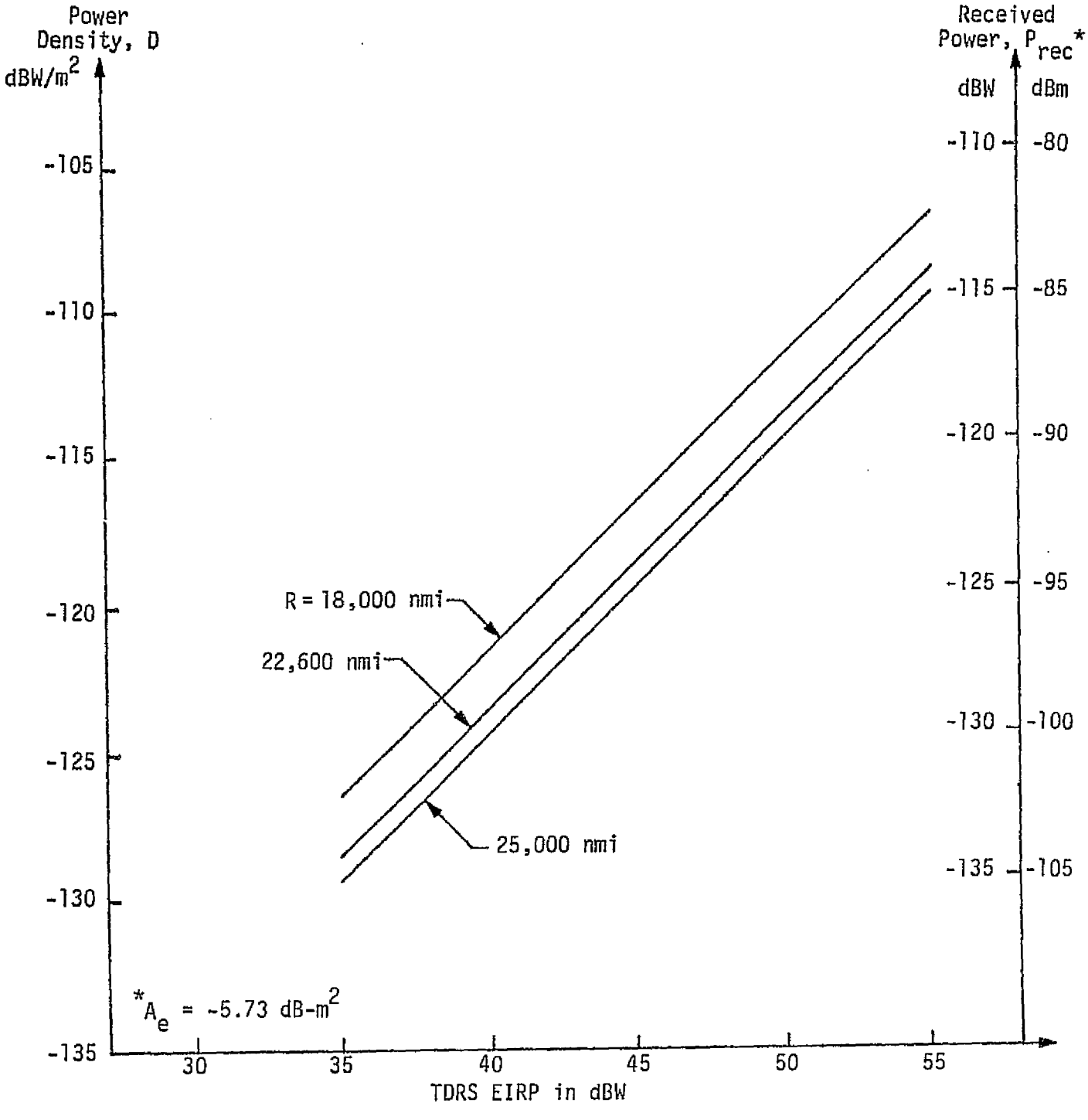

Figure 39. Power Density at Ku-Band Orbiter Antenna and Corresponding Received Power Level Versus TDRS EIRP and Range

Table 7. Path Loss Versus Orbiter-to-TDRS Range

Range (nmi)	Range (meters)	Path Loss ($dB\text{-}m^2$)	Comment
18,000	3.34×10^7	161.5	Minimum
22,600	4.19×10^7	163.5	Nominal
25,000	4.63×10^7	164.3	Maximum

Considering the EIRP variations, the higher values of EIRP (i.e., 50 to 55 dBW) are characteristic of a "hot transmitter" (a new tube, start-of-life-cycle operation) at the TDRS. These values are above a typical "high power" mode +48.5 dBW minimum output [12]. The EIRP levels below the +48.5 dBW value correspond to conditions existing when the TDRS antenna is not pointed directly at the Shuttle. Therefore, the lower values of the EIRP are the "effective" values presented to the Shuttle antenna. These values typically occur during the spatial acquisition phase of the Ku-band Orbiter/TDRS link.

Taking the values of -126.9 dBW/m^2 and -113.5 dBW/m^2 as minimum and maximum flux densities with which the receiver must meet the specifications, Table 8 summarizes the respective receive power levels in the acquisition mode, tracking mode, and minimum range mode, which is actually 2 dB above the nominal specification parameter mode based on the range of 22,600 nmi.

Table 8. Ku-Band Signal Levels at Acquisition, Tracking and Nominal Link Operation Point

	Acquisition	Tracking	Minimum Range
Incident Flux Density, dBW/m^2	-126.9	-126.9	-113.5
Antenna Area, $dB\text{-}m^2$	-5.7	-5.7	-5.7
Polarization Loss, dB	-0.2	-0.2	-0.2
Pointing Loss, dB	-3.0	-0.3	-0.3
Received Power, dBW	-135.8	-133.1	-119.7
(dBm)	(-105.8)	(-103.1)	(-89.7)

C-2

The resulting maximum power variation at the antenna is then 16.1 dB.

The single-sided noise spectral density is computed in Appendix A to be $N_0 = -196.6$ dBW/Hz; hence, the input carrier power-to-noise spectral density ratios C/N_0 are 60.8 dB-Hz, 63.5 dB-Hz, and 76.9 dB-Hz for the acquisition mode, tracking mode and minimum range mode, respectively.

Figure 40 shows the block diagram of the Ku-band receiver configuration, comprised of the DMA, DEA and EA-1. The basic architecture of the equipment is that of a two-channel monopulse receiver. One channel is used for amplifying the sum (Σ) output of a two-axis monopulse antenna; the second channel amplifies the time-multiplexed ΔAZ and ΔEL signals developed by the monopulse bridge of the antenna. The receiver utilizes double conversion with all of the data demodulation related functions performed at the second IF. The time-multiplexed angle tracking modulation, however, is detected at the first IF to minimize the overall number of the receiver components.

The gains and losses of the major subunits and the appropriate signal levels, both minimum and maximum, are indicated in Figure 40. It is important to point out that, as shown in the figure, the dynamic range of the signal levels handled by the receiver is comprised of two components: (1) the change in the input signal strength ($\approx$16 dB) and (2) the variation in the amplifier gains over the temperature range. Examination of the design review data [13] indicates that gain variations of the receiver subunits contribute an additional 10 dB dynamic range requirement over the specified range of the operating conditions. Thus, the total dynamic range requirement imposed on the automatic gain and level control is about 26 dB.

5.2 Forward Link Signal Flow in DA/EA-1

Two channels have to be considered in this discussion, the sum channel (Σ) and the difference channel (Δ).

Consider first the signal flow through the sum channel of the receiver. The received 13,775 MHz signal power output by the sum channel antenna feed, which is a part of the deployed mechanical assembly (DMA), is passed through the rotary joint and is applied to a bandpass filter (BPF 1A) and a limiter. The function of the

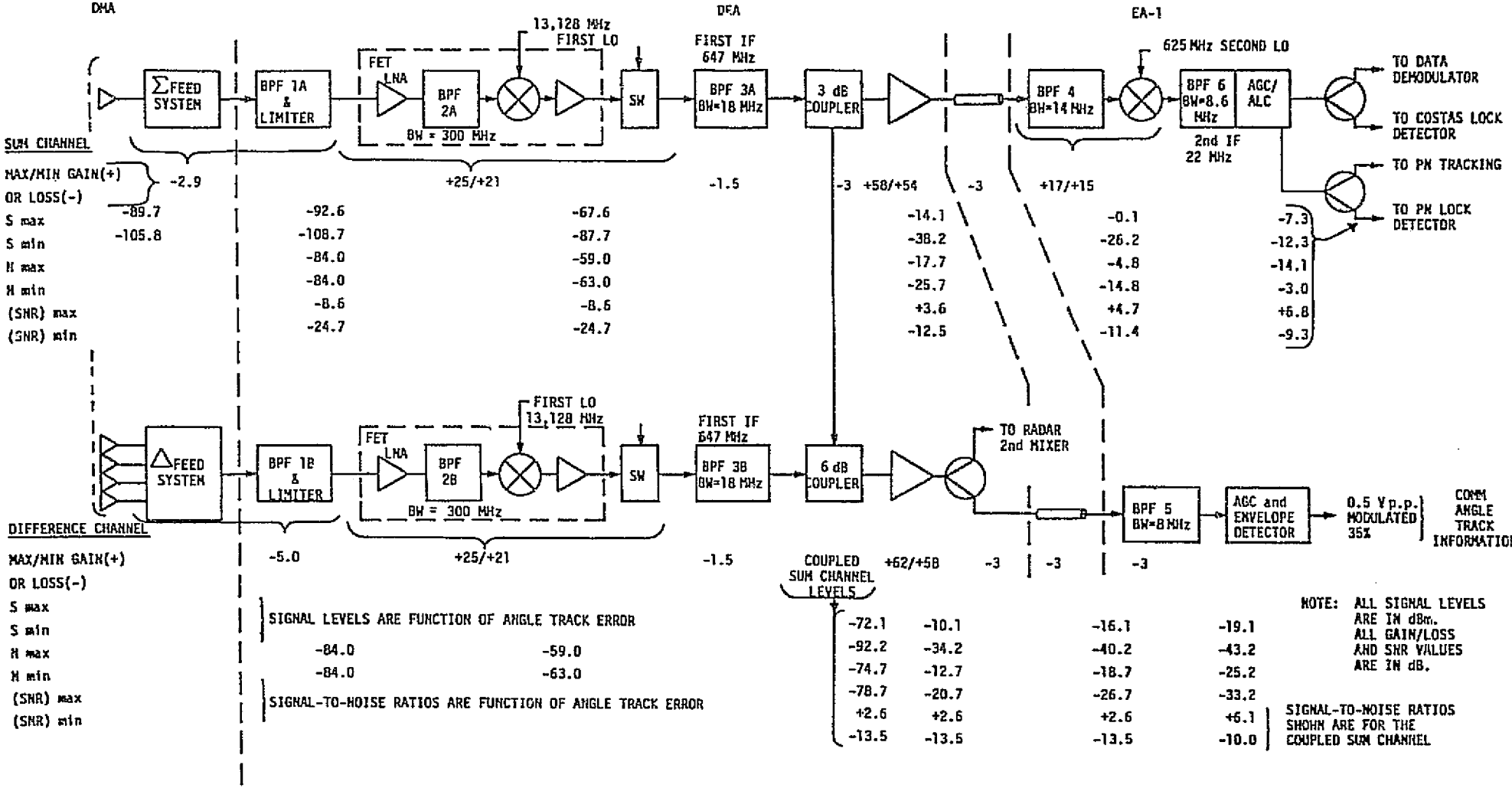

Figure 40. RF Signal Level Profile for the Forward Link Ku-Band Communication Receiver

filter is to couple the incoming 13,775 MHz signals into the receiver and to reject the communication transmitter signal. Although the bandwidth of the communication signal is less than 10 MHz, the passband of this first filter is 300 MHz wide to accommodate the frequency hopped signal of the radar which shares this channel. Also, the amplitude limiter is required primarily for the radar mode, and thus it does not affect the communication mode.

The combined loss of the antenna feed, the rotary joints, and the filter/limiter subunit is about 2.9 dB, which implies that the maximum and minimum input levels are reduced to -92.6 dBm and -168.7 dBm, respectively.

The low noise RF amplifier (LNA) which follows is a three-stage field effect transistor unit which, as explained in Appendix A, has sufficient dynamic range to handle the S-band spur as well as the signal. The bandpass filter (BPF 2A) has sufficiently wide bandwidth to accommodate the radar signal and still provide 20 dB rejection of the image frequency band.

After preselection by this bandpass filter, the received signal is applied to a single balance mixer where it is downconverted by a signal generated in the exciter to the first IF of 647 MHz. The output of the mixer is applied to a first IF preamplifier which compensates for the signal losses incurred in the prefiltering and in the downconversion.

The FET LNA, the bandpass filter (BPF 2A), the mixer, and the post-conversion preamplifier are contained in a single hermetically sealed subassembly which is located physically close to the input bandpass filter/limiter unit to reduce the RF losses. The overall RF to IF gain of this subassembly (shown by dotted lines in Figure 40) is 23 ±2 dB over the range of the environmental conditions. The corresponding range of the minimum and maximum communication signal levels is -87.7 dB and -67.5 dBm, respectively, at the output of this subassembly.

After the preamplification at the first IF of 647 MHz, the communication signal is passed through a solid-state diode blanking gate DS1 (see Section 3.3, Figure 8) and is applied to the first IF bandpass filter (BPF 3A). In the communication mode, the gate does not affect

the signal. The output of the blanking gate is fed into BPF 3A whose 3 dB bandwidth is 18 MHz. The purpose of this filter is twofold: (1) to provide sufficient rejection of the S-band spur and (2) to provide good transient response during the transmit/receive gating in the radar mode. The output of BPF 3A is applied to a 3 dB power divider. One output port of this power divider feeds the communication data IF amplifier. The signal emerging at the second output port of the power divider is summed with the IF signal of the difference (i.e., Δ) receiver channel.

The communication data IF amplifier provides a nominal gain of 56 dB with an estimated variation of ±2 dB. The amplified communication signal, which appears at the output of this amplifier, leaves the Deployed Electrical Assembly (DEA) and is routed via an interconnecting cable with 3 dB loss to the Electronics Assembly #1 (EA-1) for further amplification and processing.

The min/max levels of signal-to-noise ratios at the output of the DEA are shown in Appendix A to be -12.5 dB and 3.6 dB in the 18 MHz bandwidth.

At the input of the EA-1, the 647 MHz second IF signal is applied to a bandpass filter whose bandwidth is 14 MHz and then to a balanced mixer which downconverts it to 21.88 MHz. At this point, the min/max signal-to-noise ratios (Appendix A) are -11.4 dBm and +4.7 dBm in a 14 MHz bandwidth.

The combined effect of the automatic gain control (AGC) and the automatic level control (ALC) provide, as explained in Appendix A, enough signal level of stabilization to reduce the maximum variation at their output to ±2.5 dB.

Following the AGC/ALC unit, the second signal is applied to a series of power dividers which distribute this signal to the PN despreader, PN tracking loop, and PN lock detector. The PN despreader consists of two subsections. One subsection is used for removing the PN code from the data. This subsection is followed by the Costas loop. The second PN despreader subsection is followed by the Costas lock detector.

The min/max signal levels at the input to the PN despreader subsections are -9.8 dBm and -4.8 dBm, respectively. The min/max

levels of the signal delivered to both the PN tracking loop and the PN lock detector are -12.3 dBm and -7.3 dBm, respectively.

The detailed functional description of the PN despreader and the carrier Costas loop, as well as their performance, are explained in Appendix A. It is important to note, however, that the acquisitions of the PN code and of the carrier are carried out simultaneously and that the Costas loop can start tracking the carrier before the PN despreader has acquired the PN code.

The initial frequency search and carrier acquisition must be performed by the Costas loop regardless of the received TDRS signal which can be any of the following formats:

(a) CW carrier
(b) Data modulated carrier
(c) Spread spectrum carrier
(d) Spread spectrum plus data modulated carrier.

Figure 41 shows the functional block diagram of the polarity-type Costas loop used to acquire and track the carrier. The input to the circuit is supplied by the second IF AGC/ALC circuit and by PN code associated circuitry.

The Costas loop demodulator searches and acquires the incoming RF signal. Once the acquisition is completed, the demodulator provides coherent tracking of the phase and the frequency of the received signal. It must be noted that the initial Costas loop lockup on the incoming carrier takes place regardless of the PN code synchronization. This is due to the fact that the arm filters of the Costas loop are made wide enough to accommodate the bandwidth of the spread spectrum signal. Thus, the Costas loop handles the PN modulated carrier as a baseband "data" of 3 Mbps, and it locks up the suppressed carrier of this spread spectrum signal. The data recovery, which is the primary function of the Costas demodulator, must be preceded, however, by the PN despreading.

The capability of the Costas loop to acquire the received RF signal within a relatively short time (about 350 msec) and without needing the PN code lock makes the Costas loop the primary sensor unit for the angular acquisition of the TDRS. Specifically, as the

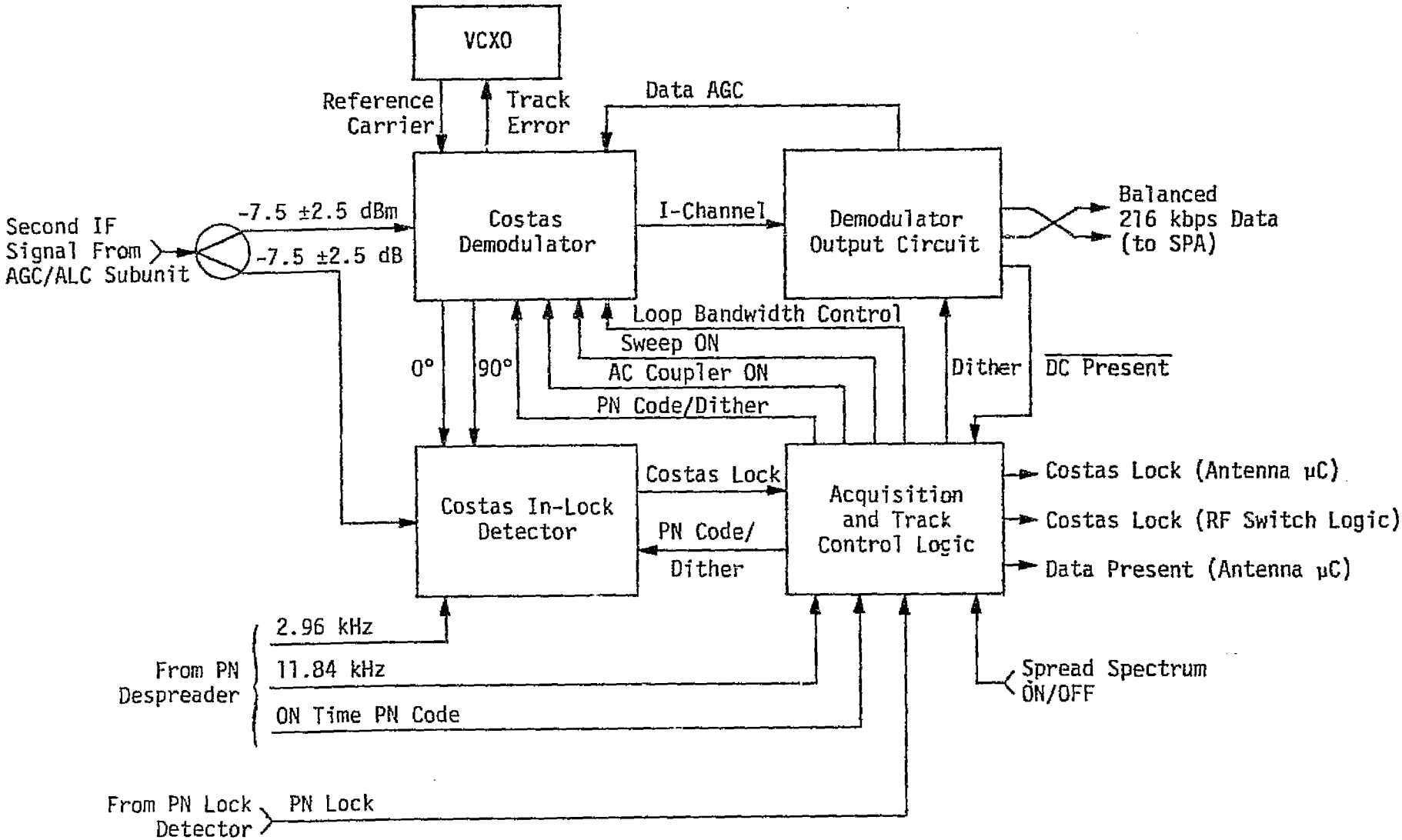

Figure 41. Functional Block Diagram of the PSK Data Demodulator

Shuttle antenna beam scans past the TDRS, the Costas loop, which is constantly swept in frequency, locks onto the TDRS signal and signals the antenna microcomputer to terminate the antenna scan. The advantage of using the Costas loop for acquisition rather than an energy sensor is that the former uses coherent detection which uniquely identifies the TDRS signal, thus eliminating possible false lockups due to earth or sun intercepts.

The actual sensing of the Costas loop signal acquisition state is performed by the Costas lock detector circuit. This circuit develops the in-phase ("I") and quadrature phase ("Q") components of the incoming signal and forms an I^2-Q^2 signal. When the Costas loop is in lock, or close to it, the condition $I^2 >> Q^2$ makes the I^2-Q^2 signal exceed a preset threshold. When this happens, the lock detector sends a "Costas lock" signal to the acquisition and track control logic.

As its name implies, the acquisition and track control logic performs the function of switching the Ku-band communication receiver from the acquisition mode to the track mode. Specifically, upon receipt of the "Costas lock" signal, the logic circuit issues commands to the antenna microcomputer and to the RF switching circuitry to terminate the antenna scan and to initiate the angle tracking, in addition to terminating the sweep, narrowing the bandwidth, and initiating tracking. (For a more detailed discussion, see Appendix A.)

The recovery of the forward link data requires the removal of the 3.03 Mbps PN code from the received signal when the incoming signal is in the spread spectrum mode. The removal of the code, in turn, requires a local replica of a code which is in a near-perfect synchronism with the incoming code. Consequently, prior to the recovery of the communication data, the Ku-band receiver must search out the phase of the incoming code and then lock its local coder to the phase of the incoming code. Once the initial synchronism is established, the local coder must remain in lock with the received code.

The function of both the code acquisition and tracking, as presented in the PDR [13], is performed by the PN tau-dither acquisition-tracking and the PN lock detector circuits whose functional block diagrams are shown in Figure 42.

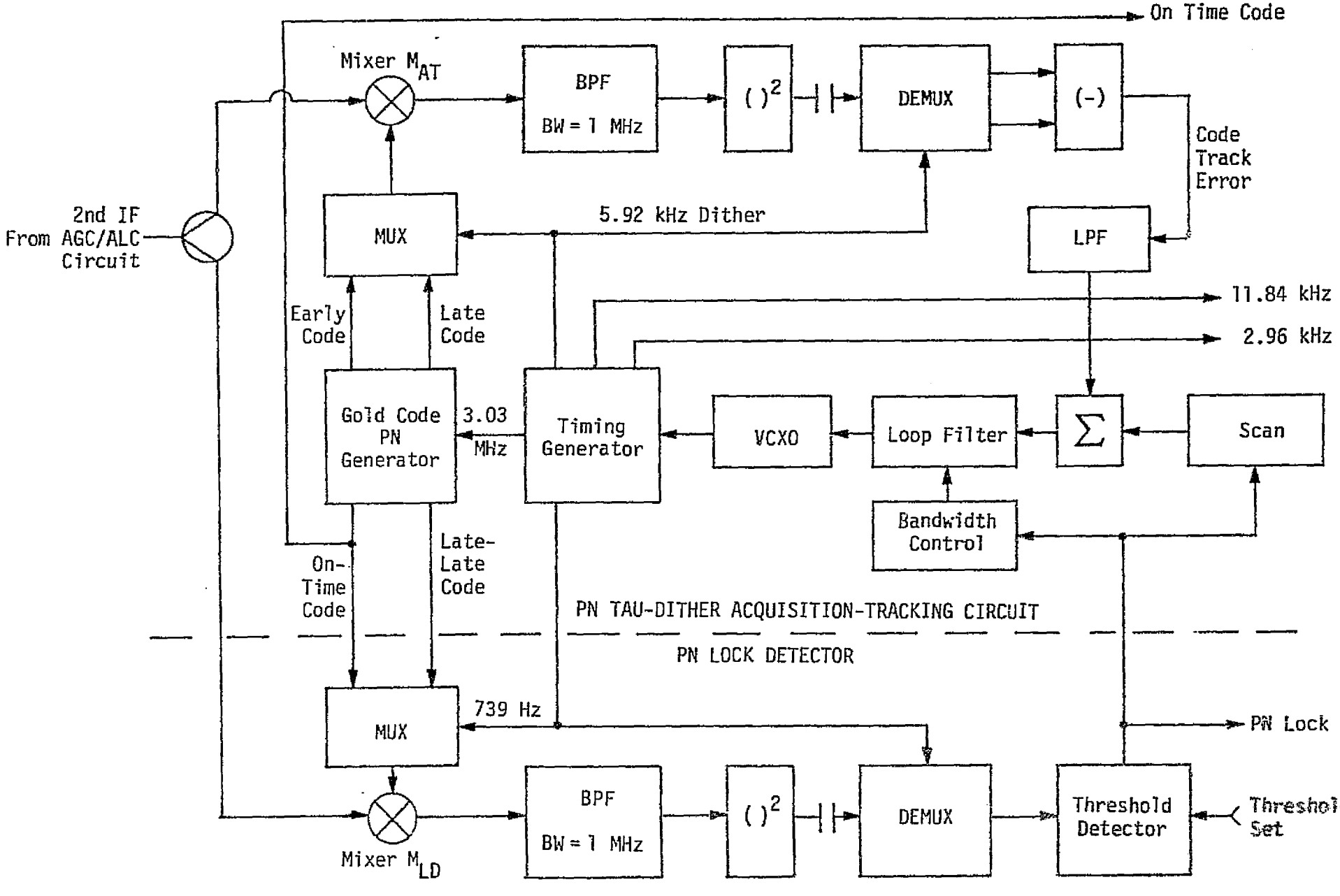

Figure 42. PN Tau-Dither Acquisition-Tracking and PN Lock Detector Functional Block Diagram

The PN tau-dither acquisition-tracking circuit is in the upper portion of Figure 42, while the lower portion shows the PN lock detector. In the tracking mode, the IF signal is applied to mixer M_{AT} where it is multiplied with the local reference. This local reference is time-multiplexed between two bi-phase signals, one modulated by the "early" code ($+\tau/2$) and the other by the "late" code ($-\tau/2$). The rate of multiplexing, which is generally referred to as the "tau-dither" rate, is equal to 5.22 kHz for this particular system.

The output of M_{AT} is bandpass filtered and applied to a square-law detector. The square-law detected signal is then AC coupled to the demultiplexer, where the detected IF outputs corresponding to the $+\tau/2$ and $-\tau/2$ conditions are separated. After separation, these two components are subtracted and the difference is filtered and applied via the loop filter to the VCXO.

The VCXO is tunable over a limited range, and the code track error developed by the tau-dither circuit is used to keep the VCXO-driven code generator in synchronism with the received code.

For the acquisition phase, the scan circuit develops a voltage which offsets the VCXO frequency from the nominal frequency of the PN code. This offset causes the local and incoming codes to slip past each other until synchronism is achieved.

Once synchronism is achieved, the tau-dither tracking function takes over and the PN code stays in lock despite the scan signal voltage. This voltage, however, is disconnected once the PN lock detector declares code lock. (For further discussion of PN acquisition and tracking, see Appendix A.)

It is important to point out that the PN code search procedure of the tau-dither acquisition-tracking circuitry described here utilizes a VCXO frequency offset which causes the code phases to slide past each other on a continuous, uninterrupted basis. Therefore, unlike the case of a stepped code search, the probability of lock cannot be defined on a discrete time basis. This fact complicates the analytical procedure for predicting the PN acquisition behavior, although it does not affect the actual tested performance [14]. The predictions made for a stepped sequential search performance [15] should thus be considered as guidelines.

The signal (Σ-channel), which is a 216 kbps bi-phase-L code, is fed into the SPA after PN despreading and carrier tracking is completed. The signal is controlled by a data-good circuit [13] which passes the data when the three following conditions are met:

(1) The PN lock detector declares PN tracking (when spreading exists).

(2) The Costas loop detector declares carrier tracking.

(3) No DC level exists.

The third requirement is included to insure that data is present and not just carrier.

The difference channel (Δ) signal is generated (Appendix A) to form (when multiplexed with the Σ-channel) the required error signal for tracking purposes in the radar and communication modes. The Δ-channel signal processing with the DEA is identical to that of the Σ-channel. The multiplexing procedure is explained in Section 3.0 and in [6].

5.3 Forward Link SPA Modes

Two modes are available in the SPA for the forward link signals—a special mode which primarily buffers* the data from EA-1 and hands it over to the NSP (1 or 2) on the Orbiter or a nominal mode which performs the following operations:

(1) Bit synchronization of the incoming 216 kbps bi-phase-L data from the EA-1.

(2) Generation of the 2×216 kbps synchronous clock with the data and solving the clock ambiguity, as well as the data (midbit, between-bit transitions).

(3) Bit detection via a bit detector.

(4) Frame synchronization and data (scientific and operational) decommutation before providing them to the Orbiter at the appropriate rates.

The mode selection is controlled by the SPA management and hardware logic.

---

*Buffering here implies amplification and impedance matching.

5.3.1 Bit Synchronization and Ambiguity Resolution

The bit synchronizer and ambiguity resolver simplified block diagram is shown in Figure 43. The objective of the circuit is to:

(1) Generate a 32×216 kHz (6.912 MHz) synchronous signal which is used to generate the 216 kbits clock, 2×216 kbits clock, and various other timing signals used in frame decommutation timing.

(2) Resolve midbit versus bit transition ambiguity of the 216 kbps bi-phase-L data, as well as the 2×216 kbps clock synchronization ambiguity.

A functional block diagram of the HAC Ku-band bit synchronizer, suitable for analysis purposes, is illustrated in Figure 44. The principles of operation of this synchronizer are summarized as follows. The synchronizer develops its timing waveforms from a twice-bit-rate clock (512 kbps), while the ambiguity resolver determines the correct timing phase of the bit rate clock obtained by dividing down the twice-bit-rate clock by 2. The input signal is multiplied by the twice-bit-rate clock and then the bit-rate clock or its complement, which are both used to gate (in each bit interval) half-bit segments of the multiplier outputs to in-phase integrate-and-dump (I&D) circuits. For the midbit I&D, the half-bit integration symmetrically (assuming perfect timing) spans the midbit position. Thus, the output of this I&D after 2-bit digitization by Digitizer 1 reflects the polarity of the NRZ data bit stream (or, alternately, the polarity of the midbit Manchester transition). For the between-bit I&D, the half-bit integration symmetrically spans the NRZ bit transition position. Thus, the output of Digitizer 2 is a measure of the polarity of the NRZ data transition. If no transition occurs, the output will be nominally zero.

The input bi-phase-L coded signal is also gated by the bit rate clock and its complement, without first being multiplied by the twice-bit-rate clock, to between-bit and midbit quadrature I&D circuits, respectively. The outputs of these I&Ds are measures of the timing offset between the input and the locally generated bit-rate clock. Multiplying the respective in-phase and quadrature I&D outputs

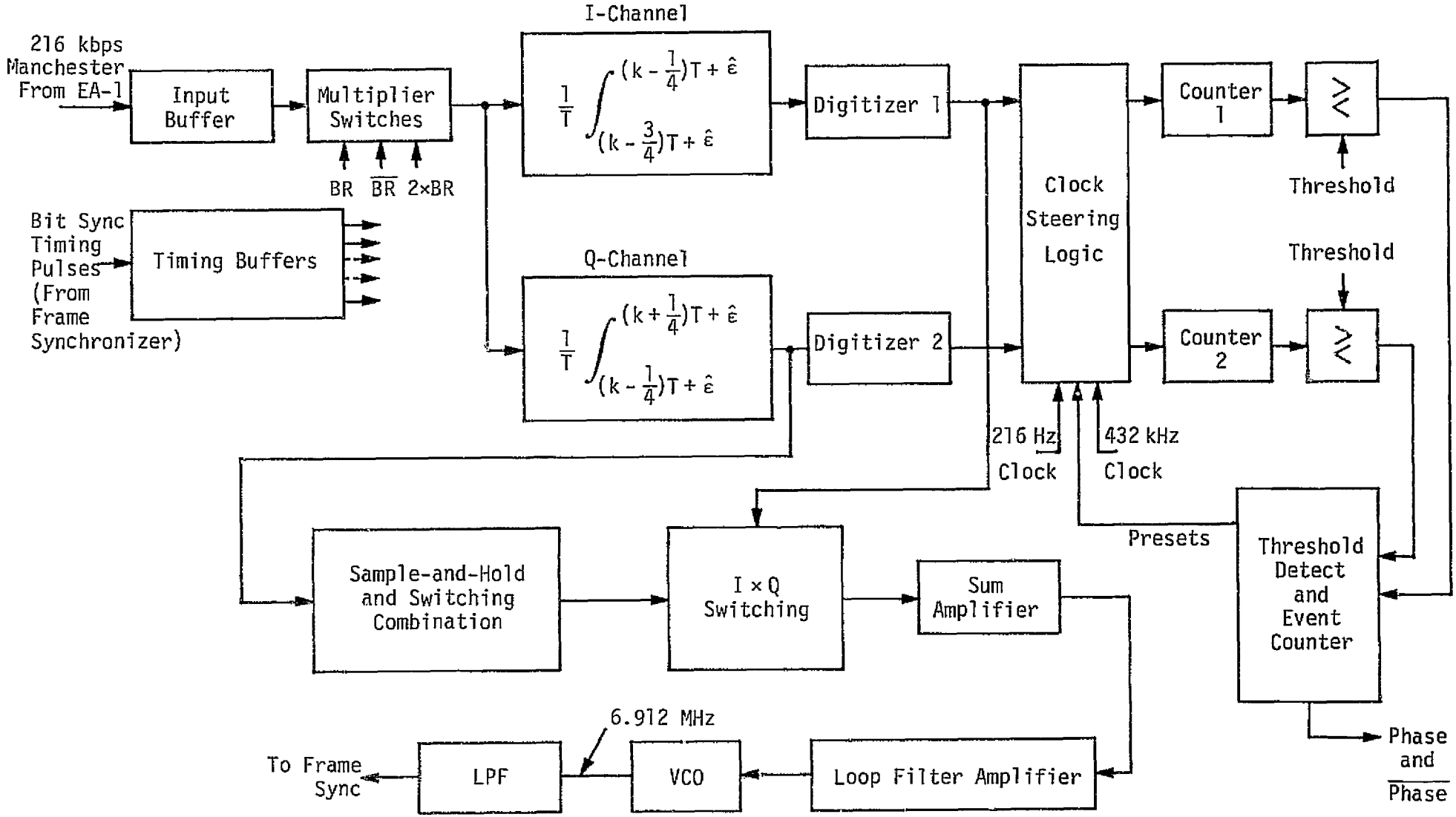

Figure 43. Bit Synchronizer and Ambiguity Resolver Block Diagram

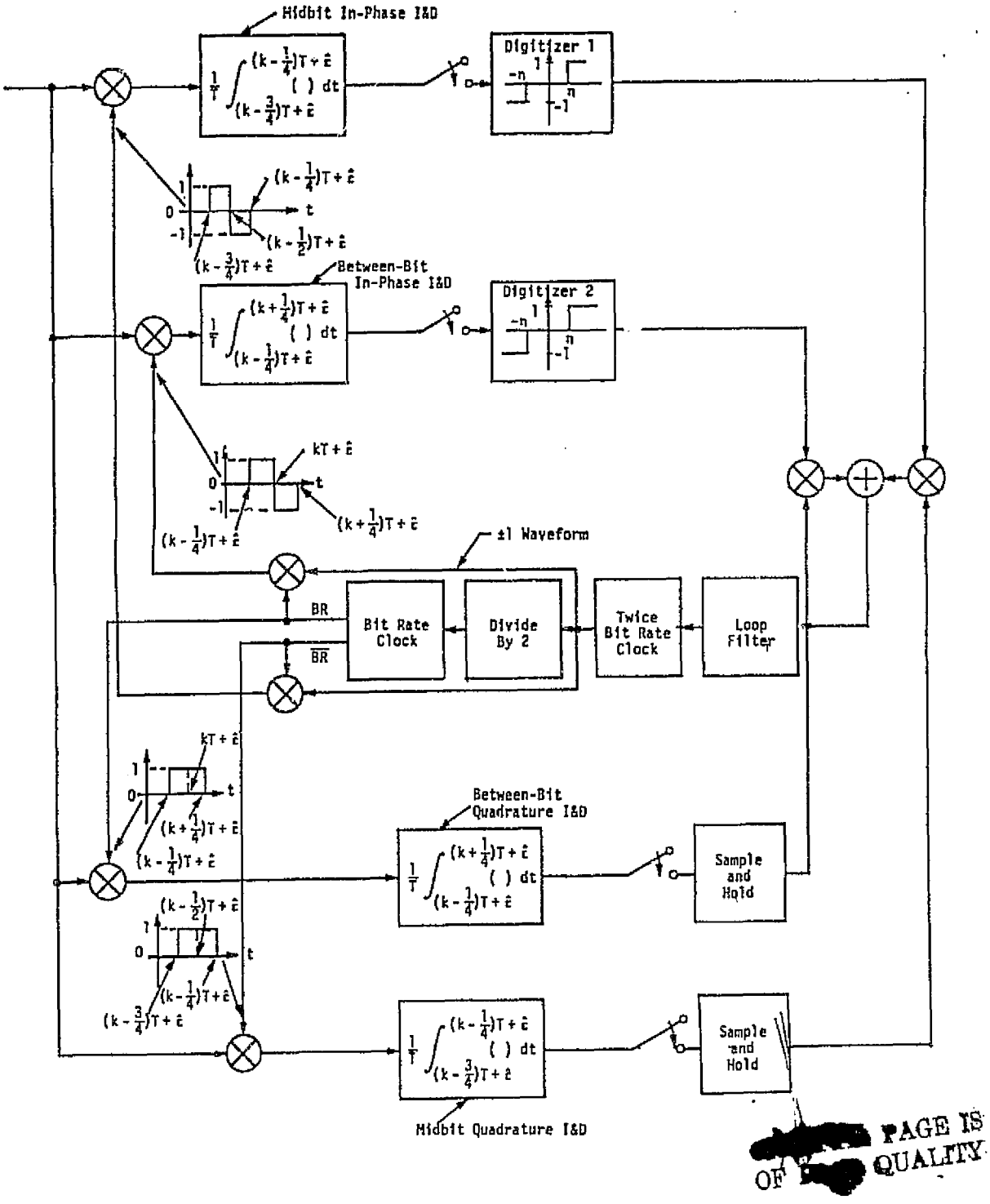

Figure 44. Bit Synchronizer Functional Block Diagram

and summing generates an error signal suitable for closing the bit sync loop.

Timing diagrams of the various waveforms formed within the loop are illustrated in Figure 45a for $0 \leq \lambda \leq \frac{1}{4} - \frac{n}{2}$ and in Figure 45b for $\frac{1}{4} + \frac{n}{2} \leq \lambda \leq \frac{1}{2}$, where λ is the relative timing error (normalized to the bit time) between the input and locally generated bit-rate clock. The corresponding loop error curve (assuming no noise) is illustrated in Figure 46 and is obtained by statistically averaging the error signal formed above over the data sequence (assuming an NRZ transition probability p_t).

Several comments are worthy of note. First, the midbit in-phase and quadrature I&D outputs are independent of the between-bit in-phase and quadrature I&D outputs because of the orthogonality (in time) of their respective integration intervals. This greatly simplifies the computation of the equivalent loop error curve and the equivalent noise spectral density at the error control point. Second, all of the above integrations occur over half-bit intervals. While it is advisable to "window" the quadrature I&Ds (half a bit in the HAC design), it is not necessarily desirable to "window" the in-phase I&Ds. In fact, windowing the in-phase I&Ds to half a bit as in the Hughes design results in a 3 dB SNR penalty for making decisions on the midbit and between-bit transitions relative to performing full-bit in-phase I&Ds as is done, for example, in [16]. In [16], four bit synchronizer configurations motivated by the application of maximum a posteriori (MAP) estimation theory are developed and their performance compared. Conceptually, the HAC bit synchronizer design is closest to Figure 5c of [16], although fundamental differences between the two do exist. Section 9.2 and Appendix E present a complete performance analysis of the HAC design.

The ambiguity resolver uses two 12-bit counters which are incremented or decremented by the absolute values of the in-phase and quadrature-phase integrate-and-dump circuits as follows (◯ refer to the signals in Figures 45a and 45b):

(1) Counter 1 is incremented by threshold crossing of ⑤ and decremented by threshold crossing of ⑦.

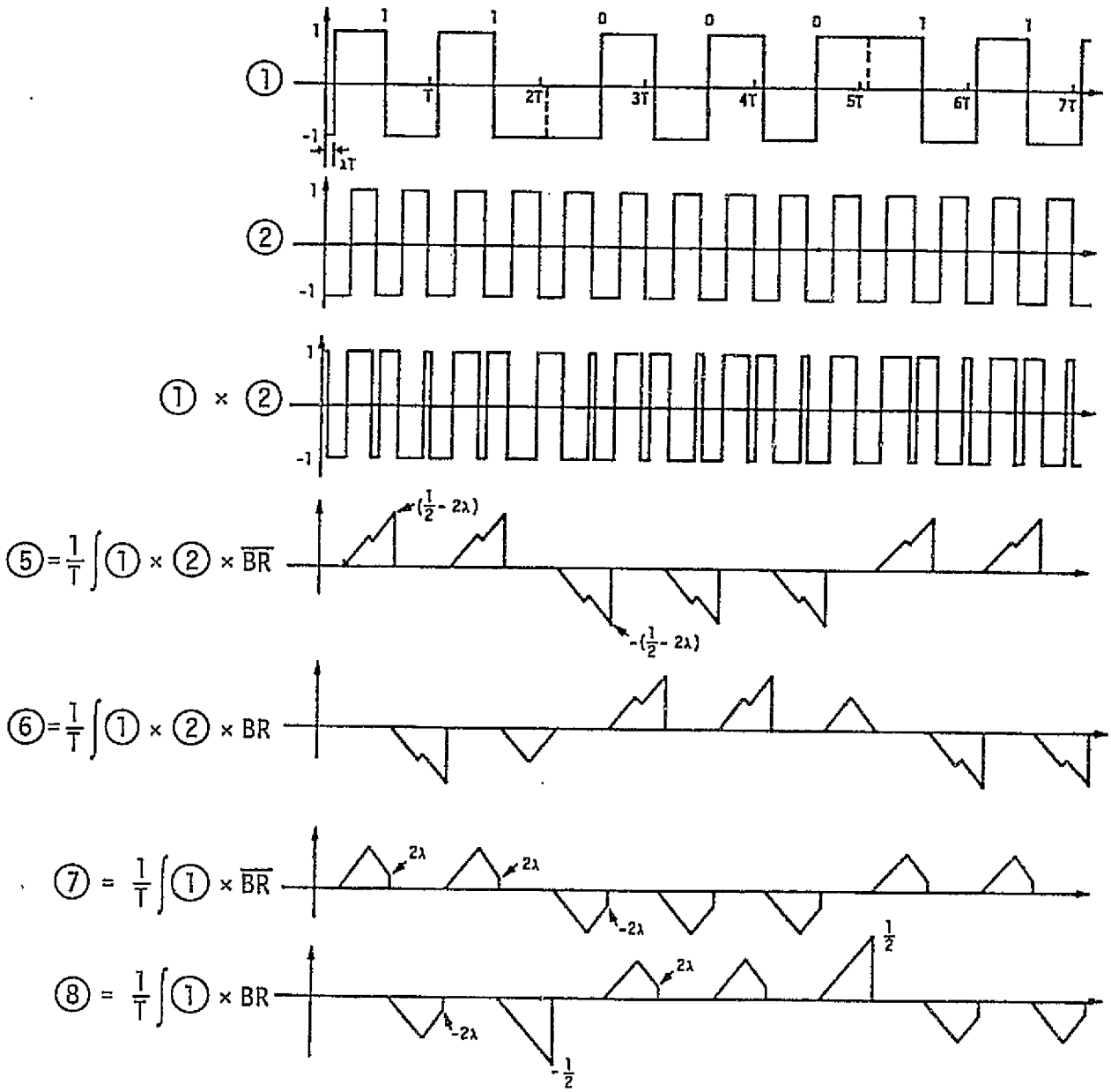

$$\lambda \triangleq \frac{\varepsilon - \hat{\varepsilon}}{T} \qquad (0 \leq \lambda \leq \frac{1}{4} - \frac{\eta}{2})$$

Figure 45a. Bit Synchronizer Timing Diagram

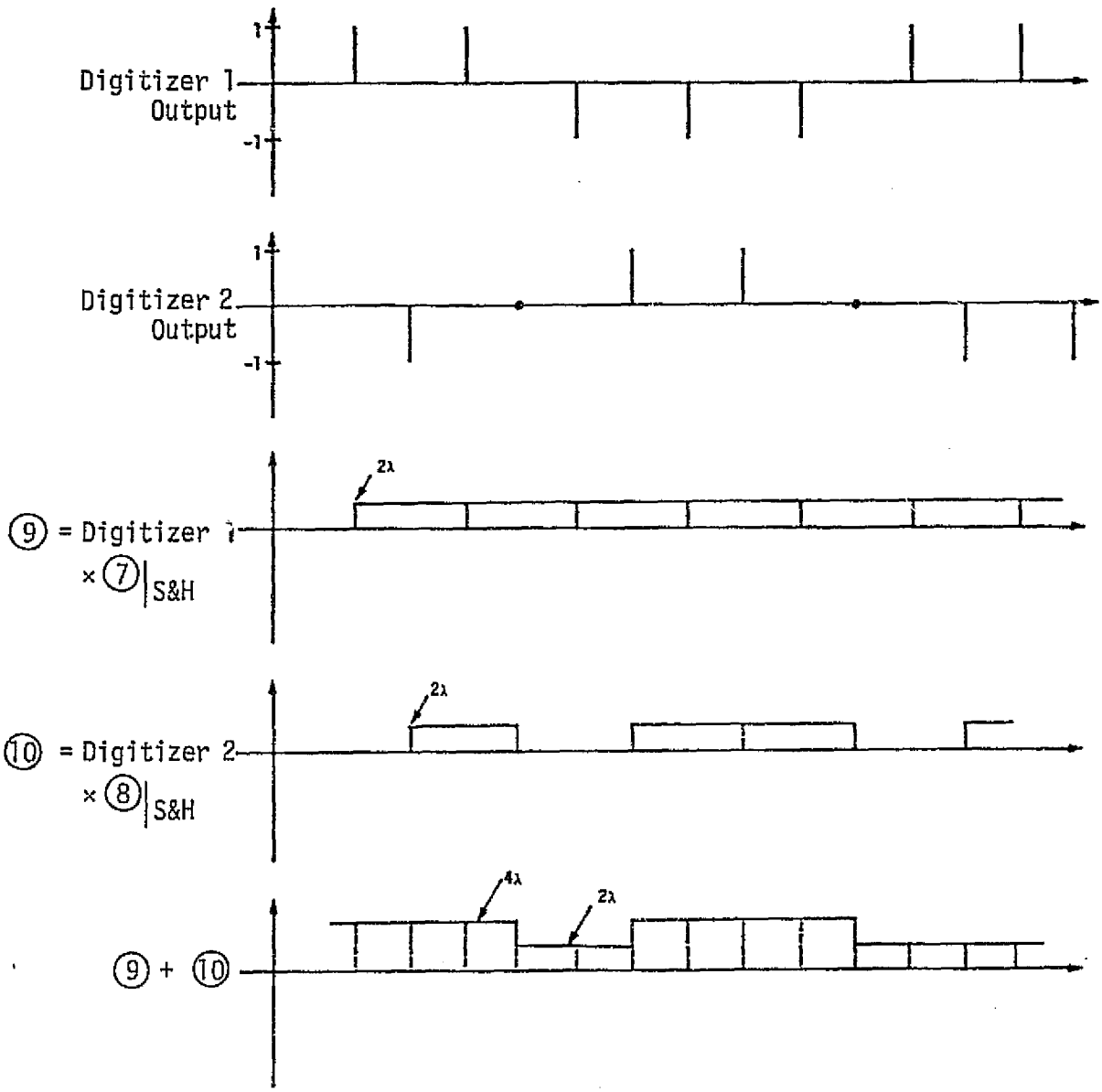

$$\overline{⑨ + ⑩} = (1 - p_t)\,4\lambda + p_t\,2\lambda = 4\lambda\left(1 - \frac{p_t}{2}\right)$$

p_t is NRZ transition probability S&H = Sample-and-Hold

Figure 45a (continued)

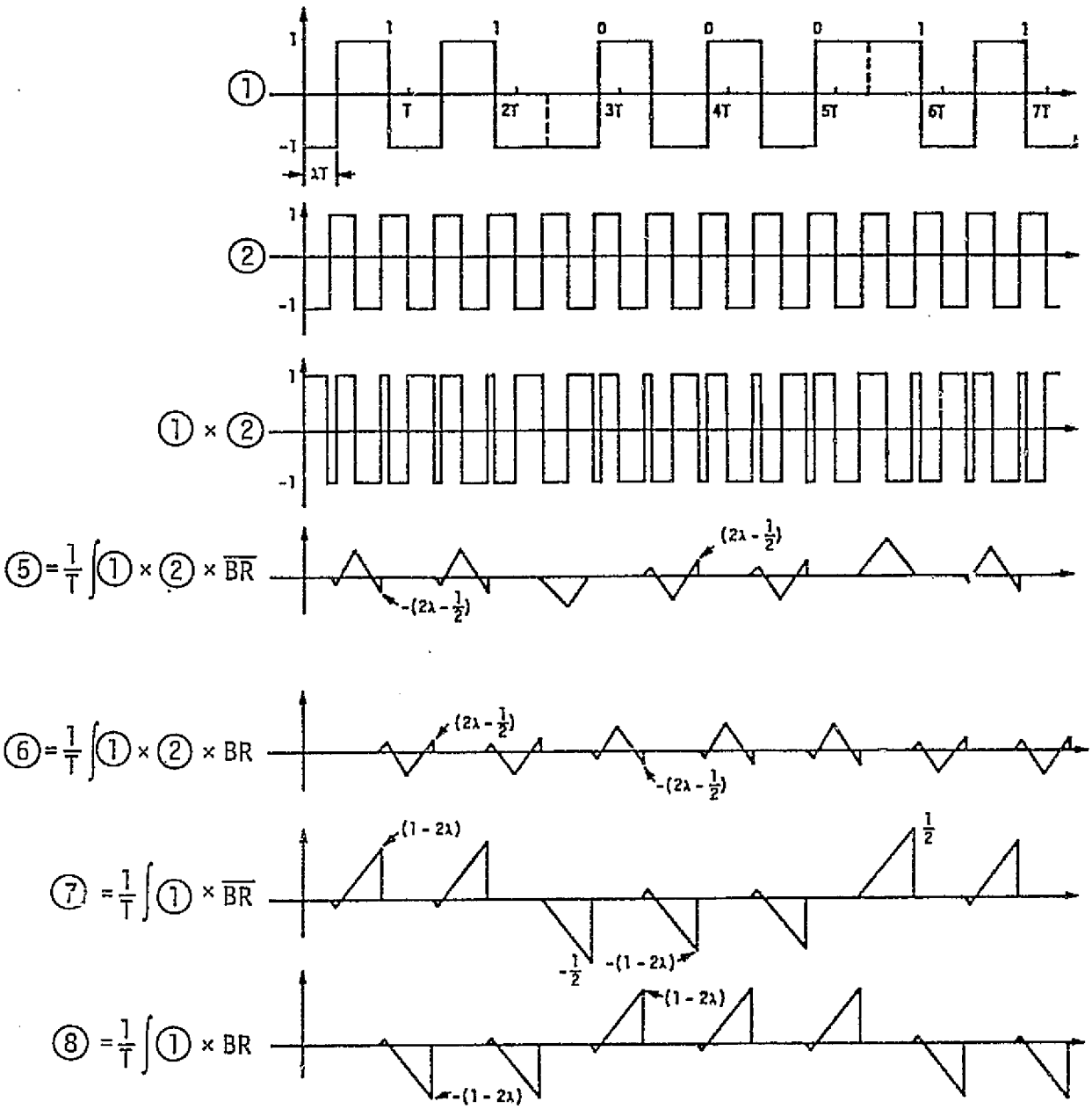

$$\left(\frac{1}{4}+\frac{n}{2} \leq \lambda \leq \frac{1}{2}\right)$$

Figure 45b. Bit Synchronizer Timing Diagram

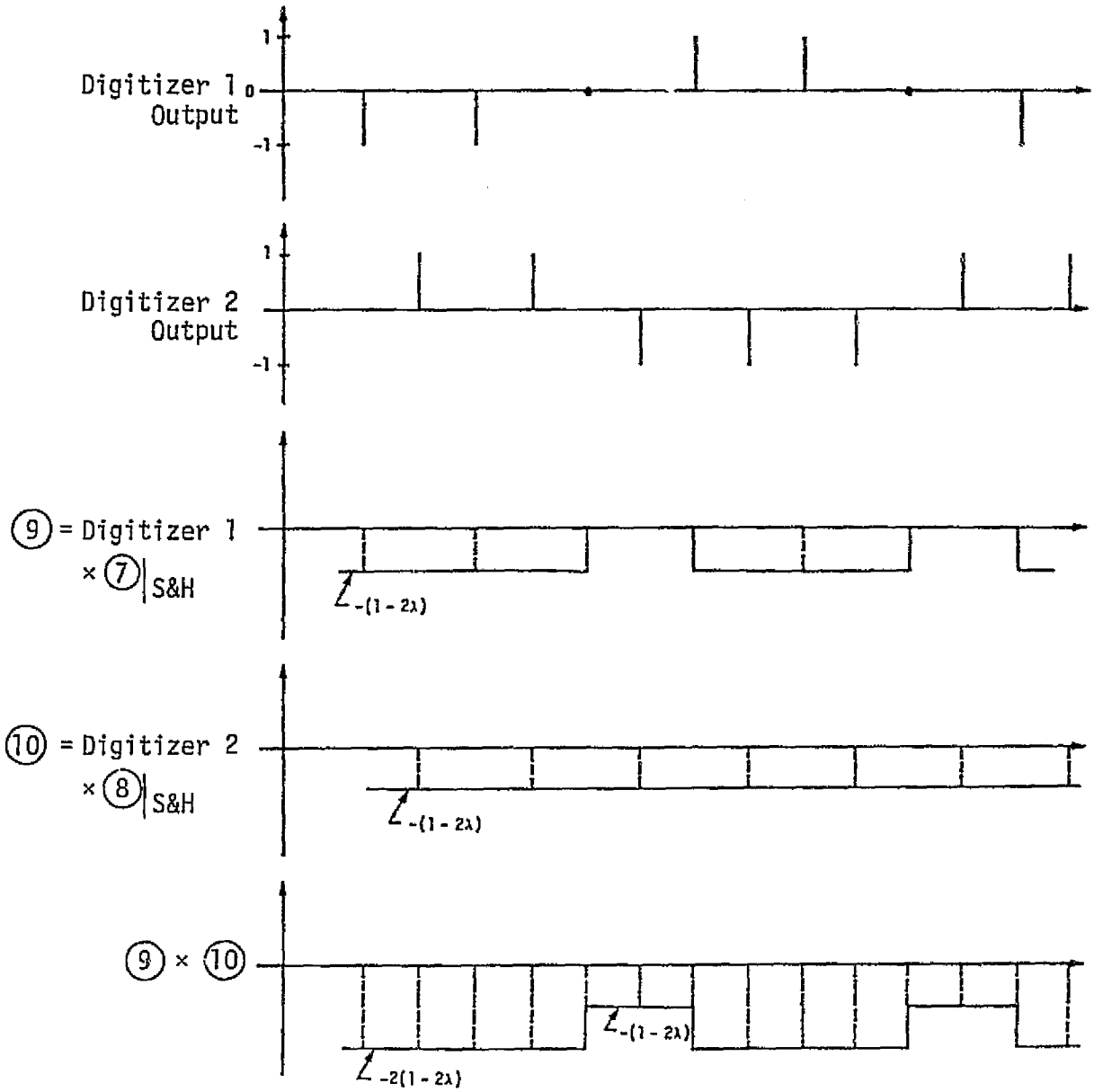

$$\overline{⑨ \times ⑩} = -(1 - p_t)\,2(1 - 2\lambda) - p_t(1 - 2\lambda) = -2(1 - 2\lambda)\left(1 - \frac{p_t}{2}\right)$$

p_t is NRZ transition probability S&H = Sample-and-Hold

Figure 45b (continued)

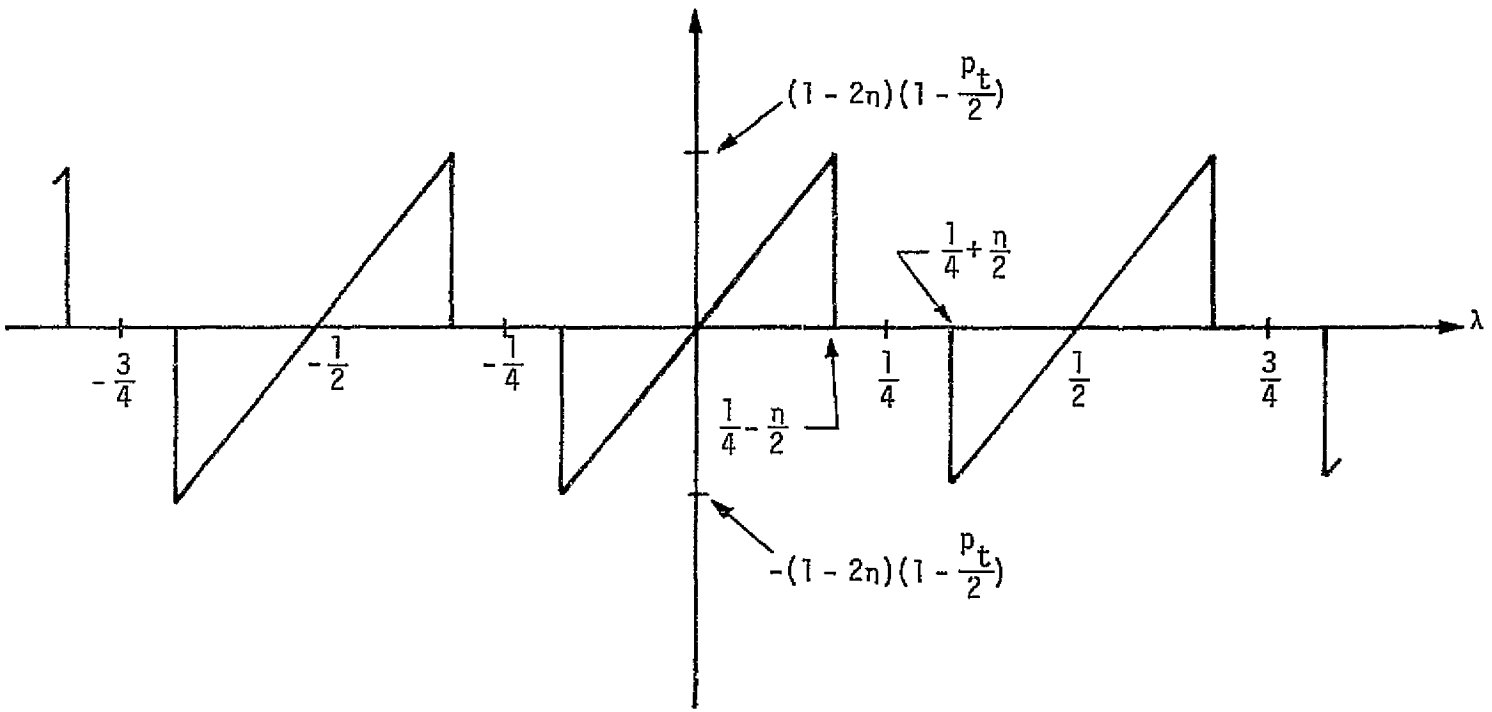

Figure 46. Equivalent Loop S-Curve (No Noise)

(2) Counter 2 is incremented by threshold crossing of ⑥ and decremented by threshold crossing of ⑧.

The resolver resolves the ambiguity once one counter overflows and exceeds the second counter by a certain count (not specified in the PDR documents). Lock is maintained unless an overflow occurs three times without exceeding the prespecified difference between the two counters which results in a signal initiating acquisition and indicating loss of lock. This implies that a long sequence of ones or zeros would cause the ambiguity resolver to lose lock while an alternate sequence of ones and zeros would help the resolver to achieve faster lock indication.

The choice of the capacity of the counter is a function of the duty factor and the expected maximum length of nonvarying data sequence. A bound on these two quantities has to be specified for an optimal counter capacity to be selected.

5.3.2 Bit Detection

After establishing bit synchronization, a conventional bit detector is used to detect the 216 kbps bi-phase-L input data and convert it to 216 kbps NRZ data by multiplying it with an in-phase bit-rate clock and using two orthogonal integrate-and-dumps to detect alternate data bits, as seen in Figure 47a. The combination of the two integrate-and-dump circuits is implemented to act as a very fast single integrate-and-dump circuit. The comparators are used as threshold devices to determine the bit polarity, and the multiplexer is used to combine the alternate outputs to form a single NRZ data stream. The equivalent bit detector is shown in Figure 47b.

5.3.3 Frame Synchronization

The data format of the forward link is shown in Figure 48. The data is time-division-multiplexed (TDM) in such a way that each frame consists of 9 bytes and each byte consists of 48 bits. There are 500 frames per second (216 kbps). The first 32 bits of byte 1 in a frame consists of a frame code which is used to establish frame synchronization. The remaining 16 bits in byte 1, as well as the last 16 bits in every other byte, are reserved for operations data

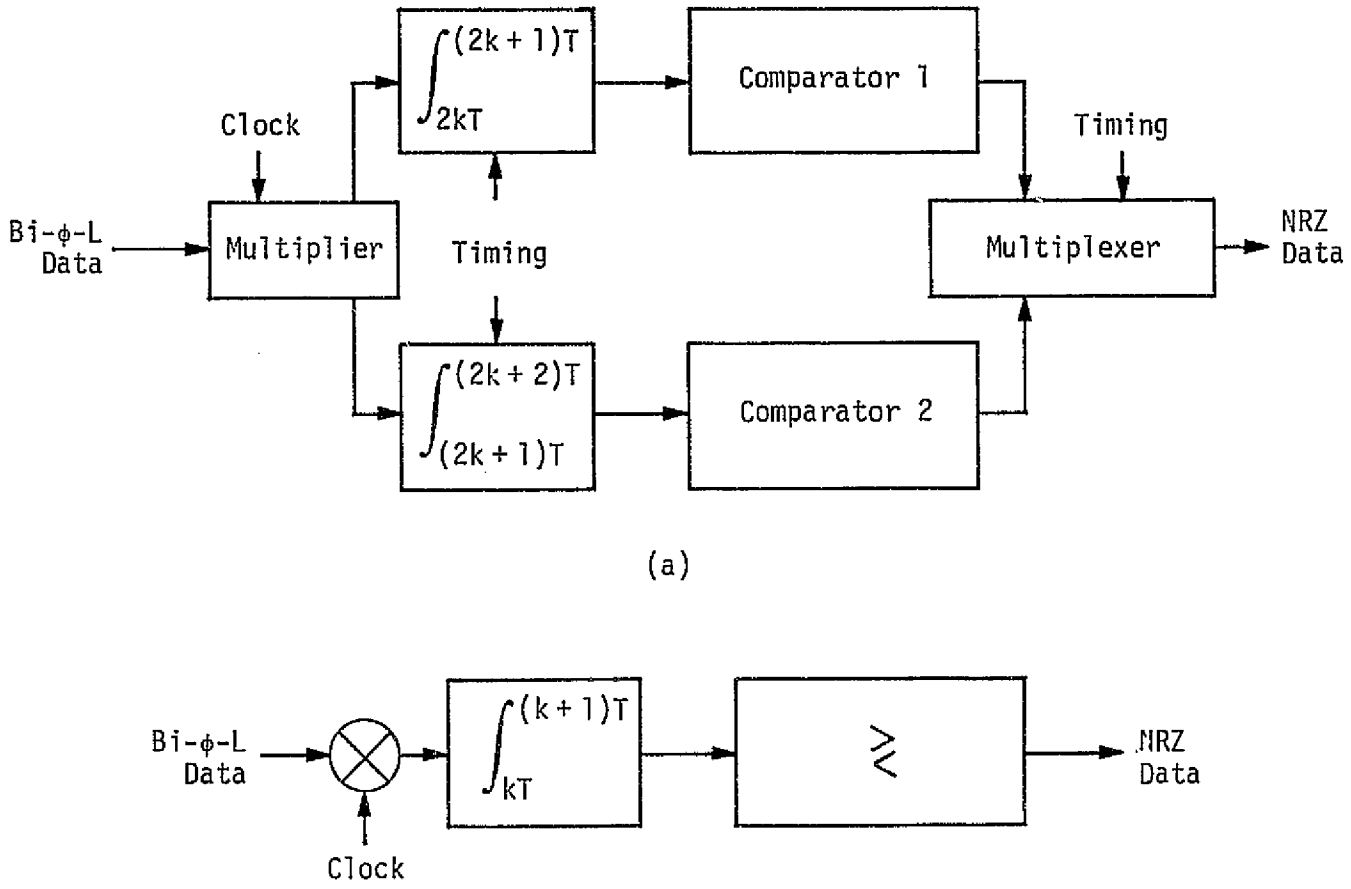

Figure 47. Bit Detector Block Diagram

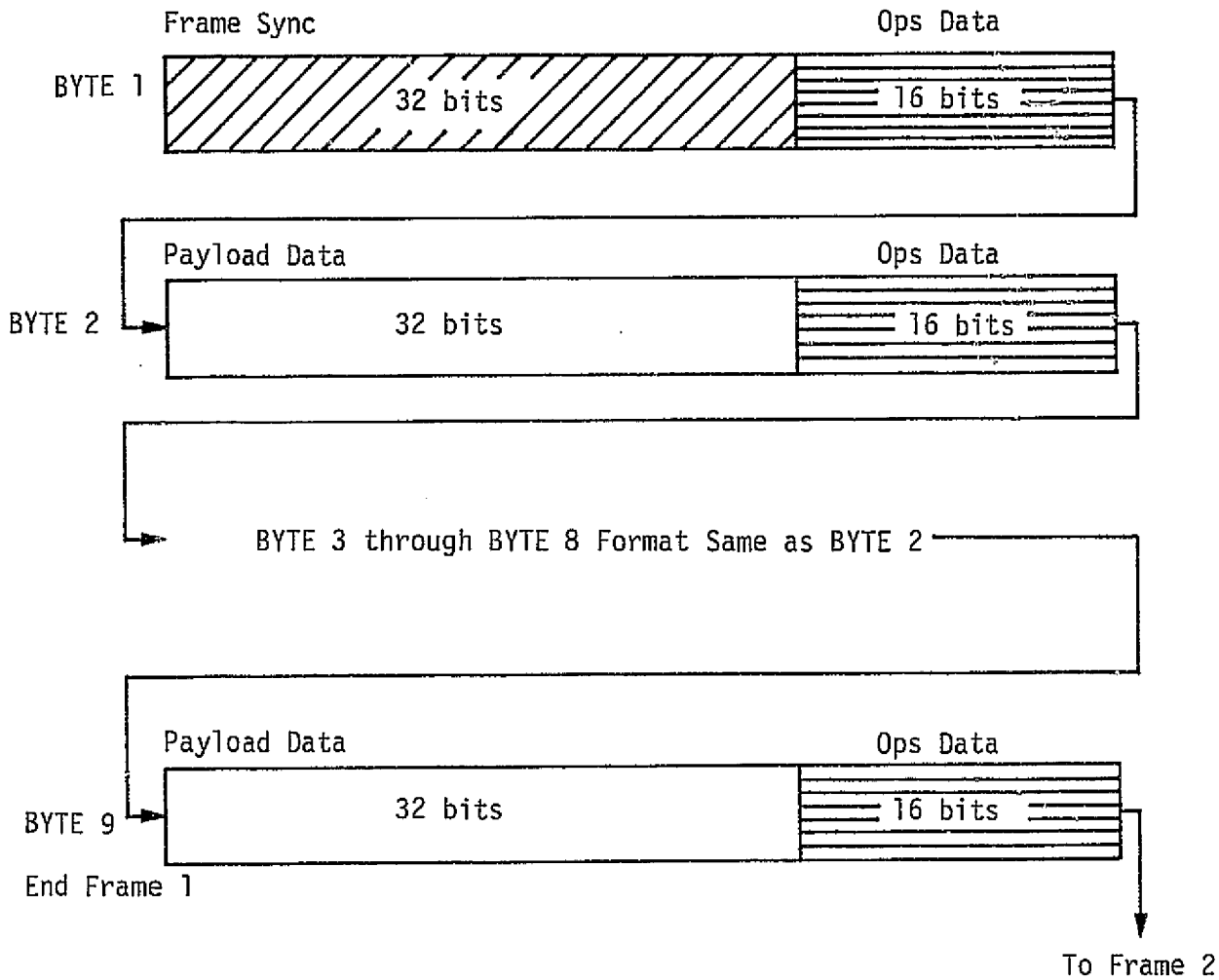

Figure 48. Forward Link 216 kbps TDM Data Format

at a rate of 72 kbps. The first 32 bits of the eight remaining bytes in a frame are used for payload data.

Frame timing (synchronization) is established via a correlation detector, as seen in Figure 49. The detector searches the various possible code positions in the first 32 bits of the first byte to detect a correlation. Two possible correlations can be declared:

(1) Positive correlation, when at least 30 bits agree with the local code.

(2) Negative correlation, when no more than 2 bits agree with the local code.

This causes the frame synchronizer to shift from the search mode to the acquisition mode with the proper data sign shift (positive or negative). If correlation is detected again after one frame time, the frame synchronizer enters the lock mode and an event counter is reset to zero. If no correlation is detected, the mode is shifted back to the search mode. Once the event counter is set to zero, it takes three consecutive correlation misses (incrementing the event counter to 3) to switch the frame synchronizer back to the search mode. The forward link timing circuits distribute the data and the required timing signals to various parts of the frame synchronizer and closes the bit synchronizer loop by sending bit synchronization timing pulses to its timing buffer, as shown in Figure 43. The frame decommutator timing uses the synchronous 6.9 MHz and 432 kHz signals to generate the required 128 kHz and 72 kHz signals for the frame decommutator, which isolates the operations data and payload data before handing it to the Orbiter at the appropriate output rate.

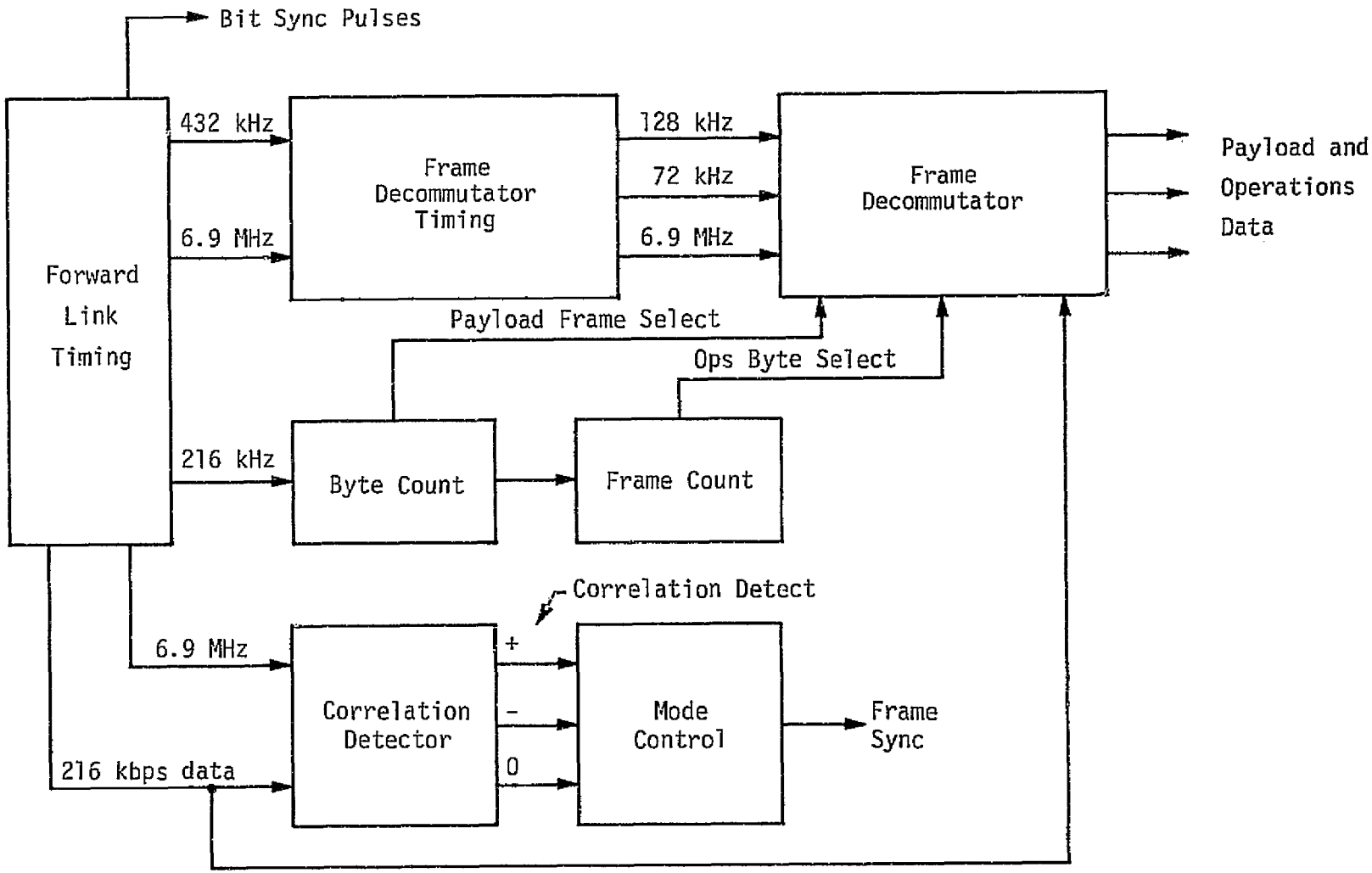

Figure 49. Frame Synchronizer Block Diagram

6.0 RETURN LINK

The return link is used by the Ku-band system to transmit data from the Orbiter to the TDRS. It has two selectable modes which multiplex three channels carrying a wide variety of data. The return link is initiated in the SPA by modulating the data in one of two modes before being upconverted to Ku-band frequencies by the DEA and transmitted by the DMA to the TDRS. In the following sections, the possible data combinations are presented, along with a description of the modes and the return link signal flow in the various Ku-band subunits. Evaluation of the performance of the link using the current design parameters is also summarized with the detailed analysis presented in Appendix B.

6.1 Signal Formats and Modes

There are three channels that can be multiplexed in one of two modes [17]. The modes are selected by a signal from the management/handover logic in the SPA, based on Orbiter commands. As seen in Figure 50, the two lower rate channels are identical in the two modes, while the higher rate channel differs according to the mode of operation.

Figure 51 illustrates the signal flow block diagram of the return link in the SPA. The two lower rate channels (Channels 1 and 2) are quadriphase-modulated on a squarewave subcarrier whose first harmonic frequency is 8.5 MHz. The subcarrier is generated by a squarewave oscillator in the SPA. The power ratio between the two channels is adjusted to give a nominal 80% to the in-phase channel (Channel 2) and 20% to the quadriphase channel (Channel 1). This is accomplished by delaying the output of the squarewave oscillator and its inverse by a nominal 17.4 nsec, which results in four squarewave carrier vectors that are located at 0°, 53.2°, 180° and 233.2° angles. Channels 1 and 2, which geometrically form the bisectors to the angles between the four vectors, are projected (multiplexed) onto these vectors to yield the appropriate (0.2,0.8) power distribution between them, respectively. This stems from the fact that $\cos^2(53.2/2) = 0.799$ (≈ 0.8) and $\sin^2(53.2/2) = 0.2005$ (≈ 0.2). The switching combination SW1, SW2, SW3 is controlled by the management and handover logic of the SPA and is used to select the desired signals from those shown in Figure 50.

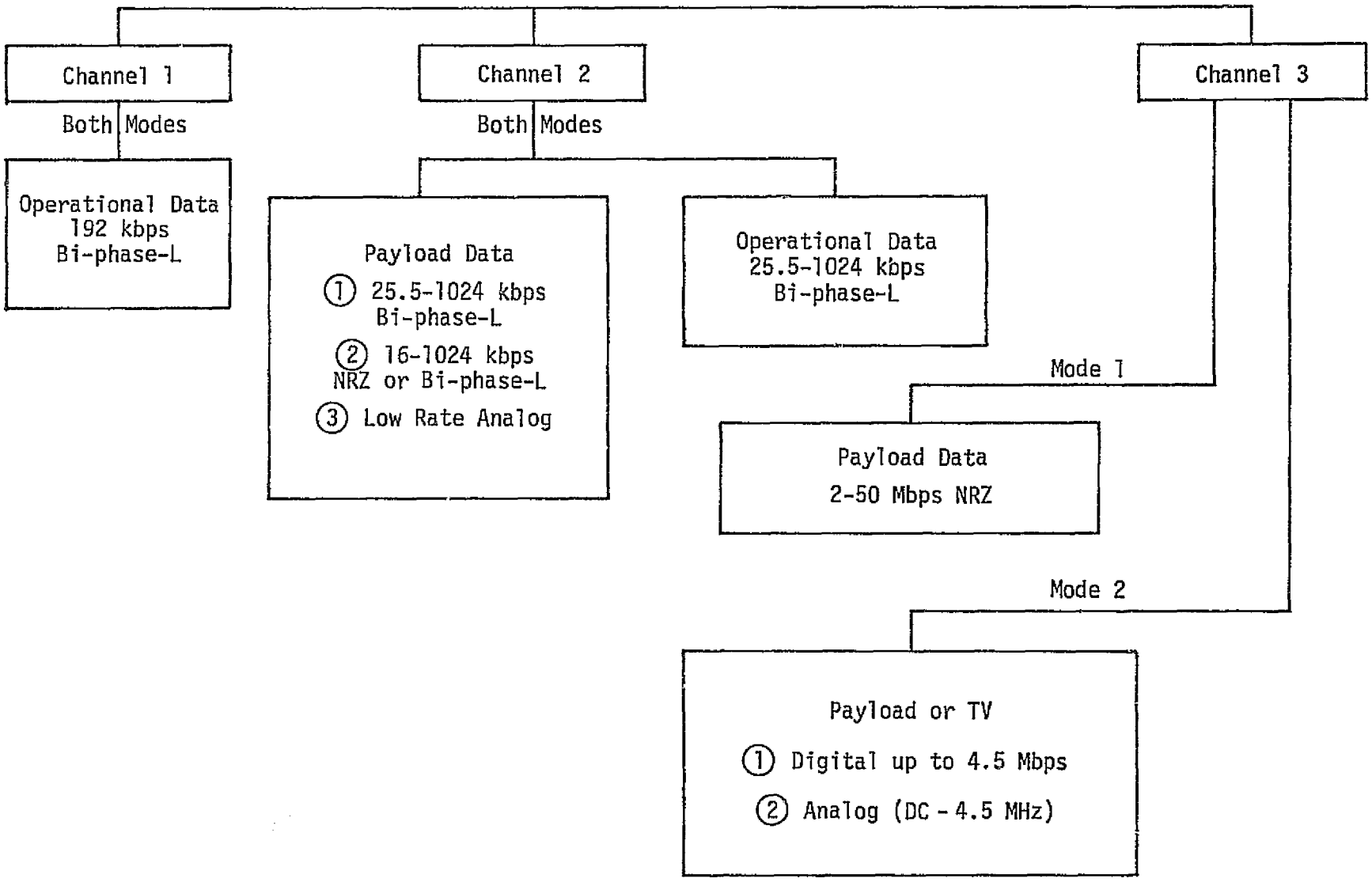

Figure 50. Return Link Signal Formats

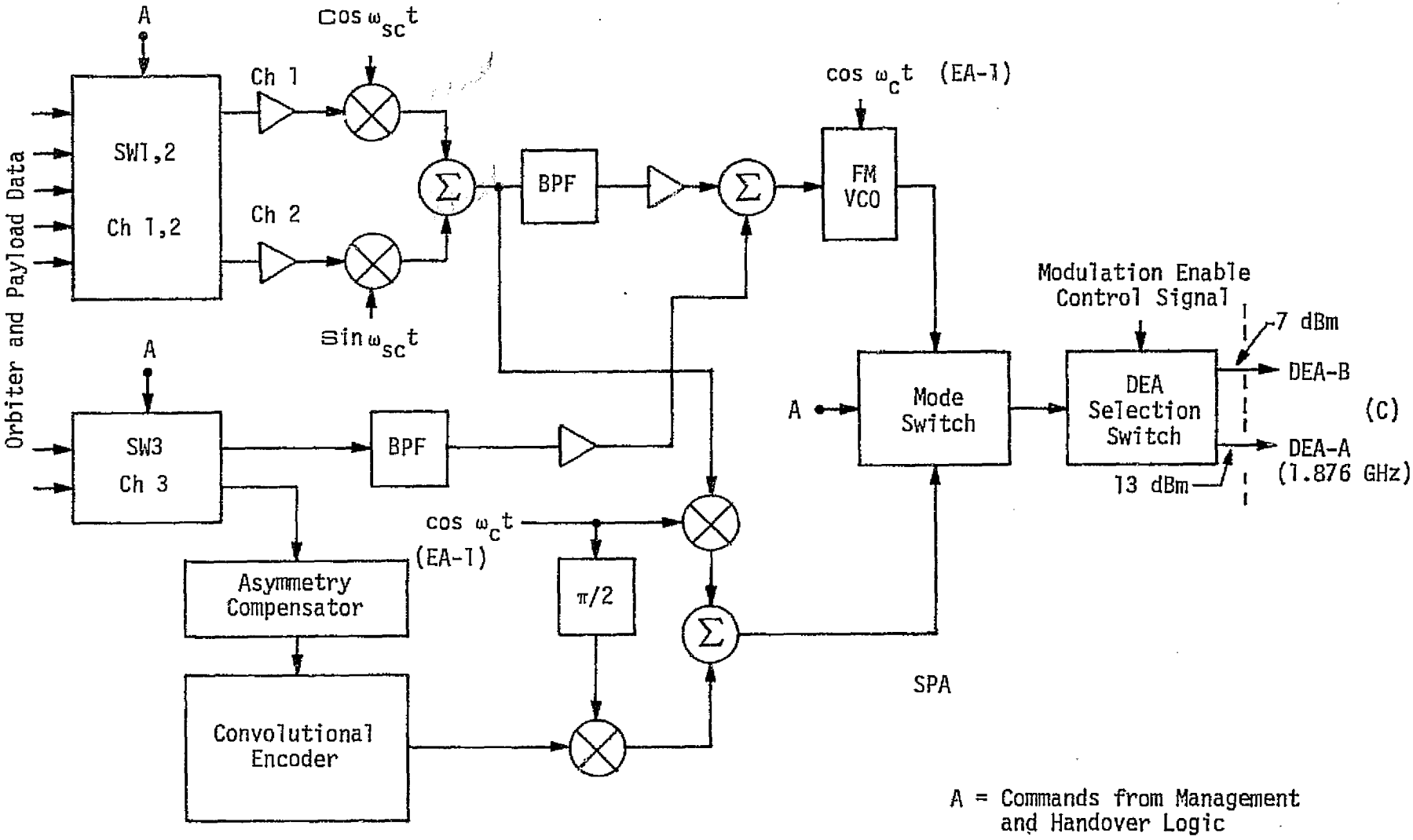

Figure 51. Return Link Block Diagram in SPA

In Mode 1, the generated quadriphase signal is modulated on the quadrature channel of a carrier frequency of 1.876 GHz derived from EA-1 while Channel 3, after passing through a convolutional encoding stage, is modulated on the in-phase channel of the carrier frequency. The resulting combination is a double quadriphase modulation with a nominal power split of 80%, 16%, and 4% for Channels 3, 2, and 1, respectively.

In Mode 2, the subcarrier quadriphase signal is bandpass filtered to obtain a sinusoidal subcarrier and then summed with the 4.5 MHz wideband Channel 3. The nominal power ratio in Mode 2 is 35% for quadriphased Channels 1 and 2 and 65% for Channel 3, while the power ratio in the subcarrier quadriphase-modulated signal remains as in Mode 1. The composite signal is then frequency modulated to produce an FM signal with the same carrier frequency as in Mode 1 (1.876 GHz) and a maximum peak-to-peak deviation of 34.0 MHz. The required mode is selected via the mode switch, and the resulting return link signal is then sent to DEA-A or DEA-B, depending on the communication enable command, for coherent up-conversion before transmission. The nominal signal level at the output of the SPA subunit is expected to be 13 dBm for DEA-A and 7 dBm for DEA-B. This is because there are no radar losses through DEA-B.

Before describing the DEA portion of the return link, the convolutional encoder is described and the effect of the variation in power distribution between various channels is analyzed.

6.2 Convolutional Encoder

The convolutional encoder is used to encode Channel 3 in Mode 1 at a rate 1/2 and constraint length 7, thus converting the 2-50 Mbps NRZ data into 4-100 Msps encoded data. This is achieved by synchronizing a received 2-50 Mbps clock with the equal amplitude, equal rate data by selecting the proper clock phase via a D flip-flop utilizing 1×clock and 2×clock frequencies. The encoder uses a 31-stage phase shift register with two modulo-2 adders and two 5-bit shift registers which are loaded at every fifth uncoded input data bit into a 10-bit buffering output shift register after passing through a delay line, as shown in Figure 52. Timing plays a very important

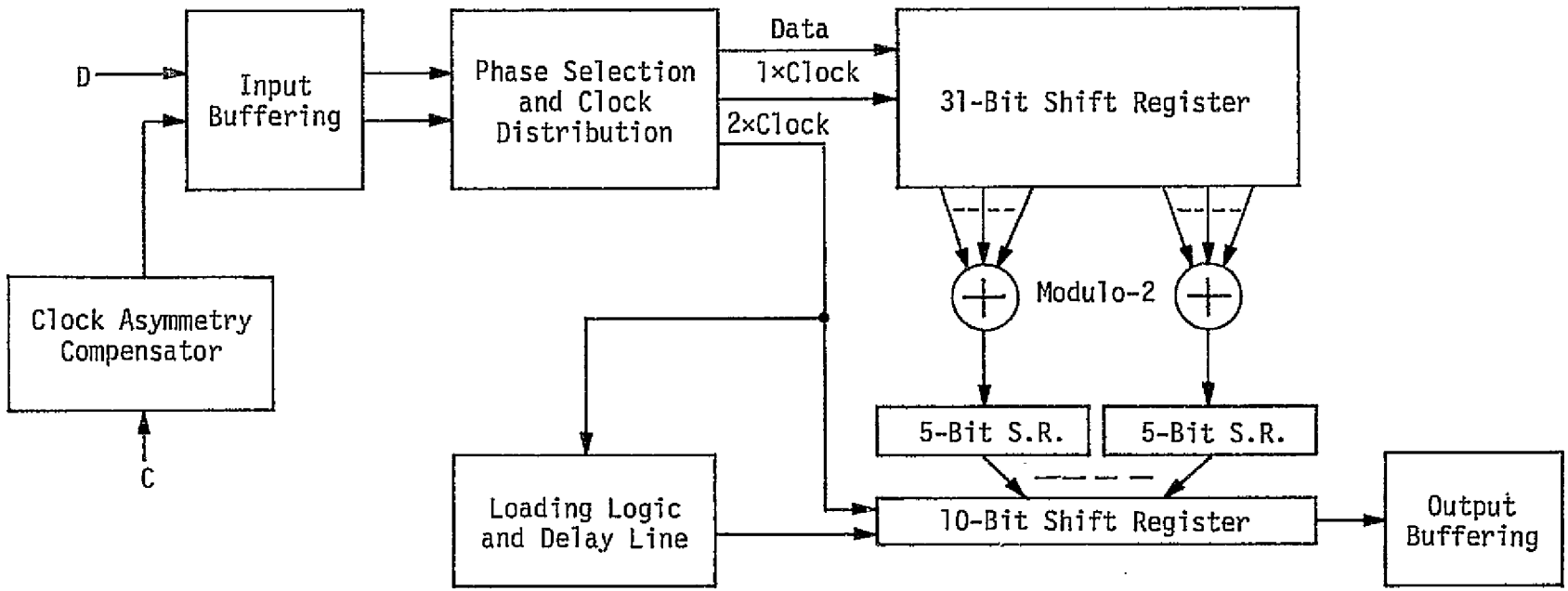

C = Clock with Same Amplitude and Rate

D = Data 2-50 Mbps NRZ (Channel 3) from Orbiter

Figure 52. Convolutional Encoder

role in the operation of the convolutional encoder. Since delay lines are used for timing purposes, care must be taken to avoid any dead zones in the operation. One such dead zone was reported at 10 Mbps.

6.3 Data Asymmetry

One area of concern in the return link is the data asymmetry produced by the 50 Mbps rate 1/2 convolutionally coded data channel over the TDRSS. This is a potential problem which can cause appreciable degradation to the demodulated data detection. This degradation is a function of the amount of asymmetry produced by the SPA return link circuitry.

The bit error rate performance of the convolutional decoder depends, among other things, on the symmetry of the modulation. Any asymmetry in the NRZ symbols entering the symbol synchronizer causes a misalignment in the symbol synchronization clock which degrades the integrate-and-dump output and any soft or hard decisions derived from it for input to the decoder. For a specified degree of asymmetry (in terms of a fraction of a symbol interval), the bit error rate degradation is dependent on the transition probability of the data. Clearly, if the data transmitted was either all ones or all minus ones, misalignment of the bit synchronization clock would have no degrading effect on the integrate-and-dump output since, for each symbol, this circuit would integrate up to its maximum value before being dumped. On the other hand, when the data is an alternating sequence, the worst-case degradation results, since the transition which occurs at the end of each symbol in combination with the symbol synchronization clock misalignment prevents the integrate-and-dump output from reaching its maximum value.

A detailed analysis of the problem was presented in [18] where two possible sample detectors were discussed taking into account the existence of data capacitive coupling which is used to restore any existing D.C. level, as well as the detector band limiting effects. A summary of the results is presented here to help in giving a complete evaluation of the effects of data asymmetry.

The first type of detector, which is the filter-sample type detector, is shown in Figure 53. Assuming NRZ data, the performance of the detector is illustrated in Figures 54 and 55, where η represents the asymmetry defined as the difference in length between the shortest and

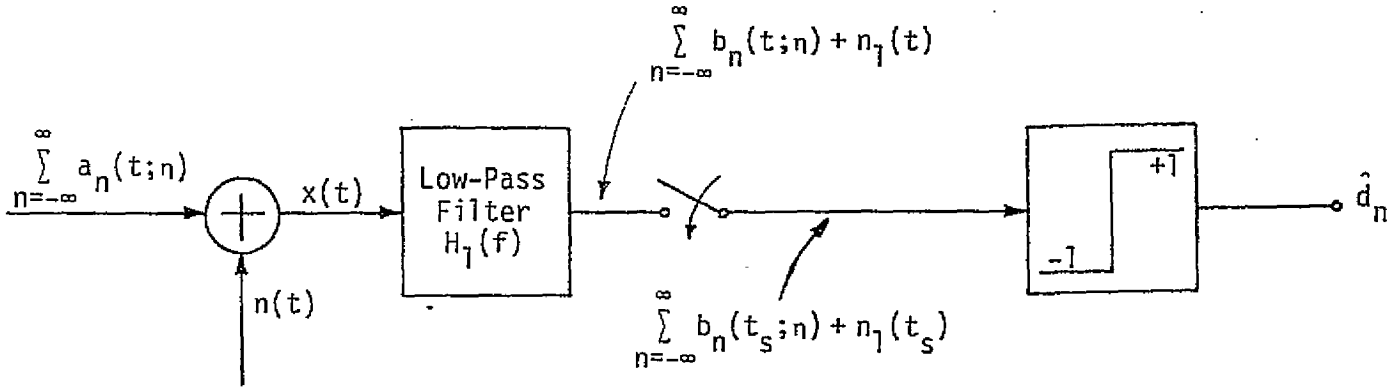

Figure 53. Band Limit and Sample Detector for Binary Data With Asymmetry

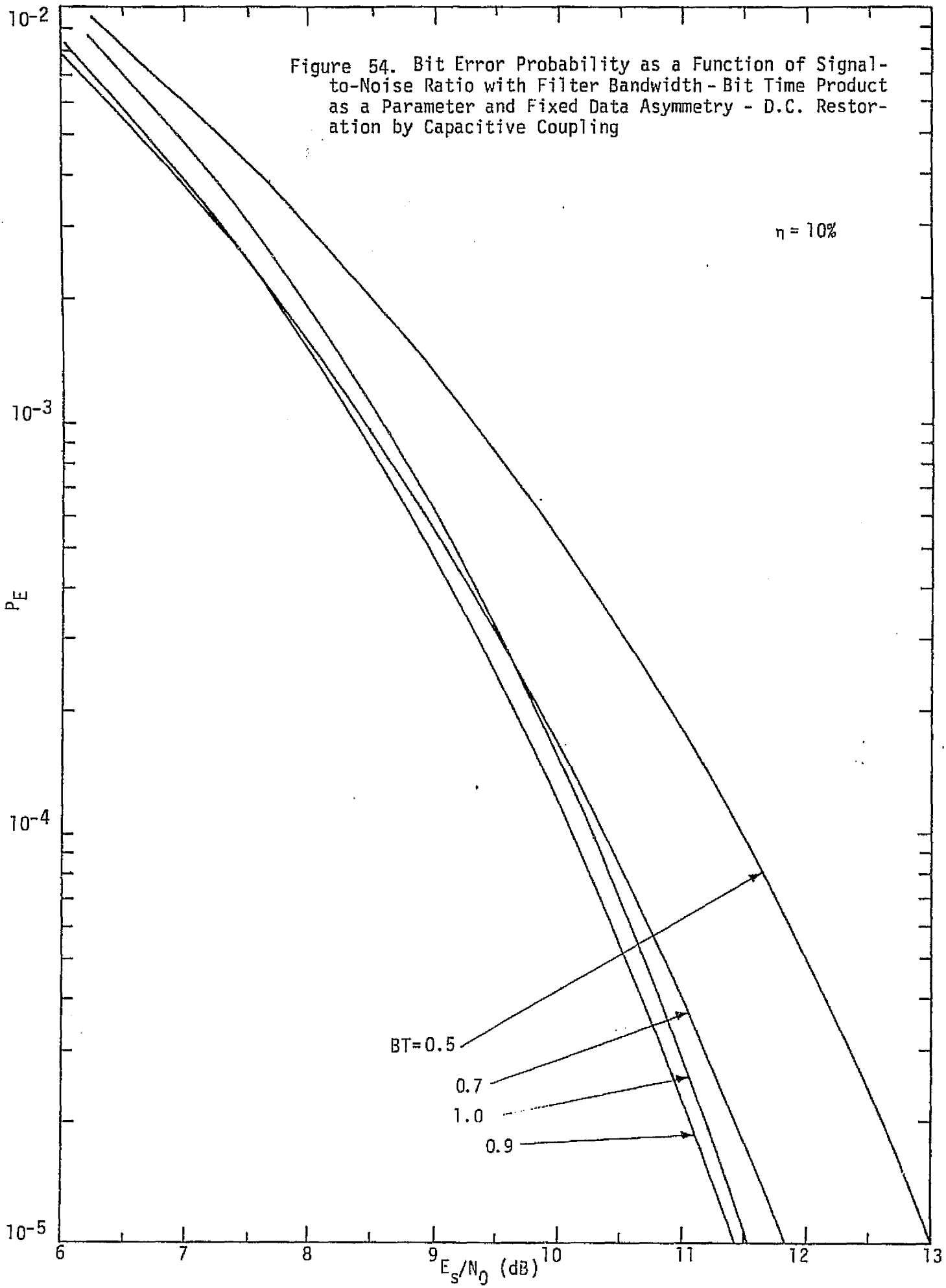

Figure 54. Bit Error Probability as a Function of Signal-to-Noise Ratio with Filter Bandwidth - Bit Time Product as a Parameter and Fixed Data Asymmetry - D.C. Restoration by Capacitive Coupling

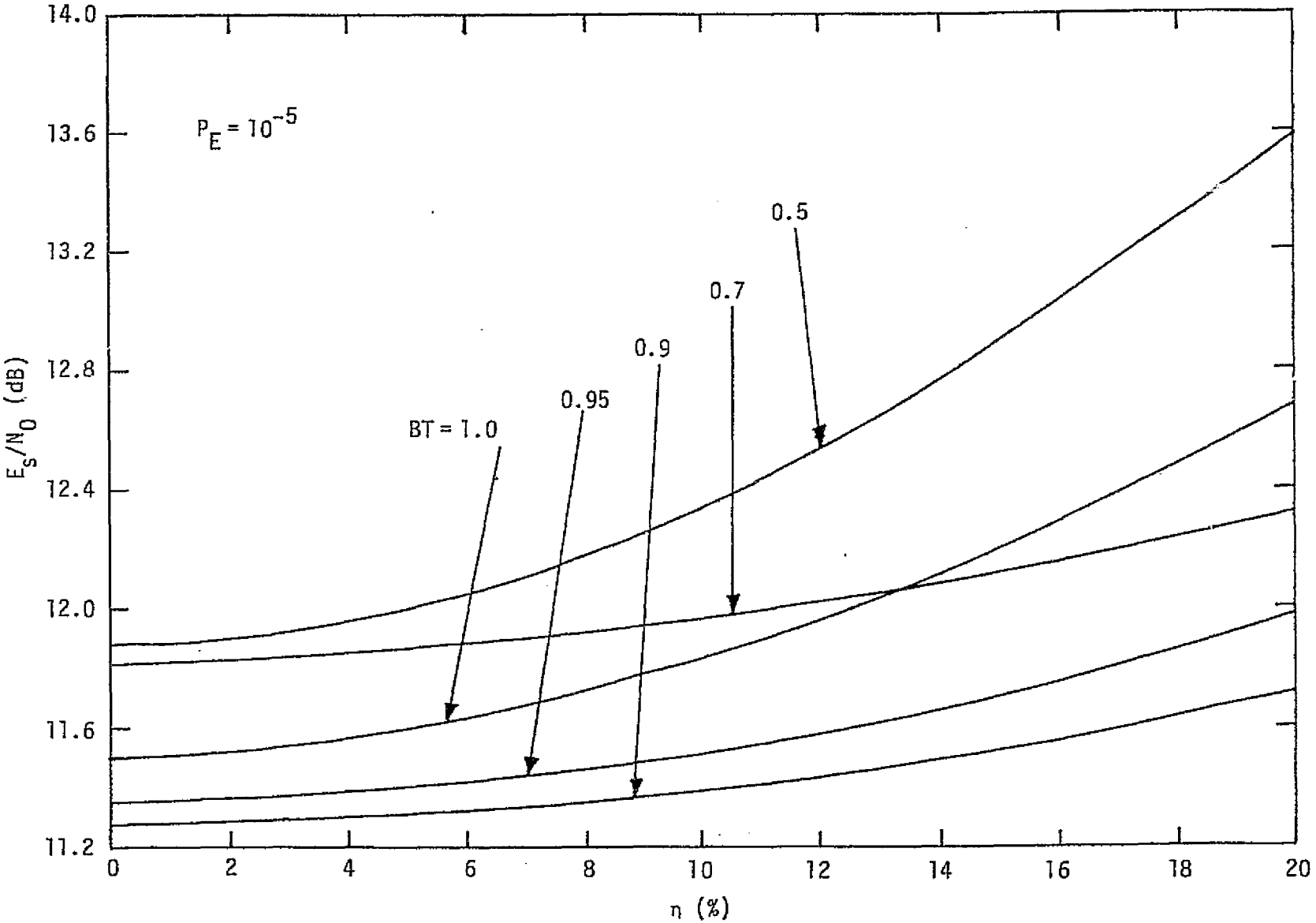

Figure 55. Energy-to-Noise Ratio as a Function of Data Asymmetry for Fixed Bit Error Probability and Filter Bandwidth - Bit Time Product as a Parameter; D.C. Restoration by Capacitive Coupling

the longest pulses in the sequence divided by their sum and E_s/N_0 is the symbol energy-to-noise spectral density ratio. It could be concluded that, for small values of asymmetry (less than about 10%), the optimum filter bandwidth-bit time product remains equal to 0.9, and the corresponding amount of energy-to-noise ratio degradation at a fixed error rate is virtually independent of whether or not D.C. restoration is present.

Using BT = 0.9, the degradation in signal energy-to-noise spectral density, which is the additional E_s/N_0 needed to achieve the required performance, is summarized in Table 9.

Table 9. E_s/N_0 Degradation with D.C. Restoration by Capacitive Coupling

$P_E = 10^{-4}$			$P_E = 10^{-5}$		
η(%)	E_s/N_0 (dB)	$\Delta E_s/N_0$ (dB)	η(%)	E_s/N_0 (dB)	$\Delta E_s/N_0$ (dB)
0	9.97	0	0	11.28	0
2.5	9.99	0.02	2.5	11.30	0.02
5.0	10.02	0.05	5.0	11.32	0.04
10.0	10.12	0.15	10.0	11.40	0.12
15.0	10.25	0.28	15.0	11.54	0.26
20.0	10.44	0.47	20.0	11.73	0.45

The table shows that for asymmetry less than 10%, the degradation does not exceed 0.15 dB.

The other possible implementation of the data detector is the gated integrate-and-dump filter shown in Figure 56. Figures 57 and 58 are the corresponding performance curves for this detector. The dotted line in Figure 58 represents the best achievable performance using the gated integrate-and dump data detector. In both figures, ε represents the fractional gate interval (relative to symbol time) at each end of the symbol.

In order to minimize the degradation and to meet the asymmetry specifications of 10%, HAC has proposed an asymmetry compensator which

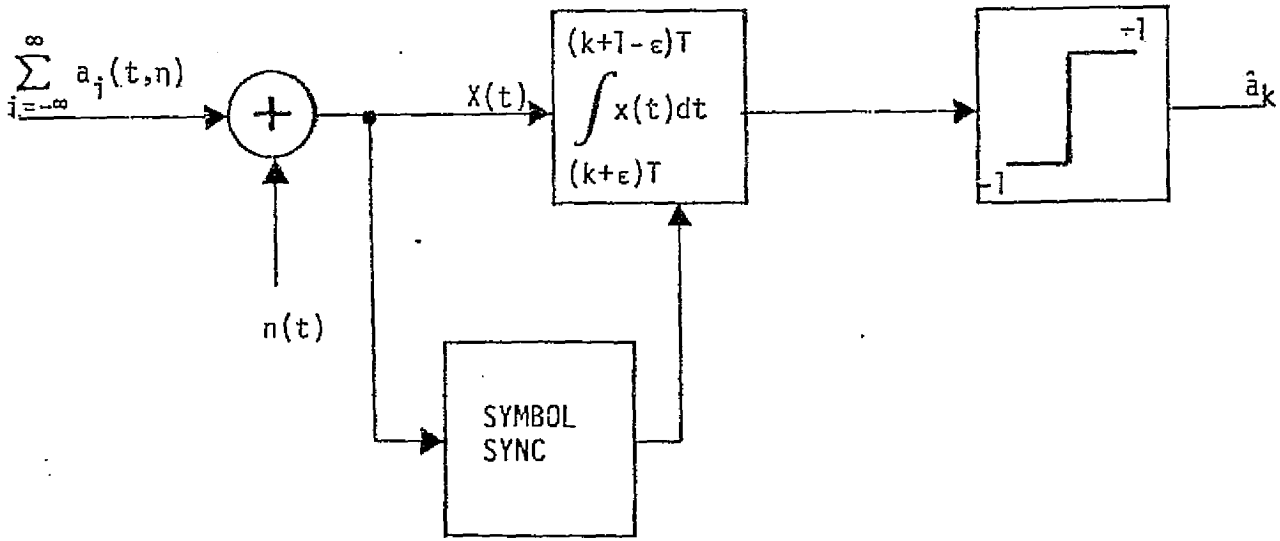

Figure 56. Gated Integrate-and-Dump Filter

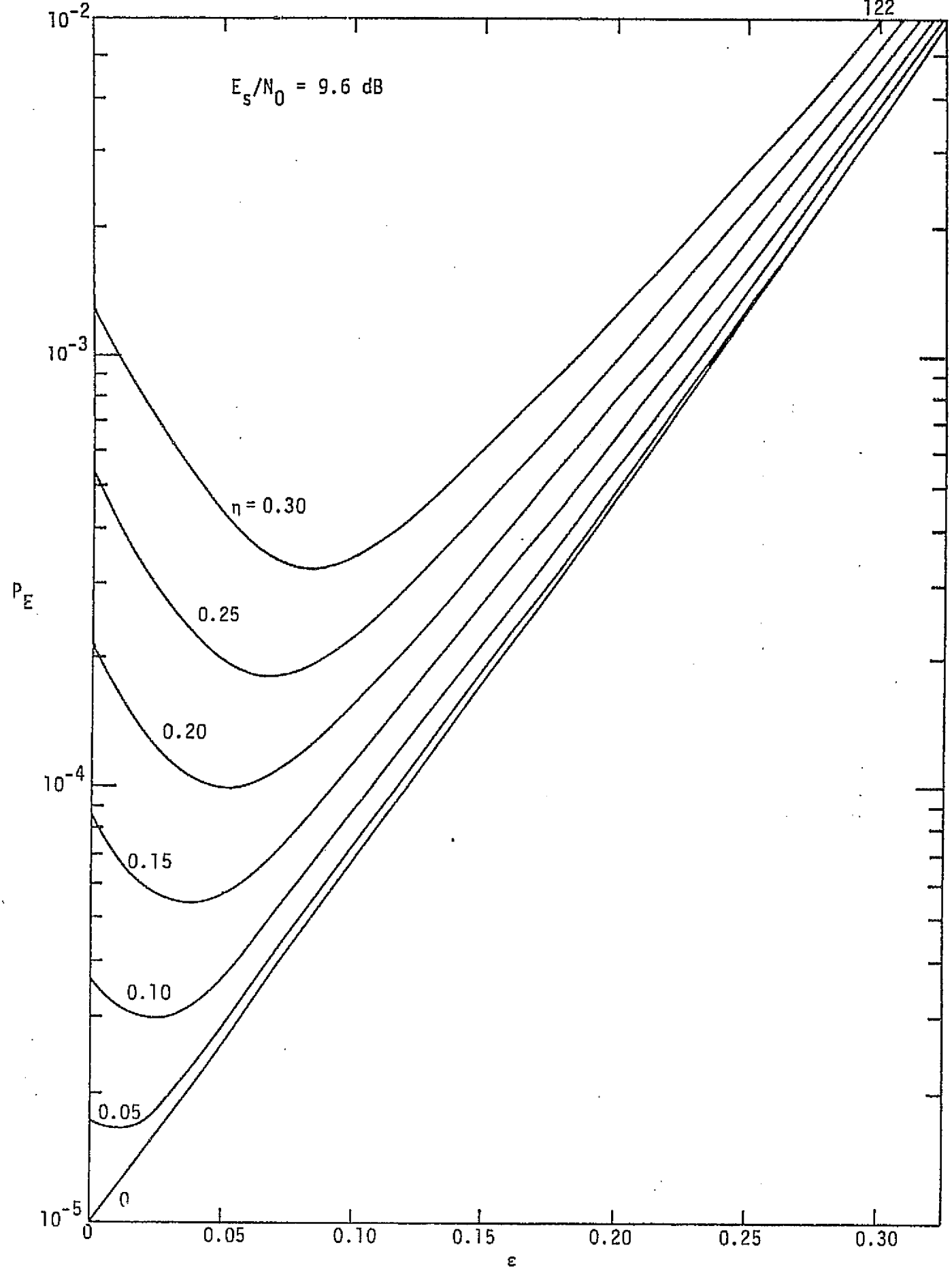

Figure 57. Average Error Probability versus Gate Interval at Symbol Edge with Data Asymmetry as a Parameter - D.C. Restoration by Capacitive Coupling

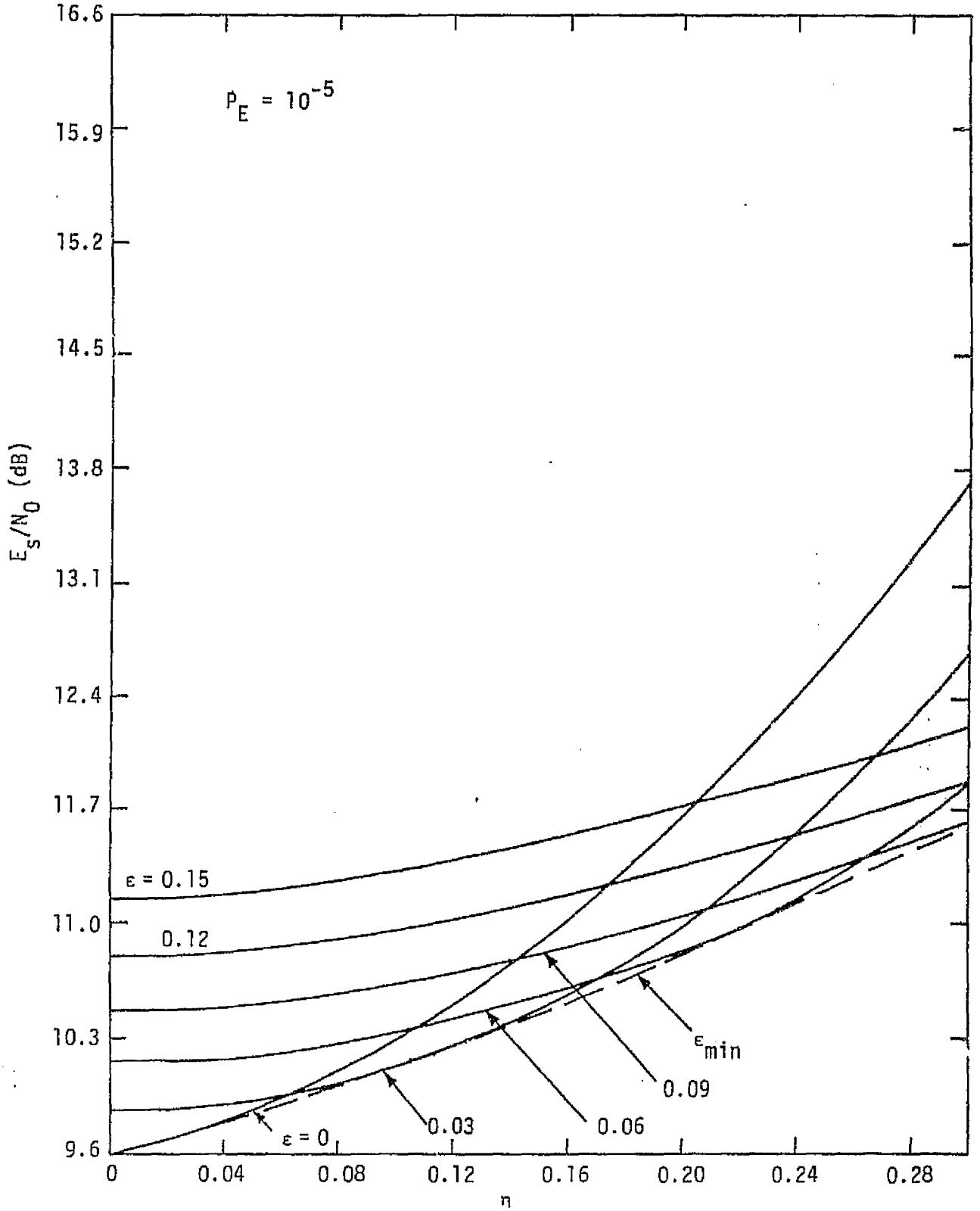

Figure 58. Symbol Energy-to-Noise Ratio versus Data Asymmetry with Gate Interval at Symbol Edge as a Parameter - D.C. Restoration by Capacitive Coupling

uses a closed loop compensator detector circuit and a D flip-flop to give a maximum asymmetry of 10%. A detailed description of the encoder and the compensator is presented in [17]. No test data pertaining to the performance of the compensator is available. It is believed, however, that the compensator output will meet the asymmetry specifications. The effects of any asymmetry test data on the probability of bit error, however, can be directly evaluated using Figures 21, 22, 25, and 26.

6.4 Effects of Deviation From the Nominal Power Ratio in Mode 1

The demodulator for the three-channel (Mode 1) configuration is a combination of two Costas loops [19] which are implemented to recover the carrier and then the subcarrier before the data can be demodulated. Appendix B presents the detailed analytical discussion of the effect of change in power distribution between the three channels on the tracking of the subcarrier loop. These changes are attributed to the inability of the hardware to maintain the exact nominal power distribution. Using the current estimates of the system losses of TDRSS, Figures 59 and 60 illustrate two cases of interest.

Channel 2 is assumed to be NRZ in the first case and biphase-L in the second, while Channel 1 is assumed to be biphase-L in both cases. The ratio of total power to the product of the single-sided spectral density and Channel 2 rate $P_T/(N_0R_2)$ is taken to be 22 dB, which is the approximate expected return signal-to-noise ratio. Different signal-to-noise ratios are shown in Appendix B. In all cases, the carrier tracking loop is optimistically assumed to be tracking perfectly. The effect of any carrier tracking error (φ_c) is an additional degradation to the rms subcarrier jitter of $\cos^2 \varphi_c$. The selected values of power ratios in the three channels are typical expected performance values of the return link modulator in the SPA [20]. Table 10 shows the nominal values, as well as the ratios used in the calculations. In deriving the values for the rms phase jitter, Channel 3 data was assumed to be NRZ data.

As is obvious from Figures 59 and 60, the subcarrier rms tracking jitter changes drastically due to the above variations in power distribution for all values of B_i/R_2, which is the ratio of the two-sided arm filter noise bandwidth to the Channel 2 data rate. The arm filter in the analysis is assumed to be a first-order Butterworth (RC) filter with

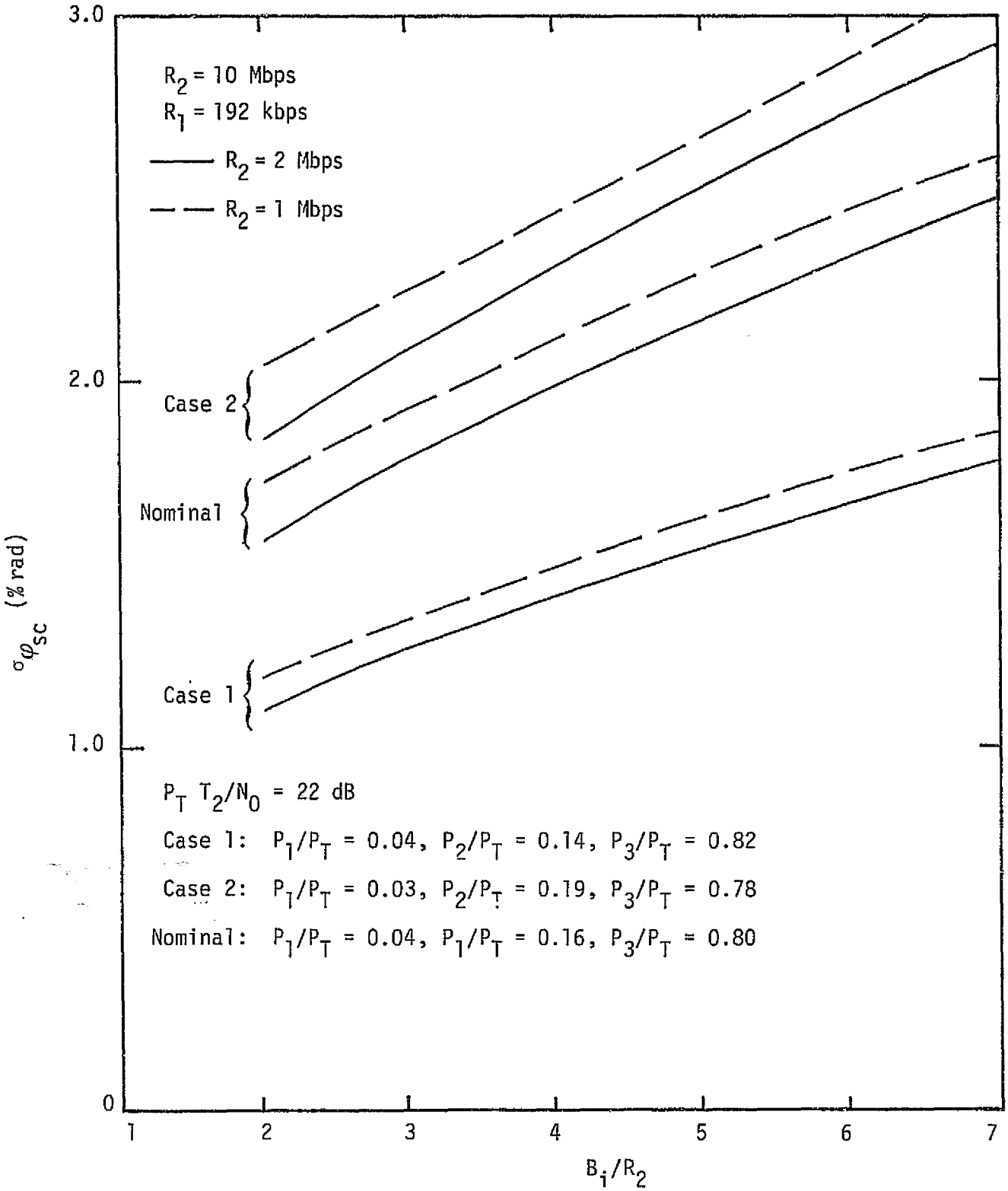

Figure 59. Subcarrier Tracking rms Jitter vs. Ratio of Arm Filter Bandwidth to High Subcarrier Data Rate R_2; R_2 is a Parameter; $m_3(t)$ and $m_2(t)$ are NRZ, $m_1(t)$ is Manchester

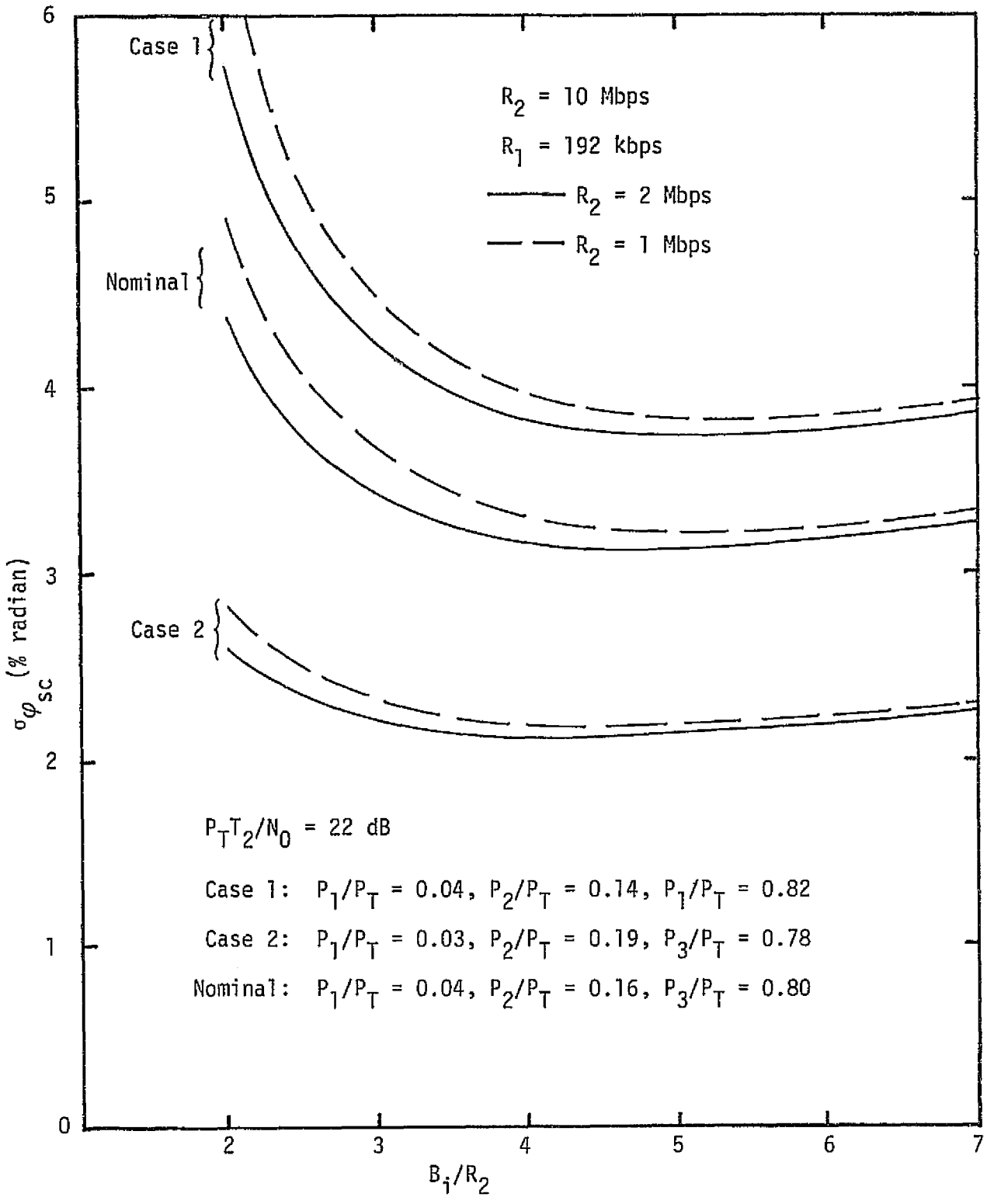

Figure 60. Subcarrier Tracking rms Jitter vs. Ratio of Arm Filter Bandwidth to High Subcarrier Data Rate R_2; R_2 is a Parameter; $m_3(t)$ is NRZ, $m_2(t)$ and $m_1(t)$ are Manchester[2]

Table 10. Power Ratios in Mode 1
($P_T = P_1 + P_2 + P_3$)

	P_3/P_T	P_2/P_T	P_1/P_T	
Nominal	0.80	0.16	0.04	
Case 1	0.82	0.14	0.04	Expected Variations
Case 2	0.78	0.19	0.03	

a typical ratio between its two-sided bandwidth (B_i) and the loop single-sided noise bandwidth (B_L) of 10^4. It should also be noted that the performance of the subcarrier tracking loop in terms of the rms jitter is worse in the case of the biphase-L data in Channel 2 than it is when the data is NRZ.

To obtain the total effect of the variation in power ratio distribution on the probabilities of bit error, however, two factors have to be taken into consideration:

(1) The variations in the loop phase jitter ($\sigma^2_{\varphi_{sc}}$) which, in turn, affects the probabilities of error. This factor, however, has been shown in [21] to be less than 0.14 dB under worst-case conditions. In other words, the deviation from the ideal tracking case is negligible.

(2) The changes in signal-to-noise ratios in the various channels. To illustrate this effect, a typical expected value of $P_T T_2/N_0 = 22$ dB is selected at the input of the subcarrier Costas loop. Choosing $R_2 = 2$ Mbps and $R_1 = 192$ kbps as an example, Appendix B shows that the resulting design margins to achieve the specified probabilities of bit error of 10^{-4} in the lower two channels are still adequate for both cases of interest. Using an estimated 2 dB for the TDRS bit synchronizer loss, the resulting design margins are summarized in Table 11.

Table 11. Return Link Lower Rate Channels Design Margins

	Channel 1	Channel 2
Case 1	6.55	2.78
Case 2	4.19	4.83

$R_3 = 10$ Mbps, $R_2 = 2$ Mbps, $R_1 = 192$ kbps

$P_T T_2/N_0 = 22$ dB

The example clearly illustrates that, in spite of the expected variations in the signal powers in the three channels, adequate design margins exist due to the high return link signal-to-noise ratios.

6.5 Return Link RF Signal Flow

In this section, the return link signal is traced through the Deployed Electronic Assembly DEA. Since parts of the DEA are shared with the radar mode, the main radar signals are pointed out with the detailed discussion presented in Section 3.0.

The modulated communication signal (Mode 1 or Mode 2) leaves the SPA unit at Point C (Figure 51) to be up-converted in the DEA exciter subunit (shown in Figure 61) to the Ku-band communication transmitter frequency of 15.003 GHz. This is accomplished by mixing the incoming 1.876 GHz signal with a 13.128 GHz signal and filtering it with a bandpass filter (BPF 1). The 13.128 GHz frequency is generated via a phase-locked loop (PLL) using the 83rd harmonic (12.972 GHz) of a 156.3 MHz reference frequency from EA-1. The loop is closed by a mixer which is used to form the difference frequency between that generated by a swept Ku-band Gunn VCO and the 12.972 GHz signal. The resulting signal is compared via a comparator whose reference level of 52.1 MHz which is derived by dividing the 156.3 MHz signal by 3. Whenever the Gunn VCO tunes to a frequency for which the output of the mixer M1 equals any integral multiple of 52 MHz, the output of the comparator will be detected by a zero beat detector (not shown in the figure) which, in turn, will stop the sweep and phase-lock the VCO. The reason behind this implementation is to allow easy generation of the five discrete radar frequencies used in the passive mode by proper bandpass filtering of the output of M1. The five radar frequencies are generated by proper VCO frequency selection which ranges from 13.128 GHz to 13.336 GHz in steps of 52 MHz and then by mixing with a 651 MHz signal which is generated from the original 156.2 MHz reference. Switches SW1 and SW2 are used to shift from the communication mode to the radar mode according to the Comm/Radar Enable command.

It should be noted that the output of the Gunn VCO is also used as a first LO frequency in the forward link (receiver) and that 573 MHz

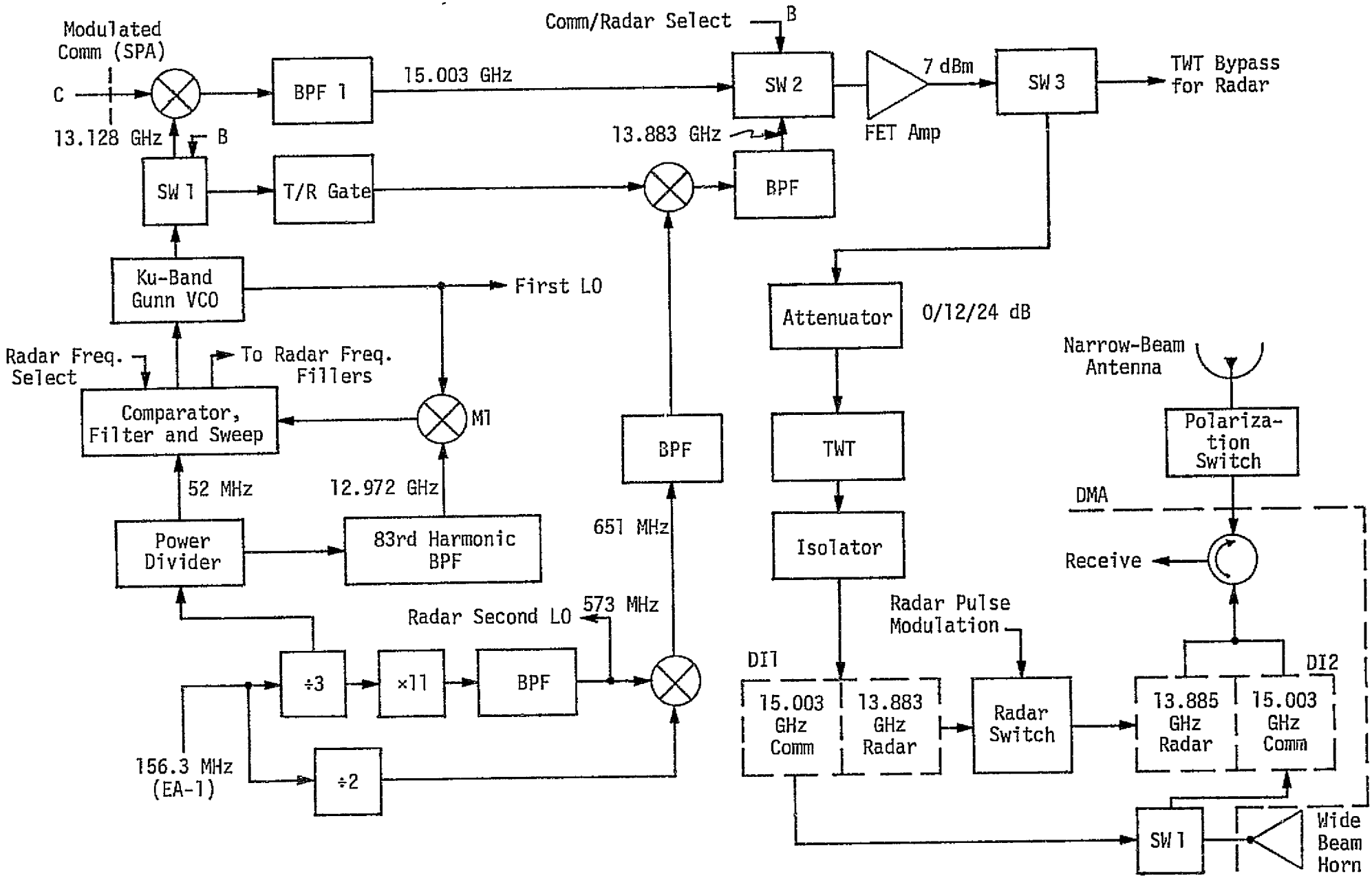

Figure 61. Return Link RF Signal Flow

is also derived from the 156.3 MHz reference for use in the radar second LO.

The up-conversion is followed in both the radar and communication modes by a four-stage, low-noise FET amplifier which is used to increase the drive power of the traveling wave tube (TWT) to 7 dBm and to reduce any amplitude modulation on the drive signal. Switch SW3 is then employed to extract a TWT bypass radar signal which is used in the radar short range operation. The signal is then passed through an adjustable attenuator which selectively provides 0 dB, 12 dB, or 24 dB of attenuation to the signal. A TWT amplifier, which operates between 14-15 GHz to accommodate both radar and communication modes, is then used to amplify the signal to a 60W nominal power at its output (55 watts in the case of the radar).

In order to turn the TWT on, two signals are needed: (1) a standby or ON command from EA-1 which enables the transmitter high voltage, the TWT filament and the TWT modulating anode power supplies and (2) a transmit enable command which enables the modulating anode after at least a three minute warm-up period following the first command.

There are isolator stages preceding and following the TWT which constitute part of the transmitter microwave subassembly in which harmonics outside the radar and communication bands are filtered. The signal then reaches the first diplexer, DI1, which consists of bandpass/band-reject filters of multicavity Chebyshev design. DI1 routes the return link signal to waveguide switch SW4 which, according to the original design, routes the signal to either the DMA wide-beam antenna in the TDRS acquisition mode or through a second similar diplexer DI2 to the narrow-beam antenna to transmit the signal to the TDRS after acquisition. In the original design, a polarization switch is also implemented to select the proper radar or communication polarization. Since the TDRSS angle tracking circuits are limited in the rate of change of received signal power, the switching from wide-beam to narrow-beam is creating a problem. It was therefore necessary to adjust the search procedure and use the GPC designate with only the narrow-beam antenna as the primary mode. Axiomatix therefore suggests that the polarization of the wide-beam antenna be changed to linear polarization, which will assist the radar mode in sidelobe discrimination.

The radar signal is routed by DI1 into a radar switching unit (ferrite circulator switch) which provides an 80 dB guard attenuation during the receive mode. The output power level of the return link signal during normal operation is approximately 50W (47 dBm).

Figure 61 shows only the necessary components of the return link. A separate discussion of the forward link is presented in Section 5.0. Also not shown in Figure 61 is the low voltage power supply subassembly [22] which is used to generate all the required DC voltages for operation of the DEA.

7.0 DEPLOYED ASSEMBLY

The DA consists of the deployed mechanical assembly (DMA) and the deployed electronics assembly (DEA). This section is devoted to describing the major functions to be performed by these units and to identifying the major signals between these units and between the Ku-band system and the Orbiter. In addition, the major potential problems are summarized wherever they might exist. In order to avoid duplication of effort and since the signal flow in the various operation modes has been discussed in Sections 3.0, 5.0, and 6.0, this section only describes the major functional blocks within each subunit without any effort to analyze the signal flow within each block. It should also be emphasized that only the major signals are included to achieve a better understanding of the system without cluttering the diagrams with extensive details.

7.1 Deployed Mechanical Assembly

7.1.1 Antenna System

The antenna system is composed of a 36-inch diameter graphite-epoxy reflector fed by a quad-ridged circular waveguide radiator. The present status is that problems exist in achieving the proper antenna pattern performance on the antenna measurement range. The initially proposed "crossed dipoles in a cup" feed was found to have unacceptable temperature increases resulting from the transmitter power levels which will be used for the integrated radar/communication system.

7.1.2 Antenna Feed Subsystem

The obvious restriction imposed by the stowage envelope within the Shuttle bay has resulted in a design with an F/D ratio of 0.28, which has created some problems in attaining the desired antenna patterns by standard experimental iteration methods. Because of the limited space available, the number of available design options and alternatives has been substantially reduced to the point where only minor adjustments in dipole spacings, sum feed aperture height above the ground plane, and effective focal point placement can be readily accomplished. The present design, with its limitations, has few modification options. A solution might be subsequently found using the present techniques but it might be prudent to first assess the existing design and then examine alternatives.

The present design consists of crossed probes in a quad-ridge waveguide section spaced such that circular polarization capabilities were attainable. The quad-ridge waveguide section allows a wider RF bandwidth and maintains isolation between the orthogonal linear polarizations. The quad-ridge section tapers into a circular waveguide section whose diameter is determined to avoid multimoding effects. The radiating aperture itself is just the open end of the circular waveguide, with no flaring or other impedance matching techniques used. This abrupt transition at the circular waveguide-free space interface is probably a significant cause of the relatively large input VSWR measured. Also, due to the short feed length, mode control is extremely difficult, and such techniques as corrugations appear to be impractical. Under these conditions, it appears difficult to control the illumination taper of the reflector and also determine the effective phase centers for the feed at the two frequencies involved except by purely experimental methods.

The incorporation of the four printed circuit dipoles composing the monopulse tracking function has complicated the design somewhat because of the mutual coupling effects between the dipoles and the quad-ridged circular waveguide sum feed, which by reciprocity affects both patterns. Again, iteration techniques must be employed to minimize this mutual coupling since isolation is essential for optimal performance.

The blockage effects of the protruding waveguide runs to the feed have had demonstrated increased sidelobe contribution effects, but this is inherent in the design and has been minimized by reducing the waveguide cross-section to that of the narrow wall, with the three waveguides stacked on edge. Also, the placement of the waveguide run is important and seems to have been adjusted accordingly. For the linearly polarized mode of operation, it is essential that the electric field vector be perpendicular to electrically conductive pods for minimum pattern disturbance. This not only applies to the waveguide run but also to support pods made of graphite epoxy, which is a relatively good electrical conductor. The shape of the pod is also critical, since a diamond wedge shaped cross-section would have minimized the blockage cross-section for an electric field vector perpendicular to the pod axis.

7.1.3 Reflector

The RMS surface tolerance and thermal characteristics of the reflector itself will not be addressed since the reflector shell is cast on a precision machined surface. Care must be taken during separation from the mold to avoid damage, and it is assumed that adequate reinforcing joints are used to satisfy shock and vibration requirements.

The two points of possible concern for the graphite-epoxy reflector are metallization of the reflector surface and uncured resin problems. Since most radar and communications applications do not require perfect reflection, it is a common practice to use the high reflection coefficient of the dielectric mismatch of the cured resin instead of an electrically conductive surface. Graphite-epoxy is conductive; however, it is highly anisotropic since it depends on the orientation of the fibers in the fabric material over which the resin is cast. Therefore, for some applications, it might be wise to consider metallizing the surface. This would be true for the case of a wide illumination angle such as 164° since the reflection coefficient might noticeably decrease at the extremes due to Brewster angle impedance-matching. A recently declassified materials measurement report also indicated that graphite-epoxy is not as electrically conductive as has been commonly assumed.

Another problem that has recently arisen and must be closely monitored is the bubbling of a graphite-epoxy surface due to uncured resins. This phenomenon, which is obviously deleterious, can be caused by a number of fabrication problems such as nonstoichiometric mixtures and nonuniform mixing. Although it appears trivial, it has become apparent on flight-qualified reflectors after antenna pattern measurements were taken on the SEASAT/NIMBUS G SMMR programs.

In addition to the above, the specifications require the antenna sidelobes to be at least 18 dB below the main lobe. The current test figures show that the sidelobes can be as high as 14 dB below the main lobe, which is a potential source of problems, especially in the radar mode.

Finally, since the primary TDRS search mode is now the GPC designate because of the inability of the TDRS angle tracking circuitry to

withstand a large rate of signal power change, it is recommended that the wide-beam horn polarization be changed to linear polarization. This would help sidelobe rejection capabilities in the radar mode.

7.1.4 Possible Alternative Antenna Concepts

Although the presently committed HAC design is probably adequate and earlier proposal studies explored various other types of feasible systems, Axiomatix would like to consider some possible modifications of the existing design.

The immediate concern for the existing design is the absence of a well-defined null in the elevation (or azimuth) plane difference channel. This phenomenon might be attributed to the geometrical relationship of the dipoles to the incoming phase front on which the monopulse tracking system is based. This phase front problem would be more apparent for lower F/D ratios of the antenna reflector systems for one orientation of linear polarization. The incoming phase front for the case of the linear polarization in the plane of incidence suffers from a lack of phase resolution since it approaches the dipole at a grazing angle. Because of this grazing angle of incidence, the phase itself cannot be well characterized by the dipole which is of the order of half a wavelength long. An attempt to pictorially describe this phenomenon is shown in Figure 62a, which shows that the phase front from the edge of the reflector is incident on the monopulse dipole at close to a grazing angle. A more detailed description is shown in Figure 62b, which shows the phase relationship of the incident wave on the dipole for the ray path designated by A. It is seen that the phase relationship cannot be well defined for this orientation of polarization and this particular dipole orientation. This is not true for the ray path designated B since the electric field vector would be oriented parallel to the dipole, and a prominent null would exist. Similarly, the gain is degraded since the incident electric field vector is not parallel to the dipole.

If this hypothesis is valid, then some corrective measures could be taken. One would be to use a curved dipole pair elevation plane monopulse system, as shown in Figure 62c. This configuration would most closely resemble the focused spherical phase front and

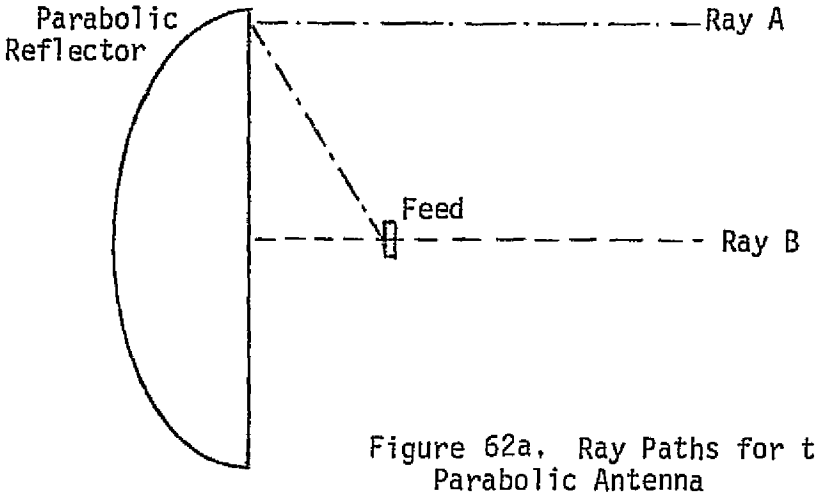

Figure 62a. Ray Paths for the Parabolic Antenna

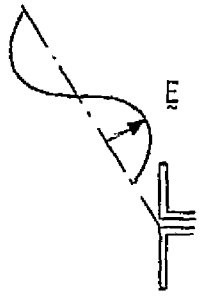

Figure 62b. Incident Electric Field on the Dipole

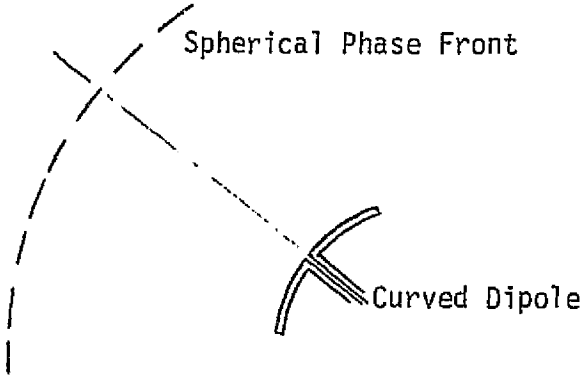

Figure 62c. Curved Dipole Configuration

would thereby avoid the null problem. This technique might be considered for correcting the present HAC design.

Another configuration which might be considered is the Cassegrain system. The argument used in the Ku-band PDR (Vol. VI, DMA and DA, Section 9-1, March 14-24, 1978) assumes that only horns would be used for the monopulse system and, therefore, because of the spacing problem, the horns would be widely separated. However, the same type of printed circuit monopulse four-linear-dipoles system can be used instead of the additional horns. The resulting larger F/D ratio would help alleviate the null problem described earlier. In addition, the absence of waveguide blockage would decrease the sidelobe levels. The 2-inch diameter of the horn is due to the flaring of the horn, which results in a better feed pattern than the abrupt open-ended 0.5-inch diameter circular waveguide, and the improved impedance matching would result in a much lower input VSWR.

7.2 Deployed Electronic Assembly

A block diagram of the Deployed Electronic Assembly (DEA) is shown in Figure 63, which includes five major blocks denoted as the low voltage power supply, the exciter, the transmitter, the transmitter/receiver microwave circuit, and the receiver. The low voltage power supply receives an unregulated 28 ±4 VDC supply from the main bus on the Orbiter to provide all the required regulated DC voltages to the DEA. The exciter uses a 156 MHz reference signal from EA-1 to generate the communication Ku-band frequencies and the five radar Ku-band frequencies and to upconvert the modulated communication signal from the SPA to the Ku-band frequency of 15,003 GHz. In the radar mode, the exciter receives three main signals from EA-2, namely,

(1) Radar power signal which controls the radar power selection by inserting 0/12/24 dB attenuation to the signal power or completely bypassing the TWT for proximity operations.

(2) Radar frequency select which chooses the required RF frequency for frequency diversity purposes.

(3) T/R signal which switches the T/R switches for transmission and reception.

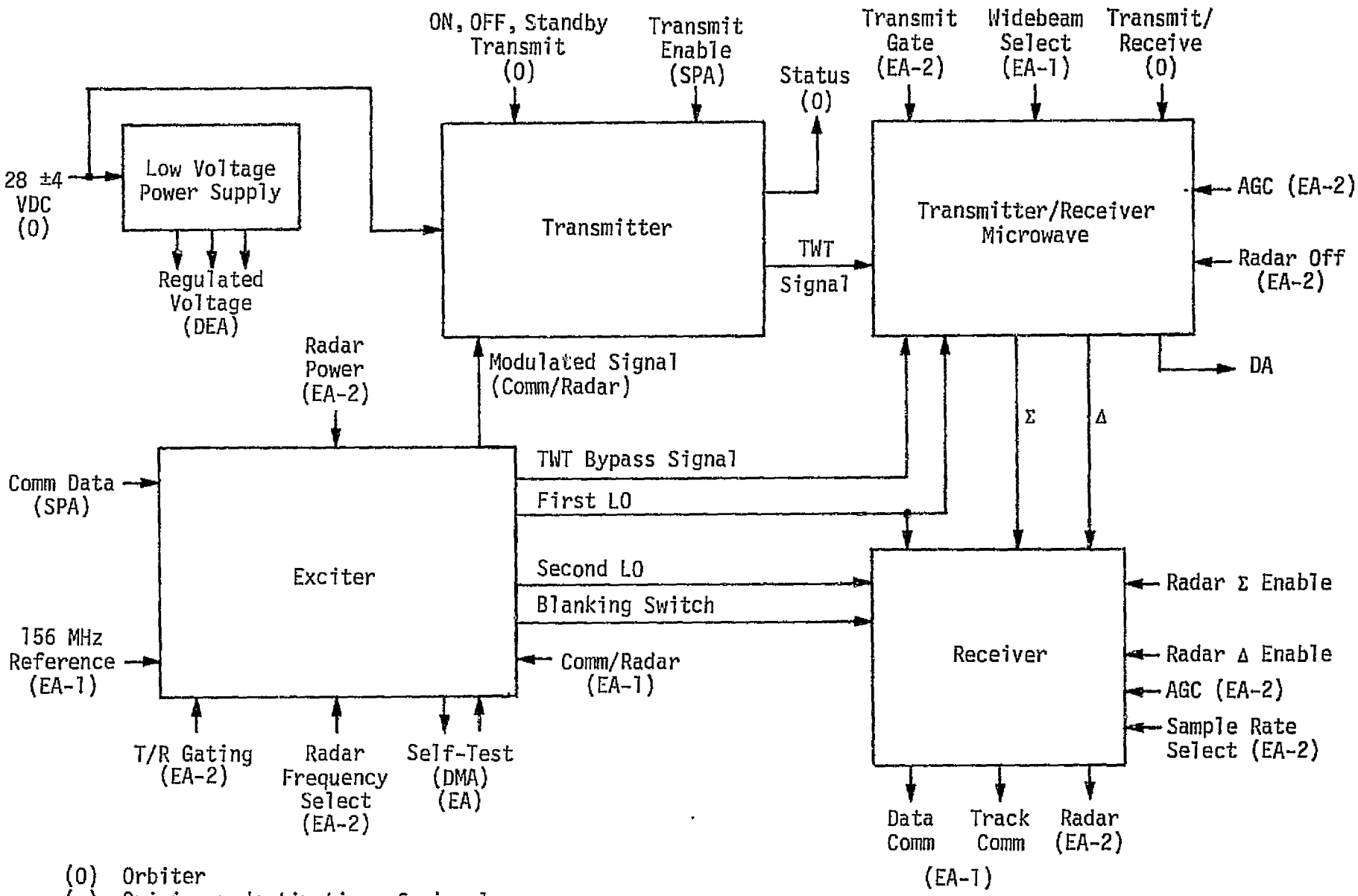

Figure 63. Deployed Electronic Assembly Block Diagram

The exciter also receives a self-test signal from EA-1 and generates a radar target which is fed to the DMA for target simulation at four selectable ranges.

The radar/communication selection is controlled by a signal from EA-1 which acts as an interface between the Orbiter and the various subunits. The exciter generates two stable frequencies for downconversion purposes. The first LO is sent to the transmitter/receiver microwave to downconvert the received signal to 651 MHz in the radar mode and to 647 MHz in the communication mode. The second LO signal is used to downconvert the multiplexed radar signal to 78 MHz. The blanking switch signal is also sent from the exciter to the receiver diode switches which are used to protect the receiver from radar transmission leaks, in addition to switching the difference (Δ) signal, the sum (Σ) signal or the multiplexed ($\Sigma + \Delta$) signal according to the mode. The upconverted modulated communication signal or radar signal is fed into the transmitter where it is amplified by the TWT. The ON/standby transmit command is used to warm up the TWT and enable the high voltage supply in the transmitter. Actual transmission does not occur, however, before the reception of the transmit enable command from the SPA.

The transmitted signal (radar or communication) leaves the transmitter to the transmitter/receiver microwave block where it is diplexed and fed into the DA for transmission using the proper antenna. EA-2 supplies the transmitter/receiver block with three main signals, namely, the radar off signal, the AGC signal to control the first bandpass filter limiters, and a transmit gate signal to assure the proper signal switching by the circulator switch in the radar mode.

The two received signals (Δ-channel and Σ-channel) in the receive mode are bandpass filtered, gain controlled, and amplified by low-noise FET amplifiers before they are sent to the receiver block. In the receiver block, the Δ-channel and Σ-channel pass the blanking diode switches that protect the receiver and receive (1) a Σ-channel enable command during radar search, (2) a Δ-channel enable command during main/sidelobe discrimination or (3) both commands during tracking. The communication channel (forward link signal) after the

first bandpass filter (647 MHz) is passed along with the multiplexed IF (647 MHz) communication track signal to EA-1. The radar signal is downconverted to 78 MHz and bandpass filtered before handing it to EA-2. The sample rate select signal from EA-2 is used to select the bandwidth of the second IF filter as a function of range (10 MHz for $R \leq 0.42$ nmi and 3 MHz for $R \geq 0.42$ nmi). It should be pointed out that the transmitter/receiver microwave block has not yet been adequately documented, which limits the ability of analyzing it in more detail for any potential problems.

8.0 ELECTRONIC ASSEMBLY 1

This section evaluates the available breadboard test data pertaining to the Electronic Assembly 1 (EA-1). The general functional description of EA-1 is presented in Section 8.1. The PN code tracking performance is analyzed in Section 8.2 and compared to the test data. Section 8.3 discusses the tracking performance of the polarity-type (hard-limited) Costas loop which is used to acquire and track the carrier, while Section 8.4 presents lower bounds on the expected pull-in time of the loop at high signal-to-noise ratios and compares it with the test data. The Costas loop lock detector performance is presented in Section 8.5. Finally, Section 8.6 summarizes the areas of concern in the antenna control electronics and points out the problems that require design modification.

8.1 Electronic Assembly 1 Functional Description

This unit is responsible for the mode control for the entire Ku-band system in addition to being the major interface between the Orbiter and the system, that is, most of the signals from the Orbiter to the Ku-band system. The EA-1 generates several reference signals for use in the various subunits, monitors the radar self-test, downconverts the communication forward link signal from the DEA receiver, acquires the forward link carrier and despreads its signal (when PN spreading exists), and generates the angle search and track servo signals which result from the communication or radar mode angle error generation. The unit also provides the Shuttle with the required computation capabilities to perform antenna coordinate transformations. Figure 64 illustrates the major EA-1 blocks and the major signals flowing into and out of these blocks.

As in all other subunits, a regulated low voltage supply is used with a 28 ±4 VDC input from the main bus to supply the unit with the required regulated voltages.

The reference frequency generator implements a crystal oscillator to generate several needed stable frequencies. A 156 MHz signal is sent to both the DEA and EA-2 and a 1.875 GHz signal is sent to the SPA. These signals are used by the respective units to generate various other signals and timing clocks. A 625 MHz signal is sent

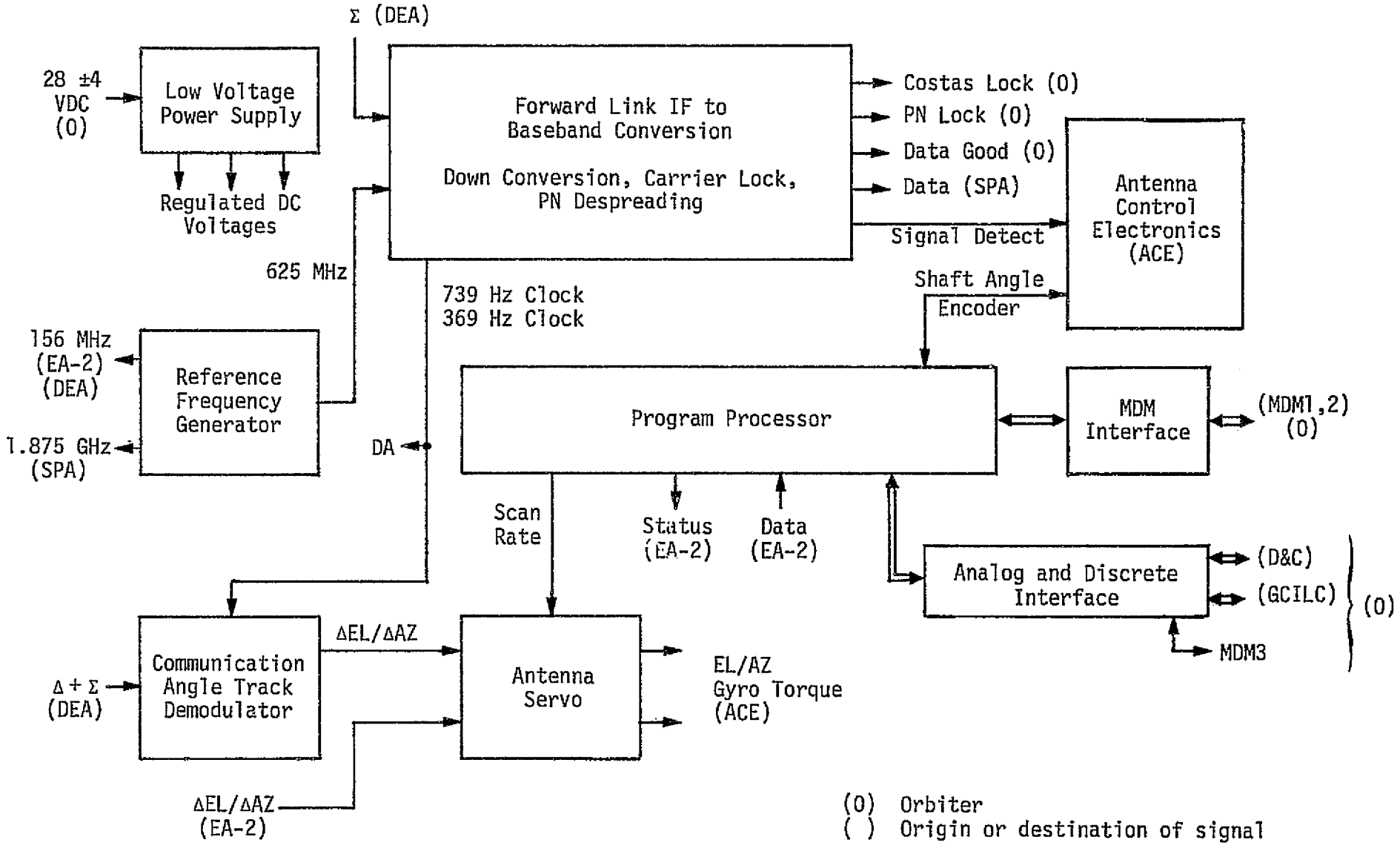

Figure 64. Electronic Assembly 1 Block Diagram

to the forward link sum channel downconverter to translate the sum channel signal from 647 MHz to 21.88 MHz. The resulting signal is processed through a swept polarity-type Costas loop to acquire and track the carrier. A lock detector is used to declare carrier acquisition and starts carrier tracking and, at the same time, supplies the antenna control electronics (ACE) with a signal detect command to stop search. When a PN code is used to spread the forward link signal, a "swept" tau-dither loop is implemented to work in parallel with the Costas loop for acquiring and tracking the PN code. A Gold code generator is used to generate the local code. A PN code lock detector is used to stop the tau-dither loop sweep and declare PN lock to the Orbiter when code acquisition is completed. A data-good circuit is added to declare that the carrier is acquired, despreading is completed (when it exists), and no residual DC voltages exist. Once this step is completed, the 216 kbps bi-phase-L baseband data is sent to the SPA for buffering and/or data detection.

The EA-1 unit contains several major interface blocks between the Orbiter and the Ku-band system. They are represented by two blocks in Figure 64: (1) the multiplex/demultiplex (MDM) interface block which interfaces with MDM1 and MDM2 and (2) the analog and discrete interface which interfaces with MDM3, the displays and controls (D&C) unit, the ground command interface logic controller (GCILC), and the antenna deployment actuator. These interfaces send most of the control and status messages to the Orbiter and receive most of the command and status signals from the Orbiter before distributing them to the various Ku-band system units. Figure 64 shows double arrows connecting the interface boxes and the EA-1 program processor, which is basically a microprocessor, to denote the numerous signals involved. The main signals involved are listed below (only major signals are listed).

(1) Signals to MDM

-Roll and pitch angle and angle rate

-Range and range rate

-Status Word 1, which includes the communication/radar mode, antenna mode, angle data validity, self-test in progress, and the Ku-band A/B select signals

-Status Word 2, which includes the range and range rate data validity, target status, data-good, frame synchronization, and radar status signals

(2) Signals from MDM

These include the GPC acquisition information word which controls the on/off switching of modes, the pitch and roll angles, and the range designation words.

(3) Signals to Display and Controls

These include roll and pitch angle and angle rate information, the radar range and range rates, the Ku-band signal strength, and the search and track status and scan warning flags.

(4) Signals from Displays and Controls

The main signals from the D&C are the search initiation signal, radar passive/active mode, radar power selection, and the roll and pitch slew rates.

The program processor also receives data from EA-2 and sends commands to EA-2 over a low rate interface. The signals involved are:

(1) Signals to EA-2

These include the antenna ready signal, slew fast or slow signal, and main or mini scans, provide the test target signal and the active or passive data signal.

(2) Signals from EA-2

These include the four radar parameters good signals (range, range rate, angle and angle rate), an angle track enable signal, a target generating signal in the self-test mode, and a miniscan signal.

The GCILC receives a forward link data present signal from the SPA and sends several signals to the SPA (see Section 9.0). The signals received by EA-1, however, are:

(1) Radar and communication ON/standby signals

(2) GPC designate, GPC acquisition, manual or autotrack signals.

The last major function of the EA-1 unit, in addition to communications and interfacing is antenna control. The communication angle track demodulation block receives two clock rates of 739 Hz and 369 Hz from the PN despreader block, which are the same as those

used in the DA to multiplex the $\Delta + \Sigma$ signal. These clocks are used to demodulate and separate the ΔAZ and ΔEL signals. The ΔAZ and ΔEL signals are used by the antenna servo circuits (in the communication mode) to generate the gyro torque control signals in the tracking mode. In the radar mode, the antenna servo uses similar signals generated by the EA-2 unit. There are two angle errors (azimuth and elevation) in either the radar mode or the communication mode. These signals are processed almost identically in two separate channels to control the motor drive and adjust the antenna position. During scanning, the program processor generates a scanning rate command which controls the antenna motion and the search pattern.

The program processor also performs the required coordinate conversion and initiates the required signals to control the self-test mode.

One aspect of the PSK data demodulator design which requires closer examination is that of using the 5.92 kHz "dither" signal in modes other than CW reception. For the CW mode, the dither signal is obviously required to provide the sideband which can be utilized by an AC coupled Costas loop for coherent carrier acquisition and tracking. However, for the case when biphase-L data is being received, the requirement for a dither waveform is questionable because the spectrum of the data does not contain DC, i.e., the carrier, anyway. Locking up to and tracking of such biphase-L data with an AC coupled loop should not present a problem.

The introduction of an asynchronous dither signal into the received IF signal by bi-phase modulation and subsequent removal of this signal from the baseband data by a chopper may result in "glitches" which, in turn, may degrade BER performance.

Consequently, it is recommended that the function of the dither signal during the reception of the biphase-L data be reexamined and, if found not justified, the use of dither in the data receive mode be discontinued.

As far as the scanning function of EA-1, the data presented at the PDR points out that the 30% overlap specification is not met. HAC digital simulation results show that the overlap is about 25% in

the radar main scan and only 12% in the communications main scan. This problem deserves special attention due to its impact on system performance in the search mode.

8.2 PN Tracking Performance

During the spread spectrum mode of the forward link, the recovery of data necessitates the removal of the 3.03 Mbps PN code from the received signal. The removal of the code, in turn, requires a local replica of a code which is in a near-perfect synchronism with the incoming one. Thus, prior to the recovery of the communication data, the Ku-band receiver searches out the phase of the incoming code and subsequently locks the local code generator to the phase of the received code. After establishing the initial synchronism, the local code generator remains in lock with the received code by implementing a tau-dither tracking loop.

The functions of code acquisition and tracking are performed by the PN lock detector and the PN tau-dither acquisition-gathering circuits, whose block diagrams are shown in Figure 65. The main emphasis in this section is placed on the performance of the circuit during tracking. Specifically, the effect of the code tracking error on data demodulation loss is considered.

In the spread spectrum mode, as shown in Figure 65, the code tracking loop supplies the punctual correlation code to the despreader mixer ahead of the Costas demodulator. The noise error within the code tracking loop introduces a certain amount of signal degradation, which ultimately affects the BER performance.

Quantitatively, the effect of the code tracking error is expressed as an effective loss L_T in dB [23]:

$$L_T = 10 \log (1 - 1.16\ \sigma_T), \tag{20}$$

where σ_T is the normalized error for the PN loop. This error, in turn, can be computed from the following expression [24]:*

$$\sigma_T^2 = \left\{0.905\,(\rho_i)^{-1} + \left[0.453 - (10T_d B_i)^{-1}\right]\left(\frac{N}{N-1}\right)^2 (\rho_i)^{-2}\right\}\frac{B_L}{B_i}, \tag{21}$$

*For a finer analysis of σ_T, see [25]. With optimized bandpass arm filter bandwidths, (21) is shown to be optimistic by about 0.9 dB.

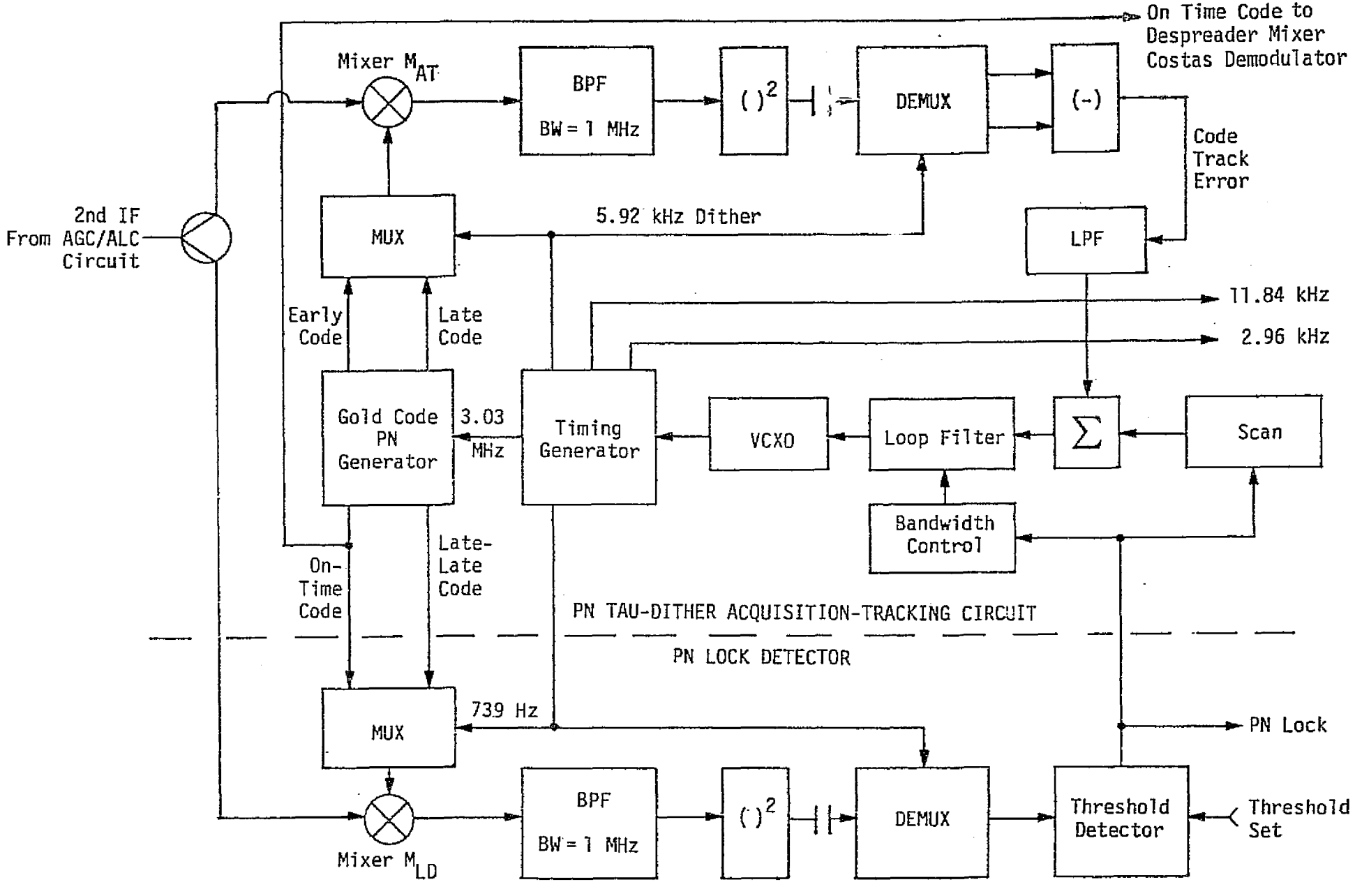

Figure 65. PN Tau-Dither Acquisition-Tracking and PN Lock Detector Functional Block Diagram

where B_i = two-sided noise bandwidth of the IF arm filters

B_L = one-sided tracking loop bandwidth

T_d = dither frequency period

N = number related to early/late code spacing ($N \geq 2$; for correlator spacing of $\pm\tau/2$, $N = 2$)

$\rho_i = \frac{C}{N_0 B_i}$, signal-to-noise ratio in the IF bandwidth.

To determine the effect of the tracking error on the data performance, we calculate, using (21), the values of σ_T as a function of the C/N_0 and then substitute these values into (20) to determine the effect of σ_T on the effective data demodulation loss. The parameters used are those of the Ku-band communication equipment:

B_i = 1 MHz

B_L = 500 Hz (acquisition), 50 Hz (tracking)

T_d = 0.168 msec (5.92 kHz)

N = 2 ($\pm$1/2 chip spacing).

Figure 66 shows the plots of both σ_T and the corresponding values of L_T as functions of the C/N_0. The measured breadboard test data for σ_T is also shown. This data was obtained by the Ku-band equipment contractor and reported during the March 14-24, 1978, Preliminary Design Review [26]. The test data shown is for a temperature of 20°C only, but it does follow the theoretical curve for B_L = 500 Hz rather well. At temperature extremes, the RMS jitter σ_T may deviate from the values shown in Figure 66, but the reduction of the tracking bandwidth to 50 Hz will provide a 5 dB reduction of the RMS value of the jitter, thus insuring that it stays below the specified value of 0.022 chips for the C/N_0 in the range from 63.5 dB-Hz to 78.9 dB-Hz.

The examination of the L_T values shown in Figure 66 indicates that, even for the tracking loop bandwidth of 500 Hz, the effective loss is relatively small compared to other typical implementation losses. Specifically, for B_L = 500 Hz, the L_T is 0.2 dB at the acquisition threshold of 60.8 dB-Hz. At the nominal tracking C/N_0 of 63.5 dB-Hz, the effective loss is 0.14 dB. With the tracking bandwidth reduced to 50 Hz, these losses are reduced to negligible values,

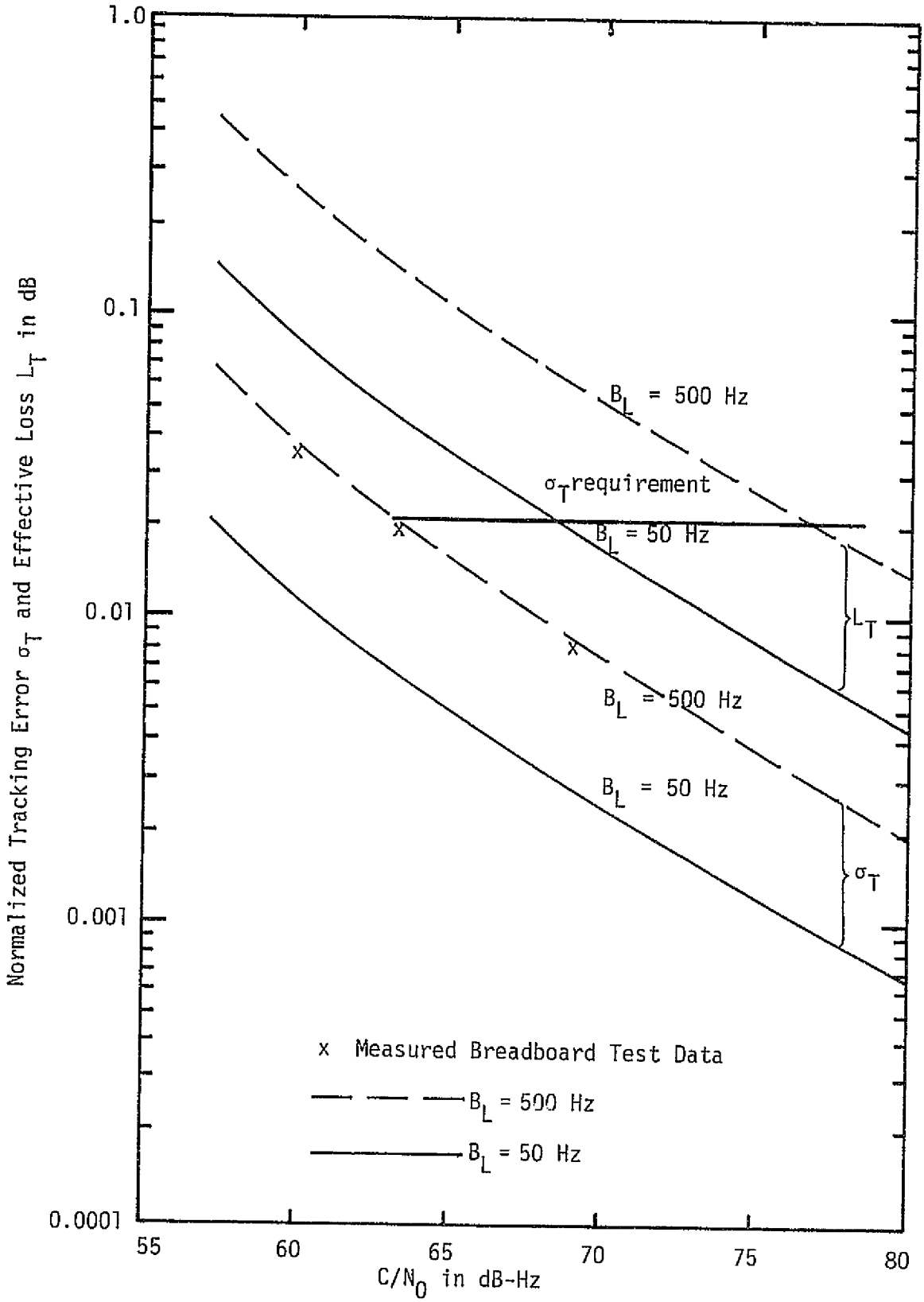

Figure 66. Normalized Tracking Error and Effective Loss for a Tau-Dither Loop Versus C/N_0

particularly at C/N_0 values above 63.5 dB-Hz. Consequently, one may conclude that the PN tracking loop contributes relatively little degradation to the forward link BER performance at C/N_0 values at and above 63.5 dB-Hz.

It is also interesting to note that, with the dither interval of 0.168 msec (5.92 kHz) and the predetection bandwidth B_i of 1 MHz, the factor $(10T_d B_i)^{-1}$ is negligible compared with 0.453:

$$(10T_d B_i)^{-1} = \left[(10)(0.168\times10^{-3})(10^6)\right]^{-1} = 5.95\times10^{-4} << 0.4. \quad (22)$$

This considerably simplifies (21) and the corresponding calculations.

8.3 Costas Demodulator Tracking Performance

The signal-to-noise ratio inside the carrier tracking loop of the Costas demodulator is an important parameter for considering the performance of the demodulator as a function of the C/N_0. Therefore, in this section, we will calculate the loop signal-to-noise ratio (SNR) using the parameters of the Costas loop demodulator employed by the Ku-band forward link receiver. The functional block diagram for this demodulator is shown in Figure 67, and the simplified diagram of the Costas loop itself is given in Figure 68.

Note that, as shown in both figures, the Costas demodulator employs a hard-limiter to shape the I-channel signal applied to the chopper multiplier. In fact, it is this feature of the Costas loop which allows the utilization of the chopper multiplier rather than an analog multiplier, the latter being a frequent source of bias error. These loops are frequently referred to as polarity-type Costas loops with passive arm filters.

Consider now the SNR within the Costas loop. The expression for this SNR is

$$\rho' = \frac{C}{N_0}\left(\frac{1}{B_L}\right)\left(\frac{1}{4}\right)S_L, \quad (23)$$

where ρ' = signal-to-noise ratio within the Costas loop

B_L = one-sided loop noise bandwidth

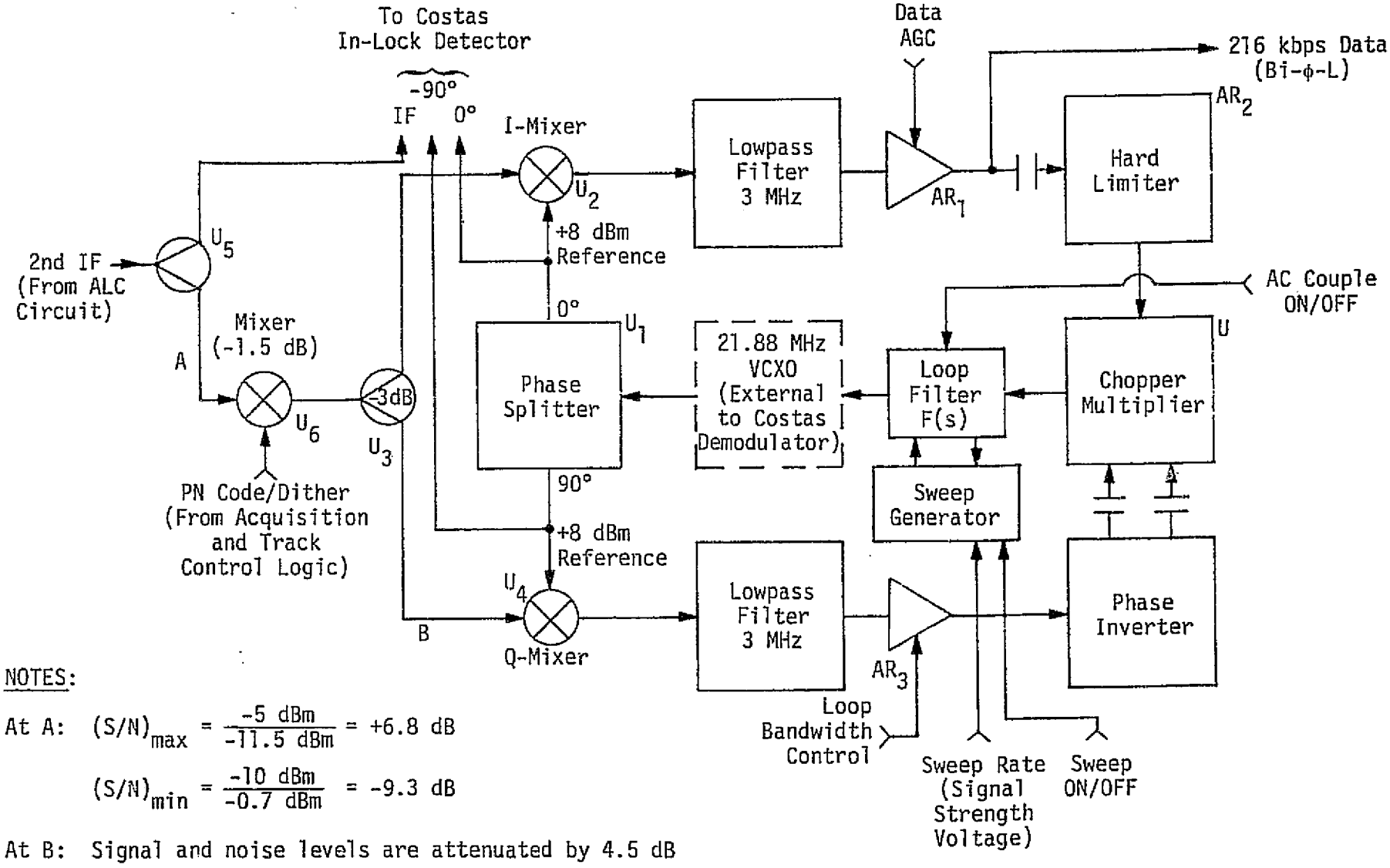

NOTES:

At A: $(S/N)_{max} = \frac{-5 \text{ dBm}}{-11.5 \text{ dBm}} = +6.8 \text{ dB}$

$(S/N)_{min} = \frac{-10 \text{ dBm}}{-0.7 \text{ dBm}} = -9.3 \text{ dB}$

At B: Signal and noise levels are attenuated by 4.5 dB

Figure 67. Costas Loop Demodulator Functional Block Diagram

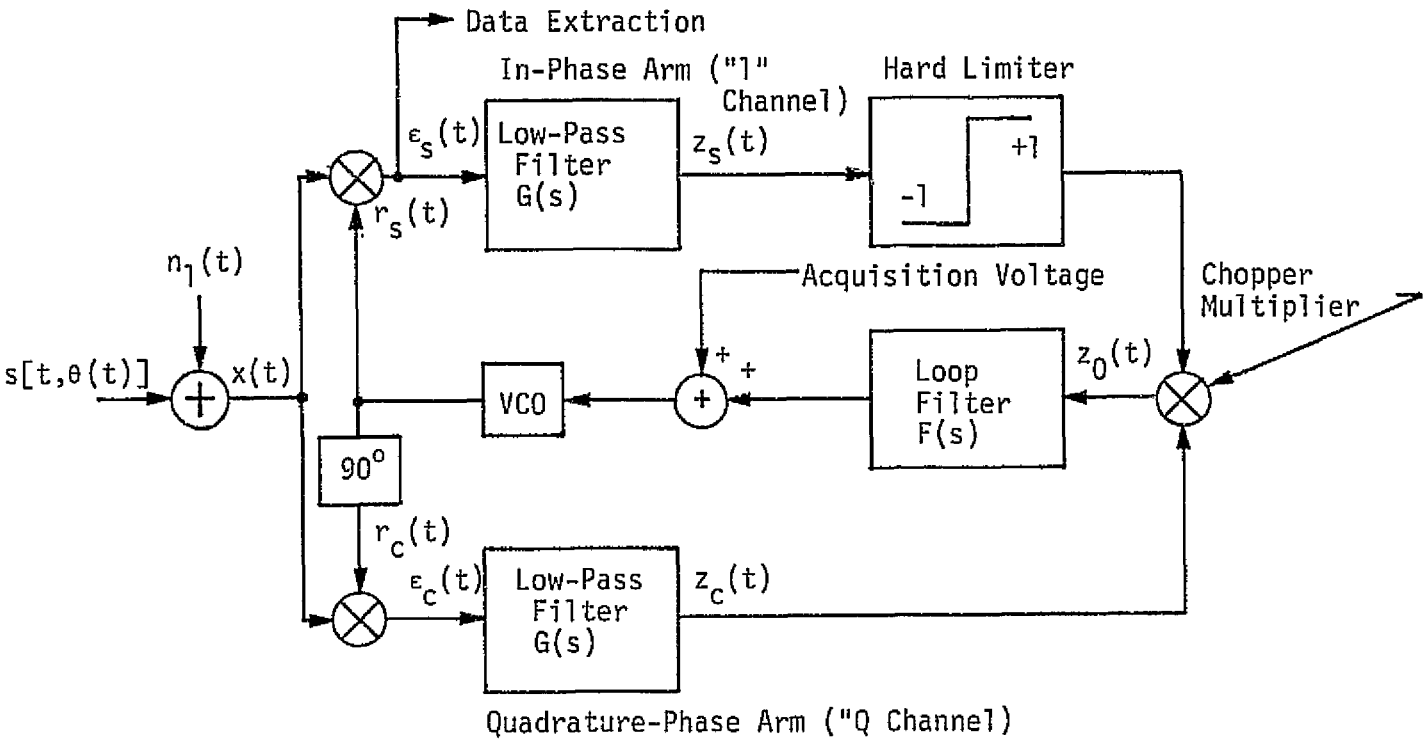

Figure 68. Costas Loop Simplified Diagram With Hard-Limited In-Phase Channel

S_L = squaring loss associated with the baseband multiplier utilized by the Costas loop.

For an analog multiplier, the expression for the squaring loss can be written in a closed form expression [27]:

$$S_L = \frac{D_m}{K_D + K_L \frac{B_i/R_s}{2R_d D_m}} \tag{24}$$

where B_i/R_s is the ratio of the two-sided arm filter noise bandwidth to data rate, R_d is the symbol signal-to-noise ratio, and D_m, K_L, K_D are factors determined by the data, the type of arm filter, and the combination of the two, respectively. However, for the Costas demodulator utilizing a hard-limiter and a chopper multiplier, the squaring loss determination is more complicated and needs involved numerical computation techniques. The results of such numerical evaluation have been published [28] and are used in our calculations.

Figure 69 shows the calculated SNR for the Costas demodulator as a function of the C/N_0. These results were obtained by reading out the values of the squaring loss S_L read out from Figures 3 and 4 of [28] and substituting these values into equation (23). For convenience, the data contained in Figures 3 and 4 are presented here as Figures 70 and 71, respectively. The abscissa in these figures is B_i/R_s, where $B_i = \pi f_c$ and R_s is the data rate, which in our case is the 3.03 Mbps NRZ PN code data. The f_c is the 3 dB cutoff frequency of the arm filters which is set equal to the code rate. Thus, for the case at hand, $B_i/R_s = \pi$ and the R_d parameter, which is the signal-to-noise ratio in the code rate bandwidth is

$$R_d = C/N_0 - 10 \log (3.03\times10^6) = C/N_0 - 64.8 \text{ dB-Hz}. \tag{25}$$

As can be seen from Figures 70 and 71, R_d and B_i/R_s are the parameters which determine the value of the squaring loss as a function of C/N_0. The magnitude of the squaring loss as a function of C/N_0 is shown in Figure 69.

Examination of the loop SNR shown in Figure 69 indicates that, at a C/N_0 of 60.8 dB-Hz, which corresponds to the acquisition threshold for the forward link, the loop SNR is about 11.2 dB for the one-sided

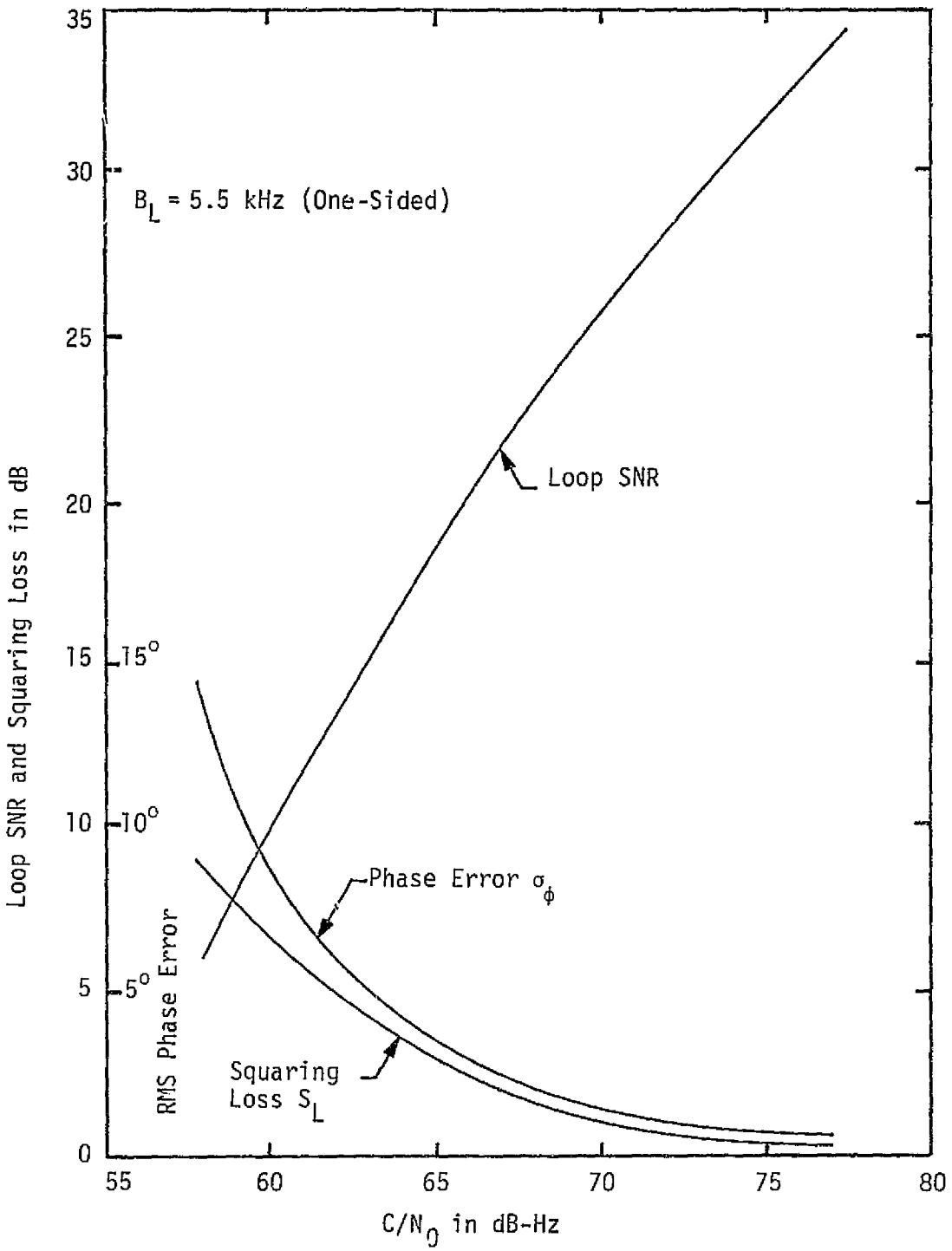

Figure 69. Loop SNR and RMS Phase Error vs. C/N_0

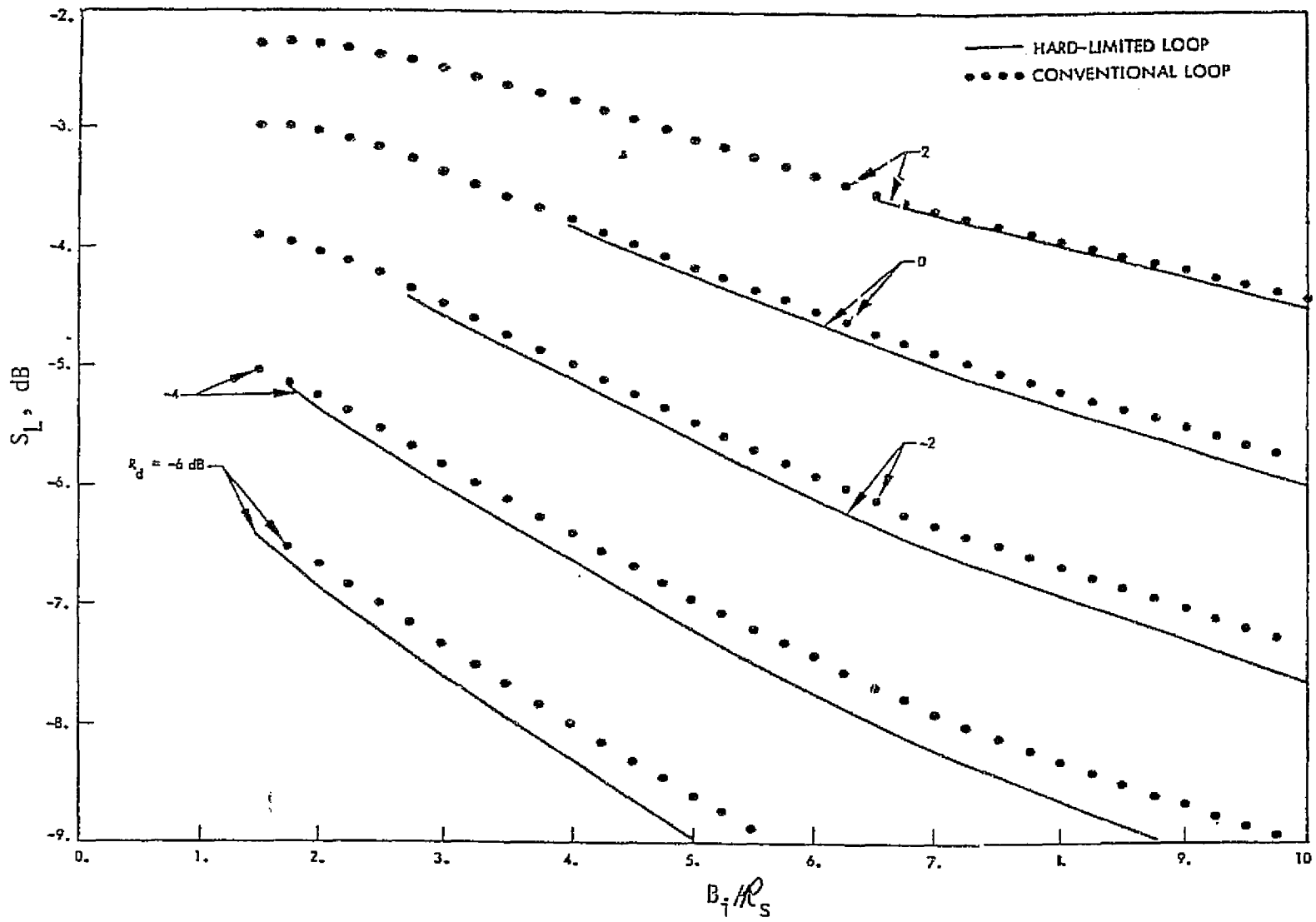

Figure 70. Squaring Loss Variations vs. B_i/R_s with R_d as a Parameter; Small ρ_i Approximation; RC Filter, NRZ Data [28]

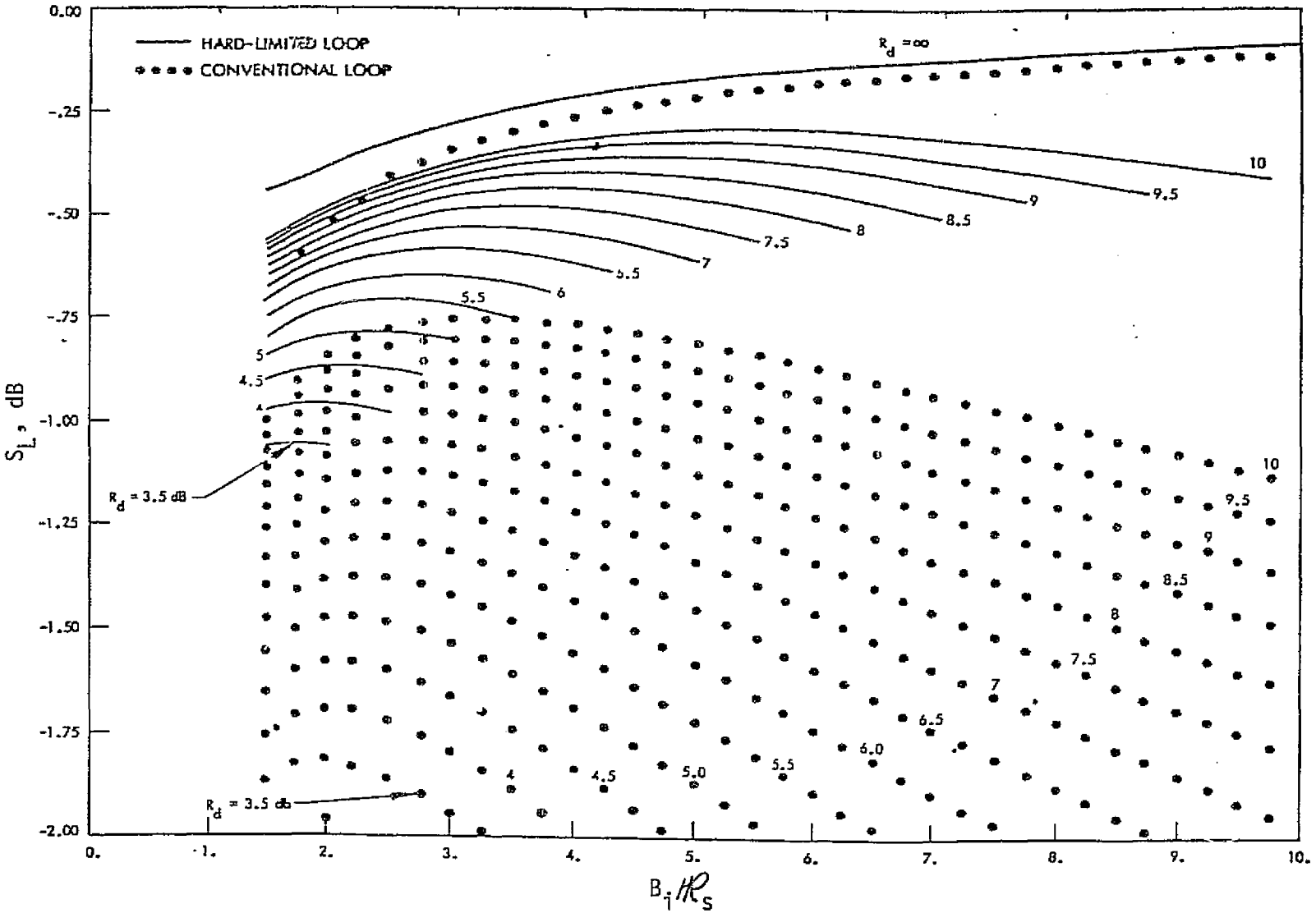

Figure 71. Squaring Loss Variations vs. B_i/R_s with R_d as a Parameter; Large ρ_i Approximation; RC Filter, NRZ Data [28]

noise loop bandwidth B_L of 5.5 kHz. This SNR is sufficient to satisfy the requirement of 0.99 probability of acquisition of the carrier. The noise bandwidth of the Costas loop, however, can be as wide as 10 kHz during acquisition [26] with the concomitant reduction in the loop SNR to 8.6 dB (i.e., a 2.6 dB reduction).

The experimental data, however, indicates that the acquisition probability of 0.99 can be achieved by the Costas loop at a C/N_0 of 61 dB-Hz over the temperature range of -20°C to +65°C and a frequency offset of ±150 kHz [26]. Consequently, the possible widening of the Costas loop bandwidth during acquisition does not seem to present a potential problem.

To determine the effect of the loop SNR on the data demodulation performance of the Costas loop, one has to consider the relationship between the loop SNR and phase noise in the I-channel detector. For a Costas loop, this relationship is

$$\sigma_\phi^2 = \frac{1}{4\rho'}, \tag{26}$$

where σ_ϕ is the RMS phase error (in radians) at the I-channel (i.e., data) detector and ρ' is the loop SNR defined by (23). The predicted values of σ_ϕ (in degrees) as a function of the C/N_0 are shown in Figure 69 along with the corresponding values of the loop SNR. As can be seen from this figure, the value of the RMS phase noise is less than 10 degrees at C/N_0 values above 60 dB-Hz.

The significance of this fact can be understood by examining the curves given in Figure 72. These curves show the relationship between the C/N_0 and the bit error rate (BER) as a function of the I-channel RMS phase error σ_ϕ. The losses ahead of the Costas demodulator are assumed to be negligible (see the discussion of the PN tracking loss) in converting the E_b/N_0 into the corresponding values of the C/N_0.

It turns out that, as shown in Figure 72, the phase error of 10 degrees or less has a relatively negligible effect on BER degradation. This degradation is about 0.15 dB at a C/N_0 of 60 dB-Hz, and it decreases rapidly above this point due to rapid decrease of the σ_ϕ magnitude with the increasing C/N_0 values. The implication is therefore

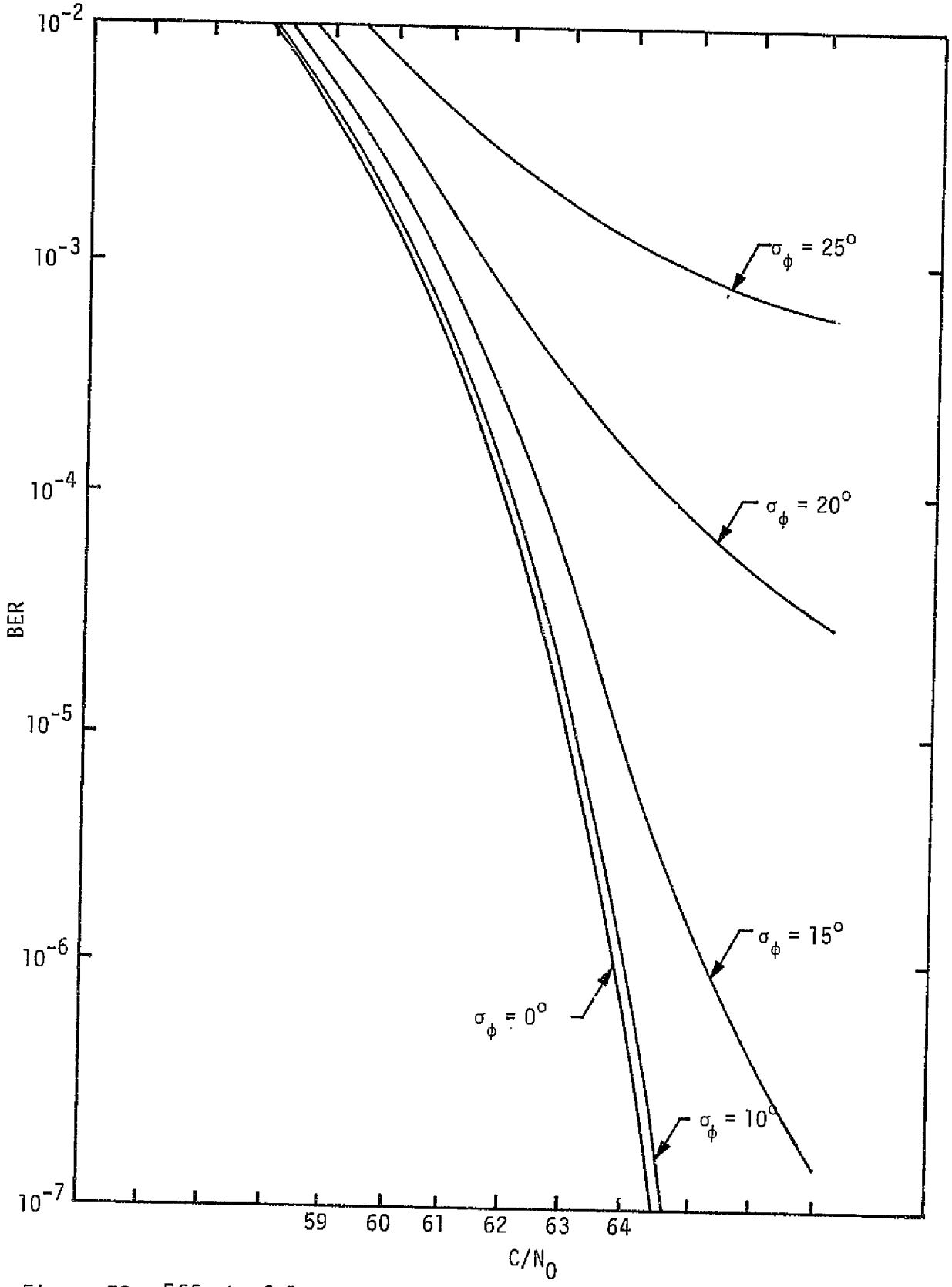

Figure 72. Effect of Increasing σ_ϕ on the Performance of the High-Rate Channel

that, with the loop SNR predicted for the Costas loop of the forward link, the data detection capability of the loop is degraded very little within the operational range of the C/N_0 values.

Additional phase errors of concern in any tracking loop are the gain imbalance and the phase imbalance in the two arms. In the case of a hard-limited loop (polarity-type), the gain imbalance does not produce any additional phase errors because of the existence of the hard-limiter in the in-phase arm. The phase imbalance along with the phase splitter and the finite DC gains are believed to produce a small phase jitter which is less than 7°. Elaborate analysis can be carried out but is believed to be unnecessary because the net phase jitter due to all the above effects is small.

8.4 Costas Loop Acquisition Time

The hard-limited Costas loop (polarity-type) used to acquire and track the carrier in EA-1 has the following acquisition mode parameters [13]:

Sweep time (T_{sw})	40-185 msec
Sweep frequency range	±175 kHz
Loop bandwidth (B_L)	5.5-10 kHz
Frequency uncertainty (Δf)	±150 kHz

which implies that the sweep rate S_f is in the range of 1.89-8.75 kHz/sec. It is important to note that the sweep is varied over a range of 4 to 1. This variation is implemented to reduce the probability of false lock at high signal-to-noise ratios. The retrace sweep time is equal to 5 msec and thus will be neglected in the following computations.

The analysis of acquisition time for second-order loops in the absence of noise has been carried out in [29], and the extension of these results to the Costas loop is discussed in detail in Appendix C. These results can be used as lower bounds on the acquisition time of the polarity-type Costas loop used in EA-1. Equation (27), which is derived in Appendix C, can be used to compute the acquisition time (T_f) in the absence of noise as a function of the frequency uncertainty (Δf) and the loop bandwidth (B_L) for a polarity-type Costas loop with a perfect integrator loop filter.

$$T_f = \frac{\Delta f}{S_f} - \frac{2}{3\pi}\frac{B_L}{S_f} + \frac{32}{27\pi^2}\left(\frac{B_L^3}{S_f^2}\right) \ln \left[\frac{\frac{9\pi}{8}\left(\frac{S_f}{B_L^2}\right) + 2}{\frac{27\pi^2}{16}\left(\frac{S_f}{B_L^2}\right)\left(\frac{\Delta f}{B_L}\right) + 2} \right] . \quad (27)$$

Figure 73 illustrates the value of $T_f B_L$ as a function of $\Delta f/B_L$ with S_f/B_L^2 as a parameter for a range of values of interest, while Table 12 shows the value of T_f for the loop parameters implemented by HAC.

It is obvious from Table 12 that, for the above parameters, the maximum acquisition time at low sweep rate and narrow loop noise bandwidth in no noise is approximately equal to 70 msec. Investigating the available Costas sweep test data [26] shows that the sweep period (acquisition time) varies between 60 and 195 msec as a function of carrier power to single noise spectral density (C/N_0) ratio which is varied between 60 dB and 80 dB. The sweep period shows little sensitivity to the variations of temperature when the temperature is varied between -20°C and +80°C.

Since the requirements specify a worst-case acquisition time of 200 msec and, since the no-noise computations show that the worst-case acquisition time with the specified Costas loop parameters does not exceed 70 msec in no-noise, it is believed that the Costas acquisition time will not present any problem.

Table 12. Acquisition Time of the Costas Loop (T_f) in msec

B_L (kHz)	S_f (kHz/sec)	
	8.75	1.89
5.5	16.27	66.33
10.0	12.94	37.40

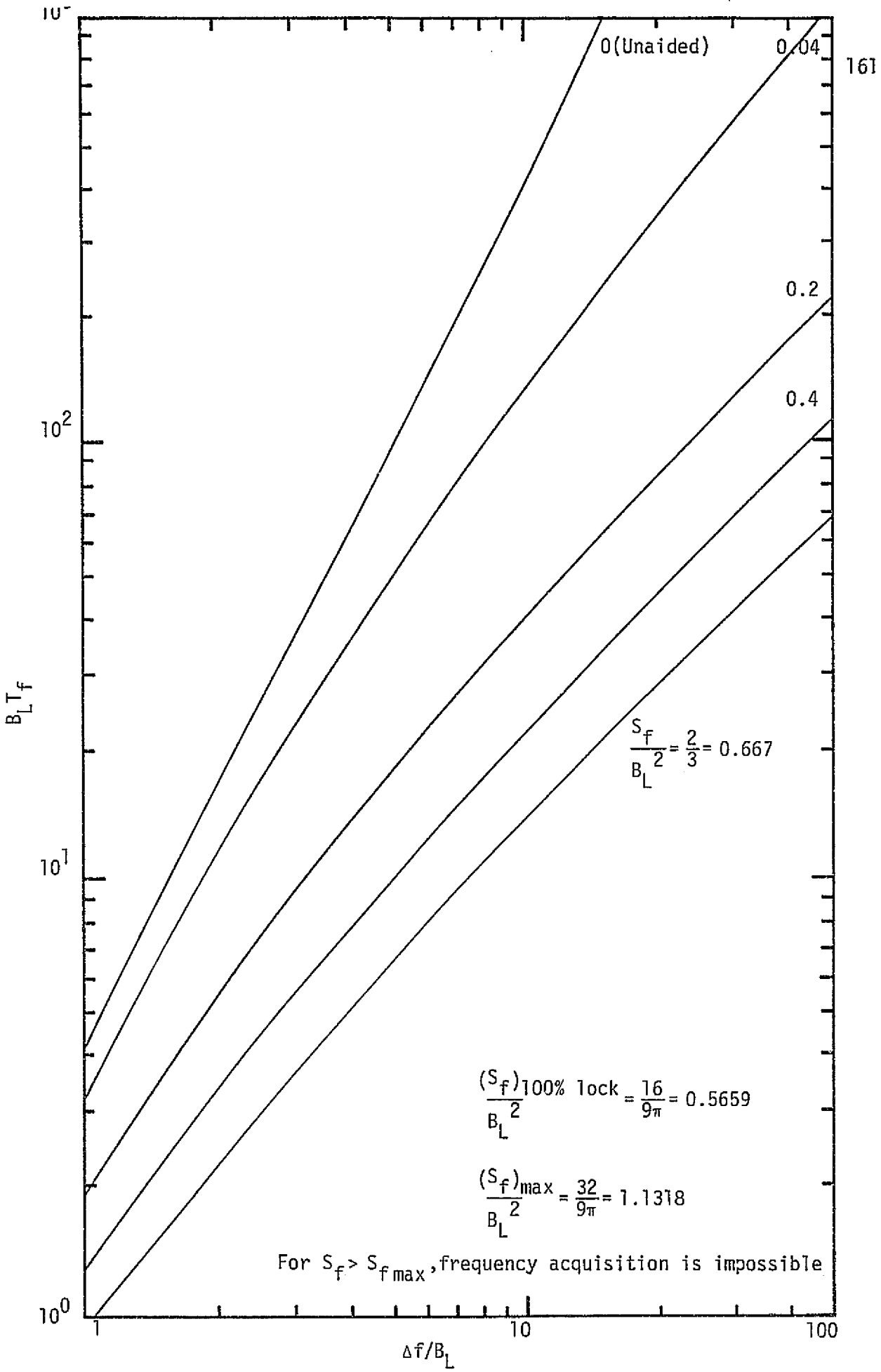

Figure 73. Frequency Acquisition Time Performance of Polarity-Type Costas Loop (No Noise)

8.5 Costas Loop Lock Detector

The primary purpose of the Costas lock detector subunit is to sense the Costas loop signal acquisition state and send a "Costas lock" signal to the acquisition and control logic when indeed it decides that the Costas loop has acquired the signal presented to its input. Since the initial frequency search and carrier acquisition must take place regardless of the type of signal format received from the TDRSS, namely, CW carrier, data modulated carrier, spread spectrum carrier, or spread spectrum data modulated carrier, the lock detector must be capable of performing its sensing function under each of these conditions.

The basic carrier lock detector employed by HAC in the Ku-band design is a dithered-type configuration and is illustrated in Figure 74. This dithered lock detector, when contrasted with the more conventional undithered $I^2 - Q^2$ type of lock detector, is not unlike a comparison between a tau-dither loop and a delay-lock loop for PN tracking in the sense that, in the former, the carrier reference (PN clock) is time-shared over a single channel while, in the latter, it is simultaneously shared by two quadrature channels. In general, dithered-type configurations (tracking loops or lock detectors) have the advantage of being insensitive to gain imbalances normally present in two channel configurations. On the other hand, because of the time sharing of the locally generated reference, they potentially suffer a 3 dB loss in performance as compared to the more conventional undithered-type configuration.

In Appendix D, the techniques used in analyzing a PN tau-dither tracking loop [25] are applied to analyzing the dithered lock detector of Figure 74. When the dither frequency is much smaller than the data rate, the results resemble those obtained by LaFlame in [30], except for a modification by a factor of 2 of the signal × noise term in the lock detector signal-to-noise ratio. On the other hand, choosing a dither frequency much closer to the data rate can overcome much of the 3 dB loss commonly associated with dither-type configurations. This conclusion has already been demonstrated in the comparison between loop signal-to-noise ratios of the PN tau-dither loop and delay-lock loop made in [25].

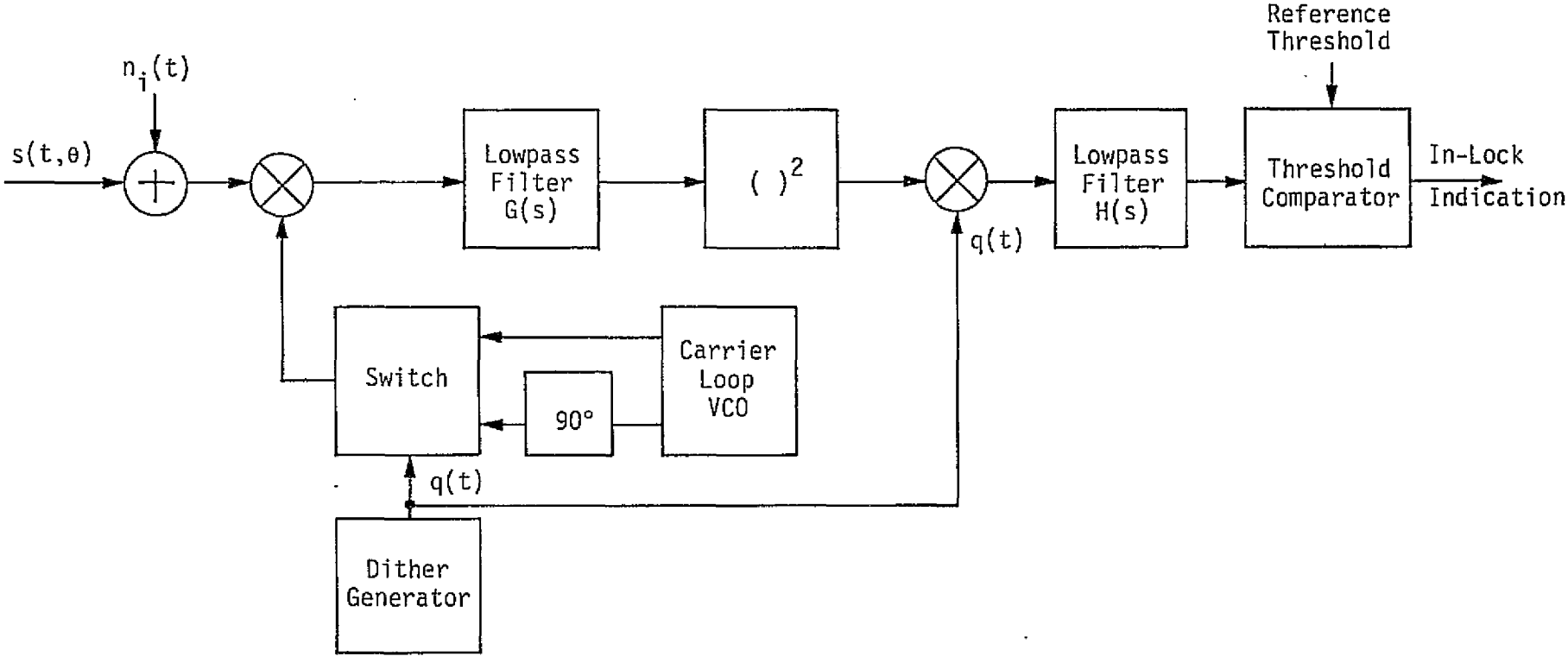

Figure 74. Dither-Type Costas Lock Detector

The actual HAC configuration includes a soft limiter [31] inserted prior to the square law detector to assist in discriminating between strong signals received through high antenna sidelobes and weak signals received through the antenna mainlobe. This is accomplished by desensitizing the front end gain variations in such a way that the lock detector detects the weakest mainlobe signal but not the strongest sidelobe signal. This configuration is considerably more difficult to analyze. It is believed, however, that the addition of the soft limiter will allow a wider sidelobe discrimination margin and hence improve the performance of the lock detector.

8.6 Antenna Control Electronics

The objective of this section is to point out problem areas in the antenna control electronics (ACE) subunit. A very brief description of this subunit is presented first in order to clearly identify the problems. A detailed description of the ACE circuits is presented in [13]. The operation of this subunit is controlled by a programmed microprocessor which receives the commands from the Orbiter and sends commands to the various parts of the subunit to perform the required task.

The commands of the microprocessor are sent to the gimbal rate servo circuit which has three major parts: the loop shaping assembly, the motor drive, and the rate integrating gyro driver (RIG).

The servo loop shaping circuit is used to provide the α and β torque commands to the gimbal motor drivers. The α and β channels are almost identical, with the only essential difference being the additional gain changing stages in the α channel. Three different error signals can be shaped to provide the torque command:

1. The $\alpha(\beta)$ coarse gyro signal.
2. The $\alpha(\beta)$ fine gyro signal, which can use either the communication track error or the radar track error, depending on the mode.
3. The fine gyro signal.

There are four shaping stages and a temperature-sensing bridge which sends a signal to the microprocessor to turn off the motor drivers in case of excessive heat. The latest figures indicate that shutting off

takes place when the temperature reaches 248°F ±10°F. Since damage to the motor can occur at temperatures higher than 250°F, it is recommended that the current design be changed in such a way as to avoid any possibility of motor damage due to heat.

The motor drivers can also be turned off if the gimbal turning rate exceeds a given threshold. The current threshold is set at 90 ±24 deg/sec. This is unacceptable because a maximum of 100 deg/sec is required for the Ku-band antenna. A change in the tachometer cut-off threshold has to be made for the system to meet specifications.

In addition, it was pointed out at the PDR that the current design of the servo system is unstable in the hold mode, which is a problem that requires a change in the design of the servo loop.

The other two parts of the gimbal rate servo unit are the motor drive, which is used to torque the gimbal motors, and the rate integrated gyro driver (RIG), which generates the required timing signals.

9.0 SIGNAL PROCESSING ASSEMBLY

This section discusses and evaluates the performance of the Signal Processing Assembly (SPA). Section 9.1 presents a general functional description of the SPA. Section 9.2 presents a summary of the expected performance of the bit synchronizer, derived in Appendix E, and compares it with the available breadboard test data. Finally, Section 9.3 presents the performance of the ambiguity resolver.

9.1 Signal Processing Assembly Functional Description

The Signal Processing Assembly (shown in Figure 75) performs data and signal processing for the forward link and return link under the direction of the management/handover logic. As is the case with the other assemblies, the SPA has its own power supply that regulates the 28 VDC it receives from the main bus on the Orbiter. The management and handover logic receives the Orbiter commands either directly from the ground control interface logic circuit (GCILC) or from EA-1 (A or B). It has an input buffer, an output buffer, a memory, an SPA controller, and a serial interface with EA-1 [17]. The main signals received from the GCILC are the A/B Ku-band select signal and numerous signals to control the selection of modes and data in both the forward link and the return link. The SPA management and handover logic outputs numerous commands to the GCILC and to various parts of the Ku-band system. The major output commands are:

- -Forward link data present to GCILC
- -Transmit enable and communications ON to the DEA
- -Modulation ON/OFF and mode select to mode selection and modulation box of the return link for Mode 2 (FM) control
- -A signal used to select a reference frequency from A or B for QPSK modulation
- -Mode select and data select to bit synchronizer for forward link mode and A/B data selection
- -Data selection command to return link switching to select the required data to be modulated.

In Mode 1 of the return link, the high data rate channel is convolutionally encoded before being modulated. Once the data is selected in the return link, three data channels are modulated in

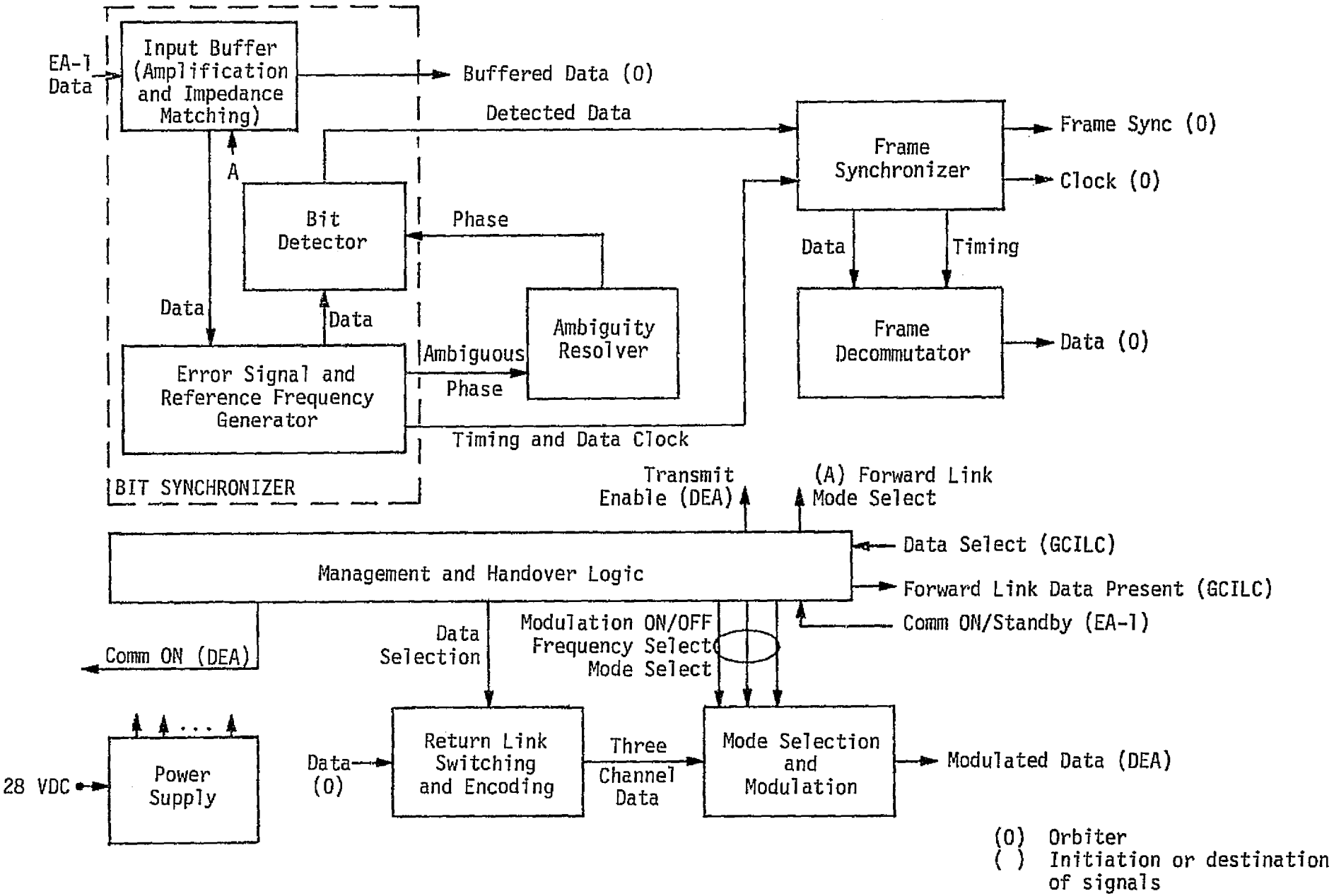

Figure 75. Signal Processing Assembly Block Diagram

one of two selected modes. In Mode 1, the three channels are double unbalanced quadriphase shift keying (UQPSK) modulated. Channels 1 and 2 are modulated on a squarewave subcarrier whose fundamental frequency is 8.5 MHz. The resulting subcarrier signal is modulated in quadrature with Channel 3 on a 1.876 GHz carrier. In Mode 2, the two lower rate channels are unbalanced QPSK modulated on an 8.5 MHz squarewave subcarrier as in Mode 1. The resulting UQPSK signal is bandpass filtered to obtain a sinusoidal subcarrier and then summed with the third channel before being frequency modulated (FM) on the 1.876 GHz carrier. The resulting modulated signal is sent in either mode to the DEA exciter for upconversion to Ku-band frequencies.

The 216 kbps forward link biphase-L data is buffered in the SPA. One of two modes is selected via a command from the management and handover logic. In Mode 2, the data is strictly amplified and impedance matched (buffered) by line drivers and handed to NSP1 or NSP2 (network signal processor) on the Orbiter, while in Mode 1 the data is detected first before sending it to the Orbiter. The data detection begins by generating a synchronous clock via an error signal generator loop which outputs a 6.912 MHz clock used in the bit synchronizer and the frame synchronizer and decommutator timing. An ambiguity resolver is used to resolve the clock ambiguity and the bi-phase-L data transition ambiguity. The bit detector receives the correct phase from the ambiguity resolver and the biphase-L data from the Costas loop and uses two integrate-and-dump circuits to detect the data bits and to convert them to NRZ data before sending them to the frame synchronizer. The frame synchronization is achieved by searching for a correlation in a frame code. The establishment of the frame synchronization enables the frame decommutator to separate the 128 kbps payload data and the 72 kbps operations data which are then sent to the Orbiter.

The major areas of concern in the Signal Processing Assembly are:

(1) The bit synchronizer is specified (Rev. A) to perform with $E_B/N_0 = 0$ dB. The Preliminary Design Review presentation concerning the bit synchronizer predicted that it will not maintain synchronization except when $E_b/N_0 > 2$ dB. This basically is not believed to be a major problem unless a higher E_b/N_0 is required

due to the aging and tolerances of the hardware. In addition there are a number of other problems pertaining to the bit synchronizer that should be pointed out:

(a) The integrations in the bit synchronizer design occur over half-bit intervals. While it is advisable to "window" the quadrature I&Ds (half a bit in the Hughes design), it is not necessarily desirable to "window" the in-phase I&Ds. In fact, windowing the in-phase I&Ds to half a bit as in the Hughes design results in a 3 dB SNR penalty for making decisions on the midbit and between-bit transitions relative to performing full-bit in-phase I&Ds [16].

(b) It is not clear how the counters in the ambiguity resolver would behave if they have a zero count and receive a decrementing signal.

(c) No definite number has been defined to what is referred to by HAC as the PR logic state in the counters when ambiguity resolution is achieved.

(d) The ambiguity resolver counters are 12-bit binary counters. This number has to be chosen depending on the data duty factor which has to be bounded to assure adequate performance of the bit synchronizer and the ambiguity resolver.

(2) The proposed asymmetry compensator should provide adequate means for reducing the asymmetry in the forward link to within the specified 10%. Test results are needed before passing a final judgment on the effectiveness of the compensator.

(3) Since the software for the Ku-band is not completed yet, the available information is not sufficient to evaluate its performance. Extensive software evaluation effort is needed once it is completed.

(4) Care must be taken in designing the convolutional encoder to eliminate the possibility of any dead zones due to timing. One such dead zone was reported at 10 Mbps.

9.2 The Bit Synchronizer

The bit synchronizer block diagram with the associated ambiguity resolver is shown in Figure 76. A detailed discussion of the

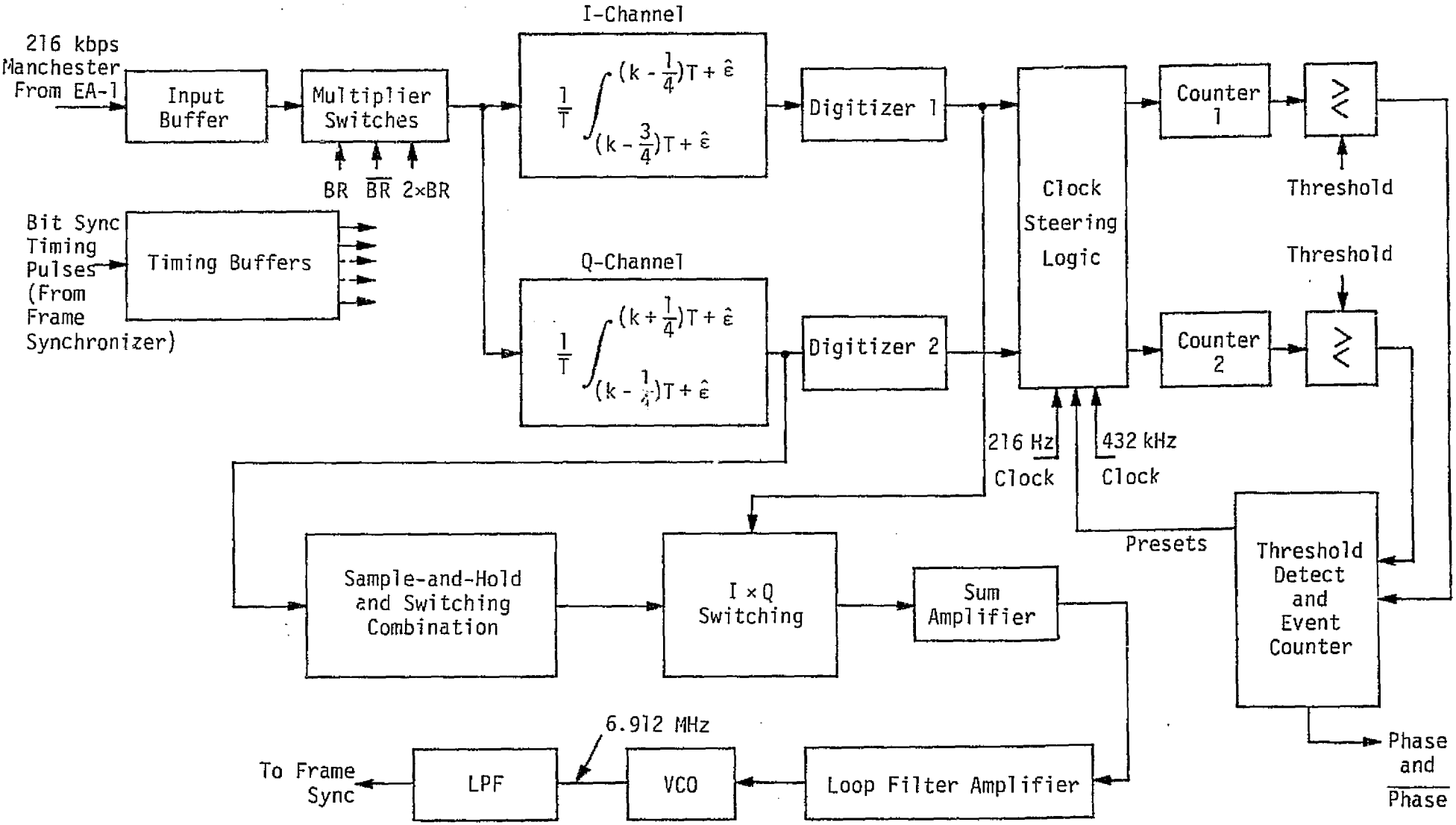

Figure 76. Bit Synchronizer and Ambiguity Resolver Block Diagram

operation of the circuit is presented in Section 5.3 and the analysis of the bit synchronizer is presented in Appendix E.

The objectives of the circuit are to:

(1) Generate a 32 x 216 kHz (6.912 MHz) synchronous signal which is used to generate the 216 kbps clock, 2 x 216 kbps clock, and various other timing signals used in frame decommutation timing.

(2) Resolve mid-bit versus bit transition ambiguity of the 216 kbps biphase-L data, as well as the 2 x 216 kbps clock synchronization ambiguity.

The principles of operation of this synchronizer are summarized as follows:

The synchronizer develops its timing waveforms from a twice-bit-rate clock (512 kbps), while the ambiguity resolver determines the correct timing phase of the bit rate clock obtained by dividing down the twice-bit-rate clock by 2. The input signal is multiplied by the twice-bit-rate clock and then the bit-rate clock or its complement, which are both used to gate (in each bit interval) half-bit segments of the multiplier outputs to in-phase integrate-and-dump (I&D) circuits. For the mid-bit I&D, the half-bit separation symmetrically (assuming perfect timing) spans the mid-bit position. Thus, the output of this I&D after 2-bit digitization by Digitizer 1 reflects the polarity of the NRZ data bit stream (or, alternately, the polarity of the mid-bit Manchester transition). For the between-bit I&D, the half-bit integration symmetrically spans the NRZ bit transition position. Thus, the output of Digitizer 2 is a measure of the polarity of the NRZ data transition. If no transition occurs, the output will be nominally zero.

The input biphase-L coded signal is also gated by the bit rate clock and its complement, without first being multiplied by the twice-bit-rate clock, to between-bit and mid-bit quadrature I&D circuits, respectively. The outputs of these I&Ds are measures of the timing offset between the input and the locally generated bit-rate clock. Multiplying the respective in-phase and quadrature I&D outputs and summing generate an error signal suitable for closing the bit synchronizer loop.

As discussed in Section 5.3, several comments are worthy of note concerning the design of the bit synchronizer loop. First, the mid-bit in-phase and quadrature I&D outputs are independent of the between-bit in-phase and quadrature I&D outputs because of the orthogonality (in time) of their respective integration intervals. This greatly simplifies the computation of the equivalent loop error curve and the equivalent noise spectral density at the error control point. Second, all of the above integrations occur over half-bit intervals. While it is advisable to "window" the quadrature I&Ds (half a bit in the Hughes design), it is not necessarily desirable to "window" the in-phase I&Ds. In fact, windowing the in-phase I&Ds to half a bit as in the Hughes design results in a 3 dB signal-to-noise ratio penalty for making decisions on the midbit and between-bit transitions relative to performing full-bit in-phase I&Ds, as is done, for example, in [16]. In [16], four bit synchronizer configurations motivated by the application of maximum a posteriori (MAP) estimation theory are developed and their performances compared. Conceptually, the Hughes bit synchronizer design is closest to Figure 5c of [16], although fundamental differences between the two do exist.

The timing diagrams, as well as the complete analysis of the tracking performance of the bit synchronizer, are discussed in Appendix E.

Figures 77 and 78 illustrate the normalized tracking jitter coefficient $f(n, R_d, p_t)$ as a function of the digitizer decision threshold (n) with the bit energy-to-single-sided spectral density defined as

$$R_d \triangleq \frac{E_b}{N_0}, \tag{28}$$

where E_b is the symbol energy and N_0 is the single-sided noise spectral density as one parameter and the data transition density (p_t) as the other parameter. The normalized tracking jitter coefficient is defined in Appendix E as

$$f(n, R_d, p_t) = 8 R_d/(B_L T)\, \sigma_\lambda^2, \tag{29}$$

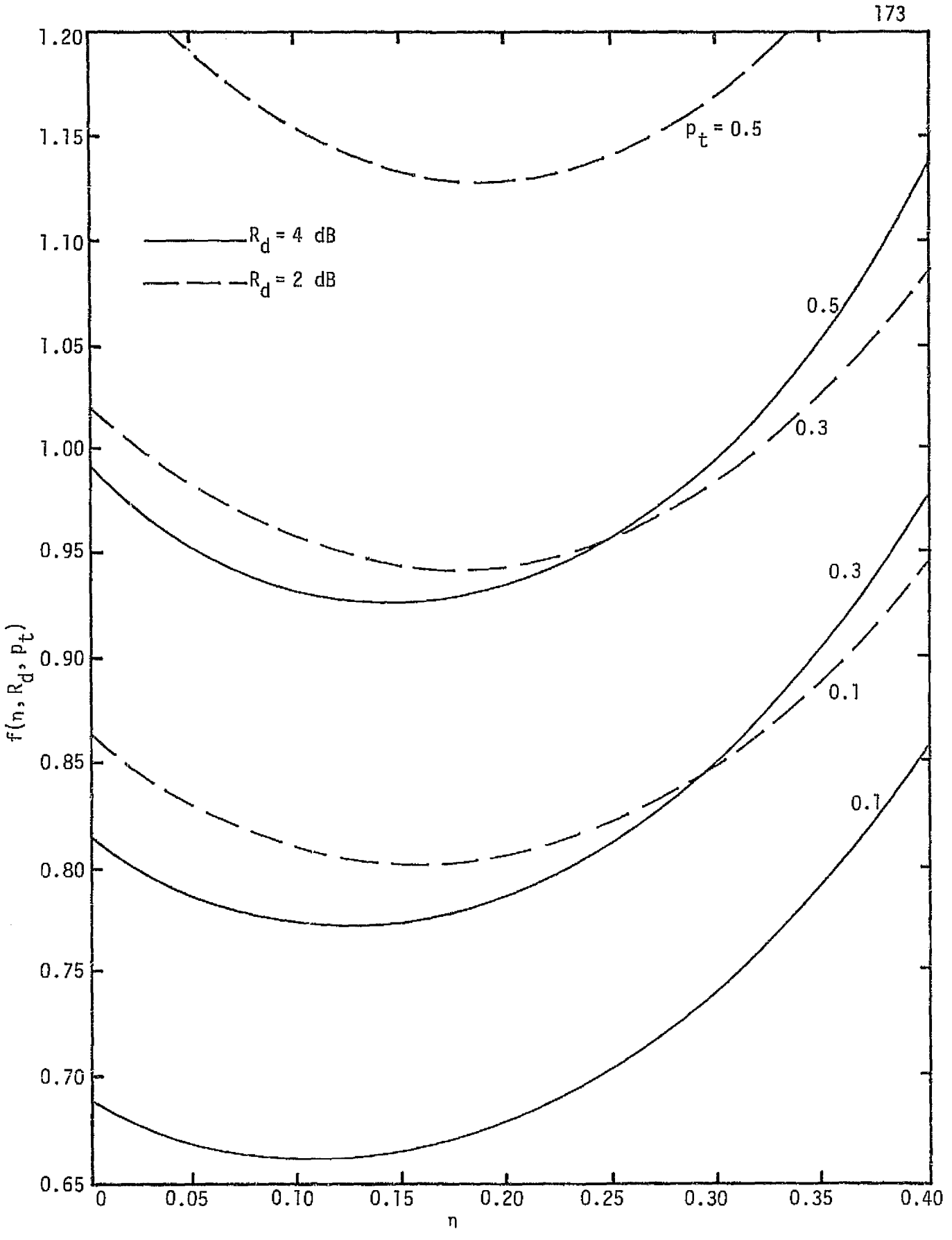

Figure 77. Normalized Tracking Jitter Coefficient vs. Detection Threshold with NRZ Transition Density and Detection Signal-to-Noise Ratio as Parameters

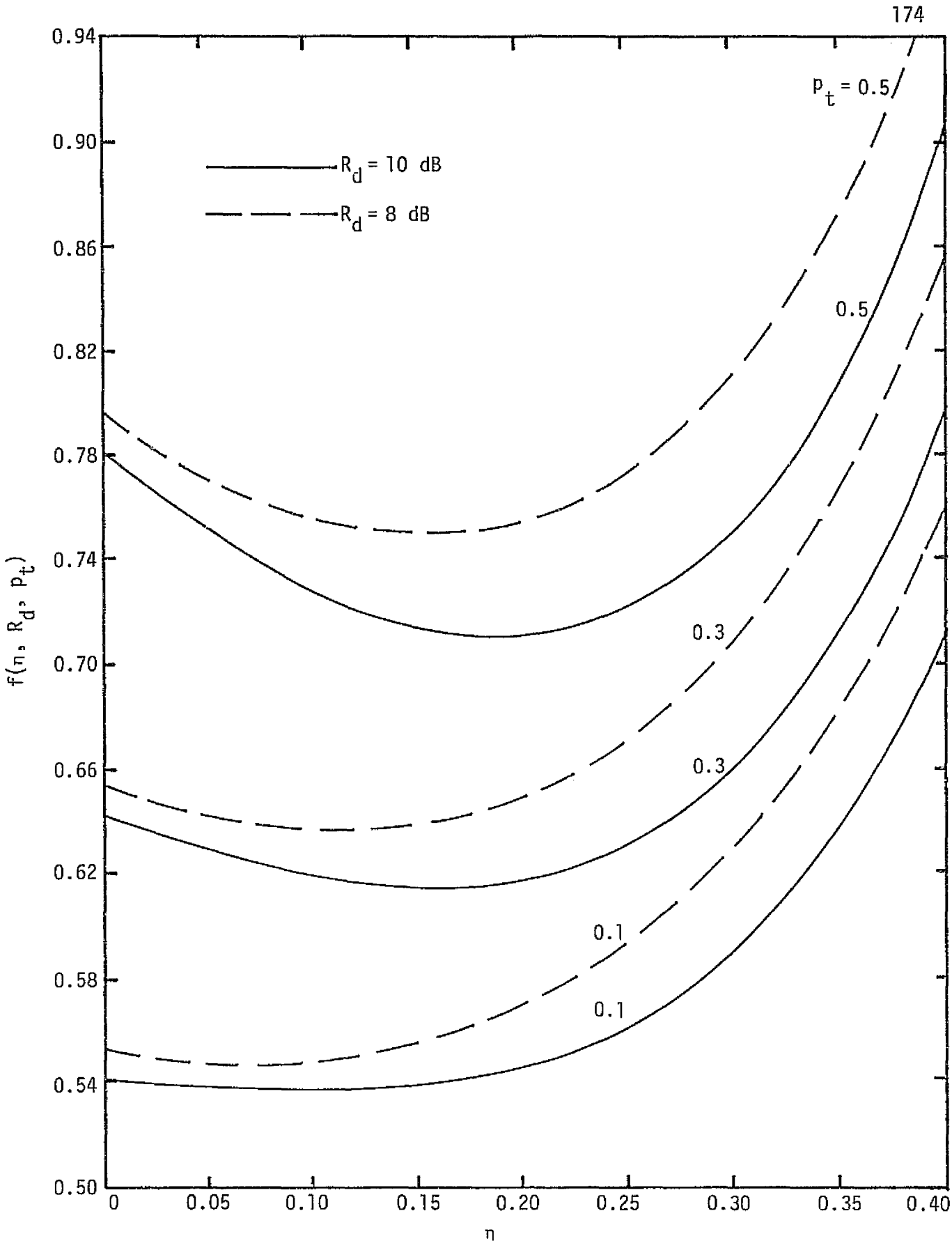

Figure 78. Normalized Tracking Jitter Coefficient vs. Detection Threshold with NRZ Transition Density and Detection Signal-to-Noise Ratio as Parameters

where B_L is the loop single-sided noise bandwidth, T is the bit time, and σ_λ is the RMS timing error normalized by the bit time.

Several observations can be made:

(1) The tracking jitter increases with the increase of the transition density p_t.

(2) For a given in-phase decision threshold (η) and a given transition density (p_t), the tracking jitter decreases with the increase of the signal-to-noise ratio R_d. This is intuitively correct because better performance should be expected at higher signal-to-noise ratios. It should be pointed out, however, that the test data supplied by HAC [20] show a reverse trend. One example is that shown in Figure 79 where the loss which is proportional to the tracking jitter is shown to increase with the increase of signal-to-noise ratio.

(3) The threshold is shown to have an optimal value which is a function of the signal-to-noise ratio and the data transition density. This optimal value is illustrated in Figure 80.

Since no threshold value has yet been supplied by HAC, a value of $\eta = 0.3$ has been selected to calculate the signal-to-noise ratio loss as a function of the input signal energy to single-sided spectral density (R_d).

Using the available documentations in [27], the random data case with $p_t = 0.5$ has been selected as an example. Since no value of the loop bandwidth (B_L) has been quoted by HAC, a typical value of $TB_L = 10^{-2}$ is selected for illustration. Table 13 summarizes the loss of signal-to-noise ratio as a function of R_d.

Table 13. Signal-to-Noise Ratio Degradation ($\Delta E_b/N_0$) as a Function of $R_d = E_b/N_0$ with Threshold $\eta = 0.3$ and a Transition Density $p_t = 0.5$

	$R_d = E_b/N_0$ (dB)			
	2	4	6	10
$\eta = 0.3$	0.75	0.65	0.35	0.30

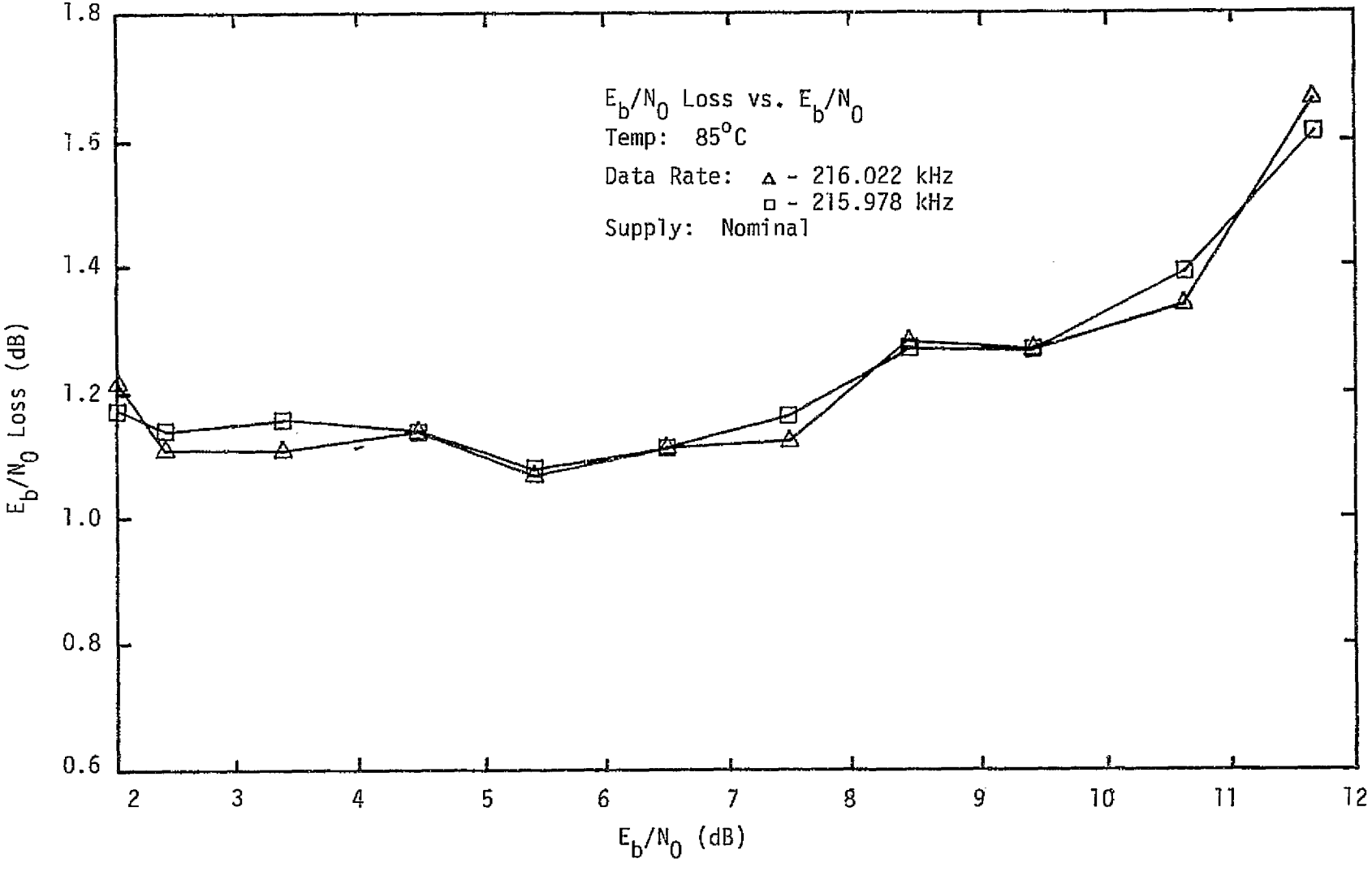

Figure 79. Signal-to-Noise Ratio Loss vs. Input Bit Energy to One-Sided Spectral Density [Data supplied by HAC]

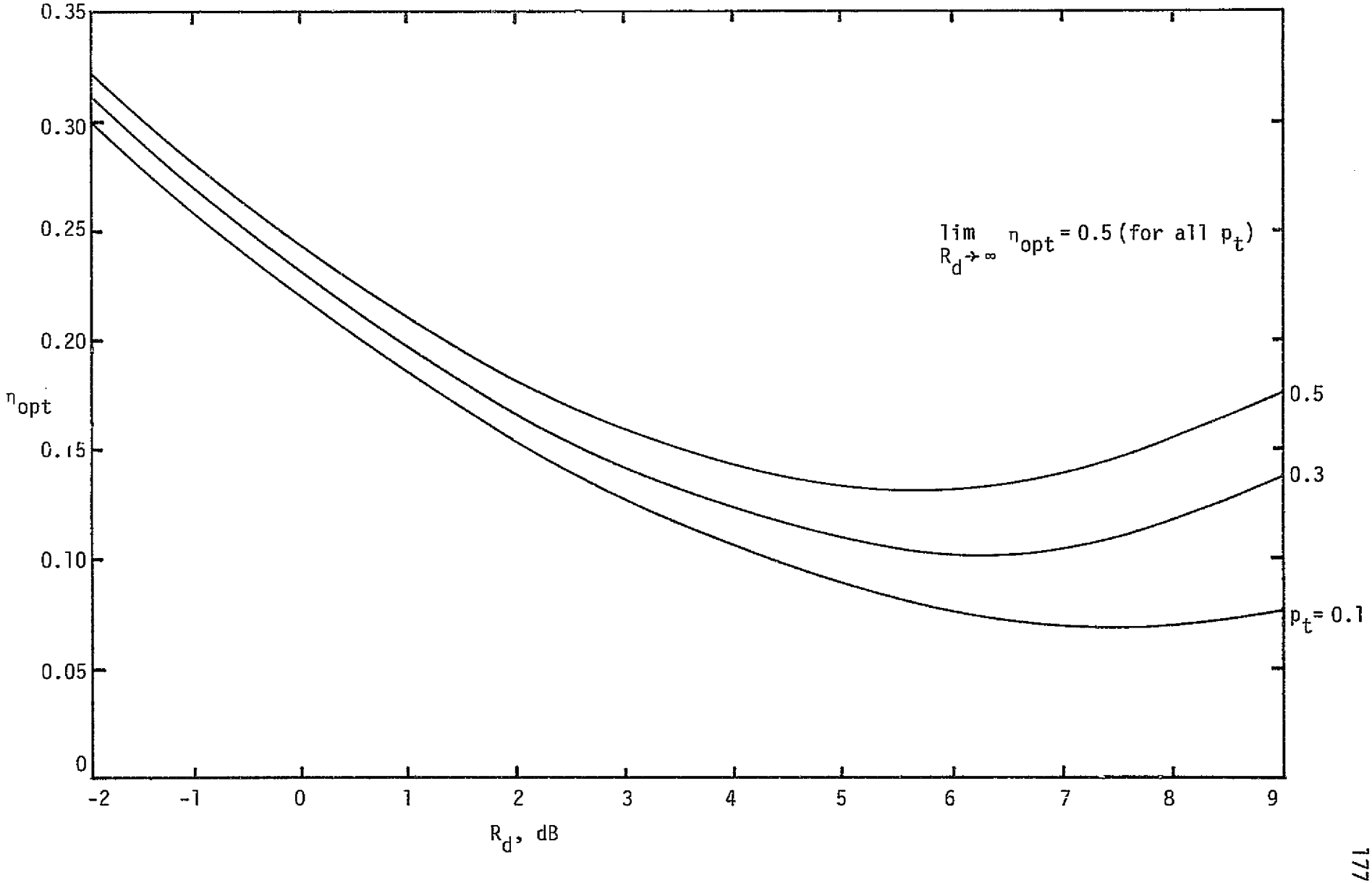

Figure 80. Optimal Decision Threshold vs. Signal-to-Noise Ratio

The table shows that, for $B_L T = 10^{-2}$, the degradation in signal-to-noise ratio due to imperfect bit timing does not exceed 0.75 dB for $R_d \geq 2$ dB, which is well below the specification value of 1.0 dB and in agreement with most of the available data. However, test data taken at 85°C show that, at this high temperature, the loss can be between 1.0 dB and 1.5 dB. Though such losses are not believed to present any problem to the overall system performance, a closer look at the data and the breadboard setting is needed to verify the validity of the test data.

It is also worth noting that the selection of the value $B_L T$ is a compromise between tracking accuracy and the ability of the loop to track long streams of ones or zeros.

The material presented in [20] quotes that, in order for the bit synchronizer loop to acquire and maintain lock over the full temperature range of -20°C to +85°C, signal-to-noise ratios (E_b/N_0) of 2 dB and 5.9 dB might be needed for random data and alternating data, respectively. The available test data at the same time [21] show that acquisition is taking place down to 0 dB with a wide frequency pull-in margin that exceeds by far the specifications of ±22 Hz. Though a possible small margin of signal-to-noise ratio above 0 dB might be warranted to allow for component aging, the value of 5.9 dB is believed to be too high for such tolerances.

An additional area of interest is the pull-in frequency range test data at various temperatures. As mentioned earlier, the data shows that the pull-in frequency range has a wide margin that can tolerate the specified ±22 Hz data rate uncertainty. Some test data, such as that shown in Figure 81, however, show an unusual behavior where, at high temperatures, the pull-in frequency range for low signal-to-noise ratios becomes higher than that at high signal-to-noise ratios. This behavior is most probably attributed to the test setup.

9.3 Results of Ambiguity Resolver Performance Analysis

The purpose of the Ku-band forward link ambiguity resolver is to distinguish between midbit transition times and data bit transition times for the 216 kbps Manchester coded data. Section 9.3.1 describes

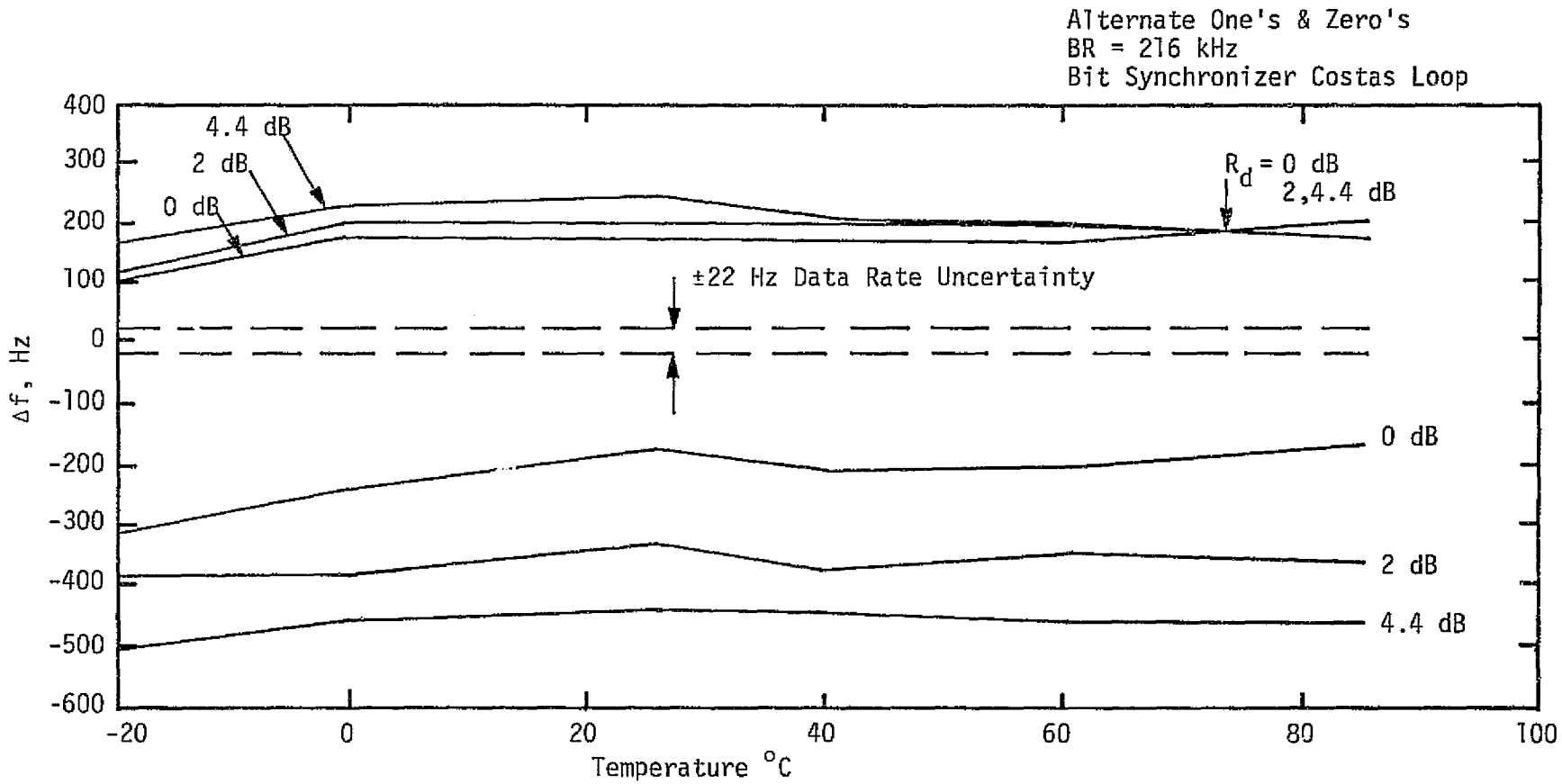

Figure 81. Hughes Test Curves on Pull-In Frequency Range of the Bit Synchronizer Loop with R_d as a Parameter

the ambiguity resolver principles of operation, Section 9.3.2 presents the results of numerical evaluation of the ambiguity performance analysis described in Appendices F and G, and Section 9.3.3 gives recommendations for future work on the ambiguity resolver.

The performance of the ambiguity resolver is a function of four parameters: η, the normalized threshold of the bit digitizer; γ, the counter decision threshold at overflow; P_t, the data transition probability; and R_d, the bit signal-to-noise ratio. The results presented show the behavior of the ambiguity resolver with respect to probability of correct resolution in one pass and the mean time to overflow in one pass as a function of the four parameters.

9.3.1 Principles of Operation

As shown in Figure 82, the ambiguity resolver consists of four integrate-and-dump (I&D) circuits, four digitizers, two counters, and threshold comparison and decision logic. The input Manchester coded data signal is mixed with a combination of the bit rate, its complement, and the twice bit rate clock to form midbit and between-bit in-phase and quadrature signals. The outputs of the I&D circuits are passed to the null zone digitizers; the output of a digitizer is 0 if the magnitude of the input is less than η_0, +1 if greater than η_0, or -1 if less than $-\eta_0$. For the purposes of analysis, the threshold is normalized to $\eta = \eta_0/A$, with A the input signal amplitude.

The magnitudes of the digitized outputs are used to increment or decrement counters 1 and 2, as shown in Figure 82. We see that midbit in-phase outputs increment counter 1 while midbit quadrature outputs decrement counter 1. Counter 2 operates in a similar manner with the between-bit outputs. The net effect, in the absence of noise and timing error, is to increment counter 1 and decrement counter 2 at each data transition, and increment both counters when no data transition occurs. If counter 1 overflows and counter 1 exceeds counter 2 by a preset threshold γ, an ambiguity decision is declared and the bit rate clock is assumed to be in-phase with the data. Similarly, if counter 2 overflows first and γ is exceeded, the complement of the bit rate clock is selected. If no decision is made at overflow, both counters are reset and the process repeats.

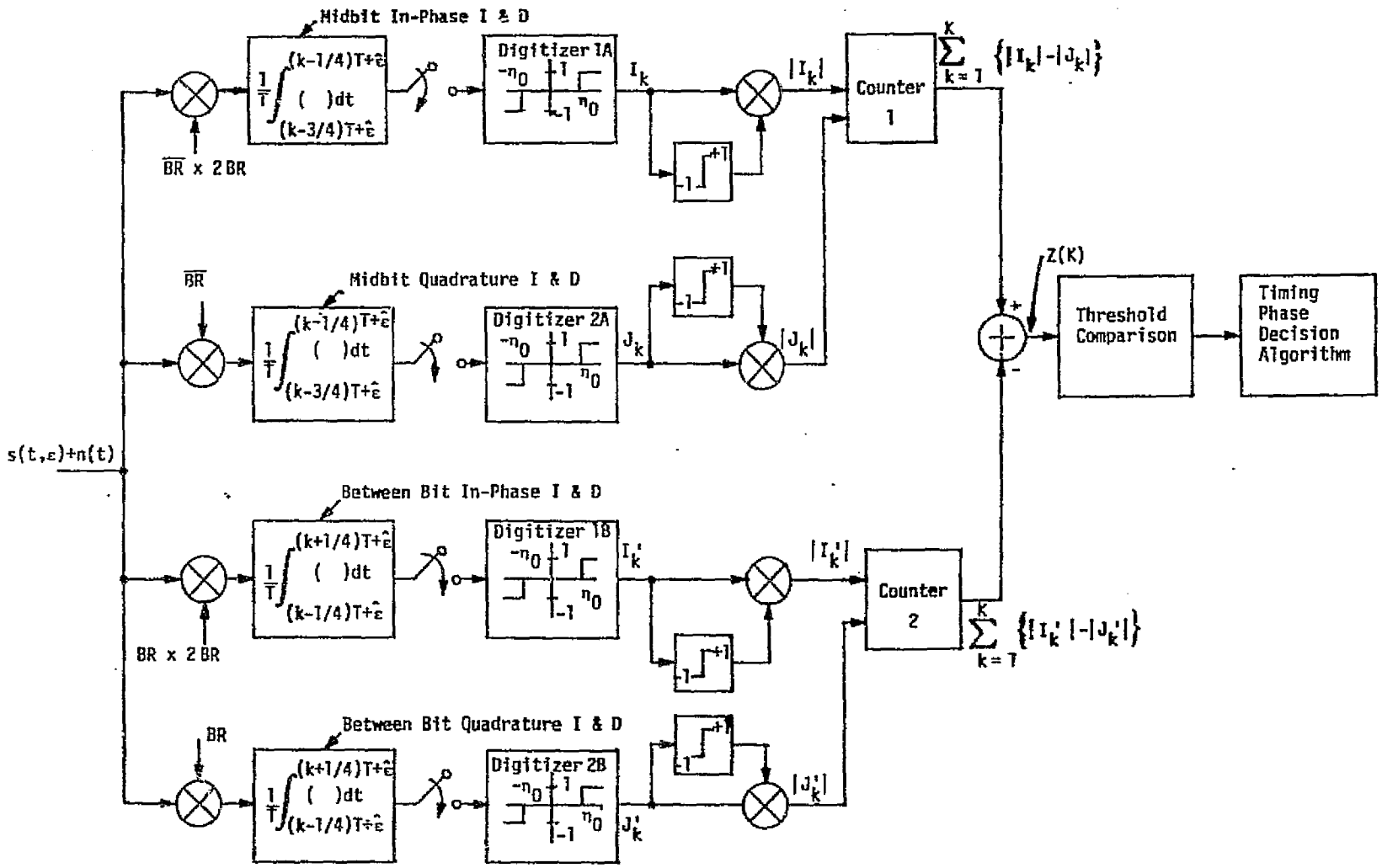

Figure 82. Timing Phase Ambiguity Resolver

The purpose of the ambiguity resolver performance analysis is to determine the performance of the ambiguity resolver in the presence of noise, and the optimum values of η and γ, the digitizer and counter thresholds. Details of the analysis are presented in Appendices F and G and summarized below.

The probability of correct ambiguity resolution in one pass is:

$$P_c = \sum_{K=K_{min}}^{\infty} P_c(K)\, p_c(K) , \tag{30}$$

with K_{min} the point of counter overflow (4096 for the 12-bit counter being used).

$P_c(K)$ is the probability that the counter difference exceeds γ at overflow on the Kth step, and $p_c(K)$ is the probability of overflow at the Kth step.

$$P_c(K) = \frac{1}{2} + \frac{1}{2} \operatorname{erf} \left[\frac{K_{min} - \gamma - \mu_c(K)}{\sqrt{2}\, \sigma_c(K)} \right] \tag{31}$$

$$p_c(K) = \left(\frac{K_{min}}{K} \right) \sum_{N=\begin{cases} 0,2,4\ldots \\ 1,3,5\ldots \end{cases}}^{K-K_{min}} \frac{K!}{\left(\frac{K + K_{min} - N}{2} \right)! \left(\frac{K - K_{min} - N}{2} \right)!\, N!} \times p_0^{(K+K_{min}-N)/2}\, q_0^{(K-K_{min}-N)/2}\, r_0^{N} ; \qquad K \geq K_{min} , \tag{32}$$

$$p_0 = \operatorname{erf} \Lambda^0 \left[\frac{1}{2} \operatorname{erfc} \Lambda^+ + \frac{1}{2} \operatorname{erfc} \Lambda^- \right] \tag{33}$$

$$q_0 = \operatorname{erf} \Lambda^0 \left[1 - \operatorname{erfc} \Lambda^+ - \frac{1}{2} \operatorname{erfc} \Lambda^- \right] \tag{34}$$

$$r_0 = \operatorname{erf} \Lambda^0 - (1 - 2 \operatorname{erfc} \Lambda^0) \left[\frac{1}{2} \operatorname{erfc} \Lambda^+ + \frac{1}{2} \operatorname{erfc} \Lambda^- \right] \tag{35}$$

$$\Lambda^0 = \sqrt{R_d/2}\,(2\eta) , \quad \Lambda^+ \triangleq \sqrt{R_d/2}\,(2\eta + 1) , \quad \Lambda^- \triangleq \sqrt{R_d/2}\,(2\eta - 1) \tag{36}$$

$$\mu_c(K) = K(1-2p_t)\left[\frac{1}{2}\operatorname{erfc}\Lambda^+ + \frac{1}{2}\operatorname{erfc}\Lambda^- - \operatorname{erfc}\Lambda^0\right] \tag{37}$$

$$\sigma_c^2(K) = K\left[\operatorname{erfc}\Lambda^0 + (1-2\operatorname{erfc}\Lambda^0)\left(\frac{1}{2}\operatorname{erfc}\Lambda^+ - \frac{1}{2}\operatorname{erfc}\Lambda^-\right)\right]$$

$$- K^2(1-2p_t)^2\left[\frac{1}{2}\operatorname{erfc}\Lambda^+ + \frac{1}{2}\operatorname{erfc}\Lambda^- - \operatorname{erfc}\Lambda^0\right]^2 . \tag{38}$$

The mean number of steps to overflow in one pass is given as:

$$m_0 = \sum_{K=K_{min}}^{\infty} K P_c(K) . \tag{39}$$

Thus, given that a correct decision has been made, the mean time to reach a correct decision in one pass is $\bar{t}_c(1) = m_0/R$, with R the data rate (216 kbps for the Ku-band system).

For the cases considered in the next section, with relatively high R_d, the probability of incorrect resolution is zero, to the accuracy of the computer. In those cases, the mean time to make a correct decision is the mean time to overflow per pass, m_0, times the expected number of passes to make a correct decision, N_c.

$$N_c = P_c + 2(1-P_c)P_c + 3(1-P_c)^2 P_c + \cdots , \quad \text{with } P_I = 0 . \tag{40}$$

Thus, $N_c = 1/P_c^2 \times P_c = 1/P_c$, and the mean time to reach a correct decision $\bar{t}_c = m_0/P_c R$.

9.3.2 Results of Performance Analysis

In this section, we discuss the numerical results of the performance analysis for selected values of R_d, η, γ, and P_t. In all cases to follow, P_t is chosen to be 1/2, i.e., equally likely ones and zeros in the data stream. The probability of correct decision and mean number of steps to correct decision are first calculated as a function of γ for fixed η and R_d; then, given a suitable γ, the calculations are performed as a function of η for fixed R_d, and finally, given a suitable γ and η, the performance is calculated as a function of R_d.

C-3

In Figure 83, P_c is plotted as a function of γ for $R_d = 10$ dB, $\eta = 0.35$, and $P_t = 0.5$. Note that P_c is relatively insensitive to γ until γ approaches the counter size, 4096. It is reasonable to expect the probability of correct decision to decrease for very large γ, as this implies little energy in counter 2 when, in fact, we expect counter 2 to be increasing. The mean number of steps has not been plotted, as the results have shown it is a constant (equal to 5104) for the values of γ selected.

In Figure 84, P_c and m_0 are plotted as a function of η for $R_d = 10$ dB, $\gamma = 3500$, and $P_t = 0.5$. P_c is a monotonically decreasing function of η as η increases, where m_0 has an "optimum" at $\eta = 0.35$, at least for $R_d = 10$ dB.

Taking into account the results of the analysis as a function of η, P_c and m_0 are plotted as a function of R_d for $\gamma = 3500$, $\eta = 0.20$, and $P_t = 0.5$ in Figure 85. As expected, the probability of correct decision increases and the mean number of steps decreases as R_d increases.

These results are also summarized in Table 14. The probability of incorrect decision, which was also calculated, is not plotted, as it is negligible for the values of R_d used.

9.3.3 Conclusions and Recommendations

The preceding results are intended as a guide to the performance of the ambiguity resolver as a function of the various relevant parameters and a verification of the analysis. The calculations are computationally intensive and, as a result, use significant amounts of computer time. In particular, as R_d goes below 6 dB, m_0 gets very large (over 10,000) and these results are not yet available.

It was hypothesized that additional precision might be needed, particularly in light of "zero" probability of incorrect decision. Single precision Fortran has a precision of 7 digits, and the calculations involve summations of many (small) probabilities. The program was modified to run double precision (17 digits), and one run was made at $R_d = 10$ dB, $\eta = 0.35$, and $\gamma = 3500$. No significant change in the results was evident. Since double precision takes longer to run and hence is more expensive, the remainder of the runs were made under single precision. However, at R_d lower than 6 dB, we may have to revert to double

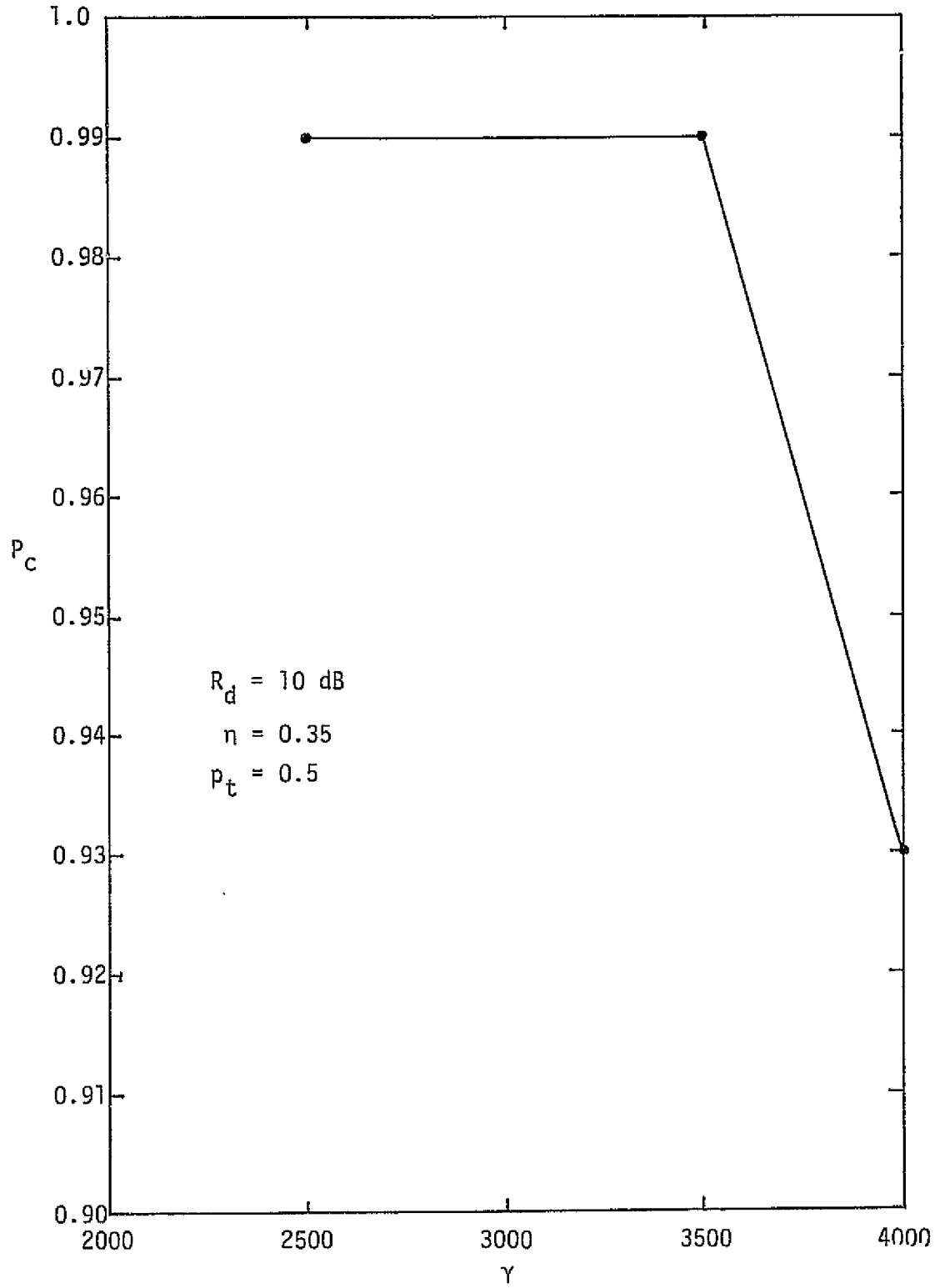

Figure 83. Probability of Correct Resolution in One Pass, P_c, Versus γ

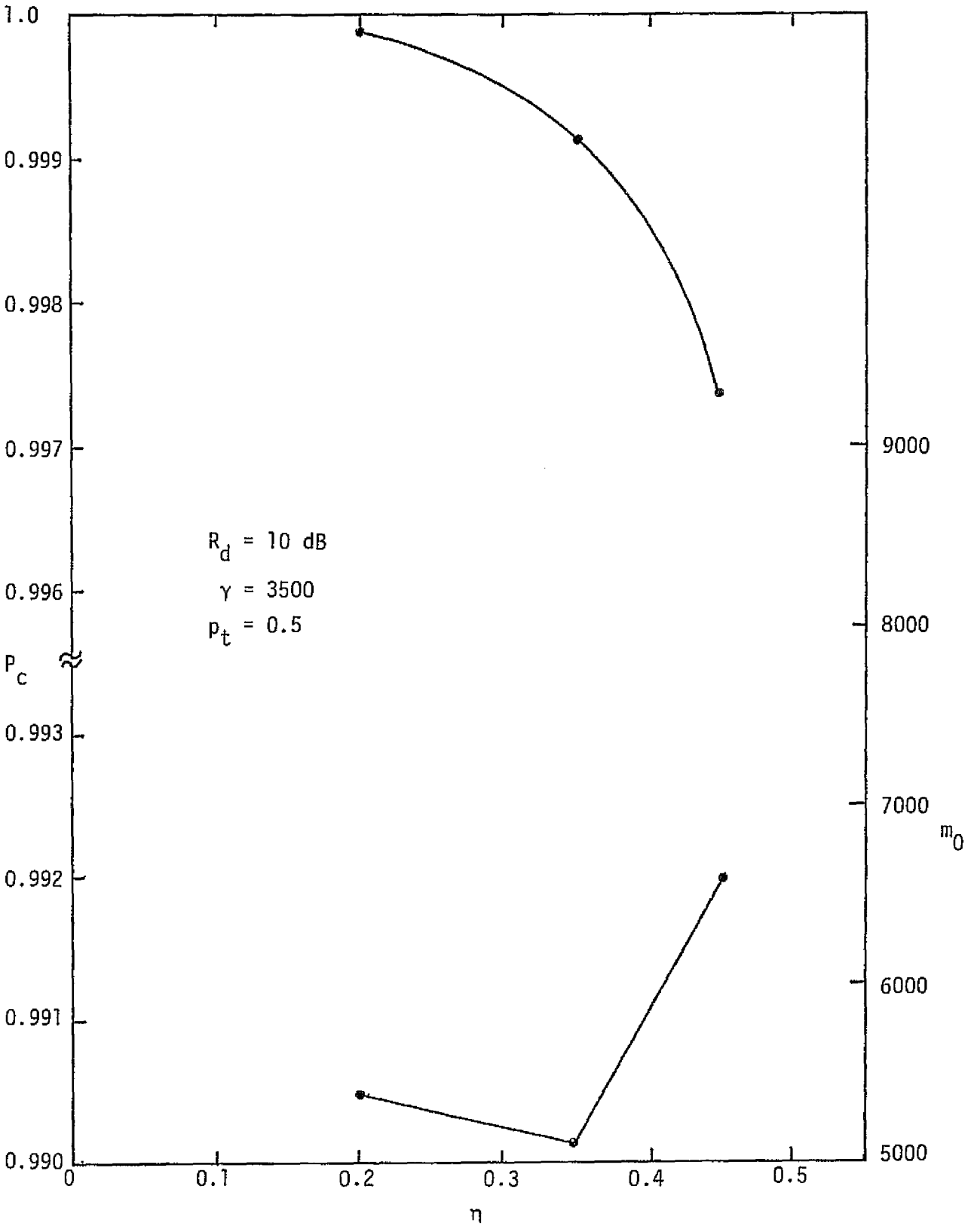

Figure 84. Probability of Correct Resolution in One Pass, P_c, and Mean Number of Steps to Overflow, m_0, versus η

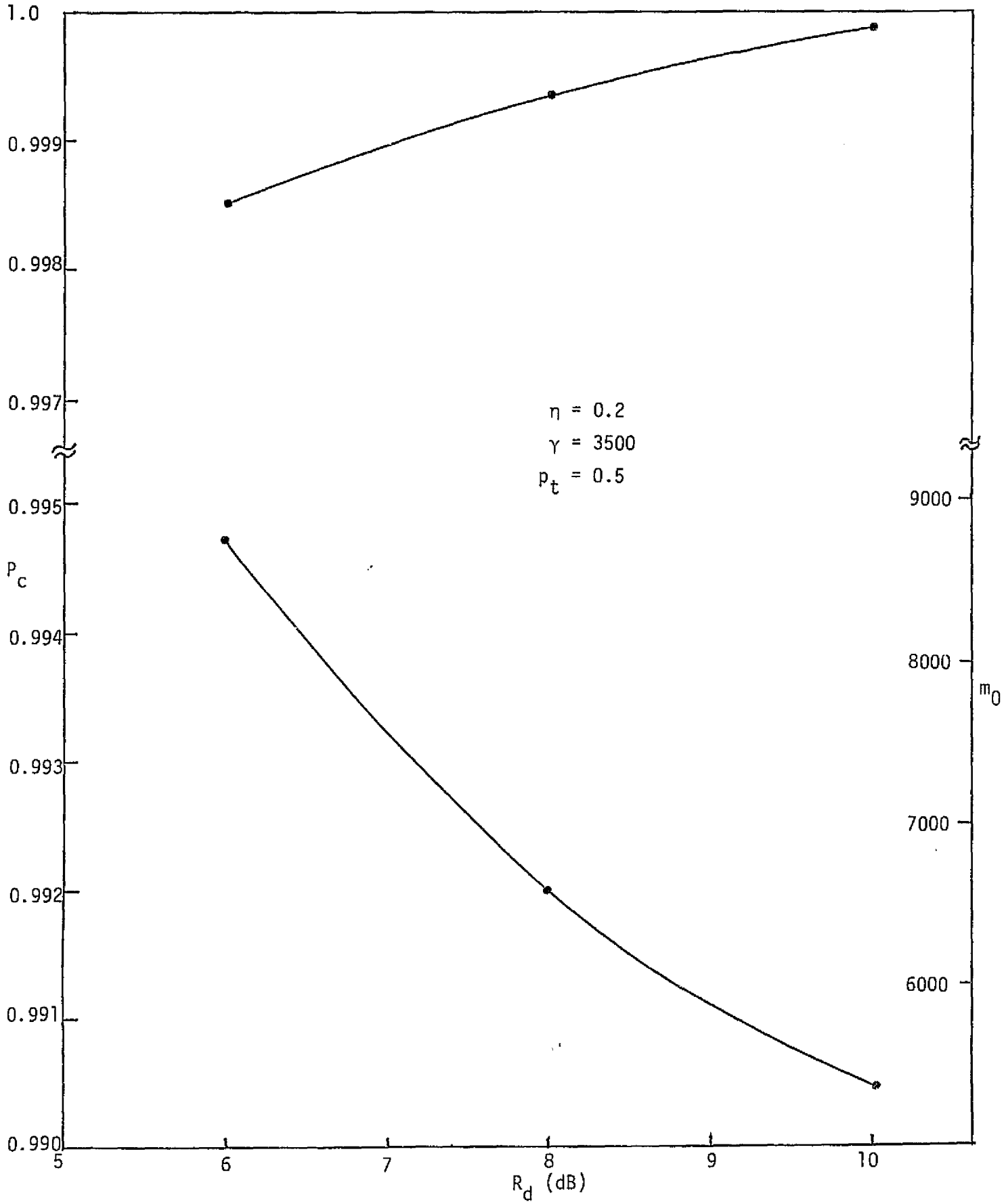

Figure 85. Probability of Correct Resolution in One Pass, P_c, and Mean Number of Steps to Overflow, m_0, versus R_d

Table 14. Probability of Correct Ambiguity Resolution in One Pass and Mean Time to Overflow as Functions of η, γ, and R_d

η	P_D	m_0	
0.2	0.99989	5352	$\gamma = 3500$
0.35	0.99914	5104.5	$p_t = 0.5$
0.45	0.99734	6592	$R_d = 10$

γ	P_D	m_0	
2500	0.99923	5104.9	$R_d = 10$
3500	0.99914	5104.5	$\eta = 0.35$
4000	0.93136	5104.9	$p_t = 0.5$

R_D	P_D	m_0	
6	0.99863	8850	$\eta = 0.2$
8	0.99934	6609	$\gamma = 3500$
10	0.99989	5352	$p_t = 0.5$

precision. The problem arises at lower R_d since the length of the sums increases and truncation errors, which propagate, may tend to dominate the calculations.

Now that the computer program to calculate the performance has been debugged and run reliably in both single and double precision, additional results can be obtained using the JSC computer in batch mode. It is suggested that additional runs be made at the expected operating point of the system (R_d = 0 to 6 dB) to determine optimum values of η and γ as a guide to HAC and to verify the performance of the ambiguity resolver when the actual performance data is made available by HAC.

10.0 PRODUCT DESIGN CONSIDERATIONS

10.1 General

This section summarizes the product design considerations for the Ku-Band Integrated Radar and Communication Equipment for the Space Shuttle Orbiter. This equipment, as designed by HAC, is comprised of four line replaceable units (LRU). One of these LRUs is a DA located within the payload bay and deployable upon the opening of the payload bay doors. The other three LRUs are installed in the avionics bay located inside the Orbiter cabin [3,13,14,22,26].

Figure 86 shows the deployed assembly. As is shown in the figure, the DA consists of two major subassemblies, namely the DMA and the DEA. The DMA includes all the necessary components for forming and steering a highly directional antenna beam. These components are the gimbals, the antenna reflector, and the feed with its support. The DEA houses the electronics for transmission and reception of the radar signals and the reception of the communication signals.

Figure 87 shows an overall configuration of an avionics bay LRU. The three LRUs are EA-1, EA-2, and the SPA. The EA-1 is devoted primarily to the communication function, but it also includes the servo electronics for both the communication and radar operations. The EA-2 is used exclusively for the radar function. The processing of the transmitted and received communications data is performed by the SPA.

With the exception of the connector configuration, the mechanical configuration of the avionics LRUs is identical.

The sections which follow contain a summarized description of the product design of the Ku-band system subunits. The details are presented in Appendix H.

10.2 Deployed Assembly

The DA comprises that portion of the Ku-band radar and communication system which attaches to the upper face of the Rockwell-supplied deployment actuator and stows in the limited space between the payload bay and the door radiators. Major elements of the DA are the DEA and DMA. The DEA is a shop-replaceable unit (SRU) of the DA LRU of the Ku-band integrated radar and communications equipment.

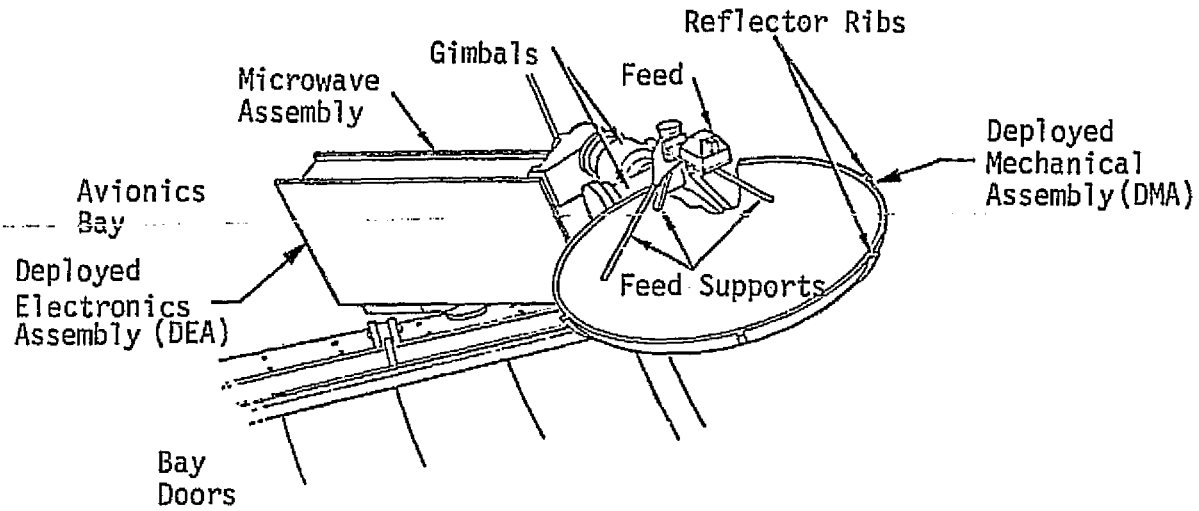

Figure 86. Deployed Assembly

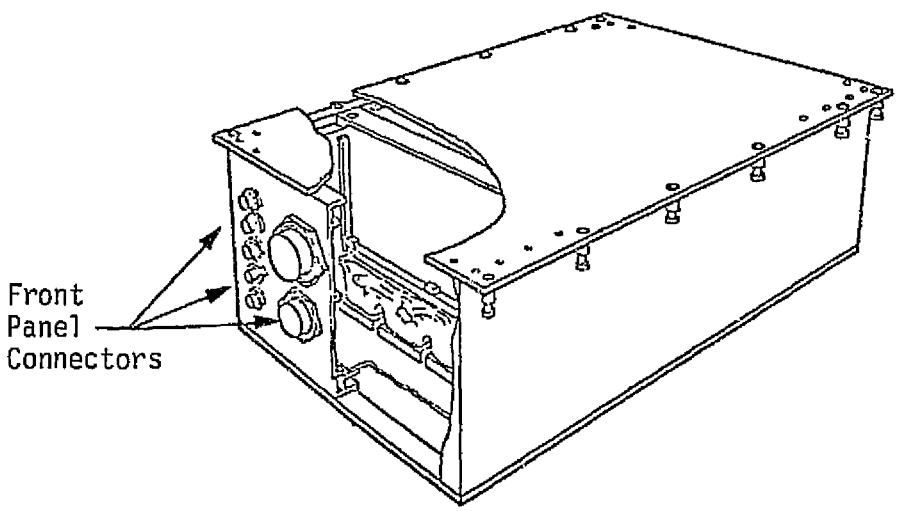

Figure 87. Avionics Bay Unit

The DA structure consists of three basic elements: the base pedestal that bolts to the Shuttle deployment mechanism and contains the electrical connector interface; a structure frame into which the DEA is secured; and a gimbal mounting bracket. These three elements of the structure are electron beam welded together to form a single assembly.

All exterior surfaces of the structure assembly are covered with 0.005" silvered teflon thermal finish material. All lightening holes in the base pedestal are closed with a film of this material to prevent the entrance of solar energy (direct or reflected) into the interior cavities. In addition, the exposed portions of the gimbal and antenna support arm are painted with a white silicon thermal control paint.

Active thermal control is utilized for cold conditions. Sensitive items on the gimbal that need to be kept above the -65°F survival level are the encoders, the rotary joints, and the waveguide switch. Heaters and thermal blankets are installed to protect these items.

10.2.1 Deployed Mechanical Assembly

The major components of the DMA are the structure, antenna, rotary joints, and gimbals.

The narrowbeam antenna assembly is a prime fed paraboloidal reflector using a five-element monopulse feed. The 36-inch parabolic reflector antenna is constructed of epoxy-impregnated graphite cloth formed over four main supporting ribs. A ring stiffener is used at the aperture plane. The epoxy-graphite construction provides a lightweight structure. The antenna shell and feed tube weight is 3.7 lb. The monopod feed support edge mounting prevents the feed from mechanically loading the reflector surface by attaching to the same edge support structure used for the parabolic surface. The overall depth of the antenna assembly is less than 12.5 inches, allowing the required envelope clearance on each side of the antenna during stowage. Figure 88 illustrates the antenna structure.

Two channels, sum and difference, of RF energy traverse the dual-axis gimbals. The sum channel remains isolated from the difference channel in a dual-channel rotary joint, which consists of two

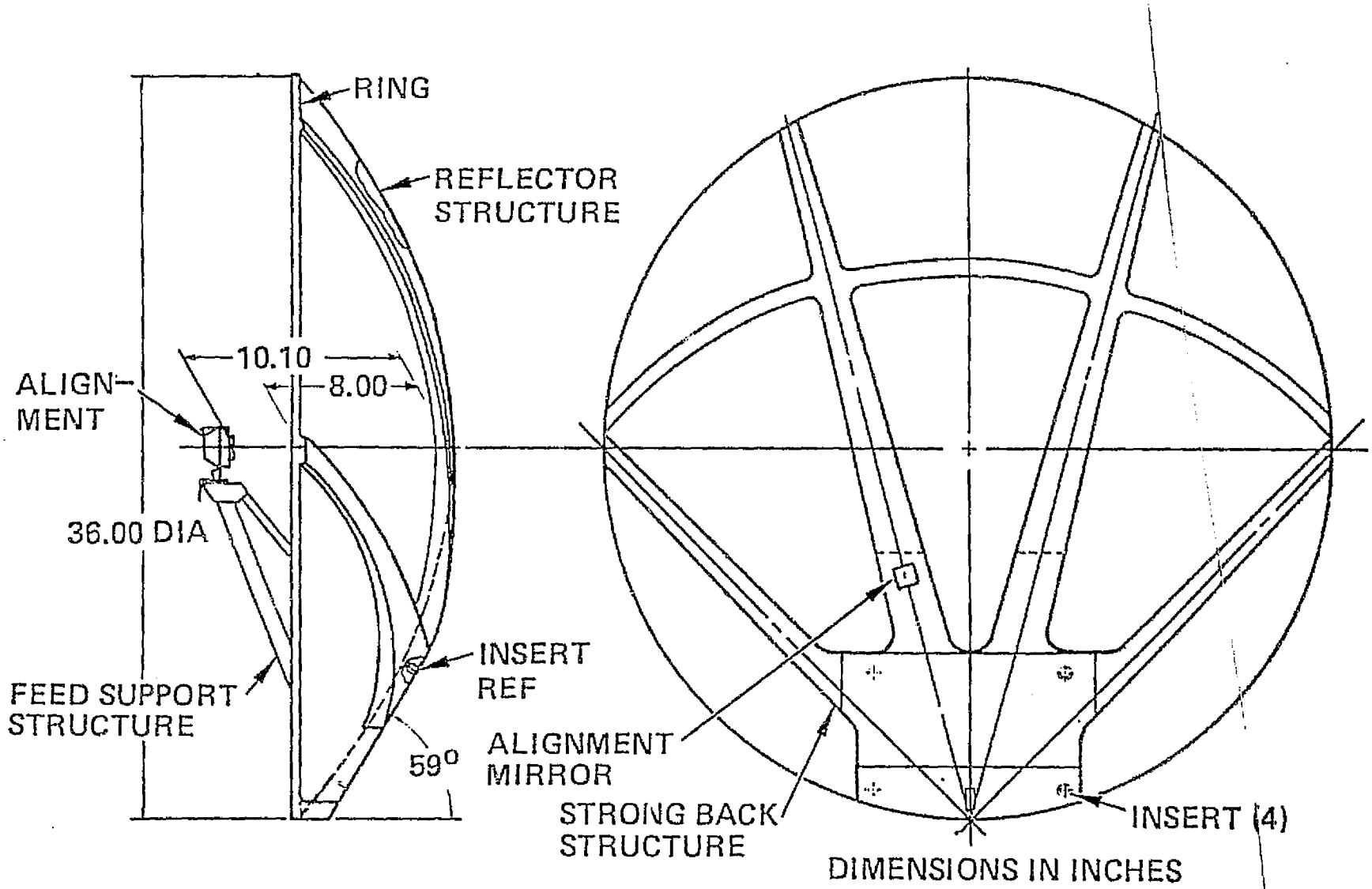

Figure 88. Antenna Structure

rotary joint subassemblies, one for each axis. These subassemblies are available as reliable off-the-shelf components. Only minor modifications in the internal bearings are required to satisfy the Shuttle temperature and vacuum requirements.

The DA gimbal assembly consists of the two-axis, servo-controlled rotating mechanical and electrical interface between the deployed boom structure and the antenna. Included are torquers, bearings, shaft encoders, waveguides, coaxial cables, and other cabling. A locking device secures the assembly in the stowed position. Minimal gimbal cost, weight, and trunnion obscuration are achieved with the edge-mounted antenna configuration.

The off-center gimbal configuration allows a maximum size (36" dia) narrowbeam antenna. Disturbance torques due to Shuttle accelerations are negligible; therefore, a centered load is not an operational constraint.

10.2.2 Deployed Electronics Assembly

The DEA (Figure 89) houses the electronics for the transmission and reception of radar and communications data. The electronics are housed in an enclosure 31 inches long, 15.5 inches high, and 4.5 inches deep. The overall estimated weight is 70.6 pounds. The enclosure is mounted to the DMA structure by a flange that extends along the perimeter of the DEA chassis baseplate; 24 torque set screws hold the flange in place.

The enclosure is a dip-brazed aluminum structure consisting of a baseplate that also serves as the prime radiating surface, ribbed side plates to which are mounted RF connectors, a front plate that serves as the mounting surface for the power and command input connectors, and a rear plate to which are mounted the waveguide output flanges and RF connectors for test access. The inside of the chassis is partitioned into cavities by a wall that extends the length of the chassis and a shorter wall that separates the receiver and exciter subassemblies. These walls provide mechanical stiffness to the structure and RF shielding between the subassemblies.

The cover for the DEA enclosure is a bonded honeycomb structure consisting of two thin aluminum face sheets, an outer and inner flange, and an aluminum honeycomb sandwich between the face sheets. The

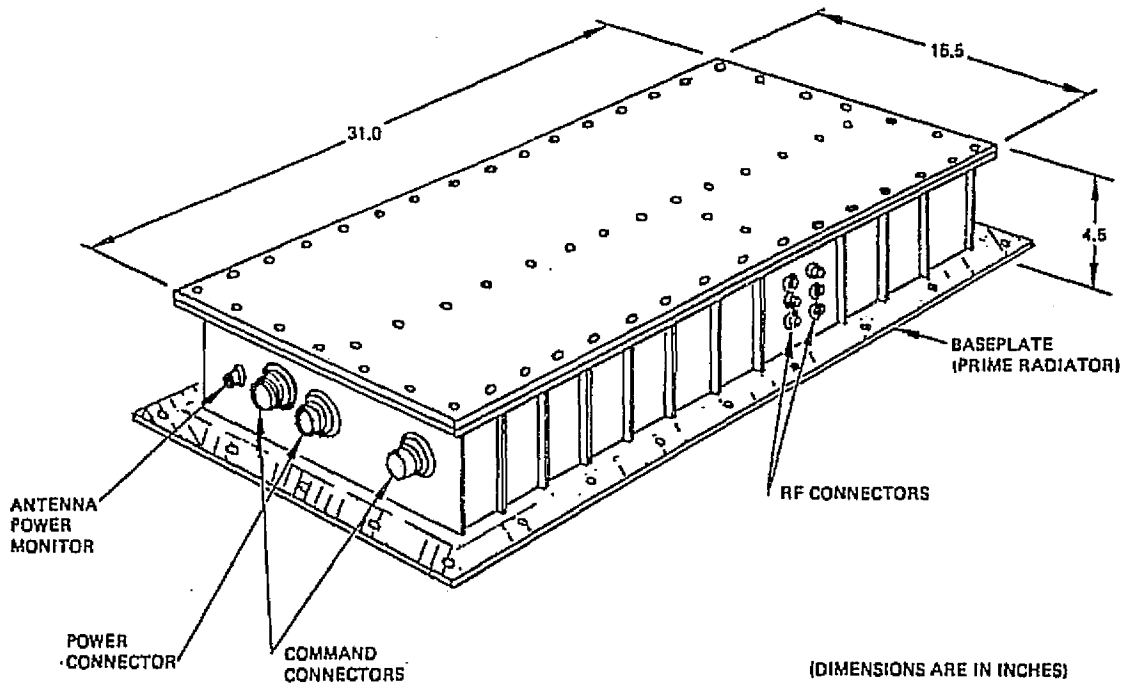

Figure 89. Deployed Electronics Assembly

enclosure walls and cover, stiffened by the ribbing and honeycomb construction, prevent excessive bending and displacement from the pressure differential resulting from the space environment.

The DEA is functionally divided into five discrete SRUs that fit into the enclosure. The subassemblies are arranged to optimize the thermal distribution, minimize the length of critical RF interconnections, and provide access for testing and maintainability. The five SRUs are plugged in and mounted directly to the base of the chassis by means of captive hardware.

The walls that partition the enclosure provide RF separation between SRUs. RF gasketing in the cover and RF shielded feed-through terminals in the walls complete the subassembly and unit level RF/EMI shielding.

Replacement of an SRU in the DEA involves removal of the cover hardware and cover. Each SRU is independently replaceably. Subassemblies are plug-in modules fastened to the chassis baseplate with captive hardware.

Active thermal control techniques are utilized in the DEA to provide adequate thermal control. During operation, internal dissipation is radiated to the space environment by the external surfaces. For nonoperating periods, the DEA will be augmented by thermostatically controlled heaters to maintain acceptable temperatures.

The present maximum power dissipation is approximately 250 W at 28 VDC input. The total radiating surface of the DEA is approximately 8.5 square feet. A silvered teflon finish is used on the prime radiating surface (base plate) to minimize solar absorptance and provide high thermal emittance. A white paint finish is used on the remainder of the external surfaces.

An extensive Hughes thermal analysis of the DEA under specular radiation from the sun has been conducted. In spite of the fact that Hughes has been directed to not consider certain flight configurations that cause the DEA to overheat, it should be emphasized that the use of some criteria as the upper allowed junction temperature of 125°C are believed to be highly unreliable. A normal junction temperature of 105°C would lead to a more acceptable reliability. In addition, tests on different other DEA modules should be conducted in order to determine whether more severe thermal conditions exist.

The DEA enclosure incorporates an environmental seal that ensures compliance to a leakage rate of 10^{-4} cc per second when the unit is filled with inert gas at a pressure of 15.2 psia at ambient temperature.

The primary seal is made by a gasket molded into a groove around the perimeter of the cover. Hermetic connectors are sealed at the enclosure interface by O-rings. Hermetically sealed ceramic windows are utilized in the waveguide adapter for the waveguide output flanges. The adapter interface and the enclosure are sealed by means of a gasket molded into a groove around the perimeter of the adapter.

10.3 Avionics Bay Assemblies - General Product Design

Chassis

Although the EA-1, EA-2, and SPA chassis are different parts (different connector patterns and different SRU/wire wrap plate mounting patterns), the general design is the same for the three units. The chassis is a dip-brazed aluminum structure (see Figure 90). There is a solid frame around each of the two access openings (SRU and wire wrap plate access), two solid end panels, and side walls consisting of two 0.040" aluminum sheets brazed to a corrugated sheet of 0.010" thick aluminum (6061-T6 alloy).

Provisions have been included in the design to avoid trapping brazing salts in the hollow side walls. Also, none of the machining operations cut into a brazed joint, so that brazing salts entrapped in the joint are not exposed to a corrosive environment.

After machining, the chassis is chromate coated per MIL-C-5541, CL 1A, and the exterior surfaces are primed and painted. The structure is also sealed per MIL-STD-276, Method B, to ensure against gas leaks at any of the brazed surfaces.

Wire Wrap Assembly

The wire wrap SRU interconnection plate is machined from 6061-T6 aluminum alloy. The plate is 0.080 inch thick with 0.30 inch high stiffening ribs between SRU connectors. This design will adequately limit deflection of the plate when the SRU connectors are engaged with or withdrawn from the receptacles. (SRU contacts are a flat blade

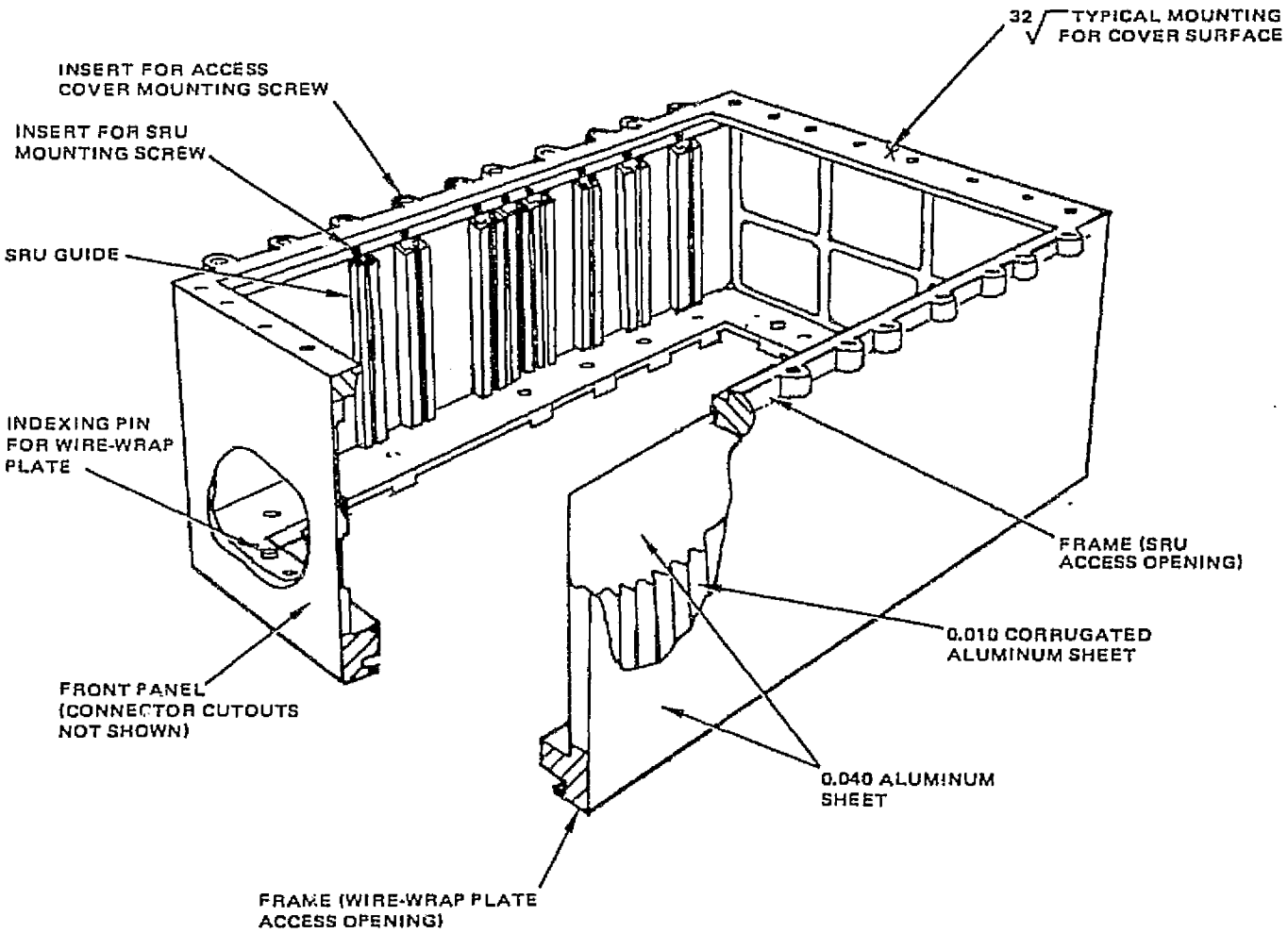

Figure 90. EA-1, EA-2, SPA Chassis

design, and the receptacles are a tuning fork design with a 0.025" square tail).

The wire wrap plate is electrically tied to the chassis, and separate bus strips are provided for +5 volts and digital return (D-RTN) signals. Each bus strip is an aluminum strip with a cross-sectional size of approximately 0.060 × 0.40 inches. The bus strips are bonded to the plate with epoxy-glass prepreg material. Electrical connection between each designated contact and the appropriate bus strip is made by installing a beryllium copper bushing over the 0.025" square contact tail and pressing this bushing into a hole in the bus strip (see Figure 91).

A separate harness is used for connections between the front panel connectors and the wire wrap plate. There are three M55302/66-50S connectors and three M55302/66-60S connectors on the harness for mating to receptacles (commercially identified as the Airborne WTAV**PW40JL series) on the wire wrap plate. The receptacle reference designators are marked on the plate, and the harness will be formed and tied so as to prevent incorrect engagement of the harness connectors.

The 28-volt input power, motor driver output power, and signals on coaxial cables are routed directly on separate harnesses without going through the wire wrap interconnect wiring. These signals each have special characteristics (high current, high frequency, and/or EMI source/susceptibility) which can be handled best in this manner.

Cutouts in the plate provide for a clearance hookup of all SMA coaxial connectors. The coaxial connectors extend from the SRU core through the interconnection plate to facilitate making this connection using conventional tools (open-end wrench). All wire wrap conductors are dressed and tied to the plate to prevent cold flow or abrasion shorting over extended periods of time.

After the plate is wired and electrical integrity is verified, the wire wrap pins and exposed conducting surfaces are conformal coated to eliminate shorting in a zero gravity environment by a foreign object. Rework procedures will allow modification to the conformally coated pins if such modification is required during the life of the LRU.

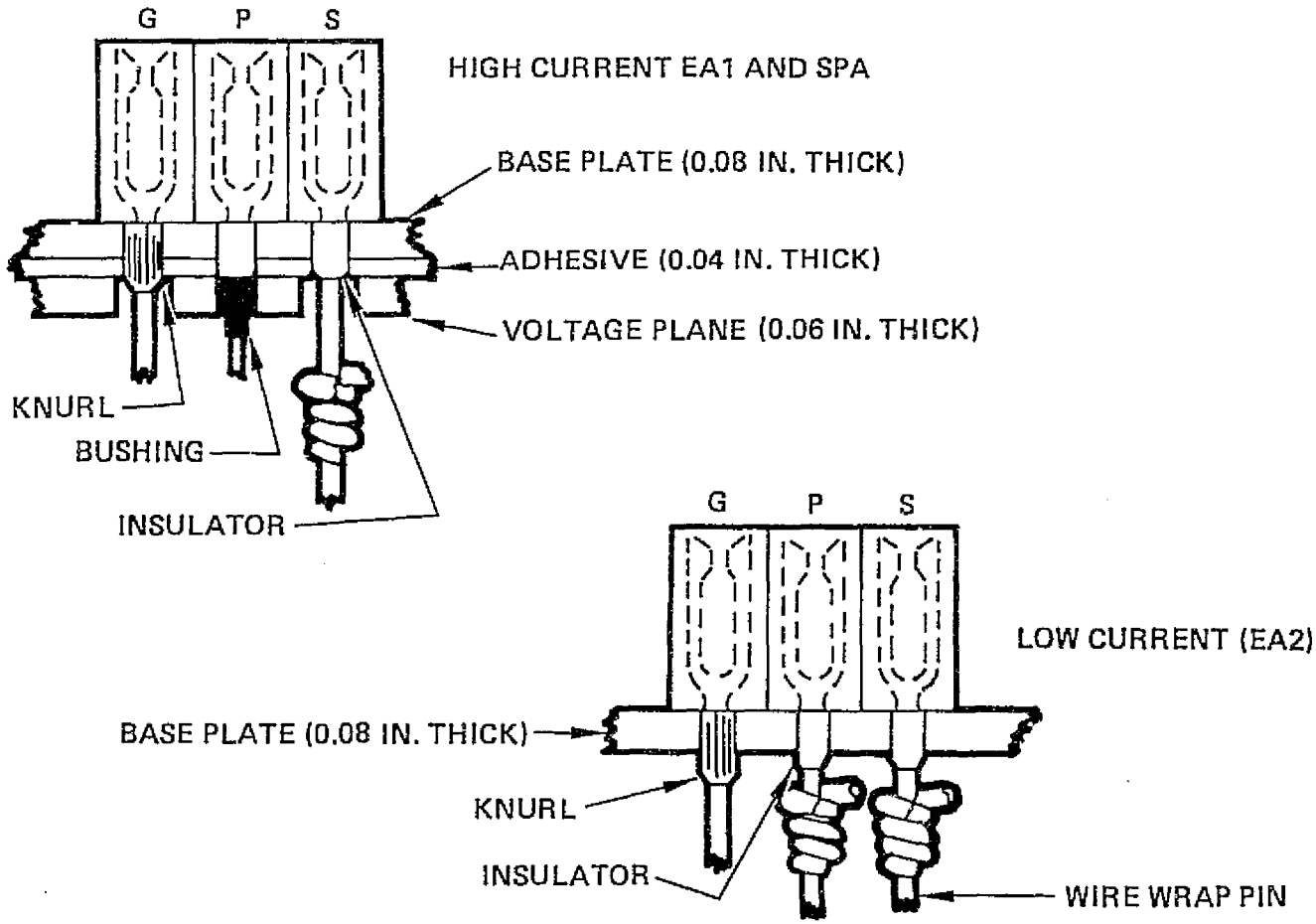

Figure 91. Wire Wrap Plate Connector Details

SRU

The two typical SRUs are shown in Figures 92 and 93. Each SRU consists of an aluminum core with a printed wiring board (PWB) bonded to each side and a connector fastened to one edge. The core is a T-shaped part with two captive mounting screws (commercially identified as Deutsch HJCT-7800-8-B-2.5) and provisions for supporting the SRU connector. The two mounting screws provide force for engagement and disengagement of the SRU connector and for ensuring a good interface for heat transfer. Since the aluminum core is the primary thermal path for cooling the components, core thickness is dictated by the SRU power dissipation.

Each PWB is a 5.3 × 8.4 inch multilayer board (4, 6, or 8 layers) with an overall thickness of approximately 0.60 inches. The boards are made from polymide-glass laminate material, and the exposed wiring lines are solder plated (solder subsequently is fused). The boards are designed for surface mounting of all components, and the plated-through holes (PTH) are not filled.

The SRU connector is fastened to the core with three screws. Tails from the connector blade contacts are preformed to fit against pads on the PWBs, and these contact tails are then reflow soldered onto the PWB pads.

Each SRU connector has two keying pins which establish a go/no-go engagement of the connector contacts. In addition to this mechanical keying system, there is a color stripe painted on the top of each SRU core in a manner such as to make a single diagonal line in the LRU. Also, the SRU reference designator is marked on the SRU core and on the wire wrap interconnection plate.

Electronic components are attached to the PWBs by reflow soldering preformed component leads to the PWB with the polysulfide adhesive-impregnated material. Larger round-bodied components and can-type devices are bonded to the PWB with an alumina-filled polysulfide paste (Hughes Aircraft Company, HP16-103, Type II). After SRU test, the PWBs and components are conformally coated with a polyurethane coating material.

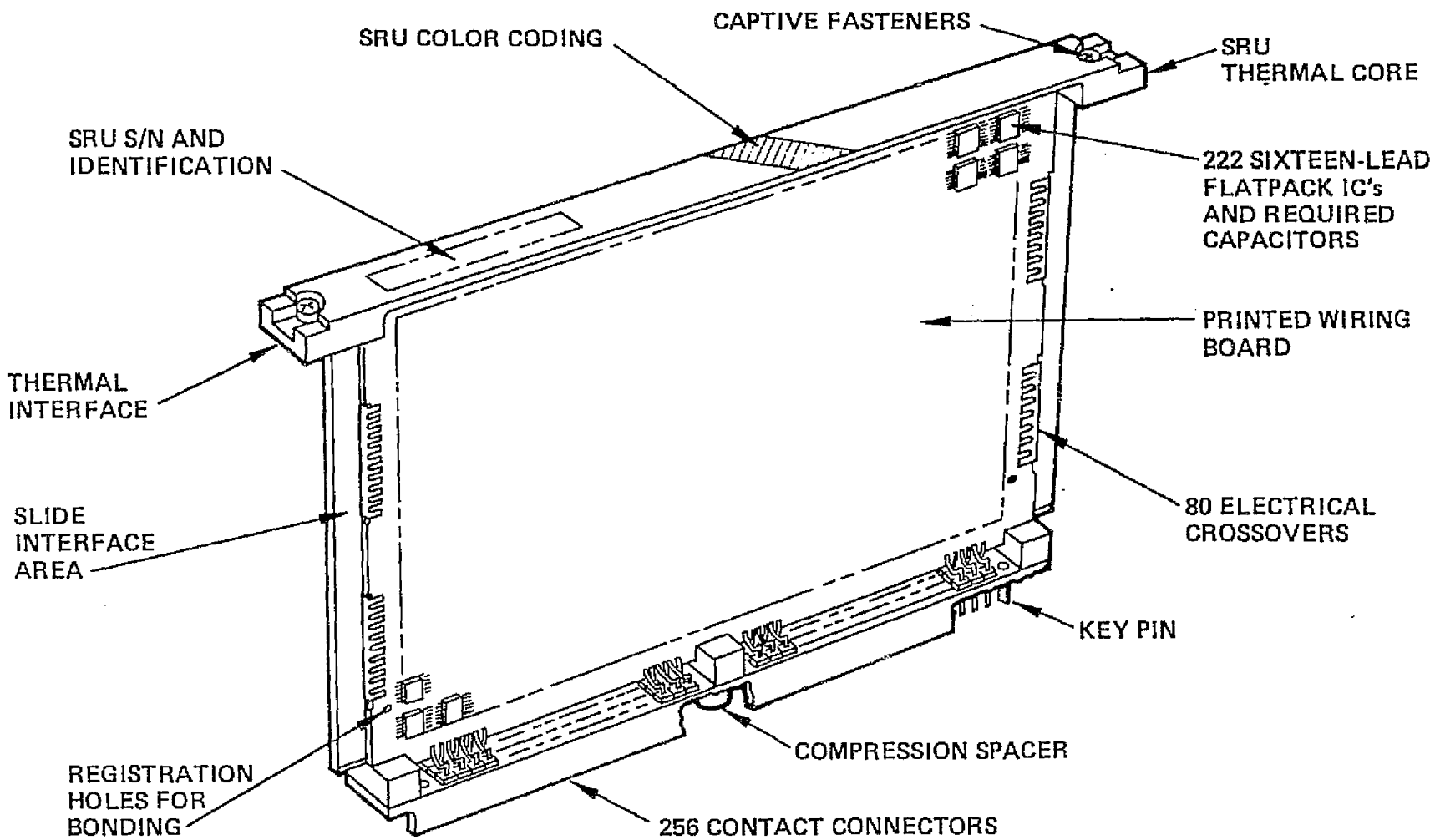

Figure 92. Typical SRU Digital Assembly

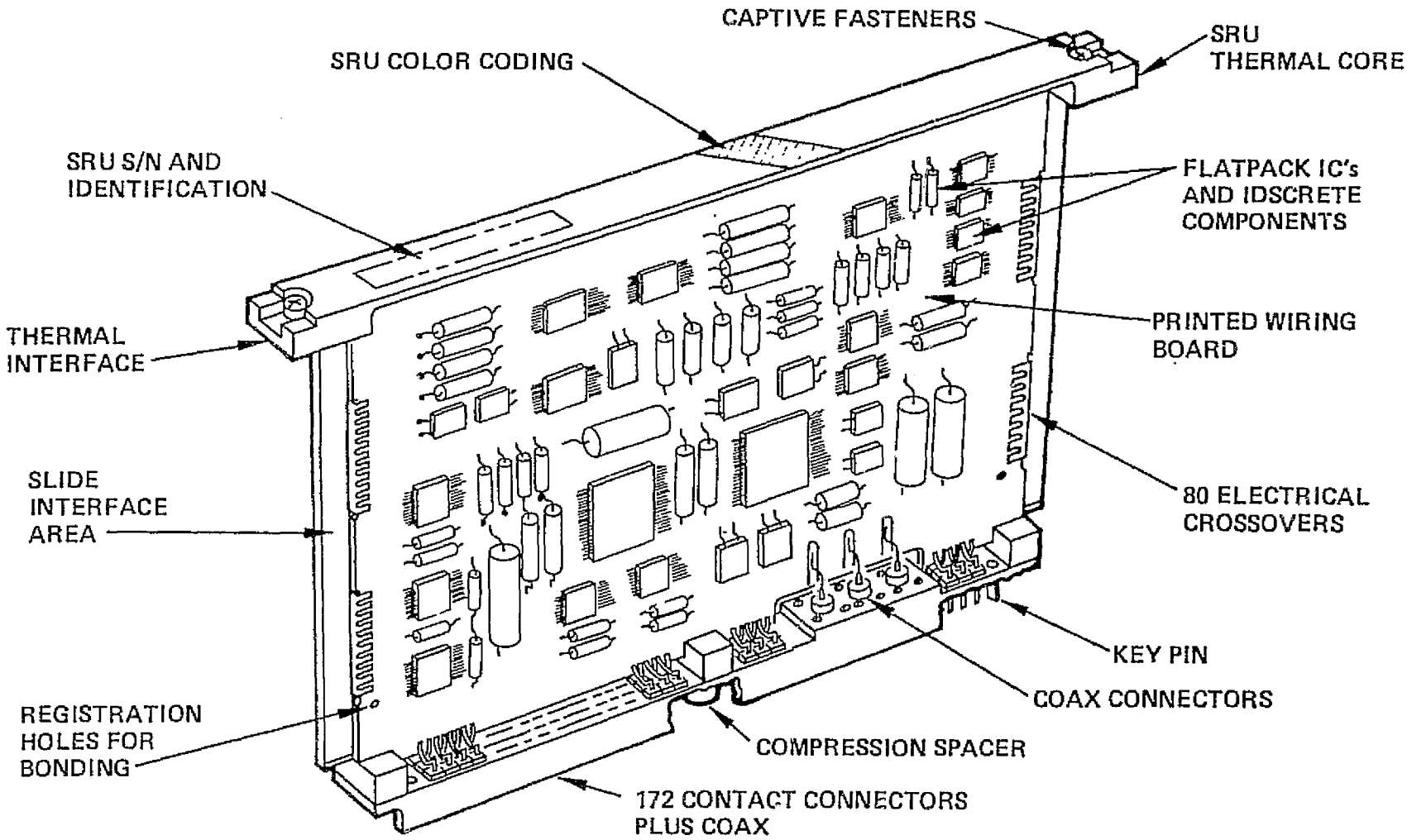

Figure 93. Typical SRU Analog Assembly

Low Voltage Power Supply

The EA-1, EA-2, and SPA low voltage power supplies are basically the same physical design for all three units. The power supply module is approximately 9.7 × 5.8 × 1.95 inches in size and weighs about 3.0 pounds. Other physical design features include (1) machined aluminum chassis for structure support and minimum thermal impedance; (2) single unit connector; and (3) captive fasteners for added maintainability.

An extensive effort was made to achieve commonality within the three modules to both reduce design cost and the number of spare parts required during the field support period. Over 98% of the parts are common to all three designs. The linear regulator/logic printed circuit board is identical in all three designs. The major differences in the three designs are the converter transformer secondary output voltage forms which are designed to meet the requirements of each LRU.

11.0 CUMULATIVE INDEX OF KU-BAND SYSTEM DOCUMENTATION

11.1 Introduction

This section consists of a cumulative index of major HAC documents describing the integrated Space Shuttle Orbiter Ku-band radar/communications system. A list of the documents covered is contained in Section 11.2, and the alphabetical index is contained in Section 11.3.

The intent of the index is to provide a cohesive reference to the various documents describing the system. Information relevant to any one of the subsystems may be contained in several documents; the index should help those who are familiar with the system to access needed information and those who are not to gain an understanding of the functions of the system.

The documents referenced in the index (listed A through L in order to make the index more compact) are defined explicitly in Section 11.2.

It is recommended that the index be expanded and updated as additional documents become available from HAC, as well as from other sources. In addition, it is suggested that block diagrams of the Ku-band system and major subsystems, including EA-1, EA-2, SPA and DA, be generated which include references to the appropriate documents describing the system. That is, each block would contain a list of the appropriate references, as would each interconnect and interface.

11.2 List of Index Documents

Document	Title	Document No.	Date
A	Hughes Preliminary Design Review Vol. 1, Ku-Band Subsystem	HS237-1531-5	3/14-24/78
B	Hughes Preliminary Design Review Vol. II, EA-1	HS237-1531	3/14-24/78
C	Hughes Preliminary Design Review Vol. III, EA-2	HS237-1531-3	3/14-24/78
D	Hughes Preliminary Design Review Vol. IV, DMA/DA	HS237-1531-1	3/14-24/78
E	Hughes Preliminary Design Review Vol. IV-A, SPA	HS237-1531-4	3/14-24/78
F	Hughes Preliminary Design Review Vol. V, DEA	HS237-1531-2	3/14-24/78
G	Hughes Preliminary Design Review Block Diagrams	HS237-890-1	3/14/78
H	Hughes Ku-Band Integrated Communications Radar Equipment	HS237-686A-1	3/16/78
I	Hughes Specifications, EA-1	HS237-710-3	11/1/78
J	Hughes Specifications, EA-2	HS237-712-2	3/2/78
K	Hughes Specifications, SPA	HS237-713-2	3/10/78
L	Hughes Specifications, Radar/ Communications DA	HS237-708-2	3/10/78

11.3 Index

Item	A	B	C	D	E	F	G	H	I	J	K	L
Baseband Data									50			
Beacon								139-140				
Bit Detector, SPA					1.17, 1.21, 9.35-9.40							
Bit Error Rate Degradation	40								50			
Bit Error Rate vs. SNR								106	52		38	
Bit Synchronizer					9.4-9.11							
Bite, DEA						1.7						
EA1									91-96			
EA2										74, 88		
Radar	167-177							147				91
Blanking, Transmit												72
Block Diagram, Ambiguity Res.					1.16							
Antenna				1.10								
Antenna Servo	138											
Bit Detector					9.36							
Bit Sync.					9.5							
Convol. Encoder					1.37-1.38							
Corr. Detector					1.29							
Costas Loop, SPA					1.10							
DA	35											7
DEA												67
EA1	36	1.3	1.13									
EA1 Ref. Gen.		1.7	1.7									
EA2 AGC			1.21									
EA2 Analog Proc.			1.3									
EA2 Angle Proc.			1.31									
EA2 Detec. Proc.			1.25									
EA2 Filter Proc.			1.14, 1.17									
EA2 Post-Detec. Integrator			1.19									
EA2 Preproc.			1.11, 1.12									
EA2 Processing										77-80		
EA2 Range Trackr			1.28									
EA2 Veloc. Proc.			1.29									
Exciter, DEA			1.32									

Item	A	B	C	D	E	F	G	H	I	J	K	L
Block Diagram, (Cd)												
FM Baseband					1.56							
FM Modulator					1.72							
FM Modulator VCO					1.74							
Forward Link	34				(1-5)			99				
Frame Sync					1.26							
Ku System	6						1-9					
LVPS						1.39						
Mgmt & Handover					1.79							
Microwave Assy.						1.23						
QPSK Modulator					1.77							
Rate Sensor, DA				1.28,2.10								
Receiver						1.26						
Return Link	55, 57											
Self-Test	172, 173											
SPA	37				(1-2),(1-5)			100				
SPA I/O Buffer					1.8							
Transmitter						1.12						
Break lock, Radar								158-159				
Buffer, SPA					1.54							

Item	A	B	C	D	E	F	G	H	I	J	K	L
DA Block Diagram	35											7
Description				1.3-1.31								
Performance	114-123											64-102
Data, Communications Interfaces								66-77				
Data Good Flag	47-48							108-109	50			
DEA, Block Diag.						1.2						
Description						1.1-1.46						
Verif. Data						8.1-8.58						
Decommutator, Frame, SPA					1.33							
Delay, RF												65-66, 70,79
Displays/Ctl.	154-165								96-110			
DMA Performance												93-102

Item	A	B	C	D	E	F	G	H	I	J	K	L
EA1, Block Diag.	36	1.3										
Ctl/Stat. Signals									78-87			
Definition		1.1-1.5	1.1-1.2						7			
Drawings		4.1-4.74										
/EA2 Serial Data									87-90			
/MDM Interf.		5.1-5.8.1							13-41			
Performance		1.4-1.5							45-111			
Ref. Gen.		1.6-1.8										
Ref. Gen., Block Diag.		1.7										
Ref. Signals		1.6							110-113			
RF Subunit		1.8-110										
/SPA Serial Data									88			
Status/Display Interf.									96-99			
Sys. Ctl.									86-90			
EA2, AGC			1.21-1.24									
Analog Proc.			1.2-1.5									
Angle Proc.			1.30-1.32									
Block Diag.			1.18							7		
Definition										6		
Detect. Proc.			1.24-1.26									
Drawings			Attachment 1									
Filter Proc.			1.13-1.17									
Interface										6, 8-40		
LOG Converter			1.20-1.21									
Performance	124-128									41-83		
Post-Detect. Integrator			1.17-1.20									
Preprocessor			1.10-1.13									
Proc. Seq.										77-80		
Range Tracker			1.26-1.28									
Status Logic										74,76-77		
Tim'g/Control			1.5-1.9									
Velocity Proc.			1.28-1.30									
EIRP, DA	19											65
EMEC	23-27											
Encoder, DMA				1.26								
Encoder Interface, DMA												61
Environmental Conditions	205, 207											
Exciter, DEA						1.31-1.36						
Exciter Gate												38-40

Item	A	B	C	D	E	F	G	H	I	J	K	L
Gimbal	146,148			1.8-1.25				184				99, 101-102
G/T	19											65
Gyro Interface												61

Item	A	B	C	D	E	F	G	H	I	J	K	L
Life Requirements								184-185				
Link Power Budget, Forward Link	39											
Losses, Impleme-mentation	65-67 115,118											
Losses, RF												66

Item	A	B	C	D	E	F	G	H	I	J	K	L
Mgmt & Handover, SPA					1.78-1.158							
Controller					1.78							
Flow Diagram					1.86-1.101							
I/O Buffer					1.82-1.84							
Logic Proc.					1.148-1.158							
Memory					1.80							
Serial Interface					1.80-1.81							
Software					1.85-1.158							
" Listing					1.102-1.147							
Manchester Code								10	102			
MDM Interface, Electrical								48-53	13-17			
MDM I/O Channel								7-18				
MDM/Ku Serial Data								7-23,25-32, 39-48				
MDM Serial Word Format								15-18	97-109			
Mechanical Interfaces								77-95	7,10-12		7,10-11, 13	10-19
Microwave Assy., DEA						1.22-1.25						
Mode Control Logic, EA1									67-77			
SPA					1.31-1.32							
Modes, Antenna Steering								143-144, 159				64-65
DA Modes												
Fwd Link								104,105			35-37,39	
Radar	115-116							123-132, 140-142				21, 30-32
Return Link	58							110-117			39-50	
Modulation, Forward Link								101				
Return Link	59-64				1.55-1.67			117-119				
Modulator, FM					1.171-1.72, 1.75							
QPSK					1.76-1.77							
Motor Drive Signals												55
Motors, Antenna Gimbal				1.25-1.26								

Item	A	B	C	D	E	F	G	H	I	J	K	L
Noise, Transmit												70, 74-74A
Noise Figure, DEA	21											77-78

Item	A	B	C	D	E	F	G	H	I	J	K	L
Obscuration Zone								180-182	64-65			
Operational Sequence, Radar								147-149				
Orbit								2				
Orbiter Maneuvering Rates								142-143, 180, 183				

Item	A	B	C	D	E	F	G	H	I	J	K	L
Phase Imbalance, DA												65,77
Phase Linearity, Comm. RF												74,77
Phase-Locked Gunn Source						9.34-9.36						
Phase Shift, DEA												85
P/N Code, Acquisition	44							107				
Forward Link	44							101-103	45, 47			
Power, DA Interface												6, 8-10
DEA						6.1-6.2						89-90
Division, Ret. Link	59-61,64											
DMA				6.1								
EA1		6.5-6.7										
EA2			6.4									
EA1 Interface									7-9,35,41			
EA2 Interface										6, 8-9		
Interface								4-6,22,32				
Ku System Monitor	14-17,28-29											74
Radar Ctl.								22, 24				
Radar Sys.	16-17							159-160				
Rate Sensor				2.13								
Rate Sensor Motor				2.9								
SPA					6.2-6.3							
SPA Interface											7-9	
Transmit	21, 52,114							111,123-124, 128-130				21,30-32, 34-35, 69-73
Power Supply, Low Voltage						1.37-1.46						
SPA					1.159-1.164							
Probability of Detection, Comm	44											
" Radar								170,172-173		63-69		
False Alarm, Comm.	44											
Radar								170,172-173				
PROM Bits, SPA					A.1-A.12							
Protocol, MDM Control Word								19-22				

Item	A	B	C	D	E	F	G	H	I	J	K	L
Radar, AGC	128									69, 73		
Amp. Estim.										69, 74-75		
Analog Proc.	124-125											
Angle Accur.	83-84, 109-110											
Angle Error Processing										48, 50-51		
Angle Track Loop Elec.										81-83		
Clutter Perf.										61		
Digital Proc.	126-127											
Equation								133				
Flags and Displays	155-156							155-158				
Margins	87,92											
Measurement Timeliness										41, 48-49		
Mode Req'mts	78,115									63-69,78-80		
Performance	77-134							119-160		41-83		119-160
Proc. Seq.	164									77-80		
Pulse Specs	115-116							125-127				30-32
Range Accur.	82-86,94-96 101-107									41-44		
Range Rate Accuracy	82-84,97-107											
RF Freq.	114											70
Search	79-80							144-177, 162-174				
Short Range						9.32-9.33						
Sidelobe Discrim.								61-63, 79				
Signal	157							123-132				21,30-33
SNR								134-135				
Status Logic										74, 76-77		
Waveforms										48, 52-61		
2nd IF	119-120									29,35,38-39		52-53
Range Status								42				
Range Rate Status								43				

Item	A	B	C	D	E	F	G	H	I	J	K	L
Rate Sensor,												
Axis Defin.				2.14								
Block Diag.				1.28, 2.10								
DA				1.27-1.28, 2.1-2.29								
Environntl				2.17-2.20								
Receive Gate												41-42
Receiver,												
Bandwidth,DEA	117											76
Description						1.6-1.7, 1.25-1.30						
Gain, DEA												76
IF												81-84
Limit'g ,DEA												75
Saturation	119											80
Reference,												
Frequency, DA												36-37
Rejection,												
Signal, DEA												79-80
Return Link,												
Ctl. Word								31-36				
Functions					1.34-1.54							
Performance	54-74							111-119				
RF Signal												34-35
Verif. Data					8.30-8.79							
Rotary Joints				1.12-1.16								94

Item	A	B	C	D	E	F	G	H	I	J	K	L
Scan	42, 72-73							162-174				
Scan Warn Stat.								44				
Search, Radar								162-174				
Servo, Antenna	137-152,123							160-152,180				
Sidelobe Disc.	74											
Signal Interfaces, DA								58-62				22-29,36, 38,42,52, 54-56,61-63
Display/EAI								54-58				
MDM/EAI								48-53,58-60				
Signal Strength	46							109-110	48-50			
Slew Rate, Antenna								28				
SNR, Radar								134-135				
SPA, Baseband - Buffer/Switch					1.54							
Block Diag.					1.3			100	3.7			
Drawings					4.1-4.38							
Functions					1.2							
Performance	49										35-54	
Power/Weight Data					6.1-6.4							
Sig. Descrip. List					5.1-5.11							
Sys. Descrip.					1.2-1.77						7-55	
Stability, RF												70,74
Status Indicators (D & F)								38-48				
Sum/Difference Channel, DEA												80
Synchronization, MDM Ctl Word								11, 14A	103			
SPA, Data					1.17-1.28						37	
Time to Acq.								107				
System Defin.								1				
Descrip.								2				

Item	A	B	C	D	E	F	G	H	I	J	K	L
VCXO, SPA					1.13-1.15							
Verif. Data DEA					8.1-8.58							
Fwd. Link					8.2-8.29							
Ret. Link					8.30-8.79							
Volume, DA Stowage								86-94				
VSWR												93-94, 96,102

Item	A	B	C	D	E	F	G	H	I	J	K	L
Waveguide Switch												90
Weight, System	12-13											
Wiring Interface								62, 77, 78				90

REFERENCES

1. Hughes Aircraft Co. "Ku-Band Preliminary Design Review - Functional Flow and Block Diagrams," HS237-890-1, March 14, 1978.

2. Hughes Aircraft Co. "Ku-Band Integrated Radar and Communication Equipment for the Space Shuttle Orbiter Vehicle," Schematic Review, Vol. I, July 19, 1977.

3. Hughes Aircraft Co. "Ku-Band Integrated Radar and Communication Equipment for the Space Shuttle Orbiter Vehicle," Ref. D7738-SCG 76075V, HS237-202, Conceptual Design Review, January 31, 1977.

4. C. L. Weber. "Maximum Likelihood Estimation of the Ratio of Powers in Two Narrowband Processes," Axiomatix Report No. R7701-3, January 31, 1977.

5. C. L. Weber. "Study to Investigate and Evaluate Means of Optimizing the Radar Function," Axiomatix Report No. R7511-3, Appendix D, November 24, 1975.

6. W. K. Alem, M. K. Simon, and C. L. Weber. "Study to Investigate and Evaluate Means of Optimizing the Ku-Band Combined Radar/Communication Functions for the Space Shuttle," Axiomatix Report No. R7710-5, October 1977.

7. W. K. Alem and C. L. Weber. "Space Shuttle Proximity Operations Sensor Study," Axiomatix Report No. R7802-2, February 1978.

8. Hughes Aircraft Co. "Radar Detection Margins," HS237-506-111, December 1977.

9. Hughes Aircraft Co. "Ku-Band Radar Angle and Angle Rate Measurement Accuracy," HS237-1411, January 1978.

10. Hughes Aircraft Co. "Ku-Band Radar Range and Velocity Accuracies," HS237-1360, December 1977.

11. Hughes Aircraft Co. "Ku-Band Integrated Radar and Communication Equipment for the Space Shuttle Orbiter Vehicle," Preliminary Design Review, Vol. III - Electronic Assembly 2, HS237-1531-3, March 14-24, 1978.

12. NASA Goddard Space Flight Center. "Tracking and Data Relay Satellite System (TDRSS) User's Guide," Rev. 3, Greenbelt, Maryland, January 1978.

13. Hughes Aircraft Co. "Ku-Band Integrated Radar and Communication Equipment for the Space Shuttle Orbiter Vehicle," Preliminary Design Review, Vol. II, Part I - Electronic Assembly 1, HS237-1531, March 14-24, 1978.

14. Hughes Aircraft Co. "Ku-Band Integrated Radar and Communication Equipment for the Space Shuttle Orbiter Vehicle," Preliminary Design Review, Vol. I - Ku-Band Subsystem, HS237-1531-5, March 14-24, 1978.

15. S. Udalov and G. K. Huth. "Integrated Source and Channel Encoded Digital Communication System Design Study," Axiomatix Report No. R7704-1, April 13, 1977.

16. M. K. Simon and W. C. Lindsey. "Tracking Performance of Symbol Synchronizers for Manchester Coded Data," IEEE Transactions on Communications, Vol. COM-25, No. 4, April 1977, pp. 393-408.

17. Hughes Aircraft Co. "Ku-Band Integrated Radar and Communication Equipment for the Space Shuttle Orbiter Vehicle," Preliminary Design Review, Vol. IV-A - Signal Processing Assembly (SPA), HS237-1531-4, March 14-24, 1978.

18. W. K. Alem, G. K. Huth, and M. K. Simon. "Integrated Source and Channel Encoded Digital Communication System Design Study," Axiomatix Report No. R7803-7, March 1978.

19. M. K. Simon and W. K. Alem. "Subcarrier Tracking Analysis for Three-Channel Orbiter Ku-Band Return Link," Axiomatix Report No. R7707-4, July 28, 1977.

20. Hughes Aircraft Co. "Ku-Band Integrated Radar and Communication Equipment for the Space Shuttle Orbiter Vehicle," Preliminary Design Review, Vol. IV, Part D - Signal Processing Assembly (Verification Data), HS237-1531-4, March 14-24, 1978.

21. M. K. Simon. "Error Probability Performance of Unbalanced QPSK Receivers," Axiomatix Report No. R7711-5, November 21, 1977.

22. Hughes Aircraft Co. "Ku-Band Integrated Radar and Communication Equipment for the Space Shuttle Orbiter Vehicle," Preliminary Design Review, Vol. V - Deployed Electronic Assembly (DEA), HS237-1531-2, March 14-24, 1978.

23. W. J. Gill. "A Comparison of Binary Delay-Lock Tracking-Loop Implementations," IEEE Transactions on Aerospace and Electronic Systems, Vol. AES-2, No. 4, July 1966, pp. 415-424.

24. H. P. Hartmann. "Analysis of Dithering Loop for PN Code Tracking," IEEE Transactions on Aerospace and Electronic Systems, Vol. AES-10, No. 1, January 1974, pp. 2-9.

25. M. K. Simon. "Noncoherent Pseudonoise Code Tracking Performance of Spread Spectrum Receivers," IEEE Transactions on Communications, Vol. COM-25, No. 3, March 1977, pp. 327-345.

26. Hughes Aircraft Co. "Ku-Band Integrated Radar and Communication Equipment for the Space Shuttle Orbiter Vehicle," Preliminary Design Review, Supplementary Material, March 14-24, 1978.

27. M. K. Simon and W. C. Lindsey. "Optimum Performance of Suppressed Carrier Receivers with Costas Loop Tracking," IEEE Transactions on Communications, Vol. COM-25, No. 2, February 1977, pp. 215-227.

28. M. K. Simon. "Tracking Performance of Costas Loops with Hard-Limited In-Phase Channel," IEEE Transactions on Communications, Vol. 26, No. 4, April 1978, pp. 420-432.

29. M. Mancrauti, F. Russo, and L. Verrazzani. "An Extension of Richman's Analysis to the Second Order SCE," Proceedings of the IEEE, March 1974, pp. 414-415.

30. D. T. LaFlame. "Costas Lock Detector Analysis," Internal HAC Memorandom, HS237-896, July 15, 1977.

31. D. T. LaFlame. "Updated Costas Lock Detector Analysis," Internal HAC Memorandum, HS237-1130, October 7, 1977.

APPENDIX A

SHUTTLE KU-BAND FORWARD LINK COMMUNICATION RECEIVER PERFORMANCE EVALUATION

APPENDIX A

SHUTTLE KU-BAND FORWARD LINK COMMUNICATION RECEIVER PERFORMANCE EVALUATION

by

Sergei Udalov

1.0 INTRODUCTION

The function of the Shuttle Ku-band forward link receiver is to acquire, track and demodulate the 13,775 MHz communication signal. Because the primary mode for this signal is that of spread spectrum, in addition to the bi-phase-L modulation, the received signal must be despread prior to recovery of the data. Also, the frequency uncertainties caused by oscillator drifts and residual doppler shifts require carrier frequency search and acquisition prior to recovery of the received data. The purpose of the material presented herein is therefore to provide a functional evaluation of the Ku-band receiver and its various subunits in terms of the specifications imposed on this equipment.

2.0 RECEIVER PERFORMANCE

2.1 Input Signal and Noise Levels

The performance of the forward link, of which the Ku-band receiver is one of the major components, depends on the C/N_0 ratio at the receiver input. To determine the range of available C/N_0 values, one must (1) calculate from the link parameters the signal levels at the output of the receiver's antenna and (2) determine the effective system noise temperature based on the RF losses of the front end and the receiver noise figure. Once the absolute values of C and N_0 are determined, the performance of the receiver itself can also be evaluated in terms of signal amplification and dynamic range capabilities. Calculations of the C and N_0 levels are presented in the following paragraphs.

2.1.1 Received Signal Power Level Calculations

The received signal appearing at the output of the antenna is a function of the forward link flux density impinging on the Ku-band antenna of the Orbiter. Multiplied by the effective area of the

antenna, the power density provides the value of the received signal delivered to the output of the antenna.

The level of power density incident on the Shuttle Ku-band receiver antenna is a function of the EIRP delivered by the TDRS, the path loss, and the pointing geometry of both the TDRS and the Shuttle antennas. To provide satisfactory forward link performance, the Shuttle Ku-band communications receiver must accommodate a range of received power levels. The purpose of the calculations presented below is to determine the absolute values of the power density and power levels expected at the Shuttle antenna over a range of operational parameters.

The one-way communication range equation provides the values of the power density and the received signal:

$$P_{rec} = \underbrace{P_t \times G_t}_{\text{EIRP}} \times \underbrace{\frac{1}{4\pi R^2}}_{\text{Path Loss}} \times \underbrace{A_{re}}_{\text{Effective Area of Receiver Antennas}} \qquad (1)$$

$$\underbrace{\qquad\qquad\qquad}_{\text{Power Density}}$$

where P_t = transmitter power (watts)

G_t = transmitter antenna gain (dB)

R = range (in selected units)

A_{re} = effective area of receiver antenna (in selected units^2).

Equation (1) shows that (a) the product of the first two terms is the EIRP of the transmitter (TDRS, in this case) and (b) the product of the first three terms is the power density incident on the receiver antenna.

For simplification of the link budget calculations, (1) is usually written in decibels; thus,

$$P_{rec}\ (\text{dBW}) = \text{EIRP}\ (\text{dBW}) - \underbrace{11\ \text{dB} - 10 \log (R^2)}_{\text{Path Loss}} + 10 \log (A_{re}). \qquad (2)$$

To proceed with the quantitative estimation of the power density and the power levels, we compute the expected values of the path

loss term. For this purpose, the range units used for path loss must be converted to the same units which are used for calculating the effective area of the receiver antenna. Because it is convenient to express the power density in watts/meter^2, we also select the meters^2 as the unit for antenna aperture. Such selection necessitates a conversion of the range units from nautical miles (used for specifying system performance) to meters. Table 1 shows this conversion along with the resulting values of path loss.

Table 1. Path Loss Versus Orbiter-to-TDRS Range

Range (nmi)	Range (meters)	Path-Loss (dB-m^2)	Comment
18,000	3.34×10^7	161.5	Minimum
22,600	4.19×10^7	163.5	Nominal
25,000	4.63×10^7	164.3	Maximum

Note that the path loss in Table 1 is expressed in units of dB-m^2 rather than in dB. The power density can thus be calculated by using the first two terms of (2) and the path loss values given in Table 1.

As an example, let us assume that TDRS EIRP = 48 dBW. Therefore, for the nominal range of 22,600 nmi, the power density is

$$D\ (\mathrm{dBW/m^2}) = 48\ \mathrm{dBW} - 163.5\ \mathrm{dB\text{-}m^2}$$

$$= -115.5\ \mathrm{dBW/m^2}. \qquad (3)$$

As the next step, the power at the output of an antenna of effective area A_e is calculated. For this, we compute A_e based on the measured gain of the Ku-band antenna at the operating frequency/wavelength of the receiver. The expression used is

$$A_e = \frac{\lambda^2 G}{4\pi}, \qquad (4)$$

where G is the measured maximum gain of the antenna and λ is the operating wavelength.

For the Ku-band forward link receiver, the values of G and λ are as follows:

G = 38.5 dB (7,080 value)

λ = 0.0218 meters (2.18 cm, f_c = 13.775 GHz).

Calculating the A_e value, one thus obtains

$$A_e = \frac{(0.022)^2(7080)}{4} = 0.267 \text{ m}^2 \quad (5)$$

or -5.73 dB-m^2.

For the previously used example of D = -115.5 dBW/m^2, one thus obtains the equivalent value of the power level at the output of the antenna:

$$P_{rec}\ (\text{dBW}) = -115.5 \text{ dBW/m}^2 - 5.73 \text{ dB-m}^2$$

$$= -121.2 \text{ dBW} \quad \text{or} \quad -91.2 \text{ dBm}. \quad (6)$$

Figure 1 shows the values of D and P_{rec} as functions of TDRS EIRP and path loss. The values of P_{rec} are for the Shuttle Ku-band communication receiver effective antenna area of 0.267 m^2.

The higher values of EIRP, i.e., 50-55 dBW, are characteristic of a "hot transmitter" (a new tube, start-of-life-cycle operation) at the TDRS. These values are above a typical "minimum range case" of +48.5 dBW minimum output [1]. The EIRP levels below the +48.5 dBW value correspond to conditions existing when the TDRS antenna is not pointed directly at the Shuttle. Therefore, the lower values of EIRP are the "effective" values presented to the Shuttle antenna. These values typically occur during the spatial acquisition phase of the Ku-band Orbiter/TDRS link.

Out of the relatively wide spread of flux density and received power levels shown in Figure 1, the values of -126.9 dBW/m^2* and -113.5 dBW/m^2 are used as the minimum and maximum flux densities with which the Ku-band receiver must meet its specifications [2]. Table 2 shows the conditions resulting in these flux densities and the corresponding differences. As shown, the two differences are

*This value is the Rev. A specification. Rev. B is currently being negotiated; this value will most probably be increased to -123.5 dBW/m^2 and the TDRS minimum EIRP will be 40.0 dBW.

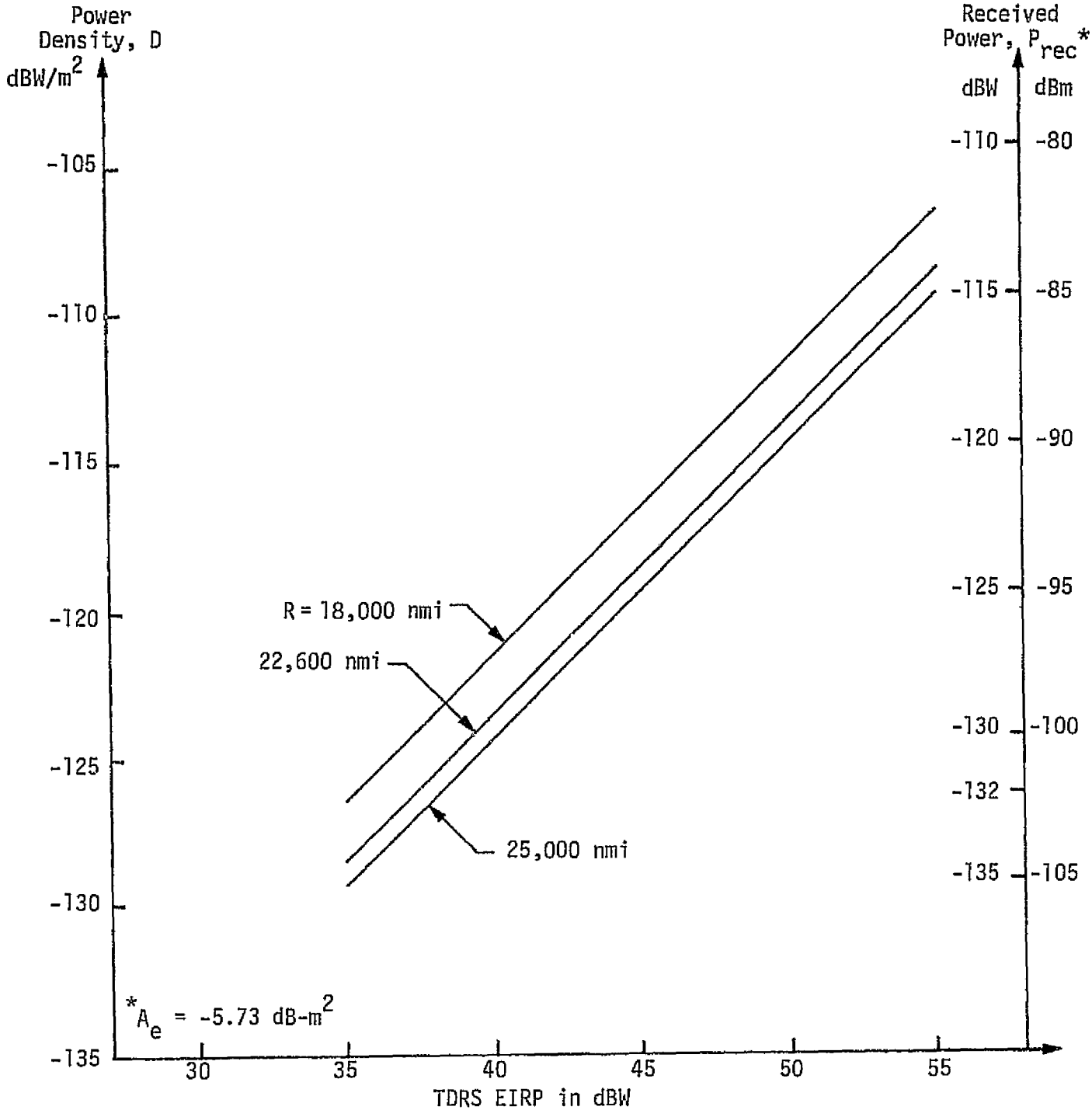

Figure 1. Power Density at Ku-Band Orbiter Antenna and Corresponding Received Power Level Versus TDRS EIRP and Range

11.4 dB due to EIRP and 2 dB due to range difference, resulting in a total variation of 13.4 dB.

Table 2. Minimum and Maximum Flux Densities at Ku-Band Antenna of Space Shuttle

Incident Flux Density (dBW/m^2)	TDRS EIRP (dBW)	Path Loss ($dB\text{-}m^2$)	Range (nmi)
-126.9	36.6	-163.5	22,600 (nominal)
-113.5	48.0	-161.5	18,000 (minimum)
Δ = 13.4 dB	Δ = 11.4 dB	Δ = 2 dB	

The actual signal levels corresponding to the specified minimum and maximum values of flux density are obtained by taking into consideration the effective antenna aperture and other pertinent loss factors existing during the acquisition, tracking and minimum range* operating modes of the Ku-band system. Table 3 shows the respective received power levels and associated conditions. The two extreme values, -105.8 dBm and -89.7 dBm, are used in the subsequent evaluations of the Ku-band link performance in general and the Ku-band receiver in particular. The intermediate value of -103.1 dBm will be used for evaluating tracking capabilities of the receiving equipment.

Table 3. Ku-Band Signal Levels at Acquisition, Tracking and Nominal Link Operation Points

	Acquisition	Tracking	Minimum Range
Incident Flux Density, dBW/m^2	-126.9	-126.9	-113.5
Antenna Area, $dB\text{-}m^2$	-5.7	-5.7	-5.7
Polarization Loss, dB	-0.2	-0.2	-0.2
Pointing Loss, dB	-3.0	-0.3	-0.3
Received Power, dBW	-135.8	-133.1	-119.7
dBm	(-105.8)	(-103.1)	(-89.7)

NOTE: Δ Received Power = -119.7 dBW - (-135.8 dBW) = 16.1 dB (Max - Min)

*The minimum range mode is actually only 2 dB above the nominal specification parameter mode which is based on TDRS EIRP of 48 dBW and the nominal range of 22,600 nmi.

2.1.2 Front-End Noise Density Calculation

The front-end single-sided noise density N_0 is calculated from the equivalent system temperature, which is a function of such parameters as the antenna temperature, the waveguide losses, and the equivalent noise temperature of the receiver itself. The corresponding equation for the system temperature is

$$T_{sys} = T_A + (L-1)T_0 + L T_e \,, \tag{7}$$

where T_A = equivalent antenna temperature
L = waveguide losses
T_0 = waveguide temperature
T_e = receiver temperature.

For the Shuttle Ku-band communications receiver, these parameters are:

T_A = 105°K
L = 2.9 dB (1.95 value)
T_0 = 290°K
T_e = 627°K (i.e., 5 dB noise figure).

Substituting these values into (7), we obtain:

$$\begin{aligned} T_{sys} &= 105 + (1.95-1)\,290 + (1.95)\,627 \\ &= 1600°K \quad \text{or} \quad 32.0\ \text{dB-°K}. \end{aligned} \tag{8}$$

The corresponding value of N_0 for the Ku-band receiver is then

$$\begin{aligned} N_0 &= k\ (\text{Boltzmann's Constant}) + 10 \log T_{sys} \\ &= -228.6\ (\text{dBW/°K-Hz}) + 32.0\ \text{dB-°K} \\ &= -196.6\ \text{dBW/Hz}. \end{aligned} \tag{9}$$

This single-sided noise density is used in the subsequent calculations of the available C/N_0 ratios.

For determining the absolute level of the receiver noise, however, the noise figure of the receiver is used. Thus, at the input to the receiver terminal (i.e., output of the antenna), the noise density is

$$N_r = -228.6\ (\text{dBW/°K-Hz}) + 10 \log\ (290°\text{K}) + \text{NF}$$
$$= -199\ \text{dBW/Hz} \quad \text{or} \quad -99.0\ \text{dBm/MHz}\ . \qquad (10)$$

From this value, the absolute levels of thermal noise at various points within the receiver can be determined by taking into account the amplification (as well as the losses) and the bandwidth. The noise values can then be compared to the corresponding values of the signal (in the same bandwidth) to determine signal-to-noise ratios.

2.1.3 Carrier-to-Noise Density (C/N_0) Ratios

Having determined the noise spectral density N_0 of the Ku-band communications receiving system, we can evaluate the C/N_0 values available for the various modes of system operation using the computed values of the received power given in Table 3. Consequently, for the acquisition, tracking and minimum range modes, we have

Acquisition Mode

$C/N_0 = -135.8\ \text{dBW} - (-196.6\ \text{dBW/Hz}) = 60.8\ \text{dB-Hz}$

Tracking Mode

$C/N_0 = -133.1\ \text{dBW} - (-196.6\ \text{dBW/Hz}) = 63.5\ \text{dB-Hz}$

Minimum Range Mode

$C/N_0 = -119.7\ \text{dBW} - (-196.6\ \text{dBW/Hz}) = 76.9\ \text{dB-Hz}\ .$

The performance of various Ku-band receiver subunits will now be examined within this range of C/N_0 values.

2.2 Signal Level Profile

The Ku-band communications signal developed by the antenna is applied to the input of the receiver where it is filtered, amplified, downconverted, and applied to a number of demodulation and tracking functions. As the signal passes through the various stages of the receiver, its level changes along with the level of the amplified noise. For proper functioning, the active components (i.e., RF preamplifiers, mixers, IF amplifiers, etc.) of the receiver must

operate within their linear ranges to avoid the intermodulation and signal suppression losses. Also, the level of the amplified noise must be kept in the proper relationship to the signal to avoid signal suppression due to noise peaks. It is for this purpose that the absolute signal levels must be traced through the receiver and compared against the signal handling capabilities of various subunits comprising the receiver amplification chain.

The specific receiver configuration considered here is that of the Ku-band Shuttle communications receiver. The basic architecture of this equipment is that of a two-channel monopulse receiver. One channel is used for amplifying the sum (Σ) output of a two-axis monopulse antenna; the second channel amplifies the time-multiplexed ΔAZ and ΔEL signals developed by the monopulse bridge of the antenna. The receiver utilizes double conversion with all of the data demodulation related functions performed at the second IF. The time-multiplexed angle tracking modulation, however, is detected at the first IF to minimize the overall number of receiver components.

Figure 2 shows the functional block diagram of the Shuttle Ku-band forward link receiver configured for the communications mode. The gains and losses of the major subunits and the appropriate signal levels, both maximum and minimum, are indicated. It is important to point out that, as shown in this figure, the dynamic range of the signal levels handled by the receiver is comprised of two components: (1) the change in the input signal strength and (2) the variation in the amplifier gains over the temperature range. As explained in Table 3, the change in signal level contributes about 16 dB of the dynamic range requirement. Furthermore, examination of the Preliminary Design Review data [3] indicates that gain variations of the receiver subunits contribute an additional 10 dB dynamic range requirement over the specified range of the operating conditions. Thus, the total dynamic range requirement imposed on the automatic gain and level control circuitry is about 26 dB.

2.2.1 Sum Channel Signal Flow

Consider first the signal flow through the sum channel of the receiver. The received 13,775 MHz signal power output by the sum

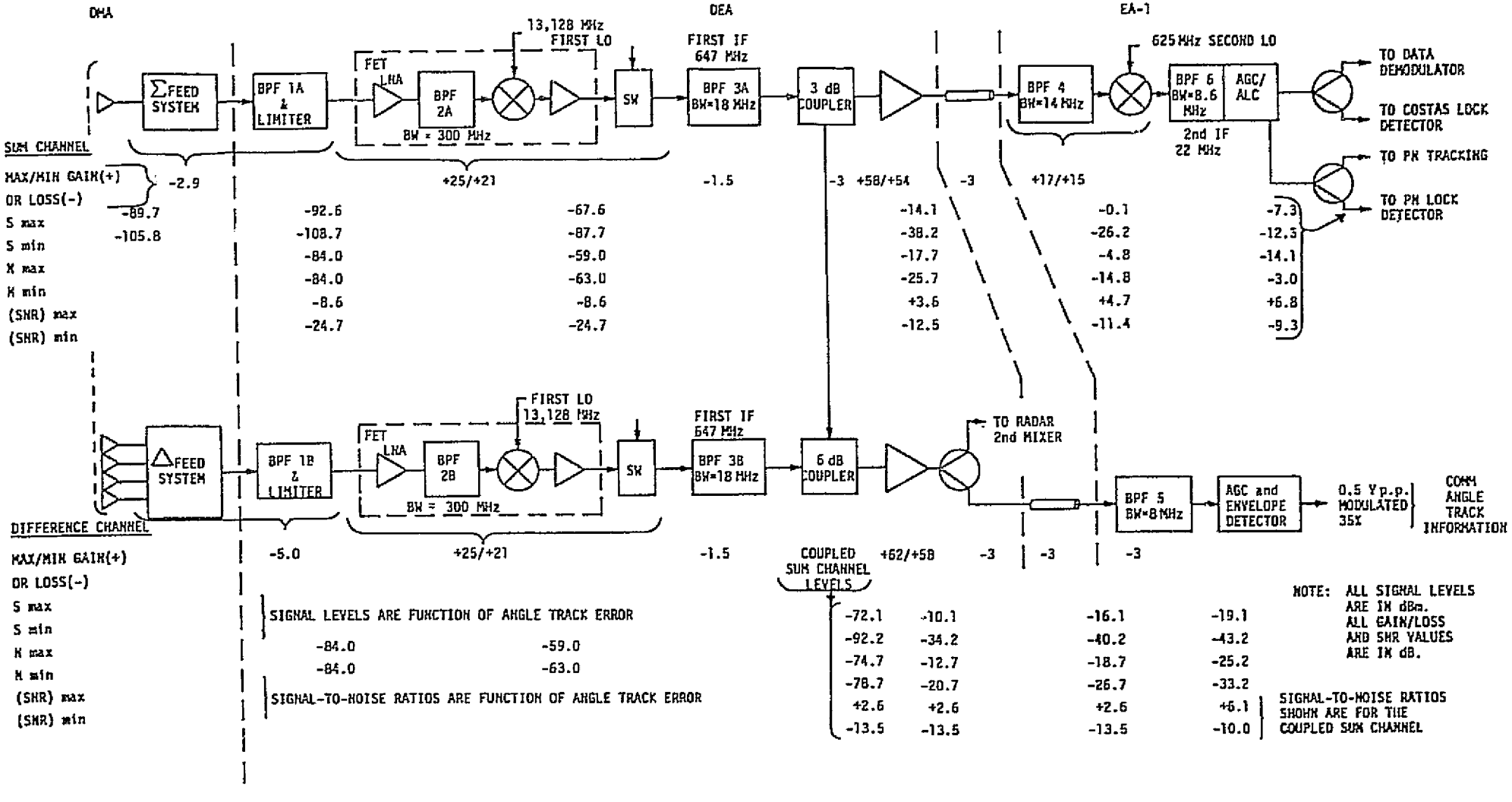

Figure 2. RF Signal Level Profile for the Forward Link Ku-Band Communication Receiver

channel antenna feed, which is a part of the deployed mechanical assembly (DMA), is passed through the rotary joint and applied to a bandpass filter (BFA 1A) and a limiter. The function of the filter is to couple the incoming 13,775 MHz signals into the receiver and to reject the communication transmitter signal. Although the bandwidth of the communication signal is less than 10 MHz, the passband of this first filter is 300 MHz wide to accommodate the frequency-hopped signal of the radar when the receiver is in the radar mode. Also, the amplitude limiter is required primarily for the radar mode, and thus it does not affect the signal amplification in the communications mode.

The combined loss of the antenna feed, the rotary joints and the filter/limiter subunit is about 2.9 dB. Consequently, the signal developed at the output of the sum channel Ku-band antenna is attenuated by this amount prior to reaching the RF low noise amplifier (LNA). Quantitatively, it implies that the maximum and minimum input levels of -89.7 dBm and -92.6 dBm are reduced to -92.6 dBm and -108.7 dBm, respectively.

The low noise RF amplifier (LNA) which follows is a three-stage, gallium-arsenide (GaAs) field effect transistor (FET) unit. The salient parameters of this amplifier unit are:

Noise Figure	5 dB
Gain	22 dB
1 dB Output Compression Point	+5 dBm.

Because the maximum input signal in the communications mode is -92.6 dBm, resulting in an output of about -70 dBm (input signal plus amplifier gain), it is evident that this amplifier does not present a dynamic range limitation to the communications signal. Furthermore, the 13,725 MHz spur (a sixth harmonic of the 2287.5 MHz S-band signal) is estimated at about -60 dBm at the input to this amplifier. This results in a -38 dBm output, which is still significantly below the 1 dB compression point. Thus, sufficient dynamic range is provided for handling the spur as well as the signal.

A bandpass filter (BPF 2A) follows the LNA. The bandwidth of this filter is sufficiently wide to accommodate the radar signal

band (about 250 MHz), yet its rolloff is such as to provide at least 20 dB of rejection of the image frequency band.

After preselection by this bandpass filter, the received signal is applied to a single balanced mixer where it is downconverted to the first IF of 647 MHz. The output of the mixer is applied to a first IF preamplifier which compensates for the signal losses incurred in the prefiltering and downconversion.

The FET LNA, bandpass filter (BPF 2A), mixer, and postconversion preamplifier are contained in a single hermetically sealed subassembly which is physically located close to the input bandpass filter/limiter unit to reduce RF losses. The overall RF-to-IF gain of this subassembly (shown by dotted lines in Figure 2) is 23 ±2 dB over the range of the environmental conditions. The corresponding range of the minimum and maximum communication signal level is from -87.7 dBm to -67.5 dBm, respectively, at the output of this subassembly. Based on a 300 MHz bandwidth, the min/max thermal noise levels at this point are -63 dBm and -59 dBm, respectively. The corresponding signal-to-noise ratios are -24.7 dB and -8.6 dB.

After preamplification at the first IF of 647 MHz, the communication signal is passed through a solid state diode blanking gate and is applied to the first IF bandpass filter (BPF 3A). In the communication mode, the gate does not affect the signal and thus the signal is passed with a minimum amount of attenuation to the filter. The purpose of this filter is twofold: (1) to provide sufficient rejection of the S-band spur and (2) to provide good transient response during the transmit/receive gating in the radar mode. For meeting the second requirement, the configuration of this filter is that of a four-pole Bessel type and the bandwidth (3 dB) is 18 MHz. The insertion loss of this filter is 1.5 dB. As a result of tne reduction of the receiver noise bandwidth from 300 MHz to 18 MHz, the signal-to-noise ratio at the output of the Bessel filter is increased by 12.2 dB.

The output of the Bessel filter is applied to a 3 dB power divider. One output port of this power divider feeds the communication data IF amplifier. The signal emerging at the second output port of the power divider is summed with the IF signal of the difference (Δ) receiver channel. (The reason for this is described in the paragraphs dealing with the difference channel.)

The communications data IF amplifier provides a nominal gain of 56 dB with an estimated variation of ±2 dB. The amplified communication signal, which appears at the output of this amplifier, leaves the deployed electronics assembly (DEA) and is routed via an interconnecting cable to the electronics assembly #1 (EA-1) for further amplification and processing.

As shown in Figure 2, the min/max levels of the amplified received signal at the output of the DEA are about -38 dBm and -14 dBm, respectively. This represents a range of 24 dB, which includes an 8 dB increase over the received signal range of 16 dB. The 8 dB increase is due to the receiver gain variations over the range of the environmental conditions. The min/max levels of the absolute noise at the output of the DEA are -25.7 dBm and -17.7 dBm, respectively. The corresponding signal-to-noise ratios are -12.5 dB and +3.6 dB. These ratios are referenced to the 18 MHz bandwidth of the IF filter located within the DEA, i.e., the four-pole Bessel filter.

From the DEA, the communication signal is fed via a cable to the input of EA-1. The cable loss is presently estimated at about 3 dB which, at a 0.12 dB/foot cable loss constant, corresponds to 25 feet of cable.

At the input of EA-1, the 647 MHz second IF communications data signal is applied to a bandpass filter whose bandwidth is 14 MHz. The passage of the signal and noise through this filter reduces the level of the noise relative to the signal by 1.1 dB. After this filtering, the signal is amplified and applied to a balanced mixer where it is downconverted to the second IF of 21.88 MHz. The net transfer gain from the first IF to EA-1 to the second IF output is 16 dB ±1 dB. Subtraction from this gain of the 3 dB cable loss results in min/max signal levels at the second IF output of about -26 dBm and 0 dBm, respectively. The absolute min/max levels of the thermal noise are -14.8 dBm and -4.8 dBm at this point. The corresponding signal-to-noise ratios in the 14 MHz bandwidth are -11.4 dBm and +4.7 dBm.

The amplification and conditioning of the second IF communications data signal continues within the automatic gain control (AGC)

and the automatic level control (ALC) subunits. The function of the AGC subunit is to compensate for the gain variations of all of the preceding circuits. This maximum variation is estimated at 10 dB.

The AGC circuit consists of a voltage controlled attenuator which is operated by a noise level sensor. The sensor is implemented by sampling the absolute value of the thermal noise within a spectral region which is relatively free of signal power. The first null of the PN spectrum is one such frequency region. Thus, within the AGC circuit, the incoming signal is filtered by a 8.6 MHz wide bandpass filter to remove undesired spectral components and then a 1 MHz wide bandpass filter is used to select the "noise" segment of the filtered spectrum. The bandpass filtered noise is detected and its level compared to a preset reference voltage. The difference voltage is used to operate the AGC attenuator.

Because the AGC attenuator is controlled by the noise, it compensates only for the signal and noise level changes caused by gain variations within the receiver. The function of leveling the output of the receiver in spite of external fluctuations is performed by another circuit, namely, the automatic level control (ALC).

The ALC unit compares the level of signal-plus-noise power to the level of noise power only. The two respective power levels are developed by detecting the outputs of two different bandpass filters. One bandpass filter is tuned to the center of the signal spectrum and the other is tuned to the "signal free" region of the IF BPF. Both filters are 1 MHz wide. The subtraction of the "signal-plus-noise" voltage from the "noise only" voltage develops a control signal which is used to stabilize the signal level at the output of the ALC unit. The minimum range of ALC correction is 16 dB.

The combined signal stabilization capability of the AGC and the ALC circuits is at least 26 dB. Out of this total range, 16 dB is due to signal input level variation and the remaining 10 dB is due to the aforementioned internal gain variation due to environmental effects. The residual level fluctuation is ±2.5 dB.

Following the AGC/ALC unit, the second IF signal is applied to a series of power dividers which distribute this signal to the PN despreader, the PN tracking loop, and the PN lock detector.

The PN despreader consists of two subsections. One is used for removing the PN code from the data. This subsection is followed by the Costas loop. The second PN despreader subsection is followed by the Costas lock detector.

The min/max signal levels at the input to the PN despreader subsections are -9.8 dBm and -4.8 dBm, respectively. The min/max levels of the signal delivered to the PN tracking loop and to the PN lock detector are -12.3 dBm and -7.3 dBm, respectively. The corresponding signal-to-noise ratios, referred to the 8.6 MHz bandpass of the AGC/ALC circuitry, are -9.3 dB and +6.8 dB.

2.2.2 Difference Channel Signal Flow

The difference (Δ) channel signal is developed by the monopulse feed system which is a part of the same high gain Ku-band antenna as is the sum channel feed. In the Shuttle Ku-band receiver, the difference channel is time-multiplexed between the ΔAZ and ΔEL tracking error signals. This reduces the total number of required channels from three to only two. However, the requirement for accurate gain and phase tracking between the sum and the time-multiplexed delta channels still exists. For this reason, all of the delta channel front end components which are located in the DEA are made identical to those of the sum channel, as shown in Figure 2.

Figure 2 also shows that, after conversion to the first IF and bandpass filtering, the sum channel signal is coupled into the difference channel. The ratio of coupling is 4 to 1 of sum to delta. The purpose of this coupling is to provide a reference carrier to the delta channel so that the time-multiplexed ΔAZ and ΔEL signals can be envelope-detected linearly. If such a reference carrier were not present, it would not be possible to determine the polarity of the delta errors and, furthermore, their detection by the envelope method would be highly nonlinear.

Because the ΔAZ and ΔEL signals are small during perfect tracking compared to the sum channel signals, the delta signal levels are not indicated in the block diagram of Figure 2. Instead, the level of the sum signal which is coupled into the delta channel is indicated starting with the 6 dB coupler where the sum signal is injected into the delta channel.

It must be noted that the absolute level of the thermal noise is increased by 1 dB at the output of the 6 dB coupler. This increase is due to the combining of the Σ-channel and the Δ-channel noise components. The combining is as follows:

$$N_{total} = N_{\Sigma} + N_{\Delta} = N_{\Sigma}(1 + \frac{1}{4}) = 1.25\ N_s \quad \text{or} \quad +1\ \text{dB}. \tag{11}$$

The one-fourth factor in the above expression is due to the 6 dB coupling ratio of the two channels.

Following the 6 dB coupler, the combined Δ + Σ signal is amplified by 60 dB ±2 dB and then applied to a 3-dB power divider. One output port of this power divider feeds the signal to the radar second mixer. The second output port feeds the cable which interconnects the DEA with the EA-1 unit. It is this second output port that is used in the communication mode to provide the angle tracking signals.

The combined Δ + Σ signal is applied to the EA-1, where it is bandpass filtered, gain controlled, and envelope detected. As shown in Figure 2, the min/max signal at the input of the EA-1 is -40.2 dBm and -16.1 dBm, respectively. The corresponding noise levels at the input to the EA-1 are -26.7 dBm and -18.7 dBm. Prior to the 8.6 MHz bandpass filtering, the signal-to-noise ratios are +2.6 dB and -13.5 dB. After passing through the 8 MHz filter, the signal-to-noise ratios are increased by 3.5 dB, resulting in a range of SNR between +6.1 dB and -10.0 dB at the input to the envelope detector. The nominal output of the envelope detector is 0.5 volts peak-to-peak across 1 kΩ. The time-multiplexed ΔAZ and ΔEL data appear as amplitude modulations superimposed on this average voltage.

2.3 PSK Data Demodulator

2.3.1 General Description

The PSK data demodulator unit of the Shuttle Ku-band communications receiver performs the following functions:

(1) Initial frequency search and acquisition of the RF carrier.

(2) Tracking of the RF carrier.

(3) Coherent demodulation of the received bi-phase modulated data.

The initial frequency search and signal carrier acquisition must be performed by the demodulator unit regardless of the type of received TDRSS signal, which can be any of the following formats:

(1) CW carrier
(2) Data modulated carrier
(3) Spread spectrum carrier
(4) Spread spectrum plus data modulated carrier.

Figure 3 shows the functional block diagram of the PSK data demodulator, which is comprised of five subunits:

(1) Costas loop demodulator
(2) Costas lock detector
(3) Acquisition and track control logic
(4) Demodulator output circuit
(5) Voltage controlled crystal oscillator (VCXO).

The inputs of these subunits are supplied by the second IF AGC/ALC circuit and by PN code associated circuitry.

The Costas loop demodulator searches and acquires the incoming RF signal. Once the acquisition is completed, the demodulator provides coherent tracking of the phase and frequency of the received signal. It must be noted that the initial Costas loop lockup on the incoming carrier takes place regardless of the PN code synchronization. This is due to the fact that the arm filters of the Costas loop are made wide enough to accommodate the bandwidth of the spread spectrum signal. Thus, the Costas loop handles the PN modulated carrier as a baseband "data" of 3 Mbps and locks up the suppressed carrier of this spread spectrum signal. The data recovery, which is the primary function of the Costas demodulator, must be preceded by PN despreading, however.

The capabilities of the Costas loop to acquire the received RF signal within a relatively short time (about 350 msec) without needing the PN code lock makes the Costas loop the primary sensor unit

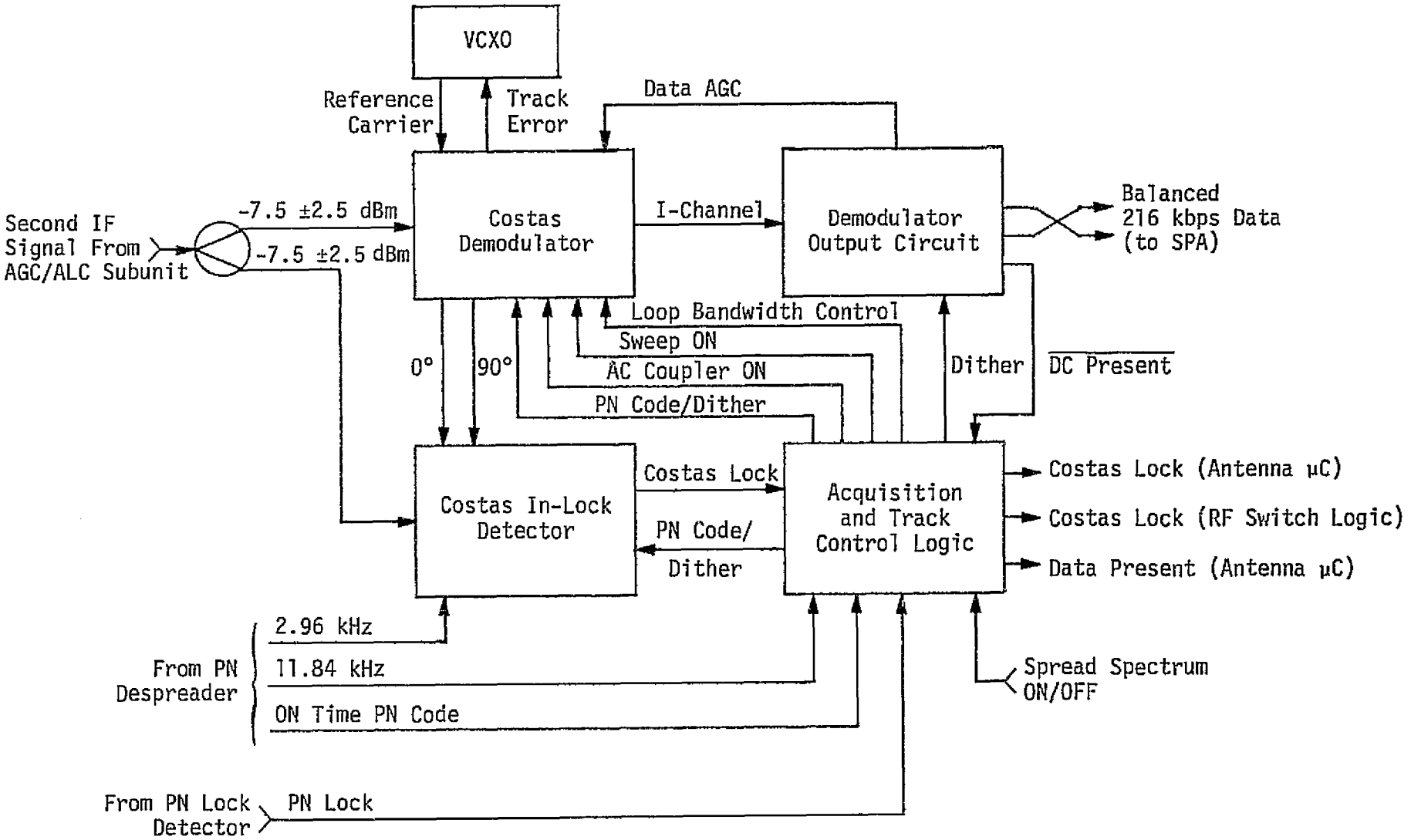

Figure 3. Functional Block Diagram of the PSK Data Demodulator

for the angular acquisition of the TDRS. Specifically, as the Shuttle antenna beam scans past the TDRS, the Costas loop, which is constantly swept in frequency, locks onto the TDRS signal and signals the antenna microcomputer to terminate the antenna scan. The advantage of using the Costas loop for acquisition rather than an energy sensor is that the former uses coherent detection which uniquely identifies the TDRS signal, thus eliminating possible false lockups due to sun or earth intercepts.

The actual sensing of the Costas loop signal acquisition state is performed by the Costas lock detector circuit. This circuit develops the in-phase ("I") and quadrature-phase ("Q") components of the incoming signal and forms an I^2-Q^2 signal. When the Costas loop is in lock, or close to it, the condition $I^2 >> Q^2$ makes the I^2-Q^2 signal exceed a preset threshold. When this happens, the lock detector sends a "Costas lock" signal to the acquisition and track control logic.

As its name implies, the acquisition and track control logic performs the function of switching the Ku-band communications receiver from the acquisition to the track mode. Specifically, upon receipt of the "Costas lock" signal, the logic circuit issues commands to the antenna microcomputer and to the RF switching circuitry to terminate the antenna scan and to initiate the angle tracking. In addition, the logic unit commands the Costas loop to (1) terminate the frequency sweep, (2) switch loop bandwidth from wide (acquisition) to narrow (track), and (3) initiate the DC tracking of the carrier phase error. Also, the logic unit provides a "data good" signal which indicates that the TDRS/Shuttle communications link has been established and that the data received is valid. The "data good" signal is generated when the following three conditions are met:

(1) Costas lock established.

(2) PN lock established (or no PN used)

(3) Incoming bi-phase-L data is properly demodulated (no DC component).

The sensing of the DC component (or absence thereof) is performed in the demodulator output circuit. This circuit accepts the

I-channel raw data from the Costas loop and conditions it for transmission to the signal processing assembly (SPA) for further processing. Furthermore, the demodulator output circuit develops the AGC voltage used by the Costas demodulator for stabilizing the data amplitude. The demodulator output circuit also samples the DC component of the demodulated data to determine the validity of the data format received from the Costas loop demodulator. Because the Ku-band forward link data is always in a bi-phase-L format, no DC component should be present at the output of the demodulator when it operates properly.

The VCXO is the fifth subunit of the PSK data demodulator. The VCXO provides a stable, yet tunable (over a limited range) source of local IF signal reference for generating the I and Q signals required by the Costas loop demodulator. A compromise between the conflicting requirements of stability and tunability is achieved in this particular design by mixing the output of a stable 4.12 MHz voltage-controlled L-C oscillator with the 26 MHz output of a crystal oscillator. The resultant difference of 21.88 MHz is used as the local reference for the Costas loop. The tuning range of this VCXO is ±220 kHz and the residual uncertainty of the nominal VCXO frequency is ±35 kHz. This residual uncertainty is well covered by the acquisition sweep range of ±175 kHz.

2.3.2 Subunit Functional Description

2.3.2.1 Costas Loop Demodulator

Figure 4 shows the functional block diagram of the Costas loop demodulator. The salient features of this demodulator are (1) AC coupling of the signals used for developing the carrier tracking error and (2) hard-limiting of the I-channel signal. These two techniques minimize the DC bias component of the carrier tracking error, thus providing for reliable loop operation over a wide range of input signal-to-noise ratios and environmental conditions.

The input to the demodulator is the 21.88 MHz second IF signal supplied by the ALC circuit. At the demodulator unit, this signal is passed through the balanced mixer U_6 and is then applied, via power divider U_3, to the I-channel and Q-channel mixers U_2 and U_4.

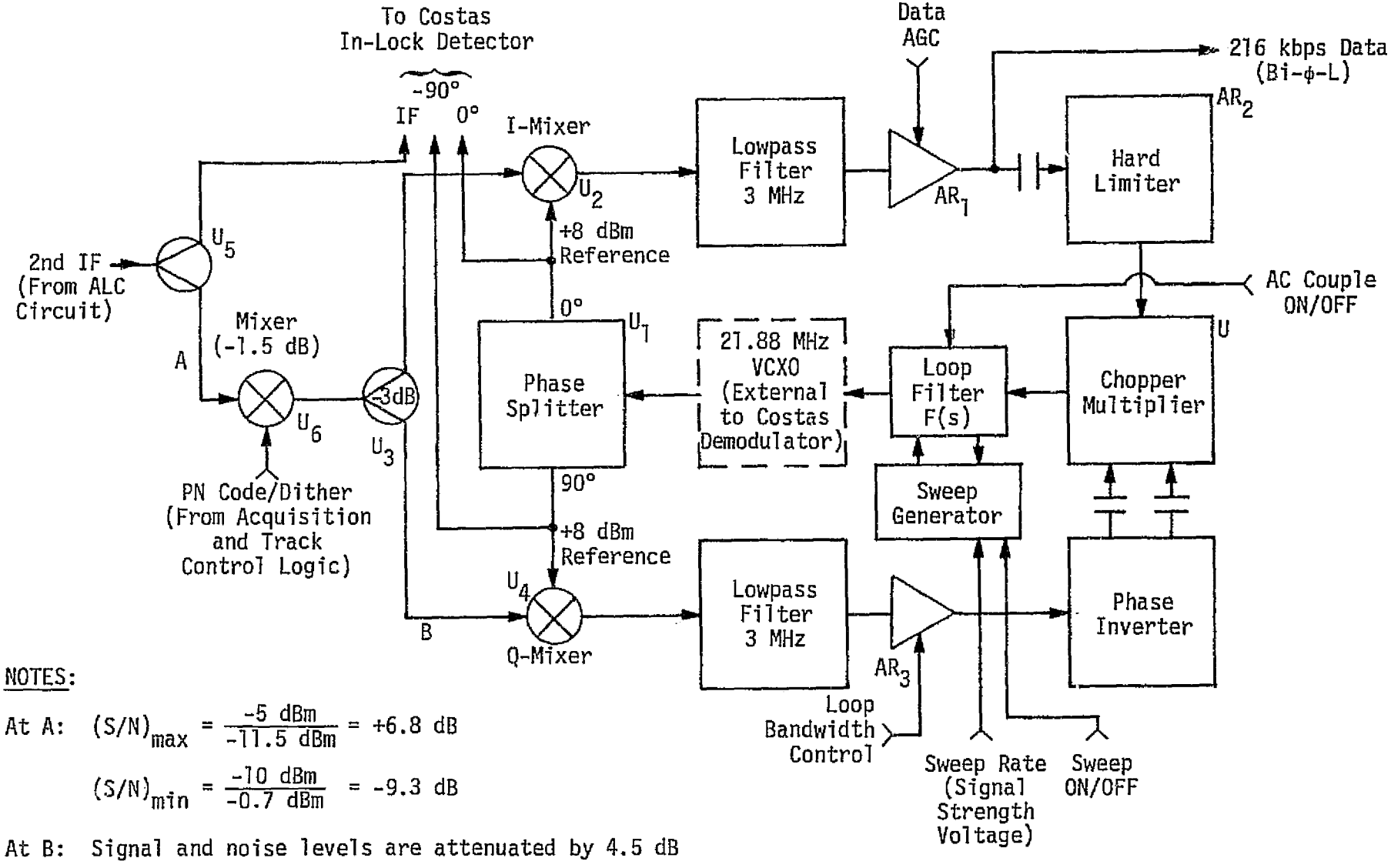

NOTES:

At A: $(S/N)_{max} = \frac{-5 \text{ dBm}}{-11.5 \text{ dBm}} = +6.8 \text{ dB}$

$(S/N)_{min} = \frac{-10 \text{ dBm}}{-0.7 \text{ dBm}} = -9.3 \text{ dB}$

At B: Signal and noise levels are attenuated by 4.5 dB

Figure 4. Costas Loop Demodulator Functional Block Diagram

The primary role of mixer U_6 is to provide PN code despreading for the data after the completion of the acquisition phase. The secondary role of this mixer is to impose the 5.92 kHz dither modulation onto the CW signal, which is one of the signals to be handled by the Costas loop. The presence of the 5.92 kHz modulation eliminates the requirement for DC tracking capability during the reception of the CW signal.

In mixer U_2, the IF signal is mixed with the 0°-phase (in-phase) of the local reference oscillator. Therefore, when the demodulator loop is in lock, i.e., it is tracking coherently the phantom carrier, the output of the I-mixer is a bipolar signal whose amplitude is proportional to the amplitude of the received signal. Depending on the nature of the received signal, the output of U_2 is either an NRZ PN code (3.03 Mbps) or a bi-phase-L data stream (up to 216 kbps) or a 5.92 kHz squarewave. The latter, of course, is the result of biphase modulating the received CW signal (if that is the mode) with a 5.92 kHz "dither" squarewave.

The mixing of the incoming signal with the 90°-phase (Q-phase) local reference is performed in mixer U_4. It is this mixer, therefore, which develops a signal proportional to the carrier tracking phase error. The error signal developed by the Q-mixer, however, changes its polarity according to the polarity reversals of the incoming signal, whether it be a PN code, a data stream, or a squarewave modulated carrier. Consequently, to remove these polarity reversals, the error signal developed by U_4 must be multiplied with the I-mixer output. This multiplication is performed by the chopper multiplier.

Prior to the application of the I and Q signals to the chopper multiplier, both of these signals are passed through the lowpass filters to remove the out-of-band noise and the higher harmonics of the IF signal. The lowpass filters are 2-pole Butterworth designs with a 3 dB cutoff frequency of 3.0 MHz, this frequency being determined by the bandwidth of the PN code.

In addition to lowpass filtering, the I-channel data is passed through a hard-limiter prior to application to the chopper multiplier. It is this limiting which permits the so-called "third multiplier" of the Costas loop to be replaced by the chopper unit. The chopper

implementation is simple and therefore provides fewer problems with DC drift, signal asymmetry and distortion.

It must also be noted that the I and Q signals are AC coupled to the chopper multiplier. Such coupling removes all the DC bias errors developed by the circuitry which precedes the chopper multiplier. Furthermore, during acquisition, the error signal developed by the chopper multiplier is also AC coupled to the control terminal of the VCXO. This removes the residual DC noise components present during the frequency search. Upon acquisition of the signal, the DC coupling is restored by the command from the Costas lock detector circuit.

The loop filter which determines the noise bandwidth of the loop during the acquisition and tracking phases is an active device with a transfer function

$$F(s) = \frac{S\tau_2 + 1}{S\tau_1(S\tau_3 + 1)}, \qquad (12)$$

where $\tau_1 = 0.84$ msec
$\tau_2 = 0.13$ msec
$\tau_3 = 0.33$ μsec .

Because $\tau_3 << \tau_1$ and τ_2, the loop is predominantly second-order, and the function of τ_3 is primarily to remove the high frequency "hash" from the control line to the VCXO.

Together with all other pertinent loop parameters, the time constants τ_1 and τ_2 determine the noise bandwidth B_L (one-sided) of the Costas loop during acquisition and tracking. The respective values of B_L are 10 kHz and 7 kHz. The reduction of the bandwidth is accomplished by lowering the gain of amplifier AR_3 upon command from the Costas lock detector.

The loop filter, being primarily an integrator, is used to generate a sawtooth voltage required for the frequency sweep of the VCXO output during acquisition. The sawtooth voltage is generated by applying a squarewave to the loop filter/integrator. The limits of the sawtooth voltage thus developed are sampled and used to reverse the sweep direction when the sweep control signal reaches its excursion

limits. The quantitative parameters of the frequency search circuit are:

Acquisition sweep range	±175 kHz
Forward sweep time	40 to 180 msec
Retrace sweep time	5 msec .

It is important to note that the forward sweep time is variable over a range of at least 4 to 1. This variability is implemented to reduce the probability of false lock at high values of C/N_0. The forward sweep time is thus controlled by summing the sweep voltage with the signal strength indicator voltage.

In concluding the functional description of the Costas loop demodulator, the consideration of the power levels at the input of the loop is in order. The levels up to and including power divider U_5 have been followed through in the earlier discussion on the signal profiles (see Section 2.2.1). Thus, at point A, the signal and noise levels, as well as their ratios, are as indicated in Figure 4. Note that these ratios correspond to the maximum signal level of -5 dBm and the maximum noise level of -0.7 dBm. Consequently, the noise power is the one that has to be handled properly by mixers U_2 and U_4 without causing their saturation.

The -0.7 dBm noise level, however, is reduced by about 1.5 dB in mixer U_6 and by another 3 dB in power divider U_3. Thus, at inputs to U_2 and U_4, the noise level is about -5.2 dBm. The local reference power level applied to these mixers is +8 dBm, resulting in a differential of 13.2 dB in favor of the local reference. This is consistent with the safe design rule which requires that the level of the LO drive be at least 10 dB above the rms noise level at the mixer IF input port.

Table 4 summarizes the Costas loop design parameters as they were presented by the Ku-band system contractor [3].

2.3.2.2 Costas In-Lock Detector

The functional block diagram of the Costas in-lock detector is shown in Figure 5. The signal applied to the detector is the 21.88 MHz second IF, which appears at the output of the power splitter U_5 shown in Figure 4. Consequently, the signal and noise levels, as

Table 4. Costas Loop Design Parameters [3]

Characteristic	Maximum	Minimum
General Parameters		
Input C/N_0 for acquisition, dB-Hz		59.5
Input C/N_0 for tracking, dB-Hz		59.0
Acquisition sweep range, kHz		±175
Forward sweep time, ms*	185	40
Retrace sweep time, ms	7	3
Maximum input signal level variation, dB	±2.5	
Maximum loop gain variation (including dynamic range), dB	±3.9	
VCXO sensitivity (nominal), kHz/V	205	
DC loop gain (tracking)		1.0×10^9
Quadrature phase error, deg	±2.3	
I/Q arm frequency response (13 dB, MHz)	3.2	2.8
Acquisition Parameters (C/N_0 = 60.8 dB-Hz)		
Phase detector gain, mV/rad	160	71
Loop stress, rad	0.15	0.06
Loop natural frequency, rad/sec	1.56×10^4	1.04×10^4
One-sided loop noise bandwidth, kHz	10	5.5
Loop signal-to-noise ratio, dB	12.7	10.1
Loop damping factor	1.05	0.70
Tracking Parameters (C/N_0 = 63.2 dB-Hz)		
Phase detector gain, mV/rad	70	32
Loop natural frequency, rad/sec	1.04×10^4	7.0×10^3
Loop damping factor	0.70	0.47
Loop noise bandwidth, kHz	7.0	5.5
Loop signal-to-noise ratio, dB	17.5	16.4
Static phase error, deg	9.3	
RMS jitter, deg	5.6	

*Depends on input C/N_0

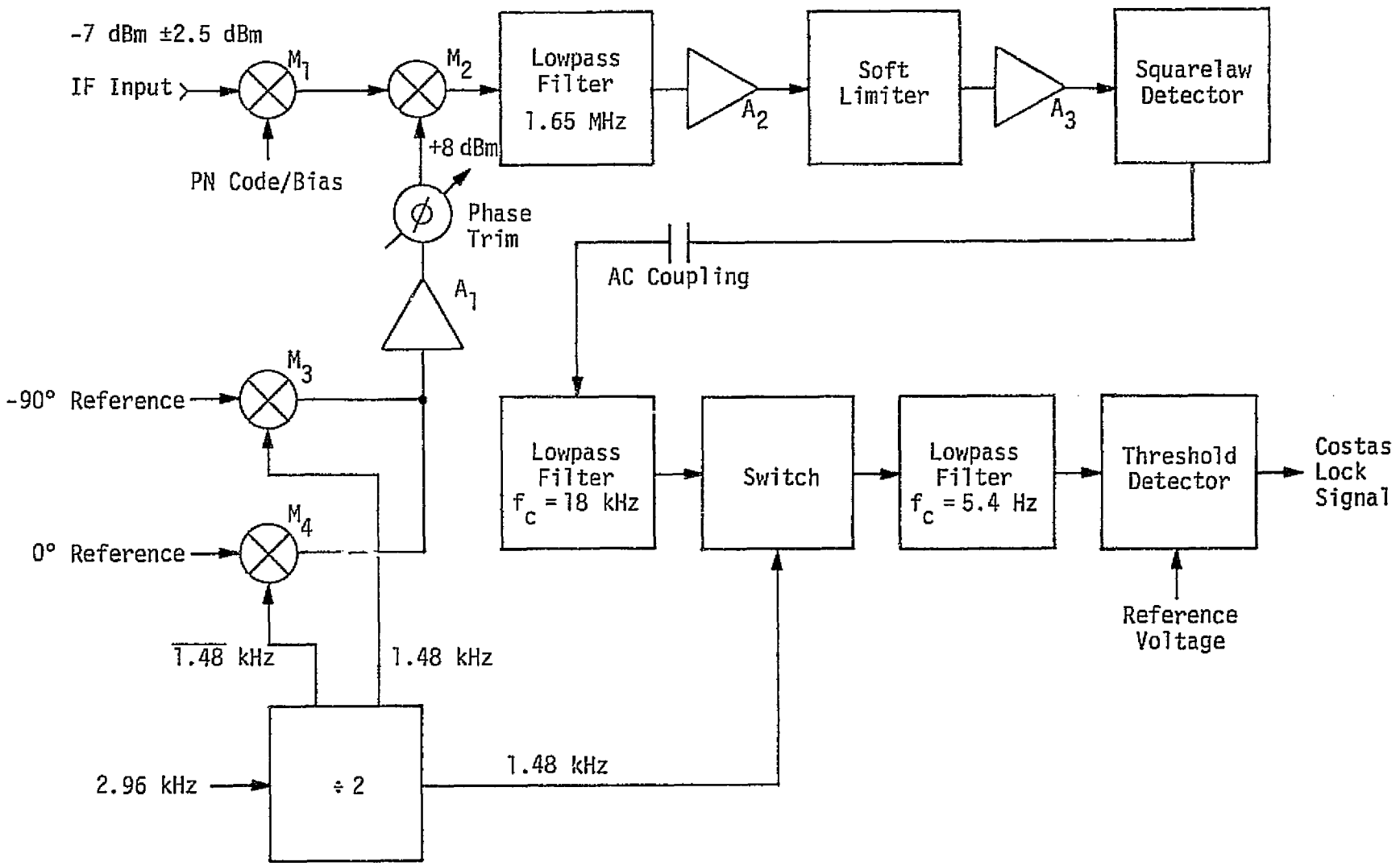

Figure 5. Costas Lock Detector Functional Block Diagram

well as their ratios, are the same as those at point A (see Figure 4) which is the input to the Costas loop demodulator.

Depending on the presence or absence of PN spectrum spreading, the incoming IF signal is either passed through mixer M_1 unaffected* (PN present) or is spread by the locally generated PN (PN absent). The reason for this function is to ensure that the detector circuitry always handles nearly the same signal regardless of the modulation mode of the received signal.

The second mixer M_2 multiplies the IF by the time-multiplexed local reference signal, which alternates between the 0° and -90° phases. Mixers M_3 and M_4, driven by the complementary phases of the 1.48 kHz dither waveform, provide the required time-multiplexed, phase-orthogonal reference signals.

Because the signal and noise levels of the input to mixer M_2 are the same as those of the Costas demodulator and because the reference level supplied to M_2 is +8 dBm, the operation of this mixer is satisfactory over the expected range of input signal variations.

The output of M_2 is lowpass filtered to 1.65 MHz, amplified and applied to a soft-limiter. The function of the soft-limiter is to provide for a better discrimination between the main lobe and sidelobe signals which are applied to the detection decision threshold. Specifically, at low C/N_0 values, the noise dominates the linear aperture of the limiter; thus, the signal is suppressed along with clipping of the noise peaks. At higher C/N_0 values, the maximum amplitude of the signal is relatively steady, and thus the signal "slides under" the limiter boundary without being considerably affected by clipping. The limiter is followed by amplifier A_3.

Because the baseband signal is bipolar from the output of M_2 to the output of amplifier A_3, regardless of the data mode, this signal has to be "rectified" before its average value can be measured to determine the "in-lock" condition. The squarelaw detector provides this rectification. The rectified output of the squarelaw detector is passed through an 18 kHz lowpass filter and is applied to a switch

*It is only attenuated by about 1.5 dB.

driven by the 1.48 kHz dither signal. The function of the switch is to provide the DC restoration to the filtered output of the squarelaw detector and to gate the I^2-Q^2 peaks into the prethreshold lowpass filter whose bandwidth is 5.4 Hz.

The filtered I^2-Q^2 output is fed to the threshold detector, which is actually a voltage comparator IC. The detector compares the magnitude of the I^2-Q^2 signal against a preset threshold and outputs the "Costas lock" signal when the threshold is exceeded. To prevent the output signal "chatter" due to noise, the comparator is provided with a small amount of hysteresis between the setting of its "ON" and "OFF" thresholds.

2.3.2.3 Acquisition and Track Control Logic

The block diagram for the acquisition and track control logic is shown in Figure 6. This logic unit receives, processes, generates and buffers various signals and commands required to control the acquisition and tracking modes associated with the receiving of the Ku-band forward link communications signal. The primary functions of the acquisition and track control logic unit are:

(1) Supplying the local, on-time PN code to the Costas loop PN code/dither mixer.

(2) Providing either the PN code (spread spectrum OFF) or the bias (spread spectrum ON) to the PN code/bias mixer of the Costas lock detector.

(3) Generating the 5.92 kHz signal for the Costas loop dither mixer and for the chopper of the demodulator output circuit.

(4) Controlling of the Costas loop bandwidth and AC coupling.

(5) Determining the "data good" status from the "Costas lock" and $\overline{\text{DC present}}$ signals.

Supplying of the local PN code to the Costas demodulator circuit takes place only after the PN lock signal is received. Before leaving the logic unit, the PN code is multiplied with the 5.92 kHz dither squarewave signal. The multiplication logic (actually modulo-2 addition) is such that, regardless of the presence or absence of the code, the dither modulation is supplied to the Costas loop demodulator. The 5.92 kHz dither waveform is developed in the

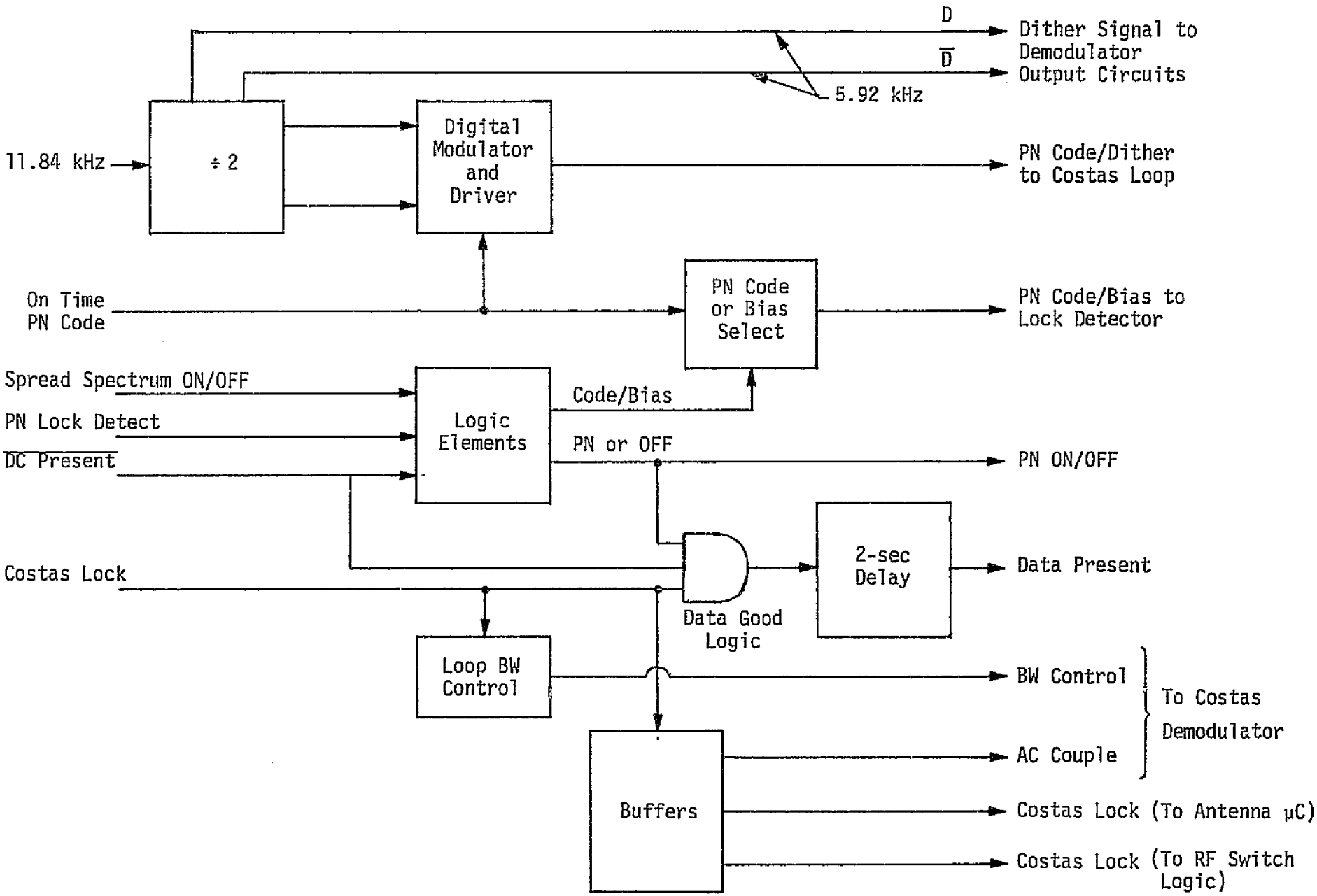

Figure 6. Acquisition and Track Control Logic Functional Block Diagram

logic circuit by dividing by 2 the incoming 11.84 kHz signal supplied by the PN master timing circuit.

The delivery of either the PN code or a bias signal to the balanced mixer located at the input of the Costas lock detector unit (Mixer M1 in Figure 5) is determined by the status of the spread spectrum ON/OFF command input to the logic unit. When the received forward link signal is spread, which is the primary mode for this link, the logic unit is commanded to provide a bias to Mixer M_1. This bias makes the mixer act as an RF gate in the "ON" state and thus the incoming spread spectrum signal is applied to the in-lock detector.

Because the in-lock detector is optimized for the spread spectrum signal, its input must be deliberately spread when the link is operating in the CW or "data only" modes. Application of the locally generated code accomplishes this function.

Table 5 summarizes the signals applied to the mixers preceding the Costas demodulator and the in-lock detector.

Table 5. Costas Loop and In-Lock Detector Mixer Drive Signals [3]

Spread Spectrum	Parameter	Costas Demodulator Mixer		In-Lock Detector Mixer	
		6 kHz*	6 kHz* Plus PN	DC Bias	PN
Off	Costas Acquisition	X			X
	Costas Track	X			X
On	Costas Acquisition	X		X	
	Costas Track	X		X	
	Costas Track and PN Lock		X	X	

*Actual value is 5.92 kHz.

Both the Costas loop bandwidth and the AC coupling control are determined by the Costas lock signal. The bandwidth control causes a narrowing of the Costas loop bandwidth after the initial signal acquisition. The AC coupling control provides for AC coupling of the carrier tracking during acquisition and, upon receipt of the Costas lock, restores DC coupling to the loop.

The "data good" logic provides the "data present" signal to the SPA. This signal is generated if, and only if, the following signals are present:

(1) Costas lock
(2) $\overline{\text{DC Present}}$
(3) PN Lock or PN OFF.

The significance of the first two signals is self-explanatory. The third signal, however, results by OR-ing the two alternate conditions. Thus, if the system is in the spread spectrum mode, "data present" does not appear until the PN lock is established. If the system is in a mode other than spread spectrum, the first and second conditions are the determining factors for declaring the "data present" condition.

2.3.2.4 Demodulator Output Circuit

Figure 7 shows the block diagram for the demodulator output circuit. The primary function of this circuit is to process the I-channel data received from the Costas demodulator and to deliver this data via a balanced, differential line to the SPA.

As shown in Figure 7, the incoming I-channel data is passed through a phase inverter (splitter) followed by a chopper multiplier which removes the dither modulation from the data. The "undithered" data is then passed through an active, 4-pole Butterworth lowpass filter and is supplied to the following three circuits:

(1) Data output driver
(2) AGC detector and amplifier
(3) Data detector.

The data output driver is a differential unit which supplies the balanced data signal to a 71-ohm cable. The outputs of this driver are protected from momentary shorts of the output lines to high voltages.

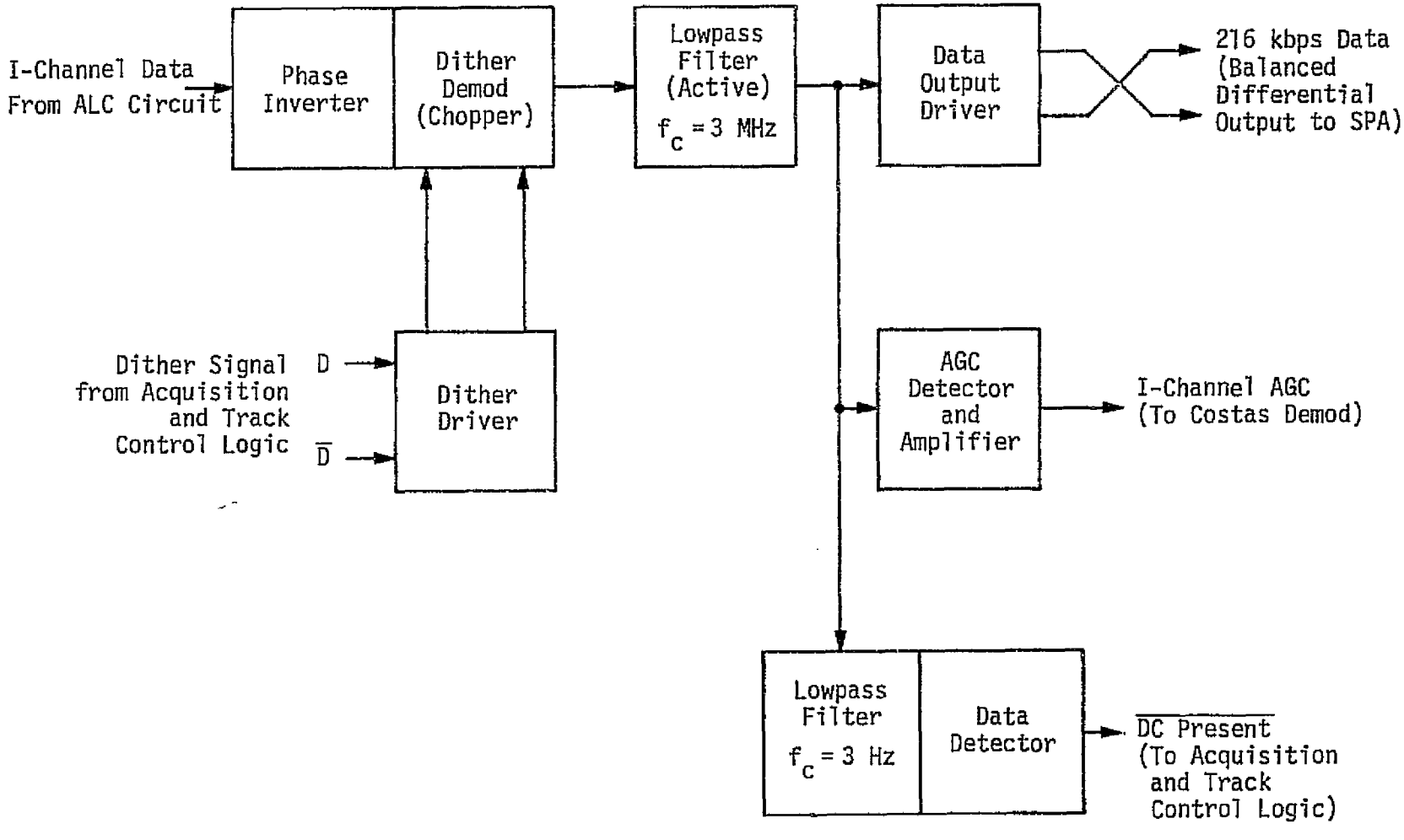

Figure 7. Demodulator Output Circuit Functional Block Diagram

The AGC detector senses the amplitude of the I-channel data signal with a pair of temperature-compensated diodes. The data applied to the amplitude detector is prefiltered by a single-pole filter with a 414 kHz 3 dB bandwidth. After detection, the AGC data is passed through an active integrator circuit whose unity gain is at approximately 10 Hz. The AGC voltage smoothed by the integrator is delivered to the gain control unit of the Costas data demodulator.

The data detector consists of two voltage comparators whose outputs are wired to provide an "OR-ed" signal. The thresholds of the comparators are set in such a manner that any positive or negative voltage exceeding a small margin gives an output indication of the presence of a positive or negative DC component of the 216 kbps bi-phase-L data. The data applied to the comparators is passed through a 3 Hz lowpass filter which provides a high degree of data smoothing.

2.4 PN Code Acquisition and Tracking Circuits

2.4.1 Functional Description

The recovery of the forward link data requires the removal of the 3.03 Mbps PN code from the received signal when the incoming signal is in the spread spectrum mode. The removal of the code, in turn, requires a local replica of a code which is in near-perfect synchronism with the incoming code. Consequently, prior to the recovery of the communications data, the Ku-band receiver must search out the phase of the incoming code and then lock its local code generator to the phase of the incoming code. Once the initial synchronism is established, the local code generator must remain in lock with the received code.

The functions of both code acquisition and tracking are performed by the PN tau-dither acquisition-tracking and PN lock detector circuits, whose functional block diagrams are shown in Figure 8. The PN tau-dither acquisition-tracking circuit is in the upper portion of the figure. Consider first the tracking mode of this circuit. The IF signal is applied to mixer M_{AT}, where it is multiplied with the local reference. This local reference is time-multiplexed between two bi-phase signals, one modulated by the "early" code ($+\tau/2$) and

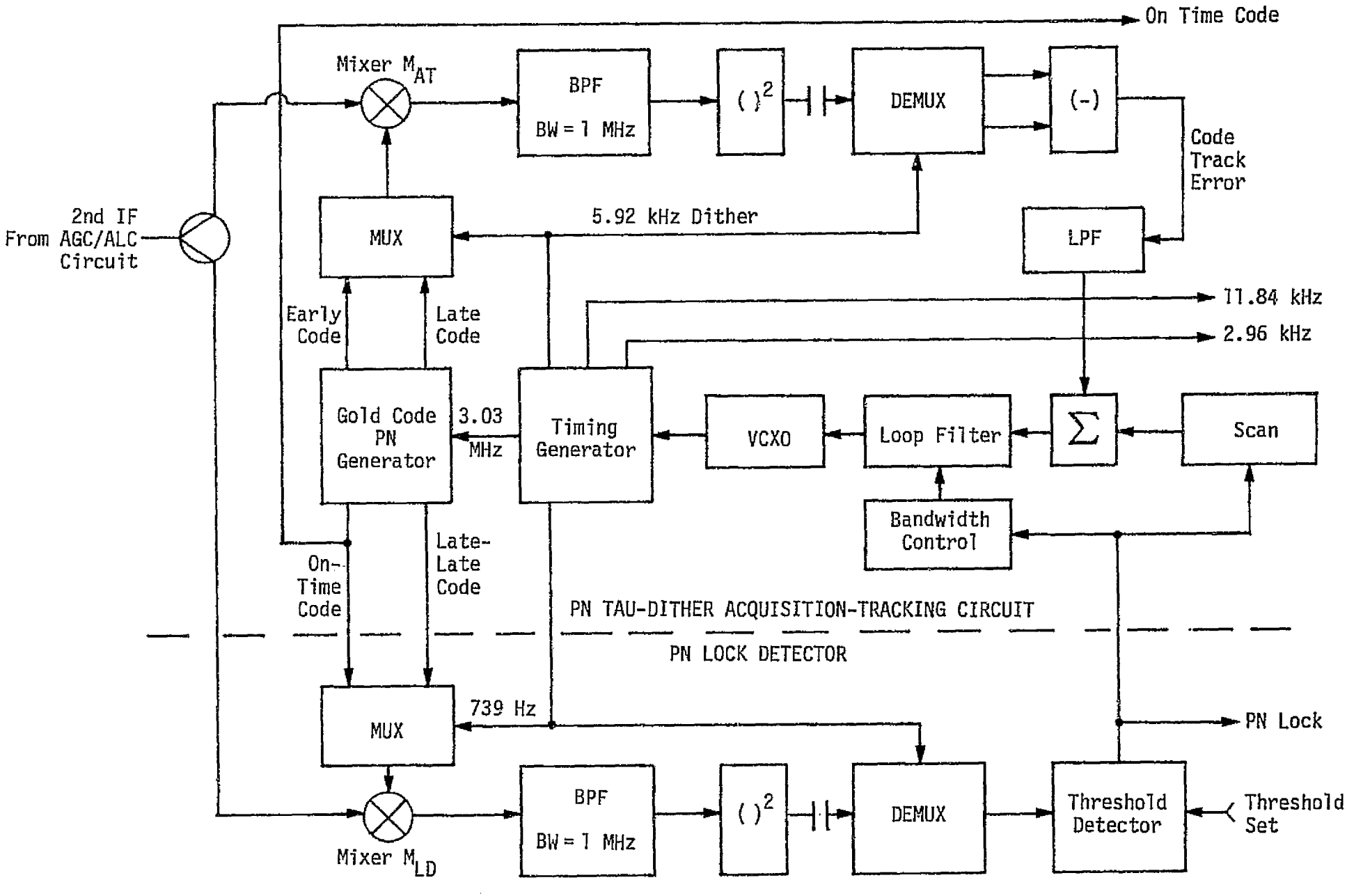

Figure 8. PN Tau-Dither Acquisition-Tracking and PN Lock Detector Functional Block Diagram

the other modulated by the "late" code ($-\tau/2$). The rate of multiplexing, which is generally referred to as the "tau-dither" rate, is equal to 5.92 kHz for this particular system.

The output of M_{AT} is bandpass filtered and applied to a squarelaw detector. The squarelaw-detected signal is then AC coupled to the demultiplexer, where the detected IF outputs corresponding to the $+\tau/2$ and $-\tau/2$ conditions are separated. After separation, these two components are subtracted and the difference filtered and applied via the loop filter to the VCXO.

The VCXO is tunable over a limited range; the code track error developed by the tau-dither circuit is used to keep the VCXO-driven code generator in synchronism with the received code.

For the acquisition phase, the scan circuit develops a voltage which offsets the VCXO frequency from the nominal frequency of the PN code. This offset causes the local and incoming codes to slip past each other until a synchronism is achieved.

Once synchronism is achieved, the tau-dither tracking function takes over and the PN code stays in lock despite the scan signal voltage. This voltage, however, is disconnected once the PN lock detector declares code lock.

As shown in Figure 8, the PN lock detector also uses time-multiplexing for developing the lock signal. The signals used for the time-multiplexed local reference are the "on-time" and the "late-late" codes. The latter is displaced from the on-time code by 1.5 chips. The multiplication of the IF signal with these two local reference signals takes place in mixer M_{LD}. The output of this mixer is bandpass filtered and rectified by a squarelaw detector. The detected signal is AC coupled to the demultiplexer. Both multiplexing and demultiplexing are done at the 739 Hz rate.

During code acquisition, both detected time-multiplexed signals provide the same voltage, namely, that due to thermal-plus-uncorrelated PN code noise. Upon code lock, the on-time signal provides considerable output, which exceeds the threshold of the threshold detector. When this happens, PN lock is declared and the scan voltage is removed from the VCXO control terminal. The bandwidth of the code tracking loop is also narrowed down for the track mode.

It must be noted that the timing generator, which is driven by the VCXO, develops all the required dither signals for both the PN code tracking/lock detection circuit (5.92 kHz and 739 Hz) and the Costas lock demodulator (11.84 kHz and 2.96 kHz).

2.4.2 PN Tracking Performance

In the spread spectrum mode, the code tracking loop supplies the punctual correlation code to the despreader mixer ahead of the Costas demodulator. The noise error within the code tracking loop introduces a certain amount of signal degradation, which ultimately affects the BER performance.

Quantitatively, the effect of the code tracking error is expressed as effective loss L_T [4]:

$$L_T = 10 \log (1 - 1.16 \sigma_T) , \tag{13}$$

where σ_T is the normalized error for the PN loop. This error, in turn, can be computed from the following expression [5]:

$$\sigma_T^2 = \left\{ 0.905 (\rho_i)^{-1} + \left[0.453 - (10 T_d B_i)^{-1} \right] \left(\frac{N}{N-1} \right)^2 (\rho_i)^{-2} \right\} \frac{B_L}{B_i} , \tag{14}$$

where B_i = Two-sided noise bandwidth of the IF arm filters

B_L = One-sided tracking loop bandwidth

T_d = Dither frequency period

N = Number related to early/late code spacing ($N \geq 2$; for $\pm\tau/2$, $N = 2$)

$$\rho_i = \frac{C}{N_0 B_i} .$$

To determine the effect of tracking error on the data performance, we calculate the value of σ_T at C/N_0 = 63.5 dB-Hz, using the following parameters:

B_i = 1 MHz

B_L = 500 Hz

T_d = 0.168 msec (5.92 kHz)

N = 2 (±1/2 chip spacing) .

Substituting the above parameters into (14), we obtain σ_T = 0.019, or 1.9%. Substituting this value into (13), we obtain a degradation of only 0.14 dB. Consequently, one may conclude that the PN tracking loop contributes relatively little degradation to the forward link performance at C/N_0 values at and above 63.5 dB-Hz.

3.0 SUMMARY AND RECOMMENDATIONS

The performance of the Ku-band forward link receiver has been examined from the standpoint of functional interaction between its subunits and also with respect to the flux density variations at the antenna.

It appears that the receiver architecture, including the data demodulation and PN despreading circuits, is consistent with meeting the required performance within the specified range of incident flux densities from -126.9 dBW/m^2 to -113.5 dBW/m^2.

One aspect of the PSK data demodulator design which requires closer examination is that of using the 5.92 kHz "dither" signal in modes other than CW reception. As was shown in Table 5, the 5.92 kHz dither signal (labeled as "6 kHz" in the table) is applied to the mixer preceding the Costas demodulator in all modes of received signals.

For the CW mode, the dither signal is obviously required to provide the sideband which can be utilized by an AC coupled Costas loop for coherent carrier acquisition and tracking. However, for the case when bi-phase-L data is being received, the requirement for a dither waveform is questionable because the spectrum of the data does not contain DC, i.e., the carrier, anyway. Locking up to and tracking of such bi-phase-L data with an AC coupled loop should not present a problem. However, the introduction of an asynchronous dither signal into the received IF signal by bi-phase modulation and subsequent removal of this signal from the baseband data by a chopper may result in "glitches" which, in turn, may degrade BER performance.

Consequently, it is recommended that the function of the dither signal during reception of bi-phase-L data be reexamined and, if found not justified, the use of dither in the data-receive mode be discontinued.

REFERENCES

1. "Tracking and Data Relay Satellite System (TDRSS) User's Guide," Rev. 3, Goddard Space Flight Center, Greenbelt, Maryland, January 1978.

2. Procurement Specification MC409-0025, "Ku-Band Integrated Radar and Communications Equipment," Vol. II, Space Division, Rockwell International, March 15, 1976.

3. Hughes Aircraft Company. "Ku-Band Integrated Radar and Communication Equipment for the Space Shuttle Orbiter Vehicle," Preliminary Design Review, Vol. II, Part I - Electronic Assembly 1, March 1978.

4. W. J. Gill. "A Comparison of Binary Delay-Lock Tracking-Loop Implementations," IEEE Transactions on Aerospace and Electronic Systems, Vol. AES-2, No. 4, July 1966, pp. 415-424.

5. H. P. Hartmann. "Analysis of a Dithering Loop for PN Code Tracking," IEEE Transactions on Aerospace and Electronic Systems, Vol. AES-10, No. 1, January 1974, pp. 2,9,

APPENDIX B

EFFECT OF POWER RATIO FLUCTUATIONS IN MODE 1 ON THE RETURN LINK SUBCARRIER TRACKING

APPENDIX B

EFFECT OF POWER RATIO FLUCTUATIONS IN MODE 1 ON THE RETURN LINK SUBCARRIER TRACKING

by

Marvin K. Simon

1.0 INTRODUCTION

This appendix presents the analysis of the effect of power ratio fluctuations in Mode 1 on the return link subcarrier tracking of TDRS. Three channels exist in Mode 1, with a nominal power distribution of 80% for the highest rate channel (Channel 3). The remaining 20% is split, with 80% going to the next highest rate channel (Channel 2) and 20% to the lowest rate channel (Channel 1); equivalently, $P_1/P_T = 0.04$, $P_2/P_T = 0.16$, and $P_3/P_T = 0.80$, where P_i is the power in the ith channel and P_T is the total power. The two higher rate channels (Channels 2 and 3) represent independent data channels, with Channel 3 being NRZ data with data rate R_3 up to 50 Mbps while Channel 2 has a rate R_2 that does not exceed 2 Mbps but can be either NRZ or bi-phase-L data. Channel 1 consists of bi-phase-L operational data at a rate R_1 of 192 kbps. Due to hardware components uncertainty, actual power ratios will differ from nominal values. Two extreme expected cases are: (1) $P_1/P_T = 0.04$, $P_2/P_T = 0.14$, $P_3/P_T = 0.82$; and (2) $P_1/P_T = 0.03$, $P_2/P_T = 0.19$, $P_3/P_T = 0.78$. The effect of this power ratio fluctuation on the tracking jitter of the subcarrier loop and the resulting error probability performance in demodulating the data are investigated.

2.0 THREE-CHANNEL MODULATIONS

The structure of the modulator in Mode 1 forms an unbalanced quadriphase signal wherein the high data rate signal $\sqrt{P_3}m_3(t)$ is biphase modulated on the in-phase carrier $\sqrt{2}\sin\omega_0 t$, and the sum of the two lower rate signals $\sqrt{P_2}m_2(t)$ and $\sqrt{P_1}m_1(t)$ (after being demodulated onto squarewave subcarriers $\mathrm{Sin}\,\omega_{sc}t$ and $\mathrm{Cos}\,\omega_{sc}t$, respectively) is biphase modulated onto the quadrature carrier $\sqrt{2}\cos\omega_0 t$. The resulting signal, now a multilevel signal $s(t)$, is then bandpass hardlimited and power amplified, as shown in Figure 1.

The modulation procedure is carried out at the SPA unit of the Ku-band communication/radar system with a carrier frequency $f_0 = 1.876$ GHz generated in EA-1 and a squarewave subcarrier first harmonic frequency of 8.5 MHz generated by a squarewave oscillator in the SPA unit.

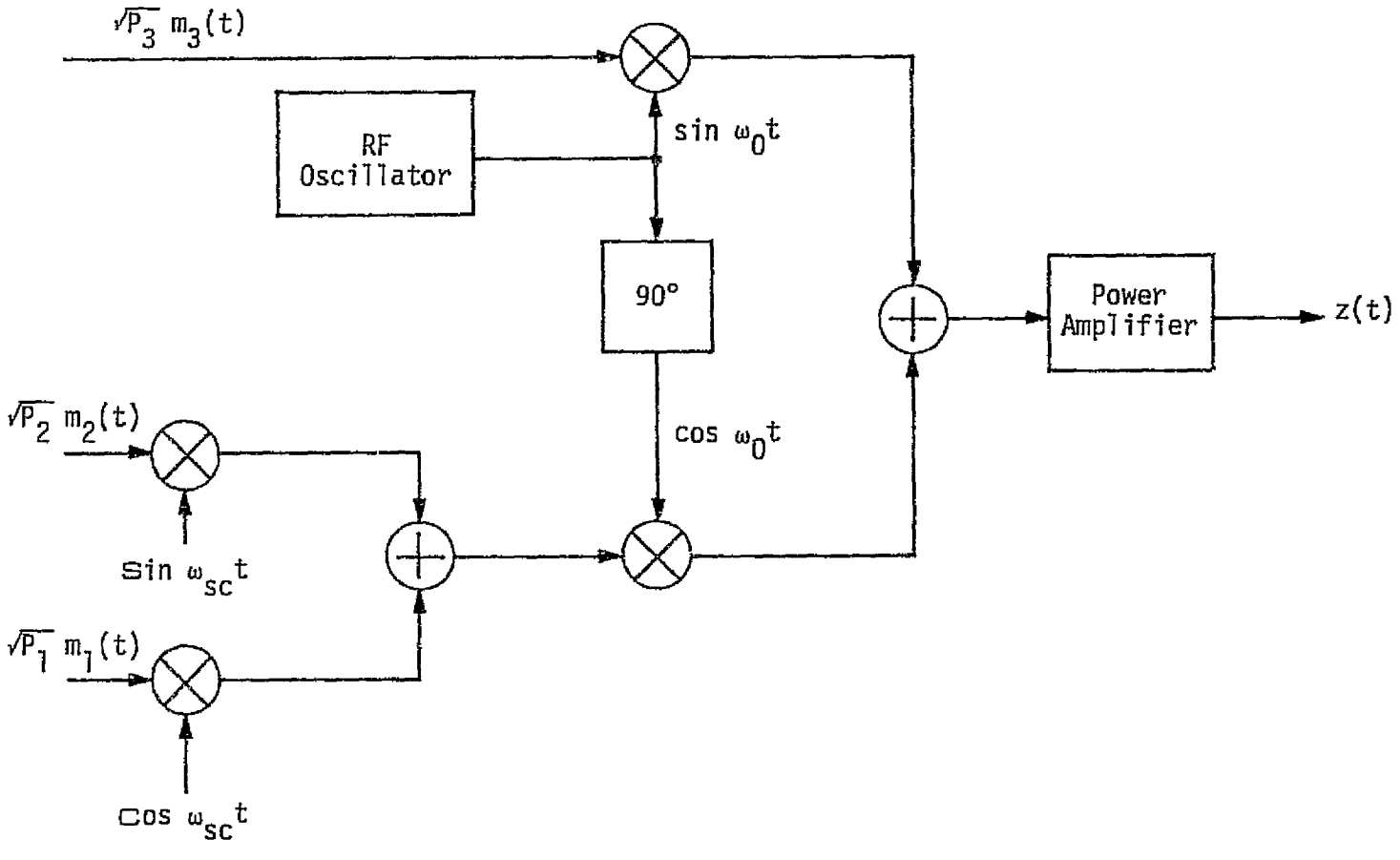

Figure 1. Three-Channel Quadrature Multiplex Modulator

The signal generated by the modulator is

$$s(t) = \sqrt{2}\,[C(t)\cos\omega_0 t + S(t)\sin\omega_0 t]\,,$$

where
$$C(t) = \sqrt{P_2}\,m_2(t)\sin\omega_{sc}t + \sqrt{P_1}\,m_1(t)\cos\omega_{sc}t$$

$$\triangleq \sqrt{P_2}\,s_2(t) + \sqrt{P_1}\,s_1(t) \qquad (1)$$

$$S(t) = \sqrt{P_3}\,m_3(t) \triangleq \sqrt{P_3}\,s_3(t)\,. \qquad (2)$$

It was shown in [1] that, due to the hardlimiting effect on the signal, the power distribution at the output of the amplifier is different from that at the input. Assuming equal output and input powers, the output signal can be written as [1]:

$$z(t) = \sqrt{2P_T}\left\{\left[C_1\sqrt{P_2/P_T} - C_2\sqrt{P_1/P_T}\right]s_2(t) + \left[C_1\sqrt{P_1/P_T} - C_2\sqrt{P_2/P_T}\right]s_1(t)\right\}\cos\omega_0 t$$
$$+ \sqrt{2P_T}\left\{C_1\sqrt{P_3/P_T}\,s_3(t) - C_2\sqrt{P_3/P_T}\,s_1(t)\,s_2(t)\,s_3(t)\right\}\sin\omega_0 t \qquad (3)$$

$$z(t) = \sqrt{2}\left\{\sqrt{\tilde{P}_3}\,s_3(t) - \sqrt{\tilde{P}_d}\,s_1(t)\,s_2(t)\,s_3(t)\right\}\sin\omega_0 t$$
$$+ \sqrt{2}\left\{\sqrt{\tilde{P}_2}\,s_2(t) + \sqrt{\tilde{P}_1}\,s_1(t)\right\}\cos\omega_0 t\,, \qquad (4)$$

where the new signal powers are

$$\tilde{P}_3 = P_3 C_1^2$$

$$\tilde{P}_2 = \left[C_1\sqrt{P_2} - C_2\sqrt{P_1}\right]^2$$

$$\tilde{P}_3 = \left[C_1\sqrt{P_1} - C_2\sqrt{P_2}\right]^2$$

$$\tilde{P}_d = P_3 C_2^2\,. \qquad (5)$$

$\tilde{P}_d$ represents the power in the cross-talk signal $s_1(t)\,s_2(t)\,s_3(t)$. In the nominal case, for example, $P_3/P_T = 0.8$, $P_2/P_T = 0.16$, and $P_1/P_T = 0.04$, which yields $\tilde{P}_3/P_T = 0.8157$, $\tilde{P}_2/P_T = 0.1503$, $\tilde{P}_1/P_T = 0.0287$, and $\tilde{P}_d/P_T = 0.00529$. If the power distribution due to hardware considerations become (as in Case 2) $P_3/P_1 = 0.78$, $P_2/P_T = 0.19$, $P_3/P_T = 0.03$, then the

output power distribution is $\tilde{P}_3/P_T = 0.7936$, $\tilde{P}_2/P_T = 0.1818$, $\tilde{P}_1/P_T = 0.0200$, and $\tilde{P}_d/P_T = 0.0046$.

The resulting signal is upconverted to a Ku-band frequency of 15.003 GHz and transmitted to the TDRS.

3.0 THREE-CHANNEL DEMODULATION

The demodulation is carried out in two steps: (1) recovering the carrier by a Costas loop, and then (2) using the quadrature arm signal as an input to a subcarrier Costas tracking loop to recover the subcarrier and allow for the demodulation of the two lower data rates $m_2(t)$ and $m_1(t)$.

Figures 2 and 3 illustrate the carrier Costas loop and the subcarrier Costas loop, respectively. The bandpass filter in Figure 3, if included to recover the first harmonic of the subcarrier, results in a loss of $(8/\pi^2)^2$ in signal power. Detailed discussion of the implementation considerations is presented in [2].

Since the subcarrier recovery is more sensitive to power ratio changes, its performance in terms of the rms phase jitter is treated next. The effect of the power ratio variations on the carrier loop is considered in [1].

To avoid repetition, the results of [3] are quoted here and applied to find the numerical evaluation of the rms phase jitter in the subcarrier loop. The rms phase jitter on the subcarrier output data streams is given by

$$\sigma^2_{\varphi_{sc}} = \frac{1}{\rho S_L}, \tag{6}$$

where, as derived in [3], ρ is the loop signal-to-noise ratio of a phase-locked (CW) loop operating on the total power $P_T \triangleq \tilde{P}_1 + \tilde{P}_2 + \tilde{P}_3 + \tilde{P}_d$ or

$$\rho = \frac{P_T}{N_0 B_L}, \tag{7}$$

with B_L denoting the equivalent single-sided loop noise bandwidth.

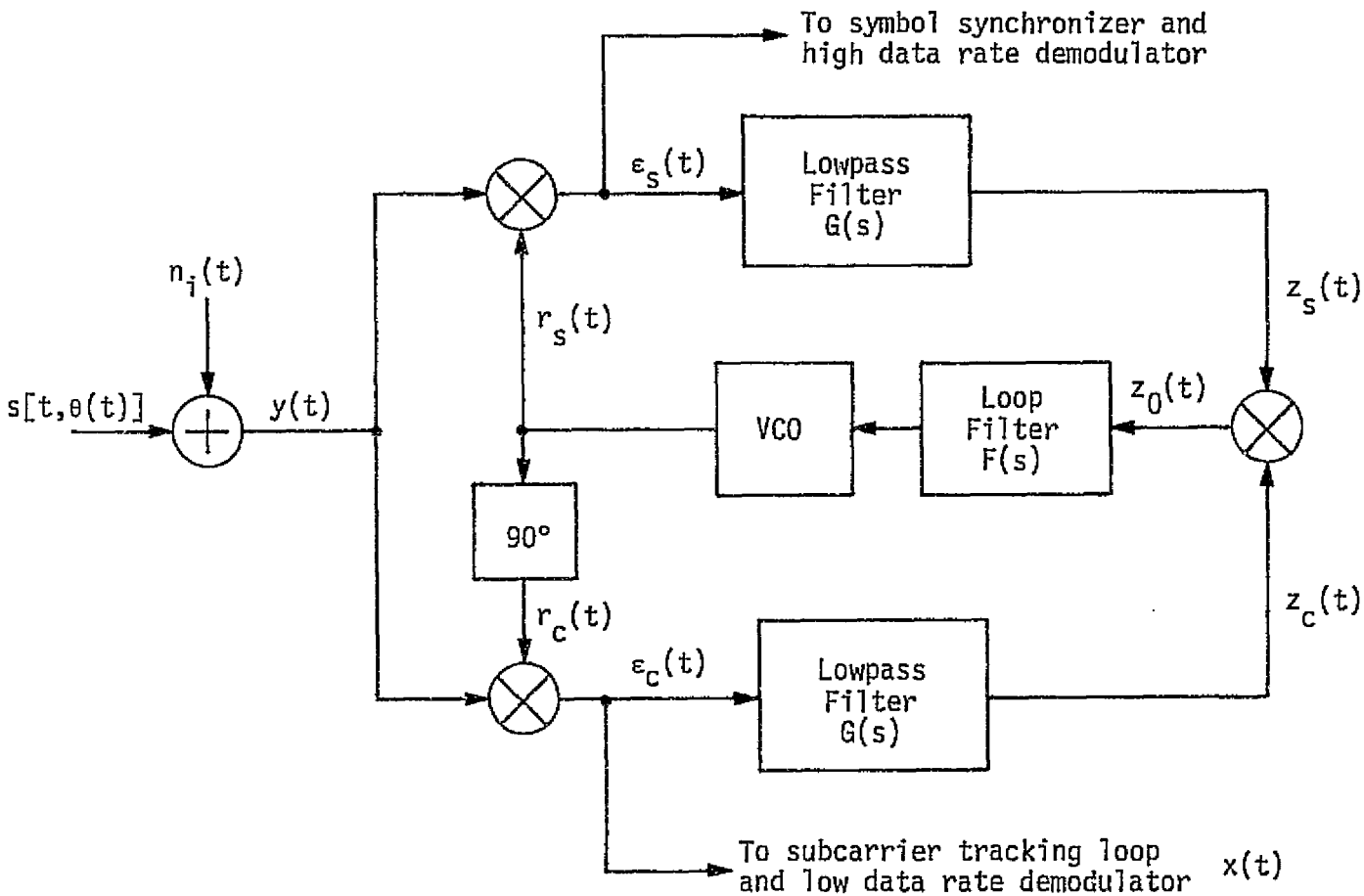

Figure 2. Costas Loop for Carrier Tracking

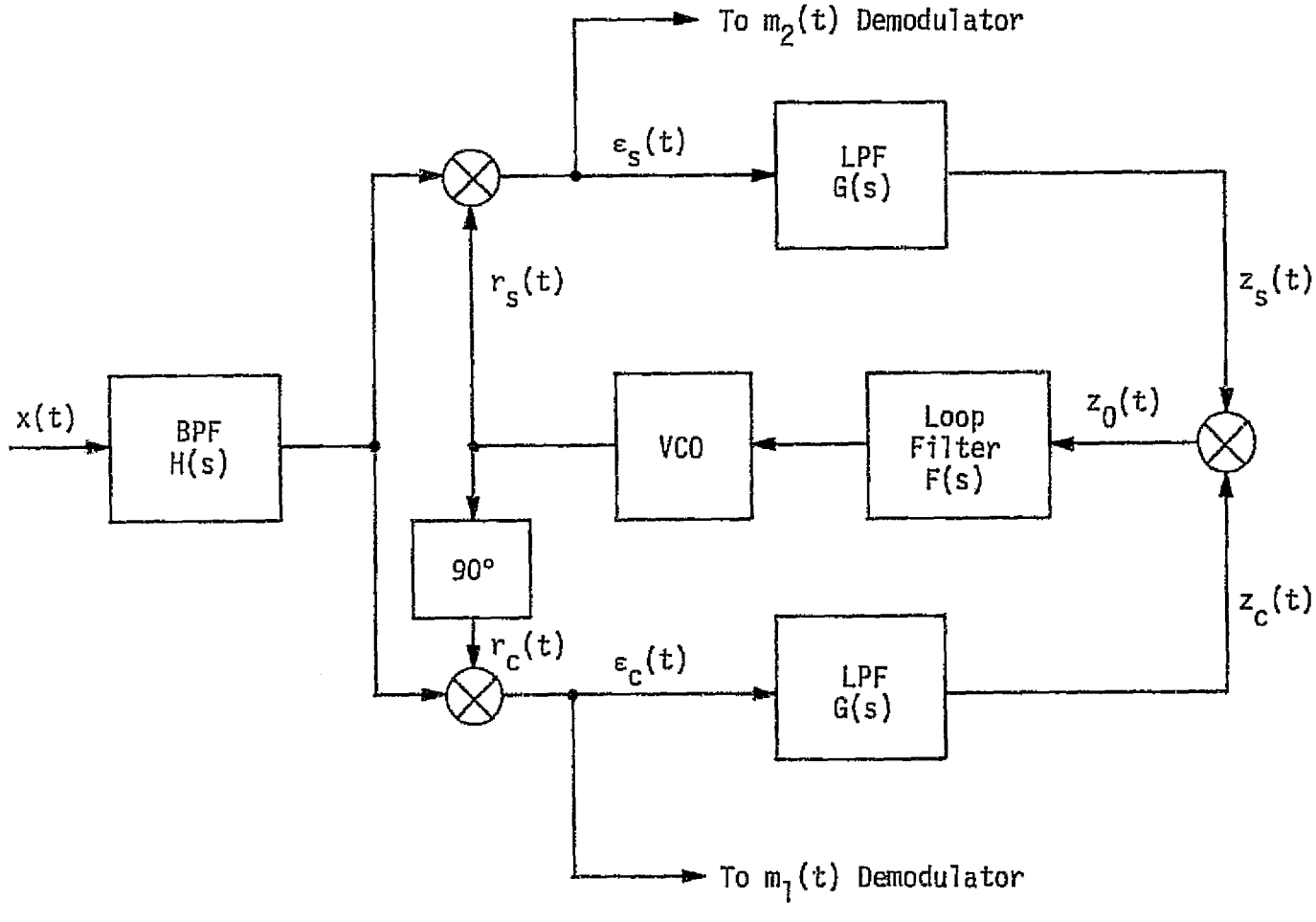

Figure 3. Costas Loop for Subcarrier Tracking

$$\mathcal{S}_L = \frac{\left\{\cos^2 \varphi_c \left(\frac{4}{\pi}\right)^2 [\eta_2 D_2 - \eta_1 D_1]\right\}^2}{A + K_L\left(\frac{B_i/R_2}{2P_T T_2/N_0}\right) + 2\left(\frac{4}{\pi}\right)^4 \eta_2 \eta_1 \left(\frac{P_T T_2}{N_0}\right) \frac{D_{12}}{T_2}} \tag{8}$$

is the loop squaring loss. The following definitions are used in (8):

$$\eta_i \triangleq \frac{\tilde{P}_i}{P_T}; \quad i = 1,2,3 \tag{9}$$

$$\eta_d \triangleq \frac{\tilde{P}_d}{P_T} \tag{10}$$

$$K_L \triangleq \frac{\int_{-\infty}^{\infty} |G_0(j\omega)|^4 \frac{d\omega}{2\pi}}{\int_{-\infty}^{\infty} |G_0(j\omega)|^2 \frac{d\omega}{2\pi}} \tag{11}$$

$$D_i \triangleq \int_{-\infty}^{\infty} S_{m_i}(\omega) \, |G_0(j\omega)|^2 \frac{d\omega}{2\pi}; \quad i = 1,2 \tag{12}$$

$$D_{12} \triangleq \int_{-\infty}^{\infty} S_{m_2}(\omega) \, S_{m_1}(\omega) \, |G_0(j\omega)|^4 \frac{d\omega}{2\pi} \tag{13}$$

$$\begin{aligned} A \triangleq \left(\frac{4}{\pi}\right)^2 \Bigg[& \eta_2 \int_{-\infty}^{\infty} S_{m_2}(\omega) \, |G_0(j\omega)|^4 \frac{d\omega}{2\pi} + \eta_1 \int_{-\infty}^{\infty} S_{m_1}(\omega) \, |G_0(j\omega)|^4 \frac{d\omega}{2\pi} \\ & + \eta_3 \int_{-\infty}^{\infty} S_{m_3}(\omega) \, |G_0[j(\omega-\omega_{sc})]|^4 \frac{d\omega}{2\pi} \\ & + \eta_d \int_{-\infty}^{\infty} S_{m_d}(\,) \, |G_0[j(\omega-\omega_{sc})]|^4 \frac{d\omega}{2\pi} \Bigg]. \end{aligned} \tag{14}$$

In equations (11) through (14), the transfer function $G_0(j\omega)$ represents the cascade effect of the bandpass filter $H(j\omega)$ and the lowpass filter $G(j\omega)$ in the subcarrier loop, and the arm filter bandwidth B_i is defined by

$$B_i \triangleq \frac{1}{2\pi} \int_{-\infty}^{\infty} |G_0(j\omega)|^2 \, d\omega \, . \tag{15}$$

In the above equations, S_{m_i} and S_{m_d} represent the power spectrums of the signals $s_i(t)$ and $s_d(t)$, respectively.

It is easy to see from (8) that the main effect of the carrier tracking loop on the subcarrier phase jitter is a degradation of $\cos^2 \varphi_c$ in the rms jitter of the subcarrier loop, where φ_c is the phase error in the carrier loop.

In order to evaluate (6) numerically to find the value of the subcarrier rms tracking jitter $\sigma_{\varphi_{sc}}$ for a fixed ratio of arm filter noise bandwidth to loop noise bandwidth (B_i/B_L), three assumptions are made:

(a) The carrier loop is tracking perfectly; thus, $\varphi_c = 0$.

(b) The bandwidth of $H(\omega)$ is much wider than that of the arm filter $G(j\omega)$.

(c) The arm filters $G(\omega)$ are assumed to be single-pole Butterworth (RC) filters, or

$$|G(j\omega)|^2 = \frac{1}{1 + (\omega/\omega_c)^2}, \tag{16}$$

where ω_c is the cutoff frequency in radians.

For illustration purposes, two sets of performance curves are drawn to demonstrate the effect of power ratio variations at the transmitter on the rms phase jitter of the subcarrier loop. Figures 4 and 5 illustrate the nominal power ratio case ($P_1/P_T = 0.04$, $P_2/P_T = 0.16$, and $P_3/P_T = 0.80$) with the signal-to-noise ratio ($P_T T_2/N_0$) as a parameter. It is observed that the changes in the subcarrier rms tracking jitter as a function of B_i/R_2 are more obvious when $m_2(t)$ and $m_1(t)$ are both Manchester codes (Figure 5) than when $m_2(t)$ is NRZ and $m_1(t)$ is Manchester.

Figures 6 through 9 illustrate the rms phase jitter for the two power ratio cases of interest, namely, Case 1 ($P_3/P_T = 0.82$, $P_2/P_T = 0.14$, $P_1/P_T = 0.04$) and Case 2 ($P_3/P_T = 0.78$, $P_2/P_T = 0.19$, $P_1/P_T = 0.03$) for two values of $P_T T_2/N_0$ and R_2 as a parameter. The chosen values of $P_T T_2/N_0$, though extremely pessimistic when compared with the actual link values, serve to illustrate the behavior of the demodulator under consideration. Figures 6 and 8 illustrate the case when $m_2(t)$ is NRZ, while Figures 7 and 9 illustrate the case when $m_2(t)$ is a Manchester code with $m_1(t)$ and $m_3(t)$ being Manchester and NRZ, respectively, for all figures, as is actually the case in

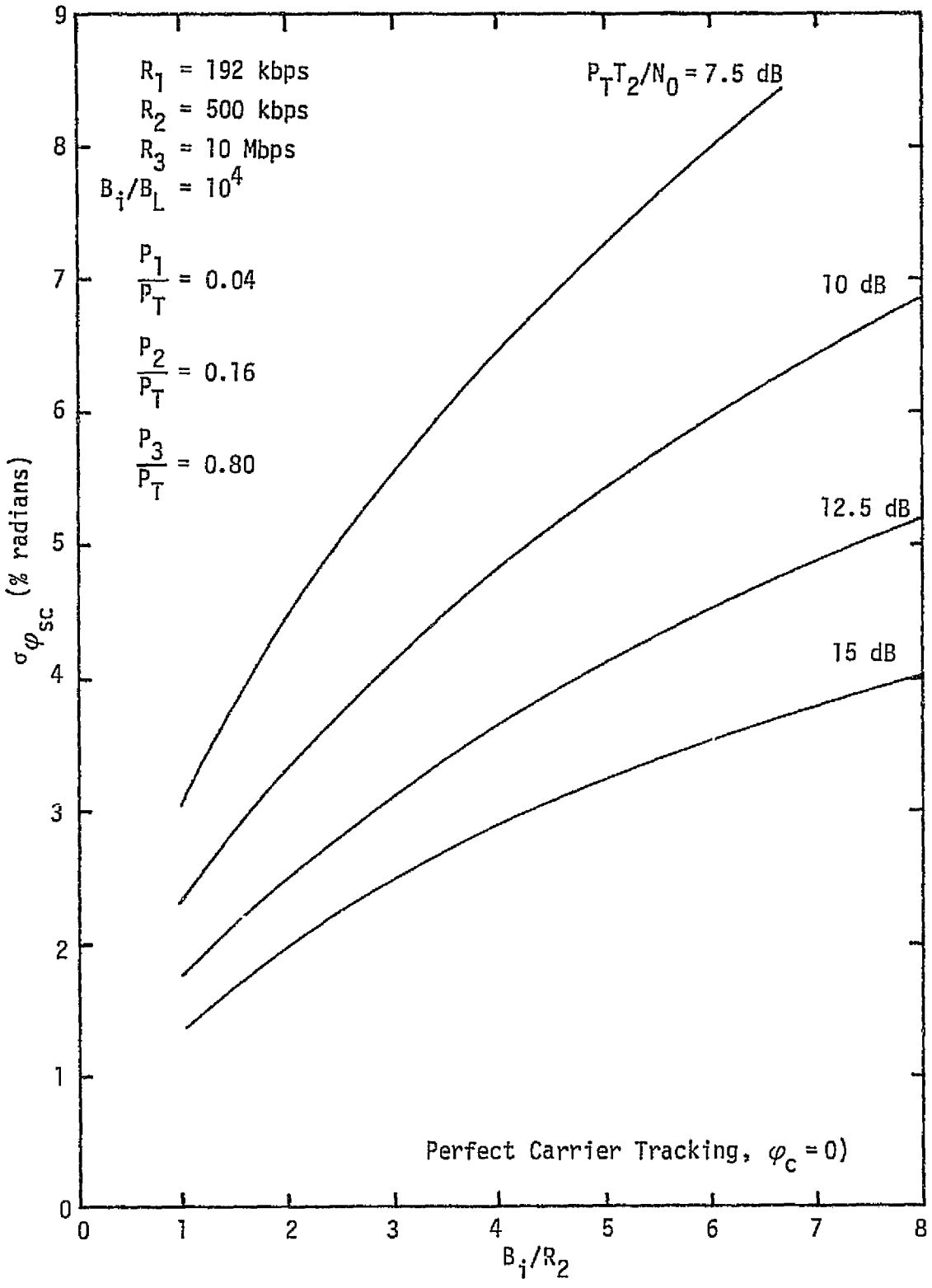

Figure 4. Subcarrier Tracking rms Jitter versus Ratio of Arm Filter Bandwidth to High Subcarrier Data Rate R_2; P_TT_2/N_0 is a parameter; $m_3(t)$ and $m_2(t)$ are NRZ, $m_1(t)$ is Manchester; $R_3 > R_2 > R_1$

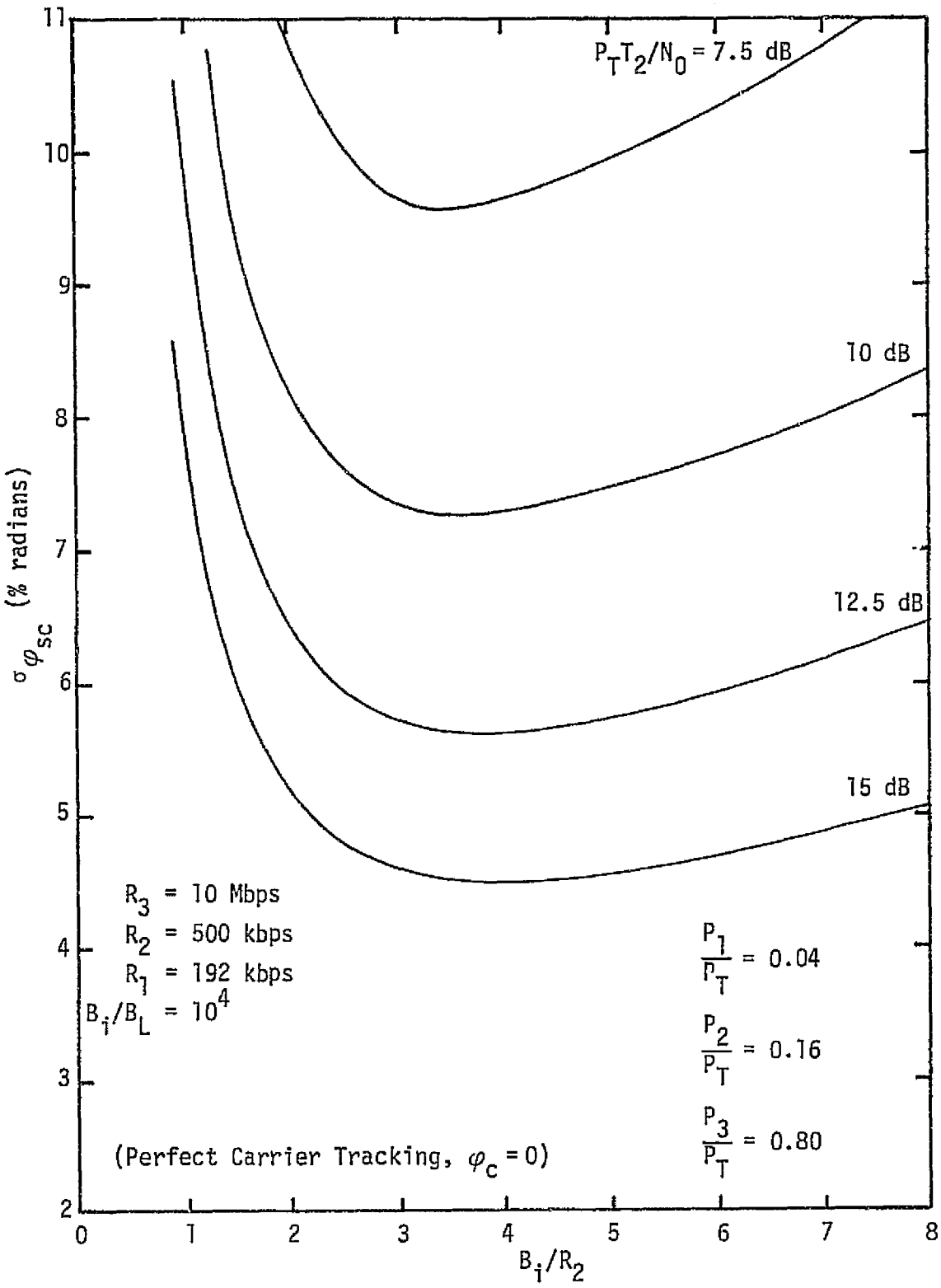

Figure 5. Subcarrier Tracking rms Jitter versus Ratio of Arm Filter Bandwidth to High Subcarrier Data Rate R_2; R_2 is a parameter; $m_3(t)$ is NRZ, $m_1(t)$ and $m_2(t)$ are Manchester codes; $R_3 > R_2 > R_1$

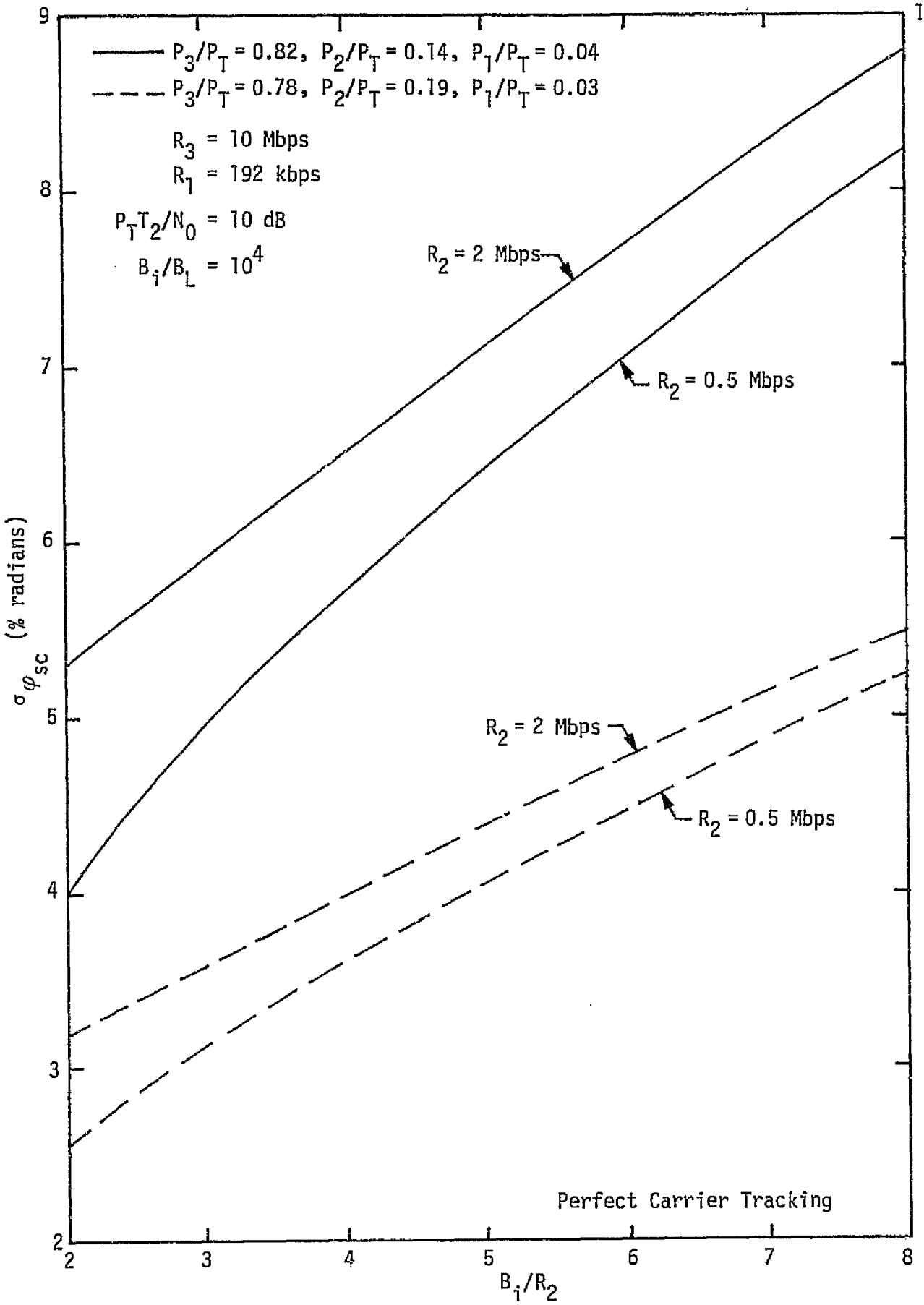

Figure 6. Subcarrier Tracking rms Jitter versus Ratio of Arm Filter Bandwidth to High Subcarrier Data Rate R_2; R_2 is a parameter; $m_3(t)$ and $m_2(t)$ are NRZ, $m_1(t)$ is Manchester

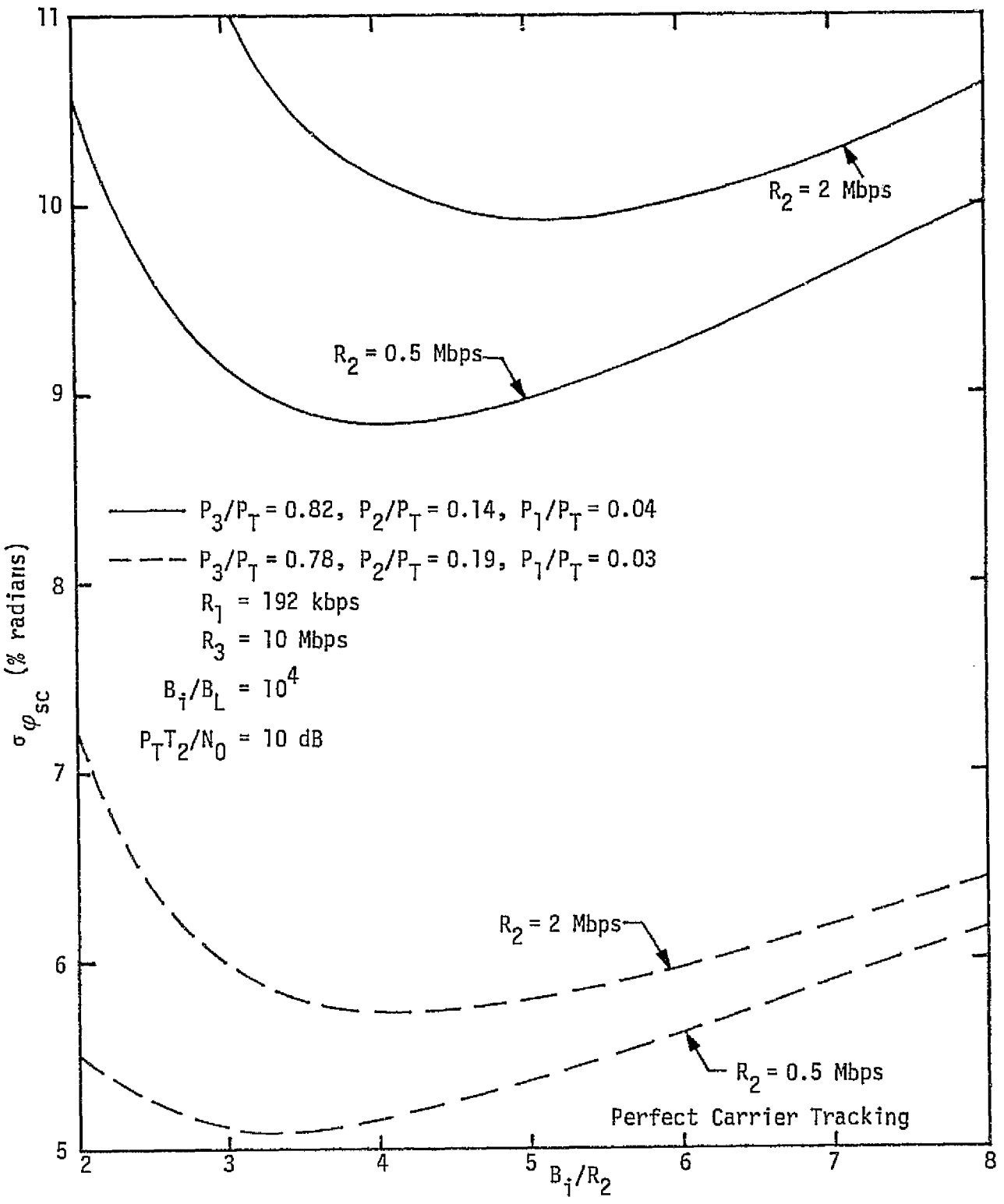

Figure 7. Subcarrier Tracking rms Jitter versus Ratio of Arm Filter Bandwidth to High Subcarrier Data Rate R_2; R_2 is a parameter; $m_3(t)$ is NRZ, $m_2(t)$ and $m_1(t)$ are Manchester

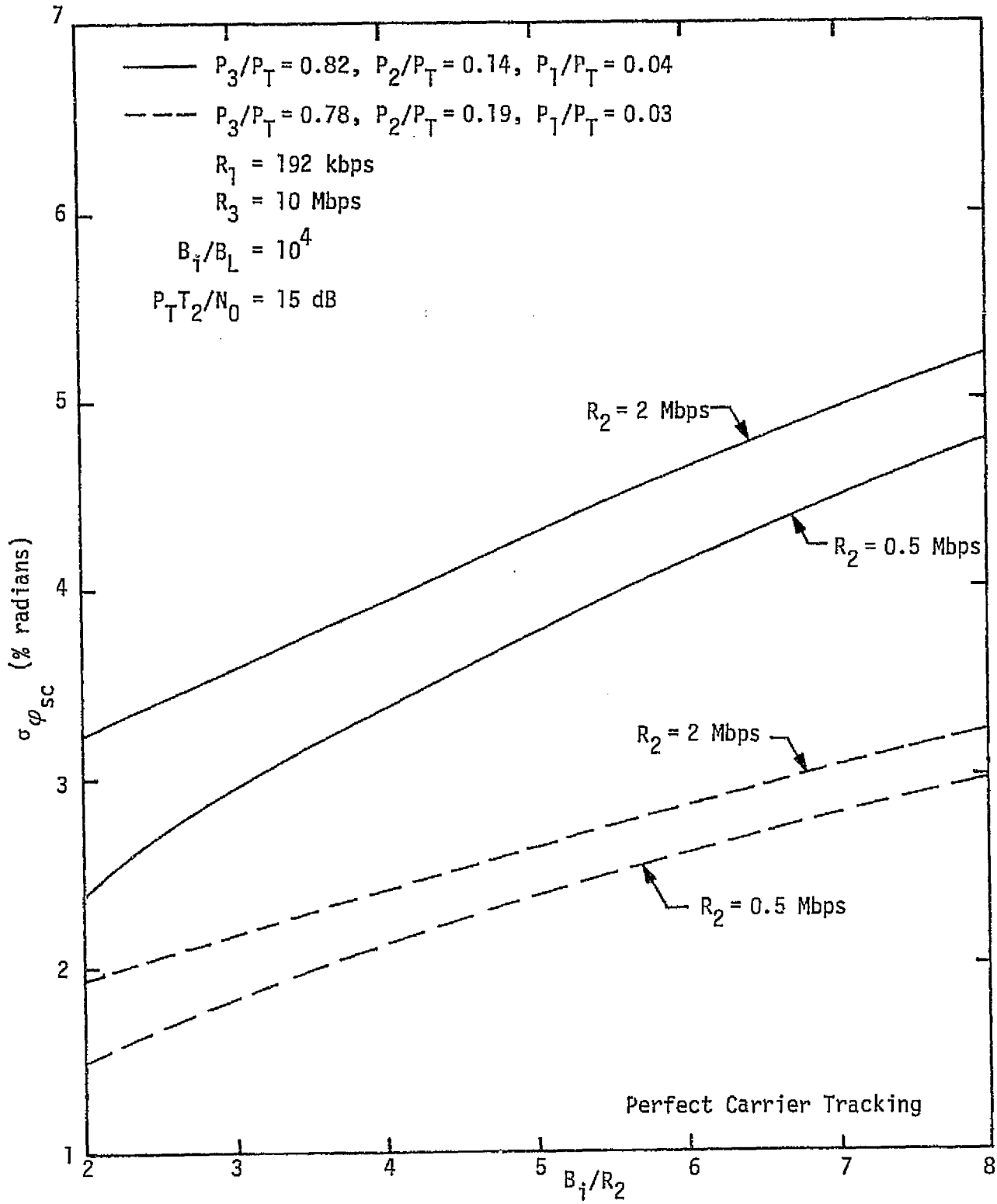

Figure 8. Subcarrier Tracking rms Jitter versus Ratio of Arm Filter Bandwidth to High Subcarrier Data Rate R_2; R_2 is a parameter; $m_3(t)$ and $m_2(t)$ are NRZ, $m_1(t)$ is Manchester

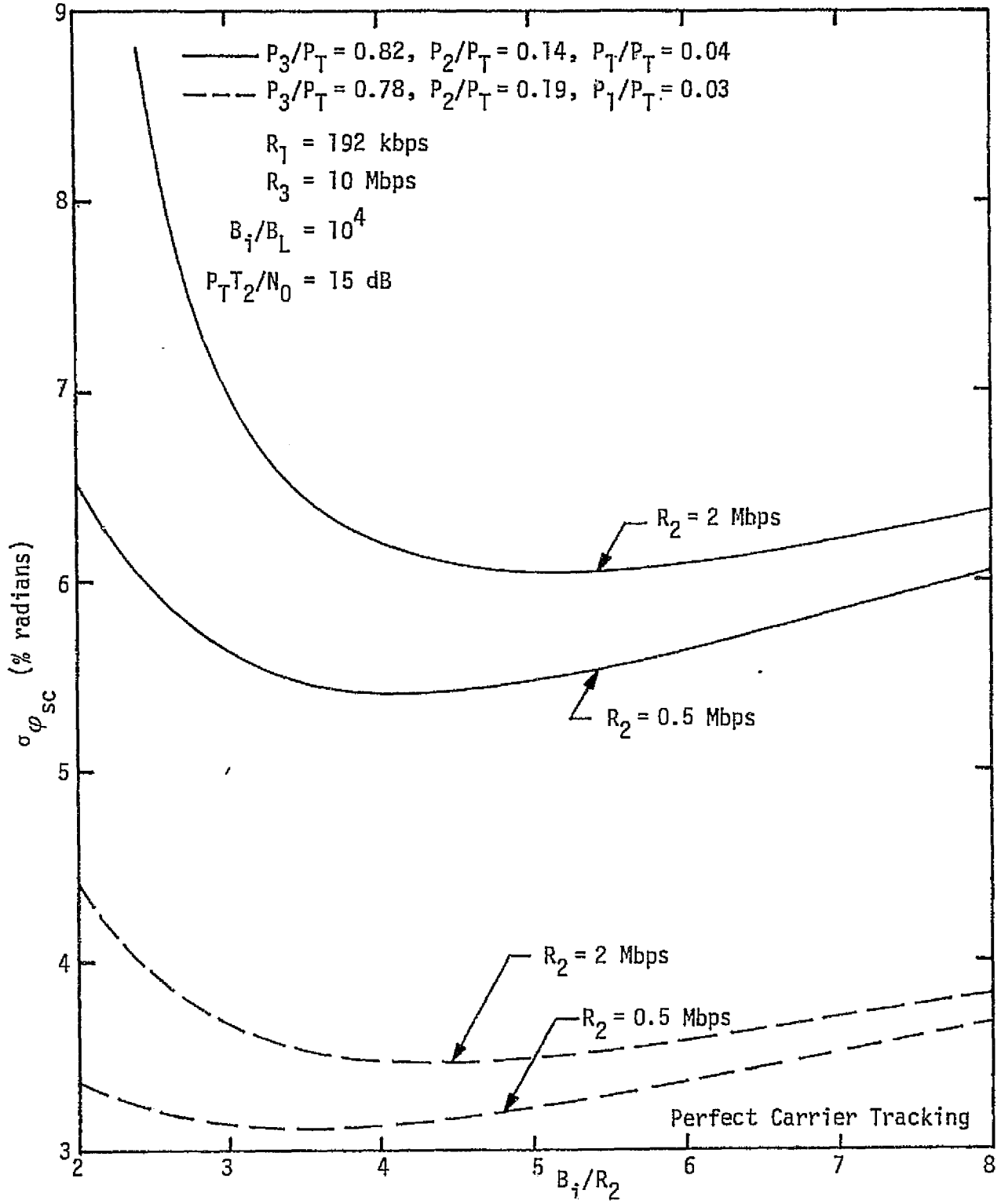

Figure 9. Subcarrier Tracking rms Jitter versus Ratio of Arm Filter Bandwidth to High Subcarrier Data Rate R_2; R_2 is a parameter; $m_3(t)$ is NRZ, $m_2(t)$ and $m_1(t)$ are Manchester

the Ku-band return link. It is obvious from the figures that the power ratio change greatly affects the subcarrier rms phase jitter; hence, care must be undertaken in designing both the transmitter and receiver to minimize the variations and to assure adequate recovery of the data in the three channels.

4.0 PROBABILITY OF ERROR PERFORMANCE

The error probability performance of unbalanced QPSK demodulators is discussed in detail in [4]. This section is devoted to obtaining numerical values for the probability of error in demodulating the data in Channels 1 and 2 with $R_2 > R_1$ for both cases of power ratios. To detect the data, the outputs of the phase detectors in the two arms of the subcarrier tracking loop are used as inputs to the channel data detectors which are assumed to be matched filters. Denoting the ratio of the two data rates by

$$\gamma_T = R_2/R_1 \geq 1, \tag{17}$$

the probabilities of error in the two channels are shown in [4] to be

$$P_{E1} = \frac{1}{2}\operatorname{erfc}\sqrt{R_{T2}\,\gamma_T\,\eta_1'} + \frac{1}{2}\sqrt{\frac{R_{T2}\,\gamma_T\,\eta_1'}{\pi}}\exp\left(-R_{T2}\,\gamma_T\,\eta_1'\right)\left[1 + 2R_{T2}\,\eta_2'\,\overline{\tilde{m}_{12}^2}\right]\sigma_{\varphi_{sc}}^2$$

$$P_{E2} = \frac{1}{2}\operatorname{erfc}\sqrt{R_{T2}\,\eta_2'} + \frac{1}{2}\sqrt{\frac{R_{T2}\,\eta_2'}{\pi}}\exp\left(-R_{T2}\,\eta_2'\right)\left[1 + 2R_{T2}\,\eta_1'\,\overline{\tilde{m}_{12}^2}\right]\sigma_{\varphi_{sc}}^2, \tag{18}$$

where $\sigma_{\varphi_{sc}}^2$ is the phase jitter calculated using (6), η_i' is defined as

$$\eta_i = \frac{\tilde{P}_i}{\tilde{P}_1 + \tilde{P}_2}; \qquad i = 1,2 \tag{19}$$

and R_{T2} is the total signal-to-noise ratio in the high subcarrier data rate bandwidth defined by

$$R_{T2} = \frac{(\tilde{P}_1 + \tilde{P}_2)}{N_0}\,T_2 .$$

The factor $\overline{\tilde{m}_{12}^2}$, which is a cross-modulation factor, is defined in [4] and shown in Table 1.

Table 1. Evaluation of $\overline{\tilde{m}_{12}^2}$; $T_1/T_2 \triangleq \gamma_T \geq 1$

$m_1(t)$ \ $m_2(t)$	Manchester	NRZ
Manchester	$\frac{1}{6}[\gamma_T^2 - \frac{5}{\gamma_T} + 12 - 6\gamma_T]$; $R_1 \leq R_2 \leq 2R_1$ $\frac{1}{2\gamma_T}$; $R_2 \geq 2R_1$	$\gamma_T - \frac{1}{6}\gamma_T^2 - 1 + \frac{1}{3\gamma_T}$; $R_1 \leq R_2 \leq 2R_1$ $1 - \frac{1}{\gamma_T}$; $R_2 \geq 2R_1$
NRZ	$\frac{1}{6\gamma_T}$	$1 - \frac{1}{3\gamma_T}$

The variation of the power ratio distribution has two effects on the probabilities of error given in (18):

(1) It causes variations in the loop phase jitter ($\sigma_{\varphi_{sc}}^2$) which, in turn, affects the probabilities of error. This effect, however, has been shown in [4] to be less than 0.14 dB under worst conditions. In other words, the deviation due to phase jitter from the theoretical value with ideal tracking is negligible.

(2) It causes changes in the signal-to-noise ratios in the various channels [the first terms in (18)]. To illustrate this effect, a typical expected value of $P_T T_2/N_0 = 22$ dB is selected at the input of the subcarrier Costas loop [5]. Choosing $R_2 = 2$ Mbps and $R_1 = 192$ kbps as an example, Table 2 summarizes the resulting bit energy-to-noise spectral density in the two cases of interest.

Table 2. Bit Energy-to-Noise Spectral Density Ratio at the Subcarrier Loop (dB)

	Channel 1	Channel 2
Case 1	16.95	13.18
Case 2	14.59	15.23

$R_3 = 10$ Mbps, $R_2 = 2$ Mbps, $R_1 = 192$ kbps

$P_T T_2/N_0 = 22$ dB

Since 8.4 dB of signal energy-to-noise spectral density is needed to achieve the specification probability of error* of 10^{-4}, a wide margin exists in both cases in spite of the expected fluctuation in power ratios. Using an estimated 2.0 dB for the TDRS bit synchronizer loss, the resulting design margins are summarized in Table 3 for the chosen data rates.

Table 3. Return Link Lower Rate Channels Design Margin

	Channel 1	Channel 2
Case 1	6.55	2.78
Case 2	4.19	4.83

$R_3 = 10$ Mbps, $R_2 = 2$ Mbps, $R_1 = 192$ kbps

$P_T T_2/N_0 = 22$ dB

To summarize, it could be concluded that, although the fluctuations in the power ratios between the three channels produce appreciable changes in the subcarrier phase jitter, adequate design margins are still expected due to the high existing signal-to-noise ratios in the return link.

*The erfc (x) is defined as

$$\text{erfc}(x) = \frac{2}{\sqrt{\pi}} \int_x^\infty \exp(-t^2)\, dt$$

REFERENCES

1. M. K. Simon. "Integrated Source and Channel Encoded Digital Communication System Design Study," Appendix C, Axiomatix Report No. R7607-3, July 31, 1976.

2. M. K. Simon. "Power Allocation Properties and Costas Loop Subcarrier Tracking Performance Associated with a Digital Phase Shift Implementation of the Three-Channel Orbiter Ku-Band Modulator," Axiomatix Report No. R7709-4, September 29, 1977.

3. M. K. Simon and W. K. Alem. "Subcarrier Tracking Analysis for Three-Channel Orbiter Ku-Band Return Link," Axiomatix Report No. R7707-4, July 28, 1977.

4. M. K. Simon. "Error Probability Performance of Unbalanced QPSK Receivers," Axiomatix Report No. R7711-5, November 21, 1977.

5. "Space Shuttle RF Link Circuit Margins," NASA publication (EJ5), January 1977.

APPENDIX C

ACQUISITION TIME PERFORMANCE OF POLARITY-TYPE COSTAS LOOPS OPERATING IN THE FREQUENCY SEARCH MODE

APPENDIX C

ACQUISITION TIME PERFORMANCE OF POLARITY-TYPE COSTAS LOOPS OPERATING IN THE FREQUENCY SEARCH MODE

APPENDIX C

ACQUISITION TIME PERFORMANCE OF POLARITY-TYPE COSTAS LOOPS OPERATING IN THE FREQUENCY SEARCH MODE

by

Marvin K. Simon

1.0 INTRODUCTION

A report by the author [1] considered the frequency acquisition performance of polarity-type Costas loops in the absence of acquisition aids of any type. As such, the initial frequency uncertainty was required to be within the pull-in range of the loop (expressions for which were derived in [1] as functions of the loop parameters). Under these conditions, equations were developed for the frequency acquisition time of second-order polarity-type Costas loops with imperfect integrating loop filters. Specific numerical results were presented for the important practical case of single-pole arm filters and both NRZ and biphase-L data formats.

More often than not, the carrier loop is required to acquire over an initial frequency uncertainty range much greater than the pull-in range of the loop itself. The loop is then said to operate in the "frequency-search mode" and an appropriate acquisition aid is employed to drive the loop voltage-controlled oscillator (VCO) toward the frequency of the incoming signal. The most common form of frequency acquisition aid consists of adding a ramp voltage $e(t) = Dt$ to the output of the loop filter (input of the VCO) where $S_\Omega \triangleq K_V D$ is referred to as the "sweeping rate" in rad/sec/sec with K_V the VCO gain in rad/sec/V. The problem then is to derive closed-form expressions (if possible) for the frequency acquisition time of a second-order polarity-type Costas loop as functions of the initial loop detuning or uncertainty, the loop parameters, e.g., loop filter time constants, loop noise bandwidth, and the sweeping rate.

In the literature, one finds two approaches which are helpful in solving this problem. The approach taken in [2] follows that used by the same author [3] to derive the acquisition performance of unaided generalized tracking systems. It was also used in [1] to derive the unaided frequency acquisition performance of polarity-type Costas loops.

Unlike [2], however, the results in [3] apply only to the case of a perfect integrating loop filter. In [4], the quasi-stationary approach suggested by Richman [5] is used to analyze the frequency acquisition time performance of second-order tracking loops with arbitrary phase detector characteristics and either perfect or imperfect integrating loop filters. Since this approach is somewhat more general in that it allows computation of acquisition time performance for either type of loop filter, we shall follow it in our attempt to characterize the acquisition performance of polarity-type Costas loops. It should be pointed out that both approaches ([2] and [4]) have the limitations concerning the absence of noise and the hypothesis of a large difference between the initial frequency of the input signal and the quiescent frequency of the VCO. Nevertheless, analogous to what was done in [1], we can partially account for the effect of noise in the case of the polarity-type Costas loop by treating it as though it were free of additive noise but possessing a phase detector characteristic which is signal-to-noise ratio dependent. With regard to the large initial loop detuning requirement, it has been found that both approaches give accurate results (when compared with the numerical solution of the differential equation of loop operation) as soon as the initial loop detuning is several times greater than the equivalent noise bandwidth of the loop.

2.0 IMPERFECT INTEGRATING LOOP FILTER

In the absence of noise, the differential equation of a second-order, sweep-aided, tracking loop with arbitrary phase detector characteristic $g(x)$ is given by (in Heaviside operator notation):

$$p\phi_\ell = \Omega - AKF(p)\, g(\phi_\ell) - S_\Omega t, \tag{1}$$

where ϕ_ℓ is the loop phase error, A^2 is the power in the synchronizing signal, K is the total open loop gain, Ω is the initial frequency detuning, and $F(s)$ is the loop filter transfer function which, for an imperfect integrating loop filter, has the form

$$F(s) = \frac{1 + \tau_2 s}{1 + \tau_1 s}. \tag{2}$$

Applying the quasi-stationary analysis approach in [2], we arrive at a general result for frequency acquisition time performance (see (10) of [2]) which when rewritten in the notation of [1], becomes

$$\mu\left(\frac{\gamma_m}{\gamma}\right)\left(\frac{T_f}{\tau_1}\right) + \left[\frac{\left(\frac{\gamma_m}{\gamma}\right)^2}{4 - 3\left(\frac{\gamma_m}{\gamma}\right)^2}\right]\left\{1 + 3\mu\left(\frac{\gamma_m}{\gamma}\right)\left[\frac{T_f}{\tau_1} - \frac{4}{4 - 3\left(\frac{\gamma_m}{\gamma}\right)^2}\right]\right.$$

$$\left. - \left[1 - \frac{12\mu\left(\frac{\gamma_m}{\gamma}\right)}{4 - 3\left(\frac{\gamma_m}{\gamma}\right)^2}\right] \exp\left[-\left(\frac{T_f}{\tau_1}\right)\left(\frac{4 - 3\left(\frac{\gamma_m}{\gamma}\right)^2}{4}\right)\right]\right\} = 1, \quad (3)$$

where T_f is the acquisition time, Ω_m is the radian pull-in range of the unaided loop, and

$$\gamma \triangleq \frac{\Omega}{AKF_0}; \qquad \gamma_m \triangleq \frac{\Omega_m}{AKF_0};$$

$$\mu \triangleq \frac{S_\Omega}{AKF_0}\left(\frac{\tau_1}{\gamma_m}\right); \qquad F_0 \triangleq \frac{\tau_2}{\tau_1}. \quad (4)$$

Since (3) is transcendental in nature, the solution for T_f/τ_1 must be found by iterative methods.

If the sweep aiding is removed (i.e., $\mu = 0$), then (3) can be solved in closed-form with the result

$$\frac{T_f}{\tau_1} = \frac{4\left(\frac{\gamma}{\gamma_m}\right)^2}{4\left(\frac{\gamma}{\gamma_m}\right)^2 - 3} \ln\left[\frac{1}{1 - \left[4\left(\frac{\gamma}{\gamma_m}\right)^2 - 3\right]}\right]. \quad (5)$$

Clearly, (5) results in real values for T_f/τ_1 only when $\gamma/\gamma_m \leq 1$, i.e., the initial loop detuning is within the pull-in range of the loop.

To allow comparison with the results for the unaided loop given in [1], it is convenient to renormalize T_f by the loop bandwidth B_L rather than the loop filter time constant τ_1. Since, for a second-order loop with imperfect integrating loop filter, we have that (see (5) of [1]):

$$B_L \cong \frac{r+1}{4\tau_2} = \left(\frac{r+1}{4F_0}\right)\frac{1}{\tau_1}, \tag{6}$$

then,

$$\frac{T_f}{\tau_1} = B_L T_f \left(\frac{4F_0}{r+1}\right), \tag{7}$$

where $r \triangleq AKF_0\tau_2$ is a parameter proportional to the loop damping. Also, from the definition of μ in (4), we have that

$$\mu\left(\frac{\gamma_m}{\gamma}\right) = \frac{S_\Omega \tau_1}{AKF_0\gamma} = \frac{S_\Omega\left(\frac{r+1}{4F_0}\right)}{\Omega B_L}$$

$$= \frac{\left(\frac{S_\Omega}{B_L^2}\right)\left(\frac{r+1}{4F_0}\right)}{\Omega/B_L}. \tag{8}$$

Alternately, in terms of the loop natural frequency ω_n, which is related to B_L by

$$\omega_n^2 \cong \frac{r}{(r+1)^2}(16 B_L^2), \tag{9}$$

equation (8) becomes

$$\mu\left(\frac{\gamma_m}{\gamma}\right) = \left(\frac{S_\Omega}{\omega_n^2/2}\right)\left(\frac{r}{r+1}\right)\left(\frac{1}{F_0}\right)\left(\frac{2}{\Omega/B_L}\right). \tag{10}$$

Finally, from (4), γ_m/γ can clearly be written as

$$\frac{\gamma_m}{\gamma} = \frac{\Omega_m/B_L}{\Omega/B_L}. \tag{11}$$

Applying the results of (3), (5), (10), and (11) to the polarity-type Costas loop, we note the following replacements,

$$S_\Omega \to 2S_\Omega\ ; \qquad \Omega_m \to 4\pi f_{acq}\ ; \qquad \Omega \to 4\pi\Delta f\ , \tag{12}$$

where f_{acq} is the actual pull-in or frequency acquisition range of the loop (see Figure 2 of [1]) and Δf is the initial frequency offset. In terms of these replacements, (10) and (11) become

$$\mu\left(\frac{\gamma_m}{\gamma}\right) = \left(\frac{S_\Omega}{\omega_n^2/2}\right)\left(\frac{r}{r+1}\right)\left(\frac{1}{\pi F_0}\right)\left(\frac{1}{\Delta f/B_L}\right) \tag{13}$$

and

$$\frac{\gamma_m}{\gamma} = \frac{f_{acq}/B_L}{\Delta f/B_L} . \tag{14}$$

Finally, substituting (7), (13), and (14) in (3) gives the desired result for $B_L T_f$ as a function of F_0, r, $\Delta f/B_L$, f_{acq}/B_L, and $S_\Omega/(\omega_n^2/2)$. Figures 1 through 4 illustrate $B_L T_f$ versus normalized frequency offset $\Delta f/B_L$ for fixed values of r and F_0 with normalized sweep rate $S_\Omega/(\omega_n^2/2)$ as a parameter. Also held fixed is the normalized unaided frequency acquisition range f_{acq}/B_L which can be related to the loop parameters r and F_0, data format, arm filter bandwidth-to-data rate ratio, and detection signal-to-noise ratio as per the results in Figure 2 of [1]. Figure 5 illustrates the acquisition time performance of the sweep-aided polarity-type Costas loop for a fixed sweep rate and several values of unaided frequency acquisition range. Clearly, as the initial frequency uncertainty Δf far exceeds the pull-in range f_{acq}, the acquisition time performance becomes independent of the latter quantity and primarily dependent on the sweep rate. In fact, asymptotically for large Δf, we would have that

$$S_\Omega T_f = 2\pi \Delta f \tag{15}$$

or, in normalized form,

$$B_L T_f = \left[\frac{\pi(r+1)^2}{4r}\right] \frac{\Delta f/B_L}{S_\Omega/(\omega_n^2/2)} . \tag{16}$$

For example, for $r = 2$ and $S_\Omega/(\omega_n^2/2) = 0.2$, (16) yields $B_L T_f = 618.5$ for $\Delta f/B_L = 35$ which agrees well with Figure 5.

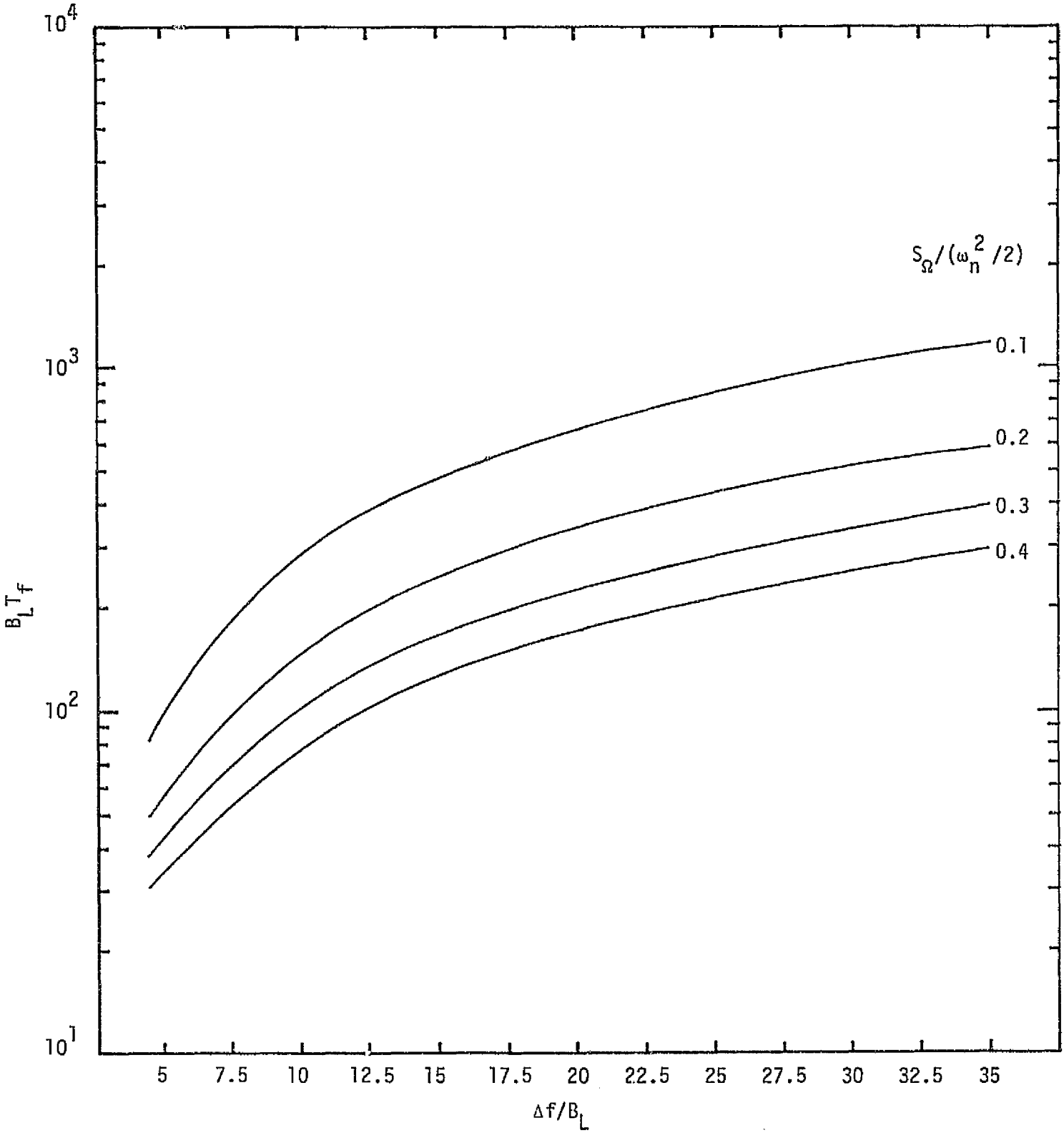

Figure 1. Frequency Acquisition Time Performance of Sweep Aided Polarity-Type Costas Loops; $r = 2$, $F_0 = 0.01$, $f_{acq}/B_L = 5$

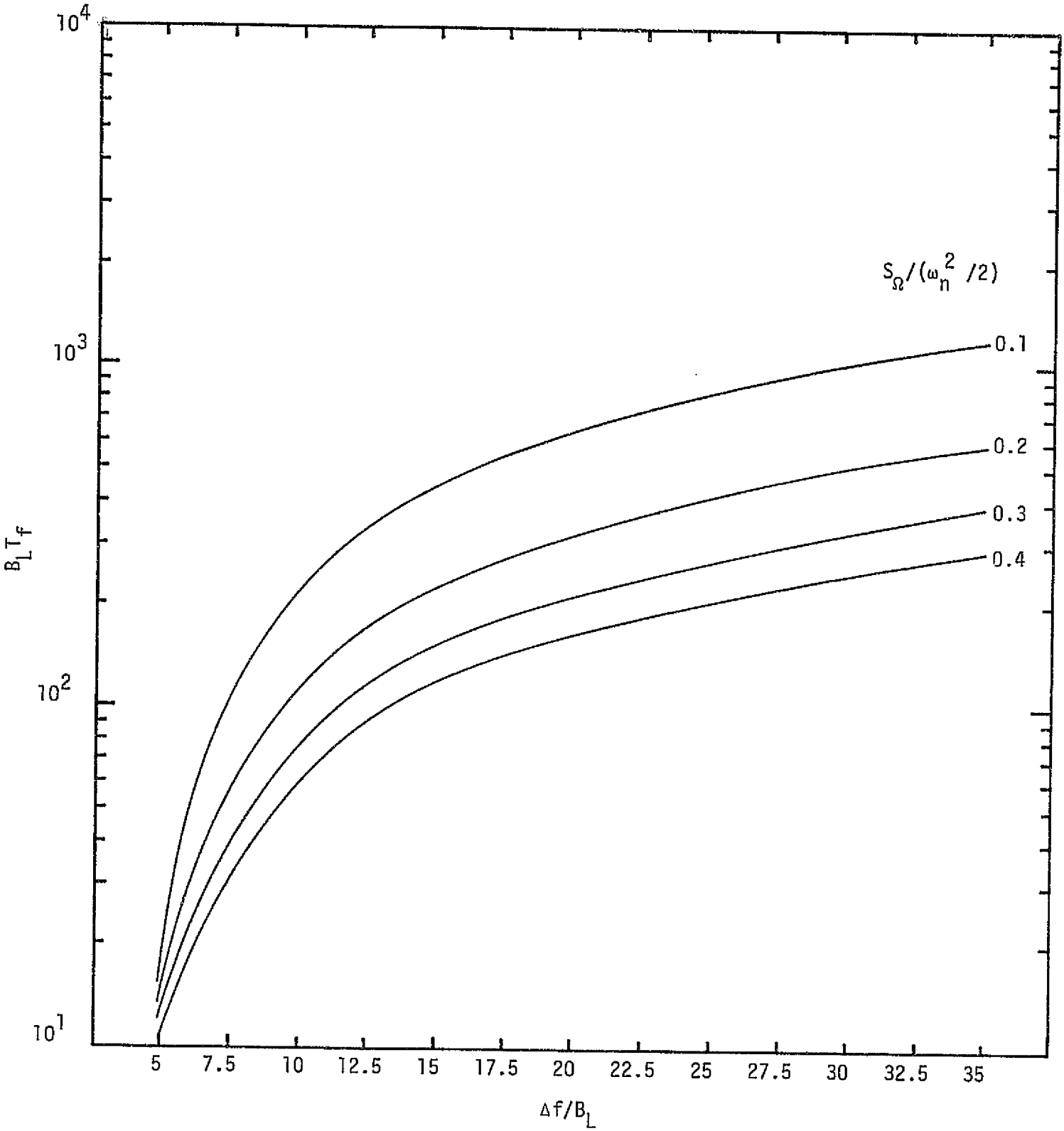

Figure 2. Frequency Acquisition Time Performance of Sweep Aided Polarity-Type Costas Loops; $r = 2$, $F_0 = 0.1$, $f_{acq}/B_L = 6$

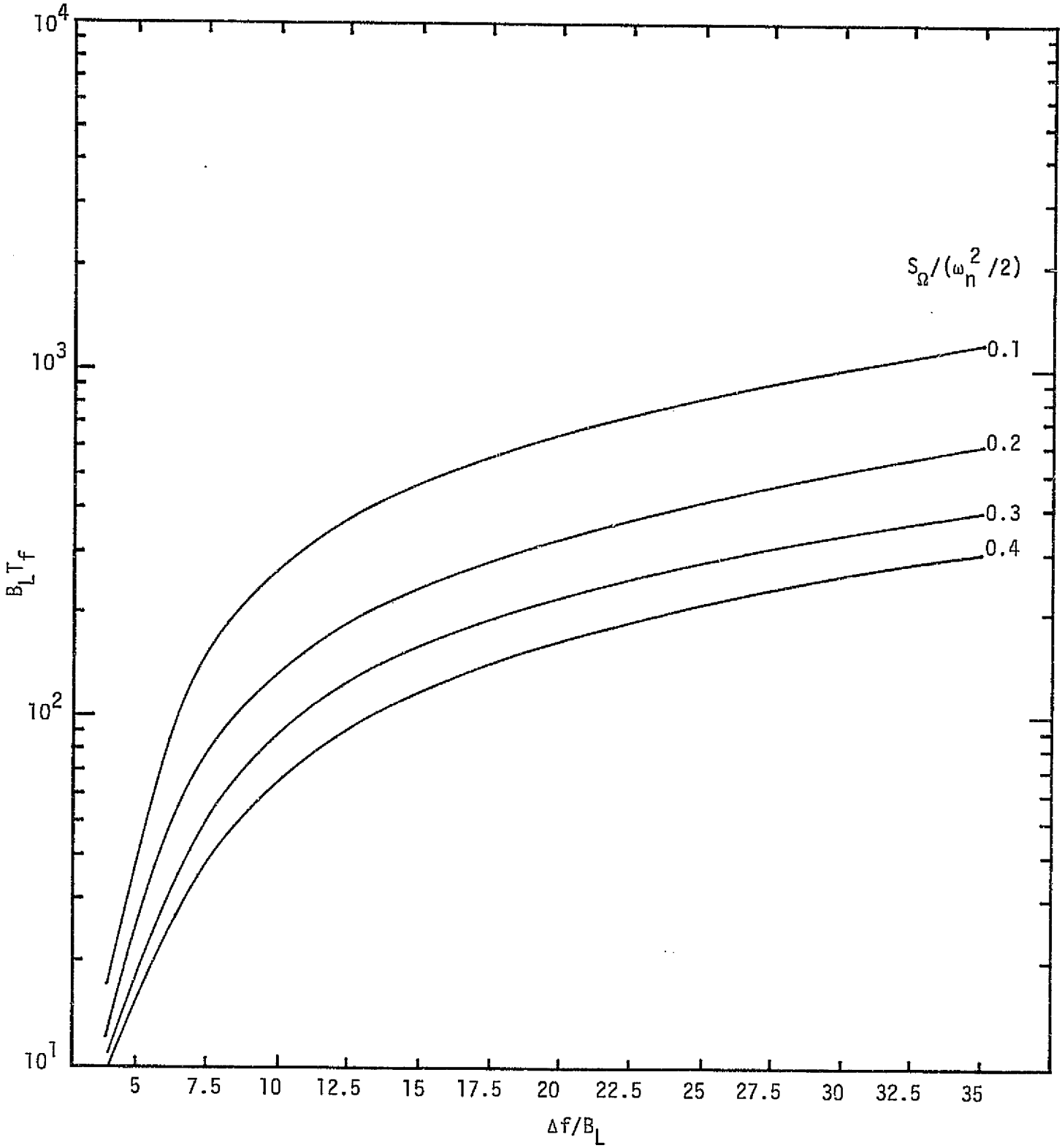

Figure 3. Frequency Acquisition Time Performance of Sweep Aided Polarity-Type Costas Loops; $r = 2$, $F_0 = 0.1$, $f_{acq}/B_L = 5$

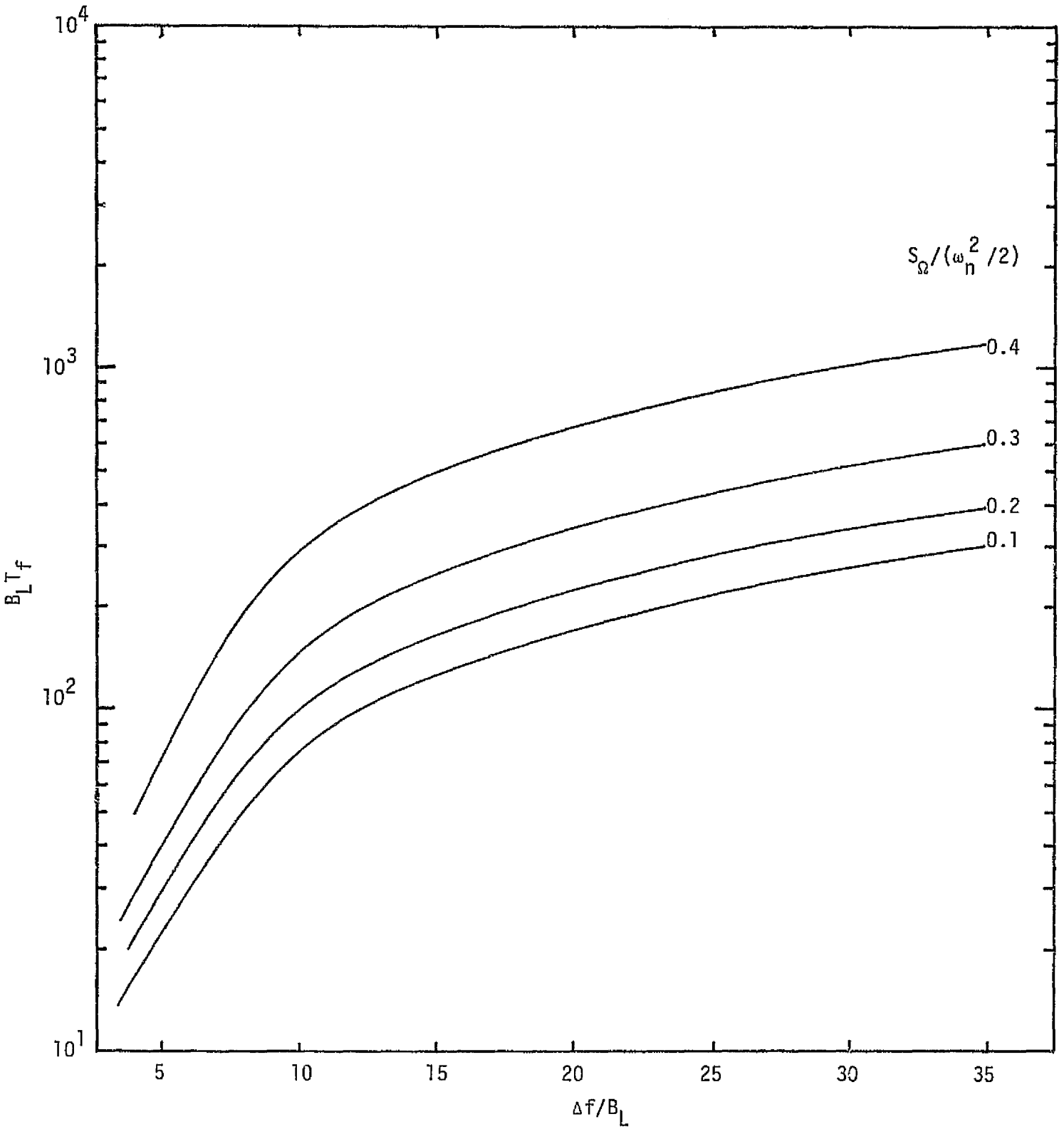

Figure 4. Frequency Acquisition Time Performance of Sweep Aided Polarity-Type Costas Loops; $r = 2$, $F_0 = 0.1$, $f_{acq}/B_L = 4$

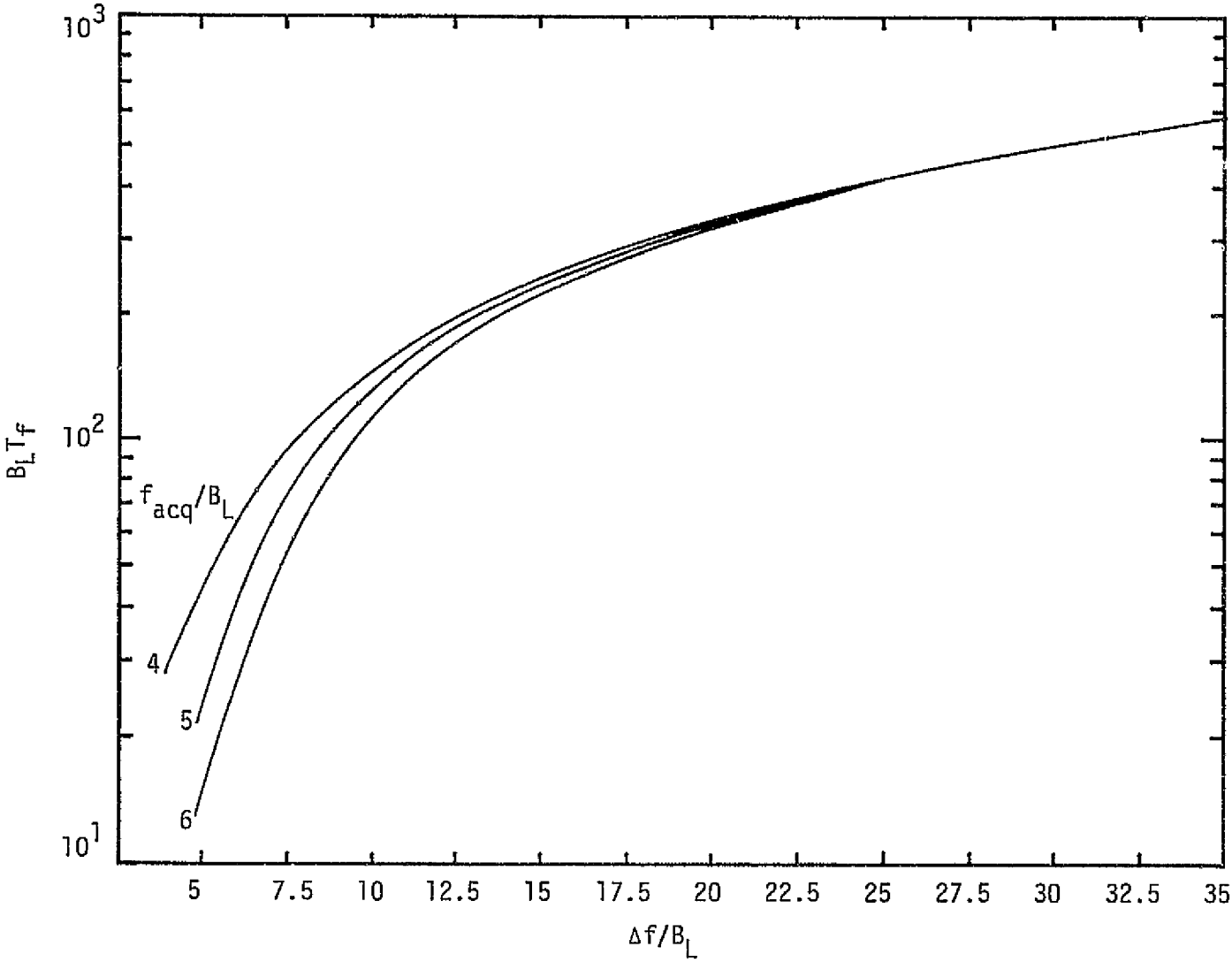

Figure 5. Frequency Acquisition Time Performance of Sweep Aided Polarity-Type Costas Loops; $r = 2$, $F_0 = 0.1$, $S_\Omega/(\omega_n^2/2) = 0.2$

3.0 PERFECT INTEGRATING LOOP FILTER

For the perfect integrating loop filter described by the transfer function

$$F(s) = \frac{1 + s\tau_2}{s\tau_1}, \tag{17}$$

the frequency acquisition time can be found as a closed-form expression (rather than by iterative solution). Again applying the quasi-stationary approach to the differential equation of (1) gives the general result (see (12) of [2] rewritten in our notation)

$$B_L T_f = B_L T_b \left[\left(\frac{\Omega}{2\pi B_L}\right) - \frac{2r}{\pi(r+1)}\right] + \frac{16\, r^2 \langle g^2(x)\rangle}{\pi^2 (r+1)^3} (B_L T_b)^2$$

$$\times \ln \left\{ \frac{\frac{\pi(r+1)^2}{8r(B_L T_b)} + \langle g^2(x)\rangle}{\frac{\pi^2(r+1)^3}{16\, r^2}\left(\frac{\Omega}{2\pi B_L}\right)\left(\frac{1}{B_L T_b}\right) + \langle g^2(x)\rangle} \right\}, \tag{18}$$

where $T_b \triangleq 2\pi B_L / S_\Omega$ is the time the VCO would take to sweep the bandwidth B_L if the loop were open. Thus,

$$B_L T_b = \frac{2\pi}{S_\Omega / B_L^2} = \frac{\frac{\pi(r+1)^2}{4r}}{S_\Omega / (\omega_n^2/2)} . \tag{19}$$

For a tracking loop with perfect integrating loop filter as in (17), it is possible to determine the maximum sweep rate to guarantee lock (in no noise) with a given probability [4,7]. In particular, to guarantee 100% lock, we require that

$$S_\Omega < \omega_n^2 \langle g^2(x)\rangle . \tag{20}$$

Furthermore, in order to acquire frequency lock at all, it is necessary that

$$S_\Omega < 2\omega_n^2 \langle g^2(x)\rangle . \tag{21}$$

Applying (18) and (19) to either the conventional or the polarity-type Costas loop requires that we first make the replacements of (12). When this is done, (18) simplifies to

$$B_L T_f = \frac{\pi(r+1)^2}{4r}\left(\frac{S_\Omega}{\omega_n^2/2}\right)^{-1}\left[\left(\frac{\Delta f}{B_L}\right) - \frac{r}{\pi(r+1)}\right] + \left(\frac{r+1}{4}\right)\left(\frac{S_\Omega}{\omega_n^2/2}\right)^{-2}\langle g^2(2\phi)\rangle$$

$$\times \ln\left\{\frac{\left(\frac{S_\Omega}{\omega_n^2/2}\right) + \langle g^2(2\phi)\rangle}{\frac{\pi(r+1)}{r}\left(\frac{\Delta f}{B_L}\right)\left(\frac{S_\Omega}{\omega_n^2/2}\right) + \langle g^2(2\phi)\rangle}\right\} . \qquad (22)$$

Then, for the conventional Costas loop (assuming no noise), we have that [1],

$$\langle g^2(2\phi)\rangle = \frac{1}{2\pi}\int_{-\pi}^{\pi} g^2(2\phi)\, d(2\phi) = \frac{1}{2} , \qquad (23)$$

with the further requirement that

$$\frac{S_\Omega}{\omega_n^2/2} < \frac{1}{2} \qquad (24)$$

for 100% lock, and

$$\frac{S_\Omega}{\omega_n^2/2} < 1 \qquad (25)$$

for frequency acquisition at all. For the polarity-type loop, we observed in [1] that (assuming no noise),

$$\langle g^2(2\phi)\rangle = 2 \qquad (26)$$

and thus, from (20) and (21) with the replacements of (12),

$$\frac{S_\Omega}{\omega_n^2/2} < 2 \qquad (27)$$

for 100% lock and

$$\frac{S_\Omega}{\omega_n^2/2} < 4 \tag{28}$$

for frequency acquisition at all. Substituting (26) into (22) and, in addition, letting $r = 2$ (the case of most practical interest) gives the frequency acquisition time performance of the sweep-aided polarity-type Costas loop with perfect integration loop filter, namely,

$$B_L T_f = \frac{9\pi}{8}\left(\frac{S_\Omega}{\omega_n^2/2}\right)^{-1}\left[\left(\frac{\Delta f}{B_L}\right) - \frac{2}{3\pi}\right] + \frac{3}{2}\left(\frac{S_\Omega}{\omega_n^2/2}\right)^{-2}$$

$$\times \ln\left\{\frac{\left(\frac{S_\Omega}{\omega_n^2/2}\right) + 2}{\frac{3\pi}{2}\left(\frac{\Delta f}{B_L}\right)\left(\frac{S_\Omega}{\omega_n^2/2}\right) + 2}\right\} . \tag{29}$$

Figure 6 illustrates $B_L T_f$ of (29) versus $\Delta f/B_L$ with $S_f/B_L^2 = (8/9\pi) \times (S_\Omega/(\omega_n^2/2))$ as a parameter. (NOTE: $S_f \triangleq S_\Omega/2\pi$ is the sweep rate in Hz/sec.) The corresponding results for the conventional Costas loop as computed from (22) together with (23) are illustrated in Figure 7. Clearly, the polarity-type loop offers superior frequency acquisition time performance relative to the conventional loop.

All that remains is to present the theory for the unaided loop frequency acquisition time performance corresponding to the curves so labeled in Figures 6 and 7. From (5) of [6], we have the general result that, as $F_0 \to 0$ and AKF_0 remains finite (limiting case of perfect integrating loop filter),

$$T_f \cong \frac{F_0 \tau_1 \gamma^2}{2\langle g^2(x)\rangle} . \tag{30}$$

Recalling the definitions of γ and B_L given in (4) and (6), respectively, we obtain after some simplification,

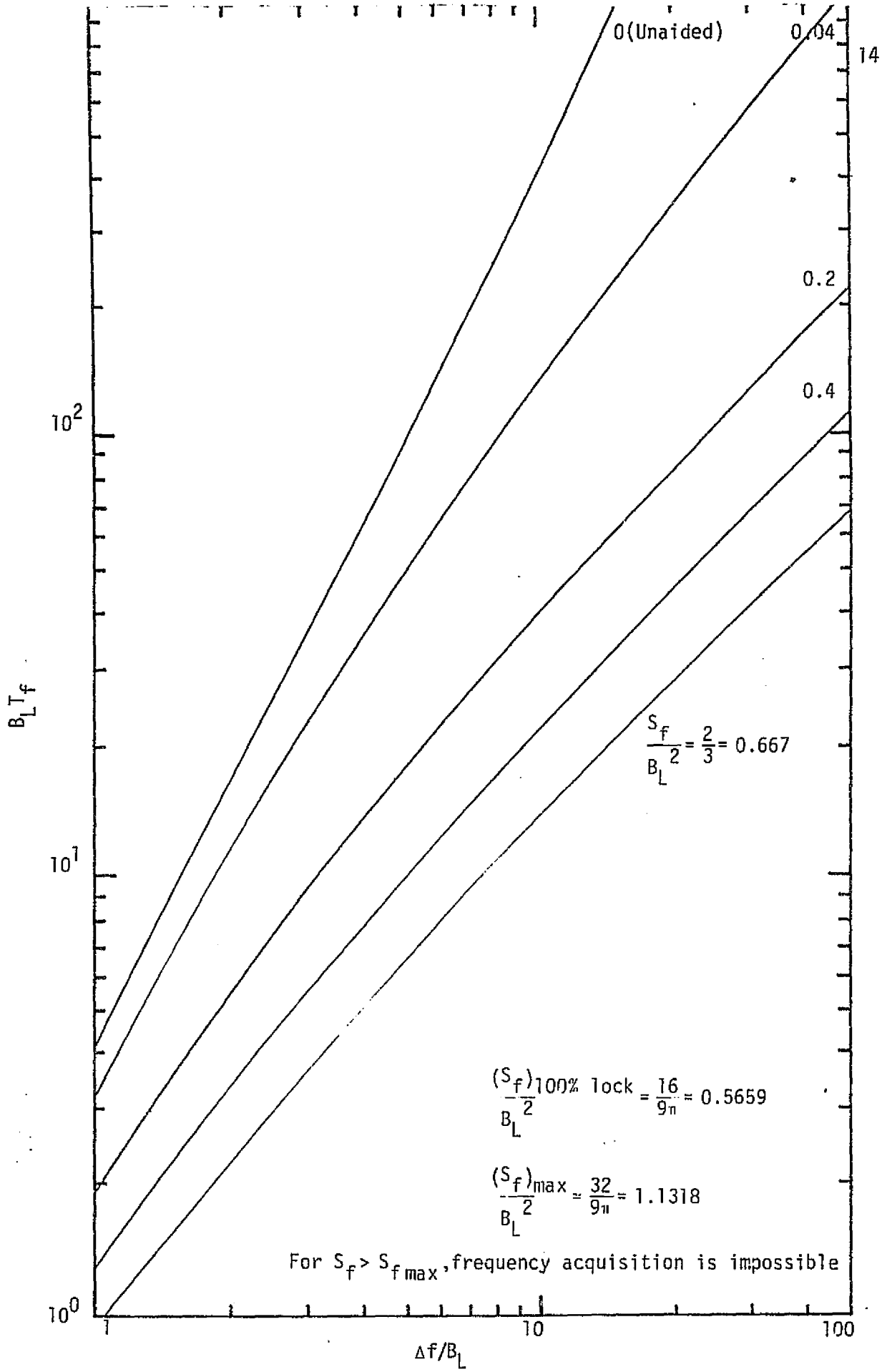

Figure 6. Frequency Acquisition Time Performance of Polarity-Type Costas Loop (No Noise)

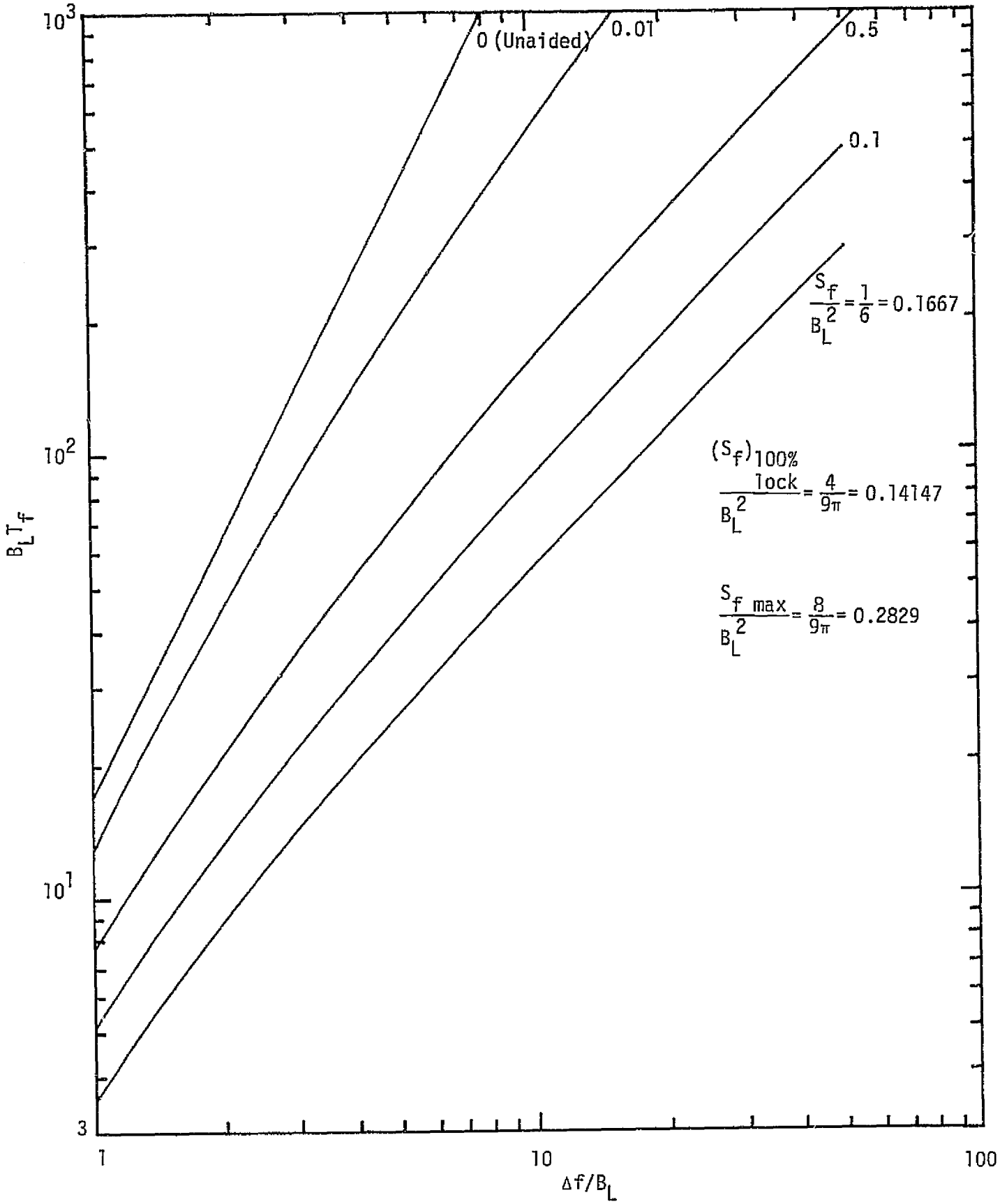

Figure 7. Frequency Acquisition Time Performance of Sweep-Aided Conventional Costas Loop (No Noise)

$$B_L T_f = \frac{(r+1)^3}{r^2}\left(\frac{1}{128\langle g^2(x)\rangle}\right)\left(\frac{\Omega}{B_L}\right)^2 . \tag{31}$$

Applying (31) to the Costas loop (conventional or polarity), we simply let $\Omega = 4\pi\Delta f$ [as was done in (12)] and $x = 2\phi$ which results in

$$B_L T_f = \frac{(r+1)^3}{r^2}\left(\frac{1}{8\langle g^2(2\phi)\rangle}\right)\left(\frac{\Delta f}{B_L}\right)^2 . \tag{32}$$

Finally, the unaided loop curves of Figures 6 and 7 are obtained by using either (26) or (23) for $\langle g^2(2\phi)\rangle$ in (32).

We conclude by noting that, analogous to the approach taken in [1], one can from (22) and (32) evaluate the frequency acquisition time performance of a polarity-type Costas loop with perfect integrating loop filter in the presence of noise. All that is necessary is to once again use the appropriate expression for $\langle g^2(2\phi)\rangle$ which is a function of data format, detection signal-to-noise ratio, and arm filter bandwidth-to-data rate ratio. We once again point out, however, that the noise is accounted for only insofar as its effect on the loop S-curve and not its additive effect.

REFERENCES

1. M. K. Simon. "Unaided Frequency Acquisition Performance of Polarity-Type Costas Loops with Imperfect Integrating Loop Filters," Axiomatix report in preparation.

2. U. Mengali. "Acquisition Time of Tracking Loops Operating in the Frequency-Search Mode," IEEE Transactions on Aerospace and Electronic Systems, Vol. AES-10, September 1974, pp. 583-587.

3. U. Mengali. "Acquisition Behavior of Generalized Tracking Systems in the Absence of Noise," IEEE Transactions on Communication Technology, Vol. COM-21, July 1973, pp. 820-826.

4. F. Russo and L. Verrazzani. "Acquisition Time of Second-Order Aided PLL," IEEE Transactions on Aerospace and Electronic Systems, Vol. AES-13, No. 1, January 1977, pp. 17-21.

5. D. Richman. "Color-Carrier Reference Phase Synchronization Accuracy in NTSC Color Television," Proceedings of the IRE, Vol. 42, January 1954, pp. 106-133.

6. M. Mancianti, F. Russo, and L. Verrazzani. "An Extension of Richman Analysis to the Second Order SCS," Proceedings of the IEEE, Vol. 62, March 1974, pp. 414-415.

7. A. Viterbi. "Acquisition and Tracking Behavior of Phase-Locked Loops," in Proceedings of the Symposium on Active Network and Feedback Systems, Polytechnic Press, New York, 1960.

APPENDIX D

IN-LOCK PERFORMANCE OF THE KU-BAND COSTAS LOCK DETECTOR

APPENDIX D

IN-LOCK PERFORMANCE OF THE KU-BAND COSTAS LOCK DETECTOR

by

Marvin K. Simon

1.0 INTRODUCTION

The PSK data demodulator unit of the Shuttle Ku-band forward link communications receiver is comprised of five subunits, one of which is a Costas lock detector. The primary purpose of this subunit is to sense the Costas loop signal acquisition state and send a "Costas lock" signal to the acquisition and track control logic when indeed it decides that the Costas loop has acquired the signal presented to its input. Since the initial frequency search and signal carrier acquisition must take place regardless of the type of signal format received from the TDRSS (CW carrier, data modulated carrier, spread spectrum carrier, or spread spectrum data modulated carrier), the lock detector must be capable of performing its sensing function under each of these conditions.

The basic carrier lock detector employed by Hughes Aircraft Company (HAC) in the Ku-band design is a dithered type configuration and is illustrated in Figure 1.* This dithered lock detector when contrasted with the more conventional $I^2 - Q^2$ type of lock detector illustrated in Figure 2 is not unlike a comparison between a tau-dither loop and a delay-lock loop for PN tracking in the sense that, in the former, the carrier reference (PN clock) is time-shared over a single channel while in the latter it is simultaneously shared by two quadrature channels. In general, dithered type configurations (tracking loops or lock detectors) have the advantage of being insensitive to gain imbalances normally present in two channel configurations. On the other hand, because of the time sharing of the locally generated reference, they potentially suffer a 3 dB loss in performance as compared to the more conventional undithered type configuration.

---

*The actual HAC configuration includes a soft limiter inserted prior to the square-law detector to desensitize this detector to front end gain variations [3]. A detailed analysis of the dithered lock detector with soft limiter is considerably more difficult than that treated here and will be discussed in a future report. Suffice it to say that the basic analysis technique used here to account for the effect of the dither can also be employed for a lock detector with soft limiter.

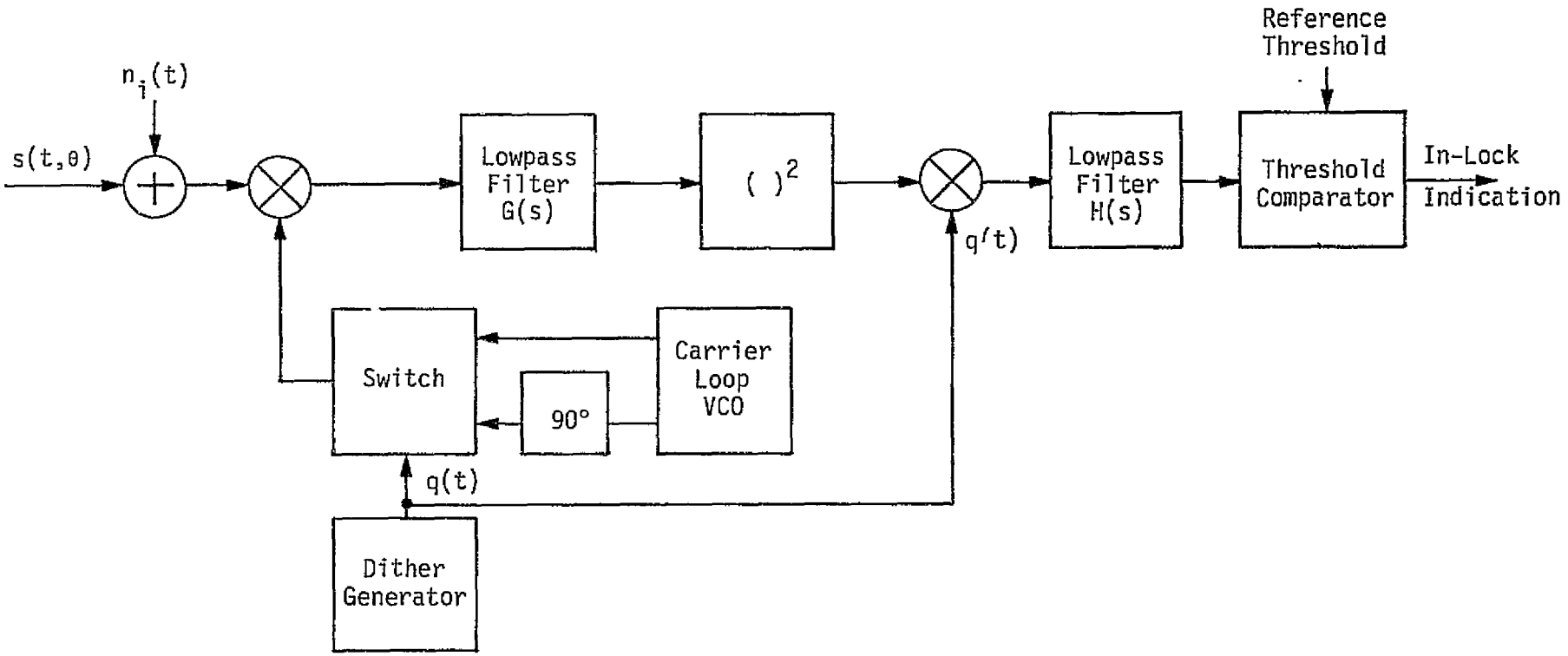

Figure 1. Dither-Type Costas Lock Detector

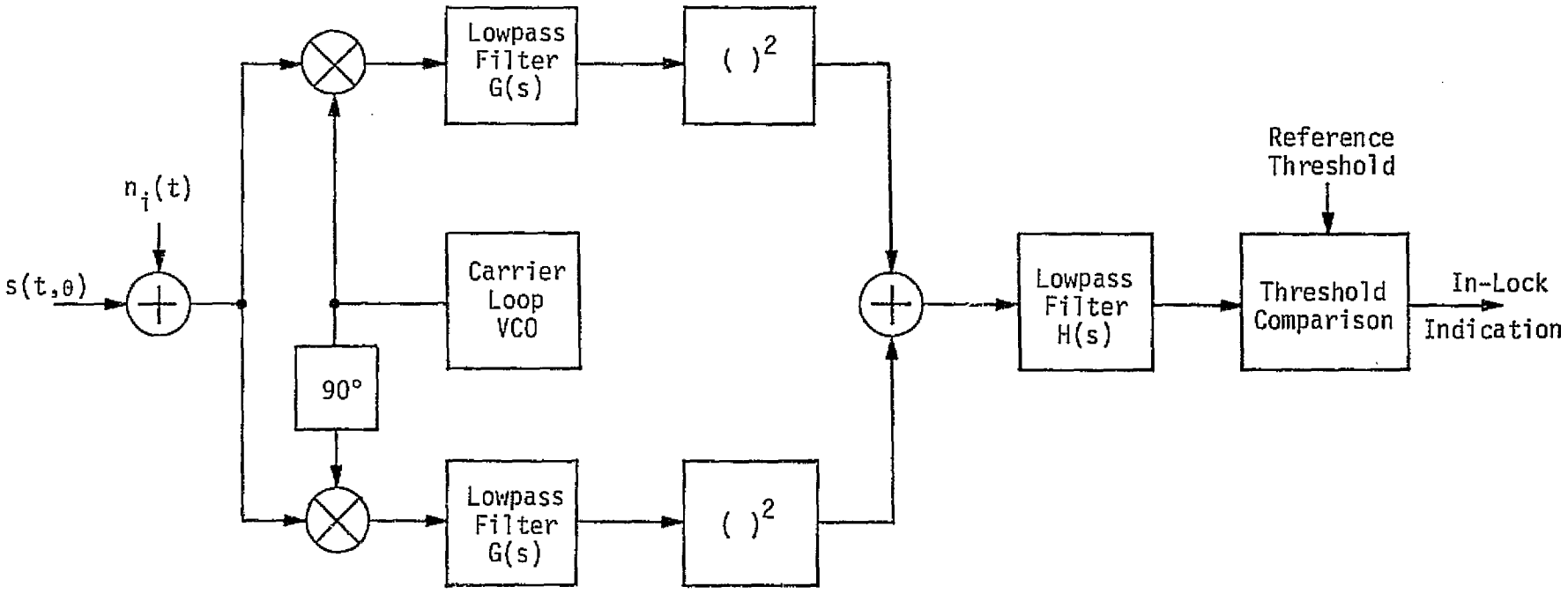

Figure 2. Conventional $I^2 - Q^2$ Type Costas Lock Detector

In this report, we apply the techniques used by the author in analyzing a PN tau-dither tracking loop [1] to analyzing the dithered lock detector of Figure 1. When the dither frequency is much smaller than the data rate, then the results resemble those obtained by LaFlame in [2] except for a modification by a factor of two of the signal × noise term in the lock detector signal-to-noise ratio. On the other hand, choosing a dither frequency much closer to the data rate can overcome much of the 3 dB loss commonly associated with dither type configurations. This conclusion has already been demonstrated in the comparison between loop signal-to-noise ratios of the PN tau-dither loop and delay-lock loop made in [1].

2.0 DITHERED LOCK DETECTOR MODEL AND ANALYSIS

Consider the dithered lock detector illustrated in Figure 1 whose operation is described as follows. The received signal plus noise is alternately (as opposed to simultaneously) correlated with quadrature (90° phase shifted) versions of the reference signal generated by the carrier tracking loop VCO. The correlation so produced is lowpass filtered, square-law detected, and alternately inverted by the dither signal $q(t)$. This gives rise to a signal which, when further lowpass filtered to remove the dither frequency and its harmonics, is (in the absence of noise) proportional to the cosine of twice the phase error between the input signal $s(t,\theta)$ and the VCO reference. Comparison of this signal (in noise) against a reference threshold allows determination of whether the loop is in-lock or out-of-lock. The remainder of this section is a mathematical characterization of the above statements.

For the purpose of analysis, it can be shown (analogous to the approach taken in [1]) that, when the dither frequency is low relative to the noise bandwidth of the lowpass filter preceding the square-law detector, then the dithered lock detector has the equivalent loop model illustrated in Figure 3. The received signal $x(t) = s(t,\theta) + n_i(t)$ can be modeled as*

*We pursue in detail here the case where the input signal is a data modulated carrier. All other cases corresponding to the other possible input signal formats can be easily deduced from the results derived and presented here.

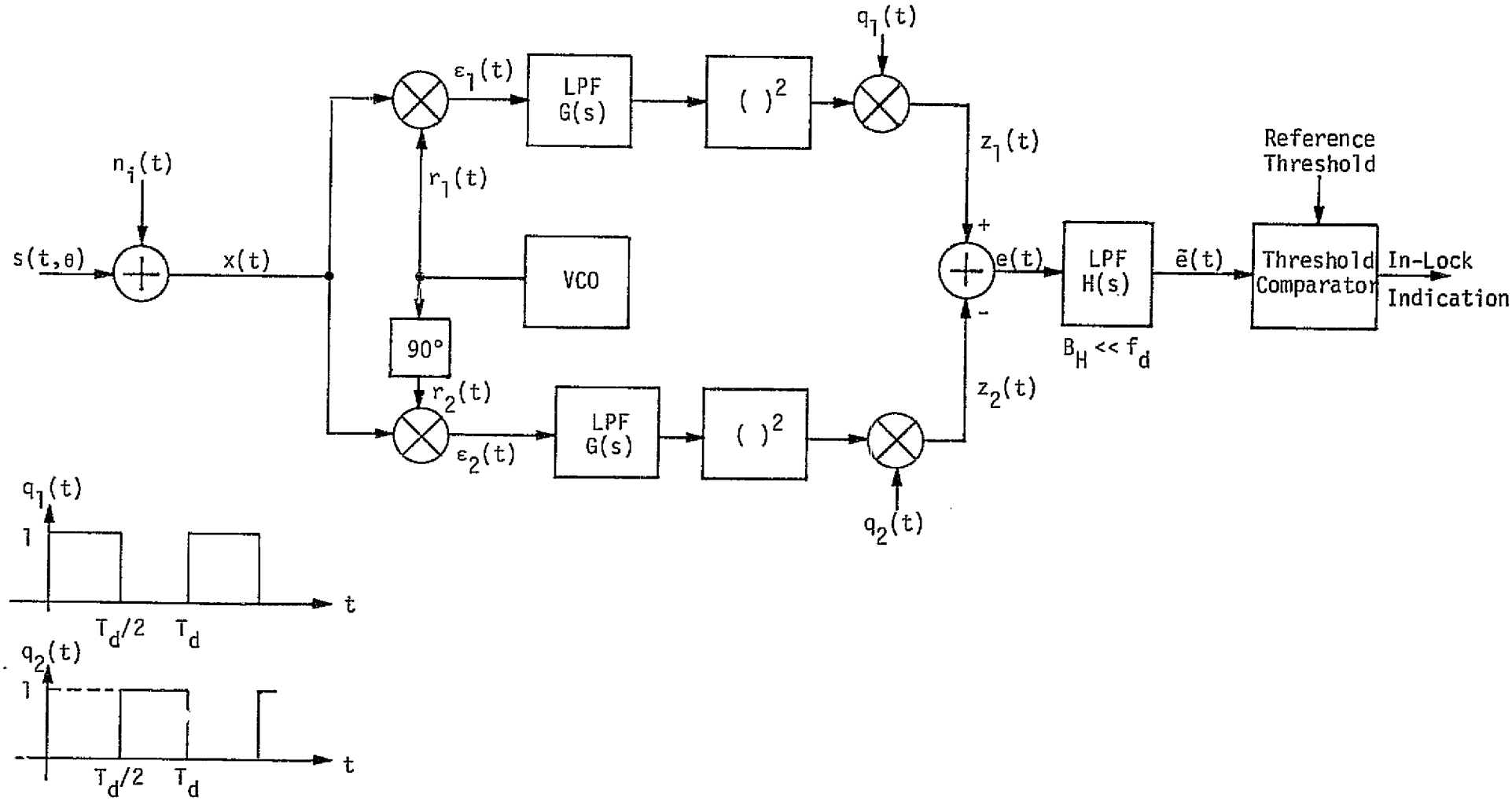

Figure 3. Equivalent Model for Dither-Type Lock Detector

$$x(t) = \sqrt{2S}\, m(t) \sin \phi(t) + n_i(t) = s(t) + n_i(t), \qquad (1)$$

where $\phi(t) \triangleq \omega_0 t + \theta(t)$ with ω_0 the radian carrier frequency and $\theta(t) = \Omega_0 t + \theta_0$ the input phase to be estimated, S is the average signal power, $m(t)$ is the data modulation (a ± 1 digital waveform), and $n_i(t)$ is the additive channel noise which can be expressed in the form of a narrowband process about the actual frequency of the input observed data, i.e.,

$$n_i(t) = \sqrt{2}\,\{N_c(t) \cos \phi(t) - N_s(t) \sin \phi(t)\}, \qquad (2)$$

where $N_c(t)$ and $N_s(t)$ are approximately statistically independent, stationary, white Gaussian noise processes with single-sided noise spectral density N_0 W/Hz and single-sided bandwidth $B < \omega_0/2\pi$. Since the equivalent of the dithered reference signals, namely, $r_1(t)$ and $r_2(t)$, can be represented as

$$\begin{aligned} r_1(t) &= \sqrt{2}\, K_1 \sin \hat{\phi}(t) \\ r_2(t) &= \sqrt{2}\, K_1 \cos \hat{\phi}(t), \end{aligned} \qquad (3)$$

then letting K_m denote the input multiplier gain and ignoring second harmonic terms, the signal input to the lowpass filter with transfer function $H(s)$ is given by

$$\begin{aligned} e(t) &= z_1(t) - z_2(t) \\ &= K_1^2 K_m^2 S \hat{m}^2(t) [q_1(t) \cos^2 \phi(t) - q_2(t) \sin^2 \phi(t)] \\ &\quad + K_1^2 K_m^2 \Big\{ \hat{N}_c^2(t) [q_1(t) \sin^2 \phi(t) - q_2(t) \cos^2 \phi(t)] \\ &\qquad + \hat{N}_s^2(t) [q_1(t) \cos^2 \phi(t) - q_2(t) \sin^2 \phi(t)] \\ &\qquad + \hat{N}_c(t) \hat{N}_s(t) \sin 2\phi(t) \\ &\qquad - 2\sqrt{S}\, \hat{m}(t) \Big[q_1(t) \cos \phi(t) (\hat{N}_c(t) \sin \phi(t) + \hat{N}_s(t) \cos \phi(t)) \\ &\qquad\qquad + q_2(t) \sin \phi(t) (\hat{N}_c(t) \cos \phi(t) - \hat{N}_s(t) \sin \phi(t)) \Big] \Big\} \end{aligned} \qquad (4)$$

where $\phi(t) \triangleq \phi(t) - \hat{\phi}(t)$ is the phase error between the input signal $s(t,\theta)$ and the equivalent VCO reference $r_1(t)$, and the "hats" on $m(t)$, $N_c(t)$ and $N_s(t)$ denote filtering by the lowpass filter with transfer function $G(s)$. The signal component of $\tilde{e}(t)$ [the result of passing $e(t)$ of (4) through $H(s)$] is easily seen to be

$$g(2\phi) = S K_1^2 K_m^2 \overline{\langle \hat{m}^2(t) \rangle} \langle [q_1(t) \cos^2 \phi(t) - q_2(t) \sin^2 \phi(t)] \rangle \quad (5)$$

where the overbar denotes statistical expectation and $\langle\rangle$ denotes time averaging produced by the lowpass nature of $H(s)$ relative to the data rate of $m(t)$ and the fundamental dither frequency $f_d = 1/T_d$ of $q_1(t)$ and $q_2(t)$. Since the loop bandwidth is ordinarily designed to be much narrower than the dither frequency, we can ignore the time dependence of $\phi(t)$ relative to that of $q_1(t)$ and $q_2(t)$. Furthermore, it has been previously shown that, for $m(t)$ a random pulse train, i.e.,

$$m(t) = \sum_{n=-\infty}^{\infty} a_n \, p(t - nT_s); \qquad a_n = \pm 1$$

$$E\{a_n a_m\} = \delta_{mn}, \quad (6)$$

with $p(t)$ denoting the symbol pulse shape, time limited on the symbol interval $(0,T_s)$, then

$$\overline{\langle \hat{m}^2(t) \rangle} \triangleq D_m = \int_{-\infty}^{\infty} S_m(f) \, |G(j2\pi f)|^2 \, df, \quad (7)$$

with $S_m(f)$ denoting the power spectral density of $m(t)$. Thus, since from the illustrations of $q_1(t)$ and $q_2(t)$ in Figure 3, it is obvious that

$$\langle q_1(t) \rangle = \langle q_2(t) \rangle = \frac{1}{2}, \quad (8)$$

we have, after combining (5), (7) and (8), the result

$$g(2\phi) = K_1^2 K_m^2 S D_m \left(\frac{\cos 2\phi}{2} \right). \quad (9)$$

The equivalent signal for the conventional $I^2 - Q^2$ lock detector of Figure 2 would be identical to (9) except multiplied by a factor of 2.

3.0 STATISTICAL CHARACTERIZATION OF THE EQUIVALENT NOISE

The equivalent noise component of e(t) (ignoring the self-modulation noise) is easily seen to be*

$$n_e(t) = K_1^2 K_m^2 n_e'(t) , \tag{10}$$

where

$$n_e'(t) = -q_2(t)\hat{N}_c^2(t) + q_1(t)\hat{N}_s^2(t) - 2\sqrt{S}\, q_1(t)\hat{m}(t)\hat{N}_s(t) . \tag{11}$$

The power spectral density N_e of the equivalent noise process at the input to the threshold comparator can be determined by approximating $n_e'(t)$ as a delta-correlated process with correlation function

$$\begin{aligned} R_e'(\tau) &\triangleq \left\langle \overline{n_e'(t)\, n_e'(t+\tau)} \right\rangle \\ &= [R_{q_1}(\tau) + R_{q_2}(\tau)][2R_{\hat{N}}^2(\tau) + R_{\hat{N}}^2(0)] \\ &\quad - R_{\hat{N}}^2(0)\left[R_{q_1q_2}(\tau) + R_{q_2q_1}(\tau)\right] + 4S\, R_{\hat{m}}(\tau)\, R_{q_1}(\tau)\, R_{\hat{N}}(\tau) , \end{aligned} \tag{12}$$

where

$$\begin{aligned} R_{q_1}(\tau) &\triangleq \overline{q_1(t)\, q_1(t+\tau)} \\ R_{q_2}(\tau) &\triangleq \overline{q_2(t)\, q_2(t+\tau)} \\ R_{q_1q_2}(\tau) &\triangleq \overline{q_1(t)\, q_2(t+\tau)} \\ R_{q_2q_1}(\tau) &\triangleq \overline{q_2(t)\, q_1(t+\tau)} \end{aligned} \tag{13}$$

and

$$R_{\hat{m}}(\tau) \triangleq \left\langle \overline{\hat{m}(t)\,\hat{m}(t+\tau)} \right\rangle = \int_{-\infty}^{\infty} S_m(f)\, |G(j2\pi f)|^2\, e^{j2\pi f\tau}\, df$$

$$R_{\hat{N}}(\tau) \triangleq \overline{\hat{N}_c(t)\,\hat{N}_c(t+\tau)} = \hat{N}_s(t)\,\hat{N}_s(t+\tau) = \frac{N_0}{2}\int_{-\infty}^{\infty} |G(j2\pi f)|^2\, e^{j2\pi f\tau}\, d\tau . \tag{14}$$

---

*Since the carrier loop signal-to-noise ratio is typically large, it is only necessary to evaluate the equivalent lock detector noise at $\phi = 0$.

Then,

$$N_e = K_1^4 K_m^4 N_e' = K_1^4 K_m^4 \left[2 \int_{-\infty}^{\infty} R_e'(\tau)\, d\tau \right], \tag{15}$$

From the defining illustrations of $q_1(t)$ and $q_2(t)$ in Figure 3 and their autocorrelation and cross-correlation functions illustrated in Figure 4, we find that

$$R_{q_1 q_2}(\tau) = R_{q_2 q_1}(\tau)$$

$$R_{q_1}(\tau) = R_{q_2}(\tau) = \frac{1}{2} - R_{q_1 q_2}(\tau) \triangleq R_q(\tau). \tag{16}$$

Substituting (16) into (12) gives

$$R_e'(\tau) = (4R_q(\tau) - 1)\, R_{\hat{N}}^2(0) + 4R_q(\tau)\, R_{\hat{N}}^2(\tau) + 4S\, R_{\hat{m}}(\tau)\, R_q(\tau)\, R_{\hat{N}}(\tau). \tag{17}$$

Noting that

$$\int_{-\infty}^{\infty} (4R_q(\tau) - 1)\, d\tau = 0 \tag{18}$$

and using Parseval's theorem gives the alternate frequency domain interpretation of N_e', namely,

$$N_e' = 8 \int_{-\infty}^{\infty} [S_{\hat{N}}(f) * S_{\hat{N}}(f)]\, S_q(-f)\, df + 8S \int_{-\infty}^{\infty} [S_{\hat{m}}(f) * S_{\hat{N}}(f)]\, S_q(-f)\, df, \tag{19}$$

where the asterisk denotes convolution and

$$S_{\hat{N}}(f) = \mathcal{F}\{R_{\hat{N}}(\tau)\} = \frac{N_0}{2} |G(j2\pi f)|^2$$

$$S_{\hat{m}}(f) = \mathcal{F}\{R_{\hat{m}}(\tau)\} = S_m(f)\, |G(j2\pi f)|^2$$

$$S_q(f) = \mathcal{F}\{R_q(\tau)\} = \frac{1}{4}\, \delta(f) + \frac{1}{4} \sum_{\substack{n=-\infty \\ n \text{ odd}}}^{\infty} \left(\frac{2}{n\pi}\right)^2 \delta\left(f - \frac{n}{T_d}\right). \tag{20}$$

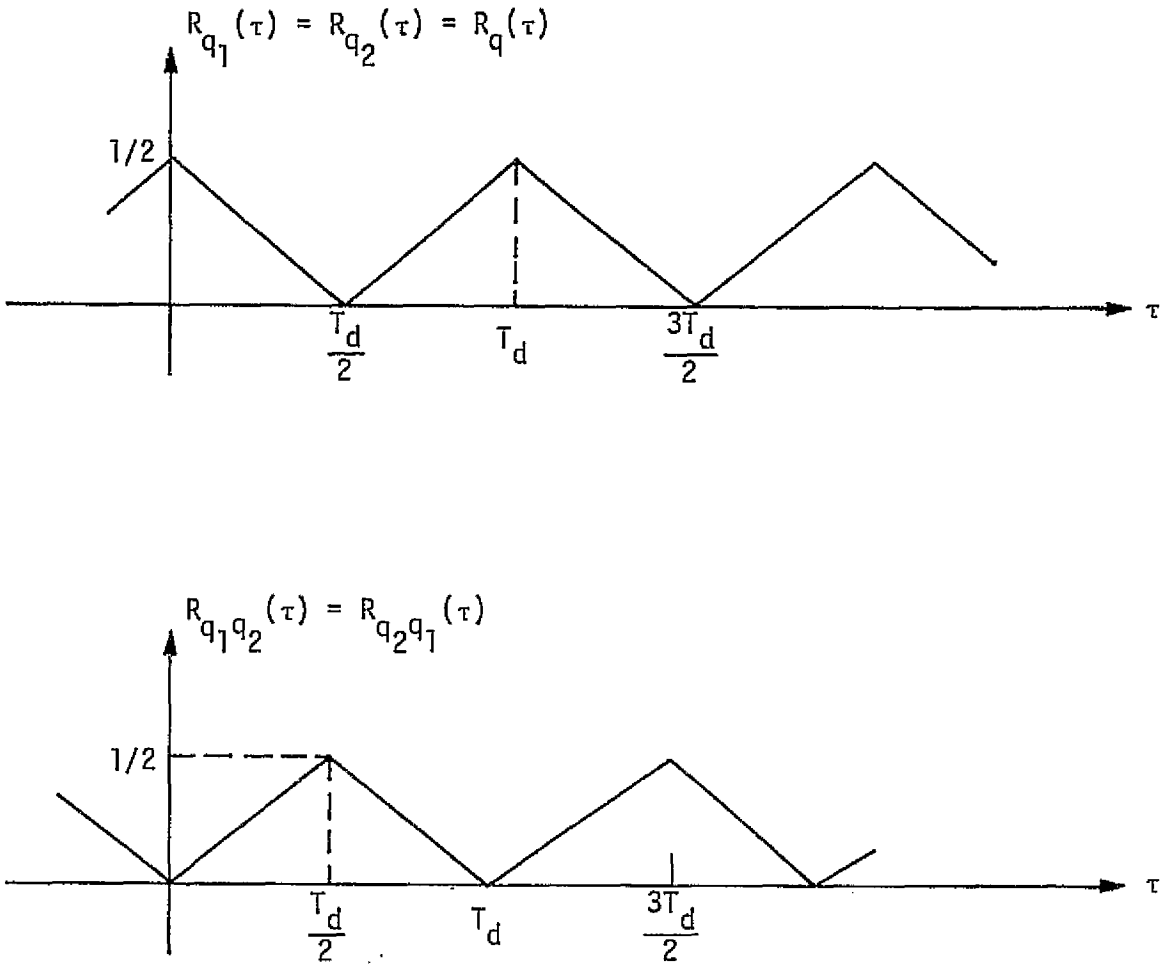

Figure 4. Autocorrelation Functions of $q_1(t)$ and $q_2(t)$ and Cross-Correlation Function of $q_1(t)$ and $q_2(t)$

Substituting (20) into (19), we obtain, after much simplification,

$$N_e' = S N_0 D_m^2 \left\{ \frac{K_D' + \frac{K_L'}{\rho_i D_m}}{D_m} \right\}, \tag{21}$$

where

$$K_D' = K_D + 2 \sum_{n=1,3,5\ldots}^{\infty} \left(\frac{2}{n\pi}\right)^2 K_{D_n}$$

$$K_L' = K_L + 2 \sum_{n=1,3,5\ldots}^{\infty} \left(\frac{2}{n\pi}\right)^2 K_{L_n}$$

$$K_{D_n} = \frac{\int_{-\infty}^{\infty} S_m(f)\, |G(j2\pi f)|^2 \left| G\left[j2\pi \left(\frac{n}{T_d} - f \right) \right] \right|^2 df}{\int_{-\infty}^{\infty} S_m(f)\, |G(j2\pi f)|^2 \, df}$$

$$K_{L_n} = \frac{\int_{-\infty}^{\infty} |G(j2\pi f)|^2 \left| G\left[j2\pi \left(\frac{n}{T_d} - f \right) \right] \right|^2 df}{\int_{-\infty}^{\infty} |G(j2\pi f)|^2 \, df} \tag{22}$$

with

$$K_D \triangleq \frac{\int_{-\infty}^{\infty} S_m(f)\, |G(j2\pi f)|^4 \, df}{\int_{-\infty}^{\infty} S_m(f)\, |G(j2\pi f)|^2 \, df}$$

$$K_L \triangleq \frac{\int_{-\infty}^{\infty} |G(j2\pi f)|^4 \, df}{\int_{-\infty}^{\infty} |G(j2\pi f)|^2 \, df}, \tag{23}$$

and B_i denoting the two-sided noise bandwidth of the arm filter $G(j2\pi f)$, i.e.,

$$B_i \triangleq \int_{-\infty}^{\infty} |G(j2\pi f)|^2 \, df. \tag{24}$$

Also, in (21),

$$\rho_i \triangleq \frac{S}{N_0 B_i} \tag{25}$$

denotes the signal-to-noise ratio in this bandwidth.

4.0 OUTPUT SIGNAL-TO-NOISE RATIO

Since the single-sided noise bandwidth B_H of the output low-pass filter H(s) is much less that the dither frequency f_d, then the output $\tilde{e}(t)$ of this filter (threshold comparator input) is a Gaussian random variable with mean $\overline{\tilde{e}(t)} = g(\phi)$ [see (9)] and variance $\sigma_{\tilde{e}}^2 = N_e B_H = K_1^4 K_m^4 N_e' B_H$ where N_e' is given by (21). Thus, the lock detector output signal-to-noise ratio ρ_0, which determines the possibility of detecting lock when the carrier loop is indeed in lock, is given by

$$\rho_0 = \frac{\overline{(\tilde{e}(t))}^2}{\sigma_{\tilde{e}}^2} = \frac{S^2 D_m^2 \cos^2 2\phi}{4 S N_0 D_m^2 \left\{ \dfrac{K_D' + \dfrac{K_L'}{\rho_i D_m}}{D_m} \right\} B_H}$$

$$= \frac{1}{4}\left(\frac{S}{N_0 B_H}\right) S_L' \cos^2 2\phi \ , \tag{26}$$

where

$$S_L' \triangleq \frac{D_m}{K_D' + \dfrac{K_L'}{\rho_i D_m}} \tag{27}$$

is the dithered lock detector "squaring loss" factor. The equivalent expressions for the conventional $I^2 - Q^2$ lock detector would be

$$\rho_0 = \frac{1}{4}\left(\frac{S}{N_0 B_H}\right) S_L \cos^2 2\phi \ , \tag{28}$$

where

$$S_L = \frac{D_m}{K_D + \dfrac{K_L}{\rho_i D_m}} \ . \tag{29}$$

Thus, a comparison of the performances of the dithered and undithered (conventional) lock detectors depends simply on the ratio of S_L' to S_L, namely,

$$\frac{S_L'}{S_L} = \frac{K_D + \dfrac{K_L}{\rho_i D_m}}{K_D' + \dfrac{K_L'}{\rho_i D_m}} . \tag{30}$$

Clearly, from the definitions of K_{D_n} and K_{L_n} as given in (22), we see that $K_{D_n} < K_D$ and $K_{L_n} < K_L$ for any n, in particular, n odd and T_d finite. Thus, from (22),

$$K_D' < K_D + \frac{8}{\pi^2} \sum_{n=1,3,5\ldots}^{\infty} \frac{1}{n^2} K_D = 2K_D$$

$$K_L' < K_L + \frac{8}{\pi^2} \sum_{n=1,3,5\ldots}^{\infty} \frac{1}{n^2} K_L = 2K_L . \tag{31}$$

Substituting the bounds of (31) into (30), we find that

$$\frac{S_L'}{S_L} > \frac{1}{2} , \tag{32}$$

or equivalently, the output signal-to-noise ratio of the dithered lock detector is, at worst, 3 dB poorer than that of the undithered type. Equation (32) approximately holds with equality when the dither frequency is chosen much lower than the data. This appears to be the case corresponding to the present Hughes Aircraft Company Costas lock detector design where the dither signal is a 1.5 kHz square wave and the data rate for a data modulated carrier is 216 kbps. Thus, for this situation, we have from (26) and (32) that

$$\rho_0 \cong \frac{1}{2}\left[\frac{1}{4}\left(\frac{S}{N_0 B_H}\right) S_L \cos^2 2\phi\right] , \tag{33}$$

with S_L given by (29). This result agrees with that obtained by LaFlame in [2] if the signal × noise term in his squaring loss (not

the same definition as used here) is divided by 2. The reason for this discrepancy between the two results is that LaFlame upper bounds the output noise rather than computing it exactly. Thus, despite the fact that he recognizes that the signal × noise term in the output noise "is absent during the second half dither period" (see page 10 of [2]), he fails to divide its contribution by 2 to account for this effect.

In conclusion, we reiterate the fact that the dithered lock detector is 3 dB worse in output signal-to-noise ratio only when the dither frequency is much less than the data rate. If the dither frequency is raised to be on the order of (but still less than) the data rate, then analogous to the results obtained in [1], the 3 dB "dither penalty" can be significantly reduced.

REFERENCES

1. M. K. Simon. "Noncoherent Pseudonoise Code Tracking Performance of Spread Spectrum Receivers," IEEE Transactions on Communications, Vol. COM-25, No. 3, March 1977, pp. 327-345.

2. D. T. LaFlame. "Costas Lock Detector Analysis," Internal HAC Memorandum HS237-896, July 15, 1977.

3. D. T. LaFlame. "Updated Costas Lock Detector Analysis," Internal HAC Memorandum HS237-1130, October 7, 1977.

APPENDIX E

PERFORMANCE ANALYSIS OF THE KU-BAND FORWARD LINK BIT SYNCHRONIZER

APPENDIX E

PERFORMANCE ANALYSIS OF THE KU-BAND FORWARD LINK BIT SYNCHRONIZER

by

Marvin K. Simon

1.0 INTRODUCTION

The Signal Processor Assembly (SPA) for the Ku-band forward link performs data and signal processing in one of two (special/nominal) operating modes. An important part of the signal processing function is the establishment of an accurate bit synchronization reference clock in order that data detection be accomplished with a small signal-to-noise ratio (SNR) degradation. Since, in the nominal mode, the data is a 216 kbps biphase-L (Manchester coded) waveform, then the bit rate clock established by the bit synchronizer will possess a half-bit phase ambiguity, i.e., the loop can lock with equal probability either in-phase or half a bit out of phase with respect to the input biphase-L waveform. Thus, the SPA must also include a phase ambiguity resolver whose purpose is to resolve which of the two possible bit rate clock phases is indeed in-phase with the input data waveform.

This appendix presents an analysis of the performance of the bit synchronizer which is proposed and being implemented by Hughes Aircraft Company (HAC) for the Ku-band forward link to the Space Shuttle Orbiter (SSO) vehicle. Preliminary analysis results obtained by members of the Space and Communications Group of HAC were reported in June 1977 [1]. A description of the principles of operation of the bit synchronizer and ambiguity resolver also appeared in that document and later in the SPA Preliminary Design Review [2]. We shall begin by reviewing these principles of operation (see also [3]) and then proceed to characterize the average loop S-curve and power spectral density of the equivalent additive noise which are both necessary to represent the bit synchronizer as an equivalent phase-locked loop. Finally, the steady-state tracking performance of this loop will be given.

2.0 BIT SYNCHRONIZER PRINCIPLES OF OPERATION

A block diagram of the Hughes Ku-band bit synchronizer suitable for analysis purposes is illustrated in Figure 1. Assuming SPA nominal mode of operation, the input is a 216 kbps Manchester coded data waveform plus additive white Gaussian noise with single-sided power spectral density N_0. The synchronizer extracts its timing information directly from the above input (data-derived or self-synchronization) and produces a twice-bit-rate (512 kHz) clock as a timing reference. The bit rate clock and its complement are obtained by dividing down the twice-bit-rate clock by a factor of 2. These three clocks (twice-bit-rate, bit-rate, and bit-rate-complement) are used to process the input in in-phase and quadrature channels whose outputs when multiplied form the components of the loop error signal. The details of this processing are described as follows.

The input signal is multiplied by the twice-bit-rate clock and then the bit-rate clock or its complement which are both used to gate (in each bit interval) half bit segments of the multiplier outputs to two in-phase integrate-and-dump (I&D) circuits. For the midbit I&D, the half-bit integration symmetrically (assuming perfect timing) spans the midbit position. The output of this I&D is two-bit digitized by Digitizer 1 in a way which is equivalent to null-zone detection of the polarity of the NRZ data bits (alternately, the polarity of the midbit Manchester transition). For the between-bit I&D, the half-bit integration symmetrically spans the NRZ bit transition position. Thus, the output of Digitizer 2 is equivalent to null-zone detection of the NRZ data transitions.

The input Manchester coded signal plus noise is also gated by the bit-rate clock and its complement, without first being multiplied by the twice-bit-rate clock, to between-bit and midbit quadrature I&D circuits, respectively. The outputs of these I&Ds are noisy measures of the timing offset between the input and the locally generated bit-rate clock. Multiplying the respective in-phase and quadrature I&D outputs and summing their sample-and-hold values generate an error signal suitable for closing the bit synchronization loop.

Timing diagrams of the various waveforms formed within the loop in the absence of noise are illustrated in Figure 2a for $0 \leq \lambda \leq \frac{1}{4} - \eta/2$

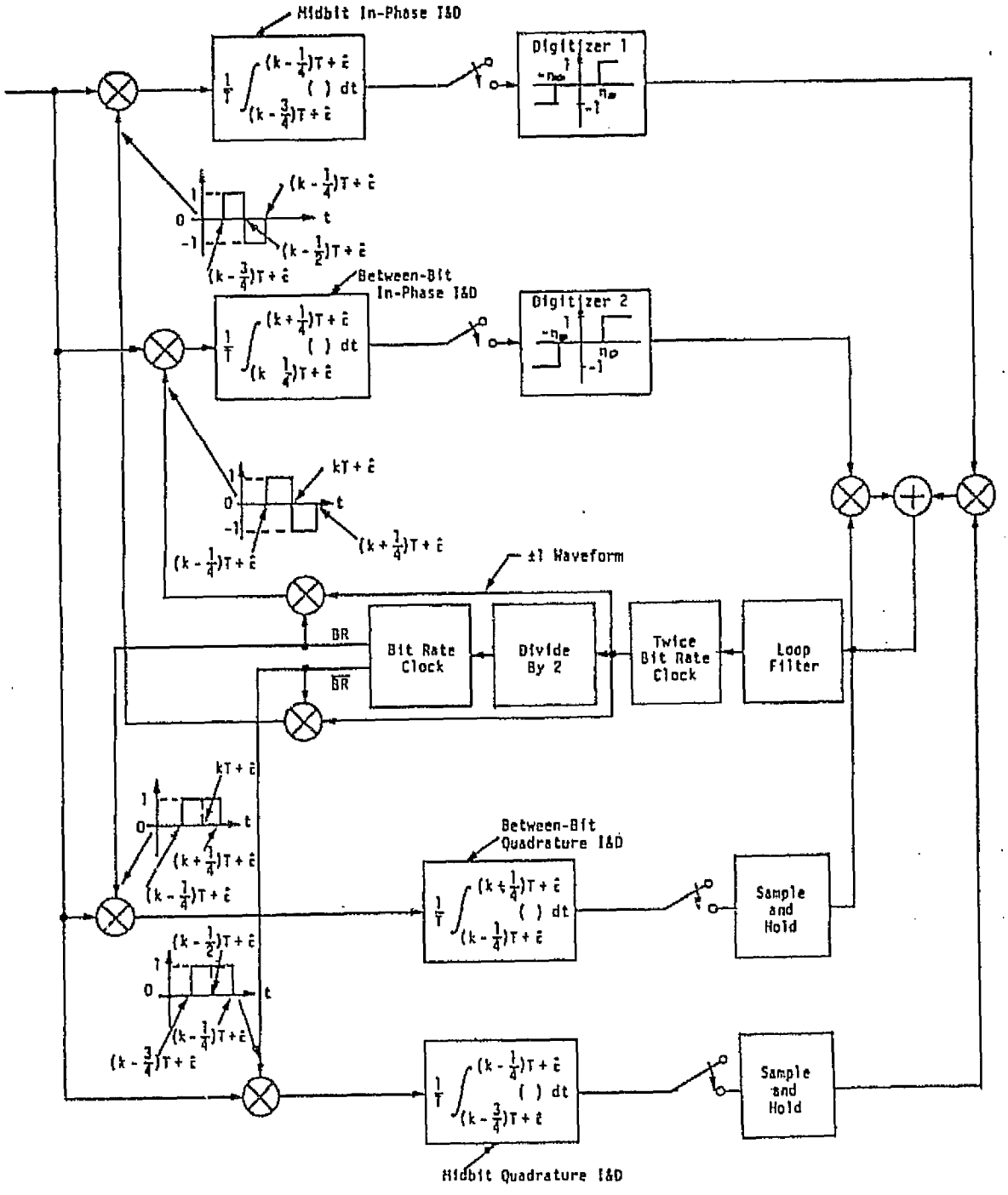

Figure 1. Bit Synchronizer Functional Block Diagram

and in Figure 2b for $\frac{1}{4} \leq \lambda \leq \frac{1}{2} - \eta/2$, where λ is the relative timing error (normalized to the bit time) between the input and locally generated bit-rate clock and η is the threshold (normalized to the signal amplitude) of the null-zone detection. The corresponding loop error curve is illustrated in Figure 3 and is obtained by statistically averaging the error signal formed above over the data sequence (assuming an NRZ transition probability p_t). For the more realistic case where additive noise is present, a more detailed analysis is required to specify the bit synchronizer performance. This analysis is the subject of the next section.

3.0 STEADY-STATE TRACKING PERFORMANCE OF THE BIT SYNCHRONIZER

The techniques that will be employed in carrying out the steady-state tracking performance analysis of the HAC Ku-band bit synchronizer are analogous to those given in [4] where they are used to characterize the comparable performance of symbol synchronizers (with Manchester coded inputs) motivated by the maximum a posteriori (MAP) estimation approach. Similar techniques were previously used by the author to characterize the performance of symbol synchronizers with NRZ inputs [5]. Namely, under the assumption that the input timing offset ε is essentially constant over a large number of bit intervals and the usual assumption that the loop response $\hat{\varepsilon}$ is very slow with respect to a bit time T (i.e., $B_L T << 1$, where B_L is the single-sided loop noise bandwidth), the bit synchronizer of Figure 1 can be mathematically modeled as the continuous phase-locked loop given in Figure 4. Developing the equivalence between Figures 1 and 4 relies on finding (1) the average loop S-curve $g(\lambda)$ as a function of the normalized timing error $\lambda \triangleq (\varepsilon - \hat{\varepsilon})/T$, and (2) the two-sided power spectral density $S(\omega,\lambda)$ of the equivalent additive noise $n_\lambda(t)$. Once having determined these quantities, the steady-state performance can be found by application of the Fokker-Planck equation [5].

Referring to Figure 1, the signal and noise components of the various I&D outputs can be expressed mathematically as follows:

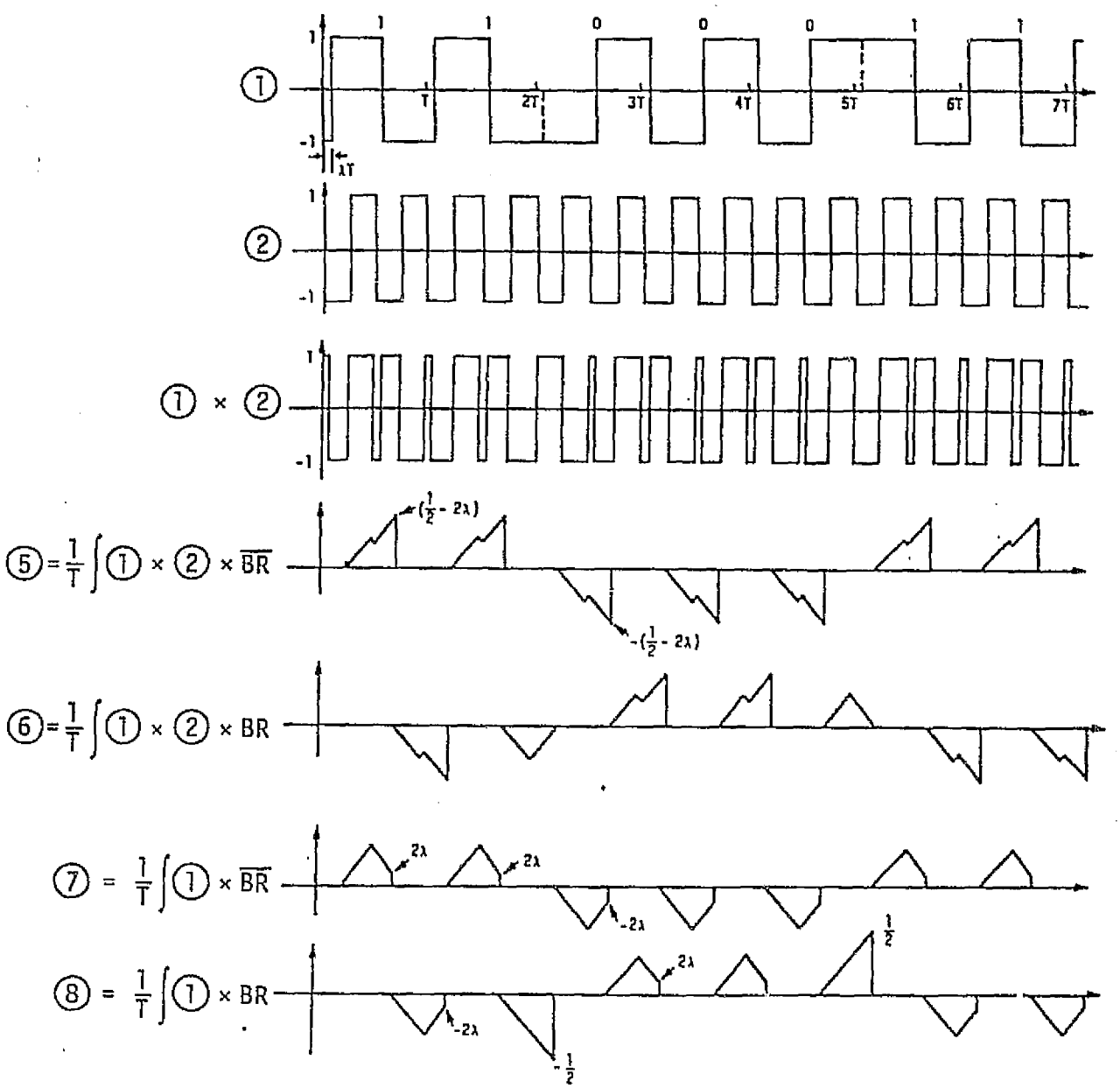

$$\lambda \triangleq \frac{\varepsilon - \hat{\varepsilon}}{T} \qquad (0 \leq \lambda \leq \frac{1}{4} - \frac{\eta}{2})$$

Figure 2a. Bit Synchronizer Timing Diagram

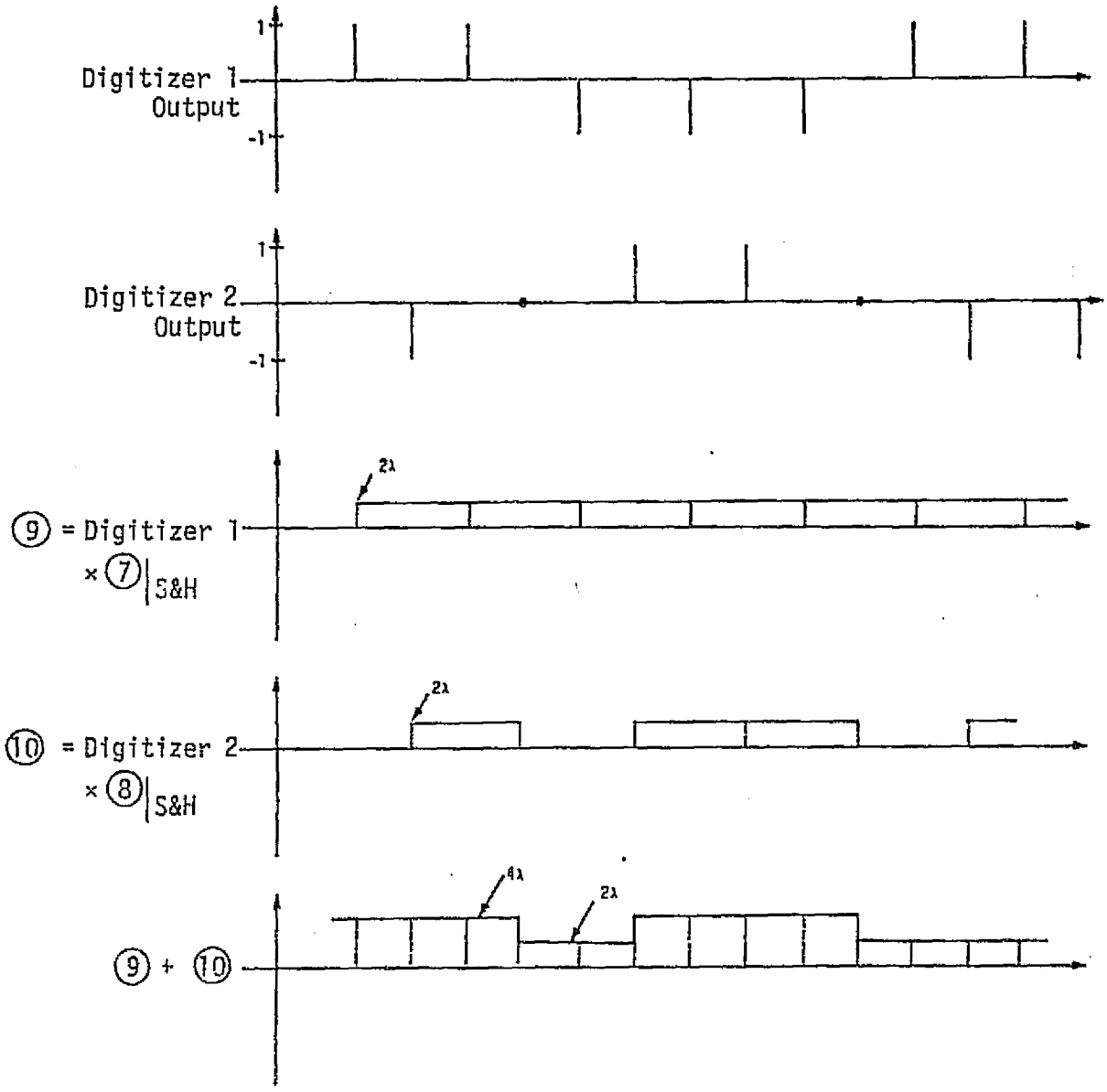

$$\overline{⑨ + ⑩} = (1 - p_t)\,4\lambda + p_t\,2\lambda = 4\lambda\left(1 - \frac{p_t}{2}\right)$$

p_t is NRZ transition probability S&H = Sample-and-Hold

Figure 2a. (continued)

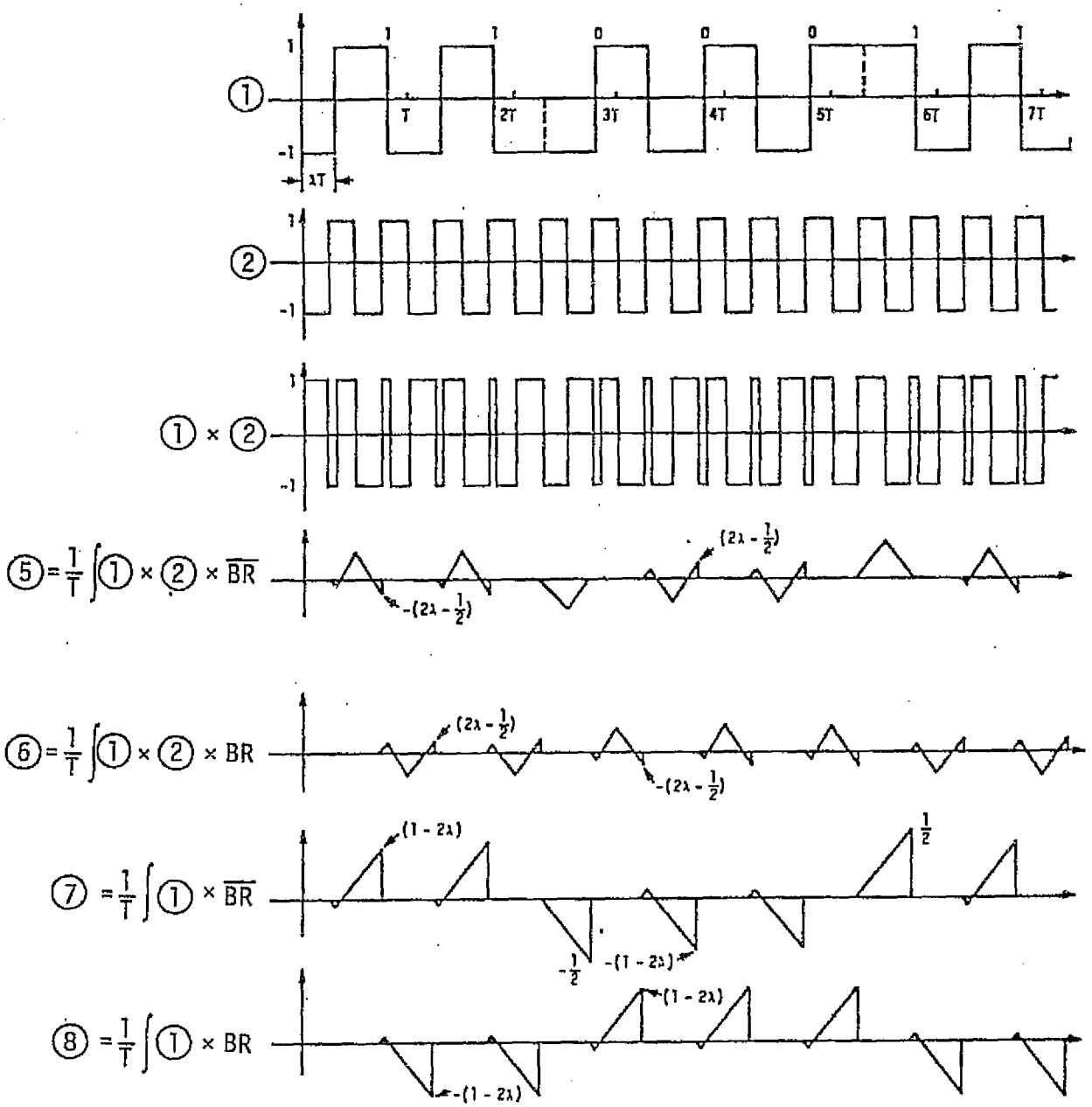

$$\left(\frac{1}{4}+\frac{n}{2} \leq \lambda \leq \frac{1}{2}\right)$$

Figure 2b. Bit Synchronizer Timing Diagram

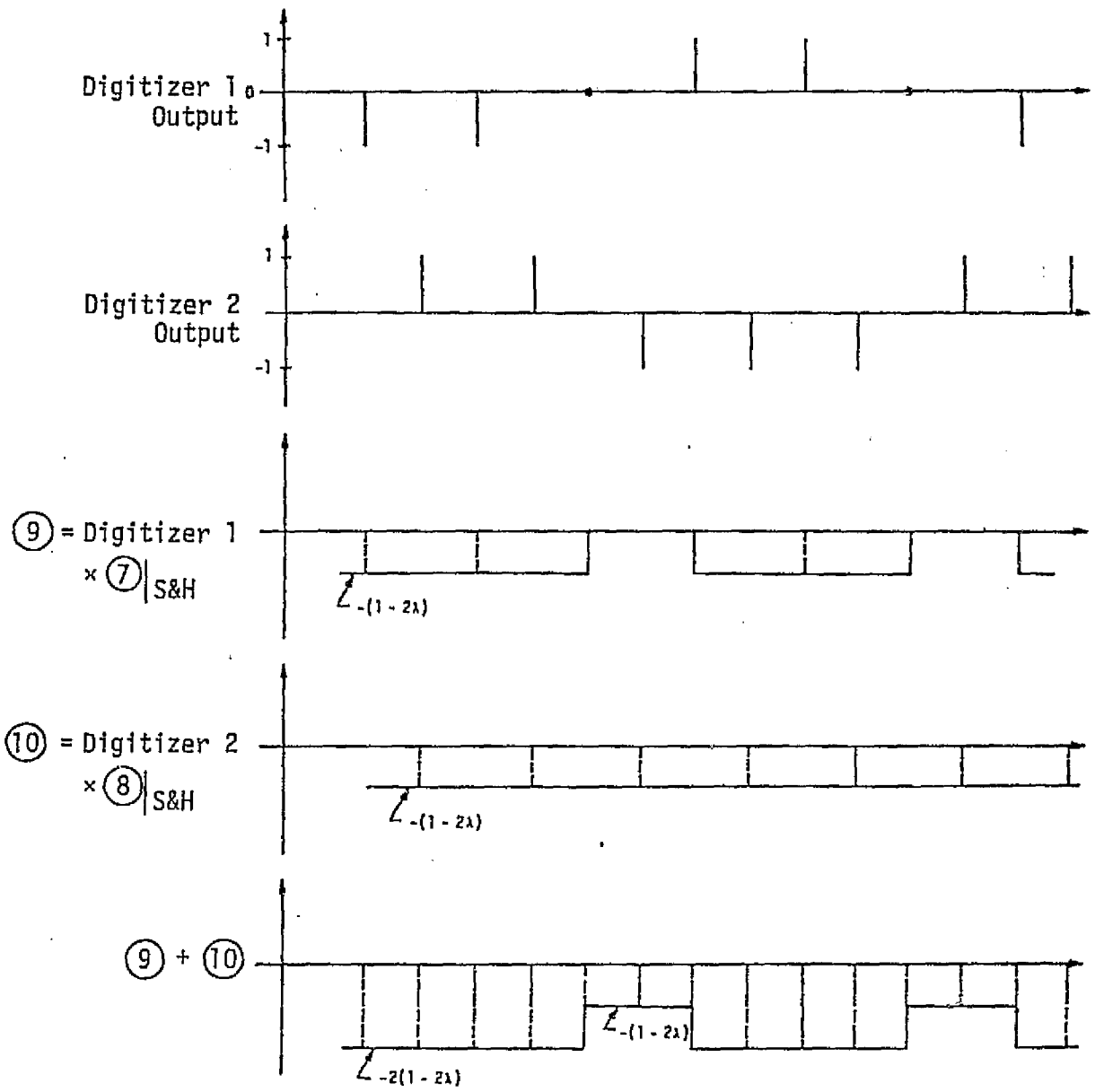

$$\overline{⑨ + ⑩} = -(1 - p_t)\,2(1 - 2\lambda) - p_t(1 - 2\lambda) = -2(1 - 2\lambda)\left(1 - \frac{p_t}{2}\right)$$

p_t is NRZ transition probability S&H = Sample-and-Hold

Figure 2b. (continued)

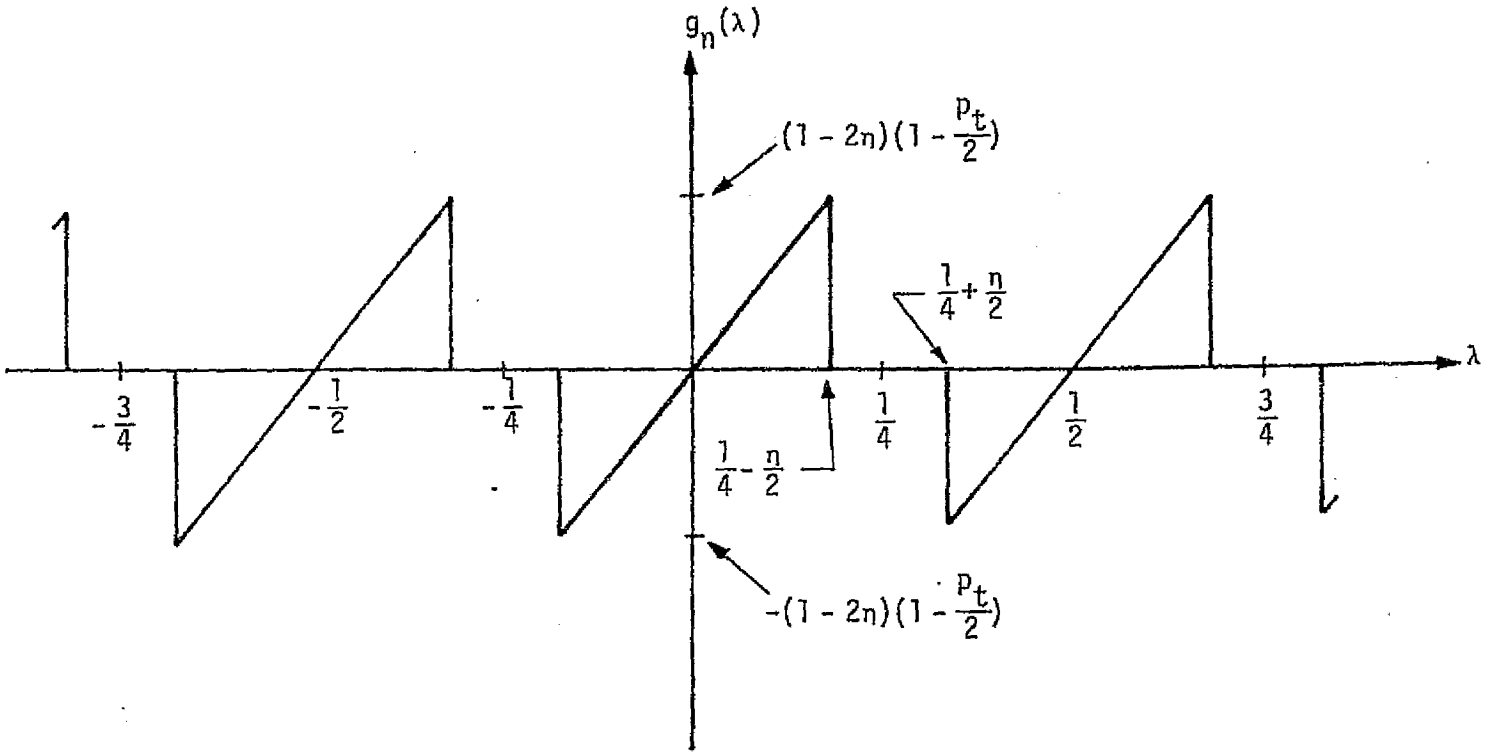

Figure 3. Equivalent Loop S-Curve (No Noise)

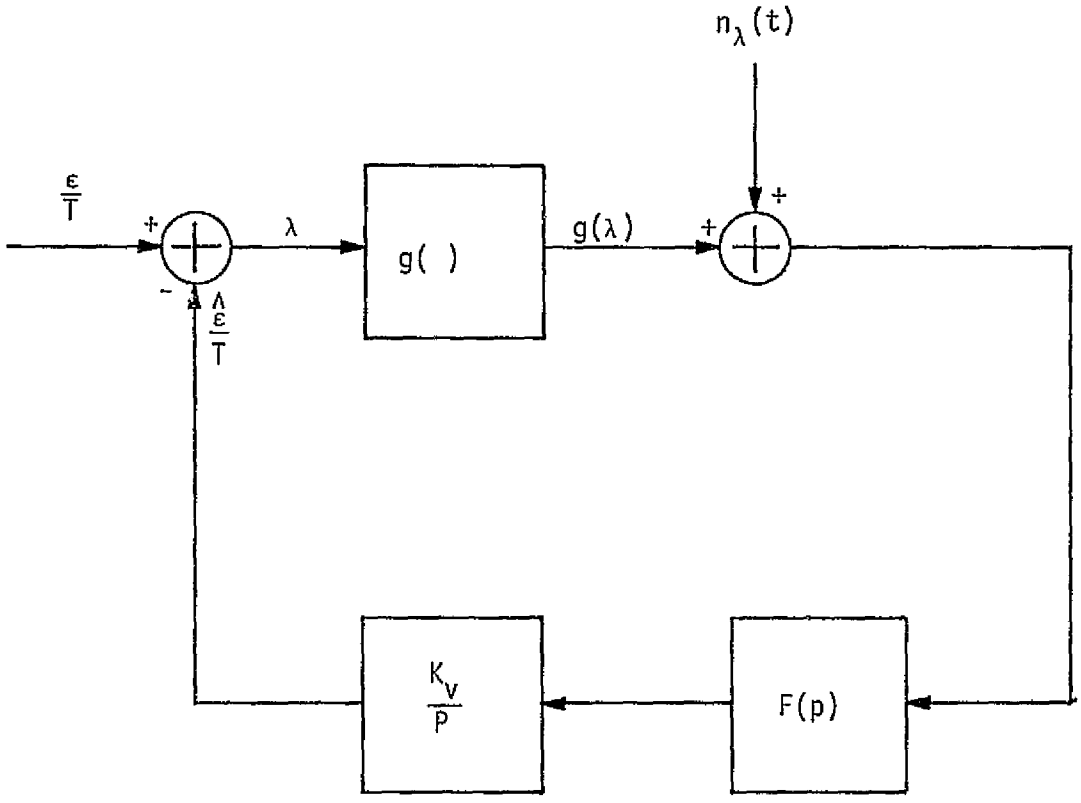

Figure 4. Equivalent Mathematical Model of a Phase-Locked Loop with Arbitrary Periodic Nonlinearity

Midbit

$$y_k \triangleq c_k + \nu_k; \qquad c_k = \frac{1}{T}\int_{(k-3/4)T+\hat{\varepsilon}}^{(k-1/2)T+\hat{\varepsilon}} s(t,\varepsilon)\,dt - \frac{1}{T}\int_{(k-1/2)T+\hat{\varepsilon}}^{(k-1/4)T+\hat{\varepsilon}} s(t,\varepsilon)\,dt$$

$$\nu_k = \underbrace{\frac{1}{T}\int_{(k-3/4)T+\hat{\varepsilon}}^{(k-1/2)T+\hat{\varepsilon}} n(t)\,dt}_{M_k} - \underbrace{\frac{1}{T}\int_{(k-1/2)T+\hat{\varepsilon}}^{(k-1/4)T+\hat{\varepsilon}} n(t)\,dt}_{N_k}$$

$$z_k \triangleq b_k + \mu_k; \qquad b_k = \frac{1}{T}\int_{(k-3/4)T+\hat{\varepsilon}}^{(k-1/4)T+\hat{\varepsilon}} s(t,\varepsilon)\,dt$$

$$\mu_k = \frac{1}{T}\int_{(k-3/4)T+\hat{\varepsilon}}^{(k-1/4)T+\hat{\varepsilon}} n(t)\,dt = M_k + N_k$$

$$I_k \triangleq \text{sgnull } y_k; \qquad e_k = z_k I_k \tag{1}$$

Between-Bit

$$y'_k \triangleq c'_k + \nu'_k; \qquad c'_k = \frac{1}{T}\int_{(k-1/4)T+\hat{\varepsilon}}^{kT+\hat{\varepsilon}} s(t,\varepsilon)\,dt - \frac{1}{T}\int_{kT+\hat{\varepsilon}}^{(k+1/4)T+\hat{\varepsilon}} s(t,\varepsilon)\,dt = c_{k+1/2}$$

$$\nu'_k = \underbrace{\frac{1}{T}\int_{(k-1/4)T+\hat{\varepsilon}}^{kT+\hat{\varepsilon}} n(t)\,dt}_{M'_k} - \underbrace{\frac{1}{T}\int_{kT+\hat{\varepsilon}}^{(k+1/4)T+\hat{\varepsilon}} n(t)\,dt}_{N'_k} = \nu_{k+1/2}$$

$$z'_k \triangleq b'_k + \mu'_k; \qquad b'_k = \frac{1}{T}\int_{(k-1/4)T+\hat{\varepsilon}}^{(k+1/4)T+\hat{\varepsilon}} s(t,\varepsilon)\,dt = b_{k+1/2}$$

$$\mu'_k = \frac{1}{T}\int_{(k-1/4)T+\hat{\varepsilon}}^{(k+1/4)T+\hat{\varepsilon}} n(t)\,dt = M'_k + N'_k = \mu_{k+1/2}$$

$$I'_k \triangleq \text{sgnull } y'_k; \qquad e'_k = z'_k I'_k. \tag{2}$$

In (1) and (2), the function "sgnull x" is the input-output characteristic of a "dead-zone" hard-limiter and is defined by

$$\text{sgnull } x = \begin{cases} 1; & x \geq \eta_0 \\ 0; & -\eta_0 \leq x < \eta_0 \\ -1; & x < -\eta_0 \end{cases} \tag{3}$$

Also, the input signal $s(t,\varepsilon)$ is the random pulse train

$$s(t,\varepsilon) = A \sum_{n=-\infty}^{\infty} d_n \, p(t - nT - \varepsilon) , \tag{4}$$

where A is the pulse amplitude, $p(t)$ is the unit Manchester pulse

$$p(t) = \begin{cases} 1; & 0 \leq t \leq \frac{T}{2} \\ -1; & \frac{T}{2} \leq t \leq T \end{cases} \tag{5}$$

and d_n is the polarity (± 1) of the nth NRZ data bit. The sequence $\{d_n\}$ is assumed to be composed of uncorrelated bits, i.e.,

$$E\{d_m d_n\} = \delta_{mn} = \begin{cases} 1; & m = n \\ 0; & m \neq n \end{cases} \tag{6}$$

with a priori probabilities $p \triangleq \text{Prob}\{d_n = 1\}$, and $q \triangleq \text{Prob}\{d_n = -1\}$. Thus, the transition probability p_t of the NRZ data sequence is given by $p_t = 2pq$.

The noise random variables ν_k, μ_k, ν'_k, μ'_k are all zero mean Gaussian with variance $\sigma^2 = N_0/4T$. Also,

$$E\{\nu_k \nu_{k+m}\} = E\{\nu'_k \nu'_{k+m}\} = E\{\mu_k \mu_{k+m}\} = E\{\mu'_k \mu'_{k+m}\} = 0 \text{ for all } m \neq 0$$

$$E\{\nu_k \nu'_{k+m}\} = E\{\nu_k \mu'_{k+m}\} = E\{\mu_k \mu'_{k+m}\} = E\{\mu_k \nu'_{k+m}\} = 0 \text{ for all } m$$

$$E\{\nu_k \mu_{k+m}\} = E\{\nu'_k \mu'_{k+m}\} = 0 \text{ for all } m . \tag{7}$$

The actual loop error signal $\xi(t)$ is a piecewise continuous function (see Figure 3) which is formed by summing the multiplications of the sample-and-hold values of the in-phase and quadrature I&D output

corresponding to the midbit and between-bit positions. In particular, if we define

$$e(t) \triangleq e_k\,; \qquad (k-\tfrac{1}{4})T+\hat{\varepsilon} \le t \le (k+\tfrac{3}{4})T+\hat{\varepsilon}$$

$$e'(t) \triangleq e'_k\,; \qquad (k+\tfrac{1}{4})T+\hat{\varepsilon} \le t \le (k+\tfrac{5}{4})T+\hat{\varepsilon}\,, \tag{8}$$

then

$$\xi(t) = e(t) + e'(t)$$

$$= \begin{cases} e_k + e'_{k-1} \triangleq \xi_k\,; & (k-\tfrac{1}{4})T+\hat{\varepsilon} \le t \le (k+\tfrac{1}{4})T+\hat{\varepsilon} \\ e_k + e'_k \triangleq \xi'_k\,; & (k+\tfrac{1}{4})T+\hat{\varepsilon} \le t \le (k+\tfrac{3}{4})T+\hat{\varepsilon}\,. \end{cases} \tag{9}$$

These relations will prove useful in deriving the equivalent loop S-curve and noise power spectral density perturbing the loop.

3.1 Characterization of the Loop Nonlinearity

We define the loop nonlinearity (S-curve), $g(\lambda)$, by

$$g(\lambda) \triangleq E_{n,s}\{\xi(t)|\lambda\} = \begin{cases} E_{n,s}\{(e_k + e'_{k-1})|\lambda\}\,; & (k-\tfrac{1}{4})T+\hat{\varepsilon} \le t \le (k+\tfrac{1}{4})T+\hat{\varepsilon} \\ E_{n,s}\{(e_k + e'_k)|\lambda\}\,; & (k+\tfrac{1}{4})T+\hat{\varepsilon} \le t \le (k+\tfrac{3}{4})T+\hat{\varepsilon} \end{cases} \tag{10}$$

where $E_{n,s}\{x|\lambda\}$ represents the conditional expectation of x on λ <u>both</u> with respect to the additive noise and the signal (bit sequence). We begin by computing the midbit component of $g(\lambda)$, namely,

$$g_{mb}(\lambda) \triangleq E_{n,s}\{e_k|\lambda\}\,. \tag{11}$$

Performing first the average on the noise, we have from (1) that

$$E_n\{e_k|\lambda\} = b_k E_n\{\text{sgnull}\,(c_k+\nu_k)\} + E_n\{\mu_k\,\text{sgnull}\,(c_k+\nu_k)\}\,. \tag{12}$$

If x is a $(0,\sigma_x)$ Gaussian random variable, then from the definition of sgnull x given in (3), it is easy to show that

$$E_x\{\text{sgnull}(a \pm x)\} = -\frac{1}{2}\,\text{erfc}\left[\frac{\eta_0 + a}{\sqrt{2}\,\sigma_x}\right] + \frac{1}{2}\,\text{erfc}\left[\frac{\eta_0 - a}{\sqrt{2}\,\sigma_x}\right], \qquad (13)$$

where

$$\text{erfc}\,x \triangleq \frac{2}{\sqrt{\pi}}\int_x^\infty \exp(-t^2)\,dt \qquad (14)$$

is the complementary error function.

Applying (13) to the first term in (12) gives

$$b_k E_n\{\text{sgnull}(c_k + \nu_k)\} = \frac{b_k}{2}\left\{-\text{erfc}\left[\frac{\eta_0 + c_k}{\sqrt{2}\,\sigma}\right] + \text{erfc}\left[\frac{\eta_0 - c_k}{\sqrt{2}\,\sigma}\right]\right\}. \qquad (15)$$

Furthermore, since from (7), μ_k and ν_k are uncorrelated, then

$$E_n\{\mu_k\,\text{sgnull}(c_k + \nu_k)\} = E_n\{\mu_k\}\,E_n\{\text{sgnull}(c_k + \nu_k)\}$$
$$= 0\,. \qquad (16)$$

Thus, substituting (15) and (16) into (12), we get

$$E_n\{e_k|\lambda\} = \frac{b_k}{2}\left\{-\text{erfc}\left[\frac{\eta_0 + c_k}{\sqrt{2}\,\sigma}\right] + \text{erfc}\left[\frac{\eta_0 - c_k}{\sqrt{2}\,\sigma}\right]\right\}. \qquad (17)$$

It now remains to average $E_n\{e_k|\lambda\}$ over the signal distribution. From (1), together with (4) and (5) (also see Figure 2), we find that

$$b_k = \begin{cases} Ad_k(2\lambda) & ; \quad 0 \le \lambda \le \frac{1}{4} \\ \left.\begin{array}{ll} Ad_k(1-2\lambda) & ; \text{ if } d_k = d_{k-1} \\ Ad_k(\frac{1}{2}) & ; \text{ if } d_k = -d_{k-1} \end{array}\right\} & ; \quad \frac{1}{4} \le \lambda \le \frac{1}{2} \end{cases}$$

$$c_k = \begin{cases} Ad_k(\frac{1}{2} - 2\lambda) & ; \quad 0 \le \lambda \le \frac{1}{4} \\ A\left(\frac{d_k + d_{k-1}}{2}\right)\left(\frac{1}{2} - 2\lambda\right) & ; \quad \frac{1}{4} \le \lambda \le \frac{1}{2} \end{cases} \qquad (18)$$

Substituting (18) into (17) and averaging over all (four) possible sequences formed from the bits d_{k-1} and d_k, we get the desired result:

$$g_{mb}(\lambda) = \begin{cases} A\lambda\left\{-\operatorname{erfc}\left[\sqrt{R_d/2}\,(2\eta+1-4\lambda)\right] + \operatorname{erfc}\left[\sqrt{R_d/2}\,(2\eta-1+4\lambda)\right]\right\}; \\ \qquad\qquad 0 \le \lambda \le \frac{1}{4} \\ \frac{A(1-p_t)}{2}(1-2\lambda)\left\{-\operatorname{erfc}\left[\sqrt{R_d/2}\,(2\eta+1-4\lambda)\right] + \operatorname{erfc}\left[\sqrt{R_d/2}\,(2\eta-1+4\lambda)\right]\right\}; \\ \qquad\qquad \frac{1}{4} \le \lambda \le \frac{1}{2} \end{cases} \tag{19}$$

where $\eta \triangleq n_0/A$ and $R_d \triangleq A^2T/N_0$ is the detection signal-to-noise ratio. Note that $g_{mb}(\lambda)$ is independent of k.

Similarly, the between-bit component of $g(\lambda)$, namely,

$$g_{bb}(\lambda) \triangleq E_{n,s}\{e_k'|\lambda\}, \tag{20}$$

can be found by applying similar averaging techniques to those used in deriving (19) from (11). In particular, the average over the noise distribution results in an equation analogous to (17), namely,

$$E_n\{e_k'|\lambda\} = \frac{b_k'}{2}\left\{-\operatorname{erfc}\left[\frac{n_0 + c_k'}{\sqrt{2}\,\sigma}\right] + \operatorname{erfc}\left[\frac{n_0 - c_k'}{\sqrt{2}\,\sigma}\right]\right\}. \tag{21}$$

Again, combining (1), (4), and (5), we can arrive at expressions for the between-bit signal components of the in-phase and quadrature integrate-and-dump outputs, namely,

$$b_k' = \begin{cases} -Ad_k(2\lambda) & ; \text{ if } d_k = d_{k+1} \\ -Ad_k(\frac{1}{2}) & ; \text{ if } d_k = -d_{k+1} \end{cases} \quad 0 \le \lambda \le \frac{1}{4}$$
$$\qquad -Ad_k(1-2\lambda)\,; \qquad \frac{1}{4} \le \lambda \le \frac{1}{2}$$

$$c_k' = \begin{cases} -A\left(\frac{d_k + d_{k+1}}{2}\right)\left(\frac{1}{2} - 2\lambda\right) & ; \quad 0 \le \lambda \le \frac{1}{4} \\ -Ad_k\left(\frac{1}{2} - 2\lambda\right) & ; \quad \frac{1}{4} \le \lambda \le \frac{1}{2} \end{cases} \tag{22}$$

Substituting (22) into (21) and averaging over the four possible sequences formed from the bits d_k and d_{k+1} gives the desired result:

$$g_{bb}(\lambda) = \begin{cases} A\lambda(1-p_t)\left\{-\operatorname{erfc}\left[\sqrt{R_d/2}\,(2n+1-4\lambda)\right] + \operatorname{erfc}\left[\sqrt{R_d/2}\,(2n-1+4\lambda)\right]\right\}; \\ \qquad\qquad 0 \le \lambda \le \frac{1}{4} \\ A\,\frac{(1-2\lambda)}{2}\left\{-\operatorname{erfc}\left[\sqrt{R_d/2}\,(2n+1-4\lambda)\right] + \operatorname{erfc}\left[\sqrt{R_d/2}\,(2n-1+4\lambda)\right]\right\}; \\ \qquad\qquad \frac{1}{4} \le \lambda \le \frac{1}{2} \end{cases} \tag{23}$$

which is independent of k.

Finally, adding (19) and (23), we get the loop nonlinearity defined in (10) or, normalizing by the signal amplitude,

$$g_n(\lambda) \triangleq \frac{g(\lambda)}{A}$$

$$= \begin{cases} 2\lambda\left(1-\frac{p_t}{2}\right)\left\{-\operatorname{erfc}\left[\sqrt{R_d/2}\,(2n+1-4\lambda)\right] + \operatorname{erfc}\left[\sqrt{R_d/2}\,(2n-1+4\lambda)\right]\right\}; \\ \qquad\qquad 0 \le \lambda \le \frac{1}{4} \\ (1-2\lambda)\left(1-\frac{p_t}{2}\right)\left\{-\operatorname{erfc}\left[\sqrt{R_d/2}\,(2n+1-4\lambda)\right] + \operatorname{erfc}\left[\sqrt{R_d/2}\,(2n-1+4\lambda)\right]\right\}; \\ \qquad\qquad \frac{1}{4} \le \lambda \le \frac{1}{2} \end{cases} \tag{24}$$

Also, it is straightforward to show that $g(-\lambda) = -g(\lambda)$. Note that, as $R_d \to \infty$ (no noise), (24) simplifies to

$$g_n(\lambda) = \begin{cases} 2(2\lambda)\left(1-\frac{p_t}{2}\right) & ; \quad 0 \le \lambda \le \frac{1}{4}-\frac{n}{2} \\ 0 & ; \frac{1}{4}-\frac{n}{2} \le \lambda \le \frac{1}{4}+\frac{n}{2} \\ -2(1-2\lambda)\left(1-\frac{p_t}{2}\right) & ; \frac{1}{4}+\frac{n}{2} \le \lambda \le \frac{1}{2} \end{cases} \tag{25}$$

For small values of λ, $g_n(\lambda)$ of (24) can be approximated by the linear function $K_g\lambda$, where K_g is the slope of the normalized loop S-curve at the origin, namely,

$$K_g = 2\left(1-\frac{p_t}{2}\right)\left\{-\operatorname{erfc}\left[\sqrt{R_d/2}\,(2n+1)\right] + \operatorname{erfc}\left[\sqrt{R_d/2}\,(2n-1)\right]\right\}. \tag{26}$$

3.2 Characterization of the Equivalent Noise Spectral Density

The two-sided spectral density $S(\omega,\lambda)$ of the equivalent additive noise $n_\lambda(t)$ is defined by

$$S(\omega,\lambda) \triangleq \mathscr{F}\{\langle R(t,\tau;\lambda)\rangle\} \; ;$$

$$R(t,\tau;\lambda) = E_{n,s}\{n_\lambda(t)\, n_\lambda(t+\tau)|\lambda\} \tag{27}$$

where the symbol $\mathscr{F}$ denotes the Fourier transform operation, the symbol $\langle\ \rangle$ denotes time average, and the equivalent noise process $n_\lambda(t)$ is defined by

$$n_\lambda(t) = \xi(t) - E_{n,s}\{\xi(t)|\lambda\} = \xi(t) - g(\lambda) . \tag{28}$$

Substituting (28) into (27), we see that

$$R(t,\tau;\lambda) = E_{n,s}\{\xi(t)\,\xi(t+\tau)|\lambda\} - g^2(\lambda) . \tag{29}$$

Evaluation of the conditional expectation needed in (29) requires [see (9)] that we study the discrete correlation functions $E_{n,s}\{\xi_k\,\xi_{k+m}|\lambda\}$, $E_{n,s}\{\xi_k\,\xi'_{k+m}|\lambda\}$, and $E_{n,s}\{\xi'_k\,\xi'_{k+m}|\lambda\}$. Using the definitions given in (9), it is straightforward to show that

$$E_{n,s}\{\xi_k\,\xi_{k+m}|\lambda\} = \begin{cases} E_{n,s}\{e_k^2|\lambda\} + E_{n,s}\{e'^2_{k-1}|\lambda\} ; & m=0 \\ 0 ; & m\neq 0 \end{cases}$$

$$E_{n,s}\{\xi_k\,\xi'_{k+m}|\lambda\} = \begin{cases} E_{n,s}\{e_k^2|\lambda\} ; & m=0 \\ E_{n,s}\{e'^2_{k-1}|\lambda\} ; & m=-1 \\ 0 ; & m\neq 0,-1 \end{cases}$$

$$E_{n,s}\{\xi'_k\,\xi'_{k+m}|\lambda\} = \begin{cases} E_{n,s}\{e_k^2|\lambda\} + E_{n,s}\{e'^2_{k}|\lambda\} ; & m=0 \\ 0 ; & m\neq 0 \end{cases} \tag{30}$$

Since $n_\lambda(t)$ is conditionally cyclostationary (i.e., its autocorrelation function $R(t,\tau;\lambda)$ is, for fixed τ and λ, periodic in t with period T), it is sufficient to evaluate $R(t,\tau;\lambda)$ over a T-sec interval. Thus, for $0 \le \tau \le T/2$,

$$R(t,\tau;\lambda) = \begin{cases} E_{n,s}\{\xi_k^2|\lambda\} - g^2(\lambda)\,; & (k-\frac{1}{4})T+\hat{\varepsilon} \le t \le (k+\frac{1}{4})T-\tau+\hat{\varepsilon} \\ E_{n,s}\{\xi_k\xi_k'|\lambda\} - g^2(\lambda)\,; & (k+\frac{1}{4})T-\tau+\hat{\varepsilon} \le t \le (k+\frac{1}{4})T+\hat{\varepsilon} \\ E_{n,s}\{\xi_k'^2|\lambda\} - g^2(\lambda)\,; & (k+\frac{1}{4})T+\hat{\varepsilon} \le t \le (k+\frac{3}{4})T-\tau+\hat{\varepsilon} \\ E_{n,s}\{\xi_k'\xi_{k+1}|\lambda\} - g^2(\lambda)\,; & (k+\frac{3}{4})T-\tau+\hat{\varepsilon} \le t \le (k+\frac{3}{4})T+\hat{\varepsilon} \end{cases} \tag{31}$$

and

$$R(\tau;\lambda) = \langle R(t,\tau;\lambda)\rangle = \frac{1}{T}\int_{(k-1/4)T+\hat{\varepsilon}}^{(k+3/4)T+\hat{\varepsilon}} R(t,\tau;\lambda)\,dt$$

$$= \left[E_{n,s}\{\xi_k^2|\lambda\} + E_{n,s}\{\xi_k'^2|\lambda\} - 2g^2(\lambda)\right]\left(\frac{1}{2}-\frac{\tau}{T}\right) + \left[E_{n,s}\{\xi_k\xi_k'|\lambda\} + E_{n,s}\{\xi_k'\xi_{k+1}|\lambda\} - 2g^2(\lambda)\right]\frac{\tau}{T}\,; \quad 0 \le \frac{\tau}{T} \le \frac{1}{2} \tag{32}$$

Similarly, for $\frac{T}{2} \le \tau \le T$,

$$R(t,\tau;\lambda) = \begin{cases} E_{n,s}\{\xi_k\xi_k'|\lambda\} - g^2(\lambda)\,; & (k-\frac{1}{4})T+\hat{\varepsilon} \le t \le (k+\frac{3}{4})T-\tau+\hat{\varepsilon} \\ 0\,; & (k+\frac{3}{4})T-\tau+\hat{\varepsilon} \le t \le (k+\frac{1}{4})T+\hat{\varepsilon} \\ E_{n,s}\{\xi_k'\xi_{k+1}|\lambda\} - g^2(\lambda)\,; & (k+\frac{1}{4})T+\hat{\varepsilon} \le t \le (k+\frac{5}{4})T-\tau+\hat{\varepsilon} \\ 0\,; & (k+\frac{5}{4})T-\tau+\hat{\varepsilon} \le t \le (k+\frac{5}{4})T+\hat{\varepsilon} \end{cases} \tag{33}$$

and, correspondingly,

$$R(\tau;\lambda) = \left[E_{n,s}\{\xi_k \xi_k' | \lambda\} + E_{n,s}\{\xi_k' \xi_{k+1}\} - 2g^2(\lambda)\right]\left(1 - \frac{\tau}{T}\right);$$

$$\frac{1}{2} \leq \frac{\tau}{T} \leq 1 . \qquad (34)$$

Finally, for $\tau \geq T$,

$$R(\tau;\lambda) = 0. \qquad (35)$$

Also, $R(\tau;\lambda)$ is an even function of τ. Thus, from the definition of $S(\omega,\lambda)$, we have that

$$S(\omega,\lambda) = 2\int_0^T R(\tau;\lambda) \cos \omega\tau \, d\tau$$

$$= 2\int_0^{T/2} \left\{R(0;\lambda)\left[1 - \frac{2\tau}{T}\right] + R\left(\frac{T}{2};\lambda\right)\left(\frac{2\tau}{T}\right)\right\} \cos \omega\tau \, d\tau$$

$$+ 2\int_{T/2}^T R\left(\frac{T}{2};\lambda\right)\left(2 - \frac{2\tau}{T}\right) \cos \omega\tau \, d\tau , \qquad (36)$$

where, from (32) and (34),

$$R(0;\lambda) = \frac{1}{2}\left[E_{n,s}\{\xi_k^2 | \lambda\} + E_{n,s}\{\xi_k'^2 | \lambda\}\right] - g^2(\lambda)$$

$$R\left(\frac{T}{2};\lambda\right) = \frac{1}{2}\left[E_{n,s}\{\xi_k \xi_k' | \lambda\} + E_{n,s}\{\xi_k' \xi_{k+1} | \lambda\}\right] - g^2(\lambda) . \qquad (37)$$

Since, as before, it is assumed that $B_L T << 1$, it is sufficient to consider only the value of $S(\omega,\lambda)$ at zero frequency—that is, $S(0,\lambda)$—and assume a flat spectrum of this value for all frequencies of interest (within the bandwidth of the bit synchronization loop). From (36), we get

$$S(0,\lambda) = \frac{T}{2}\left[R(0;\lambda) + 2R\left(\frac{T}{2};\lambda\right)\right] . \qquad (38)$$

Furthermore, since in any practical system little data degradation due to imperfect symbol synchronization can be tolerated, then extreme accuracy is required in establishing symbol synchronization. Since

this implies very large loop signal-to-noise ratios, then the value of $S(0,\lambda)$ is essentially the noise spectral density seen by the loop at $\lambda = 0$, viz., $S(0,0)$. Thus, we have that,

$$S(0,0) = \frac{T}{2}\left[\frac{1}{2}\left[E_{n,s}\{\xi_k^2\} + E_{n,s}\{\xi_k'^2\}\right] + E_{n,s}\{\xi_k \xi_k'\} + E_{n,s}\{\xi_k' \xi_{k+1}\}\right]$$

$$= \frac{T}{2}\left[2E_{n,s}\{e_k^2\} + \frac{1}{2}E_{n,s}\{e_{k-1}'^2\} + \frac{3}{2}E_{n,s}\{e_k'^2\}\right] , \qquad (39)$$

where, for simplicity of notation, we have dropped the dependency of the conditional expectations on λ, understanding that we are now specifically referring to their evaluation at $\lambda = 0$, and also recall that $g(0) = 0$.

From the definition of e_k given in (1), we compute the mean-squared value as

$$E_{n,s}\{e_k^2\} = E_{n,s}\{(b_k + \mu_k)^2 \ \text{sgnull}^2 \ (c_k + \nu_k)\}$$

$$= b_k^2 E_{n,s}\{\text{sgnull}^2 (c_k + \nu_k)\} + 2 b_k E_{n,s}\{\mu_k \ \text{sgnull}^2 (c_k + \nu_k)\}$$

$$+ E_{n,s}\{\mu_k^2 \ \text{sgnull}^2 (c_k + \nu_k)\} . \qquad (40)$$

Evaluating first the average on the noise and recalling μ_k and ν_k are uncorrelated, we have that

$$E_n\{e_k^2\} = (b_k^2 + \sigma^2) E_n\{\text{sgnull}^2 (c_k + \nu_k)\} . \qquad (41)$$

Analogous to (13), it is straightforward to show that

$$E_x\{\text{sgnull}^2 (a \pm x)\} = \frac{1}{2}\,\text{erfc}\left[\frac{n_0 + a}{\sqrt{2}\,\sigma_x}\right] + \frac{1}{2}\,\text{erfc}\left[\frac{n_0 - a}{\sqrt{2}\,\sigma_x}\right] . \qquad (42)$$

Thus, applying (42) to (41) with $x = \nu_k$ and $a = c_k$ gives the desired noise average

$$E_n\{e_k^2\} = \left(\frac{b_k^2 + \sigma^2}{2}\right)\left\{\text{erfc}\left[\frac{n_0 + c_k}{\sqrt{2}\,\sigma}\right] + \text{erfc}\left[\frac{n_0 - c_k}{\sqrt{2}\,\sigma}\right]\right\} . \qquad (43)$$

Since from (18) we have that (at $\lambda = 0$)

$$b_k = 0; \qquad c_k = A d_k \left(\frac{1}{2}\right), \tag{44}$$

then

$$E_{n,s}\{e_k^2\} = \frac{\sigma^2}{2}\left\{\text{erfc}\left[\sqrt{R_d/2}\,(2n+1)\right] + \text{erfc}\left[\sqrt{R_d/2}\,(2n-1)\right]\right\}. \tag{45}$$

which is independent of k.

Similarly, for the between-bit error signal component, we have that

$$E_n\{e_k'^2\} = \left(\frac{b_k'^2 + \sigma^2}{2}\right)\left\{\text{erfc}\left[\frac{n_0 + c_k'}{\sqrt{2}\,\sigma}\right] + \text{erfc}\left[\frac{n_0 - c_k'}{\sqrt{2}\,\sigma}\right]\right\}. \tag{46}$$

and from (22) evaluated at $\lambda = 0$,

$$b_k' = 0; \qquad c_k' = -A\left(\frac{d_k + d_{k+1}}{2}\right)\left(\frac{1}{2}\right). \tag{47}$$

Combining (46) and (47) and performing the average over the data gives

$$E_{n,s}\{e_k'^2\} = \frac{\sigma^2}{2}\left\{p_t\,\text{erfc}\left[\sqrt{R_d/2}\,(2n)\right] + (1-p_t) \times \left(\text{erfc}\left[\sqrt{R_d/2}\,(2n+1)\right] + \text{erfc}\left[\sqrt{R_d/2}\,(2n-1)\right]\right)\right\} \tag{48}$$

which is also independent of k. Finally then, substituting (45) and (48) into (39) gives the desired result for the equivalent noise spectral density, namely,

$$S(0,0) = \frac{N_0}{4}\left\{\frac{p_t}{2}\,\text{erfc}\left[\sqrt{R_d/2}\,(2n)\right] + \left(1 - \frac{p_t}{2}\right) \times \left(\text{erfc}\left[\sqrt{R_d/2}\,(2n+1)\right] + \text{erfc}\left[\sqrt{R_d/2}\,(2n-1)\right]\right)\right\}. \tag{49}$$

3.3 Application of Fokker-Planck Technique to Obtain Performance

The stochastic differential equation which describes the loop illustrated in Figure 4 is

$$\dot{\lambda} = -K F(p)\,[g(\lambda) + n_\lambda(t)]\,, \tag{50}$$

where p is the Heaviside operation, the dot denotes differentiation with respect to time, and K is the loop gain. In writing the above, we have assumed zero static timing error.

In dealing with equations of the above form one can, at best, hope to find the probability distribution of $\lambda(t)$, viz., $p(\lambda,t)$, from which the mean-squared timing jitter $\sigma_\lambda^2(t)$ can be calculated. Under the assumptions previously made regarding the equivalent additive noise process $n_\lambda(t)$, the solution for $p(\lambda,t)$ can be found via the Fokker-Planck method. In particular, for the first-order loop case, i.e., $F(p) = 1$, $\lambda(t)$ is a first-order Markov process whose probability density function satisfies the diffusion equation [5]:

$$\frac{\partial p(\lambda_0,t)}{\partial t} + \frac{\partial}{\partial \lambda_0}[K_1(\lambda_0,t)\,p(\lambda_0,t)] = \frac{1}{2}\,\frac{\partial^2}{\partial \lambda_0^2}[K_2(\lambda_0,t)\,p(\lambda_0,t)] \tag{51}$$

where $K_1(\lambda_0,t)$ and $K_2(\lambda_0,t)$ are defined by the conditional expectations

$$K_1(\lambda_0,t) = \lim_{\Delta t \to 0} \frac{1}{\Delta t}\,E\{[\lambda(t+\Delta t) - \lambda(t)]\,|\,\lambda(t) = \lambda_0\}$$

$$K_2(\lambda_0,t) = \lim_{\Delta t \to 0} \frac{1}{\Delta t}\,E\{[\lambda(t+\Delta t) - \lambda(t)]^2\,|\,\lambda(t) = \lambda_0\}\,. \tag{52}$$

Of interest is the case where $p(\lambda,t)$ converges, with time, to a stationary probability density function independent of the initial condition, which can be used to evaluate the steady-state behavior of the symbol synchronizer. Denoting

$$p_\lambda(\lambda) = \lim_{t \to \infty} p(\lambda,t)\,, \tag{53}$$

we obtain from (51) the stationary equation

$$\frac{d}{d\lambda}\left[K_1(\lambda)\, p_\lambda(\lambda)\right] = \frac{1}{2}\frac{d^2}{d\lambda^2}\left[K_2(\lambda)\, p_\lambda(\lambda)\right], \tag{54}$$

where

$$K_1(\lambda) = -Kg(\lambda)$$

$$K_2(\lambda) = K^2 S(0,\lambda) \cong K^2 S(0,0). \tag{55}$$

Substituting (55) into (54) and solving gives the probability density function

$$p_\lambda(\lambda) = C_1 \exp\left[-\frac{2\int g(\lambda)\, d\lambda}{K S(0,0)}\right]; \quad 0 \le \lambda \le \frac{1}{2}$$

$$p_\lambda(-\lambda) = p_\lambda(\lambda), \tag{56}$$

where C_1 is a normalization constant chosen such that

$$\int_{-1/2}^{1/2} p_\lambda(\lambda)\, d\lambda = 1. \tag{57}$$

Upon examination of Figure 3 and the general expression (in the presence of noise) for the loop nonlinearity $g(\lambda)$ [see (24)], we observe that $g(\lambda) = g(\lambda \pm \frac{1}{2})$. Thus, $p_\lambda(\lambda)$ as defined by (56) on the interval $-\frac{1}{2} \le \lambda \le \frac{1}{2}$ would be bimodal, i.e., the loop can lock up at $\lambda = 0$ or $\lambda = \pm\frac{1}{2}$ with equal probability. After resolution of this half-bit timing ambiguity by the ambiguity resolver (i.e., determining that, indeed, $\lambda = 0$ is the correct lock point), it is appropriate to talk only about λ modulo $\frac{1}{2}$, which has the probability density function $2p_\lambda(\lambda)$ on the interval $-\frac{1}{4} \le \lambda \le \frac{1}{4}$. For convenience of notation, we shall herein use λ to represent the modulo $\frac{1}{2}$ reduced random variable and ignore the factor of 2 in front of $p_\lambda(\lambda)$ since, instead, we can choose the normalization constant such that (57) holds when the $\pm\frac{1}{2}$ integration limits are replaced by $\pm\frac{1}{4}$.

Recalling that $g(\lambda) = A\, g_n(\lambda) = A\, K_g(g_n(\lambda)/K_g)$, where $g_n(\lambda)/K_g$ is now a nonlinearity with unit slope at the origin, then the argument of the exponential in (56) becomes

$$\frac{2\int g(\lambda)\,d\lambda}{K\,S(0,0)} = \frac{2AK_g\int \frac{g_n(\lambda)}{K_g}\,d\lambda}{N_0 K\left(\frac{S(0,0)}{N_0}\right)} \tag{58}$$

Noting that the single-sided loop bandwidth for a first-order loop is given by

$$B_L = \frac{AKK_g}{4}, \tag{59}$$

then (58) can be rewritten as

$$\begin{aligned}\frac{2\int g(\lambda)\,d\lambda}{K\,S(0,0)} &= 2\left(\frac{A^2T}{N_0}\right)\left(\frac{K_g^2}{AKK_gT}\right)\frac{\int \frac{g_n(\lambda)}{K_g}\,d\lambda}{\left(\frac{S(0,0)}{N_0}\right)} \\ &= \frac{R_d K_g^2}{2}\left(\frac{1}{B_L T}\right)\frac{\int \frac{g_n(\lambda)}{K_g}\,d\lambda}{\left(\frac{S(0,0)}{N_0}\right)} \\ &= \left(\frac{R_d\,\delta\,K_g^2}{2}\right)\frac{\int \frac{g_n(\lambda)}{K_g}\,d\lambda}{\left(\frac{S(0,0)}{N_0}\right)}, \end{aligned} \tag{60}$$

where $\delta \triangleq 1/B_L T$ is the bit rate-to-loop bandwidth ratio. For large $R_d\,\delta$ (but not necessarily large R_d), it is sufficient to replace $g_n(\lambda)$ by $K_g\lambda$; thus, under these conditions, (60) simplifies to

$$\frac{2\int g(\lambda)\,d\lambda}{K\,S(0,0)} = \left(\frac{R_d\,\delta\,K_g^2}{\frac{2S(0,0)}{N_0}}\right)\frac{\lambda^2}{2} \tag{61}$$

and, substituting (61) into (56), $p_\lambda(\lambda)$ is approximated by a Gaussian distribution with variance

$$\sigma_\lambda^2 = \frac{2\left(\frac{S(0,0)}{N_0}\right)}{R_d\,\delta\,K_g^2}. \tag{62}$$

Finally, substituting (26) and (49) into (62) gives the desired result for the mean-squared tracking jitter, namely,

$$\sigma_\lambda^2 = \left(\frac{1}{8 R_d \delta}\right) f(\eta, R_d, p_t) , \tag{63}$$

where

$$f(\eta, R_d, p_t) = \frac{\frac{p_t}{2}\operatorname{erfc}\left[\sqrt{\frac{R_d}{2}}(2\eta)\right] + (1-\frac{p_t}{2})\left\{\operatorname{erfc}\left[\sqrt{\frac{R_d}{2}}(2\eta+1)\right] + \operatorname{erfc}\left[\sqrt{\frac{R_d}{2}}(2\eta-1)\right]\right\}}{\left[(1-\frac{p_t}{2})\left\{-\operatorname{erfc}\left[\sqrt{\frac{R_d}{2}}(2\eta+1)\right] + \operatorname{erfc}\left[\sqrt{\frac{R_d}{2}}(2\eta-1)\right]\right\}\right]^2} \tag{64}$$

4.0 NUMERICAL RESULTS

Figure 5 illustrates the normalized tracking jitter coefficient $f(\eta, R_d, p_t)$ as a function of the in-phase decision threshold η with detection signal-to-noise ratio R_d and NRZ data transition probability p_t as parameters. Clearly, for given values of R_d and p_t, an optimum [in the sense of minimum $f(\eta, R_d, p_t)$ or σ_λ^2] threshold exists. Figure 6 is a plot of this optimum threshold versus R_d for three values of p_t. Several observations can be made from the results in Figure 5. First, we note that the mean-squared tracking jitter is considerably more sensitive to values of decision threshold greater than η_{opt} than it is to $\eta < \eta_{opt}$. Second, this sensitivity itself diminishes with decreasing p_t and increasing R_d. Finally, at fixed R_d, one concludes that the mean-squared tracking jitter decreases with decreasing p_t (NOTE: decreasing NRZ transition density implies increasing between-bit transitions in the Manchester coded waveform; in fact, $p_t = 0$ results in a square-wave data waveform at twice the bit rate).

Illustrated in Figure 7 are the normalized loop S-curves for random data ($p_t = 0.5$) and detection signal-to-noise ratios of 0 dB, 5 dB, and 10 dB. The values of detection threshold were, in each case, chosen equal to the optimum values as determined from Figure 6. We note the continuity of the S-curves when noise is present in comparison with the discontinuous no-noise S-curve of Figure 3 as described by (25). Also, it is clear that the slope of $g_n(\lambda)$ at the origin (namely, K_g)

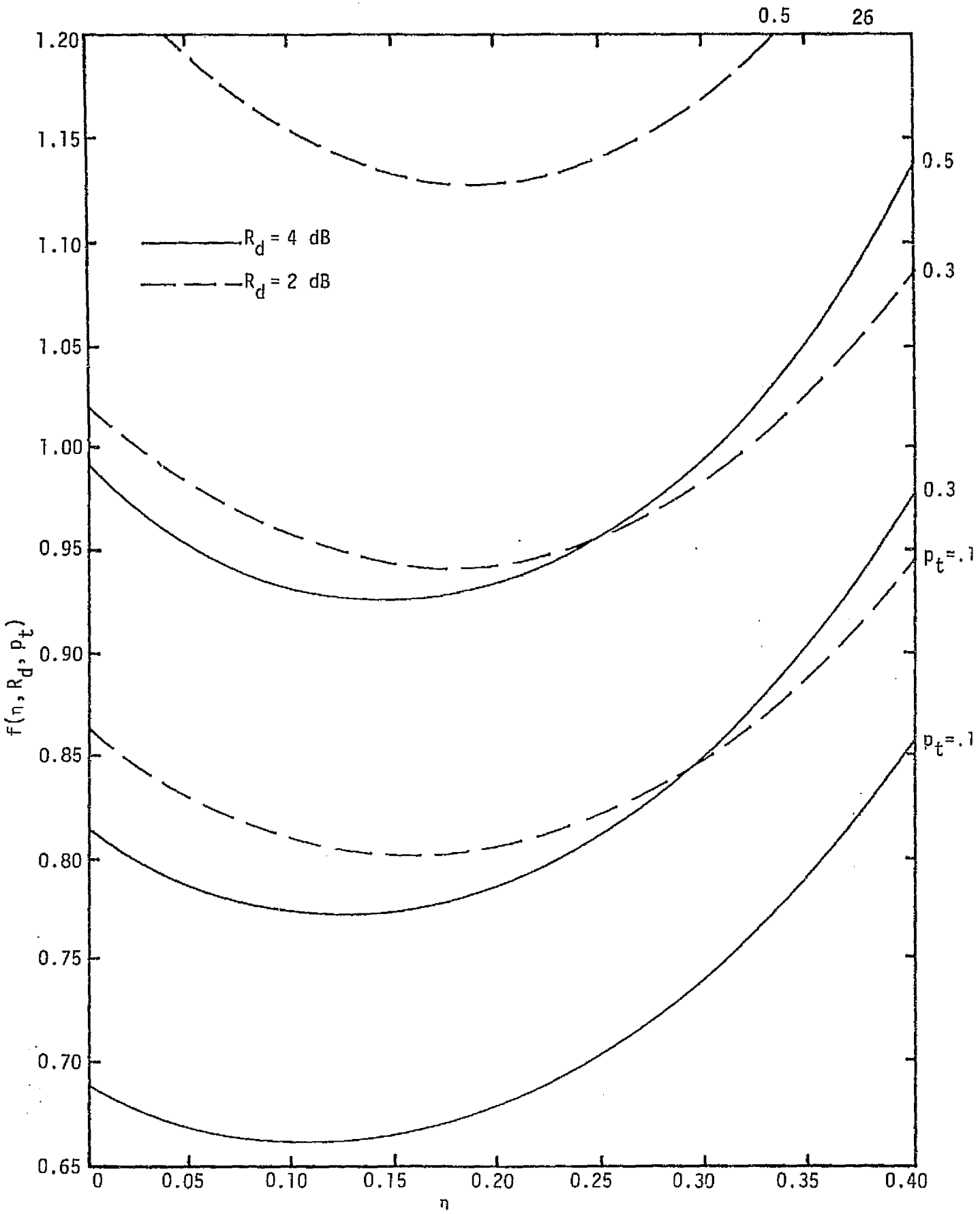

Figure 5a. Normalized Tracking Jitter Coefficient vs. Detection Threshold with NRZ Transition Density and Detection Signal-to-Noise Ratio as Parameters

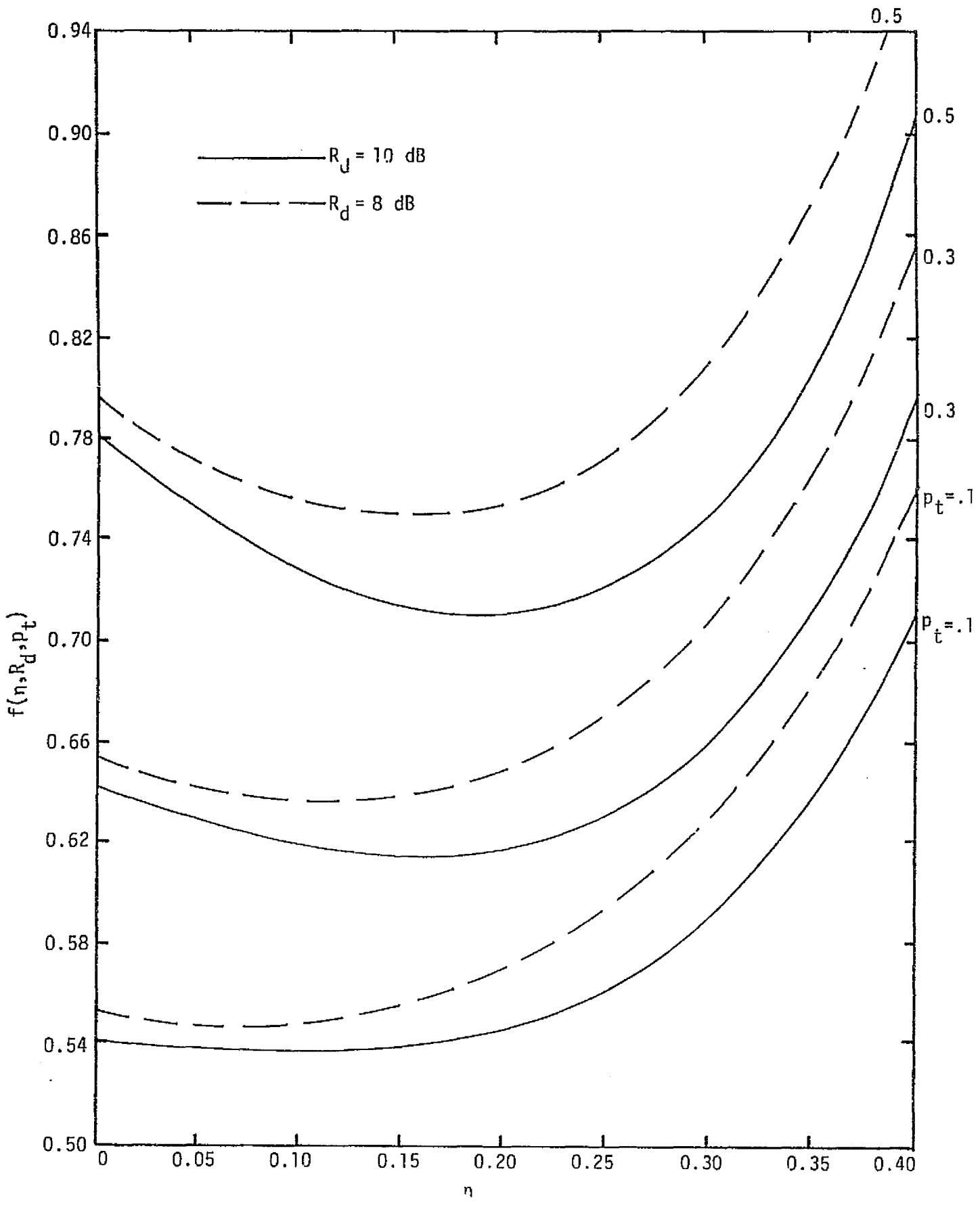

Figure 5b. Normalized Tracking Jitter Coefficient vs. Detection Threshold with NRZ Transition Density and Detection Signal-to-Noise Ratio as Parameters

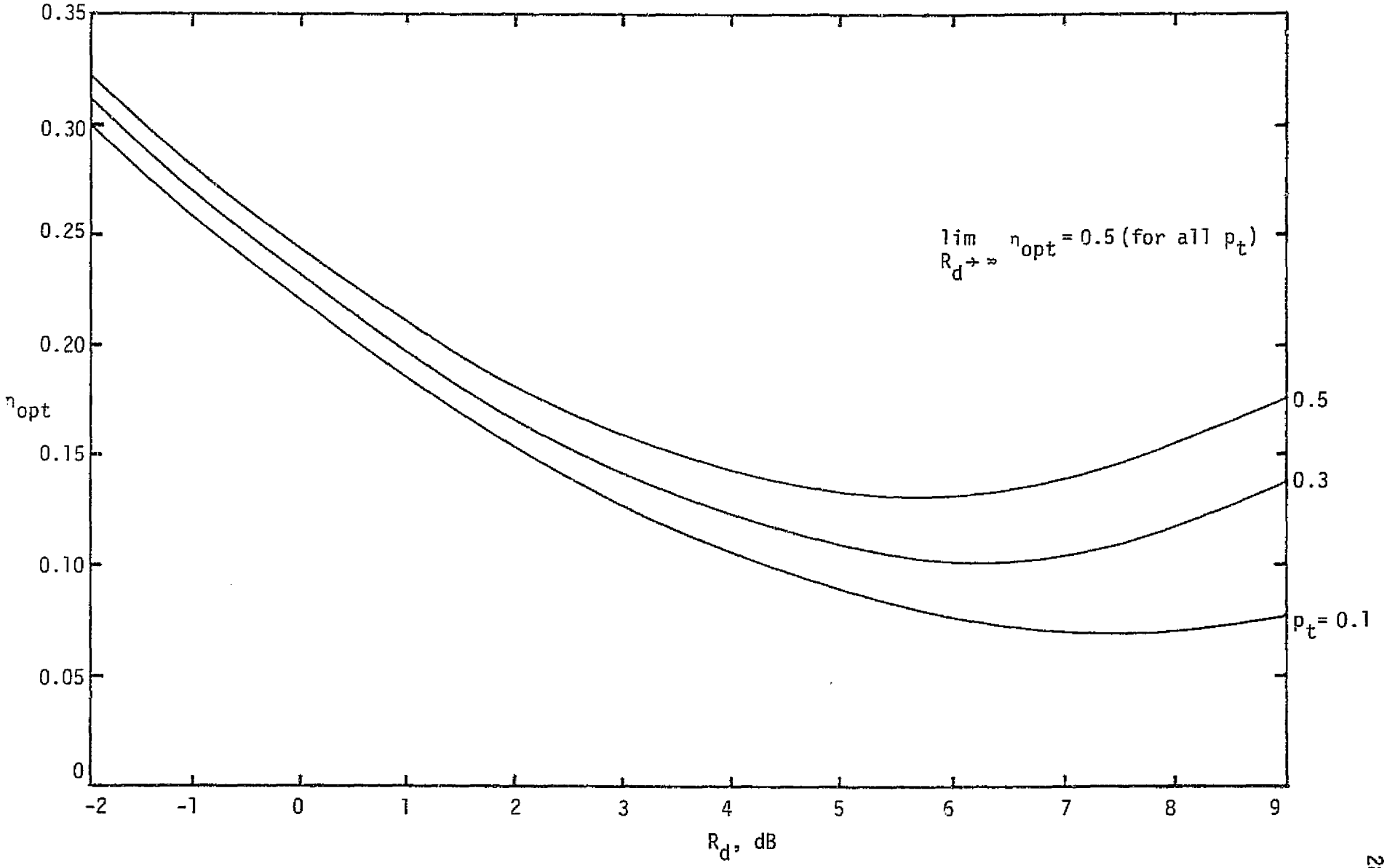

Figure 6. Optimum Detection Threshold vs. Detection Signal-to-Noise Ratio with NRZ Transition Probability as a Parameter

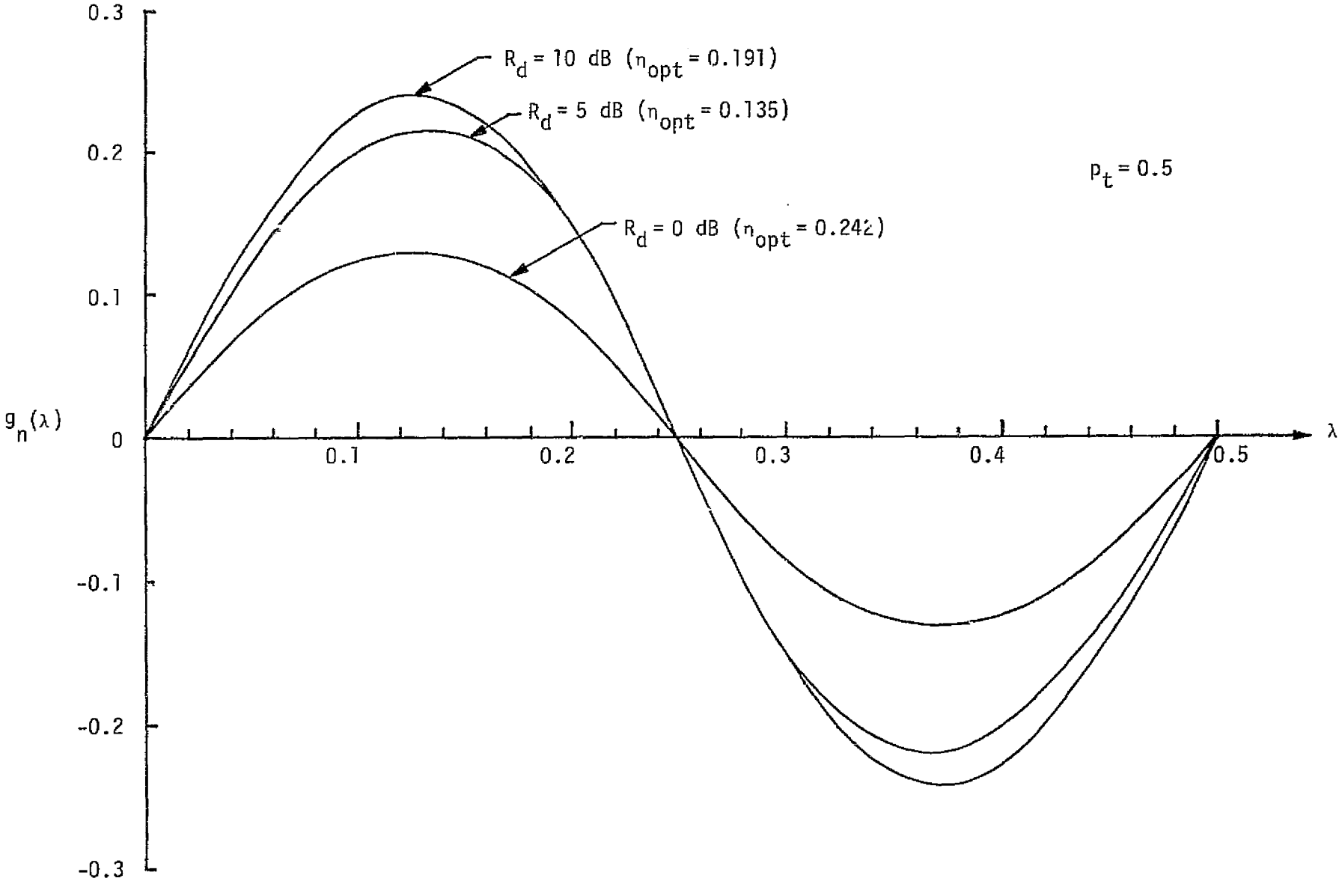

Figure 7. Normalized Loop S-Curve for Several Values of Detection Signal-to-Noise Ratio

and hence the equivalent loop gain, degrades with decreasing R_d. In fact, for small R_d, we have from (24) and (26) that

$$g_\eta(\lambda) \cong \begin{cases} 4\lambda\left(1 - \frac{p_t}{2}\right)\sqrt{\frac{2R_d}{\pi}}\ (1 - 4\lambda) & ; \quad 0 \le \lambda \le \frac{1}{4} \\ 2(1 - 2\lambda)\left(1 - \frac{p_t}{2}\right)\sqrt{\frac{2R_d}{\pi}}(1 - 4\lambda) ; & \frac{1}{4} \le \lambda \le \frac{1}{2} \end{cases} \tag{65}$$

and

$$K_g \cong 4\left(1 - \frac{p_t}{2}\right)\sqrt{\frac{2R_d}{\pi}}\ , \tag{66}$$

which are both independent of the detection threshold η.

We conclude by noting that a complete performance analysis of the accompanying phase ambiguity resolver will follow in a future report. Clearly, since the bit synchronizer and phase ambiguity resolver work hand in hand, a complete understanding of both devices and their interaction is essential to the overall performance specification of the SPA.

REFERENCES

1. Hughes Aircraft Co. "Ku-Band Bit Synchronizer Preliminary Analysis Results," Report No. HS 237-853, June 1977.

2. Hughes Aircraft Co. "Ku-Band Integrated Radar and Communication Equipment for the Space Shuttle Orbiter Vehicle," Preliminary Design Review, Vol. IV-A - Signal Processing Assembly (SPA), March 1978.

3. W. K. Alem, R. S. Iwasaki, M. K. Simon, S. Udalov, and C. L. Weber. "Shuttle Orbiter Ku-Band Radar/Communication System Design Evaluation," Axiomatix Report No. R7804-3, April 28, 1978, pp. 70-79.

4. M. K. Simon. "Tracking Performance of Symbol Synchronizers for Manchester Coded Data," IEEE Transactions on Communications, Vol. COM-25, No. 4, April 1977.

5. W. C. Lindsey and M. K. Simon. Telecommunication Systems Engineering. Englewood Cliffs, N.J.: Prentice-Hall, Inc., 1973, Ch. 9.

APPENDIX F

PERFORMANCE ANALYSIS OF THE KU-BAND FORWARD LINK AMBIGUITY RESOLVER

APPENDIX F

PERFORMANCE ANALYSIS OF THE KU-BAND FORWARD LINK AMBIGUITY RESOLVER

(Part I -- Selection of the In-Phase Bit Rate Clock)

by

Marvin K. Simon
Waddah K. Alem

1.0 INTRODUCTION

The Signal Processor Assembly (SPA) for the Ku-band forward link includes a timing phase ambiguity resolver whose purpose is to resolve which of the two possible bit rate clock phases (spaced half a bit apart) is indeed in phase with the received data waveform.* While the purpose of Appendix E was to document the performance analysis of the bit synchronizer on this link, this appendix proffers the companion analysis for the phase ambiguity resolver. Such performance characteristics as probability of counter overflow before ambiguity resolution, probability of incorrect (or correct) ambiguity resolution, and appropriate choice of counter difference threshold setting will be discussed.

2.0 AMBIGUITY RESOLVER PRINCIPLES OF OPERATION

A block diagram of the Hughes Ku-band ambiguity resolver suitable for analysis purposes is illustrated in Figure 1. Assuming SPA nominal mode of operation, the input is a 216 kbps Manchester coded data waveform $s(t,\varepsilon)$ plus additive white Gaussian noise $n(t)$ with single-sided power spectral density N_0. This total input is correlated with combinations of the bit rate clock, complement of the bit rate clock, and twice bit rate clock and processed by integrate-and-dump circuits (I&D) to produce the midbit and between-bit in-phase and quadrature signals necessary for forming the bit synchronizer error signal. Threshold crossings (positive or negative) of the midbit in-phase I&D output, as detected by digitizer 1A, increment counter 1,

*Other functions of the ambiguity resolver are to detect bit synchronization lock and loss of lock. The performance analysis of these functions will be covered in a future report.

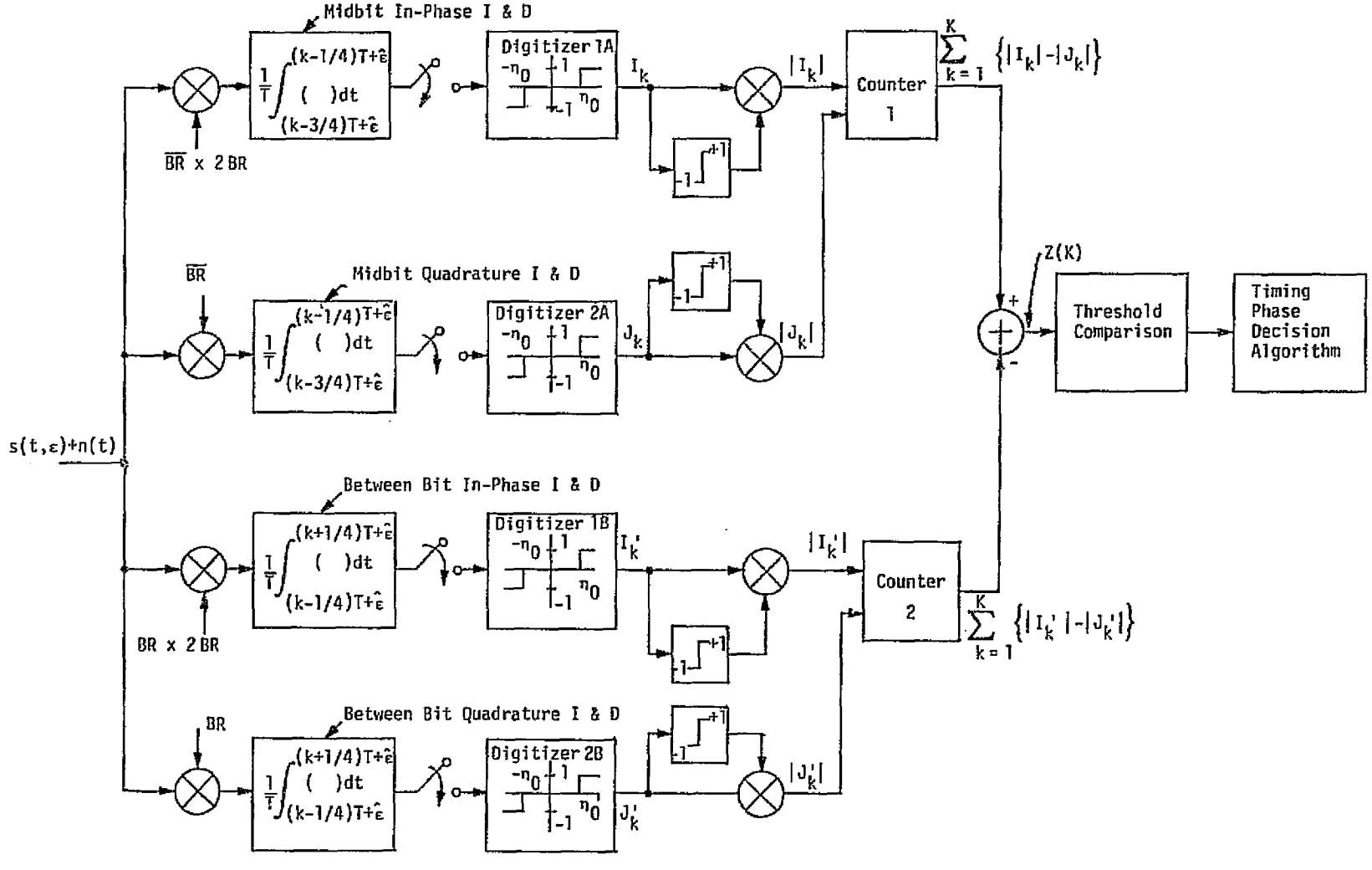

Figure 1. Timing Phase Ambiguity Resolver

while threshold crossings (positive or negative) of the midbit quadrature I&D output, as detected by digitizer 2A, decrement counter 1. Similar statements can be made for the between-bit I&D outputs with respect to counter 2. Thus, in the absence of noise and timing error, counter 1 is incremented and counter 2 is decremented each time there is a data transition. The net effect of this is to cause an increase of two counts in the contents of counter 1 relative to that of counter 2. When no data transition occurs, both counters are incremented by one count and thus the difference between the contents of the two counters is unaffected. When counter 1 overflows and the contents of counter 1 exceeds that of counter 2 by a preselected difference threshold, then a timing phase ambiguity decision is declared and the bit rate clock is assumed to be in phase with the input data stream. If counter 2 overflows and the contents of counter 2 exceed that of counter 1 by the same preselected threshold value, then the bit rate complement clock is chosen as being in phase with the input. If, however, the difference threshold is not crossed (positively or negatively) at the time either counter overflows, then both counters are reset to zero and the ambiguity search continues.

In determining the performance of the ambiguity resolver, we shall use the same notation as that used in Appendix E to characterize the bit synchronizer. Wherever possible, we shall refer to results obtained in Appendix E relative to the statistical averages of the various I&D and digitizer outputs.

3.0 PERFORMANCE ANALYSIS

3.1 Statistical Characterization of the Differenced Counter Output

Referring to Figure 1, the various digitizer outputs can be expressed mathematically as follows:

$$\begin{aligned} I_k &= \text{sgnull}\,(c_k + \nu_k) \\ J_k &= \text{sgnull}\,(b_k + \mu_k) \\ I'_k &= \text{sgnull}\,(c'_k + \nu'_k) \\ J'_k &= \text{sgnull}\,(b'_k + \mu'_k) \end{aligned} \qquad (1)$$

where the signal and noise components of the midbit in-phase and quadrature I&D outputs, namely, c_k, ν_k, b_k, and μ_k, are defined in (1) of [1] and the corresponding between-bit components c_k', ν_k', b_k', and μ_k' are defined in (2) of [1]. Further, the function "sgnull x" is the input-output characteristic of the digitizers and is defined in (3) of [1]. The inputs to counters 1 and 2 are the absolute values of the I&D outputs. In order to compute the ambiguity resolver performance, we shall need the statistical averages of these signals over the noise and data modulation probability distributions. Proceedings as in [1], we first evaluate the average over the additive noise distribution. Thus,

$$E_n\{|I_k|\} = E_n\{|\text{sgnull}\ (c_k+\nu_k)|\} = E_n\{\text{sgnull}^2\ (c_k+\nu_k)\}$$

$$= \frac{1}{2}\,\text{erfc}\left[\frac{\eta_0+c_k}{\sqrt{2}\,\sigma}\right] + \frac{1}{2}\,\text{erfc}\left[\frac{\eta_0-c_k}{\sqrt{2}\,\sigma}\right], \qquad (2)$$

where η_0 is once again the decision threshold in the bit synchronizer digitizers. Similarly,

$$E_n\{|J_k|\} = \frac{1}{2}\,\text{erfc}\left[\frac{\eta_0+b_k}{\sqrt{2}\,\sigma}\right] + \frac{1}{2}\,\text{erfc}\left[\frac{\eta_0-b_k}{\sqrt{2}\,\sigma}\right]$$

$$E_n\{|I_k'|\} = \frac{1}{2}\,\text{erfc}\left[\frac{\eta_0+c_k'}{\sqrt{2}\,\sigma}\right] + \frac{1}{2}\,\text{erfc}\left[\frac{\eta_0-c_k'}{\sqrt{2}\,\sigma}\right]$$

$$E_n\{|J_k'|\} = \frac{1}{2}\,\text{erfc}\left[\frac{\eta_0+b_k'}{\sqrt{2}\,\sigma}\right] + \frac{1}{2}\,\text{erfc}\left[\frac{\eta_0-b_k'}{\sqrt{2}\,\sigma}\right]. \qquad (3)$$

Averaging (2) and (3) over the signal distribution (see (18) and (22) of [1]) evaluated at $\lambda = 0$,*

$$E_{n,s}\{|I_k|\} = \frac{1}{2}\,\text{erfc}\left[\sqrt{\frac{R_d}{2}}\,(2\eta+1)\right] + \frac{1}{2}\,\text{erfc}\left[\sqrt{\frac{R_d}{2}}\,(2\eta-1)\right] \qquad (4a)$$

*For simplicity of analysis, we shall assume perfect bit synch insofar as the ambiguity resolver is concerned. This avoids the additional average over the probability distribution of the bit sync timing error.

$$E_{n,s}\{|J_k|\} = \text{erfc}\left[\sqrt{\frac{R_d}{2}}(2n)\right] \tag{4b}$$

$$E_{n,s}\{|I'_k|\} = p_t \,\text{erfc}\left[\sqrt{\frac{R_d}{2}}(2n)\right] + (1-p_t)\left\{\frac{1}{2}\,\text{erfc}\left[\sqrt{\frac{R_d}{2}}(2n+1)\right] + \frac{1}{2}\,\text{erfc}\left[\sqrt{\frac{R_d}{2}}(2n-1)\right]\right\} \tag{4c}$$

$$E_{n,s}\{|J'_k|\} = (1-p_t)\,\text{erfc}\left[\sqrt{\frac{R_d}{2}}(2n)\right] + p_t\left\{\frac{1}{2}\,\text{erfc}\left[\sqrt{\frac{R_d}{2}}(2n+1)\right] + \frac{1}{2}\,\text{erfc}\left[\sqrt{\frac{R_d}{2}}(2n-1)\right]\right\}. \tag{4d}$$

Defining

$$\beta_k = |I_k| - |J_k|$$

$$\beta'_k = |I'_k| - |J'_k|, \tag{5}$$

then the outputs of the two counters in Figure 1 are, respectively,

$$Y(K) \triangleq \sum_{k=1}^{K} \beta_k$$

$$Y'(K) \triangleq \sum_{k=1}^{K} \beta'_k, \tag{6}$$

where K denotes the number of bit intervals which have elapsed since the time the counters were last reset. Finally, the difference of the counter outputs is simply

$$Z(K) \triangleq Y(K) - Y'(K) = \sum_{k=1}^{K} \zeta_k$$

$$= \sum_{k=1}^{K}\left\{\left[|I_k| - |J_k|\right] - \left[|I'_k| - |J'_k|\right]\right\} \tag{7}$$

Substituting (4) into (7), it is straightforward to show that the mean of ζ_k is

$$E_{n,s}\{\zeta_k\} = 2p_t\left\{-\operatorname{erfc}\left[\sqrt{\frac{R_d}{2}}(2n)\right] + \frac{1}{2}\operatorname{erfc}\left[\sqrt{\frac{R_d}{2}}(2n+1)\right] + \frac{1}{2}\operatorname{erfc}\left[\sqrt{\frac{R_d}{2}}(2n-1)\right]\right\}$$

$$\triangleq \bar{\zeta}\ , \tag{8}$$

which is independent of k. Thus, from (7), the differenced counter output has mean

$$E_{n,s}\{Z(K)\} = 2Kp_t\left\{-\operatorname{erfc}\left[\sqrt{\frac{R_d}{2}}(2n)\right] + \frac{1}{2}\operatorname{erfc}\left[\sqrt{\frac{R_d}{2}}(2n+1)\right] + \frac{1}{2}\operatorname{erfc}\left[\sqrt{\frac{R_d}{2}}(2n-1)\right]\right\}, \tag{9}$$

which in the absence of noise ($R_d \to \infty$) reduces to $2Kp_t$, namely, two times the average number of NRZ transitions in K bits.

The variance of Z(K) is given by

$$\sigma_Z^2 \triangleq E_{n,s}\left\{\left[Z(K) - E_{n,s}\{Z(K)\}\right]^2\right\}$$

$$= E_{n,s}\left\{\sum_{k=1}^{K}\sum_{\ell=1}^{K}[\zeta_k - \bar{\zeta}][\zeta_\ell - \bar{\zeta}]\right\}. \tag{10}$$

From the definitions of I_k, J_k, I'_k, and J'_k, we observe that

$$E_{n,s}\{|I_k||I_{k+m}|\} = 0 \qquad m \neq 0$$

$$E_{n,s}\{|J_k||J_{k+m}|\} = 0 \qquad m \neq 0$$

$$E_{n,s}\{|I'_k||I'_{k+m}|\} = 0 \qquad m \neq 0$$

$$E_{n,s}\{|J'_k||J'_{k+m}|\} = 0 \qquad m \neq 0\ . \tag{11}$$

Thus, from (5), we have that

$$E_{n,s}\{\beta_k \beta_{k+m}\} = E\{\beta'_k \beta'_{k+m}\} = 0 \qquad m \neq 0 \tag{12}$$

Similarly, since for $\lambda = 0$, I_k and I'_{k+m} are uncorrelated for all m and likewise for J_k and J'_k, we further have that

$$E_{n,s}\{\beta_k \beta'_{k+m}\} = 0 \qquad \text{for all } m \ . \tag{13}$$

Thus, since from (6) and (7), ζ_k is defined by $\zeta_k = \beta_k - \beta'_k$, we conclude that ζ_k and ζ_ℓ are uncorrelated for $k \neq \ell$. In view of this, (10) simplifies to

$$\begin{aligned}
\sigma_Z^2 &= E_{n,s}\left\{\sum_{k=0}^{K} \zeta_k^2\right\} - K^2 \bar{\zeta}^2 \\
&= \sum_{k=1}^{K} E_{n,s}\{\zeta_k^2\} - K^2 \bar{\zeta}^2 \\
&= \sum_{k=1}^{K} \left[E_{n,s}\{\beta_k^2\} + E_{n,s}\{\beta_k'^2\} - 2E_{n,s}\{\beta_k\}\, E_{n,s}\{\beta'_k\}\right] - K^2 \bar{\zeta}^2 \ .
\end{aligned} \tag{14}$$

From the definitions in (5), we require evaluation of the mean square values of $|I_k|$, $|J_k|$, $|I'_k|$, and $|J'_k|$ at $\lambda = 0$. Since $|I_k|^2 = |I_k|$ and similarly for $|J_k|$, $|I'_k|$, and $|J'_k|$, we trivially obtain the results

$$E_{n,s}\{|I_k|^2\} = E_{n,s}\{|I_k|\} = \frac{1}{2}\operatorname{erfc}\left[\sqrt{\frac{R_d}{2}}\,(2n+1)\right] + \frac{1}{2}\operatorname{erfc}\left[\sqrt{\frac{R_d}{2}}\,(2n-1)\right] \tag{15a}$$

$$E_{n,s}\{|J_k|^2\} = E_{n,s}\{|J_k|\} = \operatorname{erfc}\left[\sqrt{\frac{R_d}{2}}\,(2n)\right] \tag{15b}$$

$$E_{n,s}\{|I'_k|^2\} = E_{n,s}\{|I'_k|\} = p_t \operatorname{erfc}\left[\sqrt{\frac{R_d}{2}}\,(2n)\right] + (1-p_t)\left\{\frac{1}{2}\operatorname{erfc}\left[\sqrt{\frac{R_d}{2}}\,(2n+1)\right] + \frac{1}{2}\operatorname{erfc}\left[\sqrt{\frac{R_d}{2}}\,(2n-1)\right]\right\} \tag{15c}$$

$$E_{n,s}\{|J_k'|^2\} = E_{n,s}\{|J_k'|\} = (1-p_t)\,\mathrm{erfc}\left[\sqrt{\frac{R_d}{2}}\,(2n)\right] + p_t\left\{\frac{1}{2}\mathrm{erfc}\left[\sqrt{\frac{R_d}{2}}\,(2n+1)\right] + \frac{1}{2}\,\mathrm{erfc}\left[\sqrt{\frac{R_d}{2}}\,(2n-1)\right]\right\}. \quad (15d)$$

The last evaluation that we require to obtain $\sigma^2_{Z(K)}$ from (14) is the correlation of $|I_k|$ with $|J_k|$ and similarly the correlation of $|I_k'|$ with $|J_k'|$. While it is true that $|I_k|$ and $|J_k|$ are noisewise uncorrelated and similarly for $|I_k'|$ and $|J_k'|$, these same pairs of random variables are not uncorrelated with respect to averaging over the signal distribution. Thus, from (3) and [1: (18), (22)], we have

$$E_{n,s}\{|I_k||J_k|\} = E_{n,s}\{|I_k'||J_k'|\} = \mathrm{erfc}\left[\sqrt{\frac{R_d}{2}}\,(2n)\right]\left\{\frac{1}{2}\,\mathrm{erfc}\left[\sqrt{\frac{R_d}{2}}\,(2n+1)\right] + \frac{1}{2}\,\mathrm{erfc}\left[\sqrt{\frac{R_d}{2}}\,(2n-1)\right]\right\}. \quad (16)$$

Combining (15) and (16) together with the definitions of β_k and β_k' given in (5) produces the results

$$E_{n,s}\{\beta_k^2\} = E_{n,s}\left\{\left[|I_k| - |J_k|\right]^2\right\} = E_{n,s}\{|I_k|^2\} + E_{n,s}\{|J_k|^2\} - 2E_{n,s}\{|I_k||J_k|\}$$

$$= \mathrm{erfc}\left[\sqrt{\frac{R_d}{2}}\,(2n)\right] + \frac{1}{2}\,\mathrm{erfc}\left[\sqrt{\frac{R_d}{2}}\,(2n+1)\right] + \frac{1}{2}\,\mathrm{erfc}\left[\sqrt{\frac{R_d}{2}}\,(2n-1)\right] - 2\,\mathrm{erfc}\left[\sqrt{\frac{R_d}{2}}\,(2n)\right]\left\{\frac{1}{2}\mathrm{erfc}\left[\sqrt{\frac{R_d}{2}}\,(2n+1)\right] + \frac{1}{2}\mathrm{erfc}\left[\sqrt{\frac{R_d}{2}}\,(2n-1)\right]\right\} \quad (17)$$

and

$$E_{n,s}\{\beta_k'^2\} = E_{n,s}\{\beta_k^2\}, \quad (18)$$

where both (17) and (18) are independent of k. Finally, substituting (8), (17), and (18) into (14) gives the desired result:

$$\sigma_Z^2 = 2K\left\{1 - 2\,\mathrm{erfc}\left[\sqrt{\frac{R_d}{2}}\,(2\eta)\right]\right\}\left\{\frac{1}{2}\mathrm{erfc}\left[\sqrt{\frac{R_d}{2}}\,(2\eta+1)\right] + \frac{1}{2}\mathrm{erfc}\left[\sqrt{\frac{R_d}{2}}\,(2\eta-1)\right]\right\}$$

$$+ 2K\,\mathrm{erfc}\left[\sqrt{\frac{R_d}{2}}\,(2\eta)\right]$$

$$- 2K\left[1 - 2p_t + 2K\,p_t^2\right]\left\{\frac{1}{2}\mathrm{erfc}\left[\sqrt{\frac{R_d}{2}}\,(2\eta+1)\right] + \frac{1}{2}\,\mathrm{erfc}\left[\sqrt{\frac{R_d}{2}}\,(2\eta-1)\right]\right.$$

$$\left. - \mathrm{erfc}\left[\sqrt{\frac{R_d}{2}}\,(2\eta)\right]\right\}^2 . \qquad (19)$$

For large accumulation size (K), the random variable Z(K) is approximately Gaussian distributed with mean given by (9) and variance given by (19). Similarly, when $\lambda = 1/2$, namely, the equiprobable stable lock point of the bit sync loop which is half a bit shifted from the true lock point, Z(K) is once again (for large K) Gaussian distributed with mean equal to the negative of (9) and the same variance as in (19).

3.2 Evaluation of Ambiguity Resolution Probabilities

As previously mentioned, an ambiguity decision (correct or incorrect) is made whenever the differenced counter output Z(K) exceeds a preset threshold γ where K is now a random variable which specifically represents the number of bit intervals at which either counter first overflows. In particular, the ambiguity decision algorithm may be stated as follows. If counter 1 overflows when $\lambda = 0$ (i.e., the bit rate clock is in phase with the input NRZ data transitions), then if counter 1 minus counter 2 exceeds the threshold γ, a correct ambiguity decision is made in favor of the bit rate clock. If counter 1 overflows when $\lambda = 1/2$ (i.e., the complement of the bit rate clock is in phase with the input NRZ data transitions), then if counter 1 minus counter 2 exceeds γ, an incorrect ambiguity decision is made in favor of the bit rate clock. If when counter 1 overflows, counter 1 minus counter 2 does not exceed γ, then both counters are reset to zero and the test

continues. In a similar fashion, if counter 2 overflows, then if γ is exceeded by counter 2 minus counter 1, an ambiguity decision is made in favor of the complement of the bit rate clock. This decision will be correct if it occurs when $\lambda = 1/2$ and will be incorrect if it occurs when $\lambda = 0$. Again, if counter 2 overflows and the differenced counter outputs do not exceed the threshold, then both counters are reset to zero and the test for an ambiguity resolution continues.

Because of the symmetry in the above algorithm with regard to the overflow of counters 1 and 2, it is straightforward to show that for each independent trial following reset of both counters, the conditional probability of correctly resolving the ambiguity after K bits (K large) assuming $\lambda = 0$ is given by

$$P_{c1}(K) = \text{Prob}\{Z(K) > \gamma | \lambda = 0,\ Y(K) = K_{min}\}. \tag{20}$$

Similarly, the same unconditional probability assuming $\lambda = 1/2$ is given by

$$P_{c2}(K) = \text{Prob}\{-Z(K) > \gamma | \lambda = 1/2,\ Y'(K) = K_{min}\}. \tag{21}$$

In (20) and (21), Y(K) and Y'(K) are, respectively, the outputs of counters 1 and 2 at the time of overflow and K_{min} is the capacity of each counter before overflow. For the Hughes Ku-band ambiguity resolver, $K_{min} = 2^{12}$ (12 bit storage capacity for each counter). Since from (7) we have that $Z(K) = Y(K) - Y'(K)$, then (20) and (21) can be rewritten as

$$P_{c1}(K) = \text{Prob}\{Y'(K) < K_{min} - \gamma | \lambda = 0,\ Y(K) = K_{min}\} \tag{22}$$

$$P_{c2}(K) = \text{Prob}\{Y(K) < K_{min} - \gamma | \lambda = 1/2,\ Y'(K) = K_{min}\}. \tag{23}$$

From the results of the previous section, Y(K) and Y'(K) are both Gaussian (for large K) random variables with conditional means [see (4)]

$$\mu_c(K) \triangleq E\{Y'(K) | \lambda = 0\} = E\{Y(K) | \lambda = 1/2\}$$

$$= K(1 - 2p_t)\left\{\frac{1}{2}\,\text{erfc}\,\Lambda^{+} + \frac{1}{2}\,\text{erfc}\,\Lambda^{-} - \text{erfc}\,\Lambda^{0}\right\} \tag{24}$$

and conditional variances

$$\sigma_c^2(K) \triangleq E\{[Y'(K) - \mu_c(K)]^2 | \lambda = 0\} = E\{[Y(K) - \mu_c(K)]^2 | \lambda = 1/2\}$$

$$= K\{\text{erfc } \Lambda^0 + (1 - 2 \text{ erfc } \Lambda^0)(\tfrac{1}{2} \text{ erfc } \Lambda^+ + \tfrac{1}{2} \text{ erfc } \Lambda^-)\}$$

$$- K^2(1 - 2p_t)^2 \{\tfrac{1}{2} \text{ erfc } \Lambda^+ + \tfrac{1}{2} \text{ erfc } \Lambda^- - \tfrac{1}{2} \text{ erfc } \Lambda^0\}^2 , \qquad (25)$$

where

$$\Lambda^0 \triangleq \sqrt{\frac{R_d}{2}}\,(2n)$$

$$\Lambda^+ = \sqrt{\frac{R_d}{2}}\,(2n+1)$$

$$\Lambda^- = \sqrt{\frac{R_d}{2}}\,(2n-1) . \qquad (26)$$

Thus, from the foregoing and the symmetry of the decision algorithm, we have that $P_{c1}(K) = P_{c2}(K) \triangleq P_c(K)$, where

$$P_c(K) = \frac{1}{2} + \frac{1}{2} \text{ erf} \left[\frac{K_{min} - \gamma - \mu_c(K)}{\sqrt{2}\,\sigma_c(K)}\right] . \qquad (27)$$

To obtain the unconditional probability P_c of correctly resolving the ambiguity in "one pass," we must average (22) and (23) over the probability distributions* (frequency functions) of K for counters 1 and 2. Letting

$$p_{c1}(K) = \text{Prob } \{Y(K) = K_{min} | \lambda = 0\}$$

$$p_{c2}(K) = \text{Prob } \{Y'(K) = K_{min} | \lambda = 1/2\} \qquad (28)$$

then since $\lambda = 0$ and $\lambda = 1/2$ are equally likely (each has probability of

*The frequency functions of the number of bit intervals to first cause an overflow of counters 1 and 2 will be discussed in the next section.

occurrence equal to one-half) and $p_{c1}(K) = p_{c2}(K) \triangleq p_c(K)$, we have the desired result:

$$P_c = \frac{1}{2} \sum_{K=K_{min}}^{\infty} P_{c1}(K)\, p_{c1}(K) + \frac{1}{2} \sum_{K=K_{min}}^{\infty} P_{c2}(K)\, p_{c2}(K)$$

$$= \sum_{K=K_{min}}^{\infty} P_c(K)\, p_c(K) . \tag{29}$$

By similar reasoning, the probability of incorrectly resolving the ambiguity in "one pass" is

$$P_I = \sum_{K=K_{min}}^{\infty} P_I(K)\, p_I(K) , \tag{30}$$

where

$$P_I(K) = \text{Prob}\,\{Z(K) > \gamma \,|\, \lambda = 1/2,\ Y(K) = K_{min}\}$$

$$= \text{Prob}\,\{-Z(K) > \gamma \,|\, \lambda = 0,\ Y'(K) = K_{min}\} \tag{31}$$

or

$$P_I(K) = \text{Prob}\,\{Y'(K) < K_{min} - \gamma \,|\, \lambda = 1/2,\ Y(K) = K_{min}\}$$

$$= \text{Prob}\,\{Y(K) < K_{min} - \gamma \,|\, \lambda = 0,\ Y'(K) = K_{min}\} \tag{32}$$

and

$$p_I(K) = \text{Prob}\,\{Y(K) = K_{min} \,|\, \lambda = 1/2\}$$

$$= \text{Prob}\,\{Y'(K) = K_{min} \,|\, \lambda = 0\} . \tag{33}$$

From the results of the previous section, the conditional means of $Y(K)$ and $Y'(K)$ required to evaluate (32) are

$$\mu_I(K) = E\{Y'(K) \,|\, \lambda = 1/2\} = E\{Y(K) \,|\, \lambda = 0\}$$

$$= K\left\{\frac{1}{2}\,\text{erfc}\ \Lambda^{+} + \frac{1}{2}\,\text{erfc}\ \Lambda^{-} - \text{erfc}\ \Lambda^{0}\right\} \tag{34}$$

and the corresponding conditional variances are

$$\sigma_I^2(K) \triangleq E\{[Y'(K) - \mu_I(K)]^2 | \lambda = 1/2\} = E\{[Y(K) - \mu_I(K)]^2 | \lambda = 0\}$$

$$= K\{\text{erfc } \Lambda^0 + (1 - 2\,\text{erfc } \Lambda^0)(\tfrac{1}{2}\,\text{erfc } \Lambda^+ + \tfrac{1}{2}\,\text{erfc } \Lambda^-)\}$$

$$- K^2\{\tfrac{1}{2}\,\text{erfc } \Lambda^+ + \tfrac{1}{2}\,\text{erfc } \Lambda^- - \tfrac{1}{2}\,\text{erfc } \Lambda^0\}^2 \quad . \tag{35}$$

Thus,

$$P_I(K) = \frac{1}{2} + \frac{1}{2}\,\text{erf}\left[\frac{K_{min} - \gamma - \mu_I(K)}{\sqrt{2}\,\sigma_I(K)}\right] . \tag{36}$$

Finally, the probability of <u>not</u> making an ambiguity resolution when counter 1 or counter 2 overflows for the first time is

$$\bar{P} = \sum_{K=K_{min}}^{\infty} \overline{P_c(K)}\, p_c(K) + \sum_{K=K_{min}}^{\infty} \overline{P_I(K)}\, p_I(K) , \tag{37}$$

where

$$\overline{P_c(K)} \triangleq \text{Prob}\,\{Z(K) < \gamma | \lambda = 0,\ Y(K) = K_{min}\}$$

$$= \text{Prob}\,\{-Z(K) < \gamma | \lambda = 1/2,\ Y'(K) = K_{min}\} \tag{38}$$

and

$$\overline{P_I(K)} \triangleq \text{Prob}\,\{Z(K) < \gamma | \lambda = 1/2,\ Y(K) = K_{min}\}$$

$$= \text{Prob}\,\{-Z(K) < \gamma | \lambda = 0,\ Y'(K) = K_{min}\} \tag{39}$$

Clearly, since $\overline{P_c(K)} = 1 - P_c(K)$ and $\overline{P_I(K)} = 1 - P_I(K)$, we have that

$$\bar{P} = 1 - P_c - P_I . \tag{40}$$

3.3 <u>Probability Distributions of K (The Number of Bit Intervals at Which Counter 1 or Counter 2 First Overflows)</u>

We begin this section by characterizing the random variables β_k and β_k' which <u>increment</u> counters 1 and 2, respectively. Since the digitizer outputs (see Figure 1) I_k, I_k', J_k, and J_k' can take on values $0, \pm 1$,

then from the definitions of β_k and β_k' in (5), we observe that they too take on the same values. Thus, the outputs of counters 1 and 2 behave like a particular type of random walk wherein for each bit interval, their values either remain unchanged or are incremented by +1 or -1 in accordance with the corresponding values of β_k and β_k'.

We have already evaluated the mean and variance of β_k and β_k' [see, for example, (8), (17), (18), (24), and (34)] under the hypothesis of $\lambda = 0$ and $\lambda = 1/2$. The probability distributions (frequency functions) of these random variables under the same hypotheses are readily found as follows. Letting

$$\begin{aligned} p_{\lambda_0} &= \text{Prob}\{\beta_k = +1 | \lambda = \lambda_0\} \\ r_{\lambda_0} &= \text{Prob}\{\beta_k = 0 | \lambda = \lambda_0\} \\ q_{\lambda_0} &= \text{Prob}\{\beta_k = -1 | \lambda = \lambda_0\} \end{aligned} \tag{41}$$

and

$$\begin{aligned} p'_{\lambda_0} &= \text{Prob}\{\beta'_k = +1 | \lambda = \lambda_0\} \\ r'_{\lambda_0} &= \text{Prob}\{\beta'_k = 0 | \lambda = \lambda_0\} \\ q'_{\lambda_0} &= \text{Prob}\{\beta'_k = -1 | \lambda = \lambda_0\} \end{aligned} \tag{42}$$

where $\lambda_0 = 0$ or $1/2$, depending upon whether the bit rate clock or its complement is in phase with the input data stream, then

$$E\{\beta_k | \lambda = \lambda_0\} \triangleq \overline{\beta_{\lambda_0}} = 1 \times p_{\lambda_0} + 0 \times r_{\lambda_0} + (-1) \times q_{\lambda_0} = p_{\lambda_0} - q_{\lambda_0}$$

$$E\{\beta_k^2 | \lambda = \lambda_0\} = \overline{\beta_{\lambda_0}^2} = 1^2 \times p_{\lambda_0} + 0^2 \times r_{\lambda_0} + (-1)^2 \times q_{\lambda_0} = p_{\lambda_0} + q_{\lambda_0}$$

$$p_{\lambda_0} + q_{\lambda_0} + r_{\lambda_0} = 1. \tag{43}$$

Solving for p_{λ_0}, q_{λ_0}, and r_{λ_0} gives

$$p_{\lambda_0} = \frac{1}{2}\left[\overline{\beta_{\lambda_0}^2} + \overline{\beta_{\lambda_0}}\right]$$

$$q_{\lambda_0} = \frac{1}{2}\left[\overline{\beta_{\lambda_0}^2} - \overline{\beta_{\lambda_0}}\right]$$

$$r_{\lambda_0} = 1 - \overline{\beta_{\lambda_0}^2}\,. \tag{44}$$

Similar relations to (44) hold for p'_{λ_0}, r'_{λ_0} and q'_{λ_0} in terms of $\overline{\beta'_{\lambda_0}}$ and $\beta'^2_{\lambda_0}$. Using the relations previously developed, we find that

$$p_0 = \operatorname{erf} \Lambda^0 \left[\frac{1}{2}\operatorname{erfc} \Lambda^+ + \frac{1}{2}\operatorname{erfc} \Lambda^-\right]$$

$$r_0 = \operatorname{erf} \Lambda^0 - (1 - 2\operatorname{erfc} \Lambda^0)\left[\frac{1}{2}\operatorname{erfc} \Lambda^+ + \frac{1}{2}\operatorname{erfc} \Lambda^-\right]$$

$$q_0 = \operatorname{erf} \Lambda^0 \left[1 - \frac{1}{2}\operatorname{erfc} \Lambda^+ - \frac{1}{2}\operatorname{erfc} \Lambda^-\right] \tag{45}$$

and

$$p'_{1/2} = q_0$$

$$r'_{1/2} = r_0$$

$$q'_{1/2} = p_0\,. \tag{46}$$

Also,

$$p'_0 = (\operatorname{erf} \Lambda^0 - p_t)\left[\frac{1}{2}\operatorname{erfc} \Lambda^+ + \frac{1}{2}\operatorname{erfc} \Lambda^-\right] + p_t \operatorname{erfc} \Lambda^0$$

$$r'_0 = \operatorname{erf} \Lambda^0 - (1 - 2\operatorname{erfc} \Lambda^0)\left[\frac{1}{2}\operatorname{erfc} \Lambda^+ + \frac{1}{2}\operatorname{erfc} \Lambda^-\right]$$

$$q'_0 = (\operatorname{erf} \Lambda^0 - (1 - p_t))\left[\frac{1}{2}\operatorname{erfc} \Lambda^+ + \frac{1}{2}\operatorname{erfc} \Lambda^-\right] + (1 - p_t)\operatorname{erfc} \Lambda^0 \tag{47}$$

and

$$p_{1/2} = q'_0\,; \qquad r_{1/2} = r'_0\,; \qquad q_{1/2} = p'_0\,. \tag{48}$$

From the definitions of Λ^+, Λ^0, and Λ^- in (26), we observe the following limits as $R_d \to \infty$:

$$\begin{aligned} p_0 &\to 1 & p_0' &\to (1 - p_t) \\ q_0 &\to 0 & q_0' &\to p_t \\ r_0 &\to 0 & r_0' &\to 0 \ . \end{aligned} \tag{49}$$

Using these probability distributions for the random walk random variable, we desire to compute the probability distributions of the number of bit intervals (K) at which counter 1 or counter 2 first overflows. Two approaches to this computation are discussed in Appendix D. The principal result of these discussions is as follows. If K_{min} denotes the overflow level of either counter (e.g., 2^{12} for the Ku-band ambiguity resolver), then

$$p_c(K) = \left(\frac{K_{min}}{K}\right) \sum_{N=\begin{cases}0,2,4\ldots\\1,3,5\ldots\end{cases}}^{K-K_{min}} \frac{K!}{\left(\frac{K+K_{min}-N}{2}\right)!\left(\frac{K-K_{min}-N}{2}\right)!\,N!} \times p_0^{\frac{K+K_{min}-N}{2}}\, q_0^{\frac{K-K_{min}-N}{2}}\, r_0^{N}; \qquad K \geq K_{min} \tag{50}$$

and

$$p_I(K) = \left(\frac{K_{min}}{K}\right) \sum_{N=\begin{cases}0,2,4\ldots\\1,3,5\ldots\end{cases}}^{K-K_{min}} \frac{K!}{\left(\frac{K+K_{min}-N}{2}\right)!\left(\frac{K-K_{min}-N}{2}\right)!\,N!} \times p_0'^{\frac{K+K_{min}-N}{2}}\, q_0'^{\frac{K-K_{min}-N}{2}}\, r_0'^{N}; \qquad K \geq K_{min}\ , \tag{51}$$

where the sum of N runs on the <u>even</u> integers if $K - K_{min}$ is <u>even</u> or on the <u>odd</u> integers if $K - K_{min}$ is <u>odd</u>.

3.4 Mean Time for Ambiguity Resolution

As discussed in the introduction, the ambiguity resolver declares an ambiguity decision whenever the difference between the counter that overflows in a particular pass (trial) and the other counter exceeds a threshold γ. If, however, no ambiguity decision is made, then both counters are reset to zero and the ambiguity search is continued with a new independent pass. The process is continued until ambiguity resolution is achieved.

The probability of resolving the ambiguity in n passes becomes

$$P_R(n) = P_D + (1 - P_D) P_D + \ldots + (1 - P)^{n-1} P_D \qquad (52)$$

which is a geometric series with a sum

$$P_R(n) = 1 - (1 - P_D)^n \qquad (53)$$

where P_D is the probability of resolving the ambiguity in one pass whether correctly or incorrectly; that is,

$$P_D = P_I + P_c \qquad (54)$$

where P_c and P_I are given in (29) and (30), respectively.

In order to find the mean time to achieve an overall ambiguity resolution probability in n passes $P_R(n)$, we must find the mean time for a decision per pass $\bar{t}_D$. It is easy to show that

$$\bar{t}_D = \frac{(P_c m_c + P_I m_I)}{R}, \qquad (55)$$

where m_c and m_I are the means of the probabilities of overflow of the counter leading to a correct decision and an incorrect decision, respectively; that is,

$$m_c = \sum_{K=K_{min}}^{\infty} K P_c(K) \quad \text{and} \quad m_I = \sum_{K=K_{min}}^{\infty} K P_I(K), \qquad (56)$$

where $P_c(K)$ and $P_I(K)$ are given by (50) and (51), respectively. P_c and

P_I are the unconditional probabilities of making a correct decision and incorrect decision given by (29) and (30) respectively, and R is the data rate which is also the rate at which the counters are incremented or decremented. For the Ku-band ambiguity resolver, R = 216 kbps. The numerical evaluation of the probability of correct ambiguity resolution, incorrect ambiguity resolution, and overall probability of resolution in n passes will be presented and compared to HAC test results in a future report.

APPENDIX G

MARKOV PROCESSES, RANDOM WALKS, AND THEIR APPLICATION TO THE PERFORMANCE CHARACTERIZATION OF THE KU-BAND BIT SYNC AMBIGUITY RESOLVER

APPENDIX G

MARKOV PROCESSES, RANDOM WALKS, AND THEIR APPLICATION TO THE PERFORMANCE CHARACTERIZATION OF THE KU-BAND BIT SYNC AMBIGUITY RESOLVER

by

Waddah K. Alem
Marvin K. Simon
Charles L. Weber

1.0 INTRODUCTION

Markov processes have for a long time been extremely useful as models for physical systems exhibiting random behavior. Many important features of these processes, which have emerged from their application, are best illustrated by the so-called "random walk." In most random walk problems discussed in the applications literature, the mathematical model is physically described by an individual who takes a series of steps. Each step moves one unit to the east and either one unit to the north or one unit to the south. This individual decides the direction of his walk (northeast or southeast) by making a Bernoulli trial with probability p of success and $q = 1 - p$ of failure. Arbitrarily, it is assumed that he goes northeast on a success and southeast on a failure.

A typical question of interest in such a random walk is: How many steps does it take for the individual to first reach a certain distance to the north (or south)? It is desirable to characterize this so-called "first passage time" problem by such measures as the probability distribution (frequency function) of the number of steps to first reach the boundary and the mean and variance of this distribution. Note that after n steps, the individual will be n units to the east of his starting point. His distance north relative to his starting point will be the net number of successes minus failures during the n step walk. Also, the number of successes plus failures must, of course, be equal to n. We shall shortly see that these simple properties, which come from physical reasoning, are extremely useful in a particular mathematical approach to solving the first passage time problem.

In investigating the performance of the Ku-band bit synchronization ambiguity resolver for the Space Shuttle Orbiter (SSO) Signal Processor Assembly (SPA), it became apparent that the solution to a somewhat

more complicated random walk problem was required. In physical terms, this problem can be described by an individual who once again takes a series of steps. Now, however, in addition to going east on each step, he moves one unit to the north with probability p, one unit to the south with probability q, or neither north nor south (i.e., due east) with probability $r = 1 - p - q$. As before, we are interested in the probability distribution of the time to first cross a given boundary and the mean and variance of the distribution.

It is surprising that, to the authors' best knowledge, this type of random walk and its first passage time behavior have not been formally treated in the applications literature. This appendix is an attempt to fill this gap. Several approaches for mathematically modeling this problem will be discussed and the ensuing results will be shown to be equivalent. To begin, we shall illustrate the approaches by first applying them to the classical random walk mentioned in the beginning of this introduction.

2.0 APPROACH BASED ON THE REFLECTION PRINCIPLE

2.1 Classical (Two-Way) Random Walk

Consider the typical random walk path illustrated in Figure 1 which originates ($n = 0$) at $S_0 = i$ and terminates ($n = m$) at the boundary $S_m = i + K$. Here, n denotes the number of steps taken to the east, m is the value of n at which the random walk first reaches the boundary, which is K units above the originating point, and S_n is the value of the random sum at the nth step of the walk. In mathematical terms,

$$S_n = \sum_{k=0}^{n} x_k , \tag{1}$$

where x_k is a random variable which takes on values of +1 and -1 with probability p and q, respectively. Letting N_+ represent the number of positive steps and N_- the number of negative steps in any given path from i to $i+K$, then from the properties previously discussed, it is clear that

$$N_+ - N_- = K \tag{2}$$

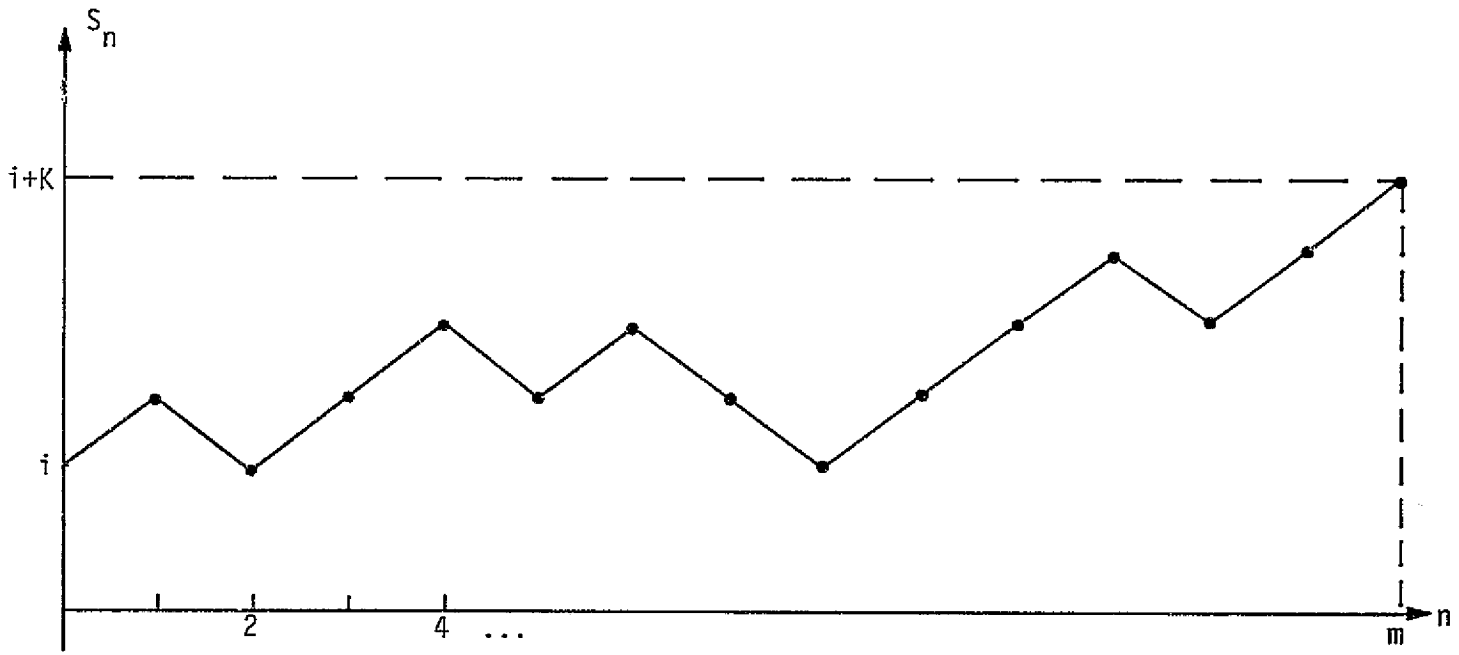

Figure 1. Typical Random Walk Path

and

$$N_+ + N_- = m . \tag{3}$$

Solving (2) and (3) for N_+ and N_- gives

$$N_+ = \frac{m+K}{2} ; \qquad N_- = \frac{m-K}{2} . \tag{4}$$

Since each positive step occurs with probability p and each negative step with probability q, then the probability of any path originating at $S_0 = i$ and terminating at $S_m = i + K$ is

$$p^{N_+} q^{N_-} = p^{(m+K)/2} (1-p)^{(m-K)/2} . \tag{5}$$

The only question that remains in order to compute the probability distribution of m is: How many paths, with probability given by (5), originate at $S_0 = i$ and reach <u>for the first time</u> the level $i+K$ at $n = m$?

The <u>total</u> number of paths $N_{i,i+K}(m)$ originating at $S_0 = i$ and ending at $S_m = i + K$ (irrespective of whether $S_n = i + K$ for any $n < m$) is equal to the number of ways of having N_+ successes in m Bernoulli trials, i.e.,

$$N_{i,i+K}(m) = \binom{m}{N_+} = \binom{m}{\frac{m+K}{2}} , \tag{6}$$

where $\binom{n}{k}$ is the binomial coefficient defined by

$$\binom{n}{k} = \frac{n!}{k!(n-k)!} . \tag{7}$$

To obtain the number of paths with $S_0 = i$, $S_m = i+K$, and $S_n < i+K$ for <u>all</u> $n < m$, we must subtract from (6) the number of paths which reach the boundary prior to $n = m$. Actually, rather than do this, we can simplify the problem one step further. Since every path which reaches $i+K$ for the first time at step m must have come from $i+K-1$ at step $m-1$ and also $i+K-2$ at step $m-2$, we can first compute the <u>total</u> number of paths originating at i and terminating at $i+K-2$ at step $m-2$ [a smaller number of paths than $N_{i,i+K}(m)$ of (6)] and then subtract off those for which $S_n = i+K$ for any $n < m-2$. This total number of paths is clearly

$$N_{i,i+K-2}(m-2) = \binom{m-2}{\frac{m-2+K-2}{2}} = \binom{m-2}{\frac{m+K}{2}-2}. \tag{8}$$

We next compute the number of paths for which $S_0 = i$, $S_{m-2} = i+K-2$, and $S_n = i+K$ for one or more values of $n < m-2$. For each such deviant path, we can select the smallest value of n (say n_0) for which $S_{n_0} = i+K$ and reflect the portion of the path preceding this value of n about the $S_n = i+K$ axis (see Figure 2). The reflected portion, together with the original portion having $n > n_0$ will form a new path with $S_0 = i+2K$ and $S_{m-2} = i+K-2$. However, <u>every</u> path with $S_0 = i+2K$ and $S_{m-2} = i+K-2$ must have $S_n = 0$ for some $0 < n < m-2$. Thus, there is a one-to-one correspondence between each deviant path between i and $i+K-2$ and <u>every</u> path between $i+2K$ and $i+K-2$. Thus, the number of deviant paths between i and $i+K-2$ is

$$N_{i+2K,i+K-2}(m-2) = \binom{m-2}{\frac{m-2+K-2-2K}{2}} = \binom{m-2}{\frac{m-K}{2}-2}. \tag{9}$$

Subtracting (9) from (8) gives the number of paths which originate at i and cross for the first time the boundary $i+K$ at $n = m$, i.e.,

$$N = \binom{m-2}{\frac{m+K}{2}-2} - \binom{m-2}{\frac{m-K}{2}-2}. \tag{10}$$

Finally then, the probability distribution of m (the number of steps to first cross the boundary K units above the originating point) is

$$p(m) = \left[\binom{m-2}{\frac{m+K}{2}-2} - \binom{m-2}{\frac{m-K}{2}-2}\right] p^{(m+K)/2}(1-p)^{(m-K)/2}; \quad m = K, K+2, K+4, \ldots \tag{11}$$

The number of paths N as computed by (10) can be simplified to

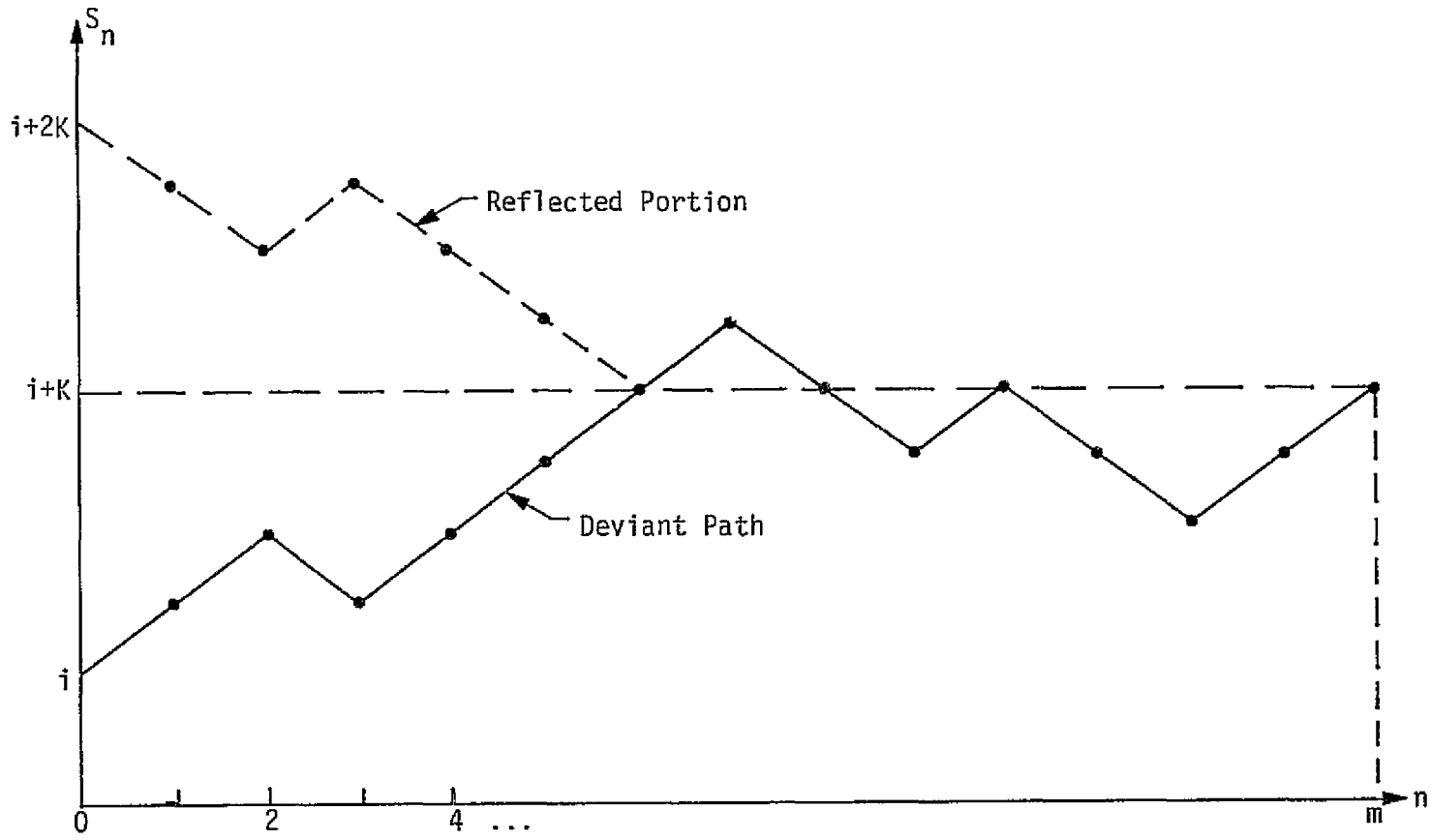

Figure 2. Deviant Path and Its Reflected Portion

$$N = \frac{K}{m}\binom{m}{\frac{m+K}{2}} = \left(\frac{K}{m}\right)\frac{m!}{(\frac{m+K}{2})!\,(\frac{m-K}{2})!} . \tag{12}$$

Thus, the final form for the probability distribution is

$$p(m) = \frac{K}{m}\binom{m}{\frac{m+K}{2}} p^{(m+K)/2}(1-p)^{(m-K)/2} ;$$

$$m = K, K+2, K+4, \ldots \tag{13}$$

The probability of first reaching the boundary in <u>any</u> number of steps is

$$P_b = \sum_{m=K,K+2,..}^{\infty} p(m) . \tag{14}$$

Substituting (13) into (14) and letting $i = (m-K)/2$ gives

$$\begin{aligned} P_b &= K \sum_{i=0}^{\infty} \left(\frac{1}{2i+K}\right)\binom{2i+K}{i+K} p^{i+K}(1-p)^i \\ &= Kp^K \sum_{i=0}^{\infty} \frac{(2i+K-1)!}{(i+K)!\,i!}[p(1-p)]^i \\ &= p^K\left\{1 + Kp(1-p) + K(K+3)\frac{[p(1-p)]^2}{2!}\right. \\ &\qquad \left. + K(K+4)(K+5)\frac{[p(1-p)]^3}{3!} + \cdots\right\} . \end{aligned} \tag{15}$$

From [1, pp. 34-35, Series No. (187)], we have that

$$1 + ny + \frac{n(n+3)}{2!}y^2 + \frac{n(n+4)(n+5)}{3!}y^3 + \cdots = \frac{1}{2^{-n}}\left\{1 + \sqrt{1-y}\right\}^{-1} . \tag{16}$$

Comparing (15) and (16) and letting $n = K$, $y = p(1-p)$, gives

$$P_b = \left\{\frac{2p}{1 + \sqrt{1-p(1-p)}}\right\}^K . \tag{17}$$

Figure 3 illustrates P_b versus p for $K = 10, 100$. Note that, for $p < 1$, there is always a finite probability of not reaching the boundary given

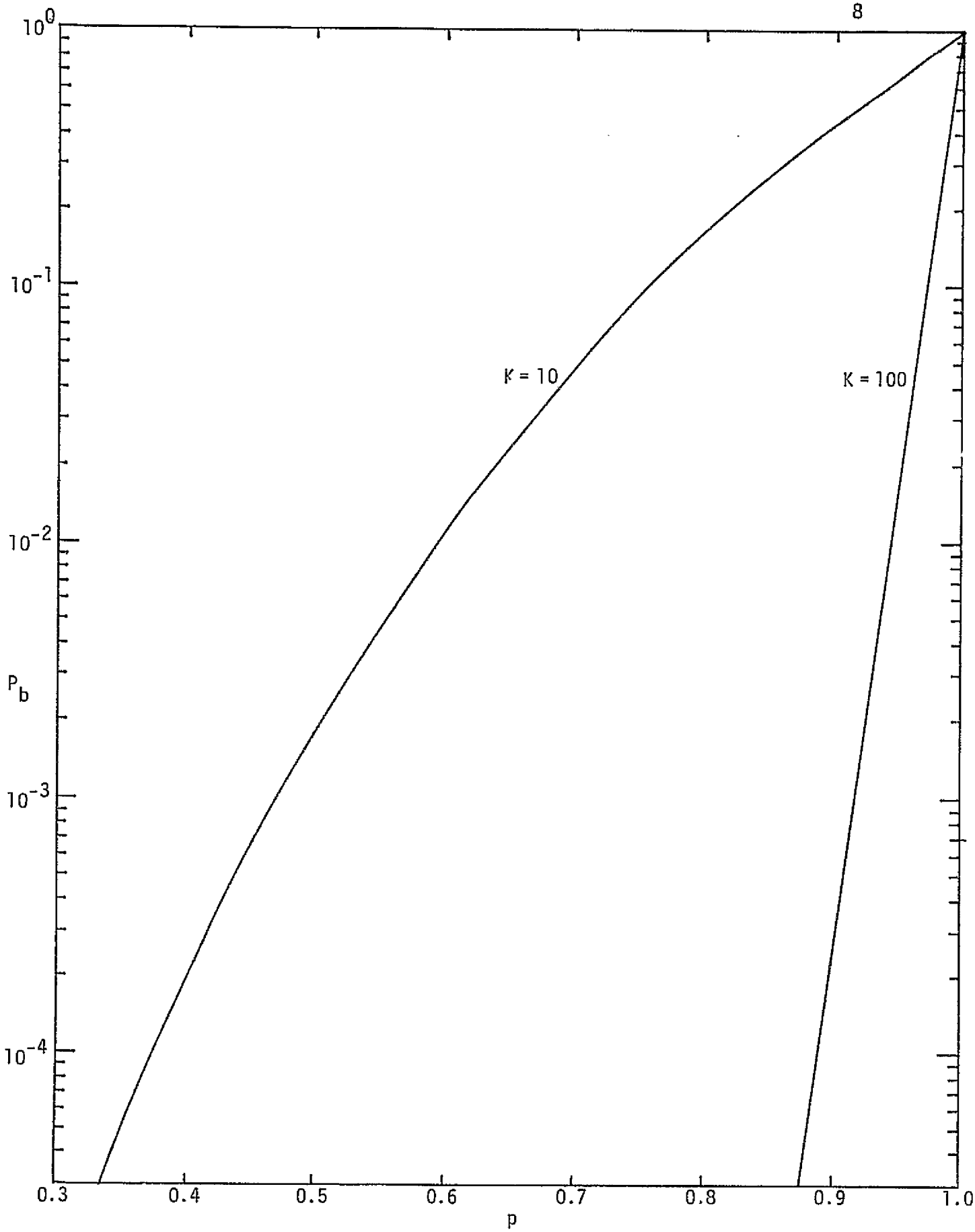

Figure 3. Probability of Reaching Boundary Versus Probability of Positive Step

by $1 - P_b$. Furthermore, as K gets large, the probability of reaching the boundary becomes an extremely sensitive function of p.

2.2 Three-Way Random Walk

Consider now the random walk at each step can proceed in one of three directions, namely, northeast with probability p, southeast with probability q, and due east with probability $r = 1 - p - q$. An example of this type of walk is illustrated in Figure 4. Once again, the net number of positive steps to reach the boundary is given by K, i.e., (2) still applies. However, the total number of steps m must now include the number of steps during which no advance in the north or south direction is made. Letting N_0 denote this number of flat steps, then the equation corresponding to (3) would be

$$N_+ + N_- + N_0 = m \, . \tag{18}$$

Solving (2) and (18) for N_+ and N_- (dependent now also on N_0) gives

$$N_+ = \frac{m + K - N_0}{2} \, ; \qquad N_- = \frac{m - K - N_0}{2} \, . \tag{19}$$

Since now each positive (north) step occurs with probability p, each negative (south) step occurs with probability q, and each zero (due east) step occurs with probability r, then the probability of any path originating at $S_0 = i$ and terminating at $S_m = i + K$ is

$$p^{N_+} q^{N_-} r^{N_0} = p^{(m+K-N_0)/2} \, q^{(m-K-N_0)/2} \, r^{N_0} \, . \tag{20}$$

Once again, to compute the probability distribution of m, we must find the number of paths which originate at i and first reach the boundary $i+K$ at step $n = m$.

The <u>total</u> number of paths $N_{i,i+K}(m;N_0)$ originating at $S_0 = i$ and ending at $S_m = i + K$ (irrespective of whether $S_n = i + K$ for any $n < m$) is a <u>trinomial</u> coefficient, namely,

$$N_{i,i+K}(m;N_0) = \frac{m!}{N_+! \, N_-! \, N_0!} = \frac{m!}{\left(\frac{m+K-N_0}{2}\right)! \left(\frac{m-K-N_0}{2}\right)! \, N_0!} \, . \tag{21}$$

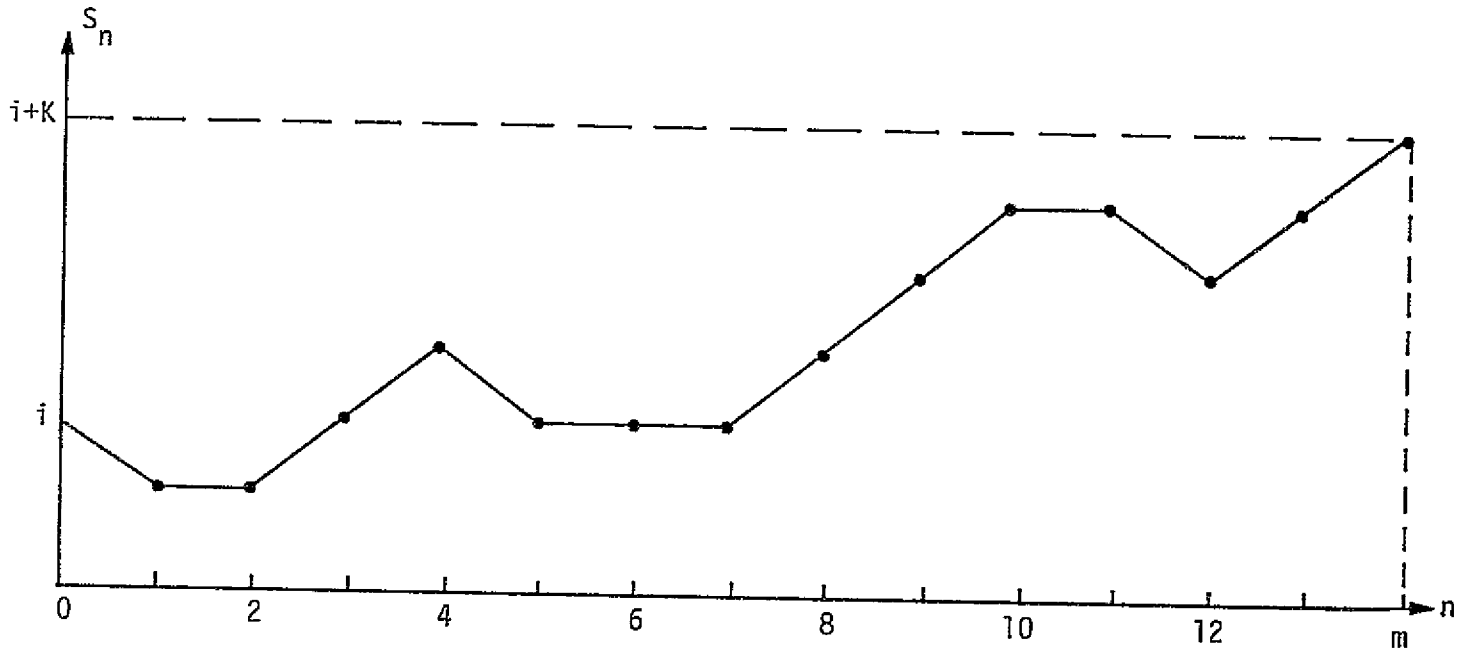

Figure 4. Typical Random Walk Path

Also, the minimum value of m for which a path can reach the boundary is $m = K + N_0$.

As in the two-way random walk, each path which reaches $i+K$ at step m for the first time must have come from $i+K-1$ at step $m-1$. Now, however, at step $m-2$, the random walk could be either $S_{m-2} = i+K-2$ or $S_{m-2} = i+K-1$. The total number of paths originating at i and terminating at $i+K-2$ is $N_{i,i+K-2}(m-2;N_0)$. Using the reflection principle once again (see Figure 5 for an example of its application), the number of deviant paths with $S_0 = i$ and $S_{m-2} = i+K-2$ is $N_{i+2K,i+K-2}(m-2;N_0)$. Thus, the number of paths N_1 with $S_0 = i$, $S_{m-2} = i+K-2$, and $S_n < i+K$ for all $i \le n < m-2$ is

$$N_1 = N_{i,i+K-2}(m-2;N_0) - N_{i+2K,i+K-2}(m-2;N_0)$$

$$= \frac{(m-2)!}{\left(\frac{m+K-N_0}{2}-2\right)!\left(\frac{m-K-N_0}{2}\right)!\,N_0!} - \frac{(m-2)!}{\left(\frac{m-K-N_0}{2}-2\right)!\left(\frac{m+K-N_0}{2}\right)!\,N_0!} . \tag{22}$$

By applying similar arguments as those above, the number of paths N_2 with $S_0 = i$, $S_{m-2} = i+K-1$ and $S_n < i+K$ for all $1 \le n < m-2$ is

$$N_2 = N_{i,i+K-1}(m-2;N_0-1) - N_{i+2K,i+K-1}(m-2;N_0-1)$$

$$= \frac{(m-2)!}{\left(\frac{m+K-N_0}{2}-1\right)!\left(\frac{m-K-N_0}{2}\right)!\,(N_0-1)!} - \frac{(m-2)!}{\left(\frac{m-K-N_0}{2}-1\right)!\left(\frac{m+K-N_0}{2}\right)!\,(N_0-1)!} . \tag{23}$$

Thus, the total number of paths N which reach the boundary for the first time at step m is $N = N_1 + N_2$, and the corresponding frequency function of m (conditioned on N_0) is

$$p(m;N_0) = N\, p^{(m+K-N_0)/2}\, q^{(m-K-N_0)/2}\, r^{N_0} . \tag{24}$$

Finally, the unconditional probability distribution of m is obtained by summing over N_0, i.e.,

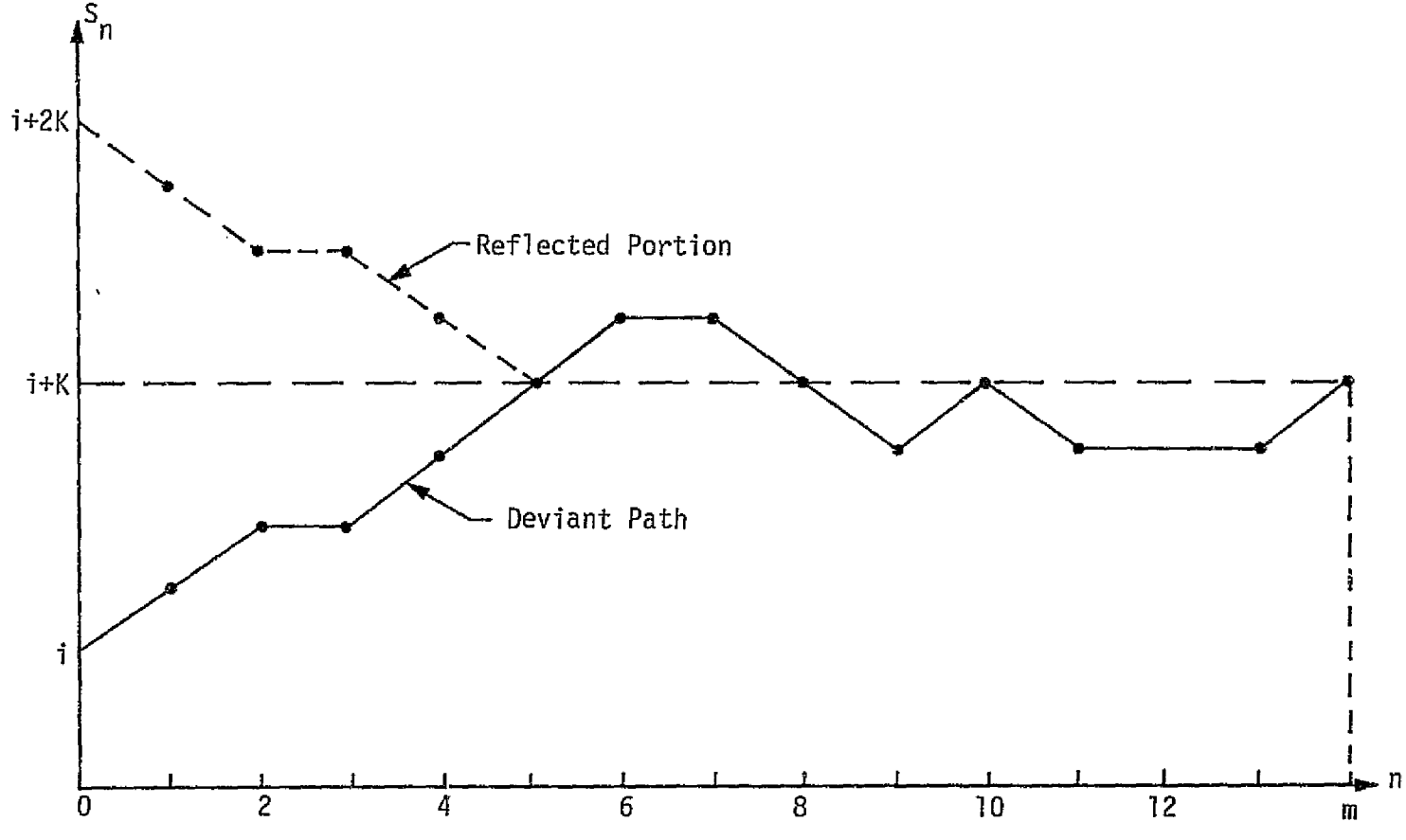

Figure 5. Deviant Path and Its Reflected Portion

$$p(m) = \begin{cases} \sum_{N_0=1,3,5,..}^{m-K} p(m;N_0) ; & m-K \text{ odd} \\ \sum_{N_0=0,2,4,..}^{m-K} p(m;N_0) ; & m-K \text{ even} \end{cases} \tag{25}$$

The defining expressions for N_1 and N_2 given in (22) and (23), respectively, can be simplified and combined to yield

$$N = N_1 + N_2 = \left(\frac{K}{m}\right) \frac{m!}{\left(\frac{m+K-N_0}{2}\right)! \left(\frac{m-K-N_0}{2}\right)! N_0!} , \tag{26}$$

which is analogous with (12). Combining (24), (25), and (26) gives the final desired result

$$p(m) = \begin{cases} \frac{K}{m} \sum_{N_0=1,3,5,..}^{m-K} \frac{m!}{\left(\frac{m+K-N_0}{2}\right)! \left(\frac{m-K-N_0}{2}\right)! N_0!} p^{(m+K-N_0)/2} q^{(m-K-N_0)/2} r^{N_0} ; \\ \qquad m = K+1, K+3, \ldots \\ \frac{K}{m} \sum_{N_0=0,2,4,..}^{m-K} \frac{m!}{\left(\frac{m+K-N_0}{2}\right)! \left(\frac{m-K-N_0}{2}\right)! N_0!} p^{(m+K-N_0)/2} q^{(m-K-N_0)/2} r^{N_0} ; \\ \qquad m = K, K+2, K+4, \ldots \end{cases} \tag{27}$$

The probability of first reaching the boundary in any number of steps is

$$P_b = \sum_{m=K}^{\infty} p(m) . \tag{28}$$

After considerable algebraic manipulation, (28) can be put in the form

$$P_b = K p^K \sum_{\ell=0}^{\infty} C_\ell \frac{[p(1-p)]^\ell}{\ell!} , \tag{29}$$

where

$$C_\ell = \sum_{i=0}^{\infty} \frac{(K+i+2\ell-1)!}{(K+\ell)!} \left(\frac{r^i}{i!}\right) . \tag{30}$$

Unfortunately, however, the authors have been unable to arrive at a closed form expression for (29) analogous to (17).

3.0 PROBABILITY DISTRIBUTION OF THE DURATION OF THE RANDOM WALK USING THE GENERATING FUNCTIONS METHOD

The probability distribution of the duration of the random walk is determined by use of generating functions [2]. The random walk is assumed to have absorbing barriers at 0 and A. The barrier at A will be allowed to extend to infinity after the probability distribution has been determined.

Assuming, as in Figure 6, that a particle starts at a height K with probability p of making a positive step to a height K+1, probability q of making a negative step to a height K-1, and probability r = 1-p-q of remaining at the same height K, the probability of reaching the zero height in m steps is developed with a finite A and then with infinite A which reduces the problem to that solved using the reflective principle approach.

It should be noted, however, that in the end result the roles of p and q should be interchanged to obtain the results in (27). This is due to the fact that, as is obvious in Figure 6, in this approach p is the probability of moving away from the crossing level, contrary to the assumption made in the first approach.

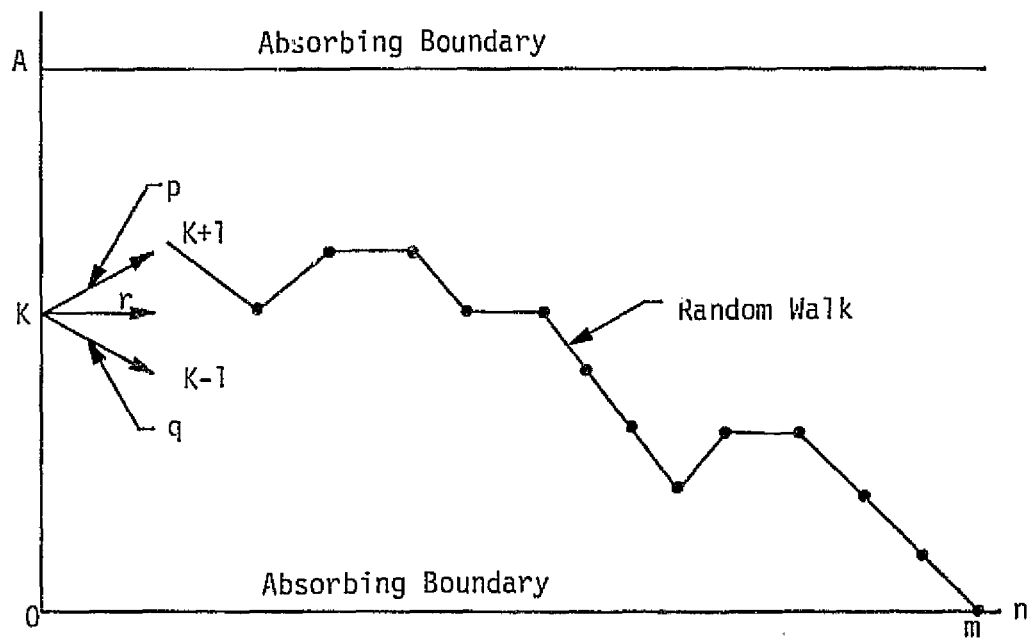

Figure 6. Notation for Generating Function Approach for the Random Walk Problem

Definition: Let $p_{K,m}$ be the probability that the random walk described in the previous section and in Figure 1 will terminate at 0 in m steps, given that the particle (or register setting) was initially placed at K, with K and m positive integers.

Definition: Let $a_0, a_1, a_2, \ldots$ be a sequence of real numbers. If

$$G(s) = \sum_{k=0}^{\infty} a_k s^k \tag{31}$$

converges in some interval $|s| < s_0$, then G(s) is called the generating function of the sequence $\{a_k\}$. The variable s itself has no significance.

Definition: Let $P_K(s)$ be the generating function for the set of probabilities $\{P_{K,m}\}$ for a given K. In particular,

$$P_K(s) \triangleq \sum_{n=0}^{\infty} P_{K,n} s^n . \tag{32}$$

Given that the random walk started at position K at m = 0, after the first step the position is K+1, K, or K-1. As a result, we conclude that, for $1 < K < A-1$ and $m \geq 1$,

$$P_{K,m+1} = p P_{K+1,m} + q P_{K-1,m} + r P_{K,m} . \tag{33}$$

This is a homogeneous difference equation depending on the two variables K and m, where K is analogous to amplitude and m is analogous to time.

The boundary conditions are

$$\begin{aligned} P_{0,m} &= 0 , & m \geq 1 \\ P_{0,0} &= 1 \\ P_{A,m} &= 0 , & m \geq 0 \\ P_{K,0} &= 0 , & K > 0 . \end{aligned} \tag{34}$$

If the generating function for the set of probabilities $\{P_{K,m}\}$ is $P_K(s)$, then the generating function for the set $\{P_{K,m+1}\}$ is

$$G(\{P_{K,m+1}\}) \triangleq \sum_{n=0}^{\infty} P_{K,n+1}\, s^n = \frac{P_K(s)}{s}. \tag{35}$$

With (35), the generating function for both sides of the difference equation in (33) can be written, with the result that

$$P_K(s) = s\,[p\,P_{K+1}(s) + q\,P_{K-1}(s) + r\,P_K(s)]\,. \tag{36}$$

The boundary conditions in (34), when converted to generating functions, lead to the following boundary conditions on $P_K(s)$:

$$\begin{aligned} P_0(s) &= 1 \\ P_A(s) &= 0\,. \end{aligned} \tag{37}$$

The evaluation of the homogeneous generating function (36) with the boundary conditions in (37) can be carried out as follows. Assume a solution of the form

$$P_K(s) = [\lambda(s)]^K \tag{38}$$

for some function $\lambda(s)$. Substituting (38) into (36), we find that $\lambda(s)$ is the solution of the quadratic equation

$$s\,p\,\lambda^2(s) - (1 - r\,s)\,\lambda(s) + s\,q = 0\,, \tag{39}$$

which has solutions

$$\lambda_1(s) = \frac{1 - r\,s + \sqrt{(1 - r\,s)^2 - 4\,p\,q\,s^2}}{2\,p\,s} \tag{40a}$$

and

$$\lambda_2(s) = \frac{1 - r\,s - \sqrt{(1 - r\,s)^2 - 4\,p\,q\,s^2}}{2\,p\,s}\,. \tag{40b}$$

Therefore, the solution for the generating function is of the form

$$P_K(s) = c_1(s)\,[\lambda_1(s)]^K + c_2(s)\,[\lambda_2(s)]^K, \tag{41}$$

where the coefficient functions of s, $c_i(s)$, $i = 1,2$, are to be determined from the boundary conditions in (37). Via direct substitution,

$$P_0(s) = 1 = c_1(s) + c_2(s) \tag{42a}$$

and

$$P_A(s) = 0 = c_1(s)[\lambda_1(s)]^A + c_2(s)[\lambda_2(s)]^A, \tag{42b}$$

from which we obtain

$$c_1(s) = \frac{[\lambda_2(s)]^A}{[\lambda_2(s)]^A - [\lambda_1(s)]^A} \tag{43a}$$

and

$$c_2(s) = \frac{-[\lambda_1(s)]^A}{[\lambda_2(s)]^A - [\lambda_1(s)]^A}. \tag{43b}$$

Substitution of (43) into (41) yields

$$P_K(s) = \frac{[\lambda_2(s)]^A[\lambda_1(s)]^K - [\lambda_1(s)]^A[\lambda_2(s)]^K}{[\lambda_2(s)]^A - [\lambda_1(s)]^A}, \tag{44}$$

where $\lambda_i(s)$ are given by (40). Using the relationship

$$\lambda_1(s)\lambda_2(s) = \frac{q}{p}, \tag{45}$$

this simplifies to

$$P_K(s) = \left(\frac{q}{p}\right)^K \left[\frac{[\lambda_1(s)]^{A-K} - [\lambda_2(s)]^{A-K}}{[\lambda_1(s)]^A - [\lambda_2(s)]^A}\right]. \tag{46}$$

This is the generating function for the probability of reaching 0 level (probability of ruin or probability of absorption at 0) at the mth step. If $P_K(s)$ could easily be expanded into a power series as in (32), then the coefficient of s^m in (46) would be $P_{K,m}$. Unfortunately, expanding (46) into a power series does not lend itself to being tractable.

4.0 SOLUTION BY THE METHOD OF PARTIAL FRACTIONS

The generating function in (46) depends formally on a square root but is actually a rational function. To see this, note initially that an application of the binomial theorem to the denominator in (46) reduces the denominator to the form

$$[\lambda_1(s)]^A - [\lambda_2(s)]^A = \left(\frac{1}{2ps}\right)^A \sqrt{(1-rs)^2 - 4pqs^2} \sum_{\substack{k=1 \\ k \text{ odd}}}^{A} \binom{A}{k}$$

$$\times (1-rs)^{A-k} [(1-rs)^2 - 4pqs^2]^{\frac{k-1}{2}}$$

$$= s^{-A} \sqrt{(1-rs)^2 - 4pqs^2}\, P_A(s) , \tag{47}$$

where $P_A(s)$ is an even polynomial of degree A-1 when A is odd and of degree A-2 when A is even. The numerator is of the same form except that A is replaced by A-k. Therefore, $P_K(s)$ is the ratio of two polynomials in s whose degrees differ at most by 1. Consequently, it is possible to develop an explicit expression for the probabilities $P_{K,m}$ by the method of partial fraction expansion.

The computations simplify greatly by the introduction of an auxiliary variable ϕ, which we define in terms of s via the relationship

$$s = \left[2\sqrt{pq}\cos\phi + r\right]^{-1} \tag{48a}$$

or, equivalently,

$$\cos\phi = \frac{1-rs}{2s\sqrt{pq}} . \tag{48b}$$

Upon substitution of (48) into (40), we obtain the simplifications

$$\lambda_1(s) = \sqrt{q/p}\ \exp(-i\phi) \tag{49a}$$

and

$$\lambda_2(s) = \sqrt{q/p}\ \exp(+i\phi) . \tag{49b}$$

As a result,

$$P_K(s) = \left(\frac{q}{p}\right)^{K/2} \frac{\sin [(A-K)\phi]}{\sin (A\phi)} . \tag{50}$$

The roots $s_0, s_1, \ldots, s_{A-1}$ of the denominator in (50) are all simple and hence there exists a partial fraction expansion of the form

$$P_K(s) = \left(\frac{q}{p}\right)^{K/2} \frac{\sin [(A-K)\phi]}{\sin (A\phi)}$$

$$= a + bs + \sum_{\nu=0}^{A-1} \frac{\rho_\nu}{s_\nu - s} . \tag{51}$$

In principle, the linear contribution a+bs must be formally written to account for the fact that the degree of the numerator may be one larger than the degree of the denominator. Since a and b contribute only to $P_{K,0}$ and $P_{K,1}$, respectively, which are both zero if $K \geq 2$, we know $a = b = 0$. Also, we should only consider the roots s_ν of the denominator which are also not roots of the numerator. If an s_ν is such a root, however, then $P_K(s)$ is continuous at $s = s_\nu$ and the corresponding $\rho_\nu = 0$. Since such canceling roots do not contribute to the right side of (51), we need not treat them separately.

The roots $s_0, s_1, \ldots, s_{A-1}$ correspond to the roots

$$\sin (A\phi) = 0 ,$$

which has solutions

$$\phi_\nu = \frac{\pi\nu}{A} , \qquad \nu = 0,\ldots,A-1 . \tag{52}$$

No additional roots need be considered, since any other values of ν in (52) will not produce any new values of s in (48). Therefore,

$$s_\nu = \left[2\sqrt{pq}\, \cos (\pi\nu/A) + r\right]^{-1} ; \qquad \nu = 0,1,\ldots,A-1 . \tag{53}$$

This expression is not valid when $r = 0$, A is even, and $\nu = A/2$. If such is the case, however, then ϕ_ν is also a root of the numerator and this

root vanishes in the final result. This lack of validity can therefore be ignored.

Since all of the roots are simple, ρ_ν can be computed from the following:

$$\begin{aligned}\rho_\nu &= \lim_{s \to s_\nu} (s_\nu - s)\, P_K(s) \\ &= \lim_{s \to s_\nu} (s_\nu - s) \left(\frac{q}{p}\right)^{K/2} \frac{\sin\,[(A-K)\,\phi]}{\sin\,(A\phi)} \\ &= \left(\frac{q}{p}\right)^{K/2} \sin\,(K\phi_\nu) \lim_{s \to s_\nu} \frac{(s - s_\nu)}{\sin\,(A\phi)}\,. \end{aligned} \tag{54}$$

The last limit can be determined from L'Hospital's rule and using implicit differentiation of (48), with the result that

$$\frac{d\phi}{dt} = \frac{1}{2\sqrt{p\,q}\; s^2 \sin\,\phi} \tag{55}$$

and

$$\rho_\nu = \left(\frac{q}{p}\right)^{K/2} \sin\,(K\phi_\nu) \lim_{s \to s_\nu} \left[\frac{1}{A \cos\,(A\phi)\, \frac{d\phi}{dt}}\right]\,. \tag{56}$$

Substituting (55) into (56),

$$\rho_\nu = \left(\frac{q}{p}\right)^{K/2} \frac{2\sqrt{p\,q}}{A} \sin\,(K\phi_\nu)\, s_\nu^2 \sin\,(\phi_\nu)\,; \qquad \nu = 0,1,\ldots,A-1\,. \tag{57}$$

Note that, since $\phi_0 = 0$, $\rho_0 = 0$, and the $\nu = 0$ term can be neglected.

The generating function $P_K(s)$ therefore has the representation

$$P_K(s) = \sum_{\nu=1}^{A-1} \frac{\rho_\nu}{s_\nu - s} = \sum_{\nu=1}^{A-1} \frac{\rho_\nu / s_\nu}{1 - s/s_\nu}\,. \tag{58}$$

Each term in the above sum can be expanded into the power series

$$\frac{\rho_\nu/s_\nu}{1 - s/s_\nu} = \left(\frac{\rho_\nu}{s_\nu}\right) \sum_{m=0}^{\infty} \left(\frac{s}{s_\nu}\right)^m . \tag{59}$$

Substituting (59) into (58),

$$P_K(s) = \sum_{m=0}^{\infty} \left[\sum_{\nu=1}^{A-1} \frac{\rho_\nu}{s_\nu^{m+1}}\right] s^m . \tag{60}$$

Comparing the power series representation of $P_K(s)$ in (60) with that in (32), we have that the probability of absorption is given by

$$P_{K,m} = \sum_{\nu=1}^{A-1} \frac{\rho_\nu}{s_\nu^{m+1}} . \tag{61}$$

Substituting (40) and (43) into (61), this probability reduces to

$$P_{K,m} = \frac{2^m}{A} q^{\frac{m+K}{2}} p^{\frac{m-K}{2}} \sum_{\nu=1}^{A-1} \sin\left(\frac{\pi\nu}{A}\right) \sin\left(\frac{\pi\nu K}{A}\right) \left[\cos\frac{\pi\nu}{A} + \frac{r}{2\sqrt{p\,q}}\right]^{m-1} . \tag{62}$$

This is the probability of absorption at 0 at the mth step, when starting at K, with an additional barrier at $A > K$.

The barrier at A is eliminated by passing to the limit as $A \to \infty$, with the result that

$$P_{K,m} = 2^m p^{\frac{m-K}{2}} q^{\frac{m+K}{2}} \int_0^1 \sin(\pi x) \sin(K\pi x) \left[\cos(\pi x) + \frac{r}{2\sqrt{p\,q}}\right]^{m-1} dx . \tag{63}$$

This can also be written as

$$P_{K,m} = 2^m p^{\frac{m-K}{2}} q^{\frac{m+K}{2}} \sum_{k=0}^{m-1} \binom{m-1}{k} \left(\frac{r}{2\sqrt{p\,q}}\right)^{m-1-k} \int_0^1 \sin(\pi x) \sin(K\pi x) [\cos(\pi x)]^k dx . \tag{64}$$

This is the probability of absorption at zero at the mth step, when starting at K, and no other absorbing barrier.

The integral in (64) can be evaluated in the following manner:

$$2^n \int_0^1 \cos^{n-1}(\pi x) \sin(\pi x) \sin(\pi i x)\, dx = \begin{cases} 0\,; & n+i \text{ odd} \\ 0\,; & n < i \\ \binom{n}{\frac{n+1}{2}} \frac{i}{n}\,; & n+i \text{ even} \end{cases} \tag{65}$$

As discussed before, interchanging the role of p and q and using (65) results in

$$P_{K,m} = p^{\frac{m+K}{2}} q^{\frac{m-K}{2}} \sum_{\substack{k=K-1 \\ k+K+1 \text{ even}}}^{m-1} \binom{m-1}{k} \left(\frac{r}{2\sqrt{p\,q}}\right)^{m-1-k} 2^{m-k-1} \binom{k+1}{\frac{K+k+1}{2}} \frac{K}{K+1}. \tag{66}$$

Changing the summation variable to $N_0 = m-1-k$ reduces (66) to (27), namely,

$$P_{K,m} = p(m) = \sum_{\substack{n=0,2.. \\ \text{or } n=1,3..}}^{m-K} \frac{m!}{\left(\frac{m+K-N_0}{2}\right)!\left(\frac{m-K-N_0}{2}\right)!N_0!} p^{\frac{m+K-N_0}{2}} q^{\frac{m-K-N_0}{2}} r^{N_0}. \tag{67}$$

5.0 NUMERICAL RESULTS AND SPECIAL CASES

Using (27), the probability of reaching the threshold K in m steps is plotted in Figures 7 and 8. Figure 7 assumes a threshold K = 10 and p = 0.7 and varies q and r such that p+q+r = 1. The mean and the variance in each case is also shown in the figure. It is obvious from these calculations that, for a constant K and p, the mean and the variance increase with the increase of q (the probability of taking a step in the wrong direction) and the decrease of r (the probability of taking a step parallel to the threshold). In Figure 8, the probabilities p, q and r are held constant and the threshold is used as a parameter.

Figure 9 illustrates the cumulative probability of crossing a threshold (K = 10) versus the number of steps for a given set of probabilities p, q and r. The cumulative probability $P^{cum}_{K,m}$ is defined as

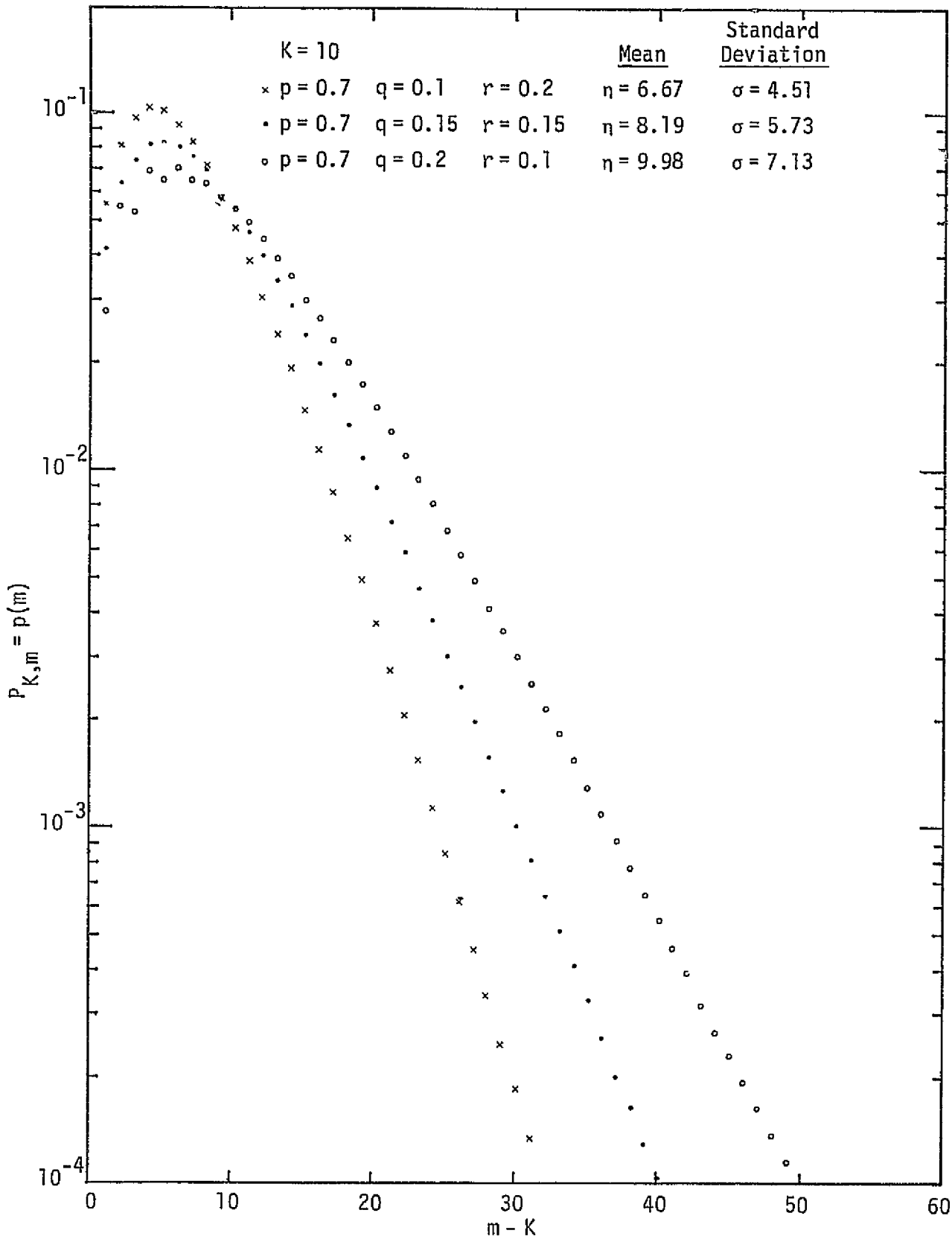

Figure 7. $P_{K,m}$ versus m-K for K = 10 and p, q, r as Parameters

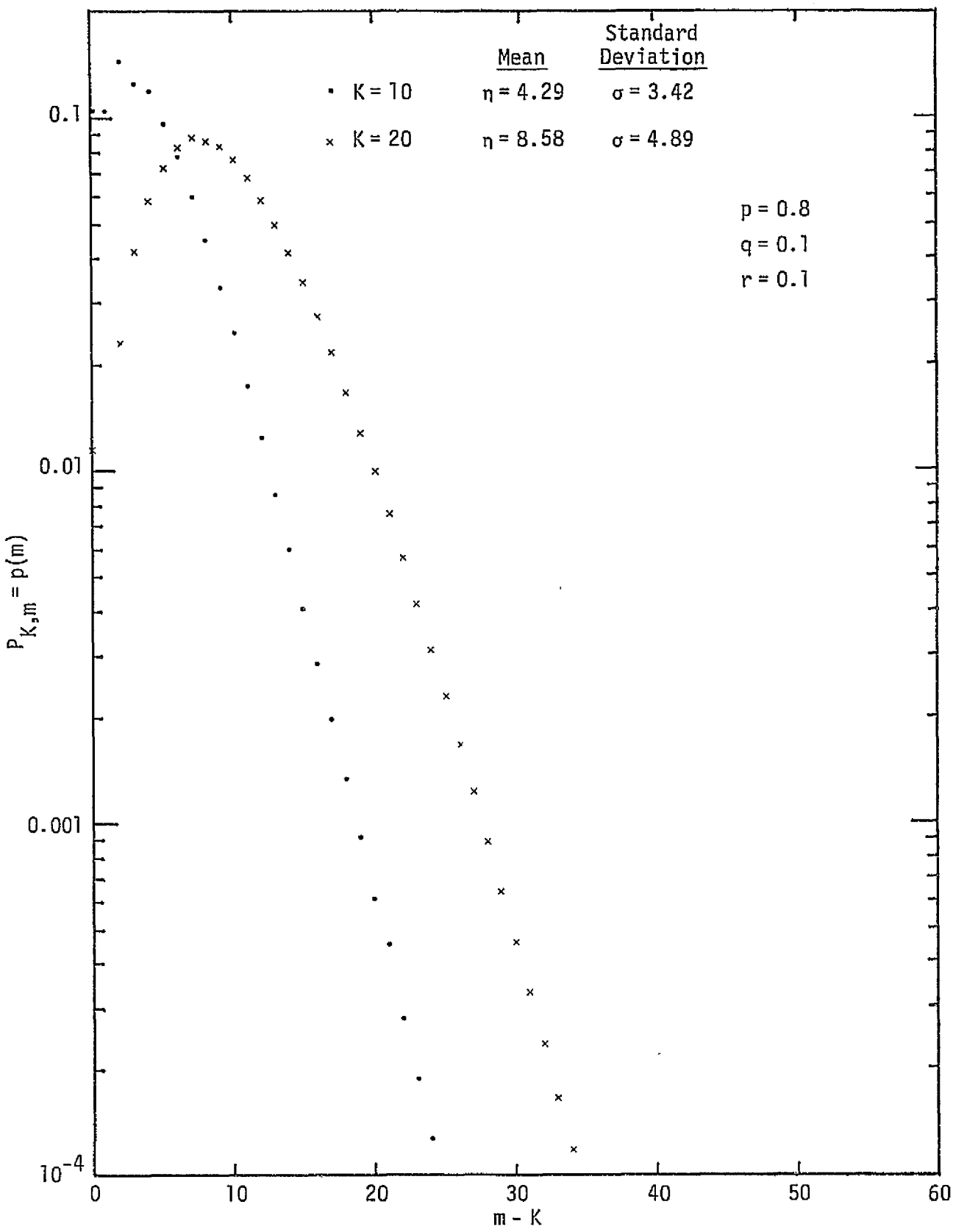

Figure 8. $P_{K,m}$ versus m-K for given p, q, and r with K as a parameter

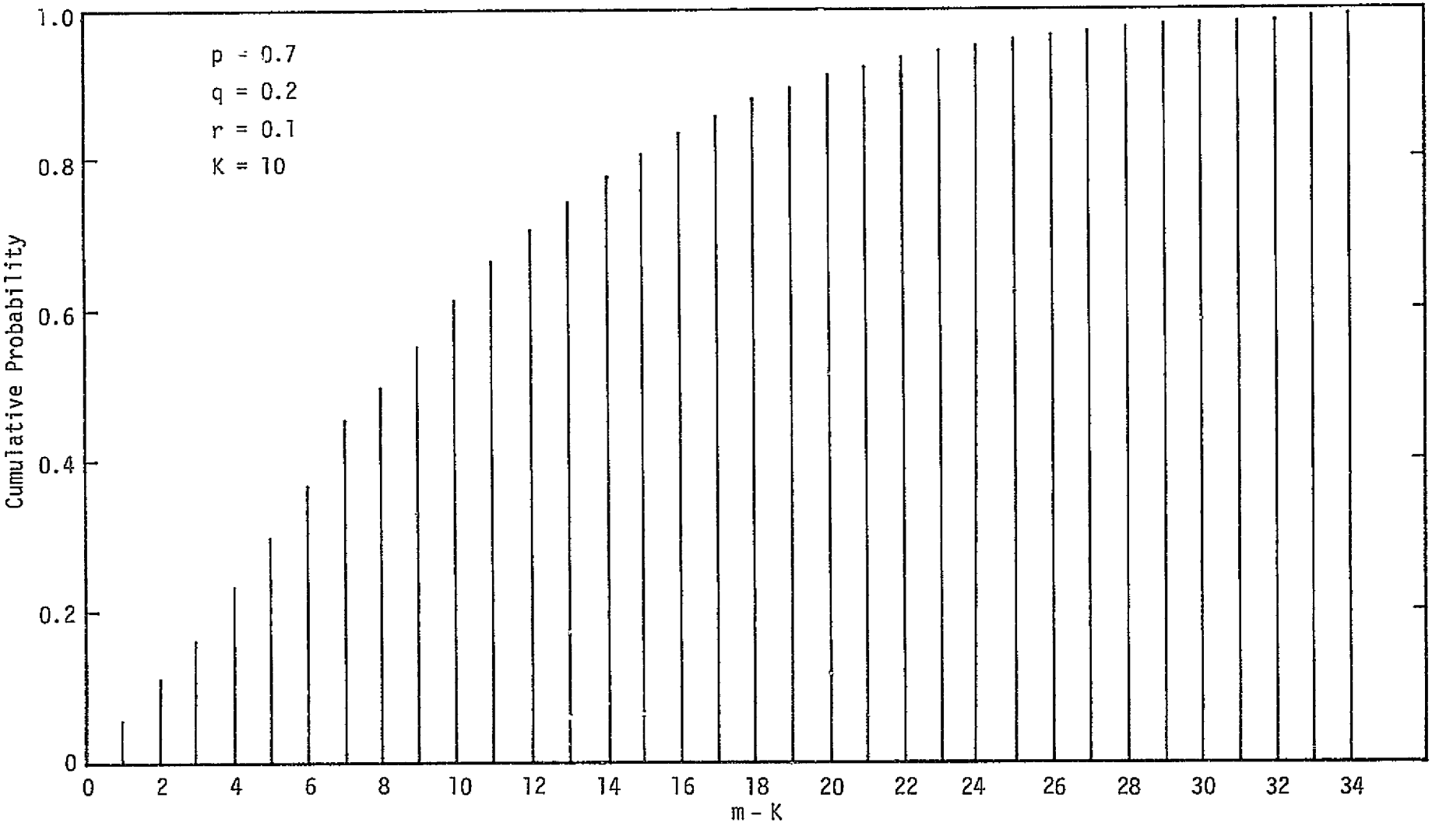

Figure 9. Cumulative Probability of Crossing Threshold

$$P_{K,m}^{cum} = \sum_{i=K}^{m-K} P_{K,i} \cdot$$

Two interesting special cases can be derived; the first is the classical two-way random walk problem and the second is a two-way random walk problem with q (the probability of going in the wrong direction) equal to 0.

A. Case 1: $r = 0$

Substituting $r = 0$ into (63) and using (65) results in

$$P_{K,m}^{(r=0)} = \frac{K}{m}\binom{m}{\frac{m+K}{2}} p^{\frac{m+K}{2}} q^{\frac{m-K}{2}} ; \qquad m = K, K+2, K+4, \ldots \tag{68}$$

which is identical to the expression in (13).

B. Case 2: $q = 0$

Substituting $q = 0$ in (67) and realizing that all the terms in the summation are 0 except when $N_0 = m-K$ results in

$$P_{K,m}^{(q=0)} = \frac{K}{m}\binom{m}{m-K} p^K r^{m-K} . \tag{69}$$

Equations (68) and (69) represent the two special cases of a two-way random walk derived from a three-way random walk.

REFERENCES:

1. L. B. W. Jolley. Summation of Series. New York: Dover Publications,

2. W. Feller. An Introduction to Probability Theory and Its Applications - Vol. I. 3rd ed. Wiley, 1968.

APPENDIX H

PRODUCT DESIGN CONSIDERATION

APPENDIX H

PRODUCT DESIGN CONSIDERATION

by

Sergei Udalov

1.0 INTRODUCTION

This appendix describes the product design considerations for the Ku-Band Integrated Radar and Communication Equipment for the Space Shuttle Orbiter.

This equipment, as designed by the contractor (Hughes Aircraft Company), is comprised of four line replaceable units (LRU). One of these LRUs is a deployed assembly (DA) located within the payload bay and deployable upon the opening of the payload bay doors. The other three LRUs are installed in the avionics bay located inside the Orbiter cabin.

Figure 1 shows the deployed assembly. As is shown in the figure, the DA consists of two major subassemblies: (1) the deployed mechanical assembly (DMA) and (2) the deployed electronics assembly (DEA). The DMA includes all the necessary components for forming and steering a highly directional antenna beam. These components are the gimbals, the antenna reflector, and the feed with its support. The DEA houses the electronics for transmission and reception of the radar signals and the reception of the communication signals.

Currently, in the baseline, each Orbiter will be equipped with two deployed assemblies, i.e., deployed assembly A and deployed assembly B. The mechanical portions of the two deployed assemblies are identical. The electronic assemblies of the A and B equipments, i.e., DEA-A and DEA-B, have identical configurations except for certain shop-replaceable units (SRU) which are radar-related. Because the B configuration equipment is used only for the reception of the communication signals, the radar-related components are removed from the B assemblies. It should be noted that there is no work being done at Hughes on the B assemblies, and NASA is reviewing the need for the B assemblies.*

---

*At the time of this report, NASA has deleted Comm B and hence the deployed assembly B. Therefore, any discussion of the B equipments reflects REV A and not future specifications.

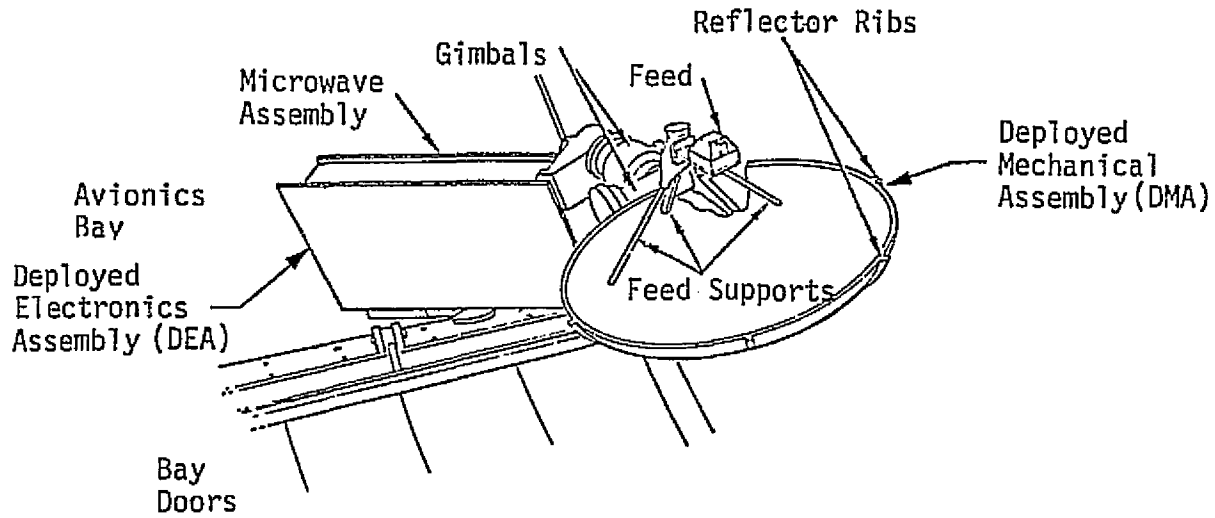

Figure 1. Deployed Assembly

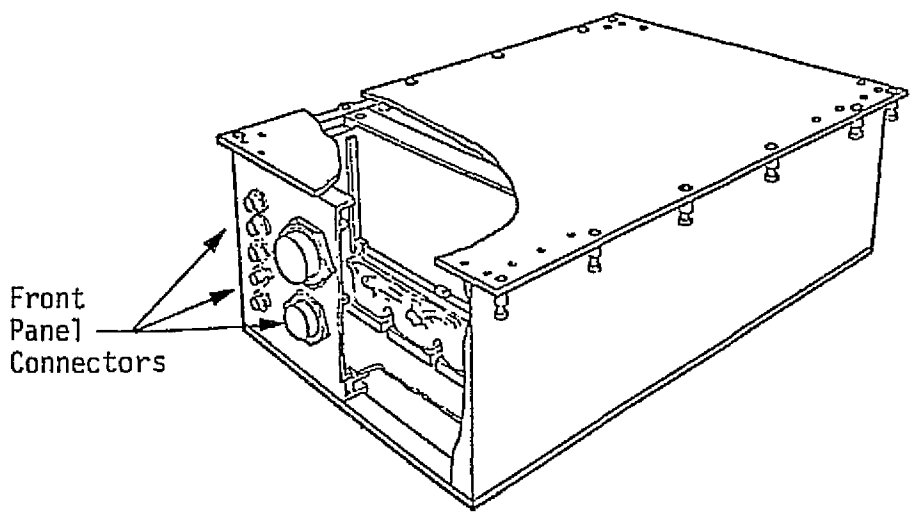

Figure 2. Avionics Bay Unit

Figure 2 shows an overall configuration of an avionics bay LRU. The three such LRUs are electronics assembly 1 (EA-1), electronics assembly 2 (EA-2), and the signal processing assembly (SPA). The EA-1 is devoted primarily to the communication function, but it also includes the servo electronics for both the communication and radar operations. The EA-2 is used exclusively for the radar function. The processing of the transmitted and received communications data is performed by the SPA. With the exception of the connector configurations, the mechanical configurations of the avionics LRUs are identical.

The detailed description of the product design for the Ku-band system subunits is presented in the sections which follow. The material included in these subsections is abstracted from the Contractor's Preliminary Design Review documents, dated March 1978.

2.0 ASSEMBLY DESCRIPTION

2.1 Deployed Assemblies

The deployed assembly (DA) comprises that portion of the Ku-band radar and communication system which attaches to the upper face of the Rockwell-supplied deployment actuator and which stows in the limited space between the payload bay and the door radiators. Major elements of the DA are the deployed electronics assembly (DEA) and the deployed mechanical assembly (DMA).

2.1.1 Deployed Electronics Assembly

The DEA is a shop-replaceable unit (SRU) of the DA line replaceable unit (LRU) of the Ku-band integrated radar and communications equipment.

2.1.1.1 Physical Description of DEA

The DEA (Figure 3) houses the electronics for the transmission and reception of radar and communications data. The electronics are housed in an enclosure 31 inches long, 15.5 inches high and 4.5 inches deep. The overall estimated weight is 70.6 pounds. The enclosure is mounted to the DMA structure by a flange that extends along the perimeter of the DEA chassis baseplate; 24 torque set screws hold the flange in place.

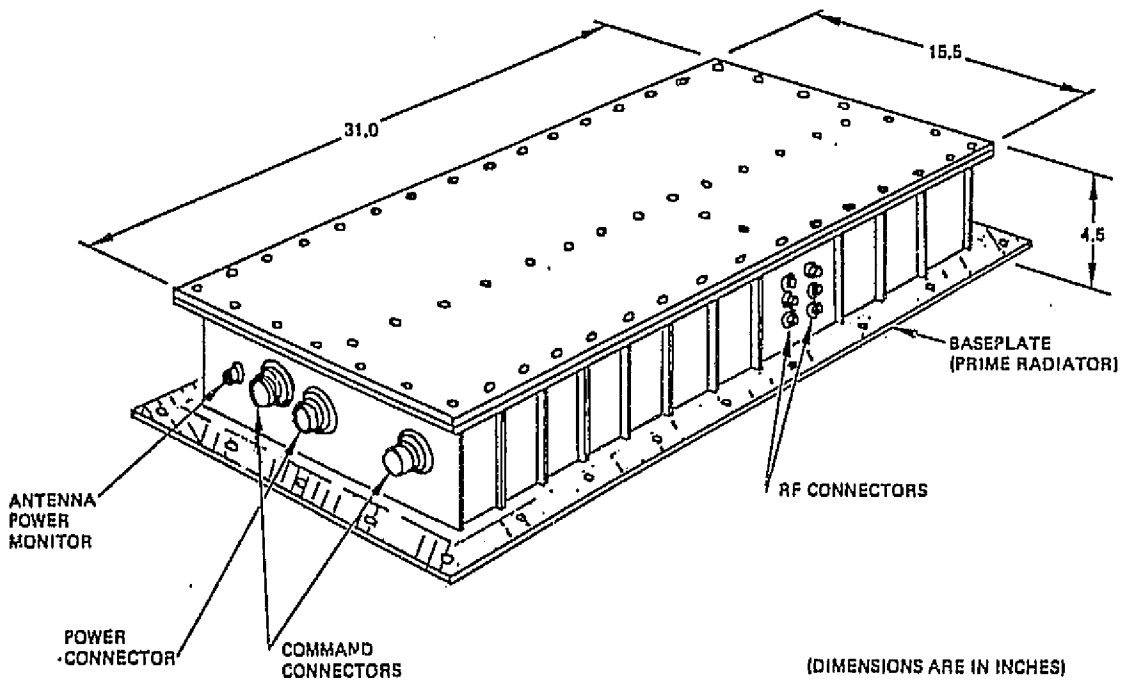

Figure 3. Deployed Electronics Assembly

2.1.1.2 Enclosure

The enclosure is a dip-brazed aluminum structure consisting of a baseplate that also serves as the prime radiating surface, ribbed side plates to which are mounted RF connectors, a front plate that serves as the mounting surface for the power and command input connectors, and a rear plate to which is mounted the waveguide output flanges and RF connectors for test access. The inside of the chassis is partitioned into cavities by a wall that extends the length of the chassis and a shorter wall that separates the receiver and exciter subassemblies. These walls provide mechanical stiffness to the structure and RF shielding between the subassemblies.

The cover for the DEA enclosure is a bonded honeycomb structure consisting of two thin aluminum face sheets, an outer and inner flange, and an aluminum honeycomb sandwich between the face sheets.

Manufacturing techniques for the DEA enclosure involve numerically controlled machining and dip-brazing procedures. The forms are

utilized in fabrication of the mounting baseplate so that SRU mounting bosses and heat flux patterns can be incorporated. Numerically controlled machining is also used in fabrication of the rib structure of the two side walls to achieve a maximum strength-to-weight ratio. The machined flange and baseplate provide the necessary jigging to position the four sides and internal partitioning for the dip-brazing process. The flange also serves as the sealing surface for the RF and environmental seal in the cover.

The enclosure walls and cover, stiffened by the ribbing and honeycomb construction, prevent excessive bending and displacement from the pressure differential resulting from the space environment.

The DEA is functionally divided into five discrete SRUs that fit into the enclosure as shown in Figure 4. The subassemblies are arranged to optimize the thermal distribution, minimize the length of critical RF interconnections, and provide access for testing and maintainability. The five SRUs are plugged in and mounted directly to the base of the chassis by means of captive hardware.

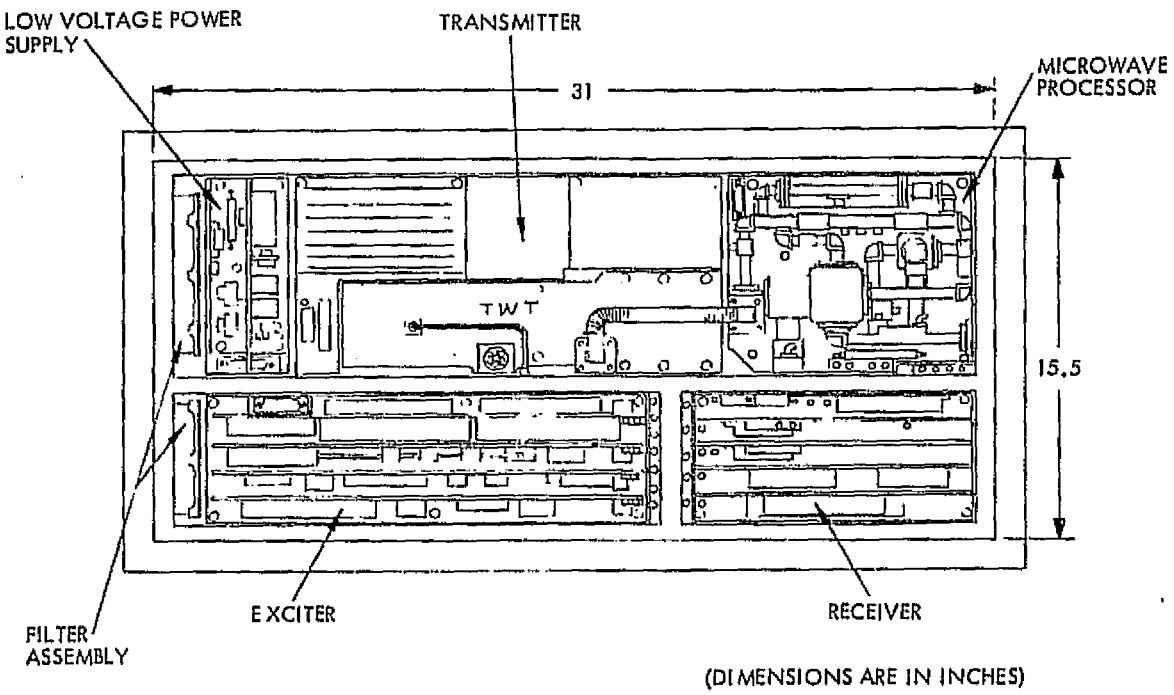

Figure 4. DEA Enclosure

The walls that partition the enclosure provide RF separation between SRUs. RF gasketing in the cover and RF shielded feed-through terminals in the walls complete the subassembly and unit level RF/EMI shielding.

Replacement of an SRU in the DEA involves removal of the cover hardware and cover. Each SRU is independently replaceable. Subassemblies are plug-in modules fastened to the chassis baseplate with captive hardware.

2.1.1.3 Thermal Design Concept

Active thermal control techniques are utilized in the DEA to provide adequate thermal control. During operation, internal dissipation is radiated to the space environment by the external surfaces. For nonoperating periods, the DEA will be augmented by thermostatically controlled heaters to maintain acceptable temperatures.

The present maximum power dissipation is approximately 250 watts at 28 VDC input. The total radiating surface of the DEA is approximately 8.5 square feet. A silvered teflon finish is used on the prime radiating surface (baseplate) to minimize solar absorptance and provide high thermal emittance. A white paint finish is used on the remainder of the external surfaces.

Hughes has extensively analyzed the thermal design of the DEA under specular radiation from the sun. It was found that, for certain Orbiter attitudes and DA positions, the solar radiation was great enough to cause the DEA to overheat. Hughes has since been directed to not consider these few Orbiter attitudes and DA positions that lead to the deleterious solar radiation in the thermal design. Therefore, Hughes is analyzing the normal operating temperatures and the qualification temperatures to determine if the thermal design is adequate. It is important for Hughes to use the right criteria for analyzing the thermal design. In previous analyses, Hughes used a junction temperature of 125°C as the upper limit allowed. However, this high a temperature during the normal thermal environment will lead to greatly decreased reliability. A normal junction temperature of 105°C would lead to a more acceptable reliability.

2.1.1.4 Environmental Sealing Techniques

The DEA enclosure incorporates an environmental seal that ensures compliance to a leakage rate of 10^{-4} cc per second when the unit is filled with inert gas at a pressure of 15.2 psia at ambient temperature.

The primary seal is made by a gasket molded into a groove around the perimeter of the cover. Hermetic connectors are sealed at the enclosure interface by O-rings. Hermetically sealed ceramic windows are utilized in the waveguide adapter for the waveguide output flanges. The adapter interface and the enclosure are sealed by means of a gasket molded into a groove around the perimeter of the adapter.

Internal module mounting is accomplished with blind hardware in the baseplate.

2.1.1.5 DEA-B Configuration

The DEA-A and DEA-B configurations are identical except for the Exciter, Receiver, and Transmitter Microwave SRUs. In the B configuration, the radar-related components are deleted from these subassemblies.

Physically, the subassemblies retain the same interconnections and mounting interface dimensions so that identical chassis and related hardware can be utilized.

Externally, the DEA is symmetrical with the exception of LRU electrical connectors. Mounting of the DEA-B to the DA boom is accomplished by rotating the unit approximately 180 degrees about its Y axis so that the RF output waveguide flanges remain oriented toward the antenna. The difference in the DEA-A and DEA-B installation is a minor shift in LRU connector locations.

2.1.2 Deployed Mechanical Assembly

The DMA descriptions are separated into discussions of antenna, rotary joints, structure, and gimbals.

2.1.2.1 Antenna

2.1.2.1.1 Narrowbeam Antenna

The narrowbeam antenna assembly is a prime fed paraboloidal reflector using a five-element monopulse feed. The 36-inch parabolic

antenna is constructed of epoxy-impregnated graphite cloth formed over four main supporting ribs. A ring stiffener is used at the aperture plane. The epoxy-graphite construction provides a lightweight structure. The antenna shell and feed tube weight is 3.7 pounds. The monopod feed support edge mounting prevents the feed from mechanically loading the reflector surface by attaching to the same edge support structure used for the parabolic surface. The overall depth of the antenna assembly is less than 12.5 inches, allowing the required envelope clearance on each side of the antenna during stowage. Figure 5 illustrates the antenna structure.

2.1.2.1.2 Monopulse Feed

The radiating feed elements are printed circuit dipoles. Thin copper clad stripline material is etched to form the dipole on one side of the dielectric and the balun circuit on the other side.

The monopulse elements and sum feed are shown in Figure 6. The four monopulse elements are single dipoles giving fixed linear polarization. They are located approximately a quarter of a wavelength above a ground plane formed by the aluminum housing for the monopulse circuitry. The sum element is a crossed probe fed horn. This quadridged, circular waveguide radiator has a 0.5 inch diameter aperture and fits into the opening between the tracking channel dipoles and is flush with the ground plane.

2.1.2.2 Rotary Joints

Two channels of RF energy traverse the dual-axis gimbals. The sum channel remains isolated from the difference channel in a dual-channel rotary joint, which consists of two rotary joint subassemblies, one for each axis. These subassemblies are available as reliable off-the-shelf components. Only minor modifications in the internal bearings are required to satisfy the Shuttle temperature and vacuum requirements.

All rotary joint interconnections are interior to the gimbal assembly housing to minimize length and provide environmental protection. All exposed surfaces are gold plated and the interior of the gimbal is vented through desiccant filled filter cartridges. Dry sealed, lead coated steel bearings with lead-tin-bronze retainers are used. Pressure release vents are provided on both sides of the bearings to minimize

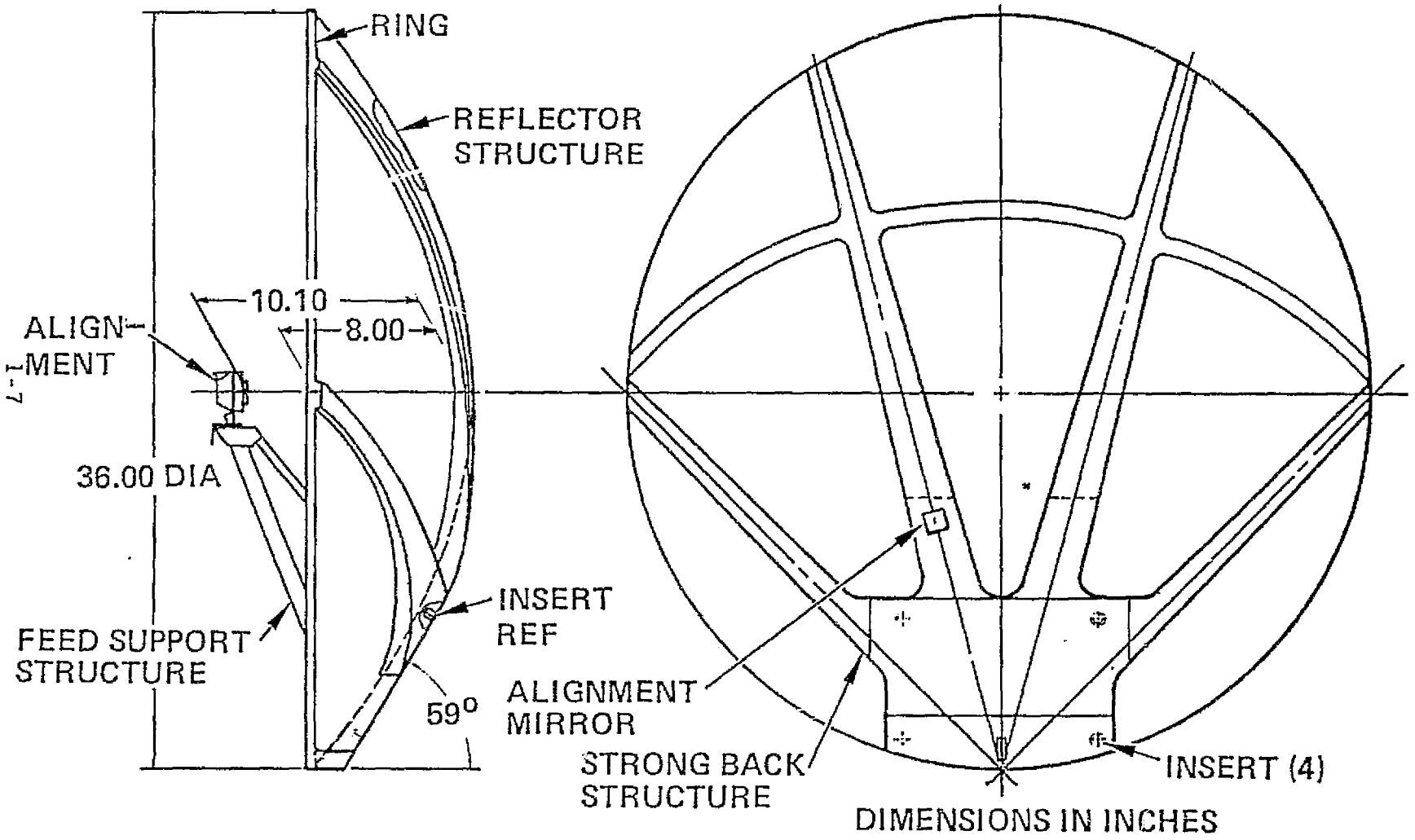

Figure 5. Antenna Structure

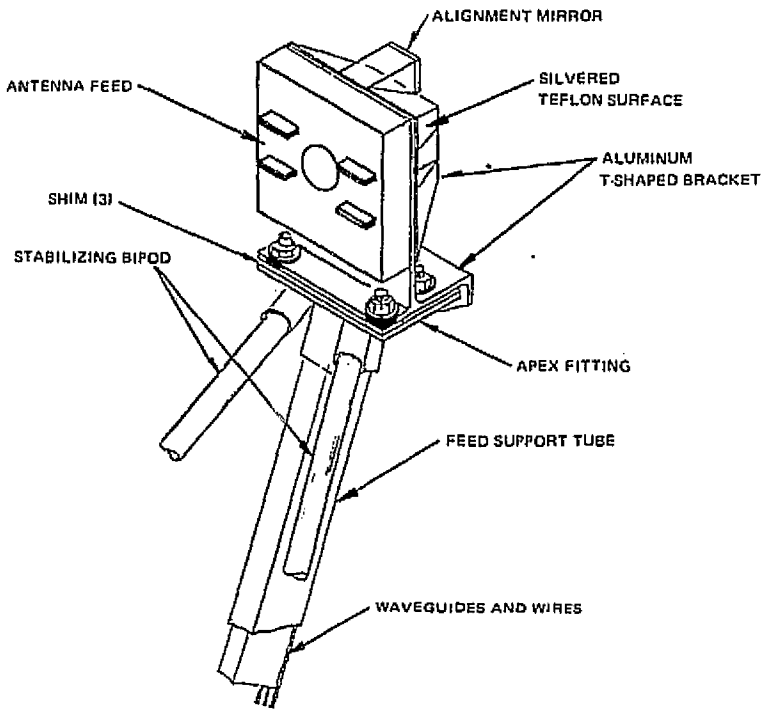

Figure 6. Antenna Feed

air in-rush across bearings during reentry pressure equalization. Waveguide windows at input and output prevent circulation of dust beyond the unsealed area.

2.1.2.3 Structure

The Deployed Assembly structure consists of three basic elements: the base pedestal that bolts to the Shuttle deployment mechanism and contains the electrical connector interface; a structural frame into which the DEA is secured; and a gimbal mounting bracket. These three elements of the structure are electron beam welded together to form a single unitized assembly.

The U channel of the frame provides the DA cable harness wire paths, the gimbal connector bulkhead, and supports the thermal shields located around the periphery. Attachment of the DEA within this frame is by 24 bolts passing through both the DEA radiator plate and the frame lip, and held by self-locking nuts in 19 places. The remaining five DEA-to-frame fasteners are blocked by the base pedestal or the gimbal mount and threaded into blind hole installed locking inserts.

All exterior surfaces of the structure assembly are covered with 0.005" silvered teflon thermal finish material. All lightening holes in the base pedestal are closed with a film of this material to prevent the entrance of solar energy (direct or reflected) into the interior cavities.

In addition, the exposed portions of the gimbal and antenna support arm are painted with a white silicon thermal control paint.

Active thermal control is utilized for cold conditions. Sensitive items on the gimbal that need to be kept above the -65°F survival level are the encoders, the rotary joints, and the waveguide switch. Heaters and thermal blankets are located to protect these items.

2.1.2.4 Gimbals

The DA gimbal assembly consists of the two-axis, servo-controlled rotating mechanical and electrical interface between the deployed boom structure and the antenna. Included are torquers, bearings, shaft encoders, waveguides, coaxial cables, and other cabling. A locking device secures the assembly in the stowed position. Minimum gimbal cost, weight, and trunnion obscuration are achieved with the edge-mounted antenna configuration.

The off-center gimbal configuration allows a maximum size (36" diameter) narrowbeam antenna. Disturbance torques due to Shuttle accelerations are negligible; therefore, a centered load is not an operational constraint.

Cabling used to pass through the gimbal is a printed circuit flat ribbon carrying 55 conductors (20 shielded groupings), and two RG 178 coax leads. The cable terminates at a terminal board on the gimbal output where the hook-up is made for distribution to the various locations on the gimballed load.

2.2 Avionics Bay Assemblies

2.2.1 General Product Design

2.2.1.1 Chassis

Although the EA-1, EA-2, and SPA chassis are different parts (different connector patterns and different SRU/wire wrap plate mounting patterns), the general design is the same for the three units. The

chassis is a dip-brazed aluminum structure (see Figure 7). There is a solid frame around each of the two access openings (SRU and wire wrap plate access), two solid end panels, and side walls consisting of two 0.040 aluminum sheets brazed to a corrugated sheet of 0.010 thick aluminum (6061-T6 alloy).

Provisions have been included in the design to avoid trapping brazing salts in the hollow side walls. Also, none of the machining operations cut into a brazed joint, so that brazing salts entrapped in the joint are not exposed to a corrosive environment.

A machined datum A is shown upon which the interconnection plate ultimately will be fastened. Both the upper and lower surfaces are machined from the A datum with a surface roughness compatible for the environmental seal integral with the two covers. Two holes that accept nonconductive registration pins are drilled in the A datum plane. These two holes constitute a datum point and line for all subsequent holes numerically machined for bushings or connectors in the chassis structure.

After machining, the chassis is chromate coated per MIL-C-5541, CL 1A, and the exterior surfaces are primed and painted. The structure is also sealed per MIL-STD-276, Method B, to ensure against gas leaks at any of the brazed interfaces.

The two nonconductive pins also align the SRU guide structures during the bonding operation, as well as the interconnection plate when installed. This control ensures precise alignment within allowable tolerance buildups. A fixture is used during the bonding operation to ensure accurate alignment with respect to the tooling pins for the wire wrap SRU interconnection plate.

All fastener holes for the enclosure covers are either outside the walls or terminated as blind holes. Self-locking inserts of the Rockwell International MD115-2002 series are used throughout. The only holes that penetrate the cavity walls are for hermetically sealed front panel connectors.

2.2.1.2 Wire Wrap Assembly

The wire wrap SRU interconnection plate is machined from 6061-T6 aluminum alloy. The plate is 0.080 inch thick with 0.30 inch high stiffening ribs between SRU connectors. This design will adequately limit

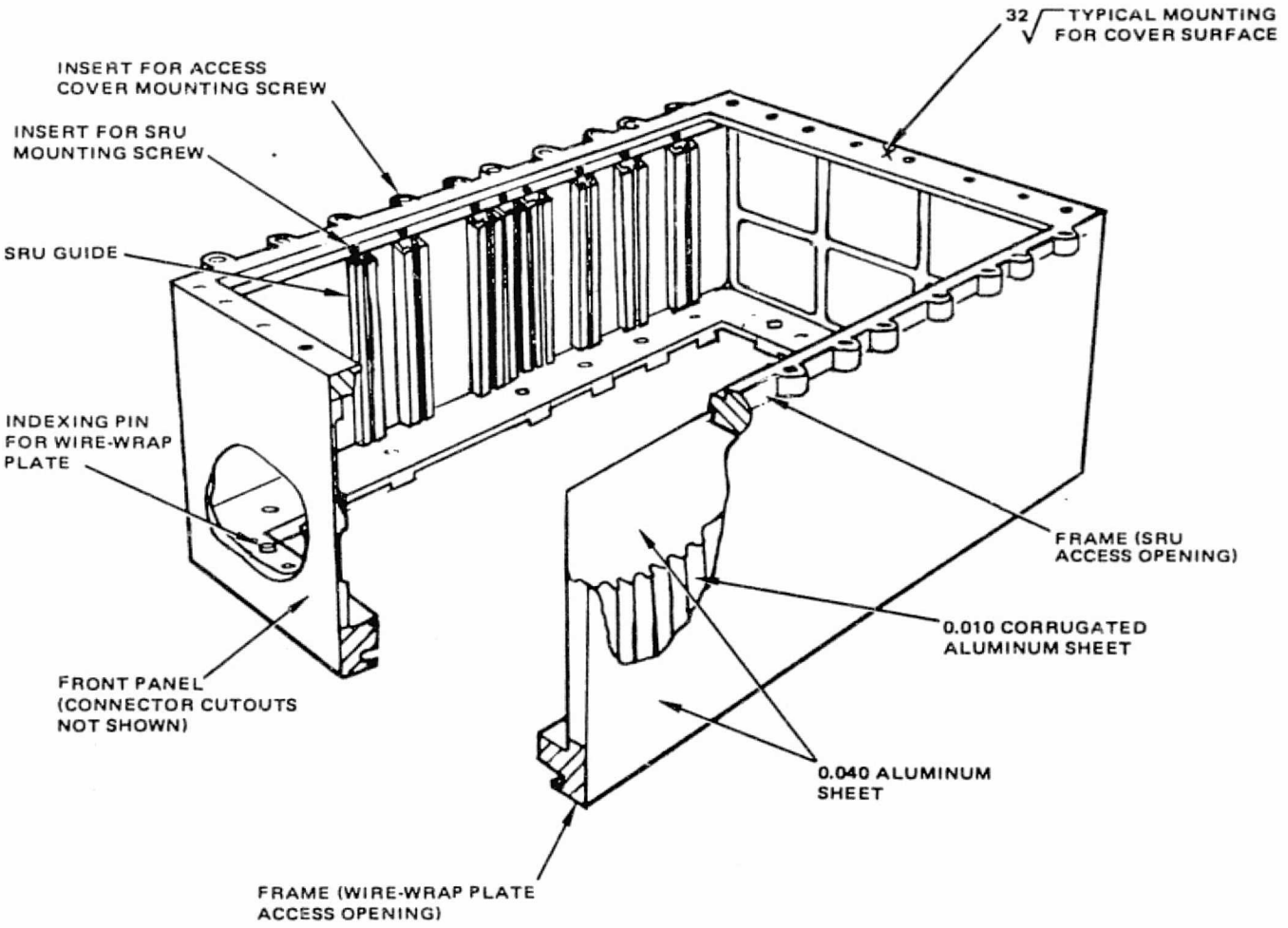

Figure 7. EA-1, EA-2, SPA Chassis

deflection of the plate when the SRU connectors are engaged with or withdrawn from the receptacles. (SRU contacts are a flat blade design, and the receptacles are a tuning fork design with a 0.025 square tail).

The wire wrap plate is electrically tied to the chassis, and separate bus strips are provided for +5 volts and digital return (D-RTN) signals. Each bus strip is an aluminum strip with a cross-sectional size of approximately 0.060 × 0.40 inches. The bus strips are bonded to the plate with epoxy-glass prepreg material. Electrical connection between each designated contact and the appropriate bus strip is made by installing a beryllium copper bushing over the 0.025 square contact tail and pressing this bushing into a hole in the bus strip (see Figure 8).

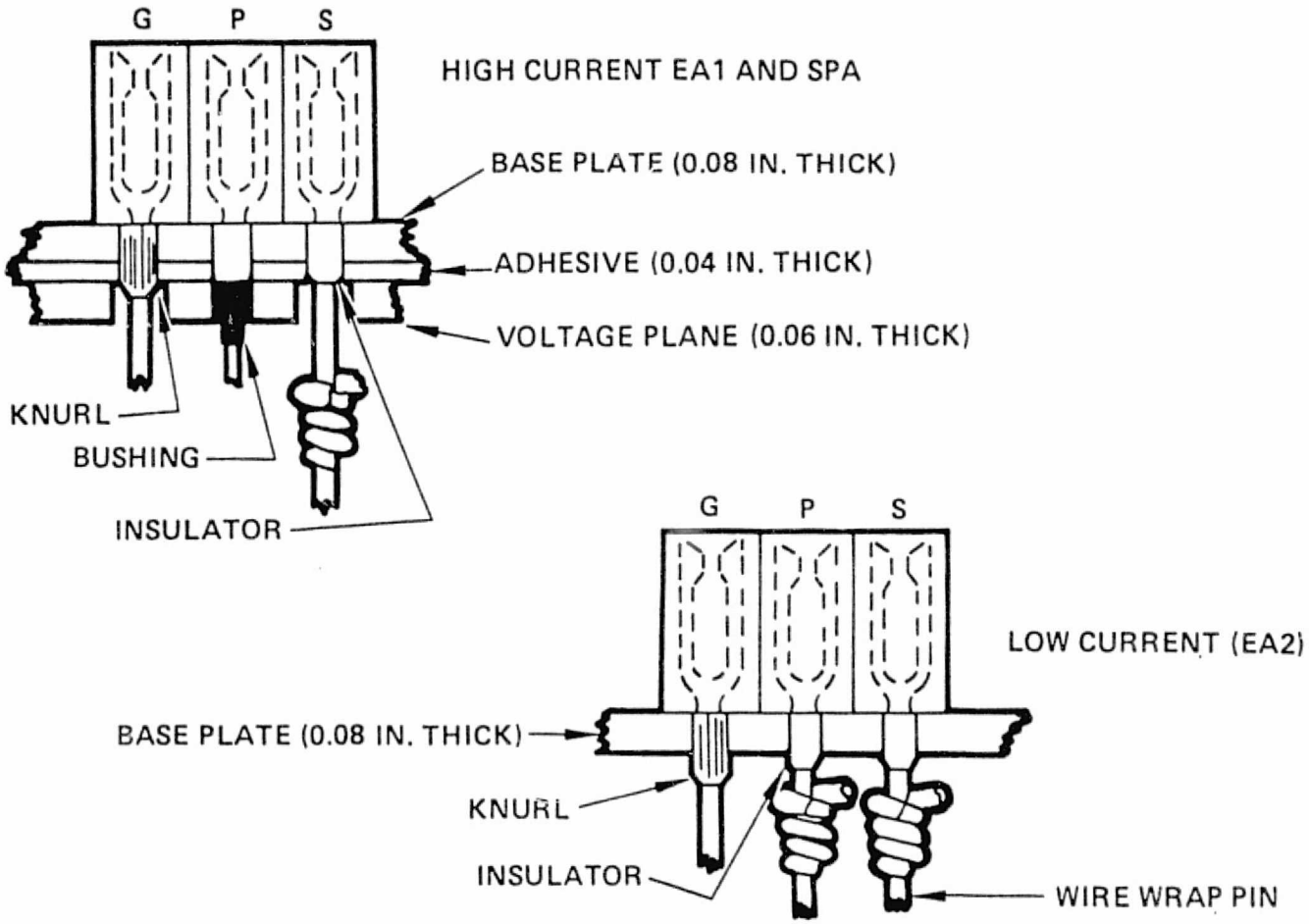

Figure 8. Wire Wrap Plate Connector Details

Finish on the plate and both bus strips is a Type II anodic coating per MIL-A-8625, except for the holes and selected areas on the plate which have a Class 1A chromate coating per MIL-C-5541. The anodic coating is applied before bonding, and the chromate coating is applied after bonding and drilling.

A separate harness is used for connections between the front panel connectors and the wire wrap plate. There are three M55302/66-50S connectors and three M55302/66-60S connectors on the harness for mating to receptacles (commercially identified as the Airborne WTAV**PW40JL series) on the wire wrap plate. The receptacle reference designators are marked on the plate, and the harness will be formed and tied so as to prevent incorrect engagement of the harness connectors.

The 28-volt input power, motor driver output power, and signals on coaxial cables are routed directly on separate harnesses without going through the wire wrap interconnect wiring. These signals each have special characteristics (high current, high frequency, and/or EMI source/susceptibility) which can be handled best in this manner.

Cutouts in the plate provide for a clearance hookup of all SMA coaxial connectors. The coaxial connectors extend from the SRU core through the interconnection plate to facilitate making this connection using conventional tools (open-end wrench).

All wire wrap conductors are dressed and tied to the plate to prevent cold flow or abrasion shorting over extended periods of time.

After the plate is wired and electrical integrity is verified, the wire wrap pins and exposed conducting surfaces are conformal coated to eliminate shorting in a zero gravity environment by a foreign object. Rework procedures will allow modification to the conformally coated pins if such modification is required during the life of the LRU.

2.2.1.3 SRU

The typical SRU (see Figures 9 and 10) consists of an aluminum core with a printed wiring board (PWB) bonded to each side and a connector fastened to one edge. The core is a T-shaped part with two captive mounting screws (commercially identified as Deutsch HJCT-7800-8-B-2.5) and provisions for supporting the SRU connector. The two mounting screws provide force for engagement and disengagement of the SRU

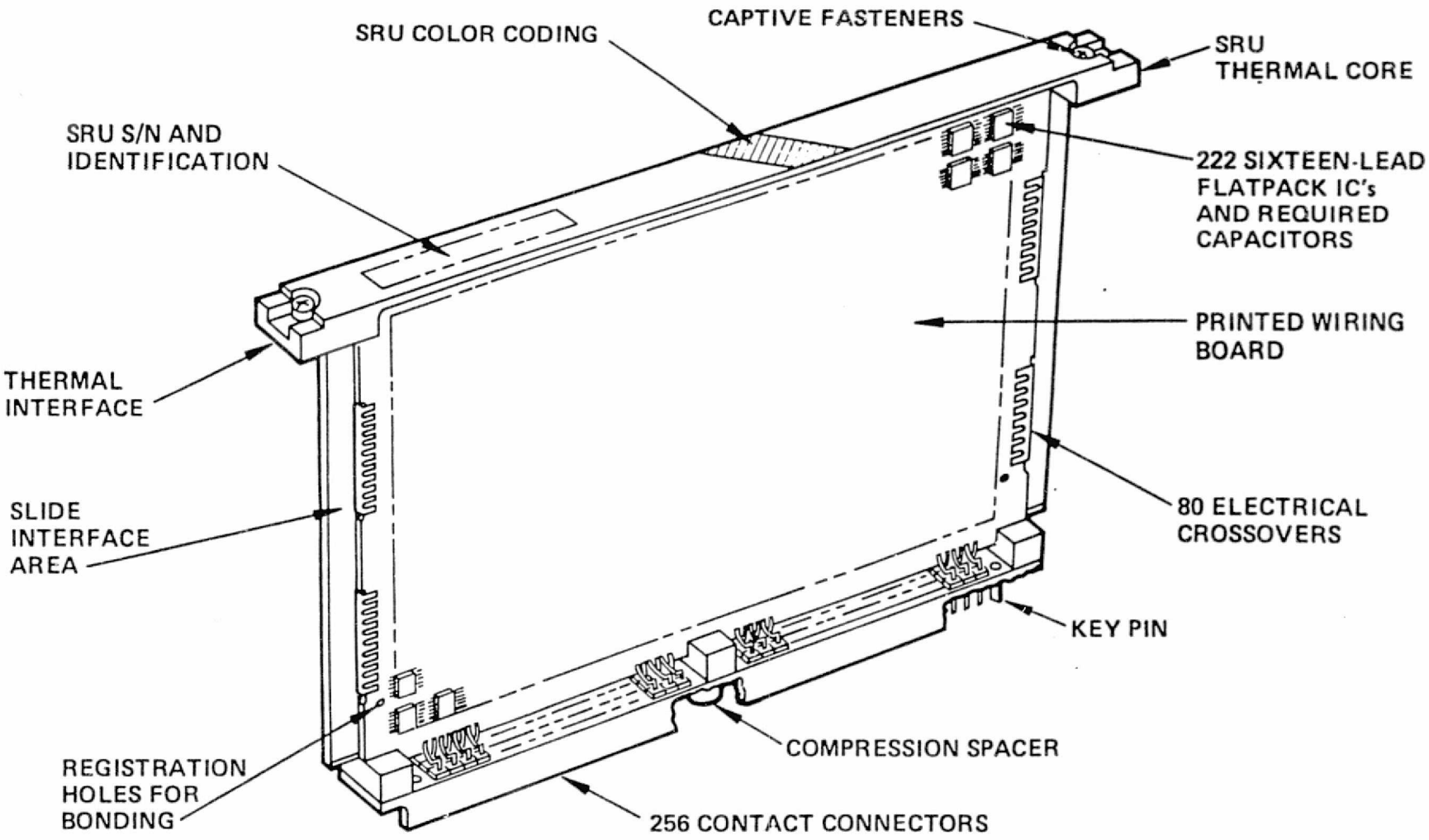

Figure 9. Typical SRU Digital Assembly

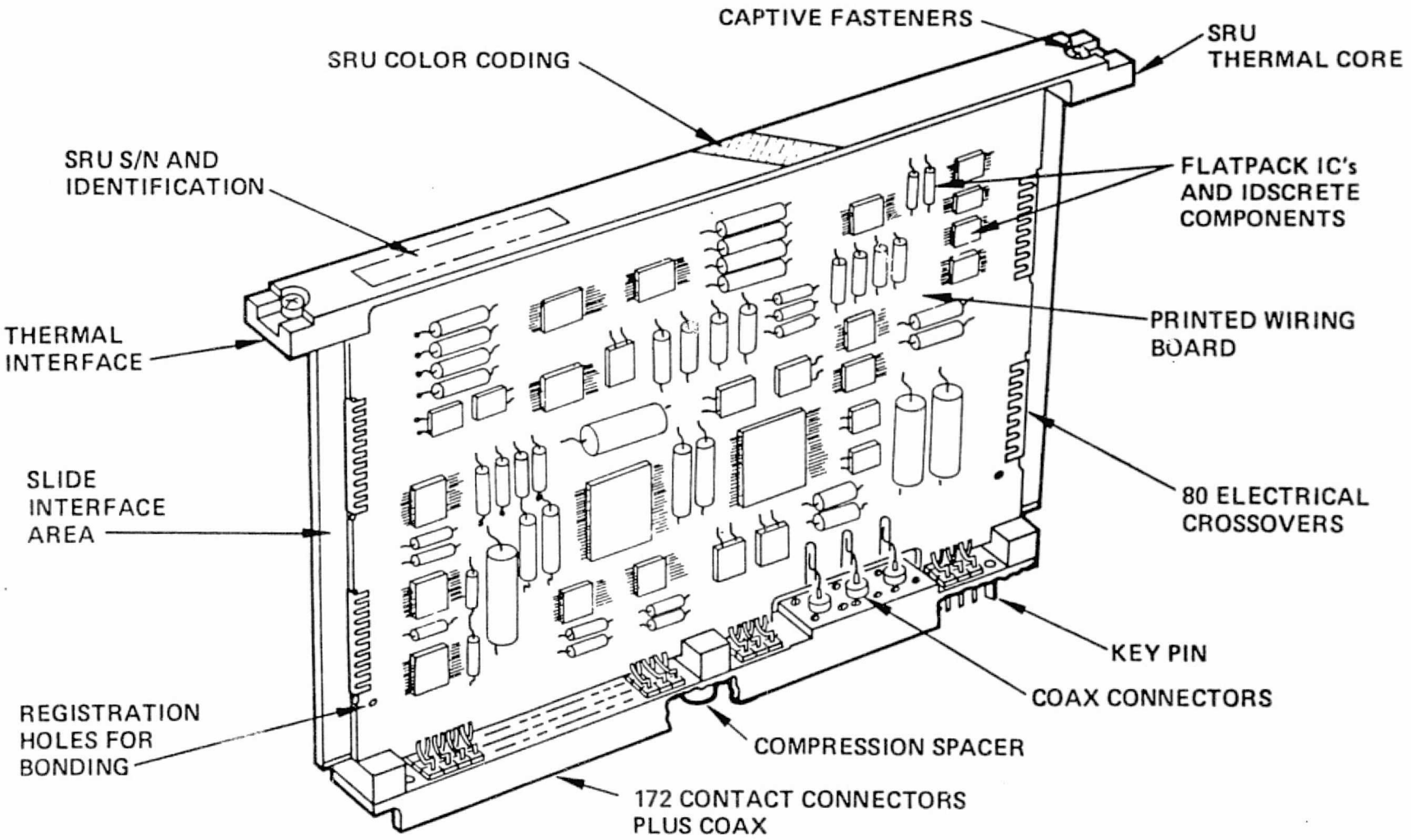

Figure 10. Typical SRU Analog Assembly

connector and for ensuring a good interface for heat transfer. Since the aluminum core is the primary thermal path for cooling the components, core thickness is dictated by the SRU power dissipation.

Each PWB is a 5.3 × 8.4 inch multilayer board (4, 6, or 8 layers) with an overall thickness of approximately 0.60 inches. The boards are made from polymide-glass laminate material, and the exposed wiring lines are solder plated (solder subsequently is fused). The boards are designed for surface mounting of all components, and the plated through holes (PTH) are not filled.

The PWBs are simultaneously bonded onto the core, in front-to-back registration under heat and pressure, maintaining electrical isolation from the metal core but retaining thermal conduction, with a polysulfide adhesive-impregnated material (Hughes Aircraft Company, HMS 16-1965, Class 1). This material provides the bonding agent and also an insulator between wiring lines and the SRU core. Other considerations are relatively low cure temperatures (200°F or less) and low bonding pressure (not more than 15 psi). These factors make it practical, if necessary, to remove and replace one PWB on a completed SRU without damage to the assembly or the components on the opposite PWB.

The SRU connector is fastened to the core with three screws. Tails from the connector blade contacts are preformed to fit against pads on the PWBs, and these contact tails are then reflow soldered onto the PWB pads.

Each SRU connector has two keying pins which establish a go/no-go engagement of the connector contacts. In addition to this mechanical keying system, there is a color stripe painted on the top of each SRU core in a manner such as to make a single diagonal line in the LRU. Also, the SRU reference designator is marked on the SRU core and on the wire wrap interconnection plate.

Electronic components are attached to the PWBs by reflow soldering preformed component leads to PWB pads. Flatpacks and other flat-bodied components are bonded to the PWB with the polysulfide adhesive-impregnated material. Larger round-bodied components and can-type devices are bonded to the PWB with an alumina-filled polysulfide paste (Hughes Aircraft Company, HP16-103, Type II). After SRU test, the PWBs and components are conformally coated with a polyurethane coating material.

2.2.1.4 Low Voltage Power Supply

The EA-1, EA-2 and SPA low voltage power supplies are basically the same physical design for all three units. The power supply module (see Figure 11) is approximately 9.7 × 5.8 × 1.95 inches in size and weighs about 3.0 pounds. Other physical design features include (1) machined aluminum chassis for structural support and minimum thermal impedance, (2) single unit connector, and (3) captive fasteners for added maintainability.

An extensive effort was made to achieve commonality within the three modules to both reduce design cost and the number of spare parts required during the field support period. Over 98% of the parts are common to all three designs. The linear regulator/logic printed circuit board is identical in all three designs. The major differences in the three designs is the converter transformer secondary output voltage forms which are designed to meet the requirements of each LRU.

Internal to each module are heavy magnetics, rectifying diodes, and power transistors. Certain portions of the circuit are packaged using printed circuit board (PCB) techniques, while the heavy components and most of the high thermal dissipating devices are mounted directly to the aluminum chassis. Those circuits which are mounted directly to the chassis are the line filter, pass stage and driver transistor for the linear regulator, the converter transformer and switching transistors, and the inductors used for the filtering of the converter transformer outputs.

Four PCBs are also used in each unit. These boards are the interconnect board, linear regulator/logic, rectifier and resistor/capacitor. The interconnect PCB is the hub of the design because it serves to distribute voltage forms to various physical locations throughout the unit, including the inputs and outputs through the connector to which it is reflow soldered. The rectifier PCB contains the rectifiers for the output voltages of the converter transformer, while the resistor/capacitor PCB contains the capacitors for the same output voltages. Also included on the resistor/capacitor PCB are bleeder and test access resistors.

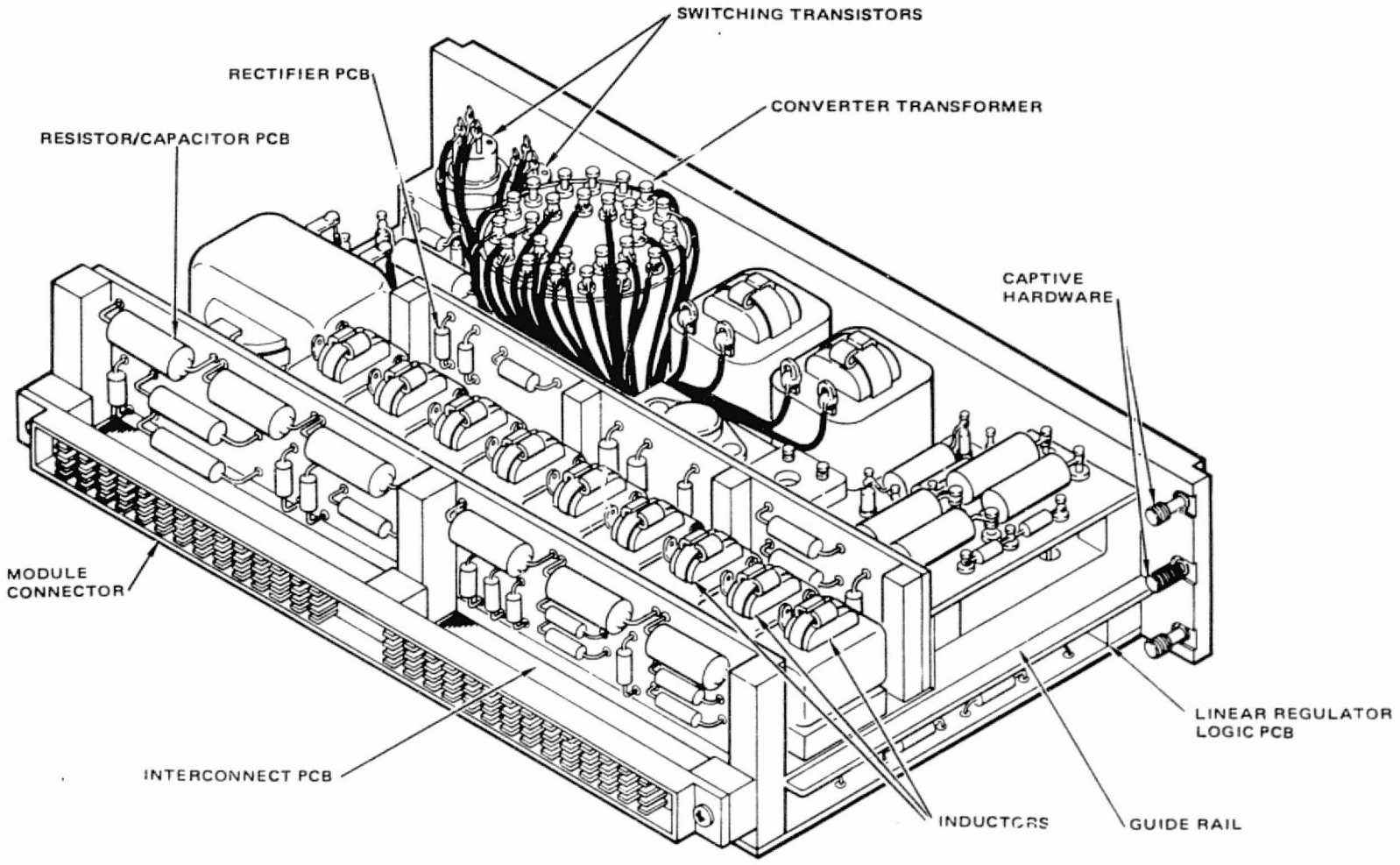

Figure 11. Layout of Low Voltage Power Supply for EA-1, EA-2, and SPA

2.2.1.5 SRU, Chassis, and Wire Wrap Plate Interface

Figure 12 shows details of the interfaces between the SRUs, chassis and wire wrap plate. Two edges of the SRU are held in the chassis guides which locate the SRU relative to the wire wrap plate. Details of the guides are shown in the inset section A-A. The guides consist of aluminum extrusions containing a low coefficient of friction sliding interface and a resilient backup material to accommodate adjustments in tolerance buildups. As mentioned earlier, the precise location of the bonded extrusions is fixtured from the two index holes in the A datum plane.

Details of the SRU edge connector mating with the wire wrap plate mounted connector are shown in the other inset of Figure 12. The force for engagement and disengagement of the connector is developed with No. 8 jacking screws on the SRU. The jacking screws engage captive inserts in the LRU chassis edge. They also insure good thermal contact from the SRU to the chassis.

The wire wrap pins are recessed below the chassis flange to prevent damage to the pins during bench handling.

2.2.1.6 Environmental Sealing

As described in the chassis section of the general product design previously, the chassis is sealed at the brazed structure and all fastener holes are outside the walls or are blind holes. O-ring seals are used at the front panel connector openings. The covers have seals molded into channels milled around the two cover perimeters.

The LRU is filled with a gas mixture of 99% nitrogen and 1% helium. Internal pressure is 15.2 ± 0.3 psia. Sealing has been designed to achieve a leak rate of less than 1×10^{-4} cc/sec of nitrogen in the pressure environment. The avionics equipment bay pressure environment specified while operating is 12.36 psia continuous, 8.0 psia for less than 165 minutes, and 18.0 psia maximum. For nonoperating conditions of transport (at 36,000 feet altitude), it is 3.28 psia and 35.8 psia during Orbiter cabin leak test.

2.2.1.7 Thermal Analysis

Heat generated in the EA-1, EA-2 and SPA LRUs is dissipated to the Shuttle cold plate. The path the heat energy takes to this sink

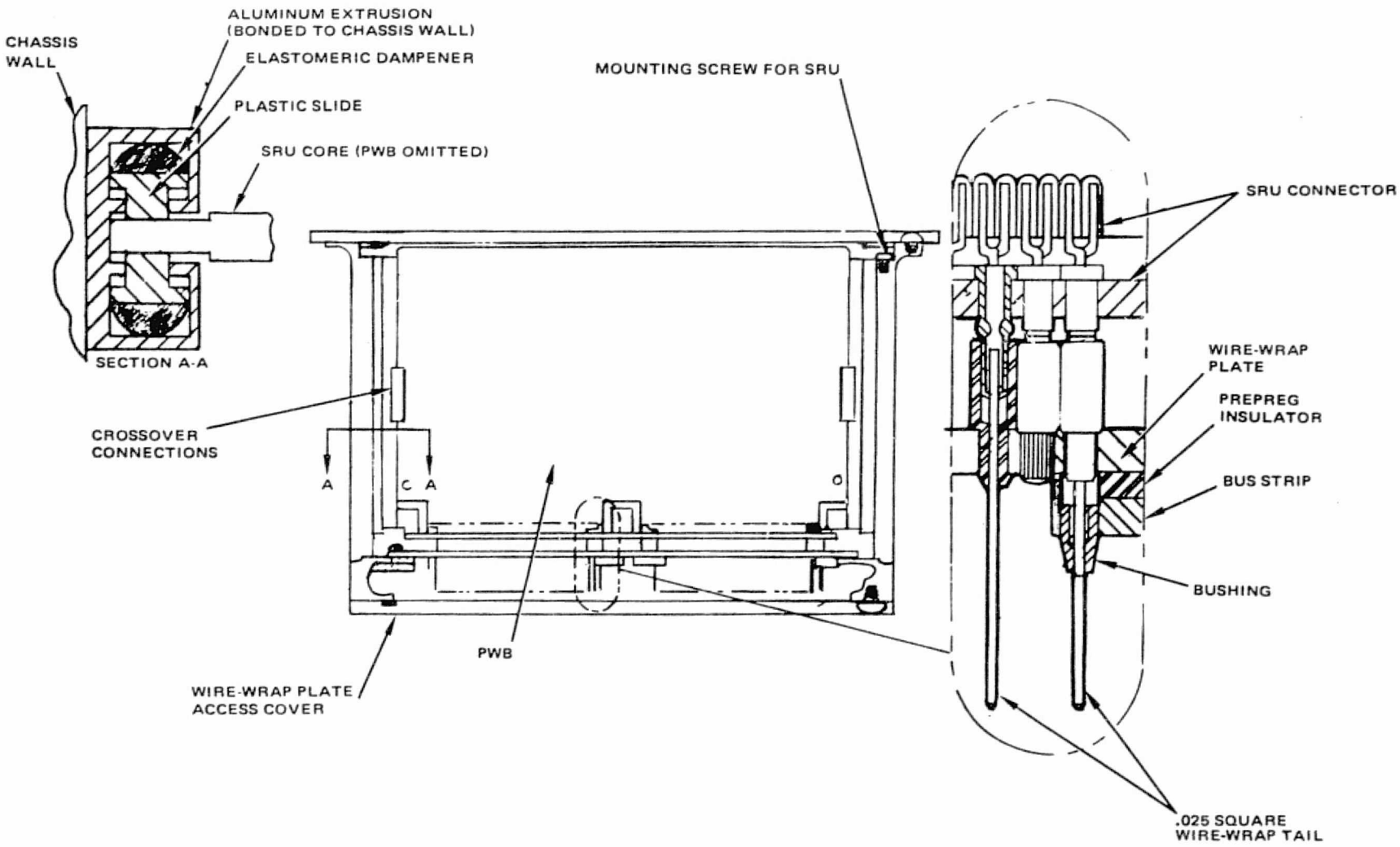

Figure 12. SRU Chassis Wire Wrap Plate Interface

was analyzed to determine the resultant temperature. A model analysis modeling the thermal resistances is illustrated in Figure 13. Heat is conducted from the SRU core to the thermal interface at the jacking screws of the SRU. From there, it goes into the chassis side walls to the LRU cover through a dry cover to chassis interface. Thence, the heat spreads laterally through the LRU cover while being simultaneously shunted to the Shuttle cold plate, also a dry interface. Both of these dry interfaces are influenced by the number of fasteners available to help conduct the heat.

Specifications for the Shuttle cold plate in the avionics bay while operating are 35°F to 120°F. A summary of the expected temperature rise given to thermal conductances of about an order of magnitude range and operating voltages of 28 and 32 volts is given in Table 1 for the EA-2 SRUs.

2.2.2 EA-1 LRU

An EA-1 LRU side view showing the 10 SRU modules in place is given in Figure 14. Mechanical details of component heights, connectors and module enclosures are shown.

2.2.3 EA-2 LRU

The EA-2 LRU is similar to that of EA-1 with 9 SRUs. No similar mechanical drawing was available for detail.

2.2.4 SPA LRU

The SPA LRU side view is shown in Figure 15. Nine SRUs and other mechanical details are shown.

3.0 SUMMARY

The above sections are a condensation of reports and engineering data which describe the product design of the deployed and avionics bay assemblies. Five basic units covered are the DEA, DMA, EA-1, EA-2, and SPA. Consideration is given to the mechanical design, produceability, thermal design, and environmental sealing.

Many of the product design features are used in common and thus are described in general sections rather than duplicated in describing each subunit.

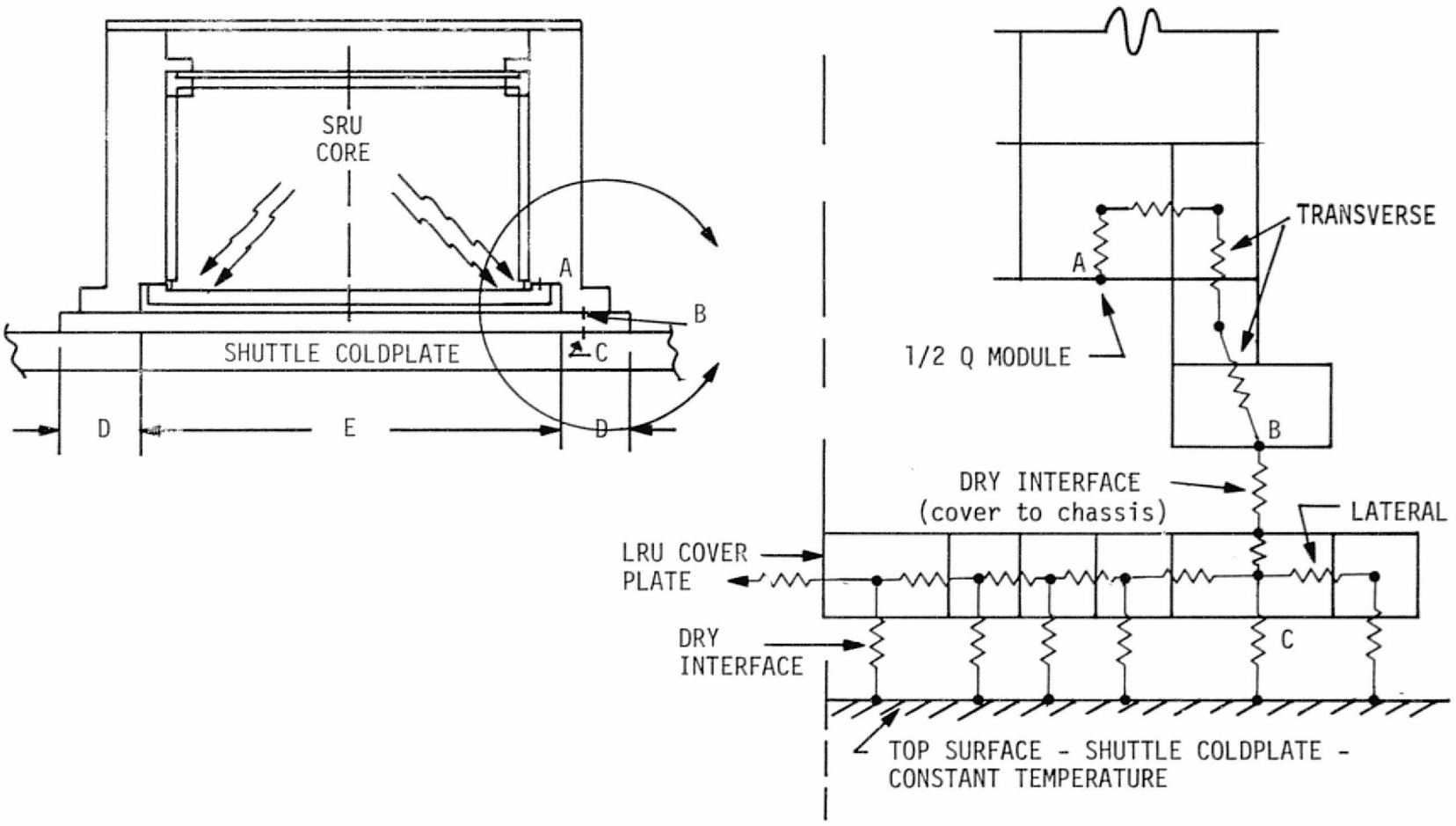

Figure 13. Analytical Model of SRU to Coldplate Thermal Path

Table 1. Summary of EA-2 SRU Temperature Rises

Module Designation	Module Name	Assembly Number	Power Dissipation (watts)		Chassis/Module Interface ΔT Above Cold Plate			
					$h = 0.549$ W/in^2 °C		$h = 5.1$ W/in^2 °C	
			28V	32V	28V	32V	28V	32V
A 1	Analog Processor	3555610	8.0	8.0	4	4	1	1
A 3	Preprocessor Control	3555620	7.0	7.0	9	9	4	4
A 4	Digital Timing	3555630	5.0	5.0	10	10	5	5
A 5	Filter Processor	3555640	2.0	2.0	10	10	4	4
A 6	Mag. PDI/Log Control	3555650	1.0	1.0	10	10	4	4
A 7	Detect. Disc. & AGC	3555660	2.0	2.0	10	11	4	4
A 8	Range & Velocity	3555670	1.0	1.0	10	11	4	4
A 9	Angle & Serial Data	3555680	2.0	2.0	11	12	4	4
A13	Low Voltage Power Supply	3555690	38.05	44.35	27	31	13	15
	TOTAL POWER		66.05	72.35				

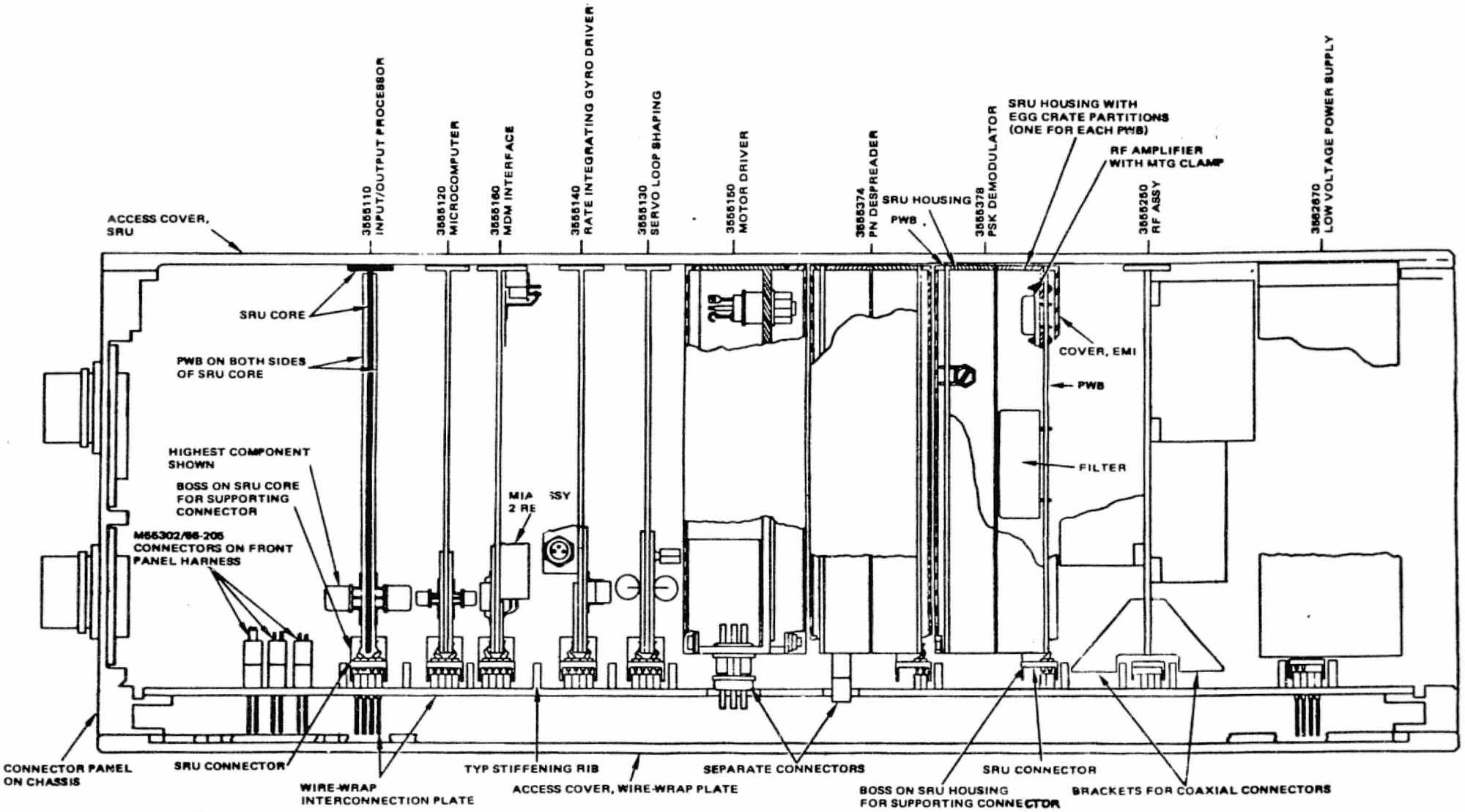

Figure 14. Side of EA-1 Line Replaceable Unit

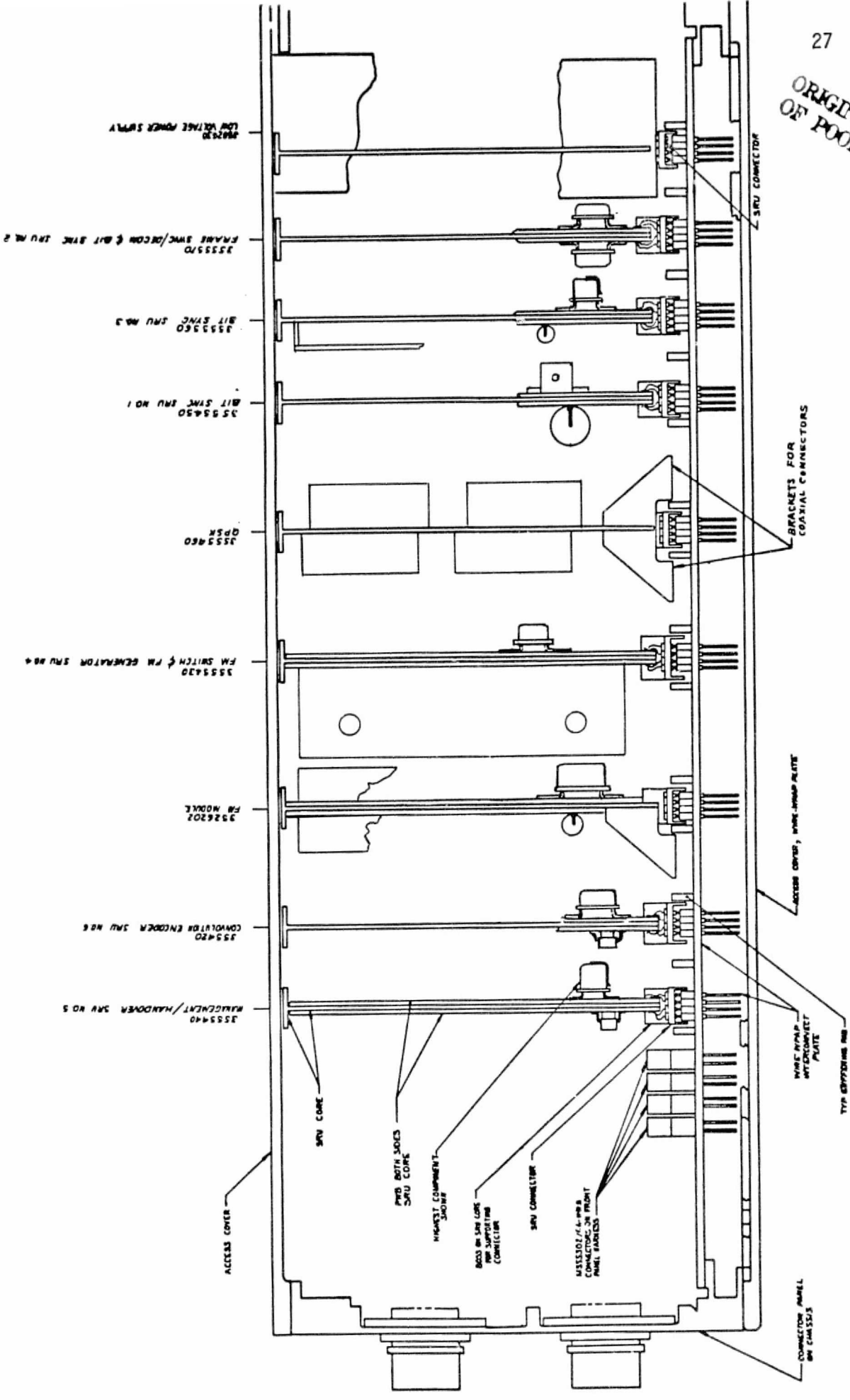

Figure 15. Side of SPA LRU